HUMAN RETINAL OXIMETRY USING SPECTRAL IMAGING

David J. Mordant

Institute of Ophthalmology

University College London

London

Submitted for the degree of Doctor of Medicine

November 2010

SIGNED DECLARATION

I David Mordant, confirm that the work presented in this thesis is my own unless stated otherwise. Where information has originated from other sources, I confirm that this has been indicated in the thesis.

Signature: *David Mordant*

The research presented in this thesis was carried in collaboration with Professor Andy Harvey's team at the School of Engineering and Physical Sciences, Heriot Watt University, Edinburgh. Their invaluable scientific contributions were central to the execution of the work presented in this thesis. The following list delineates the work that was carried out by me and Heriot Watt University. All statistical data analysis presented in this thesis was performed by myself.

Chapter 2: Heriot Watt University made important hardware and software modifications to the fundus camera which enabled the acquisition of retinal images using various wavelengths. The majority of the experiments that was performed to characterize the wavelengths of light emitted from the modified fundus camera was carried out by myself with some help of the team at Heriot Watt University. The software, programmed in *Mathematica*, used to study the wavelengths emitted from the modified fundus camera was jointly created by me and the team at Heriot Watt University.

Chapter 3: The outer casing of the model eye was created by Heriot Watt University. The inner components of the model eye, the mounting for the quartz tubes and *Spectralon* were assembled by me. The majority of the model eye experiments were performed by me, with some help from the team at Heriot Watt University and Ahmed Sallam. The algorithms, programmed in *Mathematica*, used to process the model eye images and calculate the oxygen saturation of the blood in the quartz tubes were created by Heriot Watt University. Modifications to the algorithms were performed by me. The software programmed in *Mathematica* that was used to collect the data necessary to perform the statistical analysis was created by me with the help of Heriot Watt University.

Chapter 4, Chapter 5 and Chapter 6: The algorithms, programmed in *Mathematica*, used to process the retinal images and calculate the oxygen saturation of the blood in the retinal vasculature were created by Heriot Watt University. All spectral imaging of the retina, image processing and image analysis were performed by myself. A separate *Mathematica* program was created by me with the help of Heriot Watt University to study the optical density profiles of selected retinal vessels. Analysis of the accuracy of the wavelength ranges on retinal oximetry was performed by myself and resulted in the modification to the oximetry algorithm. A *Mathematica* software was programmed by myself with the help of Heriot Watt University to extract oxygen saturation values at points along the retinal vasculature.

Signature:

David Mordant

ABSTRACT

The principal aim of the research described in this thesis was to develop a technique of non-invasively measuring the oxygen saturation within the retinal vasculature of human subjects (retinal oximetry). The evaluation of a hyperspectral fundus camera used to acquire retinal images in different wavelengths of visible light, and the image analysis techniques used to perform retinal oximetry are described.

Validation of the oximetry techniques was performed using an artificial eye containing human blood of known oxygen saturation: the calculated oxygen saturation was compared to the gold standard measurement. The mean differences between the calculated and measured oxygen saturations were small.

Hyperspectral imaging/oximetry of normal subjects was performed to characterize the oximetric features of the retinal vasculature. The mean oxygen saturation (± SD) of the temporal retinal arterioles and venules were 110.8% (± 11.8%) and 27.7% (± 3.2%) respectively.

The application of the retinal oximetry technique was explored in patients with retinal arterial and venous occlusion to determine whether oximetric changes in the retinal vasculature could be detected. Variation in measured oxygen saturation of the retinal arterioles and venules respectively were apparent, and corresponded with angiographic features of retinal capillary loss.

The techniques were applied to patients with asymmetrical primary open angle glaucoma to determine whether oximetric changes could be detected. The mean oxygen saturation of the temporal retinal venules were significantly higher [44.8% (± 24.2%)] in the more advanced glaucomatous eyes compared to normal subjects. Hyperoxia of the retinal venules suggests reduced oxygen consumption as a consequence of inner retinal dysfunction in glaucoma. However, because of the small sample size, further research on a larger population of subjects is required to support this finding.

Hyperspectral imaging could be used to detect oximetric abnormalities in the retinal vasculature in patients with retinovascular occlusion and glaucoma.

TABLE OF CONTENTS

LIST OF TABLES

LIST OF FIGURES

PUBLICATIONS

1. Mordant DJ, Alabboud I, Muyo GD, Ritchie PA, Harvey AR, McNaught AI. Validation of Human Whole Blood Oximetry Using A Hyperspectral Fundus Camera with a Model Eye. Invest Ophthalmol Vis Sci. 2011 Jan 10. [Epub ahead of print].

2. Mordant DJ, Alabboud I, Muyo GD, Ritchie PA, Harvey AR, McNaught AI. Spectral Imaging of the Retina. Eye. 2011; 25(3):309-20.

3. Alabboud I, Muyo G, Gorman A, Mordant D, McNaught A, Petres C, Petillot YR, Harvey AR. New spectral imaging techniques for blood oximetry in the retina. In: *Novel Optical Instrumentation for Biomedical Applications III*. Depeursinge CD, ed. Proceedings of the SPIE 2007;6631:66310L.

BOOK CONTRIBUTION

Scanlon P. Future advancements in the management of diabetic retinopathy. In: *A Practical Manual of Diabetic Retinopathy Management*. Scanlon P, Aldington S, Wilkinson C, Matthew D, eds. New York: Wiley-Blackwell, 2009.

PRESENTATIONS

1. D. J. Mordant, I. Al Abboud, A. R. Harvey, and A. I. McNaught. Hyperspectral Imaging of the Human Retina - Oximetric Studies. ARVO Meeting Abstracts May 10, 2007 48:148.
2. D. J. Mordant, I. Alabboud, A. R. Harvey and A. I. McNaught. Retinal oximetry using hyperspectral imaging. Oxford Ophthalmological Congress, July 2007.
3. G. Muyo, A. Gorman, I. Al Abboud, D. J. Mordant, A. I. McNaught, and A. R. Harvey. En Face Snapshot Spectral Imaging of the Retina. ARVO Meeting Abstracts May 10, 2007 48:2582.
4. I. Alabboud, III, A. McNaught, D. Mordant, and A. R. Harvey. Quantitative Spectral Imaging of the Retina. ARVO Meeting Abstracts May 10, 2007 48:2581.
5. D. J. Mordant, I. Alabboud, A. R. Harvey, and A. I. McNaught. Retinal Vessel Oximetry Using Hyperspectral Imaging in Retinovascular Disease. ARVO Meeting Abstracts April 11, 2008 49:4263.
6. D. J. Mordant, I. Alabboud, A. R. Harvey, and A. I. McNaught. Retinal Vessel Oximetry Using Hyperspectral Imaging in Retinovascular Disease. Annual Congress of the Royal College of Ophthalmologists, May 2008.
7. D. J. Mordant, I. Alabboud, A. R. Harvey, and A. I. McNaught. Retinal Vessel Oximetry Using Hyperspectral Imaging in Retinovascular Disease. Imaging in the Eye IV: Technologies and Applications, Institute of Physics, October 2008.
8. A. R. Harvey, G. D. Muyo, I. Alabboud, A. Gorman, D. Mordant, and A. I. McNaught. Development of a Clinical Snapshot Spectral Imaging Camera for Blood Oximetry. ARVO Meeting Abstracts April 11, 2008 49:4256.
9. A. R. Harvey, G. D. Muyo, I. Alabboud, A. Gorman, D. Mordant, and A. I. McNaught. Development of a Clinical Snapshot Spectral Imaging Camera for Blood Oximetry. Annual Congress of the Royal College of Ophthalmologists, May 2008.
10. A. I. McNaught, D. J. Mordant, I. Alabboud, P. A. Ritchie, G. D. Muyo, and A. R. Harvey. Development of a Model Eye to Validate Oximetric Measurements in the Human Retinal Vasculature Using Hyperspectral Imaging. ARVO Meeting Abstracts April 11, 2008 49:921.

11. Mordant, I. Alabboud, P.S. Scanlon, A.R. Harvey and A.I. McNaught. Retinal Vessel Oximetry Using Hyperspectral Imaging in Diabetic Retinopathy. D.J. Oxford EASDec 2009 Annual Conference, May 2009.
12. G. Muyo, I. Alabboud, A. Gorman, D. J. Mordant, A. I. McNaught, and A. R. Harvey. Two-dimensional Snapshot Spectral Imaging for Blood Oximetry in Retinal Vasculature. ARVO Meeting Abstracts April 11, 2009 50:3303.
13. D. J. Mordant, I. Al-Abboud, G. D. Muyo, A. R. Harvey, and A. I. McNaught. Retinal Vessel Oxygen Saturation Measurements in Asymmetrical Primary Open Angle Glaucoma Using Hyperspectral Imaging. ARVO Meeting Abstracts April 11, 2009 50:5803.
14. D. J. Mordant, I. Al-Abboud, G. D. Muyo, A. R. Harvey, and A. I. McNaught. Retinal Vessel Oxygen Saturation Measurements in Asymmetrical Primary Open Angle Glaucoma Using Hyperspectral Imaging. Annual Congress of the Royal College of Ophthalmologists, May 2009.
15. N. Shah, D.J. Mordant, I. Alabboud, G. D. Muyo, A.R. Harvey, and A. I. McNaught, Qualitative and Quantitative Retinal Vessel Oximetry Techniques in Ischaemic Retinal Vein Occlusion. Annual Congress of the Royal College of Ophthalmologists, May 2009.
16. D. J. Mordant, I. Alabboud, G. Muyo, A. Gorman, A. Harvey, Q. Mohamed, and A. McNaught. Quantitative Retinal Vessel Oximetry in Ischaemic and Non-Ischaemic Retinal Vein Occlusion. ARVO Meeting Abstracts April 11, 2010 51:2304.
17. A. Gorman, I. Alabboud, G. Muyo, D. J. Mordant, A. I. McNaught, P. Rodmell, J. Crowe, S. Morgan, and A. R. Harvey. Validation of Quantitative Retinal Vessel Oximetry Using an Eye-Phantom and Monte-Carlo Ray-Tracing. ARVO Meeting Abstracts April 11, 2010 51:5769.

ACKNOWLEDGEMENTS

I would like to express my sincere gratitude to my supervisors Andy McNaught (Cheltenham General Hospital), Andy Harvey (Heriot Watt University) and Fred Fitzke (Institute of Ophthalmology) for their support and guidance in helping me complete this research.

This thesis would not have been possible without the dedication and hard work of Ied Al-Abboud, Gonzalo Muyo and Al Gorman (Heriot Watt University) who have provided me with the technical support to enable me to carry out this research.

I am grateful to Ahmed Sallam and Peter Ritchie (Cheltenham General Hospital) who have contributed towards the model eye experiments.

I owe a huge debt of gratitude to all the staff members of the Ophthalmology Department in Cheltenham and Gloucester General Hospitals who have supported me with the clinical research.

I am deeply grateful to my parents, family and parents-in-law for their support and interest in my work over the years.

Finally, I am indebted to my wife, Emma, for having to endure the time spent away from her and our daughter, Lily, the late nights and long weekends of work. Her patience, love and support have enabled me to carry out this research to the best of my capability.

The research presented in this thesis was funded by grants from the Eye Therapy Trust, Technology Strategy Board (CHBT/007/00028) and NEAT (New and Emerging Applications of Technology - part of the i4i Invention for Innovation programme (NEAT K034) of the National Institute for Health Research.

ABBREVIATIONS

ACG: angle closure glaucoma

ADP: adenosine diphosphate

AGIS: Advanced Glaucoma Intervention Study

AOTF: acusto-optic tunable filters

ATP: adenosine triphosphate

A/V: arteriovenous

BCVA: best corrected visual acuity

BRAO: branch retinal artery occlusion

BRB: blood-retinal barrier

BRVO: Branch retinal vein occlusion

c: concentration or haematocrit

CC: choriocapillaris

CCD: charge-coupled device

CDI: Colour Doppler imaging

cGMP: cyclic guanosine monophosphate

CIGTS: Collaborative Initial Glaucoma Treatment Study

CINTGS: Collaborative Initial Normal-Tension Glaucoma

$[Cl^-]$: chloride ion concentration

CO-oximeter: cuvette oximeter

CRA: central retinal artery

CRAO: central retinal artery occlusion

CRV: central retinal vein

CRVO: central retinal vein occlusion

CSLO: Confocal Scanning Laser Ophthalmoscopy

CVOS: Central Retinal Vein Occlusion Study

d: distance/path length

D: dioptre

DNA: deoxyribonucleic acid

dd: disc diameter

ε: extinction coefficient of blood

FDT: frequency-doubling technology perimetry

FWHM: Full-Width Half Maximum

FFT: Fast Fourier Transformation

GC: ganglion cell

GCL: ganglion cell layer

GON: glaucomatous optic neuropathy

Hb: deoxyhaemoglobin

HbO_2: oxyhaemoglobin

Hct: haematocrit

HRT: Heidelberg Retina Tomograph,

HIF-1: hypoxia-inducible factor 1

INA: inferonasal arteriole

INL: inner nuclear layer

INS: inner segments;

INV: inferonasal venule

I_O: intensity of incident light

IOP: intraocular pressure

IPL: inner plexiform layer

IRIS: Image Replicating Imaging Spectrometer

ITA: inferotemporal arteriole

ITV: inferotemporal venule

I_T: intensity of light transmitted

K^+: potassium ions

$[K^+]$: potassium ion concentration

LCTF: liquid crystal tuneable filter

LDF: laser Doppler flowmetry

LDV: Laser Doppler velocimetry

LGN: Lateral geniculate nucleus

LPCA: long posterior ciliary artery

LOCS III: Lens Opacities Classification System III

LSFG: Laser speckle flowgraphy

Na^+: sodium ions

$[Na^+]$: sodium ion concentration

NFL: nerve fibre layer

NTG: normal tension glaucoma

OAG: open angle glaucoma

OCT: optical coherence tomography

$OD(\lambda)$: optical density (wavelength)

ODR: optical density ratio

ONL: outer nuclear layer;

OPL: outer plexiform layer

OS: oxygen saturation

OHTS: Ocular Hypertension Treatment Study

PCO_2: pressure of carbon dioxide/carbon dioxide tension

PO_2: pressure of oxygen/ oxygen tension

POAG: primary open angle glaucoma

RBC: red blood cells

RGC: retinal ganglion cell

RNFL: retinal nerve fibre layer

RPE: retinal pigment epithelium

SAP: standard achromatic automated perimetry

SD: standard deviation

SITA: Swedish Interactive Threshold Algorithm

SNA: superonasal arteriole

SNV: superonasal venule

SPCA: short posterior ciliary artery

SWAP: short-wavelength automated perimetry

STA: superotemporal arteriole

STV: superotemporal venule

tHb: total haemoglobin

V: retinal vessel

LIST OF EQUATIONS

$$I_T = I_O \times 10^{-(\varepsilon \times c \times d)} \quad \text{(Eq. 1.1)}$$

$$OD = -Log_{10}\left(\frac{I_T}{I_O}\right) = \varepsilon \times c \times d \quad \text{(Eq. 1.2)}$$

$$OD_{vessel} = -Log_{10}\left(\frac{I_V}{I_R}\right) \quad \text{(Eq. 1.3)}$$

$$OD(\lambda) = -Log_{10}\left(\frac{I(\lambda)}{I_O(\lambda)}\right) \quad \text{(Eq. 1.4)}$$

$$OD(\lambda) = a + \eta(\lambda)\, C_{HbTotal}\, d\, [cOS\, (\varepsilon_{oxy}(\lambda + b) - \varepsilon_{de\text{-}oxy}(\lambda + b)) + \varepsilon_{de\text{-}oxy}(\lambda + b)] \quad \text{(Eq. 1.5)}$$

$$OD(\lambda) = a\, S(\lambda) + \eta(\lambda)\, C_{HbTotal}\, d\, [cOS\, (\varepsilon_{oxy}(\lambda + b) - \varepsilon_{de\text{-}oxy}(\lambda + b)) + \varepsilon_{de\text{-}oxy}(\lambda + b)] \quad \text{(Eq. 1.6)}$$

Chapter 1: Introduction.

1.1. The Human Eye.

1.1.1. An Applied Gross Anatomy of the Human Eye and the Visual System.

The eye is a highly specialized sensory organ located in the anterior portion of the orbit which makes up the visual system. The main function of the eye is to enable vision. This is achieved by processing reflected or emitted light from objects in the environment. Light entering the eye travels through the ocular media which consists of the cornea, anterior chamber, crystalline lens and vitreous. The result is the projection of an inverted image on to the retina. Upon reaching the retina, the light photons undergo first-order processing by the photoreceptors (located in the outer retina) into neural signals. Second-order processing of the neuronal signals occurs throughout the inner layers of the retina. The neuronal information is transmitted to the ganglion cells (located in the inner most layer of the retina) which is subsequently relayed to the brain via the optic nerve, optic chiasm, optic tracts and lateral geniculate bodies. Further processing of the visual information is performed in the visual cortex, occipitotemporal, temporal, occipitoparietal, and parietal lobes of the brain. (Figure 1.1)

1.1.2. The Structure of the Eye.

The human adult eye (Figure 1.2) is approximately spherical in shape with an average anteroposterior diameter of 24 mm (range 21-26 mm) (Snell and Lemp, 1998). The eye is comprised of three coats (tunics), the corneoscleral coat, the uvea (and uveal tract) and the neural layer (retina).

The cornea is a thin and transparent structure which, due to the difference in the refractive index of between the air and tear film of the eye, constitutes two thirds of the total refractive power of the human eye (~40 D) (Sivak, 1988). The sclera is a white, avascular fibrous coat consisting of irregularly-arranged collagen fibrils. Its principle function is to protect the intraocular contents of the eye.

The uvea and uveal tract are pigmented layers consisting of the iris, ciliary body and choroid. The iris is a thin, circular structure located anterior to the lens which contains several layers of pigment cells which determine the colour of the iris and blocks light from passing through the iris to the retina.

The ciliary body is a circumferential ring of tissue comprising of the ciliary muscle and ciliary processes which extends from the sclera spur anteriorly to the ora serrata posteriorly. It has three principal functions: accommodation, aqueous humour production and production of the lens zonules and extracellular components of the vitreous.

Figure 1.1: The human visual pathway.

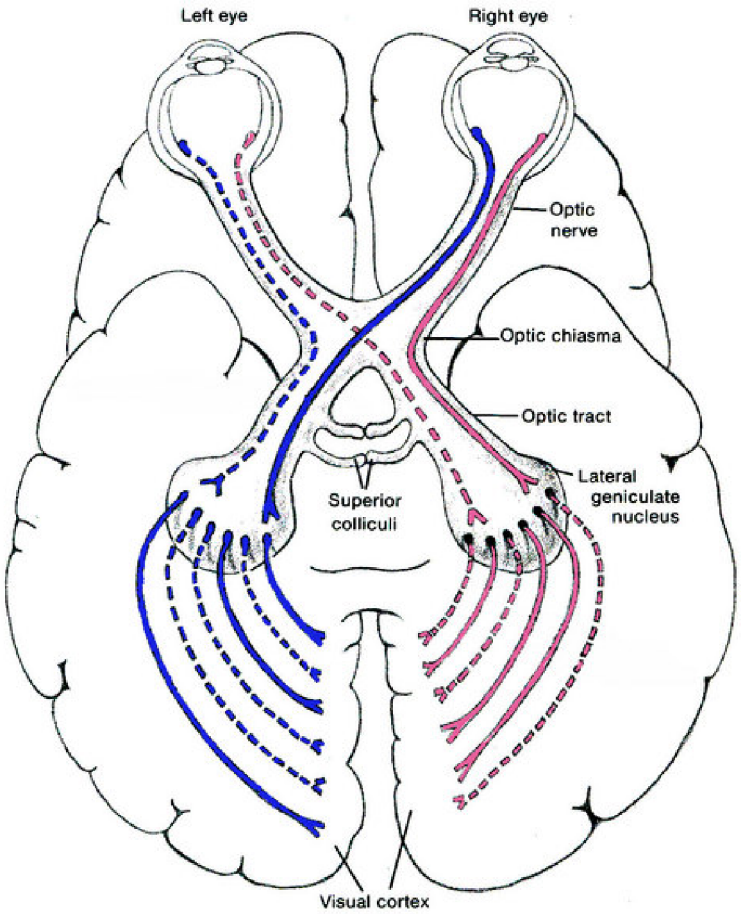

Figure 1.2: The structure of the human eye.

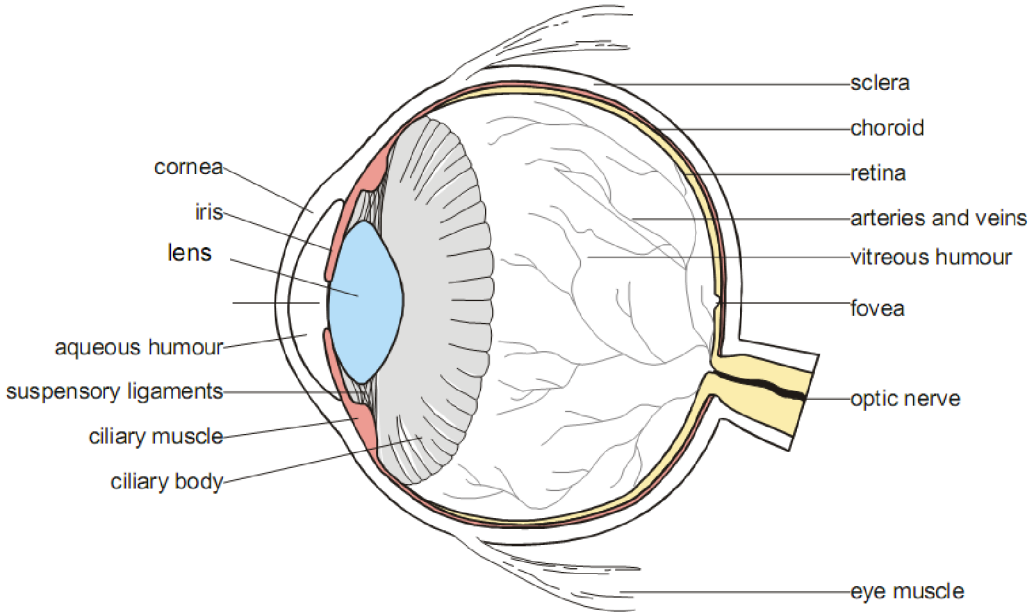

1.1.2.1. The Choroid.

The choroid, located between the retina and sclera, is comprised of a rich network of blood vessels, cells and connective tissues. Histologically, the choroid is comprised of five layers: Bruch's membrane (inner most layer), choroiocapillaris, the two vascular layers (Haller's and Sattler's), and the suprachoroid (Figure 1.3A and B) (Hogan et al., 1971). The thickness of the choroid is variable, approximately 426 µm at the subfovea (Brown et al., 2009), and is thought to be dependent on intraocular pressure (IOP)(Nickla et al., 1998; Nickla et al., 2002), refractive state of the eye (Hung et al., 2000; Troilo et al., 2000), blood flow (Fitzgerald et al., 2002) and diurnal variations (Brown et al., 2009).

The choriocapillaris is a thin (10 µm at the fovea) layer apposed to Bruch's membrane consisting of a network of wide-bore fenestrated capillaries about 20 - 40 µm wide (Bill et al., 1983). The capillaries originate from the arterioles in Sattler's layer and form a hexagonal arrangement of capillaries. The post-capillary venous channels drain the periphery of the hexagonal lobules (Figure 1.4). The flow of red blood cells is about 79% that of the velocity of red blood cells in the retinal capillaries (Wajer et al., 2000).

Figure 1.3: The choroid. **A**. A schematic illustration of the choroidal layers (Remington, 1998). **B**. Histological section of the outer retina and choroid in the primate eye. RPE: retinal pigment epithelium; CC: choriocapillaris; SL: Sattler's layer; HL: Haller's layer (Forrester et al., 2002).

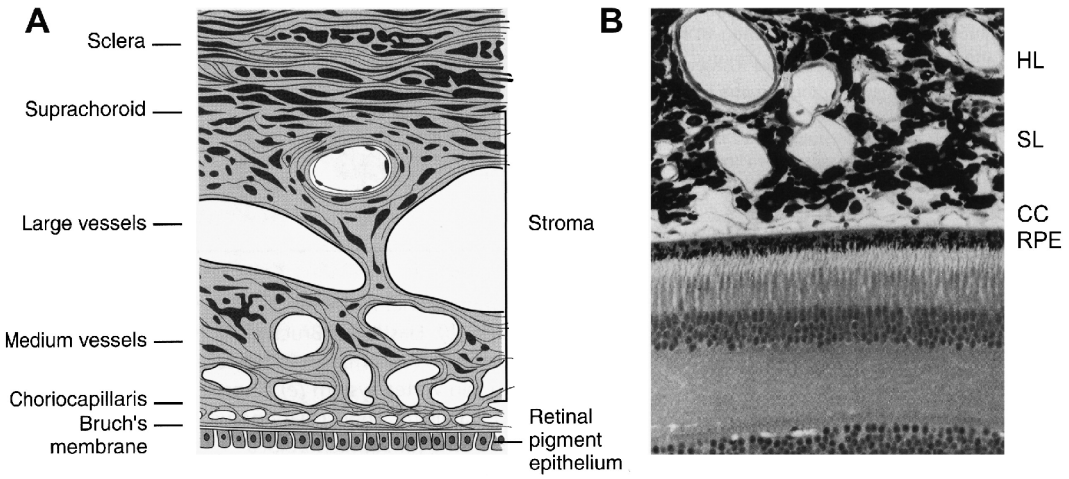

Figure 1.4: The choriocapillaris and arterioles in Sattler's layer (Forrester et al., 2002).

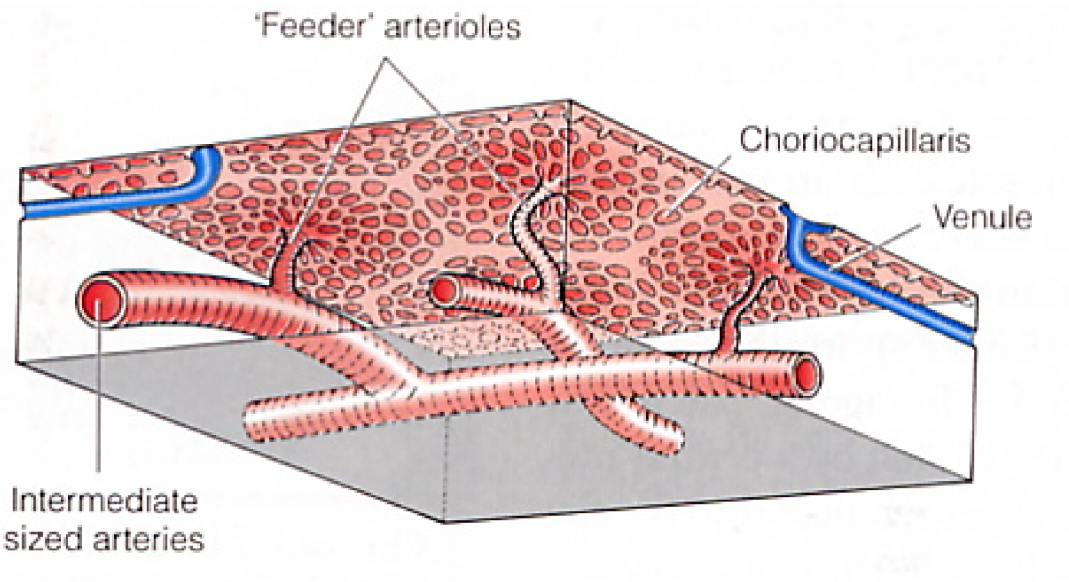

The vascular layers of the choroid consists of the outer Haller's layer of large blood vessels and the inner Sattler's layer of intermediate sized vessels that feed and drain the capillary network. Blood is supplied primarily from the long and short posterior ciliary

arteries and venous drainage occurs via a complex of large vortex veins each draining a sector of the choroid to the superior and inferior ophthalmic veins in the orbit (Figure 1.5). The suprachoroid is a 30 µm thick avascular layer containing collagen, melanocytes and fibroblasts separating the choroid from the sclera.

Figure 1.5: Arterial supply and venous drainage of the eye. (SPCA: short posterior ciliary artery; LPCA: long posterior ciliary artery) (Forrester et al., 2002).

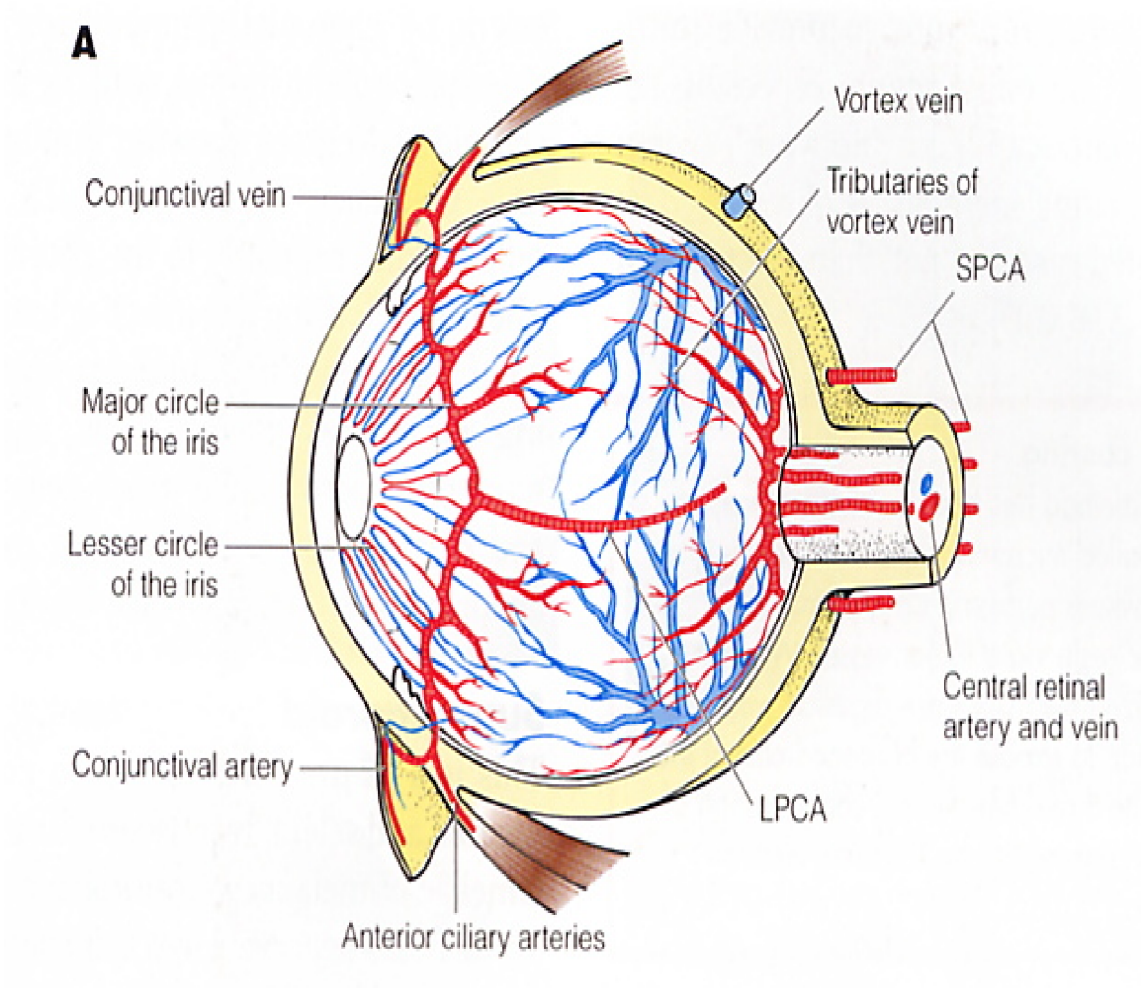

The main function of the choroid is to supply the outer two thirds of the retina with oxygen and nutrients. Other functions of the choroid include thermoregulation by heat dissipation through traversing blood vessels, drainage of aqueous humor (Alm and Nilsson, 2009), modulation of IOP via blood flow regulation and light absorption.

1.1.2.2. The Lens.

The lens consists of a thin, transparent and elastic biconvex capsule that encloses a collection of specialized cells (lens fibres). It is located posterior to the iris and anterior to the vitreous suspended by the zonular fibres attached laterally. The primary function of the lens is to enable a sharp image to be formed on the retina by changing its refractive properties (accommodation). This is achieved by the contractile state of the ciliary muscle. The refractive power of the adult human lens in its relaxed state is approximately 19D (Smith, 2003) and varies with age (Jones et al., 2005; Borja et al., 2008).

1.1.2.3. The Vitreous.

The vitreous is a transparent, virtually acellular extracellular matrix located posterior to the lens, posterior lens zonules and ciliary body; and is surrounded posteriorly by the retina and pars planar. It consists of more than 98% water and its gel-like structure is attributed by the presence of fine, unbranched collagen fibrils interspersed by a network of hyaluronan. Its physiological functions are incompletely understood, however its main role is thought to be a means to provide nutrients and oxygen to the lens (Fatti, 1977).

1.1.2.4. The Retina.

The retina is the light sensitive innermost coat of the eye which converts light photons into neural impulses that are transmitted to the brain enabling vision. The *en face* aspect of the retina can be defined into several regions with different topographical characteristics (Figure 1.6).

The posterior pole (*area centralis*) is a 5 – 6 mm circular area located between the superior and inferior temporal arterioles. It contains several layers of ganglion and bipolar cells (Spitznas, 1977).

The fovea (*macula lutea*), located 3 mm lateral to the optic disc, is a 1.5 mm diameter circular area in the posterior pole. It consists of a thin bottom and a thickened margin which represents the lateral displacement of second and third order neurons in the inner nuclear layer (mostly the cell bodies of Müller glia cells). It consists exclusively of tightly packed cone photoreceptors (150,000 per mm^2). A network of capillaries, located at the level of the

internal nuclear layer, encircle the fovea which consists of an avascular zone 250 – 600 μm wide.

The foveola is a central circular area within the lowest point of the fovea. It is 350 μm in diameter and 150 μm thick. The cone photoreceptors are enclosed by the processes of the Müller cells which, in addition to the retinal pigment epithelium (RPE) via the underlying choriocapillaris, provides nutritional support to sustain the high metabolic demand of the cones (Schubert, 2008).

The peripheral retina extends from the border of the posterior pole to the ora serrata anteriorly. It consists predominantly of rod photoreceptors (30,000 per mm^2) and is comparatively thinner (110 - 140 μm thick) than the retina at the posterior pole primarily due to the presence of only one layer of ganglion cell bodies.

The optic disc (optic nerve head) is a circular structure medial to the macula consisting of ganglion cell axons penetrating the underlying sclera (lamina cribrosa) as it enters the optic nerve. This structure is devoid of photoreceptors. The central retinal vessels, originating from the ophthalmic artery and vein, traverses through the centre of the optic disc and branches out to supply the retina (Figures 1.6 and 1.7). The short posterior ciliary arteries medial and lateral to the optic nerve, originating from the ophthalmic artery, form an arcuate anastamosis within the peripapillary sclera forming a complete circle in the majority of eyes (Olver et al., 1990; Onda et al., 1995) which is synonymous to the arterial circle described by Haller and Zinn (Zinn, 1755)(Figure 1.7). These vessels provide the blood supply to the axons in the prelaminar and laminar portions of the optic nerve.

The optic disc is often used as a landmark to separate the retina into quadrants. The temporal and nasal halves are delineated by a vertical line and the superior and inferior halves are delineated by a horizontal line passing through the centre of the optic disc (Figure 1.6). The angioarchitecture of the large retinal blood vessels can be classified according to the quadrants through which they traverse.

The retina is organized into two distinct layers: the inner neurosensory retina and an outer RPE (Figure 1.8). The neurosensory retina is a transparent layer composed predominantly of neural cells (photoreceptors, bipolar and ganglion cells). The activities of these cells are regulated by supporting cells, namely the horizontal, amacrine and Müller cells whose cell bodies and axonal processes traverse the inner and outer nuclear layers and inner and outer plexiform layers. Bipolar and horizontal cells synapse with the photoreceptors in the outer plexiform layer. Within the inner plexiform layer the bipolar and amacrine cells synapse with the dendrites of the ganglion cells. These connections represent the initial

circuitary of the visual pathway. Other cell types interspersed within the neurosensory retinal layer include vascular endothelium, pericytes, and microglia.

Figure 1.6: *En face* view of the human retina. (CRA: central retinal artery; CRV: central retinal vein; STA: superotemporal arteriole; STV: superotemporal venule; ITA: inferotemporal arteriole; ITV: inferotemporal venule; INA: inferonasal arteriole; INV: inferonasal venule; SNA: superonasal arteriole; SNV: superonasal venule).

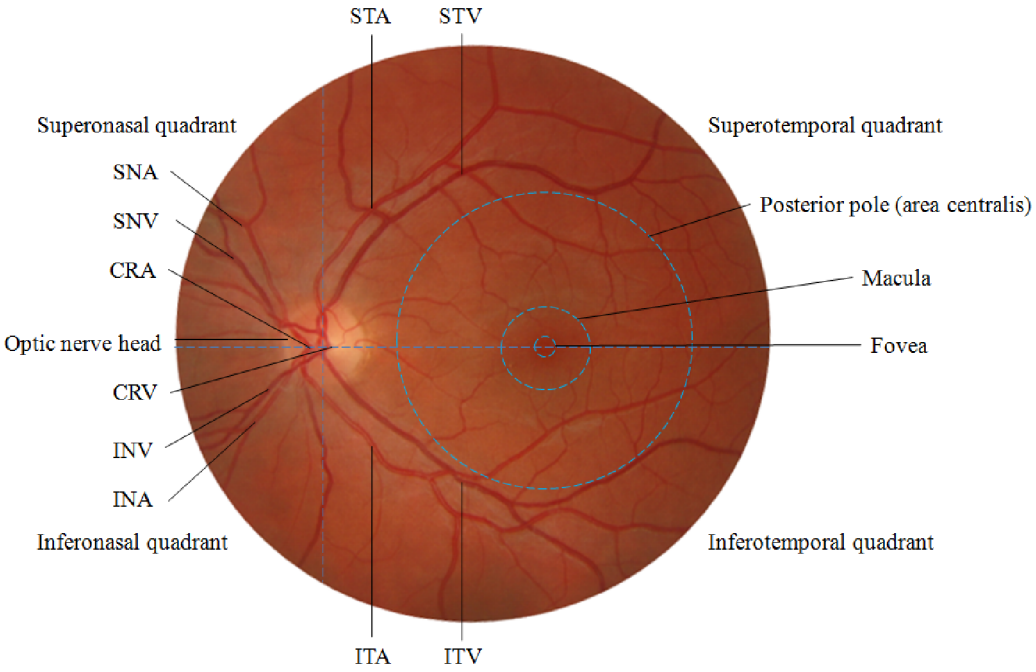

Figure 1.7: The anterior optic nerve (Sadun 2008).

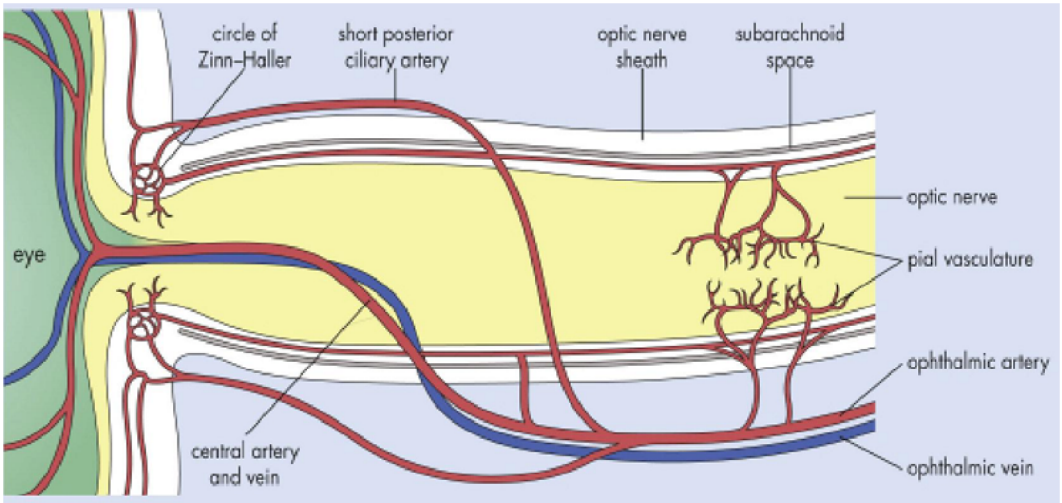

Figure 1.8: Layers of the retina and neural connections. **A**. Electron micrograph of the retina demonstrating the various layers (Forrester et al., 2002). **B**. Schematic illustration of the neuronal connections in the retina (Schubert, 2008). (GCL: ganglion cell layer; GC: ganglion cell; NFL: nerve fibre layer; V: retinal vessel; IPL: inner plexiform layer; INL: inner nuclear layer; OPL outer plexiform layer; ONL: outer nuclear layer; INS: inner segments; OS: outer segments; RPE: retinal pigment epithelium; CC: choriocapillaris).

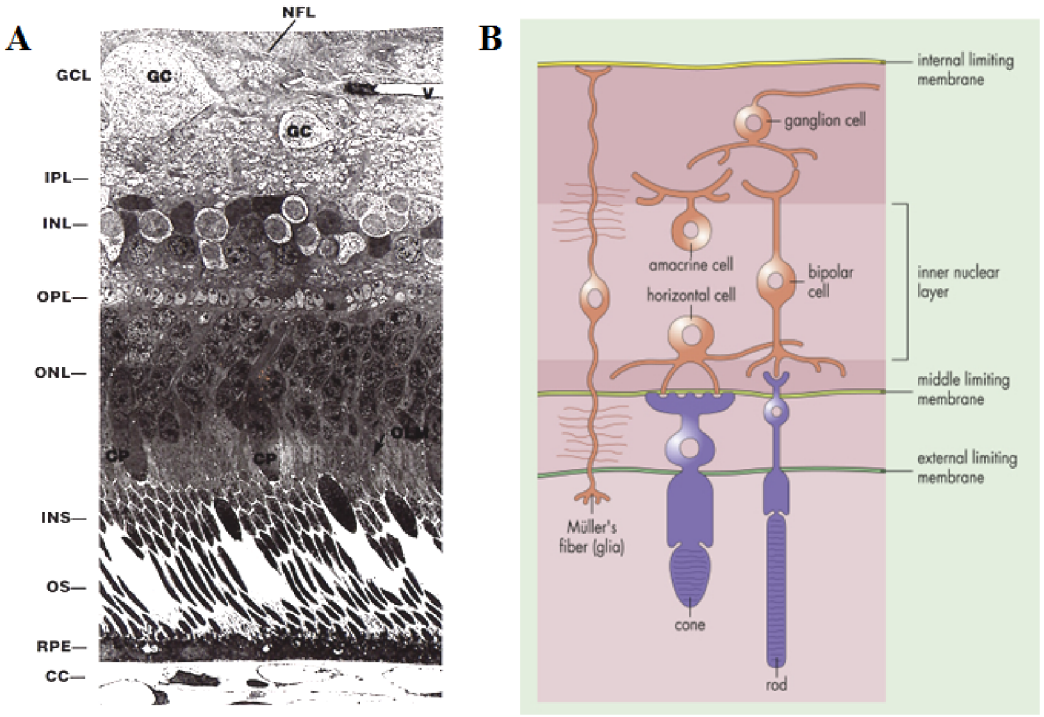

There are two main types of photoreceptors in the human eye: rods and cones. The human retina contains approximately 96 million rods and 4.6 million cones (Curcio et al., 1990). They are specialized neuronal cells capable of phototransduction – a process by which the energy from a light photon is converted into the membrane potential of the photoreceptor. Both rods and cones possess an outer and inner segment. The outer segment functions to detect light photons and the inner segment houses the important organelles for cellular metabolism. However, these cells are functionally distinct; rods have low spatial resolution, are highly sensitive to light, and are primarily responsible for sensing brightness, contrast and motion. Cones are relatively insensitive to light but have high spatial resolution and are specialized for colour, depth and visual acuity.

The retinal ganglion cells are a diverse group of specialized neurones that provide the link between the retina and the higher visual pathway, their axons exit the eye via the optic

nerve and synapse with the cell bodies of the lateral geniculate nucleus (LGN). There are several ganglion cell subtypes with a diverse range of functions. Although largely age-dependent (Harman et al., 2000; Gao and Hollyfield, 1992; Harwerth et al., 2008), there are approximately 0.7 to 1.5 million ganglion cells in the human retina (Curcio and Allen, 1990).

The RPE is the outer pigmented layer of the retina composed of a monolayer of hexagonal cells located between the photoreceptors and Bruch's membrane. It extends from the optic disc to the ora serrata and has a number of important functions. Its role in supporting the photoreceptors, such as the synthesis of enzymes for visual pigment metabolism, membrane transport of metabolites, requires a high demand of energy which is reflected by the abundance of mitochondria located towards its basal zones.

1.1.2.5. The Retinal and Choroidal Circulation.

The human retina has a dual blood supply to meet the high metabolic demands of the neural tissues and RPE. The inner two-thirds of the retina are supplied from branches of the central retinal vessels and the outer one-third of the retina is supplied by the choroid creating a watershed zone at the outer plexiform layer. The central retinal artery, derived from the ophthalmic artery (first branch of the internal carotid artery)(Heyreh, 1962), arises from the centre of the optic nerve and is in close association with the central retinal vein. It decreases to approximately 110 µm as it crosses the optic disc margin and it typically branches into superior and inferior arterioles which further divide into temporal and nasal branches.
The four major branches of the central retinal artery are usually devoid of elastic fibers and internal elastic membrane and represent functional end-arterioles which supply an area (or quadrant) of the retina with no overlap. These branches traverse across the retina within the nerve fibre layer bounded anteriorly by the inner limiting membrane.

Within the retinal layers, capillaries are organized into one to three layers of laminar meshwork (Shimizu et al., 1978), typically at the level of the ganglion cell layer and inner nuclear layer, enabling nutritional support to all retinal cells. Retinal capillaries are 5-6 µm in diameter, are more abundant at the macula compared to the peripheral retina and are absent in the fovea and capillary-free zones adjacent to large arterioles and venules. The blood-retinal barrier is formed by the tight junctions of the capillary endothelial cells and RPE which functions to prevent the intracellular movement of water-soluble molecules into the retina.

The retinal venules are located in the inner retina and follow the course of the arterioles draining into the central retinal vein. Often the arterioles cross the venules

anteriorly and at this location the two vessels share an adventitial coat. Near the optic disc the retinal veins are approximately 150 µm in diameter (Duker and Weiter, 1991).

The posterior ciliary arteries originate from the ophthalmic artery and further divide into two long posterior ciliary arteries and several short posterior ciliary arteries. The short posterior ciliary arteries enter the choroid in the submacular and peripapillary region and supply the posterior choriocapillaris. The recurrent branches of the long ciliary arteries in addition to recurrent branches of the anterior ciliary arteries supply the anterior choriocapillaris. In approximately 30% of the population a cilioretinal artery is present (Justice and Lehmann, 1976) and arises directly from the posterior ciliary artery providing an anastamotic connection between the retinal and choroidal circulation.

A network of large vortex veins located at the equator drains blood from the choroid into the superior and inferior orbital veins and into the cavernous sinus and pterygoid plexus respectively. The central retinal vein drains the retina and prelaminar portion of the optic nerve into the cavernous sinus.

The blood-retinal barrier (BRB) consists of an inner BRB (comprised of the tight junction between endothelial cells of the retinal vessels) and an outer BRB (comprised of the RPE). It is a physiological interface that selectively separates the neural tissue in the retina from the blood in order to maintain an optimal microenvironment for retinal function.

Blood flow in the choroid is regulated by the autonomic nervous system via the presence of sympathetic nerve fibre endings (Guglielmone and Cantino, 1982). In contrast, no nerve fibres are present in the walls of the retinal vessels (Ehinger, 1966) indicating that blood flow is autoregulated by the vascular tone of the resistance vessels mediated by local vasoactive substances. The retinal circulation is characterized by a low blood flow rate (80 mL/minute) and the choroid in contrast has a high level of flow (800 mL/minute) (Alm and Bill, 1973; Feke et al., 1989; Roh and Weiter, 2008). Approximately 85% of total ocular blood flow is supplied by the choroidal circulation and 4% of the total ocular blood flow is diverted to the retinal circulation (Alm and Bill, 1973). The differences between the retinal and choroidal haemodynamics reflect the topographical variations in metabolic activity throughout the layers of the retina. Over 90% of the oxygen delivered to the retina is consumed by the photoreceptors which are highly metabolically active. In the dark adapted eye, where photoreceptor metabolism is highest, over 90% of the oxygen supply is consumed to sustain the depolarized resting potential via active transport of ions across the cell membrane (Bill et al., 1983; Linsenmeier et al., 1981; Linsenmeier and Braun, 1992). Approximately 70% of oxygen and glucose consumption is supplied by the choroid (Alm,

1992). The high flow in the choroidal circulation is thought to generate and maintain a high concentration gradient of oxygen to overcome the RPE barrier that separates the choroid from the photoreceptors (Alm and Bill, 1973; Alm, 1992). As a consequence of this high flow, oxygen extraction is relatively low in comparison to the retinal circulation (arterio-venous difference of 3% versus 40% respectively) (Törnquist et al., 1979; Hickam et al., 1963).

1.2. Oxygen Physiology.

1.2.1. Oxygen Transport.

Oxygen is utilized in most tissues as a primary substrate for generating energy which is important in maintaining tissue viability and function. In humans, oxygen in the alveoli of the lungs diffuses into the pulmonary blood which in turn is transported to the tissues. Ninety-seven percent of oxygen in blood is bound to haemoglobin contained in the red blood cells. Haemoglobin is a complex iron-containing metalloprotein whereby each molecule of haemoglobin is composed of four polypeptide protein chains tightly bound to a non-protein haeme group consisting of a flat organic ring (porphyrin ring) surrounding a single iron atom (Figure 1.9). The red colour of haemoglobin is due to the red fluorescence properties of the porphyrin molecules. The four iron atoms form a weak, and reversible, co-ordinate covalent bond with a molecule of oxygen.

The amount of oxygen bound to haemoglobin (per cent saturation of haemoglobin) progressively increases as the blood oxygen concentration (pressure of oxygen - PO_2) increases. This relationship is known as the oxygen-haemoglobin dissociation curve and has a distinct sigmoid shape which describes the affinity of haemoglobin for oxygen. Several factors can displace the curve (Figure 1.10) and influence the oxygen affinity of haemoglobin. For example, an increase in blood carbon dioxide concentration and hydrogen ions reduces the affinity of haemoglobin molecules to oxygen and augments the release of oxygen from the blood into the tissues.

Arterial blood upon reaching the peripheral tissues typically has a PO_2 of 104 mm Hg. Continuous consumption of oxygen by the cells in the tissues results in the diffusion of oxygen down a concentration gradient into several compartments (oxygen cascade), before reaching the mitochondria (4 - 20 mm Hg) for energy production. Generally, oxygen partial

pressures of between 1 - 3 mm Hg is required to sustain cellular functions (Guyton and Hall, 2006), therefore in the resting state there is an abundance of oxygen for the cells to function.

Figure 1.9: The molecular structure of haemoglobin showing the α and β subunits of the haemoglobin protein (red and blue) and the iron containing haeme group (green).

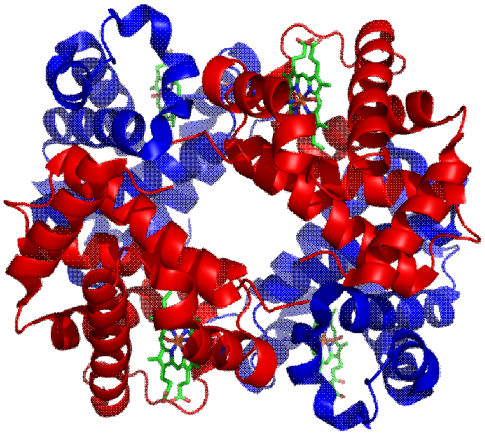

Figure 1.10: The oxygen-haemoglobin dissociation curve.

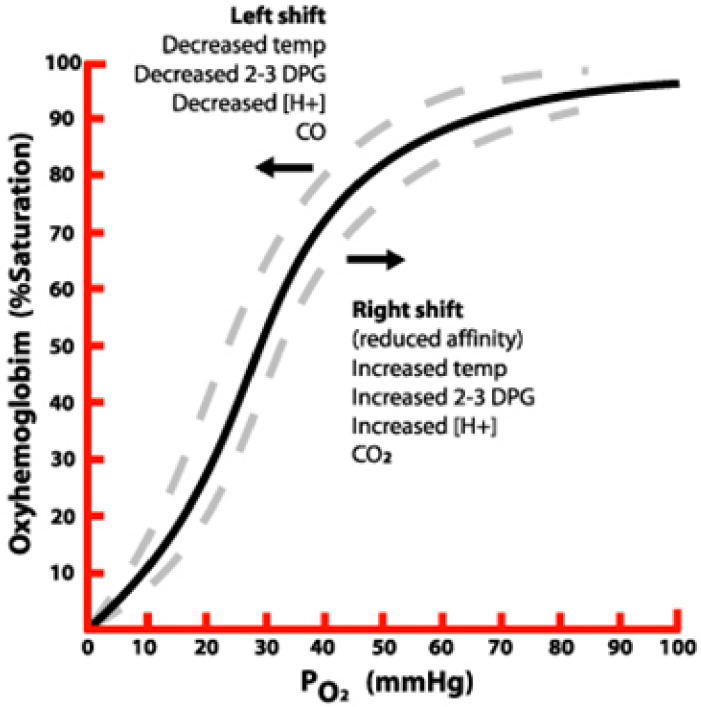

1.2.2. Cellular Metabolism of Oxygen.

Cells utilize a series of interconnected metabolic reactions to generate energy from nutrients (cellular respiration). The universal energy currency in the cell is adenosine triphosphate (ATP), a nucleotide that is repeatedly converted from it precursor adenosine diphosphate (ADP). ATP is not stored, it is converted when required and immediately consumed. Several cellular reactions use glucose, amino acids and fatty acids via the glycolytic pathway in the cytoplasm, Kreb's cycle and oxidative phosphorylation in the mitochondria of the cells to generate ATP (Figure 1.11). ATP contains high energy phosphate bonds which are readily released in an exothermic chemical reaction when ATP is hydrolyzed in endothermic cellular reactions (Ferguson et al. 2002). In the presence of oxygen, more molecules of ATP can be formed via oxidative phosphorylation in the mitochondria (aerobic respiration) compared to anaerobic respiration. ATP is used in maintaining cellular structure, synthesis and transportation of macromolecules and proteins and intracellular signalling.

In the mitochondria, a small concentration of cellular oxygen is required to enable the enzymatic chemical processes to occur. At a cellular PO_2 of greater than 1 mmHg the main limiting factor for energy production is the concentration of ADP in the cells (Guyton and Hall, 2006). When ADP concentration is increased the rate of oxygen consumption is increased. Energy consumption is therefore self-regulated by the energy requirement and expenditure of the cell.

Figure 1.11: Schematic processes of cellular respiration.

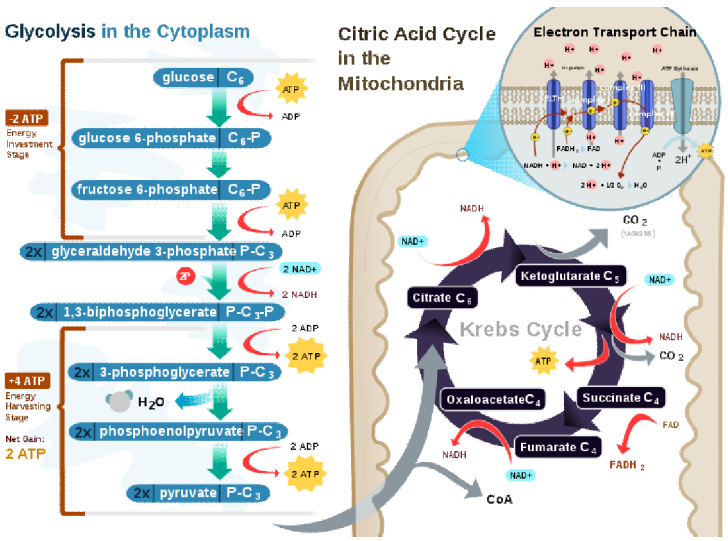

1.3. Physiology of the Retina.

1.3.1. Phototranduction and Intercellular Visual Processing

The primary function of the retina is to capture light photons and convert it into neural stimuli. This process of phototransduction begins in the outer segments of the photoreceptors and is still incompletely understood. Photoreceptors maintain a constant intracellular concentration of sodium (Na^+) and potassium (K^+) via a high density of ATP dependent Na^+/K^+ pumps located on the cell membranes of the inner segments. These pumps actively expel Na^+ ions out of the photoreceptor with an inward uptake of K^+ ions. The dark adapted photoreceptors are maintained in a constant depolarized state (-40 mV) by a continuous passage of K^+ ions through non-gated K^+-selective channels and the inward diffusion of Na^+ ions through cyclic guanosine monophosphate (cGMP) gated Na^+ channels. The depolarized state of the photoreceptor opens voltage-gated calcium (Ca^{2+}) channels which in turn increases the intracellular Ca^{2+} and stimulates the release of glutamate into the synaptic cleft between the photoreceptors and bipolar cells. Photopigment molecules (rhodopsin and iodopsin) located in the cell membranes of the photoreceptor outer segments undergo photoisomerization when exposed to a light photon. A series of molecular cascading reactions results in the hyperpolarization of the cells due to the closure of the Na^+ channels, and subsequently the closure of the voltage-gated Ca^{2+} channels. As intracellular Ca^{2+} concentration decreases the release of glutamate is reduced. Consequently, the demand for energy and oxygen consumption is greater in darkness than in light (Okawa et al., 2008; Ames et al., 1992; Wangsa-Wirawan and Linsenmeier, 2003, Yu and Cringle, 2002).

Bipolar and horizontal cells in the retina provide modulatory processing of the neural information which is relayed to the ganglion cells for higher-order processing. Amacrine cells and Müller cells are also thought to be involved in neuromodulation and further processing of the neural information (Masland, 1996). Retinal ganglion cells are spontaneously generating action potentials at the base rate which is further increased upon excitation by the retinal interneurons (Henne et al, 2000).

1.3.2. Retinal Metabolism.

The metabolic activity required to sustain dark currents, phototransduction and processing of the neural information is extremely high. These processes require energy of

which the majority is supplied in the form of ATP via oxidative phosphorylation in the mitochondria. The abundance of mitochondria in cells within the retina reflect the compartmentalized energy characteristic of its layers with the highest demand for energy in the unmyelinated ganglion cells, the outer plexiform layer, inner segments of the photoreceptors, and the RPE (Wang et al., 2003; Bristow et al., 2002; Andrews et al., 1999).

1.4. Retinal Pathologies.

1.4.1. Retinal Vascular Occlusion

1.4.1.1. Definition and Classification

Retinal venous obstructive disease is a condition in which obstruction to the retinal venous system occurs in central, hemi-central or branch retina vein. Conversely, retinal arterial obstructive disease occurs as a result of an obstruction to the central, cilio-retinal or branch retinal artery.

1.4.1.2. Retinal Vein Occlusion

Branch retinal vein occlusion (BRVO) is the most common form of retinal vein occlusion with a prevalence between 0.6% to 1.1% compared to the prevalence of central retinal vein occlusion (CRVO) between 0.1% and 0.4% (Klein et al., 2000; Mitchell et al.,1996). The incidence of BRVO and CRVO increases with age and is associated with other risk factors such as systemic hypertension, cardiovascular disease, increased body mass index, diabetes (CRVO only) and a history of glaucoma (The Eye Disease Case-Control Study Group, 1993).

The underlying pathogenesis of most forms of BRVO has been proposed to occur as a result of compression at arteriovenous (A/V) crossing sites, endothelial damage due to turbulent blood flow (Christoffersen and Larsen, 1999) with subsequent thrombus formation within veins. Retinal veins share a common adventitial sheath at A/V crossings (Frangieh et al., 1982) which can be compressed between the retina and the retinal arteries particularly in the presence of arteriosclerosis (hardening of the arterial walls) (Duker and Brown, 1989; Zhao et al., 1993). Hyperviscosity of the blood as a result of high haematocrit and other

haematological disorders have also been associated with thrombus formation in BRVO (Remky et al., 1996; Kuhli-Hattenbach et al.,2010).

The pathogenesis of CRVO is less clear but it is generally accepted that it is multifactoral with both local and systemic factors playing crucial roles in the development of thrombus formation and permanent or temporary stagnation of venous blood flow. The main contributing factors are thought to be compression of the central retinal vein by the central retinal artery within the common adventitial sheath in the optic nerve at the level of or posterior to the lamina cribrosa (Green et al., 1981), haemodynamic abnormalities such as hypotension, haematological abnormalities and primary abnormalities of the wall of the central retinal vein (inflammation or degeneration) (Heyreh, 1994; Janssen et al., 2005; Williamson, 1977).

Histopathological studies of branch (Frangieh et al., 1982) and central retinal vein occlusions (Green et al., 1981) have identified a common feature of atrophy of the inner retinal layers involving the nerve fibre layer, ganglion cell layer, and layers down to the inner aspect of the inner nuclear layer (Figure 1.12) with preservation of the outer retina (Wolter, 1961).

Figure 1.12: Histopathology of retinal vein occlusion. **A**. Atrophy of an inner retina distal to a branch retinal vein occlusion (periodic-acid Schiff, magnification x 450) (Frangieh et al., 1982). **B**. Atrophy of the inner retina in a central retinal vein occlusion (periodic-acid Schiff, magnification x 525) (Green et al., 1981). Both histological sections show atrophic changes involving the ganglion cell layer, down to the inner aspect of the inner nuclear layer.

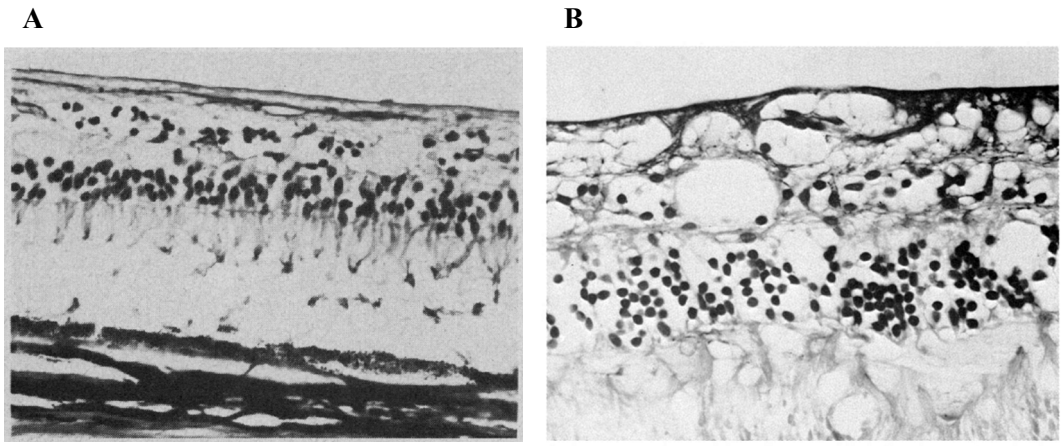

Clinically, patients with CRVO typically present with sudden onset visual disturbance or loss. The fundoscopic features of CRVO include widespread deep and superficial retinal haemorrhages, dilated and tortuous venules, cotton-wool spots and retinal oedema. In contrast, patients with BRVO may be asymptomatic or present with visual blurring and a visual field defect corresponding to the area of the affected retina. The fundoscopic features of BRVO are similar to CRVO but are confined to the region of the retina drained by the occluded vein. Old, "burnt-out" retinal vein occlusion may exhibit venous collaterals and vascular sheathing. CRVO can be further categorized into two distinct groups, ischaemic and non-ischaemic. Ischaemic CRVO is associated with poor visual acuity (6/60 or worse), a relative afferent pupillary defect, presence of multiple intense and deep intra-retinal haemorrhages and multiple cotton-wool spots. Angiography, a test that enables the visualization of anatomic structures by the passage of a fluorescent dye, is the most commonly used technique for differentiating between ischaemic and non-ischaemic CRVO. The Central Retinal Vein Occlusion Study (CVOS) delineated ischaemic and non-ischaemic CRVOs using fluorescein angiography, designating an area of capillary nonperfusion greater than 10 disc diameters as ischemic and less than 10 disc diameters as nonischaemic (The Central Vein Occlusion Study, 1993).

The prognosis of BRVO is comparatively more favourable than CRVO with 50-60% of patients maintaining vision of 6/12 or better (Gutman et al., 1974; Michels and Gass, 1974; Qunilan et al., 1990). The main causes for poor final visual acuities are chronic macular oedema, macular ischaemia, retinal neovascularization and neovascular glaucoma (The Central Vein Occlusion Study, 1993; Gutman et al., 1974; Michels and Gass, 1974; Wetzig et al., 1979; Hayreh et al., 1983). The mainstay of current treatment for retinal vein occlusion is the application of argon laser photocoagulation in the presence of macular oedema (BRVO only) and ocular neovascularization (The Branch Retinal Vein Occlusion Study Group, 1984).

1.4.1.3. Retinal Artery Occlusion

The estimated prevalence of central retinal artery occlusion (CRAO) is approximately 0.85 in 100,000 (Rumelt et al., 1999). The prevalence of branch retinal artery occlusion (BRAO) is not known, but is thought to be less prevalent than CRAO. Retinal artery occlusion commonly affect patients over 60 years of age (Sharma et al., 1998), and is

associated with atherosclerosis, systemic hypertension, and diabetes (Brown and Magaragal, 1982).

Retinal artery occlusion occurs as a result of an obstruction to the retinal arterioles, most commonly from an embolic source. Inflammation of the retinal arterioles (vasculitis) is a less frequent condition that can result in occlusion of the retinal artery.

In primates, experimental acute retinal artery occlusion is histologically associated with oedema of the inner neuronal cells within the first few hours of the insult (Figure 1.13) (Radius and Anderson, 1981). Experimental chronic arterial insufficiency results in the development of an acellular zone within the inner retina incorporating the nerve fibre layer, ganglion cell layer and inner plexiform layer with sparing of the outer plexiform and nuclear layers and photoreceptors (Hayreh et al., 2004; Zimmerman, 1965; Dahrling, 1965). The relationship between the duration of retinal ischaemia and the onset of irreversible retinal damage is unclear. Hayreh et al. (1980) demonstrated that primate retinas are able to tolerate up to 100 minutes of ischaemia.

Figure 1.13: Light micrographs of a primate retina at intervals following experimental central retinal artery occlusion. **A**. Thirty minutes after occlusion: no abnormality seen in the retinal tissue. **B**. Four hours after occlusion: thickening and oedema of the inner-retinal layers. **C**. Twenty-four hours after occlusion: disorganization of the inner retina with atrophy of the ganglion cells and nerve fibre layer (Paraphenylene diamine; magnification x200) (Radius and Anderson, 1981).

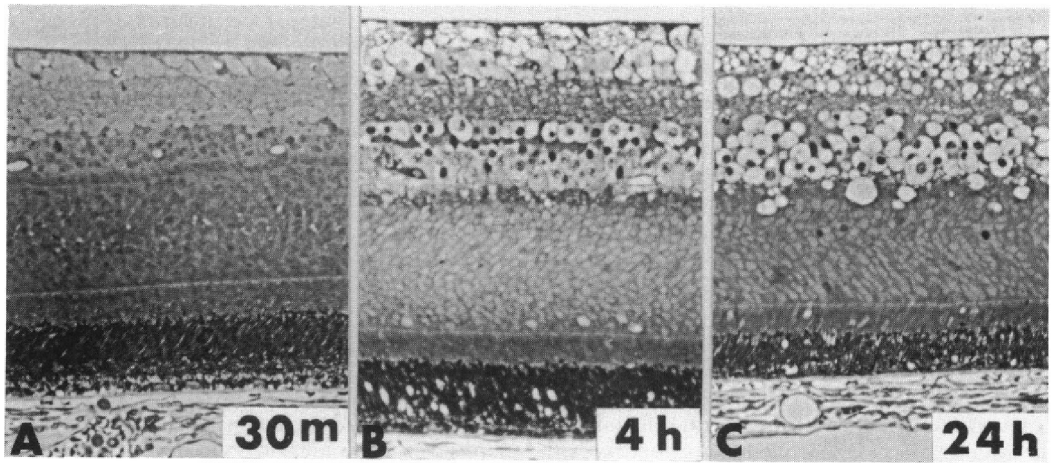

The classical presentation of a patient with a retinal artery occlusion is a sudden, painless, partial (BRAO) or profound (CRAO) visual loss. Visual field defect may be central

or sectoral. An afferent pupillary defect is usually present within seconds of a CRAO (Brown and Magaragal, 1982). The initial fundoscopic features may be unremarkable followed by a diffuse white appearance of the retina in the region supplied by the branch or central retinal artery. In CRAO, a cherry-red spot at the foveola is present due to incomplete hypoxia of the thin retina at the foveola which is supplied primarily by the choriocapillaris. The prognosis for BRAO is usually good when the fovea is unaffected, with approximately 80% of eyes achieving a final visual acuity of 6/12 or better (Brown et al., 1981). In contrast, the visual prognosis of CRAO is poor with 66% of eyes achieving a final visual acuity of 6/60 or worse (Brown and Magaragal, 1982). Currently there is no known effective treatment for CRAO (Fraser and Siriwardena et al., 2002).

1.4.2. Glaucoma

Glaucoma is a disease characterized by a combination of mid-peripheral visual field loss, structural changes to the retinal nerve fibre layer (thinning) and optic disc (excavation or cupping). Increased intra-ocular pressure (IOP) is considered a risk factor for the development of glaucoma. Glaucoma can be divided into two major subgroups: angle closure glaucoma (ACG), in which drainage of the aqueous humor through the trabecular meshwork is obstructed by apposition of the iris to the peripheral cornea; and open angle glaucoma (OAG), in which drainage of the aqueous humor through the trabecular meshwork is not obstructed by the iris, but IOP is increased because of increased intrinsic trabecular resistance to aqueous drainage. Both open-angle and closed-angle glaucoma can occur secondary to other ocular and systemic conditions. There is a further group of OAG patients, with characteristic optic nerve head and visual field changes, who nonetheless, have IOP measurements consistently within the normal range: this ‘normal tension glaucoma’(NTG) subgroup constitutes a variable proportion of the OAG patient population.

Glaucoma is the second leading cause of blindness globally (Roodhooft, 2002) and in the UK (Bunce and Wormald, 2006). The prevalence of glaucoma in 2010 is estimated to be 2.6% globally and this is expected to rise to 2.8% by 2020, because of the changing world demographic (Quigley and Broman, 2006). OAG is anticipated to continue to be the most common form of glaucoma in the developed world. This section will focus on an overview of primary open angle glaucoma (POAG).

The underlying mechanisms of the leading to the pathogenesis of POAG are not fully understood. Many risk factors have been associated with POAG including race (Buhrmann et

al, 2000; Tielsch et al., 1991), family history of POAG (Tielsch et al., 1994; McNaught et al., 2000; Wolfs et al., 1998), age over 50 years (Tielsch et al., 1991), elevated IOP (AGIS Investigators, 2000; Heijl et al., 2002; Gordon et al., 2002) and myopia (Mitchell et al., 1999).

The two main pathological features that define POAG are a characteristic pattern of damage to the optic nerve head with an associated pattern of visual field loss. Macroscopically, the optic disc in POAG becomes progressively more excavated as a result of a axonal loss, loss of the axonal myelin sheath posterior to the lamina cribrosa and posterior bowing of the lamina cribrosa (Radius and Pederson, 1984). Structural changes in the trabecular meshwork (Alvarado et al., 1984; Clark et al., 1995) is thought to contribute towards reduced aqueous outflow, and an increase in the IOP in most patients.

In glaucomatous human eyes and experimental animal models of glaucoma, it has been widely documented that degenerative retinal ganglion cells undergo apoptosis, (Kerrigan et al., 1997; Quigley et al., 1995; Garcia-Valenzuela et al., 1994; Garcia-Valenzuela et al., 1995) a slow progressive non-necrotic process of programmed cell death that is characterized by DNA cleavage by endonucleases known as caspases, chromosome clumping, cytoskeletal degeneration, cell shrinkage and plasma membrane blebbing followed by the phagocytosis of the cell by neighbouring phagocytic cells (Kerrigan et al., 1997; Okisaka et al., 1997; Tezel and Yang, 2004; Tatton et al., 2003). The underlying mechanisms that induce retinal ganglion cell apoptosis, and leads to the progression of glaucomatous optic neuropathy is unclear, but is believed to be multifactoral. These mechanisms can be broadly categorized into three groups: mechanical, biochemical, and vascular. The mechanical hypothesis of glaucomatous optic neuropathy suggests that the blockade of axoplasmic flow as a result of increased IOP impedes the transport of trophic factors, such brain-derived neurotrophic factors essential for retinal ganglion cell (RGC) viability (Lampert et al., 1968; Anderson and Hendrickson, 1974; Minckler et al., 1976; Quigley et al., 2000; Johnson et al., 2000; Pease et al., 2000). Additionally, compression and shearing of the ganglion cell axons could be caused by pressure induced structural distortions of the lamina cribrosa (Morgan et al., 1998). Numerous biochemical mechanisms have been implicated in the pathogenesis of glaucomatous optic neuropathy such as elevated glutamate as a result of excitotoxicity (Dreyer et al., 1996; Vorwerk et al., 1999; Levkovitch-Verbin et al., 2002; Wamsley et al., 2005; Lipton, 2003), oxidative stress and free radical damage as a result of mitochondrial dysfunction (Tatton et al., 2001; Tezel et al., 2005; Abu-Amero et al., 2006; Gherghel et al., 2005; Ferreira et al., 2004; Carelli et al., 2004), raised inflammatory cytokines (Yan et al.,

2000; Pang et al., 2005) and altered autoimmune status within the retina (Joachim et al., 2005; Kremmer et al., 2001; Wax et al., 1994; Tezel et al., 1999). The "vascular theory" of glaucoma implicates chronic hypoxia due to vascular dysfunction and reduced retinal blood flow (Hayreh, 1985; Osborne et al., 2001; Flammer, 1994; Chung et al., 1999; Tezel and Wax, 2004; Cioffi et al., 2004)(possibly due to compression of the capillaries [Findl et al., 1997; Pillunat et al., 1997]) in the pathogenesis of glaucomatous optic neuropathy.

A number of tests have been developed to complement the clinical evaluation of the patient in order to confirm the diagnosis of glaucoma, to monitor its progression/efficacy of treatment. Optic nerve head and retinal nerve fibre layer analysis is an integral part of the evaluation of glaucoma and is typically performed by stereo biomicroscopy. The characteristic changes of the optic disc in glaucoma are focal, or generalized, excavation of the neuroretinal rim which may be associated with optic disc haemorrhage(s), blood vessel baring and/ or bayoneting, slit-like defects in the retinal nerve fibre layer, and peripapillary atrophy.

1.4.2.1. Visual Field Assessment

Visual field testing is the mainstay of assessing the visual function of individuals with suspected glaucoma to establish a diagnosis, and for those with glaucoma it is used to determine the severity and monitor the progression of the disease. A normal visual field test indicates the presence of a high proportion of functioning retinal ganglion cells (Sample and Johnson, 2001). The essence of a visual field test is to present a light stimulus of a given intensity and size onto a background of standard luminance. The threshold light intensity eliciting a response to the stimulus indicated by the patent is measured at points throughout the field of vision. Currently, the standard achromatic automated perimetry (SAP) is the most commonly performed visual field test in glaucoma, and is considered to be the gold standard for assessing visual function in glaucoma (Delago et al., 2002). SAP is performed with one of four threshold tests. The 24-2 threshold measuring test pattern, a commonly used test for glaucoma, consists of 54 stimulus locations covering the central field (24 degrees temporally, superiorly and inferiorly; 30 degrees nasally) placed at 6 degree intervals vertically and horizontally. SAP test results, however, demonstrate long term fluctuation, particularly in regions with established visual field defects (Keltner et al., 2005; Artes et al., 2002), which means that glaucomatous progression is sometimes difficult to confirm. Fluctuation in SAP is multifactoral, and includes patient related factors such as performance, fatigue, learning

effects, changes in pupil size, incorrect refractive correction and true physiological variability. These drawbacks have led to improvements in the threshold test algorithms to improve its accuracy, repeatability and sensitivity. In particular, the application of the Swedish Interactive Threshold Algorithm (SITA), which is faster and demonstrates comparable reproducibility to the standard threshold test (Bengtsson and Heijl, 1998) has become a popular test of visual field and has been incorporated into the Humphrey Visual Field Analyzer.

Despite numerous enhancements to SAP a major limitation is that least 25% - 35% of the ganglion cells may be lost before SAP can detect functional damage (Harwerth et al., 2002) indicating that significant functional deficits are present before it could be detected. Recent advances in understanding selective ganglion cell loss in glaucoma has led to the development of other perimetry tests such as the short-wavelength automated perimetry (SWAP), frequency-doubling technology (FDT) perimetry, focussed on targeting individual ganglion cell sub-populations in the pursuit of earlier detection of glaucoma and reliable assessment of glaucomatous progression. These tests, however, have inherent limitations; SWAP, for example has been shown to have higher variability on repeated tests compared to SAP (Blumenthal et al., 2003; Wild et al., 1998). FDT perimetry has been reported to have high false-positive results in the presence of advanced cataracts and mild posterior sub capsular cataracts (Casson and James, 2006). Objective electrophysiological tests of visual function developed to detect glaucoma at an early stage have yet to be adopted for routine clinical use.

1.4.2.2. Optic Nerve Head Imaging

Imaging modalities such as stereoscopic optic disc photography, confocal scanning laser ophthalmoscopy (e.g. Heidelberg Retina Tomograph, HRT), optical coherence tomography (OCT) and scanning laser polarimetry (e.g. GDx VCC) have been developed to provide an objective and quantitative measurement of the optic nerve head and retinal nerve fibre layer. Each imaging modality have their merits and pitfalls. Stereoscopic optic disc photography has been commonly used to document the baseline appearance of the optic disc, and qualitatively identify progressive glaucomatous optic disc changes. It is however subjective, and there is reportedly significant interobserver variation (Azuara-Blanco et al., 2003; Jampel et al., 2009). It is also highly dependent on the quality of the images, which is influenced on the clarity of the ocular media and extent of the pupil dilation. However, recent

developments in digital stereoscopic optic disc analysis are more objective, reproducible, and may allow sharing of the optic disc image for teaching purposes (Sheen et al., 2004; Morgan et al., 2005). The HRT III, has been shown to have quite high sensitivity in discriminating normal from glaucomatous optic nerve heads (Zelefsky et al., 2006). Furthermore, the Confocal Scanning Laser Ophthalmoscopy (CSLO) ancillary study to the Ocular Hypertension Treatment Study (OHTS) underpinned the evidence-base for using imaging technology by demonstrating that abnormal changes of the ONH measured by the HRT were detected prior to visual field testing abnormalities (Zangwill et al., 2005). However, the early versions of the HRT had significant interoperator variability due to the subjective manual input of a contour line placed at the optic disc margin by the operator (Miglior et al., 2002; Garway-Heath et al., 1999; Iester et al., 2001). OCT has been shown to be as effective at differentiating between normal and glaucomatous eyes, as other imaging modalities, such as the HRT III and GDx VCC (Kanamori et al., 2006; Greaney et al., 2002; Zangwill et al., 2001; Medeiros et al., 2004). The value of OCT technology in monitoring the progression of glaucoma is presently uncertain due to a current lack of longitudinal studies with sufficient length of follow-up. Scanning laser polarimetry has been less commonly adopted in clinical practice and is susceptible to ocular media opacities and spurious non-RNFL (retinal nerve fibre layer) birefringence.

1.4.2.3. Evidence for the Importance of IOP in the Pathogenesis of Glaucoma

Several studies have shown that lowering IOP slows or prevents the progression of glaucoma in those with advanced glaucoma (Collaborative Initial Normal-Tension Glaucoma Study [CINTGS 1998a, 1998b] and Advanced Glaucoma Intervention Study [AGIS Investigators, 2000]), those with early to moderate glaucoma (Collaborative Initial Glaucoma Treatment Study [CIGTS Study Group, 2001] and Early Manifest Glaucoma Trial [Heijl et al., 2002; Leskea et al., 2003]), and those with high risk of developing glaucoma (Kass et al., 2002). Randomized controlled trials have shown that lowering IOP by 18% from baseline is associated with approximately 40% reduction in rates of worsening glaucoma over 5 years (Heijl et al., 2002; CINTGS 1998b; Leskea et al., 2003; CIGTS Study Group, 2001). Although these studies implicate IOP as an important factor in the pathogenesis of glaucoma, raised IOP is not an exclusive characteristic of glaucoma as some individuals have glaucomatous optic neuropathy with normal IOP and conversely some individuals have raised IOP without developing signs of glaucoma. The principal goal of current medical and

surgical treatment modalities for glaucoma is to preserve visual function by lowering of IOP. These include the use of topical medications, laser trabeculoplasty, filtration surgery or a combination of these.

1.4.2.4. Measurement of Retinal Blood Flow and Evidence for a Role in Glaucoma Pathogenesis

Clinical evidence indicating an ischaemic component in the pathophysiology of glaucoma include the association of vascular dysregulatory IOP independent factors in normal tension glaucoma such as migraine (Wang et al., 1997; Curseifen et al., 2000), Raynaud phenomenon (peripheral vascular disorders)(Gass et al., 1997; O'Brien and Butt, 1999), nocturnal hypotension (Hayreh et al., 1994), sleep apnoea (Girkin et al., 2006) and reduced cerebral blood flow (Sugiyama et al., 2006). These entities represent vascular dysregulation. Additionally, there is growing evidence to suggest that blood pressure and ocular perfusion is an important factor in the pathogenesis of POAG (Costa et al., 2009). Recent discoveries of increased concentrations of endothelin, a potent vasoconstrictor, in the aqueous humor of glaucoma patients (Iwabe et al., 2010); and hypoxia-inducible factor 1alpha (HIF-1alpha), a protein synthesized by cells in response to hypoxia, in the retina and optic nerve in post-mortem human glaucomatous eyes (Tezel and Wax, 2004) have added support to the role of chronic hypoxia or ischaemia contributing towards glaucomatous optic neuropathy (Hayreh, 1985; Osborne et al., 2001; Flammer, 1994; Chung et al., 1999). Retinal blood flow is dependent on the activity of the endothelial cells because they have no autonomic innervation. Endothelial cells release number of factors including endothelium derived vasoactive factors which regulates the tone of vascular smooth muscle. Vessel size is also regulated by neural and glial cells (neurovascular coupling)(Falsini et al., 2002).

Several techniques have been used to measure ocular blood flow. Fluorescein angiography has been used to measure mean retinal circulation transit time (Bjärnhall et al., 2007), arteriovenous transit time (Wolf et al., 1989) and to qualitatively assess the perfusion of the intraretinal and optic disc microvascular capillary beds (Spaeth, 1975; Schwartz, 1994). However, the relationship between transit times and regional retinal blood flow is not robust (Tomic et al., 2001). Blue field entopic technique measures leucocytic flow in the retinal perifoveal vessels. This method is subjective, relies heavily on the co-operation of the patient and it is unclear whether leucocytic flow is proportional to retinal blood flow

(Fuchsjäger-Mayrl et al., 2002). Laser Doppler velocimetry (LDV) determines the velocity of blood cells in larger retinal blood vessels using the optical Doppler shift of a coherent laser beam (Feke et al., 2006). Measurements of vessel diameter are required at selected measurement sites to determine volumetric blood flow. LDV is not able to measure blood flow in the optic nerve head. Laser speckle flowgraphy (LSFG)(Briers and Fercher, 1982; Tamaki et al., 1995; Tamaki et al., 1997) and laser Doppler flowmetry (LDF)(Riva and Falsini, 2008) provides an estimate of blood flow in the microcirculation of the retinal tissue illuminated by a coherent laser. These techniques require a clear media and for the subject to maintain perfect fixation. Further limitations of LSFG and LDF include its inability to measure flow in large retinal vessels, the ambiguity as to which capillary beds within the retina are being measured and whether they are pertinent to the pathogenesis of glaucoma (Caproli and Coleman, 2010). Colour Doppler imaging (CDI) measures erythrocyte velocity in the large ophthalmic vessels (such as the ophthalmic artery) and has been evaluated in glaucoma (Galassi et al., 1992). The relevance of ophthalmic artery velocity measurements is questionable since the ophthalmic artery perfuses other structures around the eye and has been shown to be unaffected when IOP is 45 mm Hg (Harris et al., 1996). Additionally, erythrocyte velocity may underestimate blood flow particularly in vasodilated vessels (Goebel et al., 1995). Furthermore, CDI measurements are highly variable and is dependent on the position of the probe (Caproli and Coleman, 2010). Despite new innovative technical advances in assessing ocular haemodynamics, there is no current gold standard for measuring ocular blood flow and ocular blood flow measurements are not currently considered suitable for the diagnosis and management of patients with glaucoma.

1.5. Retinal Oxygen.

1.5.1. Measurement of Retinal Oxygen.

The accurate quantification of retinal oxygen concentration in retinal tissues and blood vessels is currently not well established. A number of different approaches have been reported in the literature. In general, the techniques used to study retinal oxygen can be divided into invasive and non-invasive methods.

Invasive techniques include the use of oxygen sensitive microelectrodes (Briol et al., 2007; Stefánsson et al., 1992), phosphorescence quenching (Lo et al., 1996; Shonat et al., 1992; Zukerman, 1993) and functional magnetic resonance imaging (fMRI)(Duong et al., 2002). The invasiveness of these techniques has mostly limited its use to animal studies.

The mainstay of non-invasive retinal oximetry techniques involves the use of spectrophotometric systems, enabled by established knowledge of the optical properties of the haemoglobin derivatives, offers one of the most promising methods of safely deducing the oxygen saturation (OS) in the retinal tissues and vasculature. Many different spectrophotometric systems and analysis methodologies have been developed and tested. A brief overview will be discussed in later sections.

1.5.2. Principles of Photometric Oximetry.

1.5.2.1. Dual-Wavelength Oximetry.

Oximetry is defined as the measurement of the OS in either blood or in tissues. Prior to the measurement of blood OS, clinical hypoxaemia was traditionally detected by the presence of central or peripheral cyanosis by observing the colouration of the mucous membranes and the peripheral tissues. The colouration is related to the relative amounts of oxygenated and deoxygenated haemoglobin. However, it was shown that this clinical sign was a poor indicator of central hypoxaemia (Comroe et al., 1947) and more accurate measures of blood OS was required to clinically monitor patients.

The development of the photoelectric cell enabled the measurement of light absorption which contributed to the development of spectrophotometers. As a result, the spectrophotometric study of the extinction coefficients (a measurement of how much light is absorbed by a substance at a given wavelength) of reduced haemoglobin (Hb) and oxyhaemoglobin (HbO_2) was made possible; these measurements are central to the technique of oximetry.

The first documentation of the spectra of undiluted haemolysed and whole blood were made by Drabkin and Austin (1935) who was later able to demonstrate the applicability of the Lambert-Beer law in determining the OS of blood (Drabkin and Schmidt, 1945).

The Lambert-Beer law (Figure 1.14) in transmission blood oximetry assumes that for any given wavelength of light its absorption is dependent on the extinction coefficient of the blood solution (ε), its concentration or haematocrit (c) and the distance (d) the light has to travel through the solution (path length):

$$I_T = I_O \times 10^{-(\varepsilon \times c \times d)} \qquad \text{(Eq. 1.1)}$$

where, I_T is the amount of light transmitted through a solution and I_O is the amount of incident light.

Figure 1.14: The Lambert-Beer Law.

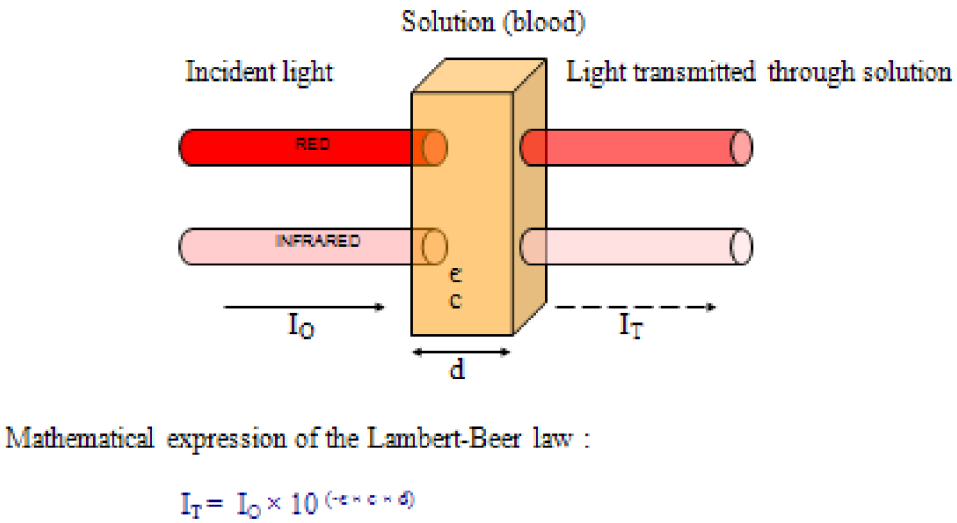

The optical density (OD) of a solution is a measure of its transmittance, and is defined by:

$$OD = -Log_{10}\left(\frac{I_T}{I_O}\right) = \varepsilon \times c \times d \qquad \text{(Eq. 1.2)}$$

where, I_T is the intensity of transmitted light (after passing through the solution), I_O is the intensity of incident light, ε is the extinction coefficeint of a solution, c is the concentration of the absorbing element in the solution, and d is the distance through the solution light has to travel (path length). Therefore the OD of a solution of blood is a function of its extinction coefficient, concentration and the path length the light has to travel.

The main absorbing component of human blood is haemoglobin, therefore its extinction coefficient is considered to be equal to that of haemoglobin. The extinction coefficients of Hb and HbO_2 have been extensively researched using various methodologies and spectrophotometric techniques. One of the most commonly used data on the extinction coefficients of Hb and HbO_2 is that published by van Assendelft (Figure 1.15)(van Assendelft, 1970). The haemoglobincyanide methods that were used to derive the extinction coefficients of the haemoglobin derivatives are today still recognized as the international standard for haemoglobinometry.

Figure 1.15: The molar extinction coefficients of deoxyhaemoglobin (Hb) and oxyhaemoglobin (HbO_2) derivatives as a function of wavelength.

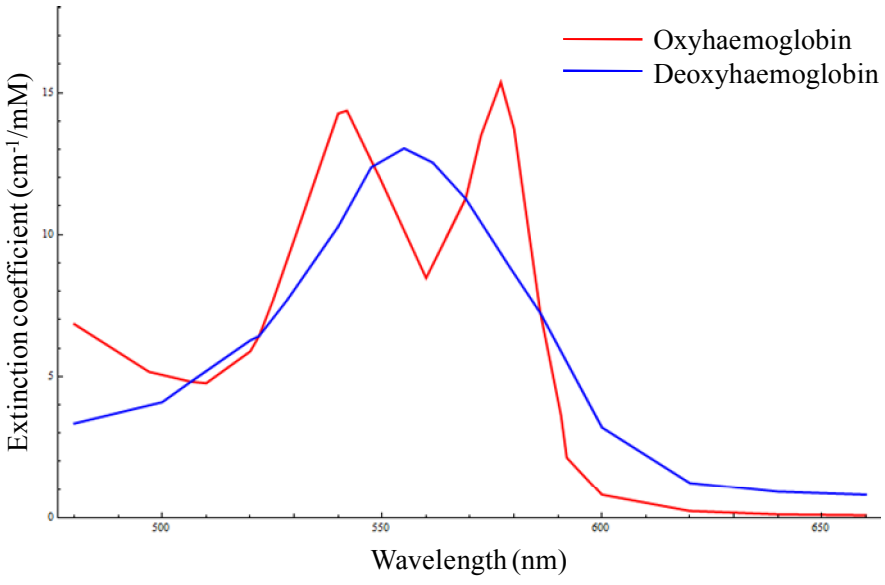

Kramer and Elam were able to demonstrate the linear relationship between the OS of blood and it absorption of red and infrared wavelengths of light (*see* Appendix 1 for the mathematical proof)(Kramer et al., 1951). This finding was pivotal in the development of clinical oximeters. Matthes and Gross (1939a, 1939b) were the first to demonstrate the use of an isosbestic wavelength (extinction of Hb and HbO_2 are equal) and an oxygen sensitive wavelength in the red and infrared regions respectively to compensate for variables such as the haematocrit, path length and light intensity. This technique of measuring the blood OS using an isosbestic and an oxygen sensitive wavelength is the basis of clinical dual-wavelength oximetry used today.

The integration of optical plethsmography (analysis of the pulsatile component of the arterial cycle) with oximetry enabled the development of pulse oximeters which are capable of measuring the arterial oxygen saturation by isolating the arterial signal from the venous, bone and tissue components (Aoyagi et al., 1974). The calibration of pulse oximeters are performed to this date using data acquired from normal subjects during induced hypoxia. That is, as soon as a constant state of hypoxia is achieved, the values of the red-infrared optical density ratios (ODR) are obtained in conjunction with the arterial blood gas measurements. Unfortunately, these calibration tests were carried out at arterial blood gas saturations of greater than 70%, the lowest tolerable state of systemic oxygenation in humans. At oxygen saturations below 70% the calibration has been estimated by linear interpolation and therefore the accuracy below this level is questionable. Sarnquist and Todd (1980) reported that pulse oximeters were overestimating the true oxygen saturation with an average reading of 70% when the true OS was 50%. This overestimation is thought to be caused by the scattering of red/infrared light in the blood vessels (Shimada et al., 1984).

The cuvette oximeter (CO-oximeter) represents the current gold standard method for photometric oximetry and is used to calibrate pulse oximeters. It is also an essential component in blood gas analyzers commonly used in the intensive care setting. This device uses multiple wavelengths to measure the OS of blood and concentrations of other haemoglobin derivatives in addition to Hb and HbO_2. Importantly, CO-oximeters achieve a high degree of accuracy because the blood is analyzed *ex vivo* under strictly controlled conditions. In addition, most CO-oximeters haemolyse the blood sample prior to oximetric measurements to remove the confounding effects of light scattering.

1.5.2.2. Light Scattering and its Implications on Photometric Oximetry.

Kramer and Elam (1951) were the first to demonstrate that although the Lambert-Beer law is true for solutions of haemoglobin it fails to accurately describe the transmission of light in whole blood and that OS had a non-linear relationship with haematocrit and optical path length. The main contributing factor to this phenomenon is thought to be the scattering effects of blood. As a consequence a number of *in vitro* studies, involving the nature of light propagation through whole blood, have attempted to describe the scattering effects of whole blood. The scattering of light in whole blood is thought to be caused by the red blood cells (RBC) and the refractive changes at the RBC-plasma interface (Zdrojkowski and Pisharoty, 1970; Johnson, 1970; Longini and Zdrojkowski, 1968) which has been shown to be dependent on wavelength, haematocrit and the path length (Johnson, 1970; Loewinger et al., 1964; Anderson and Sekelj, 1967).

Three theories have found general acceptance in its application to describe the scattering effects of whole blood. The photon diffusion theory describes the transport characteristics of wave intensities and has similarities to the diffusion of molecules in liquids. Its purpose has been used describe the propagation of photons (from collimated light) through highly scattering, dense media with a short mean free path which can be approximated by "random walk" of photons. Zdrojkowski and Pisharoty (1970) applied the theory to derive an optical density equation of whole blood. The Kubelka-Munk theory (Kubelka and Munk, 1931) describes the absorption and scattering properties of a homogenous slab of pigmented material providing a reflectance model. It makes no assumptions (phenomenological) on the characteristics of light absorption and scattering. The "two-flux" component of the theory only considers the diffuse radiation reflected from the material and assumes that the radiation scatters in two opposite directions through the medium. The Kubelka-Munk theory was applied by Janssen (1972) to assess the absorption and scattering characteristics of whole blood. A number of studies (Loewinger et al., 1964; Anderson and Sekelj, 1967) have adopted and supported Twersky's theory of multiple scattering (Twersky 1962, 1970a, 1970b), which describes the nature of light transmission in biological suspensions containing large, low-refracting and absorbing particles (red blood cells) using separate absorbing and scattering terms. In its simplest form the scattering phenomenon can be incorporated into the Lambert-Beer equation.

The *in vivo* application of an oximetry model to account for the wavelength dependent scattering component was reported by Pittman and Duling (1975a) who adopted Twersky's multiple scattering theory and demonstrated that a three-wavelength technique could be used to calculate the scattering component of blood in addition to the oxygen saturation. These techniques were applied to OS measurements on small blood vessels in hamster retractor muscles with a reported accuracy of 4.8% oxygen saturation (Pittman and Duling, 1975b).

One of the main challenges for *in vivo* oximetry has been to implement the theories and findings that account for light scattering to obtain accurate measurements of human blood oxygen saturation. This is particularly relevant in retinal oximetry.

1.5.3. Principles of Spectral Imaging

Spectral imaging is a relatively new technique which combines the capabilities of spectroscopy and imaging. Spectroscopy is an established method of analyzing materials by means of acquiring and identifying the spectral signatures of its constituents using various combinations or sequences of wavelengths. The structure of atoms and molecules is directly related to its spectrum. Various wavelengths in the electromagnetic spectrum can be used which is absorbed by molecules, resulting in atomic vibrations and rotations specific to the inter-atomic bonds. A continuous series of specific wavelengths is able to provide characteristic spectrum or spectral signature which defines of the structure of a given molecule. Spectral signatures can be obtained by acquiring and analyzing a series of wavelengths reflected or transmitted through matter to enable the identification of its constituent substance(s). Figure 1.16A illustrates the collection of a spectral signature from a single point of an object (the fundus is used in this example) using visible light. A series of multiple wavelengths are used which defines its spectral resolution and range; this determines its ability to identify specific molecules. However, the main limitation of this technique is the lack of spatial information which has restricted the use of spectroscopy to a specific subset of scientific disciplines.

Imaging is a method of obtaining spatial and temporal information from a scene. Currently, conventional digital imaging techniques involve the use of a digital camera (such as a charged-coupled device) to record data. The information from a scene is represented in

the form of a two dimensional array of intensity values. In grayscale (monochromatic) images, the intensity of each pixel represents a single wavelength (Figure 1.16B) and therefore extraction of spectral information is not possible.

Spectral imaging addresses the shortcomings of spectroscopy and imaging by combining the two methodologies to generate a number of grayscale images at various wavelengths thereby providing both spectral and spatial information. It can be broadly categorized into two distinct modalities: multispectral and hyperspectral imaging which can be performed invasively and non-invasively. Multispectral imaging uses a number of non-contiguous wavelengths at large bandwidths apart (Figure 1.16C). In contrast, hyperspectral imaging uses a large number of contiguous wavelengths at narrow bandwidths (high spectral resolution, Figure 1.16D). A multispectral or hyperspectral imaging system is capable of producing a reflectance or transmission spectrum of each pixel within the image enabling the identification of substances by means of identifying its respective spectral signature.

Both multispectral and hyperspectral imaging systems are comprised of a number of empirical components as depicted in Figures 1.16C and 1.16D. Light from a source can be dispersed into the required wavelengths before or after it reaches the scene. The reflected or transmitted light from the scene is collected into a detector, such as charged-coupled device. The subsequent series of images are subsequently processed and analyzed to detect substances contained within the scene based on the spectral signature of each pixel.

The performance of a spectral imaging system is principally dependent on a combination of its spectral and spatial resolution. Hyperspectral imaging provides a more detailed pixel spectrum which enables more information to be obtained for accurate classification and quantification compared to a multispectral pixel spectrum. A higher spatial resolution influences the accuracy of the spectral analysis by reducing the spectral distortion incurred by other substances contained within each pixel. Modern hyperspectral imaging systems usually record a stack of time-sequential images onto a two dimensional detector array, at a sequence of wavelengths forming a hyperspectral data cube. The spectral dispersion technique can be attained through a variety of filtering methods which have specific advantages and disadvantages. Discrete filters uses a succession of narrow band filters inserted in the optical path of the imaging system. Tunable filters, comprising a family of acusto-optical tunable filters (AOTFs), liquid crystal tunable filters and interferometer filters, have no moving parts and are able to be electronically tuned to any particular

wavelength. Conventional discrete filter wheels are slow, contain bulky mechanical parts, limited in colour palette, and less reliable than their electronic tunable filter counterparts. Spectral imaging systems incorporating tunable filters enables the rapid access of specific wavelengths at random. However, tunable filters have a limited spectral range, are sensitive to temperature and polarization and can attenuate the transmission of light. AOTFs have an additional effect of shifting the image during wavelength scanning.

Hyperspectral imaging requires sensitive detectors and powerful computers to enable fast processing of the images that comprise the data cube. The advancement of computer hardware and improved detectors has expanded its use from the remote sensing disciplines to laboratory and clinical research.

Figure 1.16: Principles of spectral imaging. The fundus is used as an example in the illustrations. ***A***. In spectroscopy, the spectrum at every wavelength is recorded at a single point in the scene. ***B***. In conventional grayscale imaging, the scene is projected onto detector which records the light intensity of each pixel on the 2 dimensional array. ***C***. In multispectral imaging, the scene is either illuminated by several non-contiguous wavelengths or the reflected light is filtered into several non-contiguous wavelengths by a wavelength selector. The detector records the intensity of each pixel at the respective wavelengths. ***D***. In hyperspectral imaging, the scene is either illuminated by numerous contiguous wavelengths or the reflected light is filtered into numerous contiguous wavelengths by a wavelength selector which enables the detector to record a spectrum for each pixel in the entire image plane.

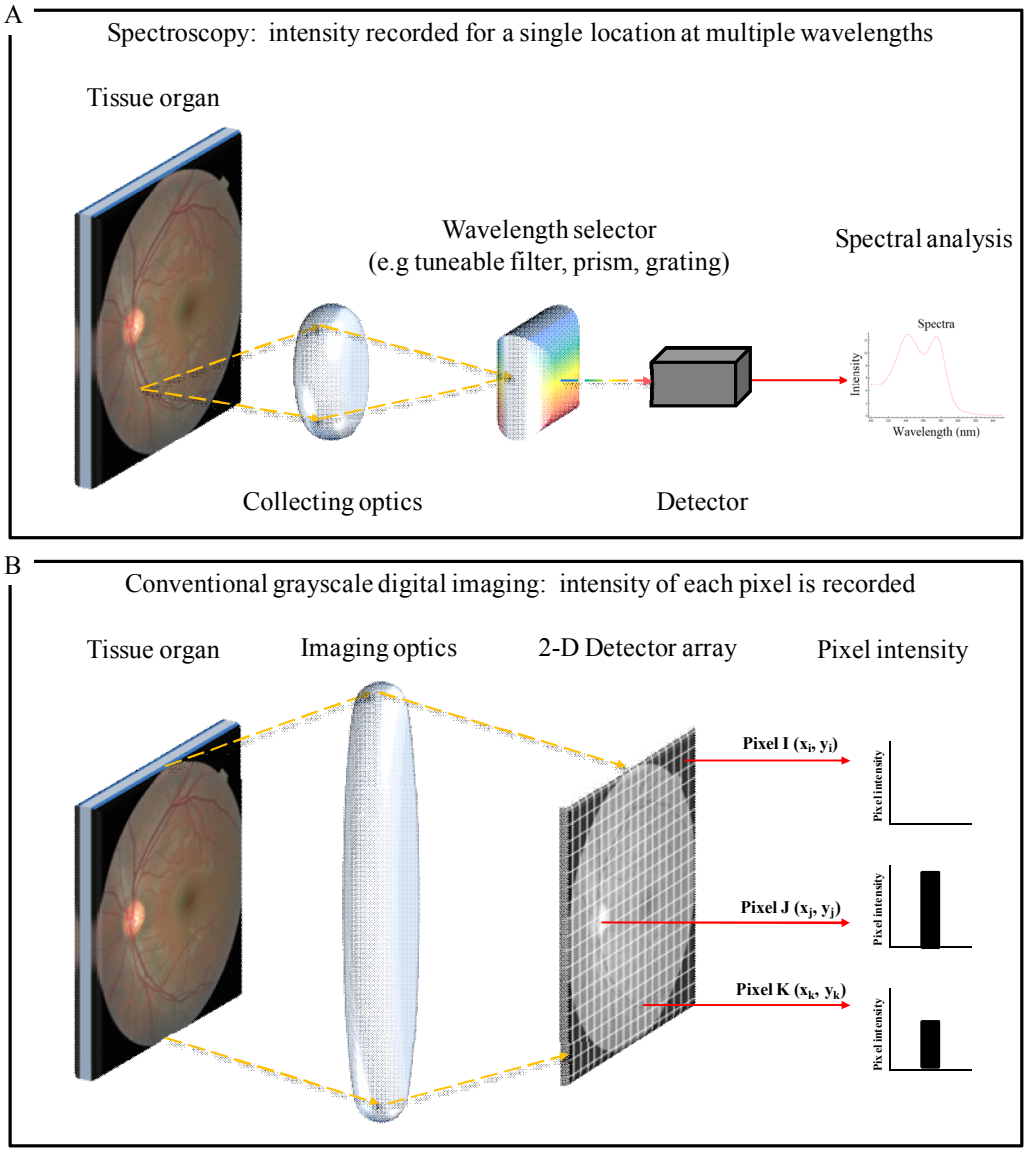

C

Multispectral imaging:
intensity recorded at multiple non-contiguous wavelengths

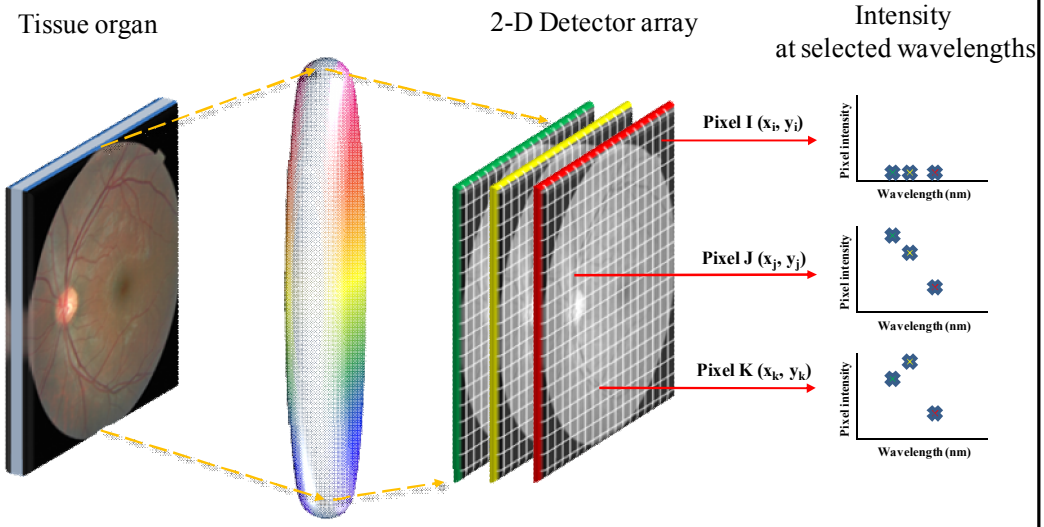

Imaging optics and wavelength selector
(non-contiguous wavelengths selected)

D

Hyperspectral imaging:
intensity recorded at multiple contiguous wavelengths

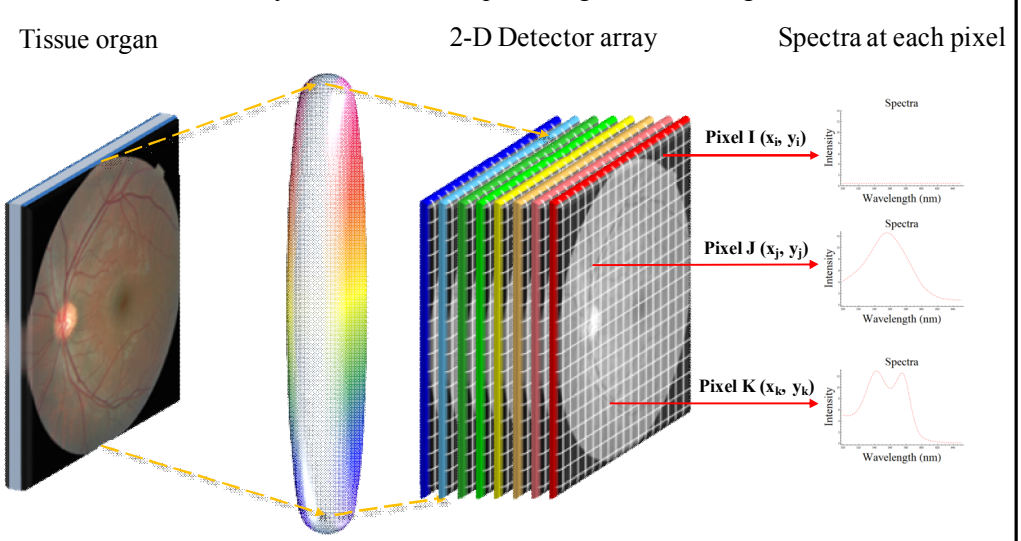

Imaging optics and wavelength selector
(contiguous wavelengths)

1.5.4. Principles of Optical Retinal Oximetry.

The optical window of the eye encompasses a broad range of wavelengths between 400 to 1400 nm (Boettner and Wolter, 1962) enabling these wavelengths to pass through the refractive components of the eye with minimal attenuation and reach the retina. In its simplest form, retinal oximetry requires an imaging system which captures images of the retina at multiple wavelengths of light. The wavelengths used in retinal oximetry (and other imaging modalities such as retinal OCT) is therefore limited by the optical window of the eye. The OD of the retinal vessels at the chosen wavelengths can be estimated using various approaches. The most common technique is to calculate the negative logarithmic ratio of the light intensity at the centre of the retinal vessel to the light intensity adjacent to the target retinal vessel:

$$OD_{vessel} = -Log_{10}\left(\frac{I_V}{I_R}\right) \quad \text{(Eq. 1.3)}$$

where I_V and I_R are the intensity of light reflected from the retinal vessel and adjacent retina respectively. The OD of the retinal vessels at the chosen wavelengths can subsequently be used to calculate the oxygen saturation, e.g. ODR of two wavelengths.

1.5.5. Retinal and Choroidal Oximetry using Spectrophotometric Techniques.

The various retinal oximeter designs that have been reported have evolved with the availability of newer technologies from standard photography, to digital photography, to the use of imaging spectroscopy and multispectral confocal slit-lamp ophthalmoscopes. Numerous dual and multiple wavelength combinations sensitive to changes in oxygen saturation have also been utilized. Subsequently, a variety of retinal oximetry analysis techniques have been described. A brief overview of influential spectrophotometric retinal oximetry studies will be described in this section with a focus on the instrument design, oximetry model and experimental/clinical findings.

1.5.5.1. Laing: The Choroidal Eye Oximeter and Photographic Eye Oximeter.

Laing and Cohen (1975) developed a "Photographic Eye Oximeter" comprising of a modified Zeiss fundus camera with a dichroic beam splitter and narrow-band interference filters that divided the reflected light from the fundus into two wavelengths centred at 470 nm (oxygen sensitive) and 515 nm (isosbestic). The retinal images at these two wavelengths were simultaneously recorded on photographic film which were scanned with a modified microdensitometer and the film's transmission at selected parts of large retinal arteries were measured. *In vivo* animal experiments were performed on eight rabbits whose systemic OS was reduced to varying levels of oxygenation determined by clinical oximetry measurements of femoral artery blood samples. Retinal photographs were captured at various oxygen saturations and the ODR of the selected retinal arteries at the two wavelengths were plotted against the measured systemic OS. An experimental calibration curve was created by least mean square fitting. The accuracy of this technique was reported to be better than 1% oxygen saturation.

Cohen and Laing (1976) subsequently modified their two wavelength Lambert-Beer oximetry model adopting functions developed by Twersky (1962, 1970a, 1970b) to account for the effect of vessel diameter and haematocrit on light scattering in blood. The double pass transmission of light passing through the blood column, reflecting from the retina and passing through the blood column a second time was also incorporated into the algorithm. The theoretical retinal oximetry model was thought to be able to correct for variations in haematocrit and vessel diameter with minimal changes in the OS. When applied to experimental calibration data (Laing and Cohen, 1975) the theoretical oximetry model was comparable at high oxygen saturations; however at low oxygen saturations the theoretical calibration line underestimated the actual oxygen saturations by up to 20%. Results of OS measurements in humans using the "Photographic Eye Oximeter" were never reported.

1.5.5.2. Hickam: The Photographic Oximetry Technique.

Hickam et al. (1963) described a photographic method to estimate the OS of the retinal veins in humans. Fundus photographs were obtained using two cameras containing different combinations of filters. A Bausch and Lomb fundus camera was modified with two

broadband filters, with wavelengths centred at 640 nm (oxygen sensitive) and 800 nm (isosbestic), enabling the capture of red-infrared retinal photographs. A second Zeiss fundus camera was adapted to obtain a combination of red-green (centred at 505 nm [isosbestic wavelength] and 640 nm) retinal photographs using a Zeiss microscope beamsplitter. The projection of the photographic negative onto a screen with a small perforation enabled density measurements to be made, using a photocell connected to a photometer, on the retinal vessels and optic disc adjacent to the vessel. The logarithmic sensitivity of photographic film enabled calculations of the vessel optical density which was performed for all the wavelengths. The ODR of two to three retinal veins at the optic disc in each eye of human subjects were calculated from red-infrared and red-green wavelength combinations.

The estimation of the OS in the retinal veins was made using data from *in vivo* human calibration experiments. This involved measuring the ODR of retinal arteries in human subjects whose arterial OS were altered by changing the inspired oxygen content with the use of various gas mixtures of oxygen and nitrogen. The OS of arterial blood was determined by analysis of brachial artery blood samples at the time of imaging and was monitored during the imaging using an ear oximeter. Several arteries were measured in each subject to derive a mean arterial ODR in each subject at various degrees of systemic oxygenation. Linear regression analysis was performed to generate a linear calibration curve describing the relationship between oxygen saturation of the arteries and red-infrared and red-green optical ODRs. The regression lines were used to calculate the retinal venous OS from the measured red-infrared and red-green ODRs. The mean (± SD) retinal venous OS was reported to be 59% (± 11%) in normal human subjects (n = 55).

In vitro validation experiments were performed by obtaining red-infrared images of heparinised venous blood samples from 4 normal subjects. The oxygenation of the venous blood was altered by exposing the venous blood to air and mixing it with venous blood not exposed to air. The OS of the sample was determined using a photometric method (Hickam and Frayser, 1949). Twenty venous blood samples with varying oxygen saturations were inserted into glass capillaries (internal diameters of 250 μm and 500 μm), placed in front of a white background and imaged through a +50D lens. A linear relationship between ODRs and the measured OS of the blood samples was confirmed. The standard deviations of the ODRs from the measured OS were relatively small: 6% and 9% OS in 500μm and 250μm glass capillaries respectively. The oximetry technique was limited by the influence of vessel diameter on the regression slopes which affected the accuracy of the OS estimation. A

decrease in the path length of light resulted in a larger change in the red-infrared ratio for a given change in OS. This was thought to result from a disproportionate change in the haemoglobin extinction coefficients at specific wavelengths for a given change in path length.

In vivo validation of the oximetry technique was performed by measuring the retinal venous OS in humans whilst breathing various mixtures of carbon dioxide and oxygen induce systemic hypoxia and hyperoxia (Frayser and Hickam, 1964). Oximetric changes in the retinal veins were detected and correlated with the concentration of inspired oxygen. However, no correction for vessel diameter (influenced by the concentration of carbon dioxide) was made in the calculation of the OS.

1.5.5.3. Delori: The Three-Wavelength Photoelectric Retinal Vessel Oximeter.

Delori (1988) described a three wavelength method to determine the OS in retinal vessels using a photoelectric oximeter. The "Retinal Vessel Oximeter" comprised of a fundus camera integrated with three interference filters (mounted on a filter wheel), a photomultiplier and a photocathode. This enabled reflected light from a small area of the fundus (1500μm in diameter) to be filtered into wavelengths centred at 558, 569 and 586 nm. A slit, 530 μm in length, scanned a selected part of the retinal vessel generating thirty-two vessel profiles at each wavelength during a period of 1.6 seconds which were subsequently aligned. The estimation of the light transmission through the vessel, using the average vessel and background fundus reflectance, enabled the calculation the optical density of the vessel at each wavelength.

The retinal vessel oximetry algorithm, incorporating the vessel transmission measurements and published haemoglobin extinction coefficients (van Assendelft, 1970), was based on the methods described by Pittman and Duling (1975a). Three simultaneous equations for each wavelength were solved to create a three wavelength oximetry algorithm. The effects of haemoglobin concentration, vessel diameter, light scattering by the red blood cells and fundus pigmentation were integrated into the algorithm.

In vitro validation experiments were performed using blood obtained from two human subjects and circulated through glass capillaries (internal diameters of 50 μm, 100 μm and

150 μm) immersed in a water-filled artificial eye model eye containing various reflecting backgrounds. The OS of the washed blood was altered using either a mixture of oxygen and nitrogen gas or by mixing it with sodium dithionite (complete desaturation of blood). Measurements of the OS using the imaging system were compared to the measured OS by a CO-oximeter. Multiple regression analysis indicated an accurate correlation between the calculated and measured OS. The three wavelength oximetry model was reported to be most accurate in the range of 50 - 100%; in the range between 0 - 50% there was a tendency towards overestimating the measured OS. Blood flow rates between 1 – 90 μlitre/min did not significantly affect the calculated blood oxygen saturation.

In vivo studies of 22 normal human subjects involved the oximetry measurements in 85 retinal arteries and 102 retinal veins. The mean (± SD) calculated OS was 98% (± 8%) and 45% (± 7%) respectively. Variability in the oximetry measurements were thought to be due to several factors: eye movements, fundus pigmentation, effect of the central retinal vessel reflex, vicinity of neighbouring structures such as the optic disc, and pulsatile changes of the vessel diameter during the cardiac cycle.

The three-wavelength oximetry technique was applied in a clinical study of seven patients with unilateral optic disc atrophy with nerve fibre layer defects (Sebag et al., 1989). The OS of several temporal and nasal retinal veins were compared to corresponding retinal veins in the unaffected fellow eye. Retinal arterial OS was not measured but was assumed to be constant at 97%. The mean arterio-venous difference in OS was significantly higher in the affected eye (indicating lower venous OS) compared to the fellow eye. This finding, in conjunction with laser Doppler velocimetry findings of reduced blood flow, indicated a reduction in the supply of oxygen in affected eyes.

1.5.5.4. Schweitzer: The Imaging Ophthalmospectrometer.

Schweitzer et al. (1992) developed an imaging ophthalmospectrometer, which consisted of a modified fundus camera with an attached spectrograph. The instrument illuminated the retina with a small (40 μm x 1.5 mm) slit of light and scattering by the ocular media was reduced by the confocal arrangement. A grating component within the spectrograph spectrally dispersed the reflected light from the fundus. An intensified charged-coupled device was used to capture the reflectance spectrum (spectral range from 450 to 700

nm; spectral resolution of 2 nm) from the spectrograph in 10 ms which was then used to perform quantitative oximetric measurements of the retinal blood vessels (Schweitzer et al., 1999). The complex oximetry model used was based on detailed research on the properties of fundal reflectance and the multiple light pathways in the eye (Hammer et al., 2001).

In vitro experiments, using whole blood contained in quartz cuvettes of varying thicknesses, studied the influence of various simulated physiological conditions on the behaviour of the light paths in the retina (Schweitzer et al., 1999). At wavelengths between 450 nm and 700 nm the light transmission through blood was reported to decrease with increasing cuvette thicknesses and haematocrit. The reflectance spectrum of flowing blood was found to increase in proportion to an increase in blood velocity of up to 6mm/s. The characteristics of internal reflectance of light were also described. At wavelengths between 500 nm to 600 nm (absorption-dominated wavelengths) the internal reflectance was found to be independent on cuvette thickness. At wavelengths between 600 nm to 700 nm (scattering-dominated wavelengths) the internal reflectance increased with increased cuvette thickness.

An oximetry algorithm was developed using wavelengths between 510 nm and 586 nm where the internal reflectance was assumed to be constant and the light transmission is solely dependent on the vessel size and the haematocrit. The transmission and internal reflectance spectra of fully oxygenated and deoxygenated whole blood that were determined under experimental conditions were incorporated into the oximetry algorithm in place of published extinction coefficients of Hb and HbO_2 (Schweitzer et al., 1999). Several other parameters were taken into account including the vessel size, haematocrit, reflectance of the fundus background and specular reflection of light. Seventy-six equations, obtained from each wavelength, were iteratively solved to calculate a number of unknown parameters which included the OS (Thamm et al., 1998).

In vivo measurements of retinal vessel oxygen saturation were performed using the oximetry algorithm in 30 eyes of healthy subjects (Schweitzer et al., 1999). The mean (± SD) OS of 126 retinal arteries and 139 retinal veins were 92.2% (± 4.1%) and 57.9% (± 9.9%) respectively. The OS measured at points along the vessel away from the optic disc showed that the arterial oxygen saturation was constant up to a distance of 3 disc diameters. However, the retinal venous OS was found to be significantly lower at 1 disc diameter from the optic disc compared to the OS measurements performed at 2 disc diameters.

Clinical studies using the oximetry technique was applied to compare patients with dry (n = 32 eyes) and wet (n = 14 eyes) age-related macular degeneration to a control group comprising of the offspring of the ARMD patients (n = 30 eyes) and normal subjects (n = 21 eyes)(Schweitzer et al. 2000, 2001). The mean OS of the central retinal arteries were not significantly different between the compared groups whereas mean central retinal venous OS was significantly higher in the patients with age-related macular degeneration compared to the controls.

1.5.5.5. Michelson: Retinal Oximetry using the Imaging Ophthalmospectrometer in Glaucoma.

Michelson and Scibor (2006) used the imaging ophthalmospectrometer to compare the oxygen saturation of selected retinal vessels between patients with primary open-angle glaucoma (POAG) and a control group of normal subjects. Fifty-eight normal subjects, 49 patients with "normal tension POAG" and 45 patients with "high tension POAG" were recruited. OS measurements were made at the supero-temporal retinal arteries and veins 1-3 mm from the disc margin. A simplified oximetry model was used to calculate the OS which compensated for light scattering by the blood cells and retinal tissues, and light absorption by melanin in the retinal pigment epithelium and choroid (Hammer et al., 2002). The reflectance spectra of the analyzed retinal vessel was transformed linearly such that the reflectance values at the isosbestic wavelengths (522nm, 569nm and 586nm), were mapped onto the isosbestic reflectance values of the reference spectra (determined experimentally). This was assumed to correct for the influence of light scattering and absorption by melanin on the measured vessel reflectance. A fourth measuring wavelength (560nm), whose reflectance value was assumed to be linearly related to the OS, was used to calculate OS of the retinal vessel.

The mean (± SD) retinal arteriolar and venular OS in the control group of normal subjects were 92.3% (± 3.4%) and 55.7% (± 6.8%) respectively. Repeatability of the retinal arteriolar OS measurements was demonstrated, however, the retinal venular OS were found to be more varied. The mean (± SD) retinal arteriolar OS in eyes with "normal tension POAG" [89.7% (± 5.4%)] was significantly lower than the control group, no difference was not found between the "high tension POAG" group [91.4% (± 4.0%)] and the control group.

The mean (± SD) retinal venular OS in the "normal tension POAG" [56% (± 8.3%)] and "high tension POAG" [58.3% (± 10.5%)] groups were not significantly different to the control group. Further analysis of the oximetry data showed that there was a significant correlation between the OS in the retinal arterioles and the neuroretinal rim area measured by HRT, such that a lower OS was associated with smaller rim areas. No significant relationship between the venular OS and neuroretinal rim area was found.

1.5.5.6. Denninghoff: The Scanning Laser Eye Oximeter and Intravitreal Retinal Oximeter.

Denninghoff et al. developed an "Eye Oximeter" consisting of four diode lasers emitting wavelengths centred at 629, 678, 821 and 899 nm (Drewes et al., 1999). The wavelength selection was influenced by complex theoretical calculations and analysis of the optimal wavelength combinations for retinal vessel oximetry (Smith, 1999). Specular reflection in the vessel wall, thought to contribute to errors in the oximetry calculation, was reduced using a horizontal polarizer positioned in front of the detector (Denninghoff and Smith, 2000). Calibration of the modified Eye Oximeter involved a series of model eye experiments using whole human blood from one human subject which was then modified to create blood samples of varying haemoglobin concentrations (Drewes et al., 1999). The OS of the blood samples were altered by mixing with various combinations of nitrogen and oxygen gas concentrations providing a range of saturations from 6% -87% which was verified using a CO-oximeter. The blood samples were injected into micropipettes of varying internal diameters (110 – 268 μm) and placed in front of a 100% reflective *Spectralon* background within a model eye filled with index matched fluid. The extinction values of the various combinations of blood samples in the model eye were determined at the four wavelengths (629, 678, 821 and 899 nm). An oximetry model based on the Lambert-Beer law was derived which accounted for the wavelength dependence of red blood cell scattering, haematocrit and the path length of transmitted light. The accuracy of the oximetry model was determined by comparing the mean calculated OS to the measured OS of the blood samples. The reported error was small at measured oxygen saturations of 83% (± 4% error) but increased with lower oxygen saturations to a maximum at measured oxygen saturations of 0% (± 52%). Retinal vessel measurements using the modified Eye Oximeter was only performed on one human subject. The mean oxygen saturation of the retinal veins and

arteries on the optic disc were 65% and 101 - 102% respectively. The mean oxygen saturation in the retinal veins and arteries away from the optic disc were 63% and 98% respectively. Variations in the fundal background reflectivity were acknowledged by the authors to contribute to calculation errors.

Salyer et al. (2006) explored the potential of intravitreal illumination on retinal oximetry. An intravitreal light source attached to a scanning monochromator was used to obliquely illuminate the retina. The advantage of this technique was to remove the confounding effects of specular vessel reflection and double-pass light paths on the oximetry calculation – although paracentral reflexes were evident in some vessels. Two anaesthetized pigs were subjected to graded hypoxia (from 100% to 50%) and multispectral images of a small section of the fundus containing a selected retinal artery and vein were captured using a digital camera. The OS in the aorta and inferior vena cava were measured using a CO-oximeter at the time of retinal vessel measurements. The monochromator enabled intravitreal illumination of the fundus section with wavelengths of light ranging from 420 nm to 700 nm in 10 nm steps. Sequential multispectral fundal images were captured in synchrony with the cardiac cycle which minimized the effect of changing vessel diameter and potential alterations in the vessel OS at different points in the cardiac cycle. The registered images were used to measure the normalized single-pass transmittance spectra of the vessels studied. The OS was calculated by applying the Leavenburg-Marquard technique to fit the measured vessel transmission to a theoretical transmission model which incorporated the Lambert-Beer law and the published extinction coefficients of Hb and HbO_2 (van Assendelft, 1970). This oximetry technique accounted for the scattering effects of the red blood cells and ocular media.

In vivo experiments, using the multispectral intravitreal system, were performed on anaesthetized pigs and the transmittance spectral profiles of the retinal vessels were measured and characterized at a various systemic oxygen saturation levels. The transmission spectral profiles of the retinal arteries were shown to change at different oxygen saturations. Two main characteristics were noted: firstly, as the oxygen saturation decreases the local maximum of the transmission spectral profile in the 460 - 520 nm range moved from 510 nm to 480 nm and secondly the two minima at 542 nm and 577 nm converge to a broad minimum at 555 nm. The latter characteristic suggested the transition of the spectral profile of oxyhaemoglobin to reduced haemoglobin.

The calculated retinal arterial oxygen saturations were shown to have a strong correlation with the measured arterial oxygen saturations. However, the retinal venous OS did not correlate with the mixed venous (inferior vena cava) OS. This was thought to have been caused by the creation of an oxygen diffusion gradient from the retinal veins into the vitreous cavity during the vitrectomy as the balanced salt solution is instilled, resulting in an underestimation of retinal venous oxygenation. Vascular autoregulation as a result of the increased oxygen diffusion could also have contributed to errors in calculating the retinal venous OS.

1.5.5.7. Beach: Digital Multispectral and Hyperspectral Imaging of the Retina.

Beach et al. (1999) developed a two wavelength retinal imaging system which consisted of a fundus camera and an optical beam splitter enabling the simultaneous generation of two retinal images which were subsequently filtered using two interference filters, centred at 569 nm (isosbestic) and 600 nm (oxygen sensitive), and recorded with a digital camera. A vessel detection algorithm enabled the calculation of the optical densities, at each wavelength, along the retinal blood vessel. Oxygen saturations along the retinal vessels were calculated from the optical density ratio ($ODR = OD_{600} / OD_{569}$) which has a linear relationship with the measured OS (Pittman and Duling 1975a, 1975b). Confirmation of the linear relationship between the ODR and OS was demonstrated using the retinal oximeter in one healthy human subject during graded hypoxia. A strong negative correlation between the measured pulse oximetry OS and the measured ODR in the retinal arteries was demonstrated.

Clinical studies were performed to measure the ODRs in 12 diabetic human subjects without clinical evidence of diabetic retinopathy during normoglycaemia and hyperglycaemia (Tiedeman et al., 1998). The ODRs of the retinal arteries did not change; however, the ODRs of the retinal veins were shown to increase during acute hyperglycaemia indicating a decrease in venular OS. It was thought that this was due to increased consumption of oxygen.

The influence of fundal pigmentation on the oximetry calculations was explored in 7 healthy human subjects exposed to graded hypoxia using various mixtures of oxygen and nitrogen (Beach et al., 1999). An ear oximeter was used to measure the systemic OS. The accuracy of three methods of calculating the optical densities and ODR of the retinal arteries

were compared. It was concluded that the introduction of a correcting factor which estimated the amount of fundal pigmentation was the most accurate method. However, these methods were acknowledged to be sensitive to vessel size, particularly in the range of 80 – 200 μm. Using the modified ODR the mean (± SD) retinal venous OS in 5 human subjects during normoxia and hyperoxia (100% inspired oxygen) were 19.2% (± 2.9%) and 55% (± 3.38%) respectively.

Beach et al. subsequently developed a hyperspectral imaging system which consisted of a fundus camera with an attached prism-grating-prism spectrograph coupled to a digital camera (Khoobehi et al., 2004). The system was used in a study involving two anaesthetized monkeys. A sequence of line scans across a small area of the optic disc were recorded by moving the imaging system and the data was processed to generate a three dimensional "hyperspectral data cube", consisting of a sequence of images each representing a single wavelength from 410 nm to 950 nm with a spectral resolution of 2.5 nm. The hyperspectral signatures of the optic disc under normoxic and hyperoxic conditions (100% oxygen saturation) were compared in one monkey. In the second monkey hyperspectral signatures of the optic disc were generated at normal intraocular pressures and high intraocular pressures (induced through an infusion of saline in the anterior chamber) and compared. The reflectance spectral profile (between 450 nm and 600 nm) of the retinal vessels and temporal and nasal sections of the optic nerve head were analyzed. Under hyperoxic conditions increases in blood oxygen was found in the retinal arteries, retinal veins and optic nerve head tissue. Under high intraocular pressures the analysis indicated a reduction in oxygenated blood in the retinal vessels and optic nerve head tissues. Semi-quantitative OS maps, derived from complex analysis of the spectral profiles, illustrated the significant increased oxygenation of the retinal vessels and optic nerve head tissues during hyperoxia and decreased oxygenation during increased intraocular pressure. Subsequent modifications to the oximetry algorithm, applied to further experiments involving 5 anaesthetized monkeys at normal and high intraocular pressures, indicated that capillary blood OS in the optic nerve head at normal intraocular pressures were intermediate to that of the retinal arteries and retinal veins (Beach et al., 2006). At high intraocular pressures there was a reduction in the OS of the retinal vessels and optic nerve head tissues.

This hyperspectral imaging system was acknowledged to be susceptible to motion artefacts which limit its use to anaesthetized animal experiments and results from human studies have not been reported.

1.5.5.8. Stefánsson: Dual-Wavelength Digital Retinal Oximetry.

The two-wavelength oximetry technique described by Beach et al. (1999) was adopted by Stefánsson and co-workers (Hardarson et al., 2006) who developed a retinal oximeter that produced simultaneous retinal images at four wavelengths. This was performed using a beam splitter which linked a fundus camera to a digital camera and enabled the separation of the original retinal image into four retinal images each representing wavelengths centred at 542, 558, 586 and 605 nm. Image processing algorithms aligned the images and a vessel detection algorithm enabled ODR calculations, along the retinal the blood vessels to be performed using only the 586 nm and 605 nm wavelengths. Optical density ratios from first degree retinal arterioles and venules of 18 normal eyes were measured and used to generate a quantitative oximetry model. Calibration of the model was performed by averaging the data from previously published OS calculations of the retinal arteries (Schweitzer et al., 2001; de Kock et al., 1993; Delori, 1988) and veins (Hickam et al., 1963; Schweitzer et al., 2001; Beach et al., 1999; Delori, 1988). Several clinical studies in humans have been reported using this oximetry system.

Retinal vessel oxygen saturations were performed on 16 normal eyes whilst breathing room air followed by systemic hyperoxia (100% oxygen saturation)(Beach et al., 1999). The mean (± SD) retinal arteriolar oxygen saturation significantly increased from 96% (± 9%) to 101% (± 8%) and the retinal venules significantly increased from 55% (± 14%) to 78% (± 15%). Further experiments comparing retinal vessel OS in human subjects in light and dark conditions (n = 13 dark to light; n = 19 light to dark) showed that the OS of the retinal arterioles and venules were significantly higher in the dark adapted eye (Hardarson et al., 2009). This was thought to be due to increased outer retinal demand for oxygen.

Siesky et al. (2008) performed a randomized study comparing the effects of brinzolamide and dorzolamide on retinal oxygen saturation in 13 patients with POAG. The ODR of the retinal veins were significantly lower whilst on either brinzolamide or dorzolamide than that recorded at a baseline value (on timolol) indicating an increase in venous oxygenation. A subsequent randomized study of 13 patients with OAG or ocular hypertension demonstrated that the addition of dorzolamide to the patients already on timolol had no significant effect on the OS in the retinal arterioles, venules and arteriovenous differences (Traustason et al., 2009). However, a significant reduction in the retinal arteriolar

and venular OS was found when the treatment of the glaucoma subjects were changed from a dorzolamide-timolol combination to timolol monotherapy. More recently, Siesky et al. (2010) studied the effect of dorzolamide and timolol on the OS of the retinal vessels in 11 normal subjects and 11 POAG patients over an 8 month period. The OS of the retinal vessels did not change in both the normal and glaucoma groups with the addition of timolol and dorzolamide to timolol. However, increased blood flow in the superficial retina was found upon the addition of timolol to dorzolamide. The findings were thought to indicate an increased delivery of oxygen to the retina with the addition of dorzolamide to timolol.

This dual-wavelength retinal oximeter was also used to determine the effects of glaucoma filtration surgery (n = 19) on the OS in the retinal arterioles and venules (Hardarson et al., 2009). No significant differences were found in the OS of the retinal arterioles and venules before and after surgery.

1.5.5.9. Hammer: Dual-Wavelength "Oxygen Module".

Hammer et al. (2009) reported the use of a dual wavelength retinal oximeter comprised of a fundus camera with an attached filter with transmission wavelengths centred at 548 nm and 610 nm. Retinal images were recorded onto a colour digital camera and an oximetry model, using the ODRs at the two wavelengths, was used. Compensation for the effects of vessel diameter and fundus pigmentation were incorporated into the oximetry model by using methods previously described by Beach et al.(1999). and calibrating the ODR to normoxic and hyperoxic (100% OS) measurements in 20 normal subjects. The OS measurements along retinal arterioles and venules were demonstrated to be highly reproducible in 10 normal subjects. The mean (± SD) arteriolar and venular OS under normoxic conditions were 98% (± 10.1%) and 65% (± 11.7%) respectively. Inhalation of 100% oxygen increased the mean arteriolar and venular OS by 2% and 7% respectively.

The oximetry system was applied to study the OS in diabetic patients (Hammer et al., 2009). Forty-one diabetic patients with a range of retinopathy severity from mild non-proliferative to proliferative diabetic retinopathy (DR) were compared to 12 age-matched controls. No significant difference in the arteriolar OS was reported between the controls and subjects with diabetic retinopathy of all severities. Venular OS increased with the severity of diabetic retinopathy with a mean (± SD) OS of 69% (± 7%) in subjects with mild non-

proliferative DR and 75 (± 8%) in subjects with proliferative DR. This finding was thought to be due to arterio-venous shunting of blood.

Gehlert et al. (2010) applied the retinal oximetry system to a cohort of 11 patients with retinal artery occlusion and reported a significant increase in arterial OS over a time from a mean (± SD) baseline OS of 73% (± 16%) to 87% (± 11%) five days after medical treatment.

1.5.5.10. Yoneya: Fourier Transform Spectral Retinal Imager.

Yoneya et al. (2002) developed a Fourier transform spectral imaging system which consisted of a interferometer coupled to a fundus camera and a digital camera enabling the collection of spectral data from two dimensional retinal images. Eleven subjects with recent onset CRVO were examined and compared to 4 normal fellow eyes. Reflectance data, at wavelengths between 480 nm and 600 nm, from each pixel in the retinal image were analyzed using an oximetry model based on the Lambert-Beer law which used the published extinction coefficients of haemoglobin (van Assendelft, 1970). Additional parameters accounted for the wavelength dependent scattering of light in the eye. Quantitative OS maps of the retinal tissues and vasculature was demonstrated. The OS of the retinal arteries and veins in the fellow eyes were calculated between 90 - 98% and 60% - 70% respectively. Oxygen saturations of less than 40% were detected in the retinal tissues that corresponded to areas of capillary non-perfusion and leakage seen in the fluorescein angiograms. In addition, it was shown that both hemispheres of the retina appeared hypoxic in hemi-CRVO.

Further clinical studies using this imaging system compared oximetric retinal features between normal eyes (n = 20) and eyes with OAG (n = 15 low tension glaucoma and n = 41 high tension glaucoma)(Ito et al., 2008). The mean (± SD) OS of the juxta-papillary retinal tissues in eyes with normal tension glaucoma [78% (± 8%)] and high tension glaucoma [(82% (± 10%)] were significantly lower than in normal eyes [88% (± 8%)]. There were no significant differences in the OS of the retinal arteries and veins between the groups. In the high tension glaucoma group, worsening of the visual field (mean deviation) was associated with a reduction in the inferotemporal and superotemporal retinal OS.

More recently, Tsuchiashi et al. studied oximetric changes in the retinal tissues in the macular region of 22 patients with age-related macular degeneration (Tsuchihashi et al., 2009). The main findings were a reduction in tissue OS 1 week following verteporfin photodynamic therapy in 11 patients which recovered to pre-treatment levels at 1 month. The study also found significantly higher tissue OS in patients with neovascular age-related macular degeneration compared to aged-matched normal subjects.

This retinal imaging system is, however, limited by its spatial resolution in which each pixel in the image represents an area of 40 μm^2. Therefore oximetric quantification of small retinal vessels could not be performed. Additionally, it was acknowledged that the influence of the choroidal circulation on the retinal tissue oxygen calculations is unclear.

1.5.5.11. Other Retinal Oximetry Systems.

A number of other retinal oximetry systems have been previously reported which are either in the experimental or early clinical stage of their development. The various designs have included dual wavelength (de Kock et al., 1993; Crittin et al., 2002; Nelson et al., 2005), multiwavelength (Ramella-Roman and Matthews, 2007; Muqit et al., 2010) and hyperspectral (Johnson et al., 2007; Arimoto et al., 2007) imaging systems. Numerous different methods of calculating the OS of the retinal vessel have also been described. Further investigations are required on these systems to establish their performance as a retinal oximeter. The use of a modified optical coherence tomography (Kagemann et al., 2007) and modified multiwavelength scanning laser ophthalmoscope (Ashman et al., 2001) has also been reported but the results demonstrated that these systems were not suited for retinal oximetry.

1.6. Summary.

Photometric oximetry is an established and important tool used is clinical medicine today. Its development has stemmed from years of detailed research which has enhanced our understanding of the optical properties of the functional haemoglobin derivatives. The theories and methods used to calculate the oxygen saturation of human blood have been exploited in retinal oximetry. The underlying premise for retinal oximetry is to determine the

characteristic distribution of oxygen within the retina in health and disease. Since the retina has a high metabolic demand for energy, and subsequently that of oxygen, to meet its functional role; the detection of abnormal oxygen supply and demand has the potential to provide a useful indicator of the functional status of the retina. Various retinal oximetry methodologies have been adopted which reflect the uncertainties and challenges of establishing a gold standard retinal oximetric technique. Nevertheless, previous retinal oximetry studies have provided a useful insight into the potential usefulness of retinal oximetry in providing an enhanced understanding of the normal physiology of the retina and pathophysiological mechanisms of common sight threatening ocular diseases such as glaucoma. In addition, oximetry of the retina could potentially inform on the effects of established treatment modalities on retinal function and influence the development of future treatments of sight threatening retinal diseases.

1.7. Aims of the Research.

The research that will be reported in the thesis will describe the development of techniques used to measure the OS in the retinal vessels using a hyperspectral imaging system.

The aims of the research are:

- to evaluate the wide-field hyperspectral retinal imaging system
- to develop a robust and accurate method of measuring the OS in the retinal vasculature using image analysis techniques
- to apply the oximetry techniques to human retinal images acquired by the hyperspectral retinal imaging system
- to determine the ability of our oximetry technique to detect abnormal OS in the retinal vasculature in retinal diseases.

Chapter 2: The Hyperspectral Fundus Camera.

2.1. Introduction.

2.1.1. Clinical Applications of Multispectral and Hyperspectral Imaging.

The widespread application of multispectral and hyperspectral imaging systems has encompassed a number of bio-medical fields such as cytogenetics (Nuffer et al., 2006; Timlin et al., 2005; Huebschman et al., 2002; Schultz et al., 2001), pathology (Goodacre et al., 1998) and oncology (Martin et al., 2006; Sorg et al., 2005). In particular, clinical oximetric research using spectral imaging has grown in popularity. This has originated from the appreciation of dissimilar spectral properties of oxygenated and deoxygenated haemoglobin which can be used to calculate the oxygen saturation (OS). The feasibility of oximetry using hyperspectral imaging has been tested in a variety of clinical sub-specialties such as assessing haemorrhagic shock (Cancio et al., 2006), tissue perfusion (Zuzak et al., 2001 and 2002) and microvascular disease in diabetes (Greenman et al., 2005) and sickle cell anaemia (Zuzak et al., 2003).

2.1.2. Retinal Vessel Oximetry using Spectral Imaging.

Since the first retinal vessel oximetry experiments reported in the late 1950s various approaches have been undertaken to non-invasively measure the OS of blood in the retinal vessels (described in Chapter 1). The calibration methods of these oximetry systems have ranged from *in vitro* model eye experiments to *in vivo* hypoxia and hyperoxia experiments on animals and humans. Numerous oximetry techniques have been developed and reported but as yet there is no agreed gold standard method of calculating the OS in the retinal blood vessels. However, it is apparent that there are two main requirements: firstly an imaging system capable of accurately extracting spectral data from the retinal blood vessels; and secondly, a robust and accurate method of calculating the OS that accounts for the confounding influence of the complex light interactions within the retinal vessels, retinal tissues and ocular media. These requirements represent the main challenge to the development of a mainstream clinical retinal oximeter.

The aims of this chapter are:

- to describe the principle components of the hyperspectral fundus camera that was constructed by Heriot Watt University and used for the experimental and clinical oximetry research described in this thesis.
- The ability this hyperspectral fundus camera to emit wavelengths of light within the visible spectrum is integral to its function as hyperspectral imaging system. Therefore, experiments performed to establish the performance of the hyperspectral in relation to its ability to generate light of various wavelengths are also described and the findings reported in this chapter.

2.2. The Hyperspectral Fundus Camera

2.2.1. Fundus Camera

The hyperspectral imaging system consists of a commercial mydriatic fundus camera (Canon CF-60Z, Tokyo, Japan) which was modified to integrate a liquid crystal tuneable filter (LCTF) into the optical path of the camera enabling the illumination of the retina using a number of user selected wavelengths of visible light (Figure 2.1).

The basic optical system of the fundus camera consists of an annular illumination which projects light through the dilated pupil (Figure 2.2 *left*). The reflected light from the retina exits the pupil through the centre of annular illumination and continues through the optical components of the fundus camera forming a retinal image at the image plane. The observation and focusing system of the fundus camera transfers the retinal image onto the detector plane (Figure 2.2 *right*).

Two sources of illumination were incorporated into the design of the hyperspectral fundus camera. A tungsten bulb provided a continuous light source for viewing the retina and a xenon flash tube was used to illuminate the retina to enable the capture of a retinal image. The spectral transmission of the hyperspectal imaging system without the LCTF is shown in Figure 2.3.

The safety of the hyperspectral imaging system was independently assessed and approved for use in humans by the chair of medical physics from Aberdeen University as a requisite for attaining local ethical approval.

Figure 2.1: Photograph of the hyperspectral fundus camera in operation and its main components. (LCTF: liquid crystal tunable filter; CCD: charge-coupled device).

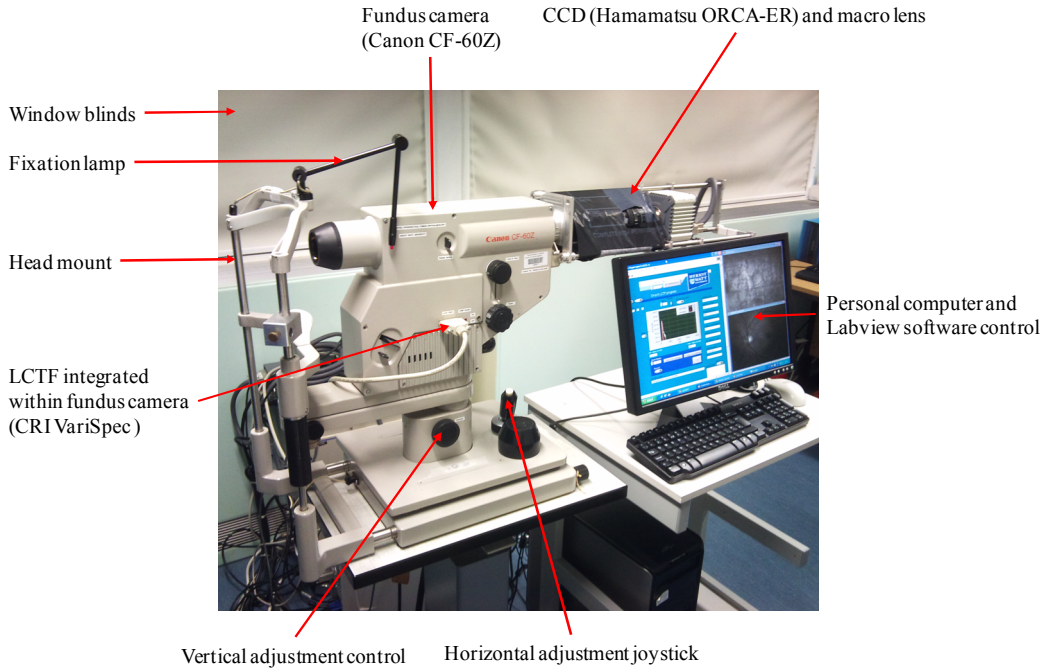

Figure 2.2: The main optical paths of the fundus camera. (*Left*) A schematic of the annular illumination of the retina. (*Right*) The optical paths of the illumination, observation and focusing system within the fundus camera.

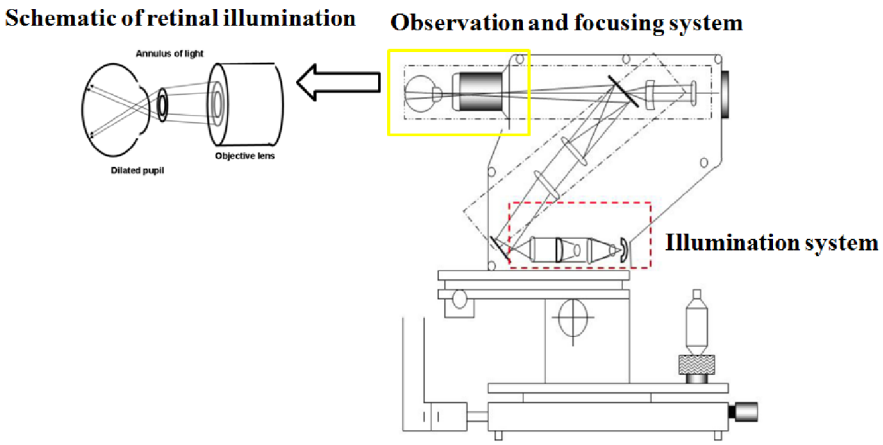

Figure 2.3: Spectral transmission of the hyperspectral imaging system without the LCTF.

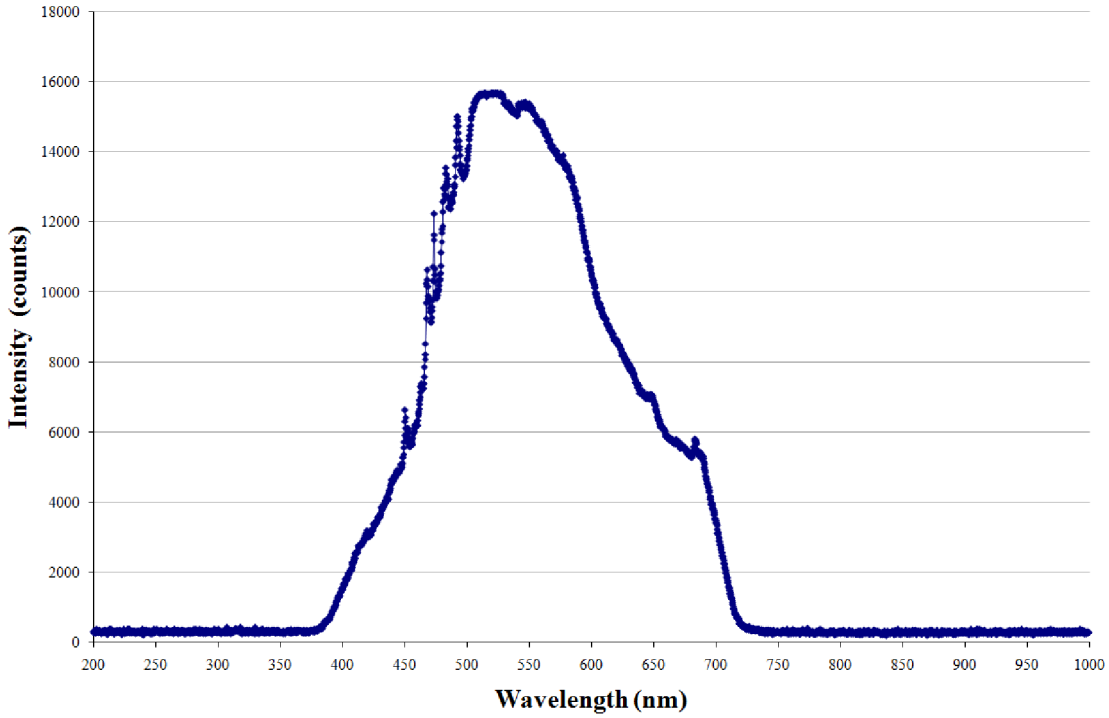

2.2.2. Liquid Crystal tuneable filter (LCTF).

Liquid crystal tuneable filters are based on a Lyot filter (Lyot, 1933) which consists of a series of birefringent retarders located between two parallel polarisers. A liquid crystal layer in each Lyot cell (Figure 2.4) enables variable changes to the retardance and provides the spectral tuning ability. Each Lyot cell transmits light that varies sinusoidally as a function of wavelength. Within the selected wavelength bandwidth, the transmitted light adds constructively and outside the bandwidth there is destructive interference. The typical transmission outside the bandwidth is 0.01% or less. The liquid crystal component enables the transparent bandwidth to be shifted throughout the spectral range of the filter.

The LCTF chosen to be incorporated into the fundus camera was a CRI VariSpec (Woburn, MA, USA). The LCTF filter is able to transmit wavelengths between the visible and near-infrared region (400 – 700 nm) with a wavelength dependent bandwidth of approximately 10 nm. Importantly, the LCTF is electronically tunable enabling fast random access of the desired wavelength via a personal computer, contains no moving parts and has and operating ambient temperature range of between 10 °C to 40 °C. The LCTF was integrated in an optimized position within the optical path of the incident light of the fundus camera.

Figure 2.4: A single Lyot cell consisting of two linear polarisers, a fixed birefringent retarder and a liquid crystal waveplate.

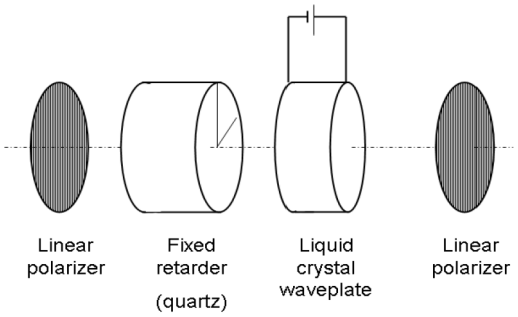

2.2.3. Charge-Coupled Device.

A low noise charge-coupled device (CCD) camera (Hamamatsu ORCA-ER, Hamamatsu Photonics K.K., Hamamatsu City, Japan) was incorporated into the fundus camera to enable the electronic capture of retinal images (Figure 2.5). The CCD has a high resolution of approximately 1.3 million pixels and a dynamic range of 12 bits. The CCD is peltier cooled with a vacuum seal to reduce dark noise and thermal drift, and has a high quantum efficiency in the visible and near-infrared wavelengths. A linear polarizer is attached to the front of the CCD to reduce a fixed pattern artefact caused by the specular reflection from the two surfaces of the objective lens within the fundus camera. A macro lens is inserted between the CCD and the fundus camera to maintain a field of view of approximately 40º onto the CCD detector chip with dimensions of 6.6 x 8.9 mm^2 (Figure 2.5).

Figure 2.5: Incorporation of the CCD and macro lens into the fundus camera.

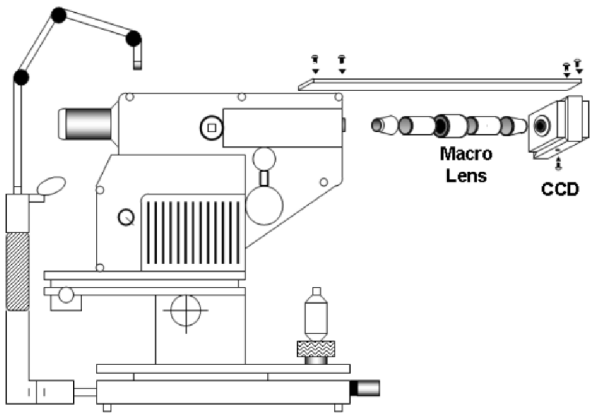

2.2.4. LabView software interface

A customized software programmed using LabView (National Instruments, Austin, Tx, USA) controls the LCTF, xenon flash and CCD camera. (Figure 2.6). The LCTF was controlled typically by changing the desired wavelengths in 10 nm increments or decrements. The xenon flash, engaged using the software, was integrated with the simultaneous capture of CCD images. A saturation histograph, live feed of the CCD recording and image of a captured image are displayed on the software interface (Figure 2.6, *centre of the image*). The captured images were stored onto a personal computer in 12-bit Portable Network Graphics (PNG) format.

Figure 2.6: The customized LabView software interface. The control interface window (*left*), an acquired retinal image at 580 nm (*bottom right*) and the live feed window (*top right;* retina not displayed in the live feed) are shown on the computer screen.

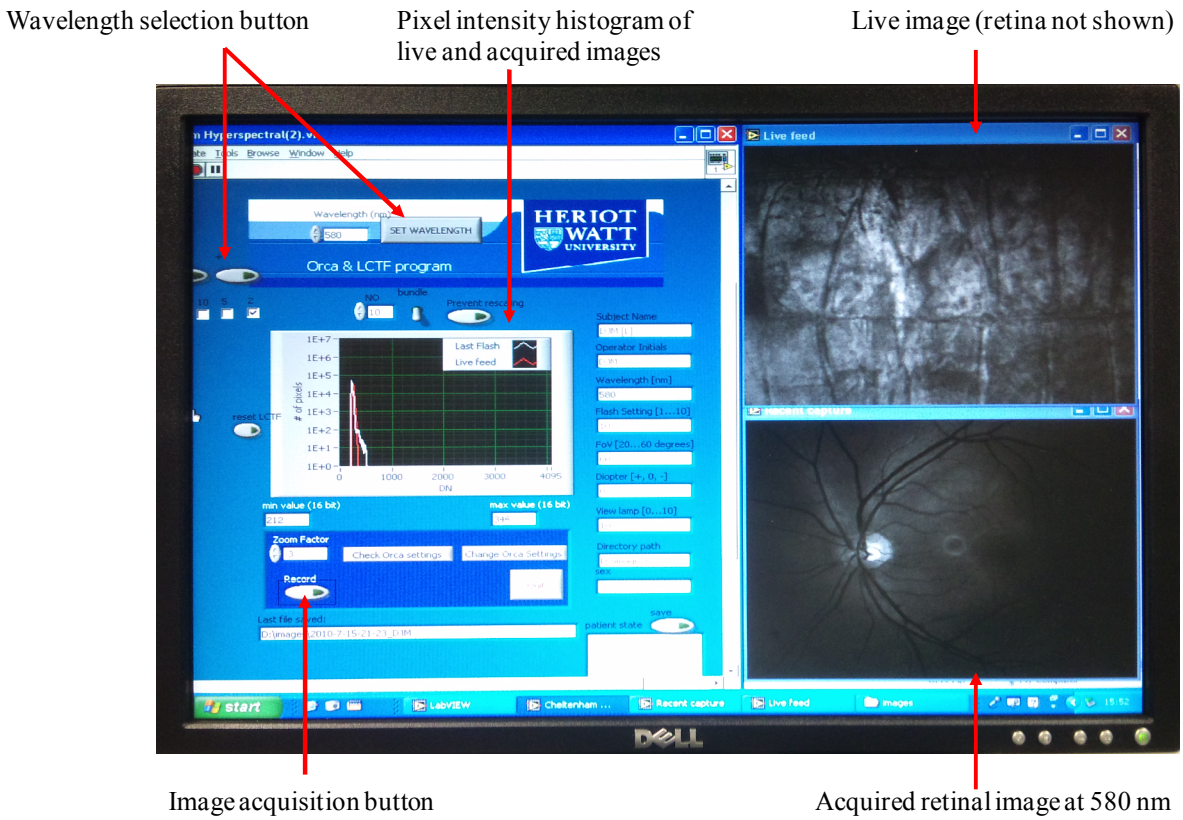

2.2.5. Spectrometer Measurements of the Hyperspectral Fundus Camera.

To establish that the wavelengths of light transmitted through the LCTF corresponded to the wavelengths that were programmed in the LabView software, a series of 4 experiments were performed to characterize the spectral performance of the hyperspectral fundus camera.

A spectrometer (Ocean Optics S2000, Dunedin, Florida, USA) was positioned in the illumination path in front of the hyperspectral fundus camera to record the actual wavelength of light transmitted through the LCTF for a given programmed wavelength. During each spectrometer experiment, the LCTF was changed sequentially using the programmed software from "500 nm" to "700 nm" in 10 nm incremental steps. At each programmed wavelength the xenon flash was engaged five times to enable 5 spectrometer measurements to be recorded by the spectrometer. The LCTF was then changed to "502 nm" and the sequential spectrometer recording sequence was repeated up to "702 nm". This process was repeated until sequence of programmed wavelengths from 500 nm to 708 nm in 2 nm incremental steps were recorded by the spectrometer. The importance of changing LCTF wavelengths in 10 nm steps was to ensure that the LCTF responded to the programmed commands. From initial experience with the hyperspectral fundus camera, the LCTF had a tendency to be unresponsive to the programmed commands when the wavelengths were changed too quickly (usually less than 3 seconds). Furthermore, by changing the LCTF in 10 nm increments, it was possible to visually confirm the response of the LCTF by viewing the shift of the spectrometer signal on a computer display showing the transmission of the LCTF (from the tungsten light source) in real time. The spectrometer experiment was repeated on four occasions over three separate days. Two experiments were performed on the same day 2 hours apart.

2.2.6. Analysis of the Spectrometer Measurements.

The processing and analysis of the spectrometer raw data was performed using *Mathematica* (ver. 5.2 Wolfram Research, Champaign, IL, USA). Each spectrometer measurement of a programmed wavelength was saved as a separate file consisting of the programmed wavelength (located in the filename) and the measured intensity data between

340.92 nm and 1000.07 nm (Figure 2.7). The spectrometer measurement data, therefore, represented the spectral transmission of the LCTF at the programmed wavelength.

A systematic offset present in the intensity count of each spectrometer measurement was corrected by subtracting the mean intensity in the wavelength range between 900 nm and 1000 nm from the raw data (Figure 2.7). The wavelength corresponding to the maximum intensity count (peak wavelength) was extracted from each corrected spectrometer measurement (Figure 2.8).

The data points in each spectrometer file was fitted using a second degree polynomial curve fit (Figure 2.9A). The interpolation of the data points was used to calculate the two wavelengths of the spectrometer signal at half the intensity of the peak wavelength. The difference between the wavelengths was used to calculate the Full-Width Half Maximum (FWHM) value (Figure 2.9B). The peak measured wavelength and corresponding FWHM were calculated for each programmed wavelength between 500 and 700 nm (in 2 nm increments).

Figure 2.7: A plot of a spectrometer measurement from the hyperspectral fundus camera programmed at 500 nm. Each spectrometer measurement data consists of the measured light intensity (*y*-axis) at each discrete wavelengths between 340.92 nm and 1000.07 nm (*x*-axis). A systematic offset in the intensity can be seen which was corrected by subtracting the mean intensity count in the wavelength range between 900 and 1000 nm.

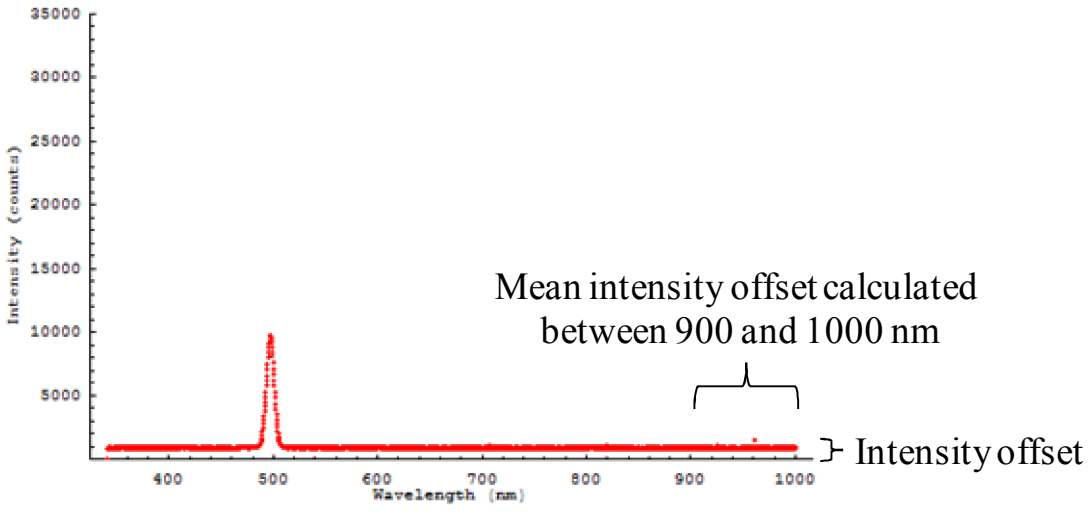

Figure 2.8: Extracting the peak wavelength from the corrected spectrometer measurement data. **A**. Plot of the corrected spectrometer measurement from the hyperspectral fundus camera programmed at 500 nm. The measured peak wavelength is 497.57 nm (*red filled circle)*. **B**. A magnified view of the corrected spectrometer measurement data between 480 nm and 515 nm and the corresponding measured peak wavelength (*red filled circle)*.

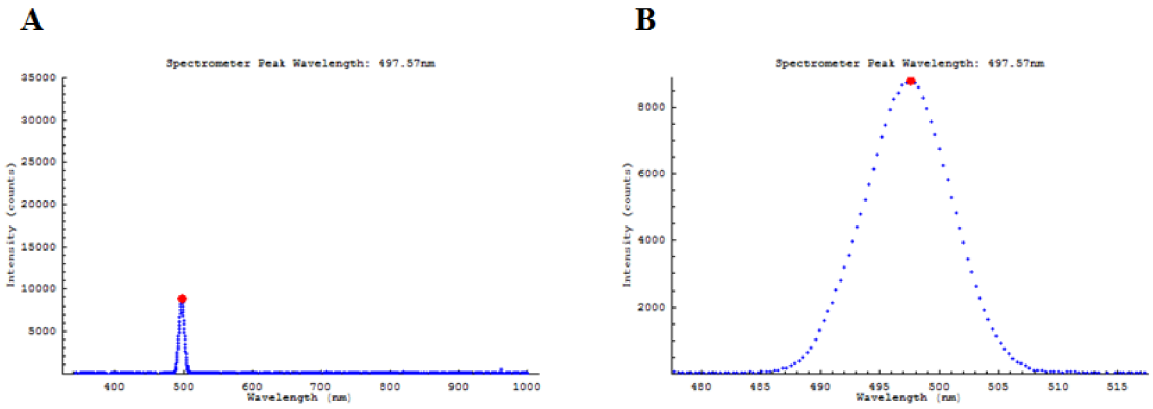

Figure 2.9: Calculation of the Full-Width Half Maximum (FWHM) of a spectrometer measurement at one programmed wavelength. **A**. A second degree polynomial curve fit is used to interpolate the spectrometer data. **B**. Calculation of the FWHM from the spectrometer data. The wavelengths at the half maximum (*green filled circles*) were set to zero to displace the signal downwards enabling the calculation of the half maximum wavelengths which are in this example: 493.07 nm and 501.69 nm. The FWHM is 8.62 nm.

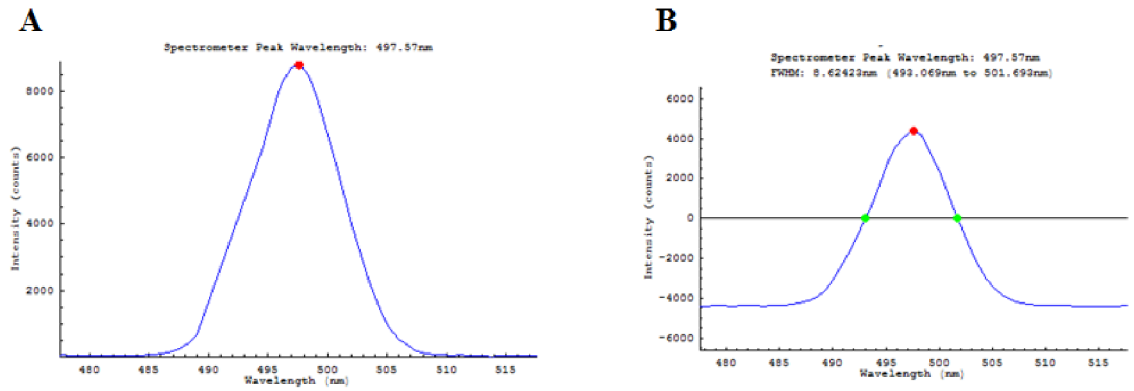

2.2.7. Statistical analysis

All statistical analyses were performed using *Mathematica* (ver. 5.2 Wolfram Research, Champaign, IL, USA). The mean peak measured wavelength, and mean FWHM for each programmed wavelength (from all 4 experiments) was calculated to determine the actual wavelengths (and FWHM) transmitted through the LCTF. To determine the variation of the 5 measured peak wavelengths for each programmed wavelength, the SD of the respective peak wavelengths were calculated. The average SD across the programmed wavelength range was calculated to determine the variability of the peak measured wavelength. A Pearson correlation was calculated between the mean measured wavelength and respective programmed wavelength. The Bland-Altman method (Bland and Altman, 1986) was used (programmed minus mean measured wavelength vs. average of the two wavelengths), for each experiment separately, to assess the agreement and variability between the programmed and measured wavelengths.

2.3. Results

The hyperspectral fundus camera is capable of illuminating the fundus with various user-selected wavelengths of light in the visible spectrum. The variability at each programmed wavelength was 0.32 nm. That is, for a given programmed wavelength, the SD of the measured peak wavelength was on average 0.32 nm.

A strong positive correlation was observed between the programmed and measured peak wavelengths ($R^2 = 0.99$, $P = < 0.0001$, Figure 2.10 *filled circles*). The mean FWHM of all four experiments for each programmed wavelength is also shown in Figure 2.10 (*vertical error bars*). The mean (± SD) FWHM across the full programmed wavelength range was 12.59 nm (± 2.57 nm).

Figure 2.10: Plot of the programmed wavelength against the mean measured peak wavelength of all four experiments. *Vertical error bars* are the mean FWHM at each programmed wavelength.

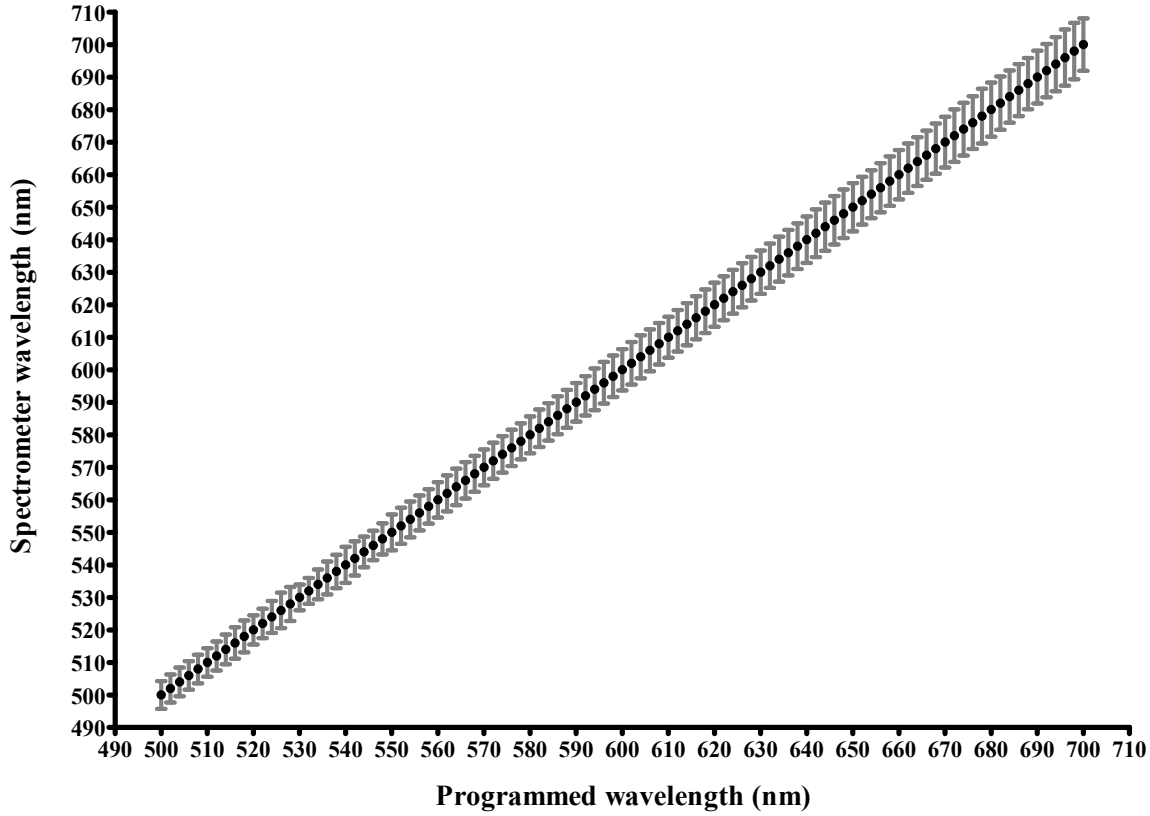

The agreement between the programmed and measured wavelength within each experiment are shown in the Bland-Altman plots in Figure 2.11. The mean difference (bias) ± SD between the programmed and measured wavelengths in Experiments 1 to 4 were 4.16 ± 1.67 nm, 3.30 ± 0.89 nm, 3.40 nm ± 1.24 nm and 4.16 ± 1.07 nm respectively (95% limits of agreement were: 0.88 – 7.44 nm, 1.55 – 5.05 nm, 1.55 – 5.05 nm and 2.36 – 6.54 nm respectively). Overall, the mean difference (±SD) between the programmed wavelength and measured wavelengths in all four experiments across the full programmed wavelength range (500 – 700 nm) was 3.84 nm (± 1.34 nm).

Figure 2.11: Bland-Altman plot (programmed minus measured wavelength vs. average wavelength) demonstrating the agreement between the programmed and measured wavelength. The mean differences (bias) are shown in each plot as *solid horizontal lines*, and the 95% limits of agreement are shown as *dashed horizontal lines*.

Experiment 1

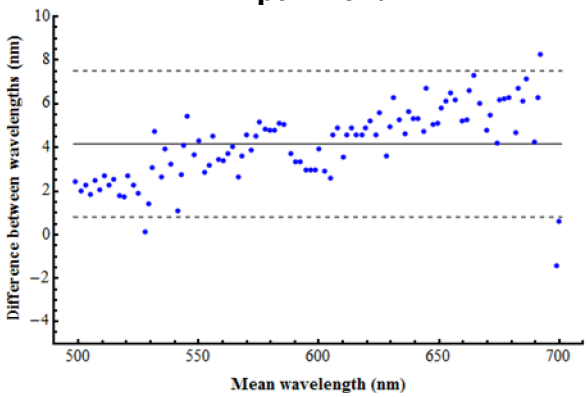

Bias	4.16 nm
SD of bias	1.67 nm
95% Limits of Agreement	0.88 – 7.44 nm

Experiment 2

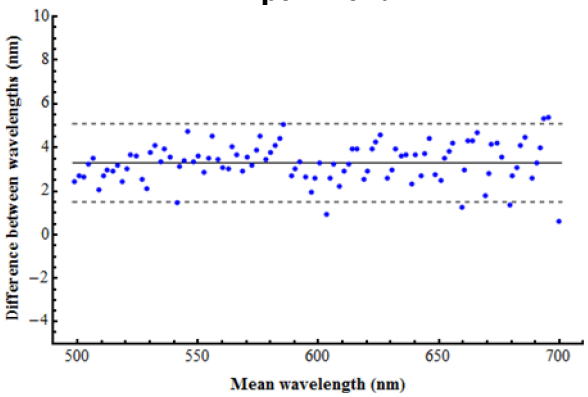

Bias	3.30 nm
SD of bias	0.89 nm
95% Limits of Agreement	1.55 – 5.05 nm

Experiment 3

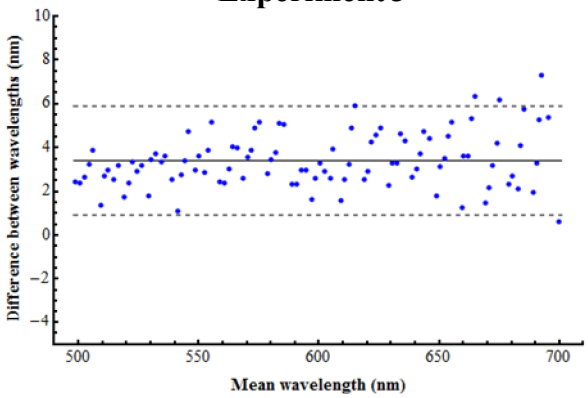

Bias	3.40 nm
SD of bias	1.24 nm
95% Limits of Agreement	0.96 – 5.84 nm

Experiment 4

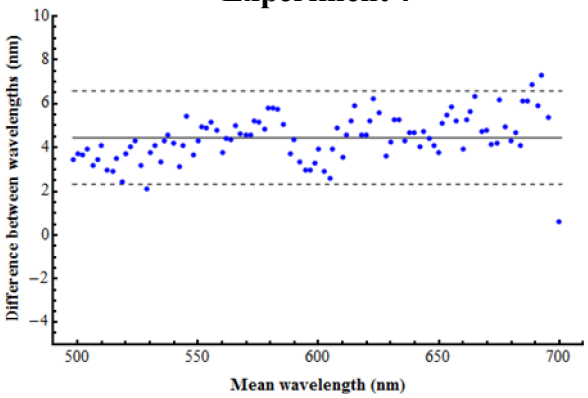

Bias	4.45 nm
SD of bias	1.07 nm
95% Limits of Agreement	2.36 – 6.54 nm

2.4. Discussion

This chapter has described the essential components used to construct the hyperspectral fundus camera. However, the ability of the hyperspectral fundus camera to generate light of various wavelengths is essential for it to function as a hyperspectral imaging system. Experiments to test this ability were performed to establish whether there was a difference between the programmed wavelength and the measured (actual) wavelength and study its characteristics.

At a given programmed wavelength, the repeated spectrometer measurements indicated that the LCTF was stable with an average SD of the peak wavelength of 0.34 nm. That is, when the hyperspectral fundus camera was programmed to illuminate a scene repeatedly at one wavelength, the peak wavelength remained relatively constant over 5 measurements. The stability of the LCTF is important as it would be undesirable to have large temporal fluctuations in the wavelength when the LCTF was set at one wavelength. The source of the variability is uncertain, but could originate from the detector of the spectrometer, the calculation of the peak wavelength from the spectrometer data and fluctuations in the structural properties of the LCTF. Although further research may be required to establish and correct for the source of the variability, this was considered to be small and possibly not significant.

A strong positive correlation between the programmed and measured wavelengths was found ($R^2 = 0.99$, $P = < 0.0001$) which demonstrates that, as expected, incrementally or decrementally changing the programmed wavelength resulted in corresponding changes in the measured wavelength. This demonstrates, to some extent, the controllability of the desired wavelength. However, as mentioned previously, it was found that changing the programmed wavelength too rapidly often led to the LCTF becoming unresponsive. This feature could originate from either the software (response of the program to a command) or hardware (response of the LCTF or computer). The practical importance of this finding was to ensure that imaging was conducted slowly to ensure that the LCTF had adequate time to respond to the commands.

To evaluate the performance of the hyperspectral fundus camera in detail, further tests were conducted to assess whether the selected programmed wavelength accurately depicted

the actual measured wavelength of light emitted from the imaging system. This is of particular importance, since the operating routine of the hyperspectral fundus camera was to generate spectral images which were stored onto a computer and the wavelengths used to acquire them were labelled as the programmed wavelength. The correlation analysis did not analyze this adequately and further detailed investigation was warranted since the analysis of spectral images is critically dependent on the wavelengths used. Four experiments were conducted to compare the accuracy of the programmed wavelength to depict the actual measured wavelength and the Bland-Altman method was used to demonstrate the results (Figure 2.11). In each experiment, there is a systematic tendency of the measured wavelength to be less than the programmed wavelength (Figure 2.11). Amongst all the experiments the average overestimation of the measured wavelength by the programmed wavelength was 3.84 nm (± 1.34 nm) across the wavelength range. A constant overestimation of the measured wavelength would be relatively simple to correct by adding a constant factor in the spectral analysis algorithm. However, closer inspection of the Bland-Altman plots reveals a number of important characteristics of the fundus camera. Firstly, the overestimation appears to increase as the programmed wavelength increases (particularly evident in Experiment 1 and 4, Figure 2.11). Secondly, there is variability in the overestimation between the experiments. This overestimation and variability are unlikely to have been caused by the analysis of data as the measurements of each programmed wavelength was performed five times, averaged and the SD of each measurement for a given programmed wavelength was low. A possible cause for the overestimation is likely to be due to the inaccurate calibration of the software to the true wavelength. The variability of the overestimation, however, could also be explained by flaws in the LCTF which may be temperature dependent. This finding is critical as it indicates that the true wavelength cannot be accurately described by the programmed wavelength. Prior knowledge of the wavelengths used to acquire spectral images is crucial to hyperspectral image analysis algorithms, in particular that of oximetry which relies on incorporating the wavelength specific extinction coefficients of oxy- and deoxyhaemoglobin into the algorithms. This characteristic of the hyperspectral fundus camera was not ideal. Unfortunately, this phenomenon was not discovered until half-way through this research project during the creation of the oximetry algorithms. At this stage over half of the model eye experiments and retinal images had been collected, and changing the design of the camera (i.e. using a new filter) would have been time-consuming and would have made the existing data redundant.

To adjust for the design flaw of the hyperspectral camera, spectral images at 2 nm increments apart were acquired as part of the imaging protocol. Fortunately, this had already been performed at the outset of the research project and therefore existing data were available for analysis. The explanation for the compensation is reflected in Figure 2.10 which plots the mean measured wavelength and mean FWHM for each programmed wavelength. It can be seen that for a given wavelength there is an overlap of the measured FWHM (mean 12.59 nm) with approximately four to five adjacent peak measured wavelengths. This would represent an oversampling of each wavelength thereby, to a limited extent, correcting for the variability of the measured wavelength which is in the order of 3.84 nm (mean bias of all experiments). In addition, as will be described in the next chapter, the algorithm used to calculate the OS incorporates a means of allowing the wavelength to be a free parameter thereby compensating for the variable offset in the wavelength. Although, these uncertainties in the hyperspectral imaging system are not ideal, it will be shown in later chapters that the acquired spectra of blood can be processed and is comparable to the published extinction coefficients of haemoglobin. Furthermore, from the acquired spectra, the oximetry algorithm can be applied to calculate the oxygen saturation of blood with some accuracy.

Chapter 3: Model Eye Experiments.

3.1. Introduction.

Numerous retinal oximeter designs using dual and multiple wavelength combinations sensitive to changes in oxygen saturation (OS) have been previously reported and was reviewed in Chapter 1. One of the main challenges of retinal vessel oximetry is the development of a robust and accurate oximetry technique that accounts for the complex interaction of light within the retinal vessels, retinal tissues and ocular media. As a result there is currently no agreed method of calculating the OS in the retinal blood vessels.

Model eyes provide a means of simulating the ocular optical system and anatomy for various ophthalmic experiments. The design and complexities of model eyes are driven by the nature of the research which may require the simulation of a specific functional property of the real eye or require high anatomical fidelity. In relation to retinal oximetry, model eyes provide a useful platform to evaluate new imaging systems and establish the validity of the oximetry methods. *In vitro* validation of a number of retinal oximetry systems have been previously reported using various model eye configurations (Hickam and Frayser, 1949; Delori, 1988; Schweitzer et al., 1999; Drewes et al., 1999; de Kock et al., 1993; Ramella-Roman et al., 2008; Hirohara et al., 2007; Smith et al., 2000) and most have been briefly described in Chapter 1.

The purpose of this study were:

- to determine the accuracy of our OS calculations of arterial and venous human blood of known OS from spectral images acquired by the hyperspectral fundus camera using a model eye
- to establish the effects of the background reflectance, and blood column thickness, on the accuracy of the OS calculations.

3.2. Methods

This study was approved by the Gloucestershire Research Ethics Committee (COREC reference: 06/Q2005/131) and all procedures were carried out in accordance with the tenets of the *Declaration of Helsinki*.

3.2.1. The Hyperspectral Fundus Camera

The hyperspectral fundus camera was described in detail in Chapter 2. In summary, it is a commercial fundus camera (Canon CF-60Z, Tokyo, Japan) in which a liquid-crystal tuneable filter (VariSpec, CRI, Woburn, MA, USA) enables the acquisition of spectral images between 400 nm to 700 nm on to a CCD digital camera.

3.2.2. The Model Eye

A model eye was constructed to simulate the salient optical properties of the human eye (Figure 3.1). It is comprised of a water-tight black aluminum outer casing and a +62.5D doublet convex achromatic lens (Thorlabs, Ltd. UK; AC080-016-A1 series) inserted through an opening in its front surface, such that when distilled water was instilled into the model eye chamber to simulate the vitreous, the effective focal length is approximately 22 mm. To determine the effects of the reflectivity on the accuracy of the OS calculation, a background surface was built using *Spectralon* (Labsphere Inc., New Hampshire, USA) segments with Lambertion albedos of 20%, 60% and 99% (Figure 3.2).

Blood-filled, fused quartz tubes (VitroCom, New Jersey, USA) could be positioned vertically within the model eye approximately 300 μm in front of the surface of the *Spectralon* background surface. The refractive index of the quartz tube is 1.46. Data was recorded for quartz tubes with internal diameters of 50 μm, 100 μm and 150 μm (outer diameters of 80 μm, 170 μm and 250 μm respectively), which enabled evaluation of the influence of simulated vessel diameter on the accuracy of the OS calculations.

Figure 3.1: The model eye. **A.** The model eye viewed from the top containing the *Spectralon* background and human blood in 150 µm quartz tubes. **B.** Schematic cross-section of the model eye.

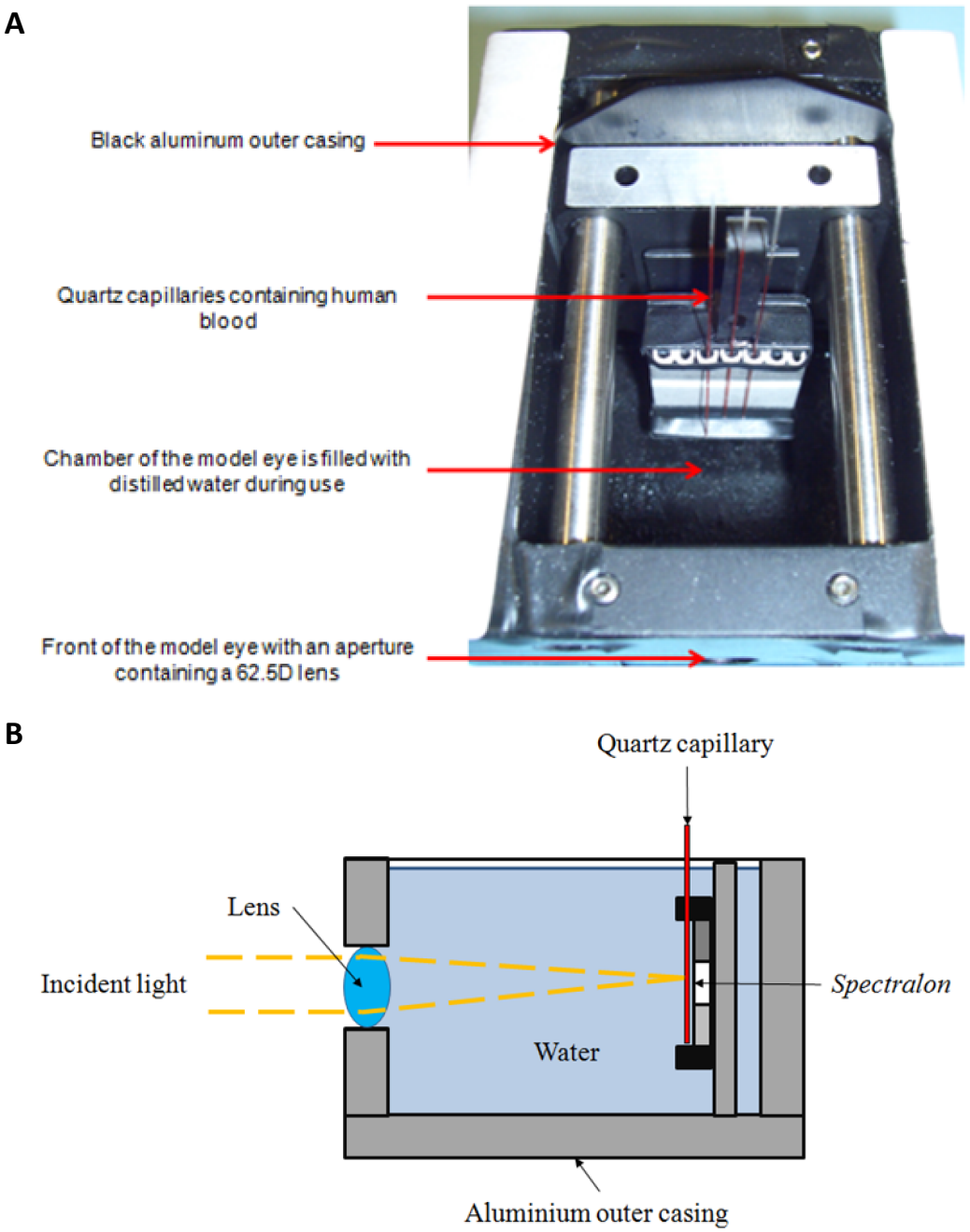

Figure 3.2: Configuration of the *Spectralon* background and internal components of the model eye.

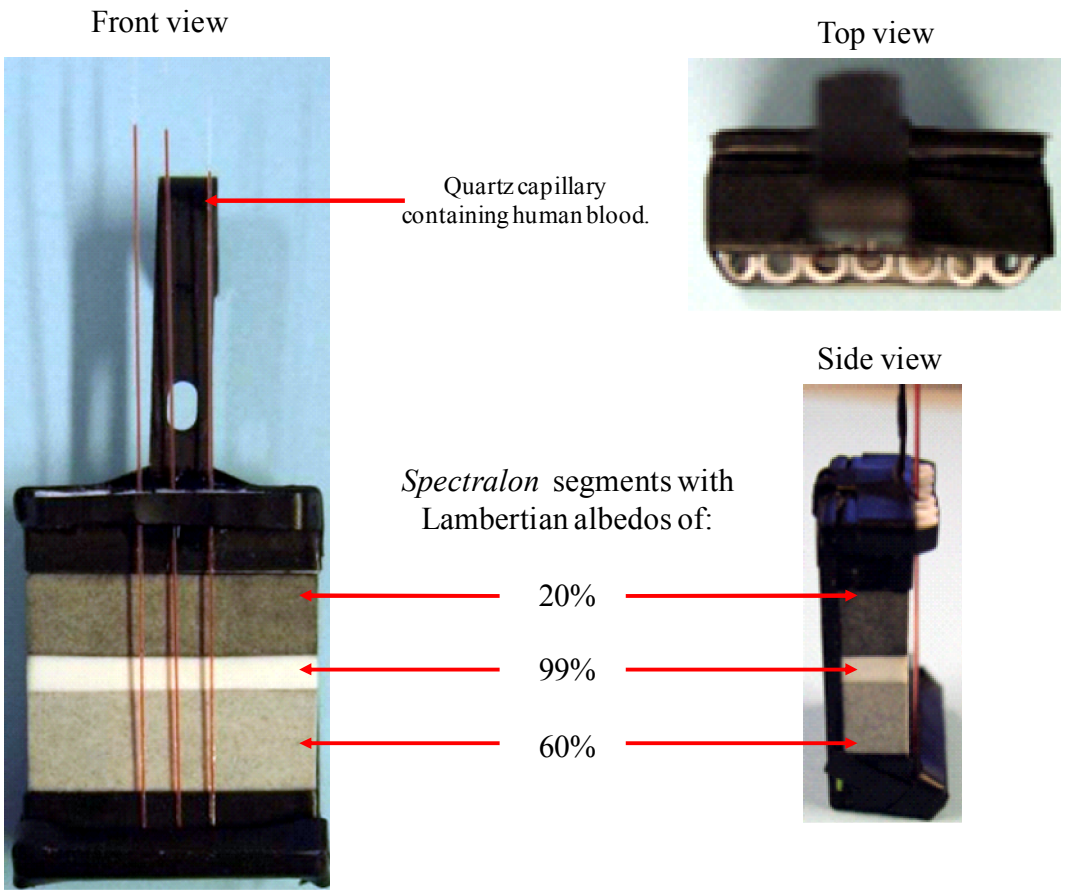

3.2.3. The Model-Eye Experiments.

The model eye was located in the conventional imaging position in front of the hyperspectral fundus camera. A straight metal wire (approximately 100 µm in diameter) placed in front of the *Spectralon* was used to help achieve optimal focus. The position of the fundus camera was also adjusted to attain optimal diffuse illumination (i.e. with minimal vignetting) within the model eye.

Two arterial and five venous blood samples, contained in a syringe lined with 2 ml of lithium heparin (Sarstedt, Monovette ® 2 ml LH), were collected from seven human subjects in the intensive care unit in Cheltenham General Hospital. Blood-gas analysis of each blood sample was performed using a CO-oximeter (Gem Premier 4000, Instrumentation Laboratory, MA, USA) at the time of collection. A small sample of the blood was inserted into 100 µm and 150 µm quartz tubes, the ends of the tubes were sealed with petroleum jelly

and the tubes were located in the model eye in front of the *Spectralon* background. Time-sequential hyperspectral images were acquired at wavelengths from 500 to 650 nm at 2 nm intervals. The mean (± SD) time taken to acquire a complete set of images was 5 minutes 52 seconds (± 1 minutes 22 seconds). This process was repeated using the same blood sample inserted into 50 μm quartz tubes. Several repeated attempts to fill 50 μm quartz tubes with blood yielded only broken blood columns in the tube which were considered unsuitable for oximetry and consequently these images were not included in the study.

To enable the analysis of blood at intermediate OS between the higher and lower saturations commonly found in unmixed arterial, or unmixed venous blood respectively, three of the venous blood samples were mixed with varying volumes of atmospheric air over a period of thirty to forty-five minutes. This process resulted in an increase in the measured OS of the venous blood samples. Subsequent to the blood-gas analysis with the CO-oximeter, the small air bubbles were removed from the syringe, which was then sealed to maintain a stable level of oxygenation prior to its use in the model eye. Samples of this blood were then imaged within the quartz tubes, in the model eye, as described above.

Blood-gas analyses of all of the blood samples were performed again by the CO-oximeter after imaging and the mean spectrophotometric measurement of OS before and after imaging was calculated to determine the gold-standard measured OS. The mean (± SD) time taken to perform the initial blood-gas measurement before imaging and re-measurement after imaging was 51 minutes 31 seconds (± 10 minutes 31 seconds). The mean difference (± SD) between the measured OS before and after imaging was 0.49% (± 0.76%).

In total 20 blood-filled quartz tubes (ten 100 μm quartz tubes and ten 150 μm quartz tubes) were imaged. Table 1 summarizes the number of blood samples that were imaged for each type of blood and tube size. The measured OS range (mean ± SD) of the arterial and venous blood samples were 97.9 - 98.9% (98.4 ± 0.7%) and 23.4 - 97.5% (69.7 ± 25.3%) respectively. The total hemoglobin concentration ranges (mean ± SD) were 9.9 – 10.7 g/dL (10.3 ± 0.5 g/dL) and 7.1 - 18.3 g/dL (13.7 ± 3.7 g/dL) for the arterial and venous blood samples respectively. The hematocrit range (mean ± SD) of the arterial and venous blood samples were 28.5 – 30.5% (29.5 ± 1.4%) and 32.5 - 57.5% (46.9 ± 8.1%) respectively.

Table 1. Number of blood sample types and quartz tubes used.

Blood sample type	Number of blood filled quartz tubes imaged			
	100µm quartz tubes	150µm quartz tubes		
Arterial	2	2	4	Total
Venous	8	8	16	
	10	10		
	Total			

3.2.4. Image Processing and Quantitative Oximetry Calculation.

All raw spectral images of the model eye were saved as 12-bit Portable-Network-Graphics (PNG) format. Further processing and analysis of the raw images was performed using *Mathematica* (ver. 5.2; Wolfram Research, Inc., Champaign, IL). Dark calibration of each raw image was performed to remove the dark-current offset from the CCD output. Figure 3.3 illustrates the subtraction of a dark image from a model eye image at the same wavelength (580 nm) to generate a dark calibrated image. In the dark image there is central annular artefact (not apparent in the model eye image due to the reflectivity of the *Spectralon*) which is fixed in position irrespective of the wavelength used and position of the fundus camera. The fixed pattern artefact is a result of reflections from the internal components of the fundus camera and is reduced, in addition to the CCD noise, as a consequence of the dark calibration. A vessel-tracking algorithm implemented in C++ (Microsoft, Inc., Redmond, WA) and integrated with the *Mathematica* software was used to

determine the centreline co-ordinates along the quartz tubes and a series transverse intensity profiles were obtained orthogonal to the tubes (Figure 3.4).

Figure 3.3: Dark calibration of a model eye image obtained at 580 nm. **A.** A raw image of the model eye obtained at 580 nm and an intensity profile along a linear region of interest (*red solid line*). The annular central artefact is not apparent due to the high reflectivity of the *Spectralon*. **B.** A dark image obtained at 580 nm and an intensity profile along a linear region of interest (*red solid line*). The annular central artefact is apparent and its intensity profile is shown in the plot below. **C.** Subsequent dark calibrated image at 580 nm obtained by subtracting the dark image obtained at 580 nm from the raw image of the model eye obtained at 580 nm. An intensity profile along a linear region of interest (*red solid line*) is shown in the plot below.

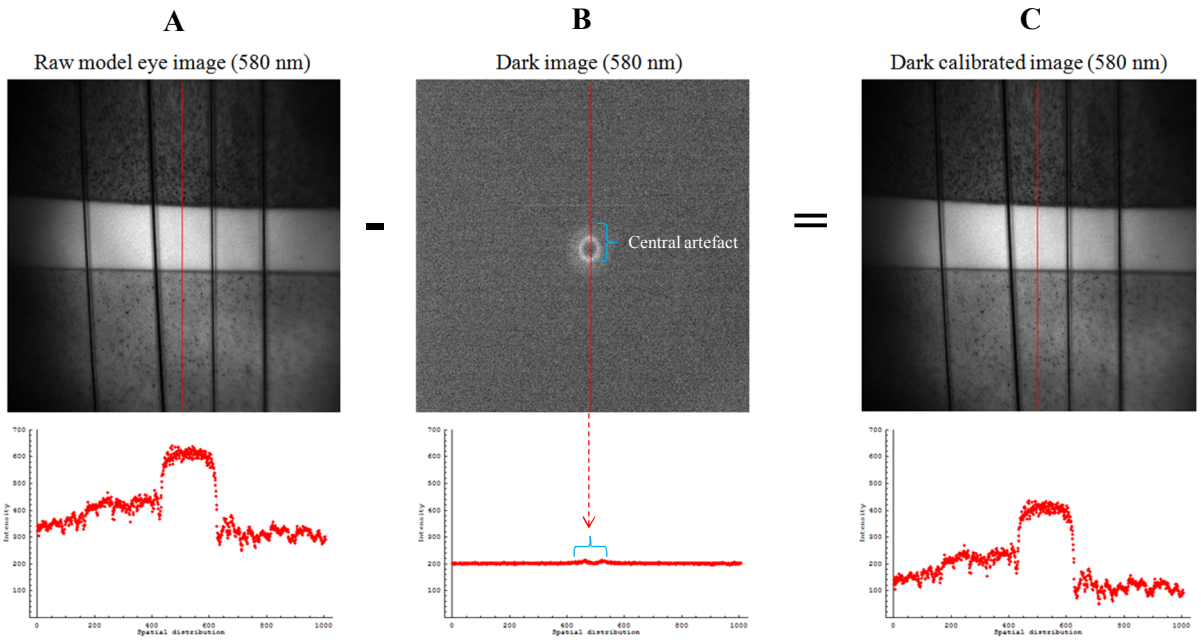

Figure 3.4: Linear profiles (*red lines*) orthogonal to the centreline of the tracked quartz tubes.

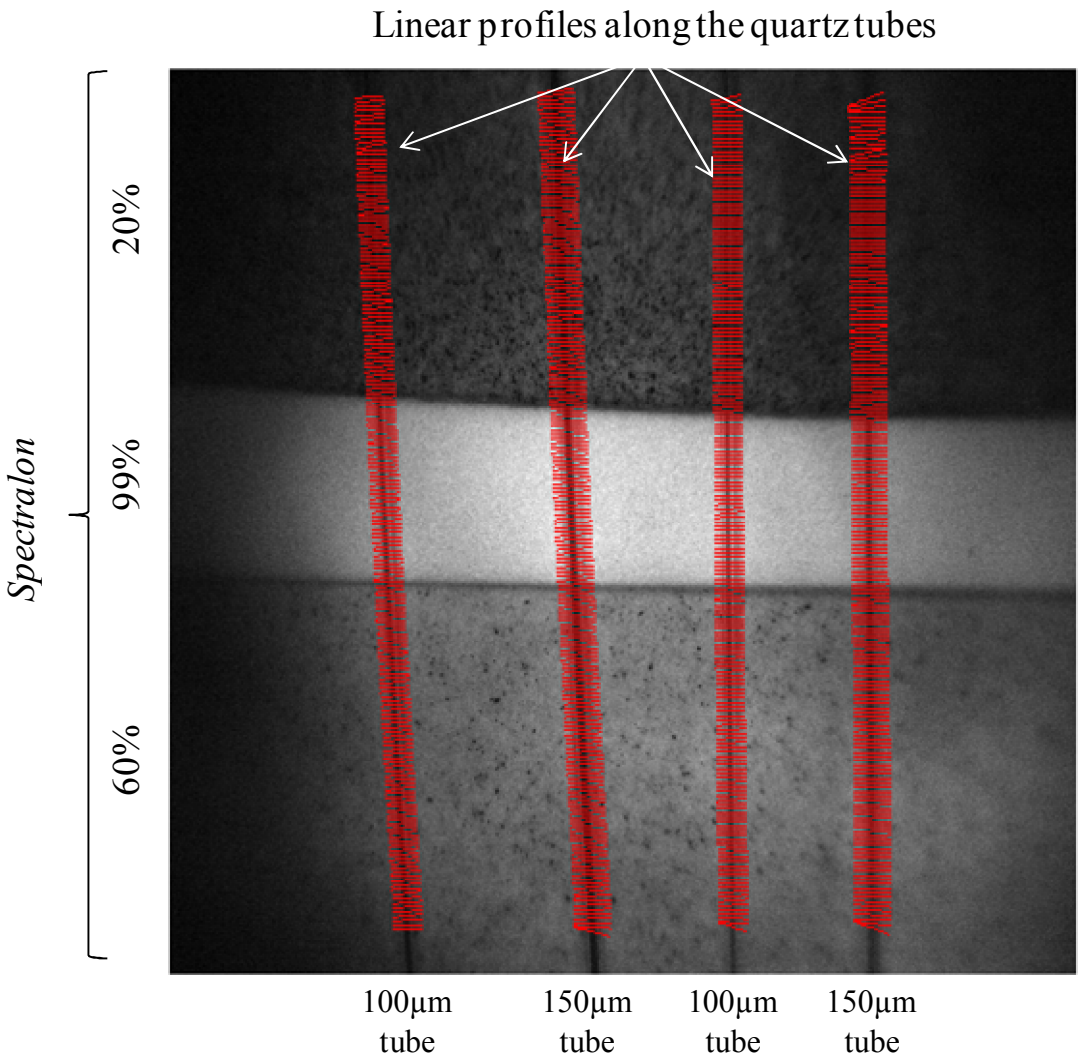

For each gray-scale intensity profile, fitting algorithms were used to estimate the intensity at the centre of the tube (minima of the non-linear curve) and intensity of the background adjacent to the tube (gray-scale value of the linear fit at the center of the tube) to enable an estimate the optical density of the tube center (Figure 3.5), given by:

$$OD(\lambda) = -Log_{10}\left(\frac{I(\lambda)}{I_o(\lambda)}\right) \qquad \text{(Eq. 1.4)}$$

where, $I(\lambda)$ is the estimated intensity at wavelength λ at the center of the tube, and $I_o(\lambda)$ is the estimate of intensity at the same position obtained by interpolation of the intensities either side of the tube – that is an estimate of the intensity in the absence of the tube. The effects of reflections (e.g. specular reflection or refractive index mismatch between the water-quartz-blood interfaces) on the quartz tubes are minimized by the curve fitting

technique to used estimate the intensity at the centre of the blood column. The optical densities of a given point were estimated across the wavelength range (500 nm – 650 nm) to calculate the optical density spectral variation, $OD(\lambda)$ (Figure 3.6). This was repeated at multiple points along all the quartz tubes.

Figure 3.5: Analysis of the grayscale intensity profile across a given point in the quartz tube at one wavelength. **A.** Image of the model eye containing blood filled quartz tubes acquired at 500 nm. The location of the linear profile across a quartz tube (*red solid line*) to be analyzed is shown. **B.** A plot of the intensity values along the linear profile. A curve fitting algorithm (*blue dashed line*) is applied to the grayscale intensity profile to estimate the grayscale intensity at the center of the tube. The value $I(\lambda)$ is determined from the minimum value of the curve. A linear fitting algorithm (*green solid line*) is used to estimate the intensity of the background in the absence of the quartz tube [$I_o(\lambda)$].

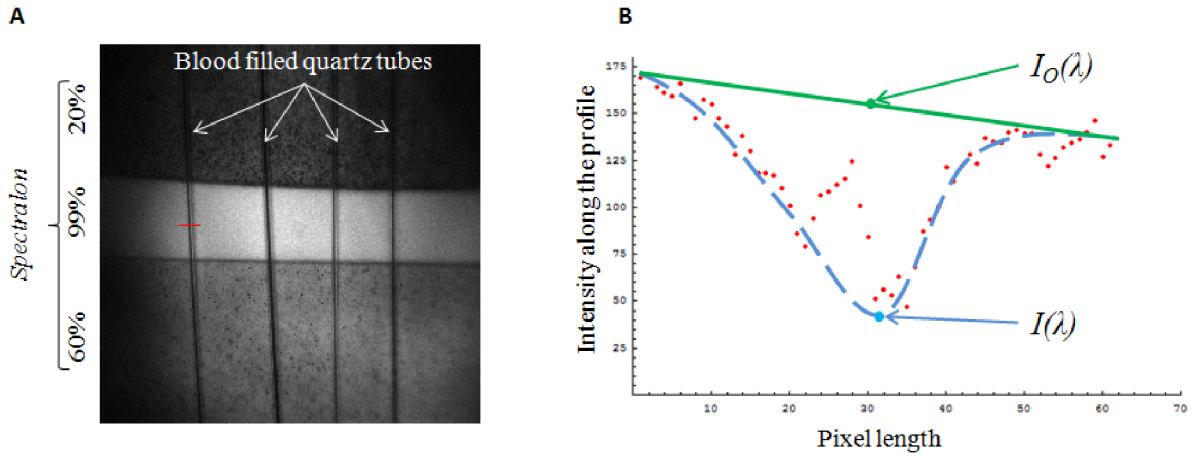

Figure 3.6: Calculation of the optical density profile. **A.** Analysis of the intensity along the linear profile is used to estimate the optical density in the centre of the quartz tube (*blue dot*). This analysis is performed on all the spectral images (500 - 650nm in 2nm increments). **B.** Plotting all the optical densities across the wavelength range generates an optical density profile at the respective location in the tube.

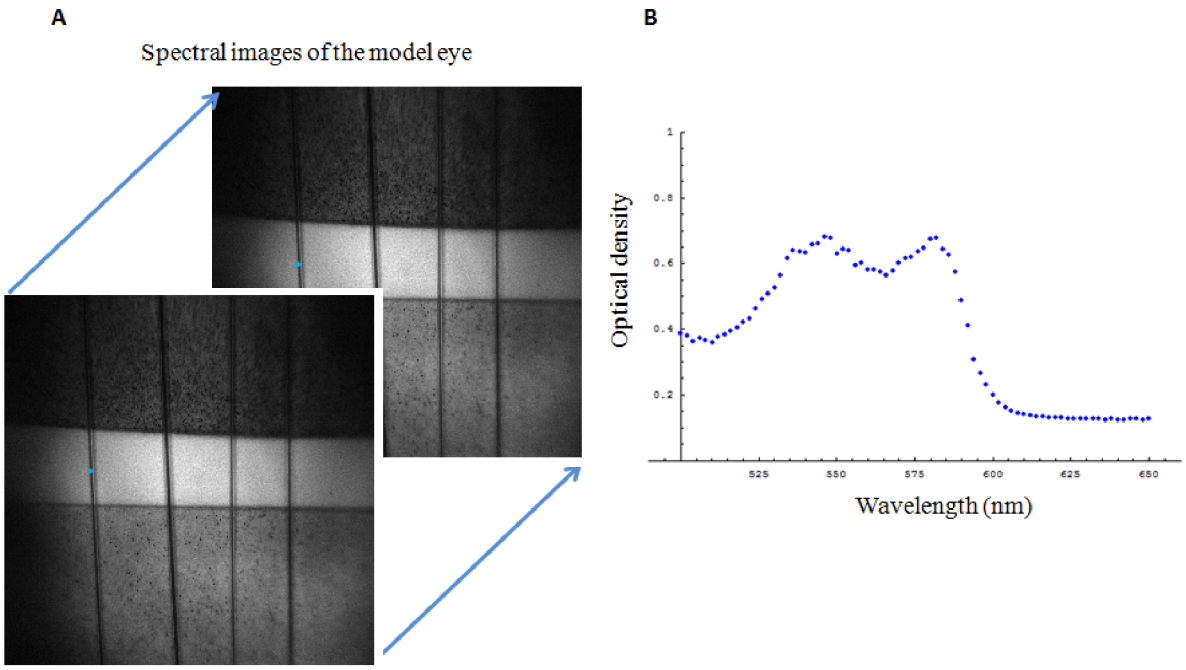

Calculation of the OS along the length of the quartz tubes was performed using the complete set of $OD(\lambda)$. Two oximetry models were tested to determine the most accurate model. The first oximetry model is given by the Equation 1.5 and the second oximetry model by the Equation 1.6.

Oximetry model 1.

$$OD(\lambda) = a + \eta(\lambda)\, C_{HbTotal}\, d\, [cOS\, (\varepsilon_{oxy}(\lambda + b) - \varepsilon_{de\text{-}oxy}(\lambda + b)) + \varepsilon_{de\text{-}oxy}(\lambda + b)] \qquad \text{(Eq. 1.5)}$$

Oximetry model 2.

$$OD(\lambda) = a\, S(\lambda) + \eta(\lambda)\, C_{HbTotal}\, d\, [cOS\, (\varepsilon_{oxy}(\lambda + b) - \varepsilon_{de\text{-}oxy}(\lambda + b)) + \varepsilon_{de\text{-}oxy}(\lambda + b)] \qquad \text{(Eq. 1.6)}$$

where, $C_{HbTotal}$ is the total concentration of haemoglobin, ε_{oxy}, and $\varepsilon_{de\text{-}oxy}$ are the extinction coefficients of oxygenated and deoxygenated haemoglobin (van Assendelft, 1970) respectively corrected for convolution with the spectral response of the liquid crystal tunable filter, d is the vessel diameter, cOS is the calculated oxygen saturation, η is the effective optical path-length contribution (Smith et al., 2000) and a is a scaling constant of the curve along the y-axis. Importantly, b is a scaling constant of the curve along the x-axis which compensates for the variability of the liquid crystal tunable filter which was described in Chapter 2. The difference between the two oximetry models is the presence of a scattering function. In Oximetry model 1 there is no scattering function. In Oximetry model 2, the function S accounts for the backscatter by of red blood cells. Wavelength dependent optical scattering values published by Meinke et al. (2007) were used in this oximetry model. In essence, this algorithm estimates the free parameters based on the Levenberg-Marquardt non-linear fit to $OD(\lambda)$ to yield an estimate of cOS.

3.2.5. Statistical Analysis

The normality of the data distribution was confirmed using the Shapiro-Wilk normality test, with the cutoff for non-normality set at $P < 0.05$. To determine the effect of the light scattering parameter (S) on the accuracy of the oximetry model, a two-tailed paired t-test was used to compare the mean OS difference (difference between the measured and calculated OS) calculated by Oximetry model 1 and 2 in the 100 µm and 150 µm quartz tubes. The most accurate oximetry model was used in subsequent analyses.

A multiple linear regression analysis was performed for the mean OS differences along the length of each quartz tube with the independent variables capillary size and blood gas analysis parameters (total haemoglobin (tHb), pH, carbon dioxide tension (pCO_2), PO_2, sodium ion concentration ($[Na^+]$), potassium ion concentration ($[K^+]$), chloride ion concentration ($[Cl^-]$), haematocrit (Hct) and lactate, using the "enter" method.

To determine the effect of the background reflectivity and tube size, the mean OS differences for segments of the 100 µm and 150 µm quartz tubes overlying the three different background reflectivities were calculated. A repeated-measures, two-way analysis of variance (ANOVA) was performed to compare the effect of tube size and background reflectivity on the mean OS difference. A *post-hoc* power analysis using the mean OS difference in each

group (n = 6; three background reflectivities for each tube size), the average observed SD and a 0.05 significance level was performed using a software program developed by Faul et al. (2009)(Gpower program ver. 3.1). Pearson's correlation between the measured OS and mean calculated OS along the length of each tube were calculated.

The Bland-Altman method was used to assess the agreement between the CO-oximeter and the values obtained from the chosen oximetry model in 100 µm quartz tubes. The mean calculated OS of each segment of the tube overlying the 3 *Spectralon* background reflectivities was calculated and the mean of the measured and calculated OS was plotted against the difference between the two methods. Statistical analyses (except the power analysis) were calculated using commercial software (SPSS, ver. 16.0; SPSS Inc., Chicago, IL).

3.3. Results.

3.3.1. Hyperspectral Images of Arterial and Venous Blood in the Model Eye.

Representative narrow-band images of the model eye containing human arterial and venous whole-blood in 150 µm quartz tubes obtained at wavelengths of 586, 600, 620 and 650 nm are shown in Figure 3.7. The vertical dark lines are the quartz tubes containing human blood. Each of the blood-filled quartz tubes spans the three reflective grades of *Spectralon*. Figure 3.7A shows a tube containing arterial blood with a measured OS of 97.9%. Figure 3.7B shows a tube containing venous blood with a measured OS of 23.6%. It can be observed, as expected, that at the isosbestic wavelength of 586 nm (where the absorbance of oxyhemoglobin and deoxyhemoglobin are equal), both arterial and venous blood appear to have similar optical densities, and, that the arterial blood has a lower optical density at wavelengths of 600, 620 and 650 nm compared to venous blood.

Figure 3.7. Cropped dark calibrated spectral images of the model eye containing (**A**) arterial and (**B**) venous blood filled 150 µm quartz tubes. The spectral images shown were acquired at 586, 600, 620 and 650 nm. Each tube is located in front of 3 reflective grades of *Spectralon*.

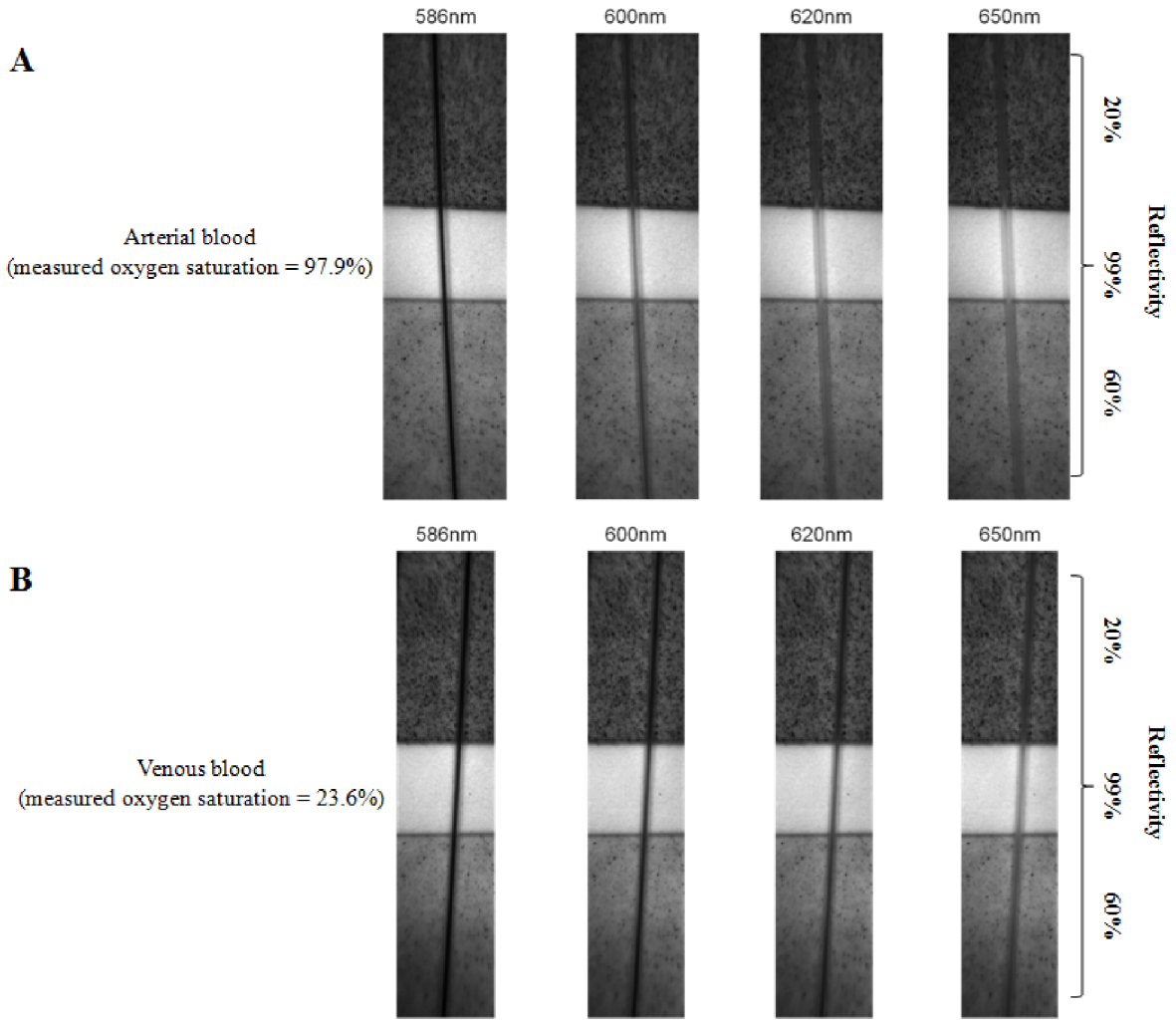

3.3.2. Determining the effects of light scattering on the accuracy of the oximetry model.

The mean OS differences calculated by the two oximetry models were significantly different in both 100 µm and 150 µm quartz tubes ($P < 0.0001$, two-tailed paired *t*-test) (Figures 3.8 and 3.9). Table 2 summarises the mean OS differences in the 100 µm and 150 µm tubes calculated using the two oximetry models. The mean (± SD) OS differences, using Oximetry model 1 (no scattering function), were -11.8% (± 6.0%) and -11.4% (± 9.7%) in the

100 µm and 150 µm tubes respectively. The mean (± SD) OS differences, using Oximetry model 2 (scattering function), were -7.1% (± 7.1%) and -6.2% (± 10.2%) in the 100 µm and 150 µm tubes respectively. Oximetry model 2 was used for subsequent OS calculations because the mean OS difference was smaller than the mean OS difference in Oximetry model 1.

Figure 3.8: A scatter plot of the mean oxygen saturation (OS) differences calculated by Oximetry model 1 (no scattering function) and 2 (scattering function) in 100 µm quartz tubes.

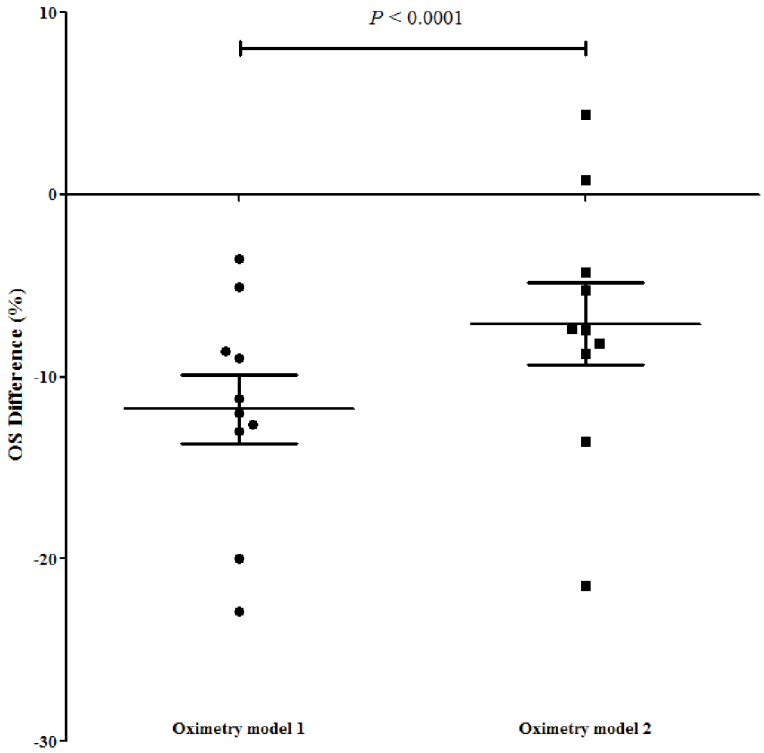

Figure 3.9: A scatter plot of the mean oxygen saturation (OS) differences calculated by Oximetry model 1 (no scattering function) and 2 (scattering function) in 150 µm quartz tubes.

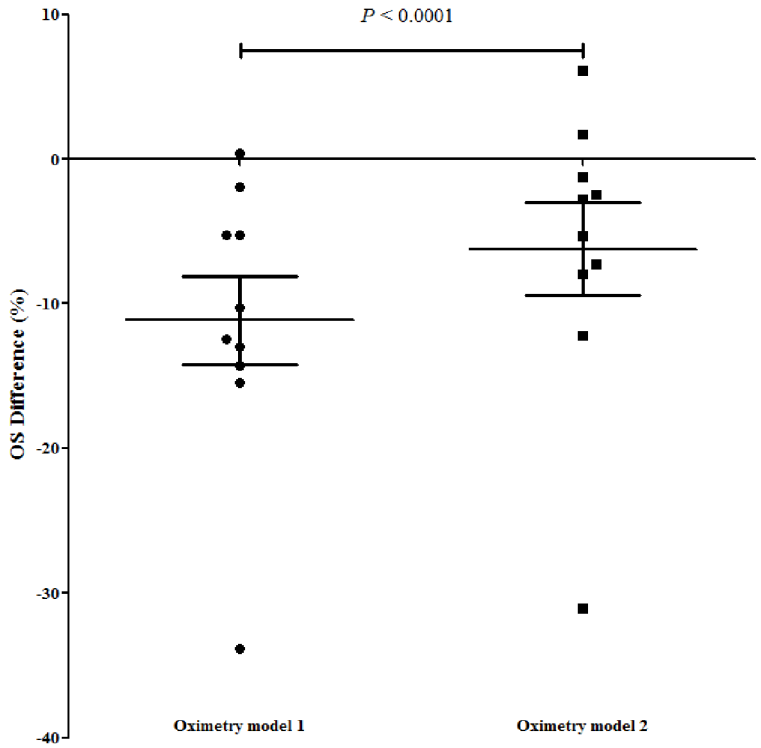

Table 2. The mean oxygen saturation difference (OS) in 100 µm and 150 µm quartz tubes using oximetry model 1 (no scattering function) and 2 (scattering function).

Oximetry Model	100 µm quartz tubes Mean OS difference (± SD)	150 µm quartz tubes Mean OS difference (± SD)
1 (no scattering function)	-11.8% (± 6.0%)	-11.4% (± 9.7%)
2 (scattering function)	-7.1% (± 7.1%)	-6.2% (± 10.2%)

3.3.3. Oxygen Saturation Calculation of Blood Along the Quartz Tubes.

Figures 3.10 and 3.11 show the variation of calculated OS along the length of 100 μm quartz tubes containing arterial (measured OS = 98%) and venous (measured oxygen OS = 23%) blood respectively. Processing and analysis of the model eye images was used to produce a pseudocolour image with a coloured representation of the calculated OS overlaid on the tube and sequential calculated OS values shown to the left of the tube (Figures 3.10A and 3.11A). Examples of the non-linear fitting of the oximetry model (Figures 3.10B and 3.11B red lines) to the mean optical density profile along the length of each tube are illustrated with the calculated oxygen saturation. The calculated OS values along the length of each tube are also shown in a plot (Figures 3.10C and 3.11C) and demonstrate small fluctuations along its length. These fluctuations were comparatively higher in segments of the arterial and venous blood overlying the 20% reflective background (SD 1.40% and 1.05% respectively), possibly due to the effect of increased texture in the *Spectralon* background, however these fluctuations were small. In the quartz tubes containing arterial and venous blood the mean calculated OS along their lengths (± SD) was 106% ± 1.13% (n = 1,891 measurements) and 45% ± 0.94% (n = 1,940 measurements) respectively.

Figure 3.10: Calculated oxygen saturation (OS) along the length of a quartz tube containing arterial blood. (**A**) A cropped pseudocolour image of the model eye with a 100 µm tube containing arterial blood (measured OS = 98%). A coloured representation of the calculated OS has been overlayed on the tube with sequential calculated OS values to the left of the tube. (**B**) Mean optical density profile (*blue dots*) of the whole tube and the non-linear fitting oximetry algorithm (*red line)* to derive the calculated OS (106%). (**C**) Calculated OS (*red line)* along the length of the tube (mean calculated OS ± SD was 106% ± 1.13%). The locations of the different *Spectralon* reflective backgrounds with respect to the calculated OS are indicated in the legends within the graph. The table shows the mean calculated OS (± SD) of the blood column over segments of the *Spectralon* and along the whole length of the quartz tube.

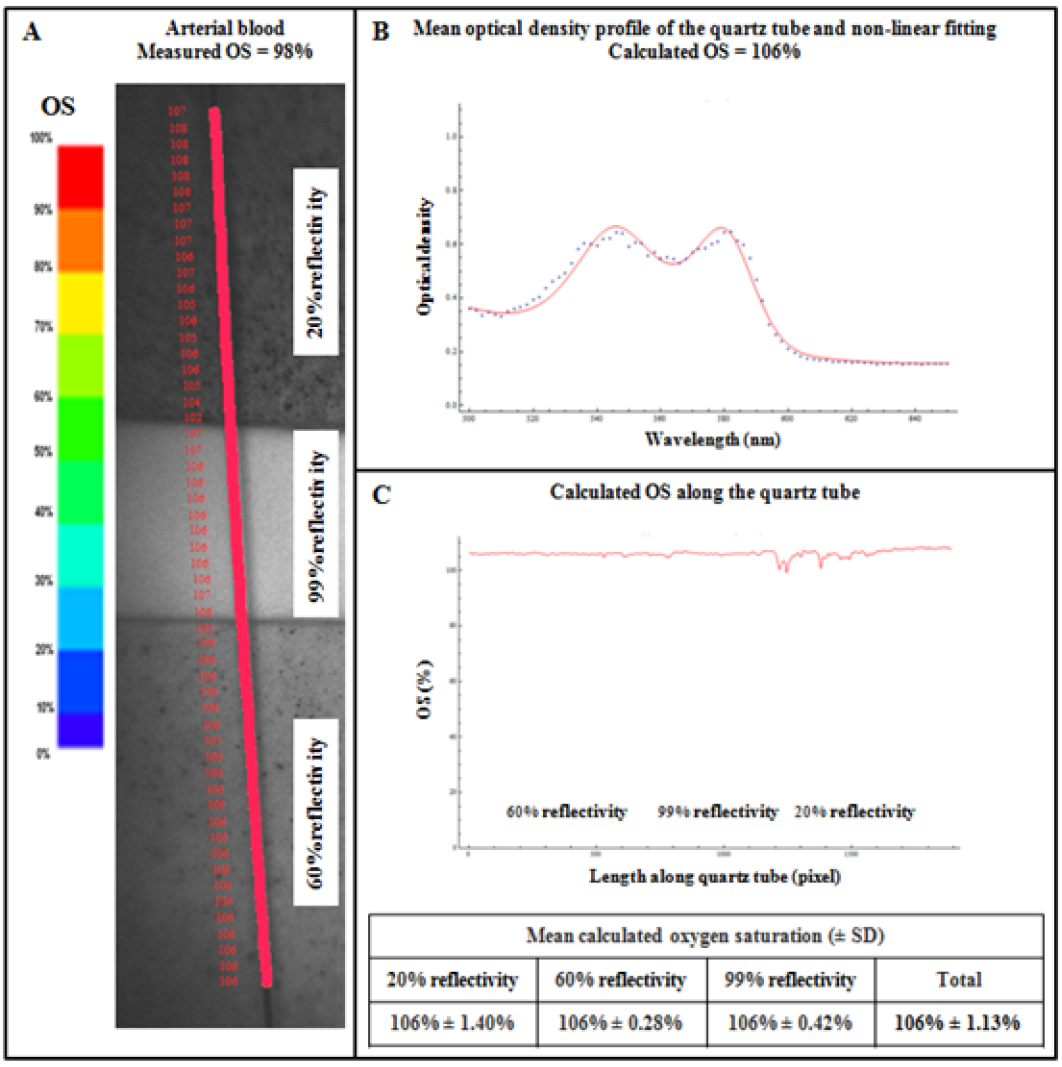

Mean calculated oxygen saturation (± SD)			
20% reflectivity	60% reflectivity	99% reflectivity	Total
106% ± 1.40%	106% ± 0.28%	106% ± 0.42%	106% ± 1.13%

Figure 3.11: Calculated oxygen saturation (OS) along the length of a quartz tube containing venous blood. (**A**) A cropped pseudocolour image of the model eye with a 100 µm tube containing venous blood (measured OS = 23%). A coloured representation of the calculated OS has been overlayed on the tube with sequential calculated OS values to the left of the tube. (**B**) Mean optical density profile (*blue dots*) of the whole tube and the non-linear fitting oximetry algorithm (*red line*) to derive the calculated OS (45%). (**C**) Calculated OS (*red line*) along the length of the tube, (mean calculated OS ± SD was 45% ± 0.94%). The locations of the different *Spectralon* reflective backgrounds with respect to the calculated OS are indicated in the legends within the graph. The table shows the mean calculated OS (± SD) of the blood column over segments of the *Spectralon* and along the whole length of the quartz tube.

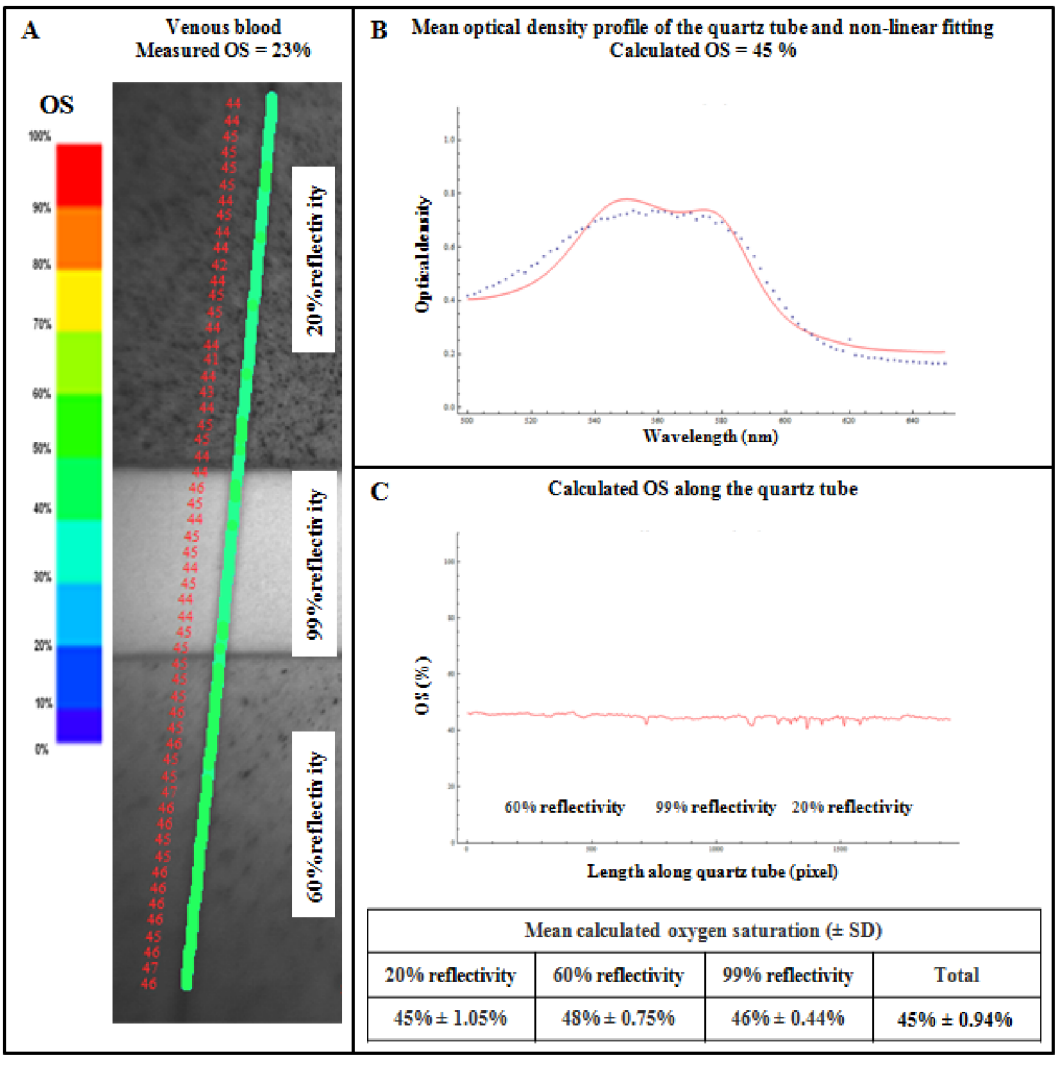

Mean calculated oxygen saturation (± SD)			
20% reflectivity	60% reflectivity	99% reflectivity	Total
45% ± 1.05%	48% ± 0.75%	46% ± 0.44%	45% ± 0.94%

3.3.4. Influence of the Blood Gas Parameters, Background Reflectivity and Quartz Tube Size on the Accuracy of the Calculated Oxygen Saturation.

A significant multiple linear regression model was used ($F = 4.54$, $P = 0.02$, adjusted R squared = 0.65) to assess the relationship between the mean OS difference and capillary size and blood gas analysis parameters (tHb, pH, PCO_2, PO_2,$[Na^+]$,$[K^+]$,$[Cl^-]$, Hct and lactate). In Table 3 the standardized coefficients of the independent variables - tHb, pH, PCO_2, PO_2,$[Na^+]$,$[K^+]$,$[Cl^-]$, Hct and lactate are presented. The independent variables were not a significant predictor of the model.

Table 3. Standardized regression coefficients derived from multiple linear regression analysis with mean OS difference as the dependent variable.

Predictor variable	Standardized coefficients	*P*
Quartz tube internal diameter (100µm and 150µm)	0.05	0.71
tHb	0.36	0.42
pH	-1.54	0.11
pCO2	-1.34	0.33
pO2	0.07	0.86
Na+	-1.23	0.38
K+	-0.98	0.05
Cl-	1.45	0.18
Hct	-0.36	0.48
lactate	0.66	0.49

The mean differences between the measured and calculated oxygen saturations for segments of the 100 µm and 150 µm quartz tubes overlying the different reflective backgrounds are expressed as histograms ± SEM in Figure 3.12. A comparison between the groups using a two-way ANOVA showed that the *Spectralon* reflectance and quartz tube sizes had no significant effect on the mean OS difference ($P = 0.18$ and $P = 0.99$ respectively). The *post-hoc* power calculation of the ANOVA analysis was 0.07.

Figure 3.12: Mean differences between the measured and calculated oxygen saturations (± SEM) in segments of the 100 µm ($n = 10$) and 150 µm ($n = 10$) quartz tubes overlying the 3 background reflectivities.

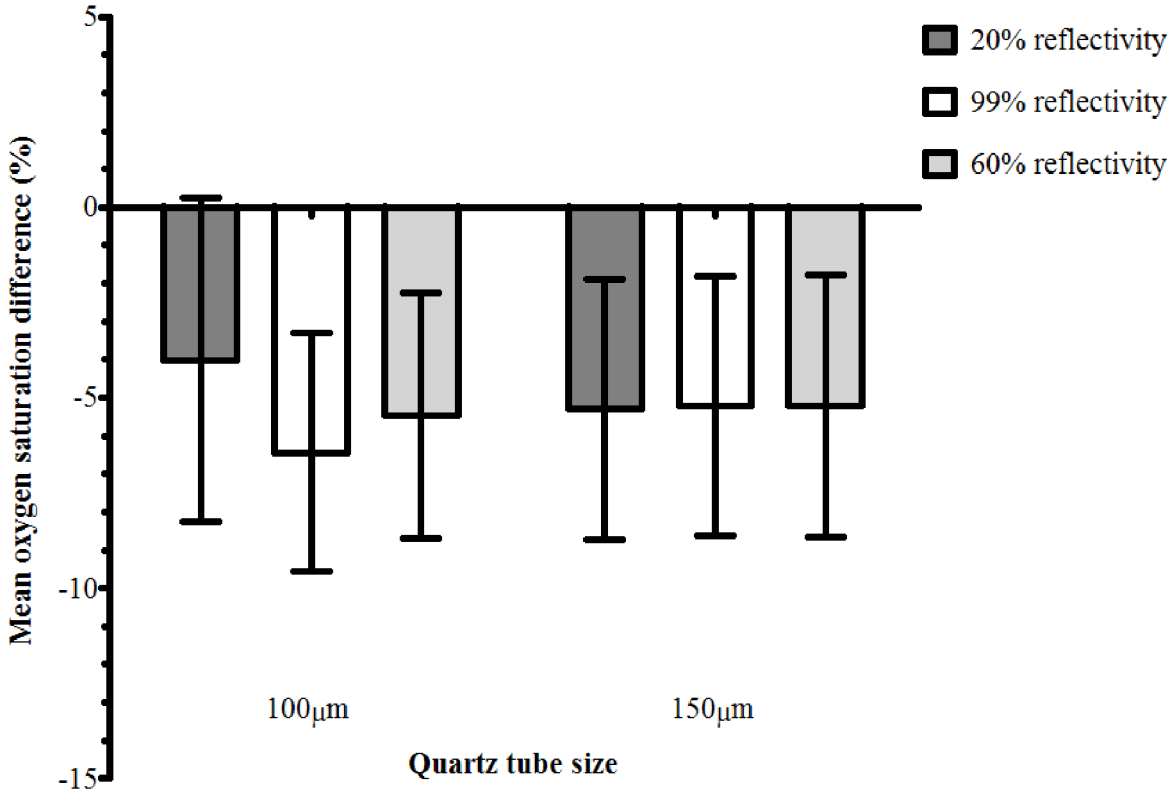

3.3.5. Correlation Between the Measured and Calculated Oxygen Saturation.

A significant and strong correlation between the measured oxygen saturation and respective mean calculated oxygen saturation of all 10 blood-filled 100 μm (r^2 = 0.96, P = 0.000008) and 10 blood-filled 150 μm quartz tubes was found (r^2 = 0.95, P = 0.000035).

3.3.6. Accuracy of the Blood Oxygen Saturation Calculations in the Model Eye.

Figure 3.13 shows Bland-Altman plots for segments of the 100 μm quartz tubes overlying the reflective backgrounds. The mean differences (± SD) between the measured and calculated OS in segments of the 100 μm and 150 μm tubes overlying the 20%, 60% and 99% background reflectivities were -4.0% (± 13.4%), -6.4% (± 9.9%), -5.5% (± 10.2%) and -5.3% (± 10.8%), -5.2% (± 10.7%), -5.2% (± 10.9%) respectively (95% limits of agreement were -30.2 – 22.3%, -25.9 - 13.0%, -25.4 – 14.8% for the 100 μm tubes and -26.5 – 15.9%, -26.3 – 15.8%, -26.5 – 16.1% for the 150 μm tubes).

Figure 3.13: Bland-Altman plots showing the agreement between the measured and calculated oxygen saturations in 100 µm quartz tubes. Each plot represents separate analysis of segments of the quartz tubes overlying the 3 reflective backgrounds: (**A**) 20% (**B**) 60% and (**C**) 99%. The mean of each corresponding measured and calculated oxygen saturations are plotted against the difference between the measured and calculated oxygen saturations.

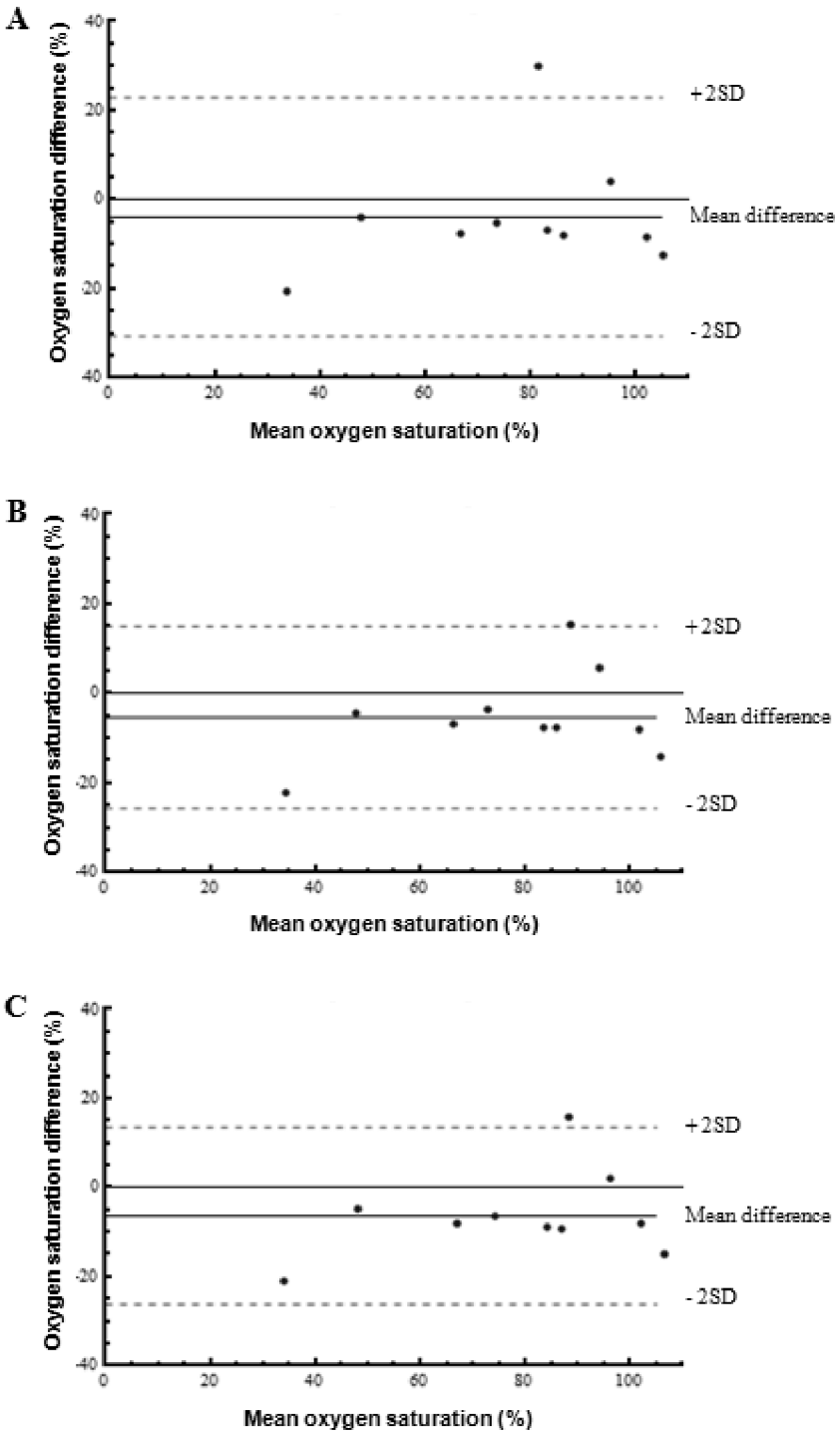

3.2. Discussion

This study demonstrates the ability of our hyperspectral imaging system and oximetry analysis to yield oxygen saturation calculations and evaluates its accuracy using a model eye.

The model eye provided a useful platform to acquire spectral images of blood samples with varying oxygenation. Although it represents a simple optical model of the eye, it has been a useful tool in determining the applicability of hyperspectral imaging to perform oximetry and determine the accuracy of our oximetry model using ground truth, *a posteriori* knowledge. Figure 3.7 illustrates an example where both arterial and venous blood can be visibly distinguished from the dark calibrated spectral images. In this example, both arterial and venous blood appear to have equal optical density at 586 nm, however, at wavelengths of 600, 620 and 650 nm, the arterial blood appears to be optically, less dense than venous blood. This is due to lower extinction coefficients of oxygenated blood at these wavelengths. This correlates with published descriptions of the extinction properties of fully oxygenated and fully de-oxygenated hemolyzed blood (van Assendelft, 1970), however, these observations provide only qualitative information regarding the OS of blood.

Our quantitative determination of the blood OS used a non-linear fitting oximetry model applied to the estimated $OD(\lambda)$ along a given column of blood. Importantly, we have made attempts to account for variables that influence the propagation of light in the retina, such as scattering by the red blood cells, the optical path length, hemoglobin concentration, and vessel diameter. In particular, this study has demonstrated that the incorporation of a scattering factor into the oximetry model improves its accuracy in calculating the OS of blood.

We have shown that the optical density profiles of arterial and venous blood (Figures 3.10B and 3.11B respectively) are spectrally distinguishable, and conforms to the published extinction coefficients of fully oxygenated and fully de-oxygenated hemoglobin (van Assendelft, 1970). This similarity of the optical density profiles to the published extinction coefficients suggests that the acquisition of spectral images at 2 nm intervals compensates, to some extent, for the variability of the liquid crystal tunable filter. Furthermore, the close approximation of the non-linear curve to the measured optical densities suggests that introducing a free parameter, *b*, into the oximetry model enables the non-linear curve to be

translated in a horizontal direction, thereby also compensating for the variability of the liquid crystal tunable filter.

This study has demonstrated that the oximetry model is capable of producing consistent calculated OS values along the length of each quartz tube (Figures 3.10C and 3.11C). The standard deviation of the calculated OS along each of the quartz tubes shown are small and the fluctuations in the calculated OS values can be explained by the texture in the background reflectance and/or physiological noise (scattering within the blood column due to red blood cells or other component of blood such as bilirubin, or physiological fluctuations in the oxygen saturation along the blood column). In the multiple linear regression analysis, no significant association was found between the OS difference and the blood gas parameters (tHb, pH, PCO_2, PO_2,$[Na^+]$,$[K^+]$,$[Cl^-]$, Hct and lactate) indicating that these independent variables were unlikely to influence the accuracy of the OS calculation.

Fluctuations in the calculated OS were more prominent in segments of the quartz tubes overlying the 20% reflective background and this can be explained by the increased contrast of the texture in the low albedo *Spectralon*. Further analysis of the effect of the background reflectivity and tube size on the mean OS differences in all quartz tubes was subsequently performed using a repeated measures, two-way ANOVA. The results indicated that the effect of the background reflectivity and tube size on the mean OS differences was not significant ($P = 0.18$ and $P = 0.99$ respectively). The consistency in the calculated OS along the length of the quartz tubes (Figures 3.10C and 3.11C) further illustrates the robustness of the oximetry model to variations in the background reflectivities. The oximetry model can, therefore, be considered to be robust to differences in the background reflectivity and tube diameter. These two features are commonly encountered in the retina where there are variable vessel diameters and variable amounts of fundal pigmentation resulting in different background reflectivities. The configuration of the *Spectralon* background within the model eye was specifically intended to broadly mimic the variability in fundal pigmentation (20% and 60% background reflectivity *Spectralon*) and the optic disc (99% background reflectivity) which is relevant to evaluating the applicability of the oximetry model to a wide population of subjects. The power of the ANOVA analysis was 0.07 according to the post-hoc power calculation and an undetected real difference in the accuracy of the OS calculation due to the small sample size could also explain the non-significant effect of the background reflectivity and tube size. In addition, the reflectivity of the *Spectralon* cannot be considered as a precise simulant of the fundus, which has distinct

spectral characteristic due to the presence of visual pigments, blood and other retinal chromophors. Further, investigation is required to determine the accuracy of the oximetry technique in the human eye. A further limitation of this study was that tests of repeatability could not be performed with a high degree of precision. The main reasons for this were, firstly, that the oxygenation of a given blood sample changed (albeit by a small percentage) over a time period between re-imaging. Secondly, the process of imaging the blood samples was carried out within a few minutes. From experience, we found that prolonging the imaging process would lead to segmentation of the blood column in the quartz tubes which could lead to undesirable and uncontrolled changes in the OS of the blood column within the tube.

We have demonstrated a significant and strong correlation between the measured and calculated OS in 100 μm and 150 μm quartz tubes ($P < 0.01$ in both tube sizes). However, to assess the agreement between the measured and calculated OS, the Bland-Altman method was used for each segment of the 100μm (Figure 3.13) and 150 μm quartz tubes overlying the different reflective backgrounds.

The limits of agreement are high from a clinical point of view. It is unlikely that the limits of agreement were affected by the variability of the measured OS as the mean difference ± SD between the measured OS before and after imaging was small (0.49% ± 0.76%). This figure may have been adversely affected by systematic effects; two plausible reasons are: the oxygenation of the blood in the tube may have changed upon transfer from the blood gas syringe to the quartz tube – however this is unlikely as the transfer of the blood samples to the quartz tubes occurs in a few seconds and secondly, and most plausibly, the oximetry model may be overestimating the true OS through an imperfect match between the optical model for $OD(\lambda)$ and the data. This is illustrated in Figure 3.11B in which a sample of venous blood with a measured OS of 23% is analyzed. The spectral variation in optical density for the whole tube (blue dots) appears to have a distinct "bell" shape; however the oximetry model fits a curve to the data which exhibits a distinctive "double-hump" (red line), which is redolent of fully oxygenated blood. It is therefore likely that a fitting error for venous blood may have contributed towards an overestimation of its true OS. However, this does not necessarily provide a full explanation of the wide limits of agreement as it can be observed in Figure 3.13 that there are two underestimates of the measured OS at the higher end of the oxygen saturation scale. It is unlikely that the limits of agreement were affected by the variability of the measured OS as the mean difference ± SD between the measured OS

before and after imaging was small. Additionally, the systematic effect of a fitting error does not address the variability and high SD in the mean differences between the measured and calculated OS. Further experiments and evaluation of the fitting technique would be required to establish a comprehensive explanation for our findings. Our future research will initially focus on refining the physical model to remove the effects of this systematic error, particularly at lower oxygen saturations.

The phenomenon of overestimating the true OS has been previously reported in studies on other types of photometric oximeters. Sarnquist et al. (1980) reported that pulse oximeters were overestimating the actual OS with an average reading of 70% at 50% actual OS. This overestimation in pulse oximeters is thought to be caused by the scattering of red or infrared light in the blood vessels (Shimada et al., 1984). Additionally, Drewes et al. (1999) reported an error of ±52% at 0% blood OS in a model eye using an Eye Oximeter and Delori et al. (1988). reported overestimations of the true OS, particularly at lower OS, in *in vitro* tests of the Retinal Vessel Oximeter. In light of this, the accuracy of our oximetry model is comparable to these reports. Errors of this magnitude are higher than is desirable since accuracy in the determination of both the arteriolar and venular oxygen saturation is important in determining the functional status of the inner retina. This limitation of our oximetry model to lower blood OS could be improved by further research to enable accurate characterization of scattering effects within and around the blood column. A comparison of the accuracy of the model eye experiments reported in this thesis to model eye experiments reported by other authors (described in Chapter 1) is shown in Table 4.

Further limitations of this study include the lack of control of the blood sample properties such as its temperature during imaging, pH, haemoglobin concentration, haematocrit and mean corpuscular volume. In addition, the light scattering influences of segmentation within the blood column (including platelet aggregation) during imaging and the shape of the red blood cells in the quartz tubes of varying internal diameters requires further attention on its effects on the accuracy of the oximetry technique in future studies. Further improvements to the model eye, to more accurately simulate the optical characteristics of the human retina, would be desirable in order to achieve a more detailed appraisal of the oximetry technique.

Table 4. Comparison of the accuracy of the model eye results reported in this thesis to the accuracy of model eye experiments reported by other authors.

Author	Accuracy
This thesis	The mean (± SD) OS differences were -7.1% (± 7.1%) and -6.2% (± 10.2%) in the 100 µm and 150 µm tubes respectively.
Laing and Cohen (1975) Cohen and Laing (1976)	Better than 1% oxygen saturation. Oximetry model was comparable at high oxygen saturations. At low oxygen saturations the theoretical calibration line underestimated the actual oxygen saturations by up to 20%.
Hickam and Frayser (1949)	The standard deviations of the ODRs from the measured OS were relatively small: 6% and 9% OS in 500µm and 250µm glass capillaries respectively.
Delori (1988)	Oximetry model was most accurate in the range of 50 - 100%. In the range between 0 - 50% there was a tendency towards overestimating the measured OS.
Schweitzer et al. (1999)	No accuracy reported.
Drewes et al. (1999) (Denninghoff)	The reported error was small at measured oxygen saturations of 83% (± 4% error) but increased with lower oxygen saturations to a maximum at measured oxygen saturations of 0% (± 52%)
de Kock et al. (1993)	A linear relationship was demonstrated between the R/IR ratios and the measured blood oxygen saturations from 100% to 85%. However, at blood oxygen saturations below 85%, a non-linear relationship with the R/IR ratios.

In summary, the model eye has been a useful test bed for evaluating our method of measuring the OS of blood using a hyperspectral fundus camera. Our oximetry technique was shown to be reasonably accurate and robust to variable features such as background reflectivity and quartz tube diameter. Further studies will be described in the subsequent chapters which apply these oximetry techniques on spectral images of the human retina.

Chapter 4: Human Imaging and Spectral Image Analysis.

4.1. Introduction.

The aims of this chapter are to describe:

- the use of the hyperspectral fundus camera to acquire hyperspectral retinal images from healthy subjects
- the application of the image processing and analysis algorithms to calculate the oxygen saturation (OS) of the retinal vasculature.

4.2. Methods.

This study was conducted in accordance with the ethical standards of the Declaration of Helsinki and was approved by the local Research and Ethics Committees at Gloucestershire Hospitals NHS Foundation Trust (REC reference number: 06/Q2005/132)

4.2.1. Recruitment, Assessment and Preparation of Volunteers.

Twenty-three healthy subjects were recruited from the eye departments in Cheltenham and Gloucester General Hospitals between 2006 and 2010. Healthy subjects also included staff members from Cheltenham and Gloucester General Hospitals who volunteered to participate in the research. These volunteers responded to poster advertising placed in the respective eye departments. Written informed consent was obtained from all volunteers.

All normal subjects were assessed by the study investigator. The best corrected visual acuity (BCVA) was measured using a Snellen chart to record the distance vision. Intraocular pressures (IOP) of both eyes were measured using Goldmann applanation tonometry. Slit-lamp biomicroscopy was used to assess the anterior segment. The pupils of the normal subjects were dilated with 1% tropicamide (Minims; Chauvin Pharmaceuticals, Romford, UK). The Lens Opacities Classification System III (LOCS III) (Chylack et al., 1993) was used to grade the degree of lens opacity. Dilated fundoscopy was performed by slit-lamp

biomicroscopy using a 78D lens. Oximetry measurements of the index finger were performed in all volunteers using a pulse oximeter (Biox 3740, Ohmeda, Louisville, CO). Brachial blood pressure of all normal subjects was measured using an aneroid sphygmomanometer (Accoson 0342: A.C. Cossor & Son (Surgical) Ltd., Essex, UK).

Inclusion criteria were BCVA 6/9 or better, open anterior chamber angle, absence of any ocular pathology, IOP <21 mm Hg, normal optic disc appearance. Exclusion criteria included history of intraocular surgery, ocular pathology, diabetes mellitus, stroke, hypertension, glaucoma family history.

4.2.2. Acquisition of Hyperspectral Retinal Images.

The hyperspectral fundus camera has been previously described in detail in Chapter 2. Spectral images of the retina were acquired using wavelengths between 500 nm and 650 nm at 2 nm intervals. To obtain the optimal focus of the retina, images at 580 nm were acquired and viewed in real time. Fine adjustments to the camera focusing was performed until the edges of the retinal blood vessels within and around the optic disc and macular appeared sharp. The subjects were instructed to maintain their head position on a head mount with their forehead firmly pressed against a forehead strap until the complete set of spectral retinal images were acquired. Eye fixation was maintained by instructing the subject to fixate on a red fixation light with the contralateral eye. The positioning of the optic disc within the retinal image was achieved by positioning the red fixation light in front of the contralateral eye such that the location of the optic disc in the retinal images in all normal subjects was approximately midway between the centre and the image border (right image border for the right eye and left image border for the left eye). This ensured that the macula region was captured within each image.

At wavelengths between 500 – 550 nm and 620 - 650 nm the contrast of the retinal blood vessels to the retinal background was low. At these wavelengths, it was difficult to determine the focus of the images. Therefore the imaging sequence protocol started at 580 nm and spectral images were acquired by changing the LCTF wavelengths in 10 nm steps up to 650 nm. The LCTF was then changed to 582 nm to ensure optimal focus and spectral images were again acquired by changing the LCTF wavelengths in 10 nm steps up to 648 nm. This procedure was repeated to obtain spectral retinal images between 580 nm and 650 nm in 2 nm intervals. The same procedure of changing the LCTF wavelengths was performed to

obtain spectral retinal images between 580 nm and 500 nm in 2 nm intervals. Significant head movements and eye movements caused changes in the focus of the images. Defocused images were identified by viewing the captured images in turn on the computer screen. The defocused retinal image at the given wavelength was reacquired by adjusting the camera focus and/or repositioning the subject's head.

Early experience with the hyperspectral fundus camera showed that if the wavelength was changed too rapidly the LCTF had a tendency not to respond to the command resulting in an image acquired labelled with the wrong wavelength. Associating the retinal image with the corresponding wavelength is an essential part of the image processing and analysis algorithms. Therefore, a 3 - 4 second time interval between changing the LCTF wavelength, and acquiring an image was used to ensure that the LCTF had responded. Furthermore, by imaging the retina in 10 nm intervals the characteristic spectral changes within the retinal image could be viewed to ensure that the LCTF had responded (Figure 4.1). Sequential imaging often resulted in images that are poor quality due to small eye movements, head movements and eyelid blinking. To ensure that the best quality images were obtained, two good quality images (determined by the operator) for each wavelength were acquired before the wavelengths were changed. This imaging protocol ensured that all spectral images of the retina were of the highest quality prior to processing. The mean (± SD) time to acquire a series of spectral images of the retina between 500 – 650 nm was 11 minutes 5 seconds (± 7 minutes 41 seconds).

4.2.3. Selection and Processing of Hyperspectral Retinal Images.

Selection of the best retinal images for each wavelength was performed manually. This was done by inspecting the raw 12-bit retinal images on a computer using an image viewing software (Windows picture and fax viewer, Microsoft, Redmond, WA). Appendix 2 illustrates examples of the image selection process. Appendix 3 illustrates histrogram of a sample raw retinal image acquired at 580 nm .

The majority of the image processing algorithms applied to the retinal images were the same as the algorithms applied the model eye images described in Chapter 3. The specific image processing algorithms that were applied to the retinal images are described in the following sections.

Figure 4.1: Spectral images of a normal retina acquired using wavelengths between 580 and 618 nm. Characteristic spectral changes of the optic disc and retinal blood vessels (appear lighter) are more obvious as the wavelengths are changed in 10 nm increments. The characteristic spectral changes are less obvious in 2 nm increments.

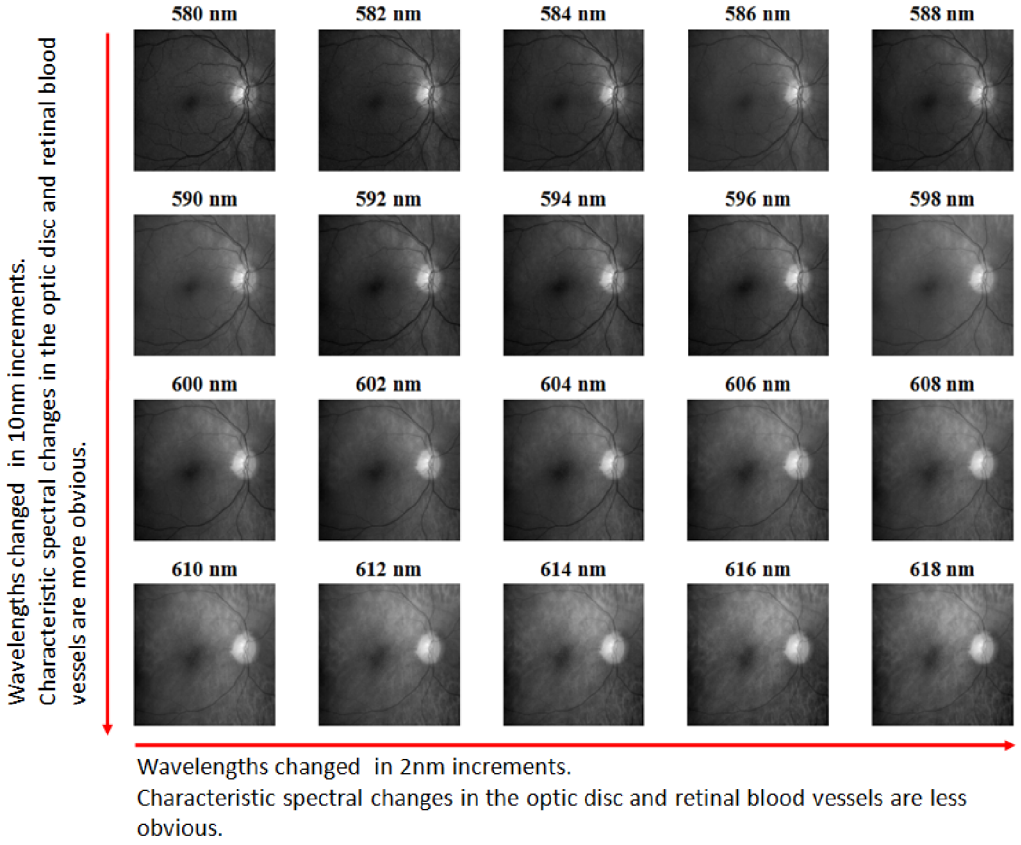

4.2.3.1. Dark Calibration.

The method of dark calibration was described in Chapter 3. However, the effectiveness of the dark calibration in removing noise from the optical system (especially the central annular artefact) was not obvious in the model eye images due to the presence of the highly reflective *Spectralon* in the centre of the image field. In the retinal images, the central annular artefact is located over the macular and can project onto the vascular structures. Figure 4.2 illustrates the effect of the dark calibration in reducing the signal of the central annular artefact in an example retinal image acquired at 580 nm.

Figure 4.2: Dark calibration of a retinal image. An image of a normal right retina acquired at 580 nm before (*top left*) and after (*top right*) dark calibration (subtraction of a dark image at the corresponding wavelength). Line profiles of the intensity across the fixed pattern artefact in the retinal image before (*bottom left*) and after (*bottom right*) dark calibration are shown below each image. The central artefact is less apparent in the dark calibrated image and its signature in the intensity line profile has been attenuated.

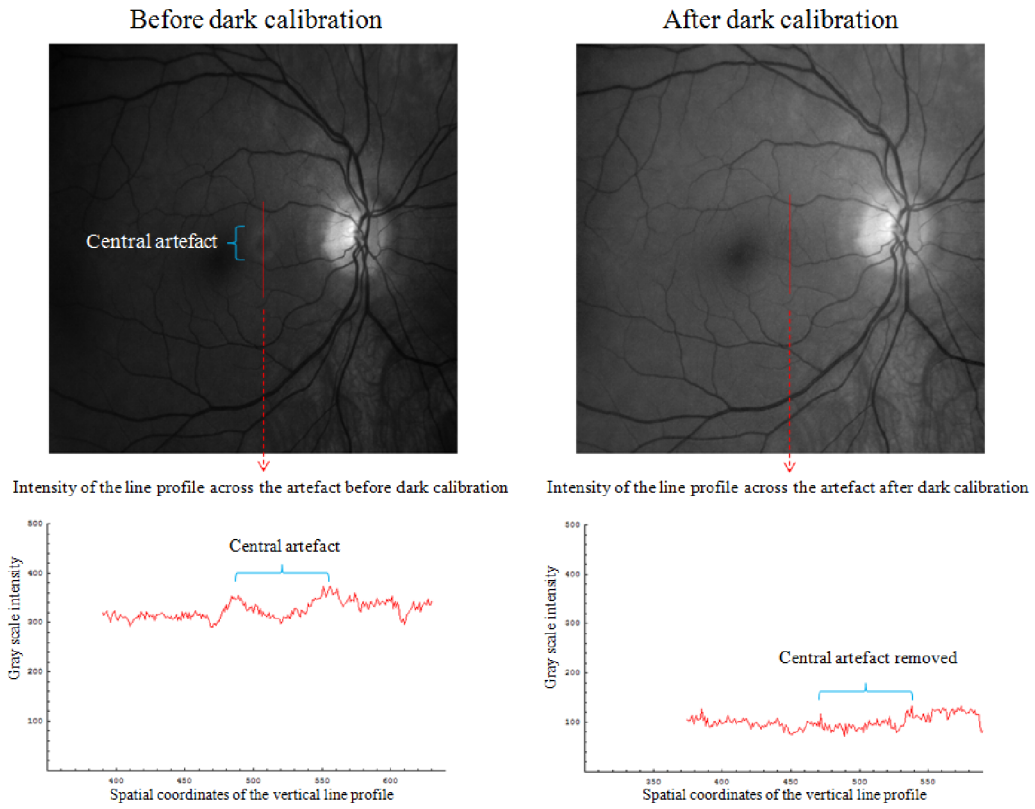

4.2.3.2. Image Registration.

Image registration is a method of aligning images of the same scene into one common coordinate system. Numerous methods have been used to align different types of images and various approaches have been applied to the registration of retinal images. An in depth discussion of these methods is beyond the scope of this thesis but they can be broadly categorized into intensity-based (Maes et al., 1997; Matsopoulos et al., 1999; Ritter et al., 1999; Lloret et al., 2000; Cideciyan, 1995; Ballerini, 1997; Skokan et al., 2002) and feature – based (Stewart et al., 2003; Sofka and Stewart, 2006; Xu et al., 2007; Li and Chutatape, 2007; Can et al., 2002; Zana and Klein, 1999) methodologies. The main problem in time-sequential

imaging is the misalignment of the raw spectral retinal images due to the saccadic movements of the eye. The alignment of the spectral retinal images is of paramount importance to enable the measurement of the oxygen saturation at a given point in the retinal image plane.

The image registration method that was used in this research employed a cross-correlation technique. A customized image processing routine written in *Mathematica* (ver. 5.2; Wolfram Research, Inc., Champaign, IL) was used to perform the image registration. The cross-correlation technique measures the degree of similarity between two images. A reference image is chosen, usually at 580 nm where the appearances of the arterioles and venules are equally as dark and have a higher contrast in comparison to the retinal background. All of the other spectral retinal images are aligned to the coordinates of the reference image. The maximum of the cross-correlation of each image is searched by rotating and translating the images and comparing it to the reference image. The amount of translation and rotation required to align each image to the reference image is calculated from the maximum cross-correlation between each images and the reference image. The cross-correlation technique requires features within each image to be similar in appearance irrespective of the wavelength. However, the appearance of the spectral retinal images change in relation to the wavelengths used to acquire them (Figure 4.3). Hence, a number of pre-processing steps were implemented during the image registration process. Firstly, sequential spectral retinal images were acquired such that the main features of the retinal images (optic disc and large retinal vessels) were located in approximately the same position in the image field. Secondly, the vascular network and the optic disc were used as features within each image and enhanced to enable accurate cross-correlation between the reference retinal image and the sequential spectral images. These features were enhanced using customized passband and edge detection (Laplacian of Gaussian [Marr and Hildreth, 1980]) filters. Lastly, the enhanced images were converted into the frequency domain using fast Fourier transformation (FFT). These Fourier transformed enhanced images were used in the cross-correlation image registration process to reduce the time required for the calculation of the maximum correlation between the spectral images and the reference image. A flow chart of the image registration algorithm is shown in Figure 4.4. An illustration of 6 spectral images from one normal eye, before and after image registration is shown in Figures 4.5A and 4.5B respectively. In Figure 4.5, landmark retinal features were manually selected from a reference retinal image to illustrate the misalignment of the retinal images before the image registration (Figure 4.5A) and their alignment after image registration (Figure 4.5B).

Figure 4.3: Spectral images of a normal right retina at six wavelengths.

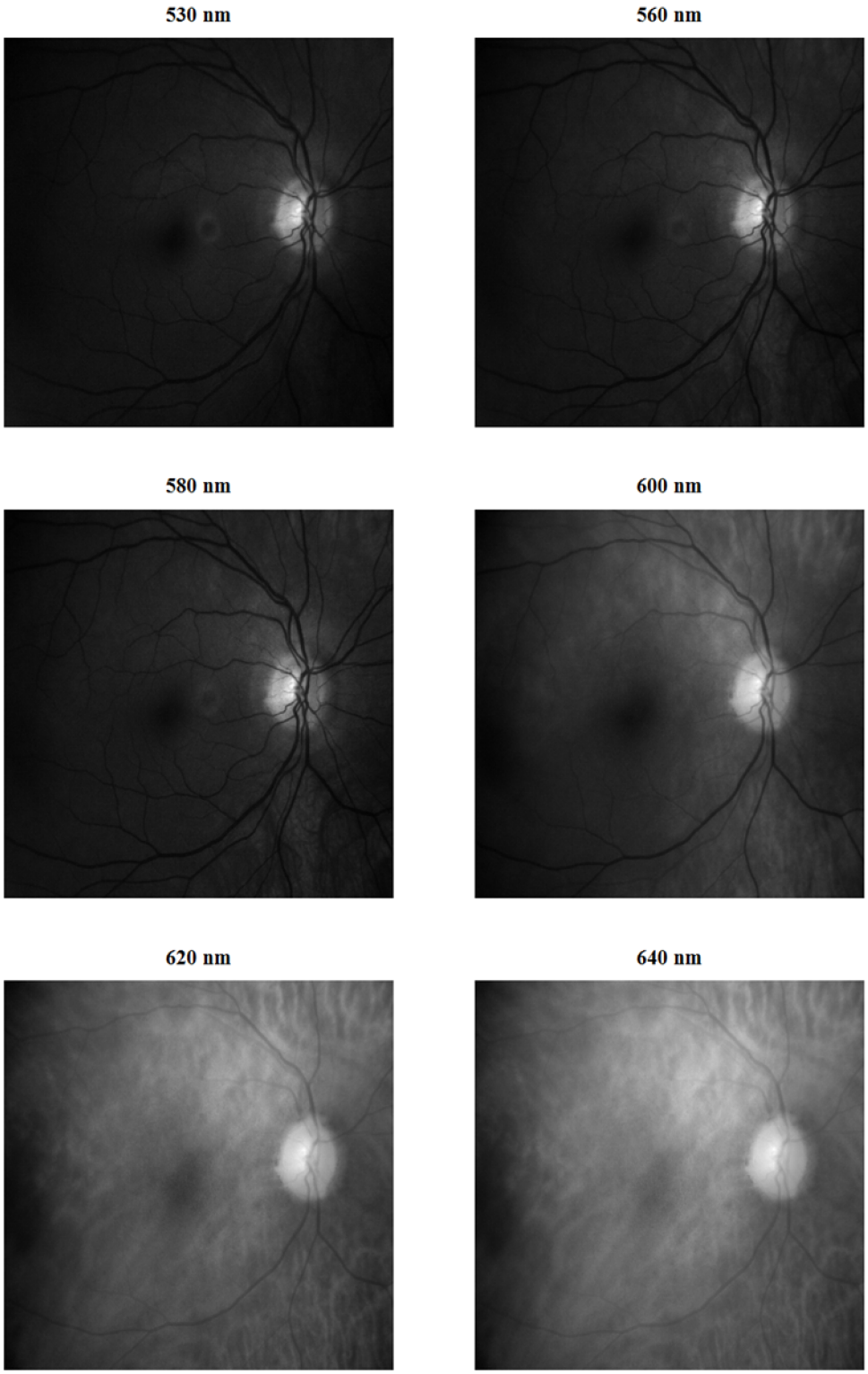

Figure 4.4: Flow chart of the registration algorithm.

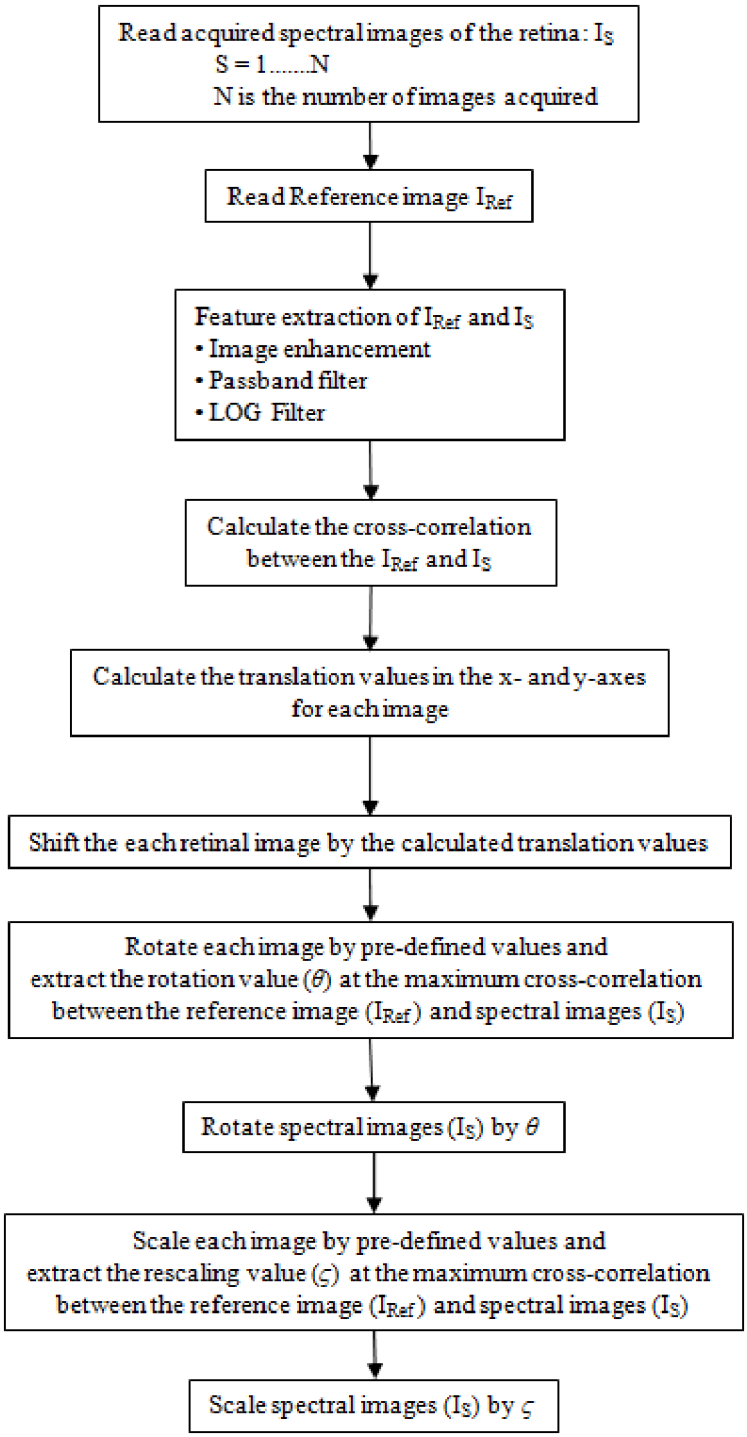

Figure 4.5: Spectral retinal images before and after registration. ***A***. Unregistered raw spectral images of a normal right retina at six wavelengths. Six coordinate points (*red dots*) selected manually from the reference image (580 nm – *red square border*) overlying the retinal blood vessels and the corresponding coordinate points are displayed in the retinal images acquired at 530, 560, 600, 620 and 640 nm. The images are misaligned. ***B.*** Registered dark calibrated spectral images of a normal right retina at the 6 wavelengths. The six manually selected coordinate points (*red dots*) overlie the same landmark structures demonstrating the alignment of the retinal images.

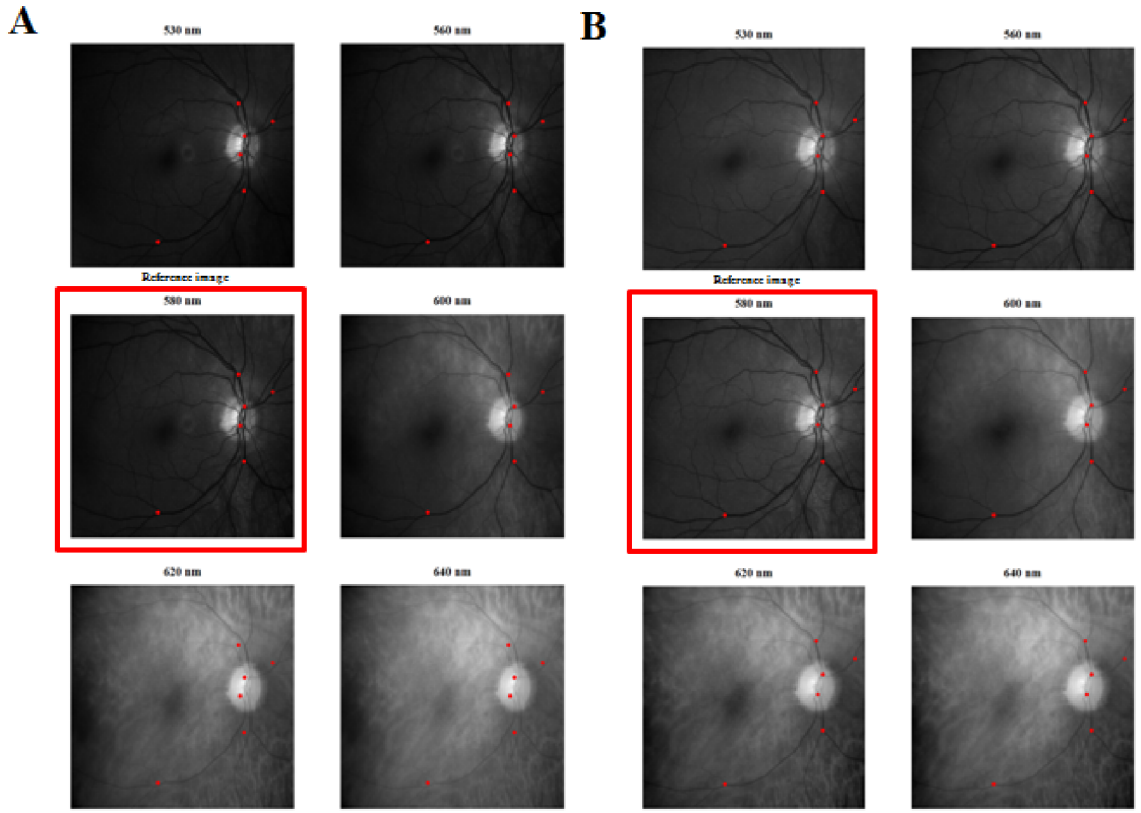

Subsequent to the registration of all the spectral images, the registered images were checked visually by comparing the alignment of the registered images to the reference image. Images that appeared to be significantly misregistered were removed from further processing and analysis. In total 19 (0.01%) images were removed due to misregistration from all the images collected (n = 1784).

4.2.3.3. Vessel Detection and Tracking.

The coordinates of the centreline of the retinal vasculature were calculated by manually detecting the retinal blood vessels and applying a semi-automated vessel tracking routine. The vessel tracking technique is based on the Fast Marching Method (Sethian, 1999) which searches for pixels between two points with the lowest intensities and finds its shortest path. To enable accurate tracking of the retinal vasculature a reference retinal image (580 nm) was converted into an image which highlighted the retinal blood vessels by assigning the lowest pixel values to the vessels in contrast to higher pixel values to the retinal background (Figure 4.6). Two points along the length of a given blood vessel segment within the reference image were manually selected and the vessel tracking algorithm was applied.

Figure 4.6: Conversion of an image of a normal left retina into an image which highlights the retinal blood vessels. (*Right*) Dark calibrated registered reference image of a normal left retinal acquired at 580 nm. (*Left*) Processed image highlighting the retinal vasculature.

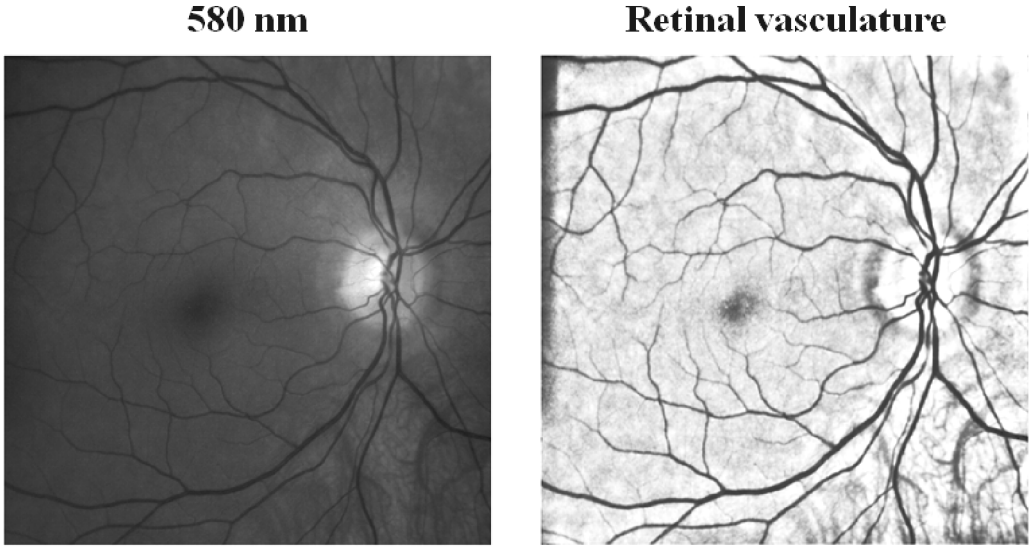

The vessel tracking algorithm was frequently unable to distinguish between two vessels that were in close proximity to or crossed each other. The result lead to the vessel tracking of two different vessels. This often occurred when tracking arterioles in close proximity to or crossing over large venules resulting in the tracking of the larger venules.

To prevent this from occurring, my method was to select two points at short distances apart (as opposed to the whole length of a vessel), apply the vessel tracking algorithm and repeat the procedure along the length of a given blood vessel. This was particularly useful for arterioles and smaller venules. For the larger 1st degree venules, the vessel tracking algorithm was capable of following the course of the whole vessel along its length (Figure 4.7, *top images in the third and fourth columns*).

Figure 4.7: Semi-automated vessel detection of the superotemporal and inferotemporal arterioles and venules. Each image illustrates the results of the vessel tracking for a segment of the retinal blood vessel. The vessel tracking program identifies coordinates in the centre of the vessel along the segment (*red line*). The coordinates of a series of linear profiles orthogonal to two adjacent centreline coordinates are subsequently calculated (*blue lines*).

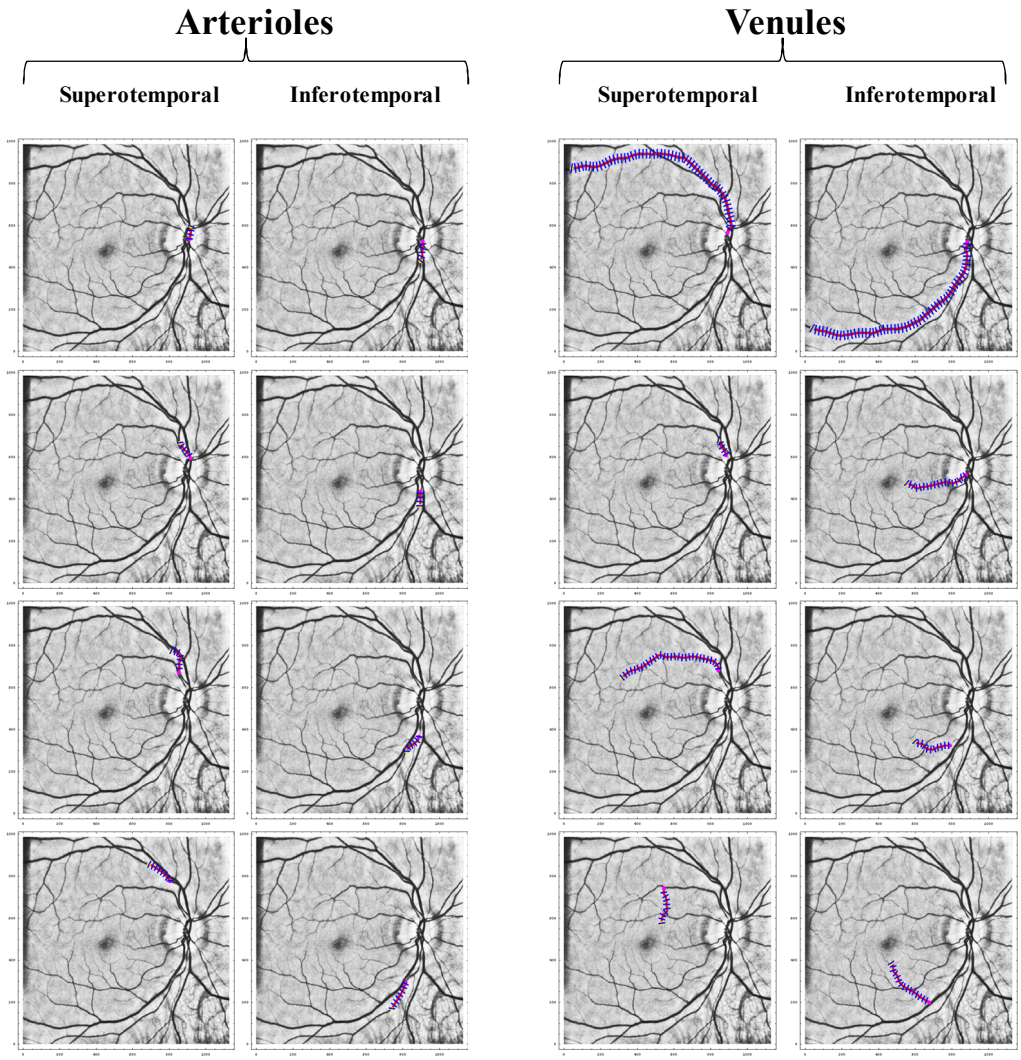

The vessel tracking procedure was repeated until the majority of the retinal vasculature was identified (Figure 4.8). Small arterioles and venules were often the most difficult to obtain accurate tracking and therefore tracking of some of the smaller blood vessels were omitted due to vessel tracking errors. The vessel tracking algorithm enabled an estimate of the centreline coordinates of the retinal blood vessels.

Figure 4.8: Completed vessel tracking of the retinal vasculature in an image of a normal left retina. The different colours indicate segments of the vessels that were tracked separately.

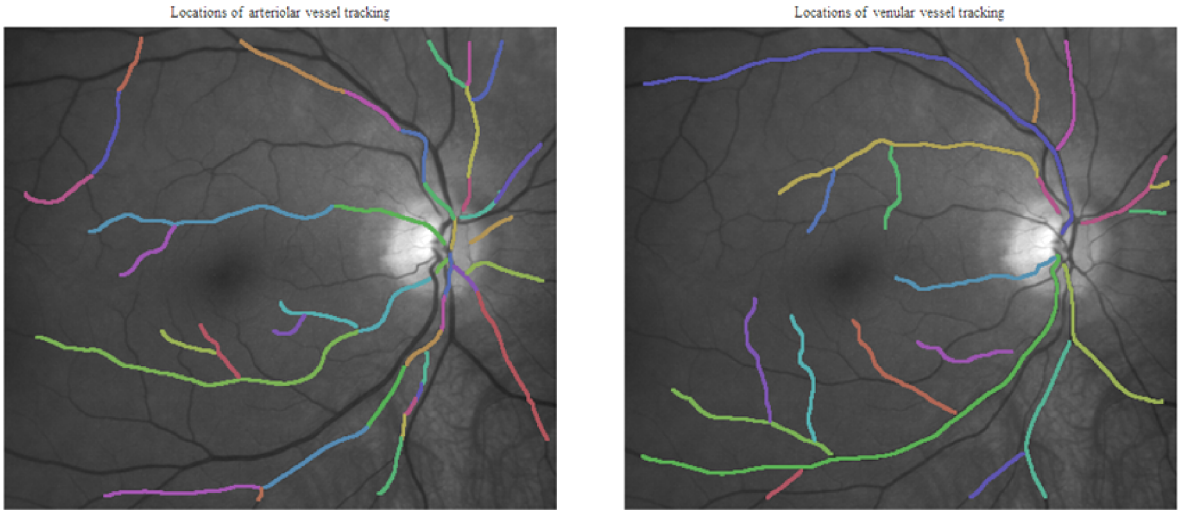

4.2.3.4. Vessel Profile Extraction and Calculation of the Light Transmission of the Retinal Vasculature.

The centreline coordinates along each blood vessel was subsequently used to calculate the coordinates of a series of linear profiles orthogonal to the vessels. This was performed by calculating the perpendicular of the gradient between two successive points along the centre of a given blood vessel (Figure 4.9). The result was a series of linear profiles perpendicular to the blood vessels in the retinal vascular network (Figure 4.10). The length of the profile was manually selected depending on the size of the blood vessel and was approximately 2-3 times the estimated width of the blood vessel. The intensity values along the length of each linear profile were extracted (Figure 4.11). This was repeated for all the spectral images (Figure 4.12) such that for each linear profile in a given blood vessel the intensity values along that profile were extracted for all wavelengths.

Figure 4.9: Calculation of the perpendicular of the gradient between two successive points along the centre of a given blood vessel

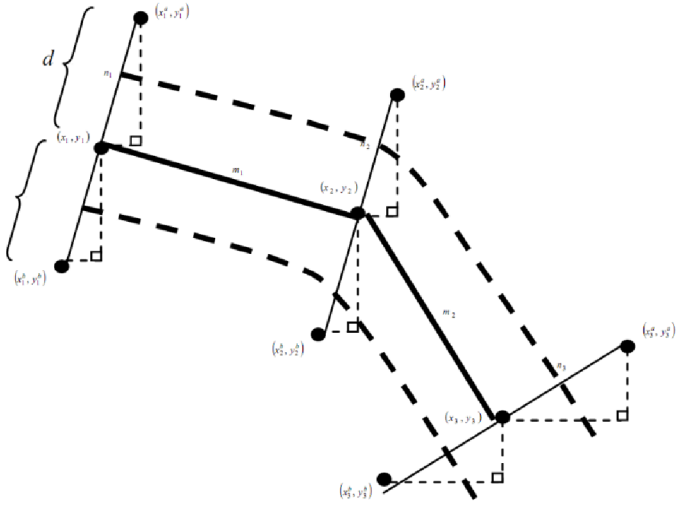

Figure 4.10: Linear profiles perpendicular to the retinal blood vessels in an image of a normal left retina.

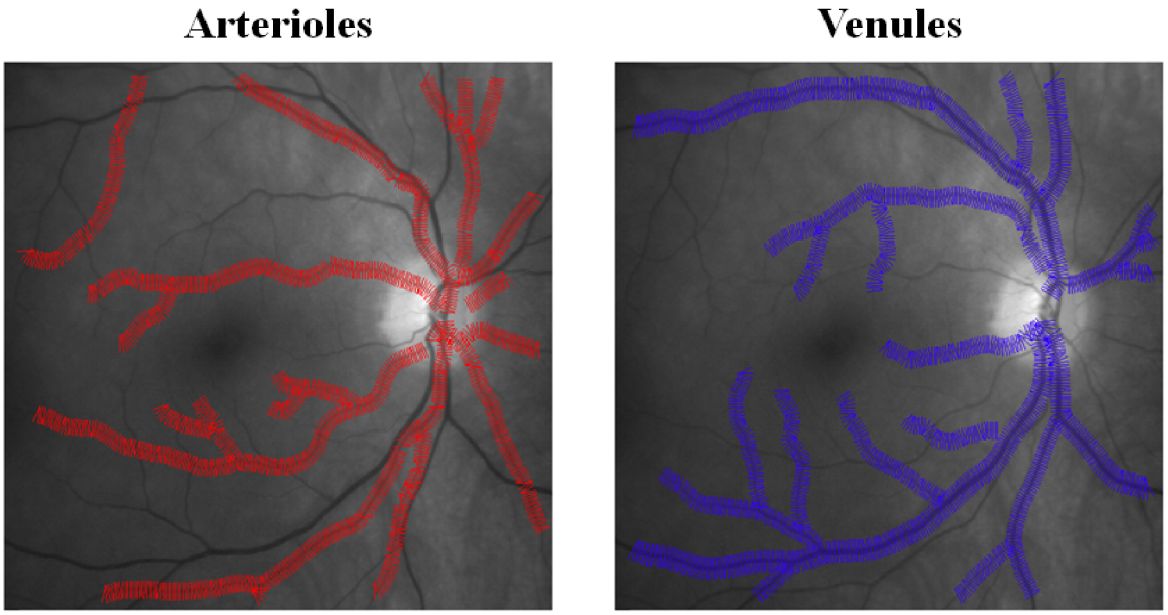

Figure 4.11: Intensity along a given profile of a point in a retinal blood vessel at 580nm.

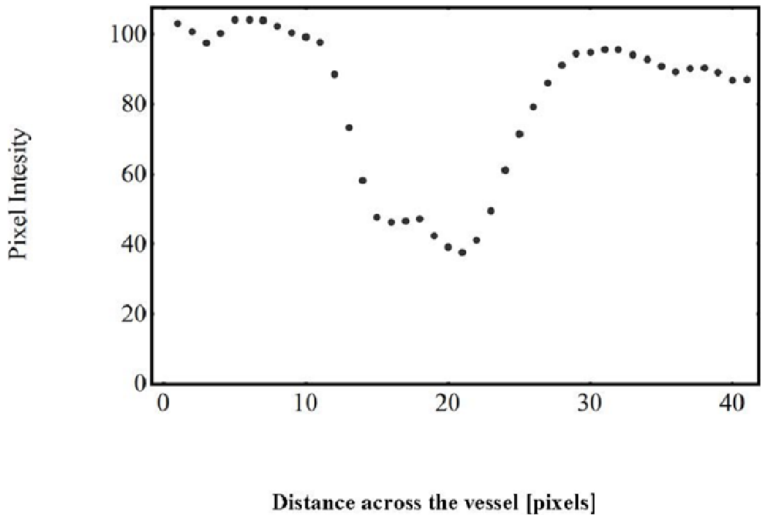

Figure 4.12: Intensity of a given profile of a point in a retinal blood vessel at various wavelengths.

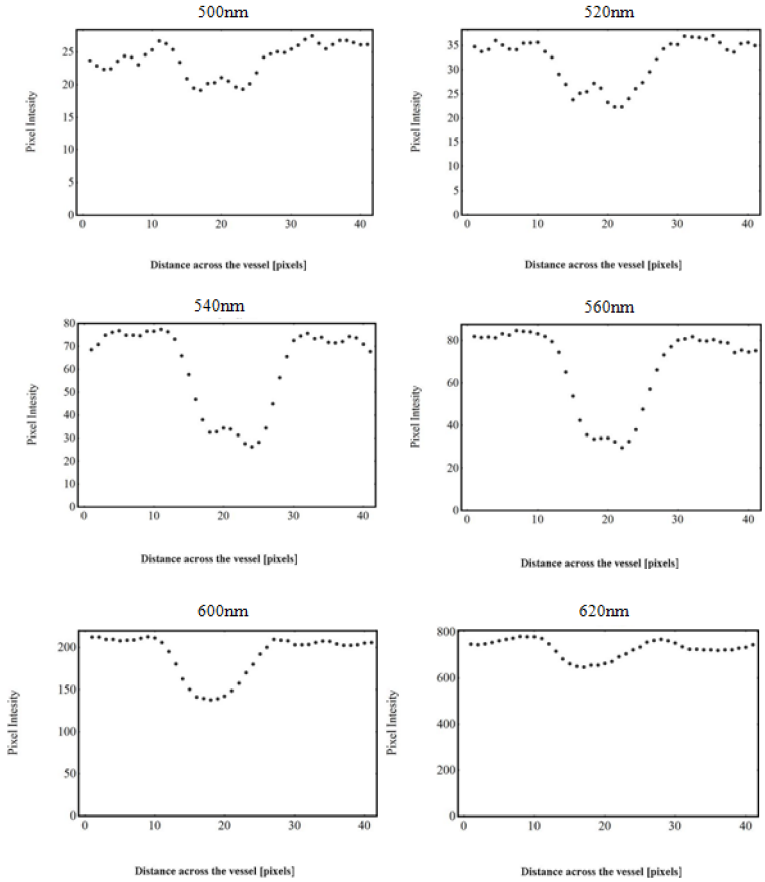

4.2.3.5. Optical Density Estimation.

The method used to estimate the optical density in the centre of a given point in a blood vessel was the same as that described in Chapter 3 for the model eye experiments. Briefly, fitting algorithms were applied to each gray-scale intensity profile to estimate the intensity at the centre of the blood vessel (minima of the non-linear curve) and intensity of the background adjacent to the blood vessel (gray-scale value of the linear fit at the centre of the blood vessel). The optical densities of a given point were estimated across the wavelength range (500 – 650 nm) to calculate the optical density profile. This was repeated at all points along all the selected blood vessels.

4.2.3.6. Oxygen Saturation Calculation.

The method used to calculate the OS along the length of the retinal blood vessels was the same as that described in Chapter 3 for the model eye experiments. This was performed by using an algorithm based on the Levenberg-Marquardt non-linear fit to the complete set of OD(λ) for a given point on the tracked blood vessel in the equation,

$$OD(\lambda) = a\,S(\lambda) + \eta(\lambda)\,C_{HbTotal}\,d\,[cOS\,(\varepsilon_{oxy}(\lambda + b) - \varepsilon_{de\text{-}oxy}(\lambda + b)) + \varepsilon_{de\text{-}oxy}(\lambda + b)] \quad \text{(Eq. 1.6)}$$

where, $C_{HbTotal}$ is the total concentration of haemoglobin, ε_{oxy}, and $\varepsilon_{de\text{-}oxy}$ are the extinction coefficients of oxygenated and deoxygenated haemoglobin (van Assendelft, 1970)[193] respectively corrected for convolution with the spectral response of the liquid crystal tunable filter, d is the vessel diameter, cOS is the calculated oxygen saturation, η is the effective optical path-length contribution (Smith et al., 2000) and a is a scaling constant of the curve along the y-axis. Importantly, b is a scaling constant of the curve along the x-axis which compensates for the variability of the liquid crystal tunable filter which was described in Chapter 2. Wavelength dependent optical scattering values published by Meinke et al. (2007). were used in this oximetry model.

4.2.3.7. Determining the Wavelength Range for Retinal Oximetry.

An evaluation of the OS calculations in normal eyes at an early stage of the research project revealed that when a wavelength range between 500 and 650nm was used it frequently calculated lower than expected oxygen saturations of the retinal arterioles (about 70 – 80%). It was therefore important to determine the wavelength range that would yield the most accurate OS calculations.

Retinal images from 3 normal subjects were used to determine the most accurate wavelength range. For each subject, optical density profiles (n = 101) were generated from selected segments of the retinal arterioles and averaged (Figure 4.13). The mean optical density profile was used to calculate the OS using the oximetry algorithm.

Figure 4.13: Generation of the mean optical density profile of a selected segment of retinal arteriole in a normal subject. (*Left*) An image of the retina acquired using 580 nm. The location of the range of extracted optical density profiles are shown in the image (*orange lines; red line*: centre optical density profile). (*Right*) The mean optical density profile at wavelengths between 500 and 650 nm.

Location of the selected optical density profiles

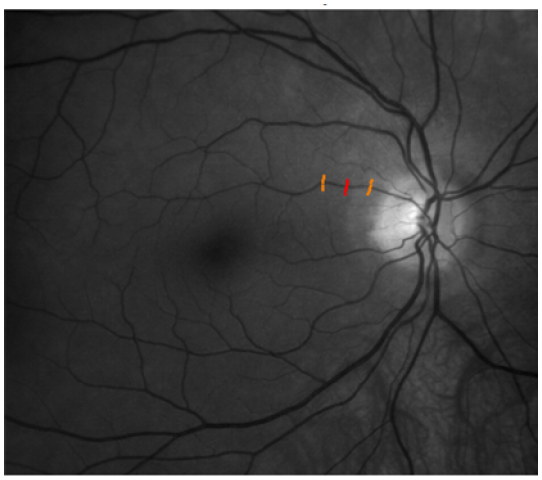

Mean optical density profile

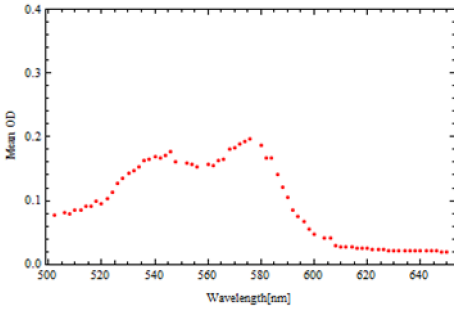

The wavelength range of the mean optical density profile was changed and the oxygen saturations calculated for each range. Firstly, the starting wavelength of the range was changed from 500 nm to wavelengths in increments up to 640 nm. The end wavelength was kept at 650 nm. For each wavelength range the OS was calculated. Plots illustrating the effect of changing the starting wavelength in the wavelength range on the non-linear fit and OS calculation are shown in Figure 4.14. In the plots, the oximetry model (described by the curve fit; *red line*) was applied to the optical denisty data at specific wavelength ranges. To enable a visual comparison of the fitted curves between the wavelength ranges, the wavelength range of the fitting curves were kept constant between 500 – 650 nm. Figure 4.15 shows a plot of the wavelength range (the intial wavelength is modified, the last wavelength is kept constant at 650 nm) versus the calculated OS for the given optical density profile of the retinal arteriole shown in Figure 4.13 (*right*).

The most appropriate starting wavelength of the wavelength range was decided to be 556 nm. The rationale for this decision is multifactoral. Firstly, it yields the most appropriate OS of the retinal arteriole in a normal eye (wavelength range 556 - 650 nm; oxygen saturation 94%). It can be seen in Figures 4.14 and 4.15 that using a wavelength range with the initial wavelength starting between 500 and 540 nm resulted lower than expected oxygen saturations for the retinal arterioles. Similarly, using a wavelength range with the initial wavelength starting between 560 nm and 640 nm resulted inaccurate oxygen saturation calculations for the selected retinal arteriole. Secondly, when the mean optical density profile (Figure 4.13, *right*) is compared to the modified extinction coefficient (Figure 4.16) an important difference exists. The first local maxima of the optical density profile appear to be lower than the second local maxima. In contrast, the first local maxima of the modified extinction coefficient is higher than the second local maxima. Thirdly, the wavelength range of 556 – 650 nm incorporates important features of the modified extinction coefficient curves of oxyhaemoglobin (local minima and the second local maxima) and deoxyhaemoglobin (local maxima), that could be used accurately calculate the oxygen saturation of a given point in a retinal blood vessel (Figure 4.16, r*ight*).

Figure 4.14: Nonlinear fitting (*red line*) of the mean optical density profile (*blue dots*) with incremental changes to the starting wavelength to generate the oxygen saturation (OS) calculation. The oximetry model (described by the curve fit; *red line*) is applied to the optical denisty data at specific wavelength range. The wavelength range of the fitting curves are kept constant between 500 – 650 nm to enable a visual comparison of the fitted curves between the wavelength ranges. In each plot the optical densities outside the wavelength range is show as *gray dots*.

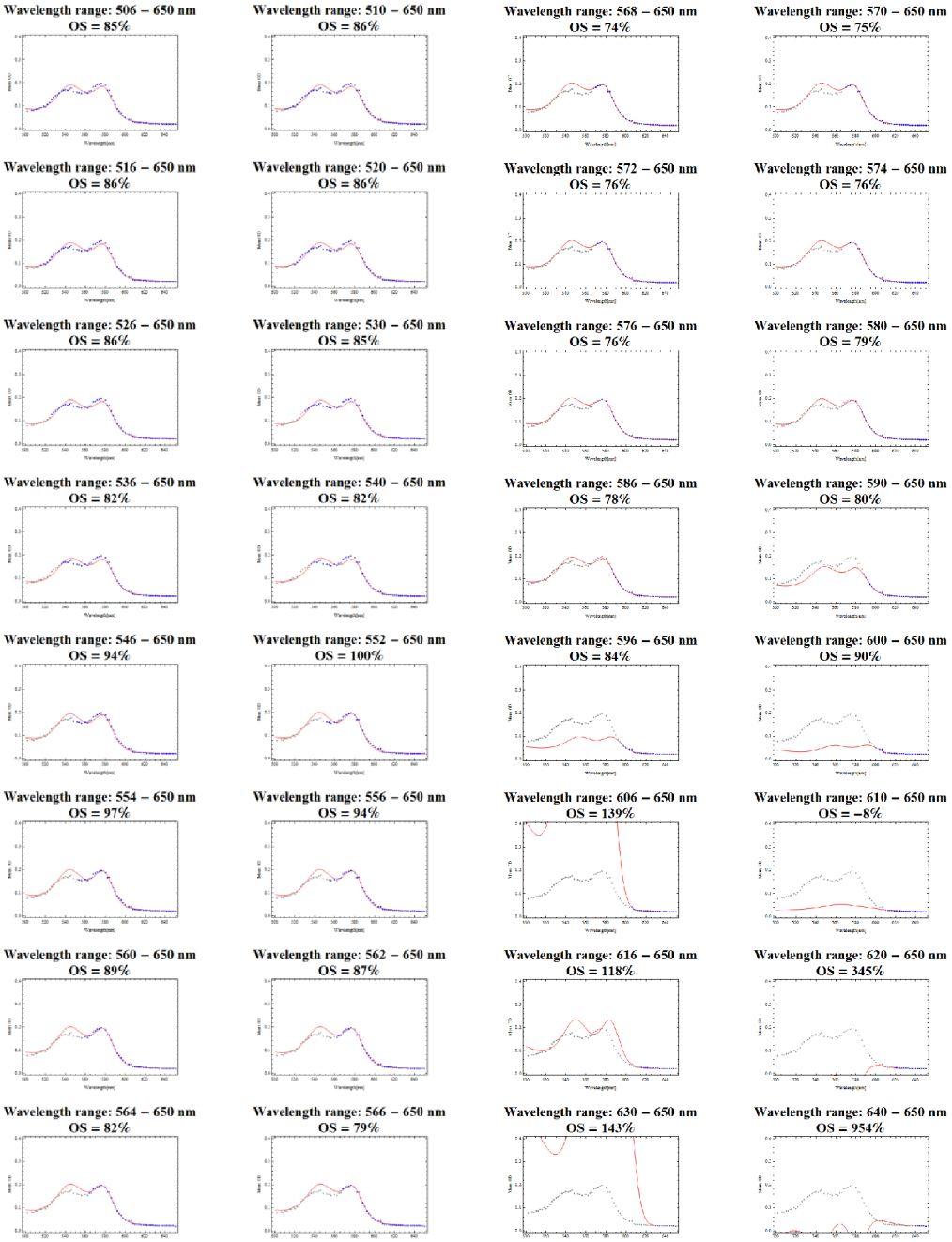

Figure 4.15: A plot showing the effect of changing the starting wavelength in the wavelength range on the oxygen saturation calculation (OS). The range of the *y*-axis has been cropped from 0 – 150%.

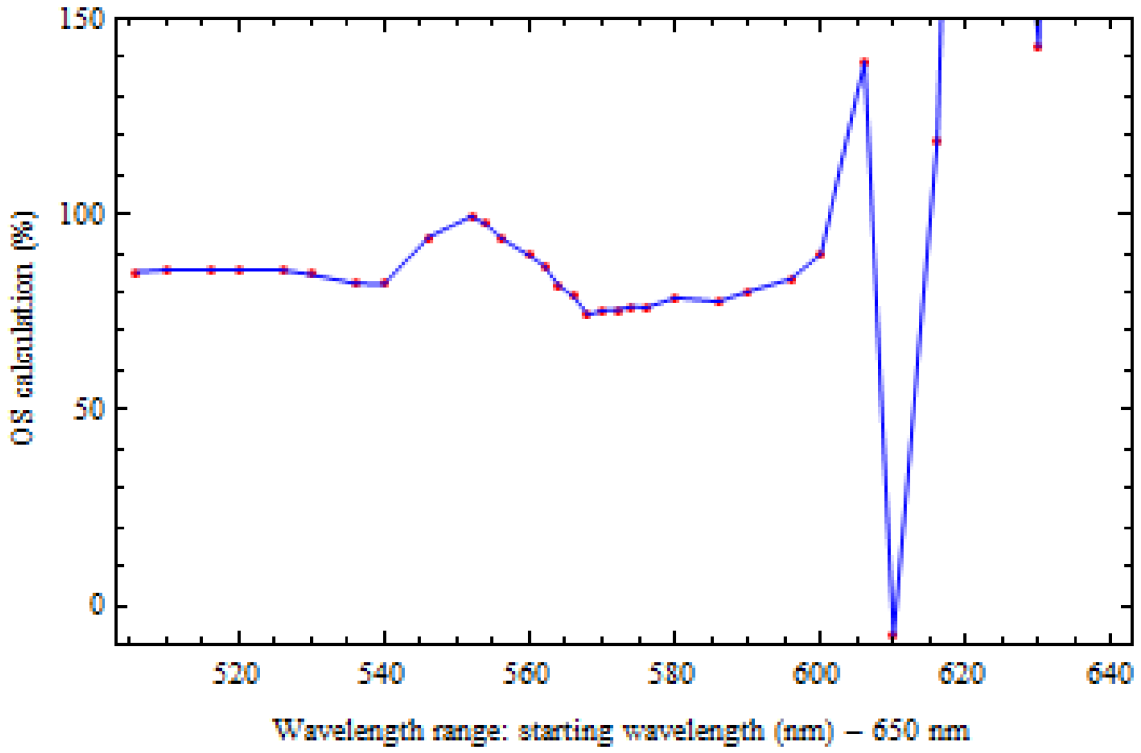

Figure 4.16: Modified extinction coefficients of oxyhaemoglobin (*red line*), deoxyhaemoglobin (*blue line*) and haemoglobin at 50% oxygen saturation (*green line*). (*Left*) Modified extinction coefficients at wavelengths between 500 and 650 nm. (*Right*) Modified extinction coefficients at wavelengths between 556 and 650 nm.

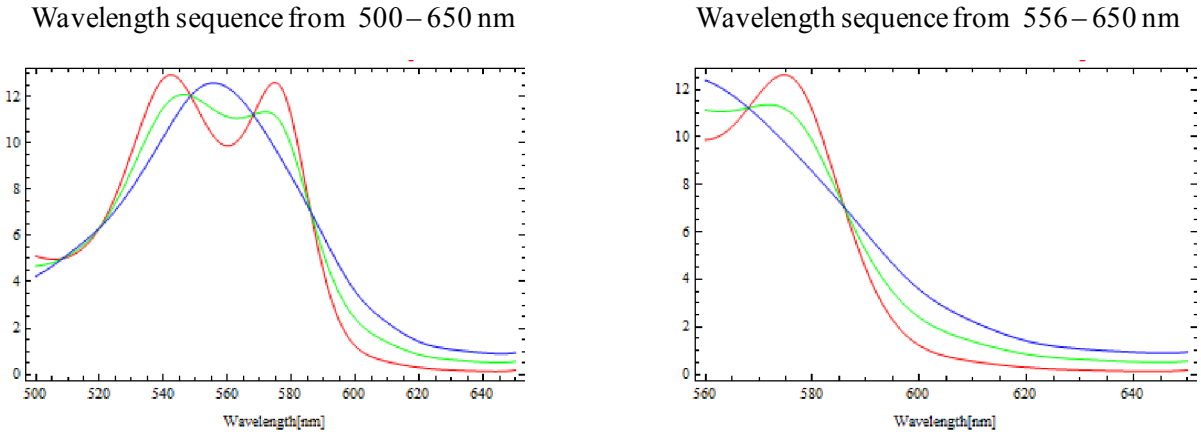

The end wavelength of the range was subsequently changed from 568 nm to wavelengths in sequential increments up to 640 nm. The starting wavelength was kept at 556 nm. For each wavelength range the oxygen saturation was calculated. Plots illustrating the effect of changing the end wavelength in the wavelength range on the non-linear fit and OS calculation are shown in Figure 4.17. The oximetry model (described by the curve fit; *red line*) is applied to the optical denisty data at specific wavelength ranges. The wavelength range of the fitting curves are kept constant between 500 – 650 nm to enable a visual comparison of the fitted curves the between the wavelength ranges. Figure 4.18 shows a plot of the wavelength range (the intial wavelength is kept constant at 556 nm, the last wavelength is kept is modified from 568 nm) versus the calculated OS for the given optical density profile of the retinal arteriole shown in Figure 4.13 (*right*).

The most appropriate end wavelength of the wavelength range was decided to be 650 nm because it yielded the most appropriate oxygen saturation for the retinal arteriole. It can be seen in Figures 4.17 and 4.18 that using a wavelength range with the end wavelength between 568 and 620 nm yields less accurate calculations of the OS for the retinal arterioles.

Therefore, to enable accurate calculations of the oxygen saturation of the retinal vessels, the optimal wavelength range of the optical density profiles used to calculate the OS were chosen between 556 and 650 nm.

Figure 4.17: Nonlinear fitting (*red line*) of the mean optical density profile (*blue dots*) with incremental changes to the end wavelength to generate the oxygen saturation (OS) calculation. The oximetry model (described by the curve fit; *red line*) is applied to the optical denisty data at specific wavelength ranges. The wavelength range of the fitting curves are kept constant between 500 – 650 nm to enable a visual comparison of the fitted curves between the wavelength ranges. In each plot the optical densities outside the wavelength range is show as *gray dots*.

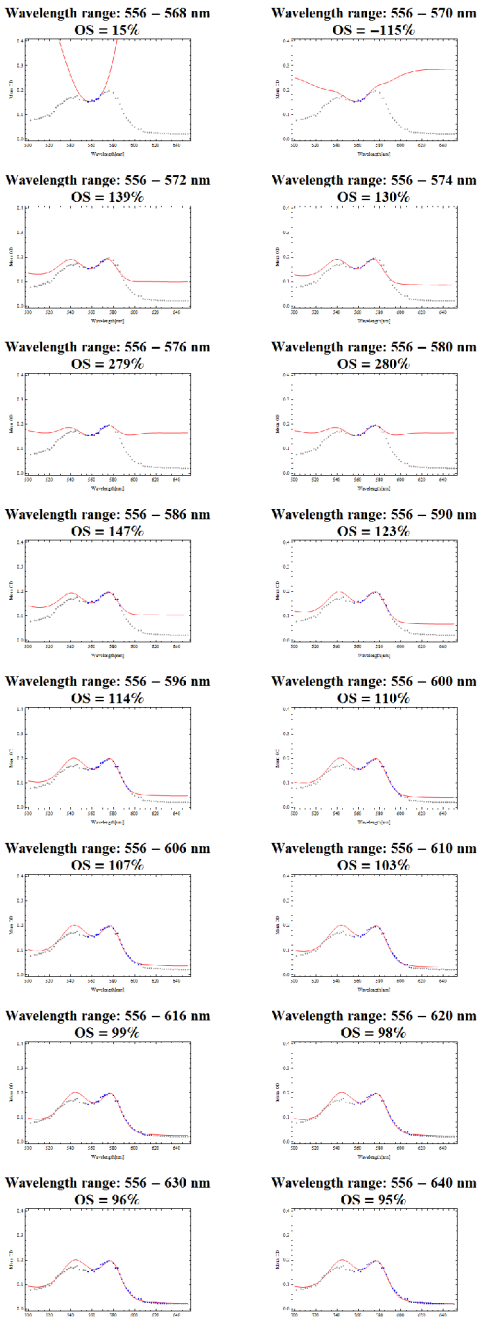

Figure 4.18: A plot showing the effect of changing the end wavelength in the wavelength range (initial wavelength maintained at 556 nm) on the oxygen saturation calculation. The range of the *y*-axis has been cropped to 0 – 150%.

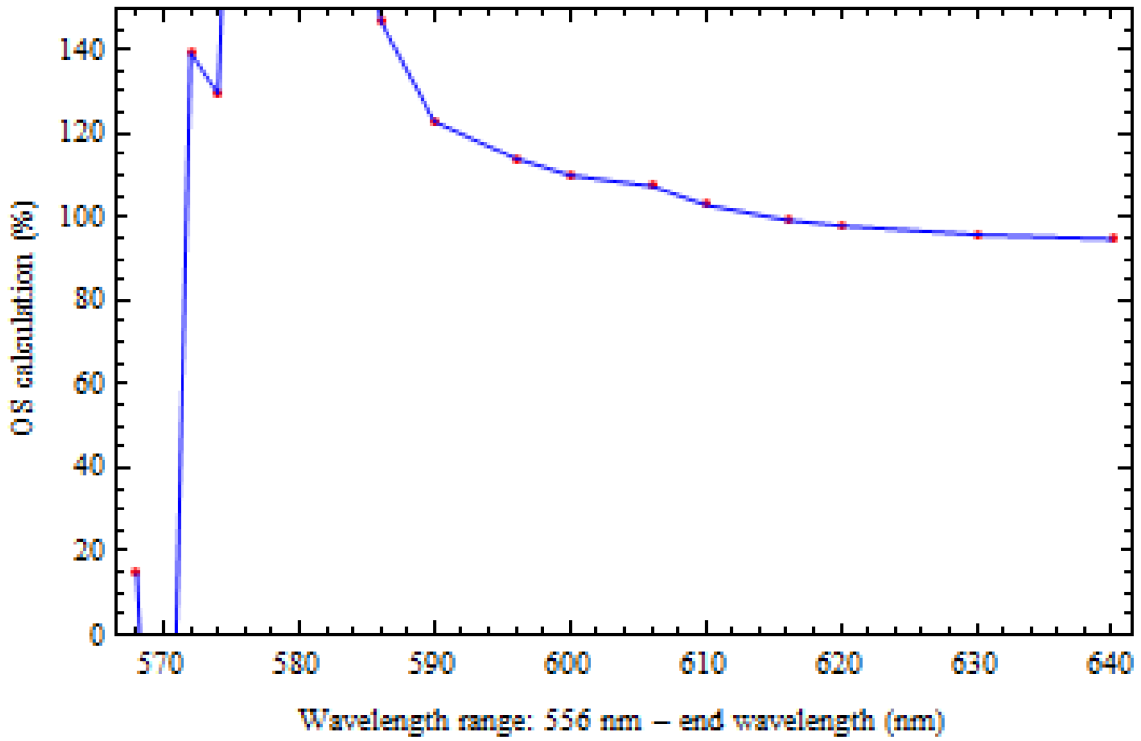

4.2.3.8. Analysis of the Oxygen Saturation Data.

The OS calculations and corresponding coordinates of the centre of the tracked retinal blood vessels were used to generate oximetric pseudocolour maps of the retinal vasculature.

To enable further studies of the OS data, a semi-automated program was written in *Mathematica* (ver. 5.2; Wolfram Research, Inc., Champaign, IL) to enable the extraction of calculated OS values at given points in the retinal arterioles and venules defined by the distance from the optic disc margin (see Appendix 4 for the *Mathematica* programming code).

Initially, five circular "lines of interest" were generated to segment each retinal image (Figure 4.19).The first circle defined the margin of the optic disc. This was performed by

determining the centre of the optic disc and its radius (*r*). Four additional circles with increasing radii (*2r, 3r, 4r, 5r*) about the point in the centre of the optic disc corresponded to the regions ½ disc diameter (*dd*), 1 dd, 1½ dd and 2 dd from the disc margin respectively (Figure 4.20).

Figure 4.19: Annular regions of interest defining regions of the retina corresponding to the disc margin, ½ disc diameter (*dd*), 1 dd, 1½ dd and 2 dd from the disc margin.

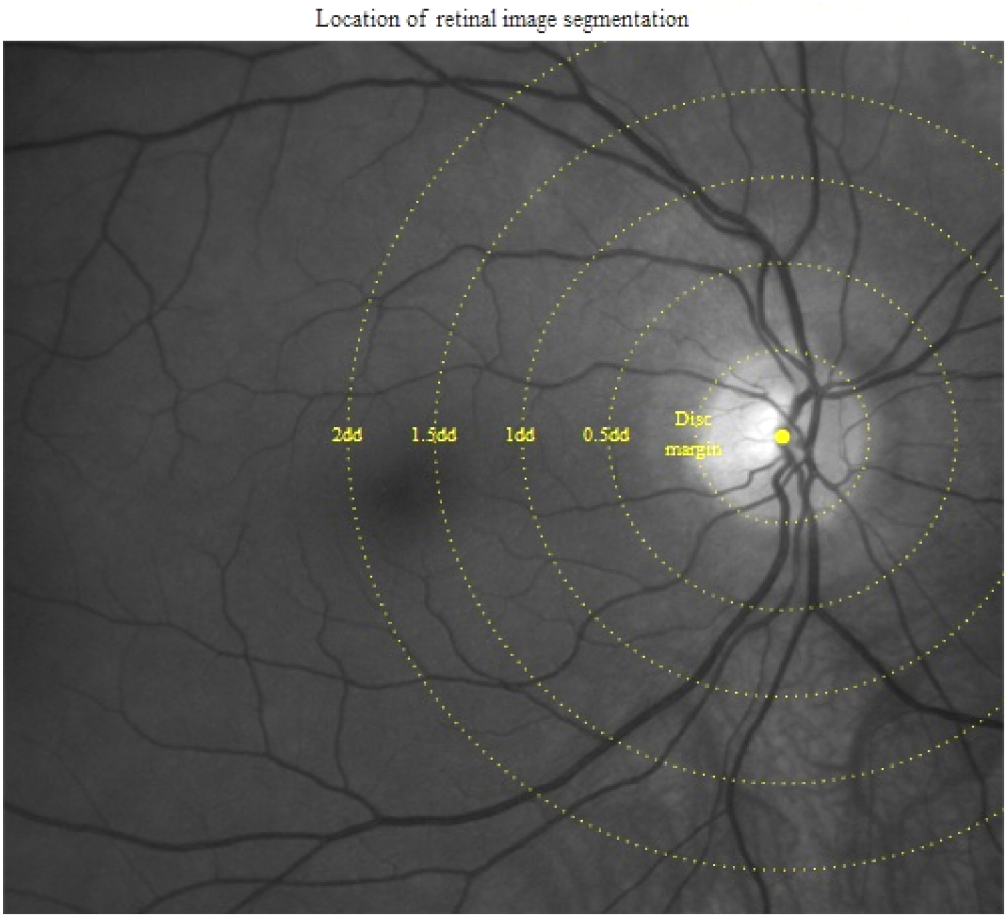

The positions of the intersection between the retinal segmentation "lines of interest" and the main retinal blood vessels were identified manually. Only 1st and 2nd degree superotemporal, inferotemporal, superonasal and inferonasal blood vessels (arterioles and venules) were included. First degree vessels were preferentially chosen over 2nd degree vessels. The optical density profiles at these intersections and 10 consecutive optical density profiles proximal to and distal to these points were calculated. Where the positions of the intersection between the segmentation "lines of interest" and retinal blood vessel extended beyond the field of view of the retinal image, arbitrary positions were created at the periphery

of the vessels (to ensure that the software program would continue to execute the command) but were not included for further analysis.

Figure 4.20: Segmentation "lines of interest" (*yellow dots*) overlaid on an image of a normal right retinal image. The linear profiles orthogonal to the centre of the blood vessels (*red and orange lines*) shown correspond to the positions of the intersection between the retinal segmentation "lines of interest" and the main retinal blood vessel. Only 1st and 2nd degree superotemporal, inferotemporal, superonasal and inferonasal retinal vessels were included. (The coloured lines overlying the retinal arterioles (*left*) and venules (*right*) indicate the locations of the semi-automated tracking of the centre of the blood vessels.)

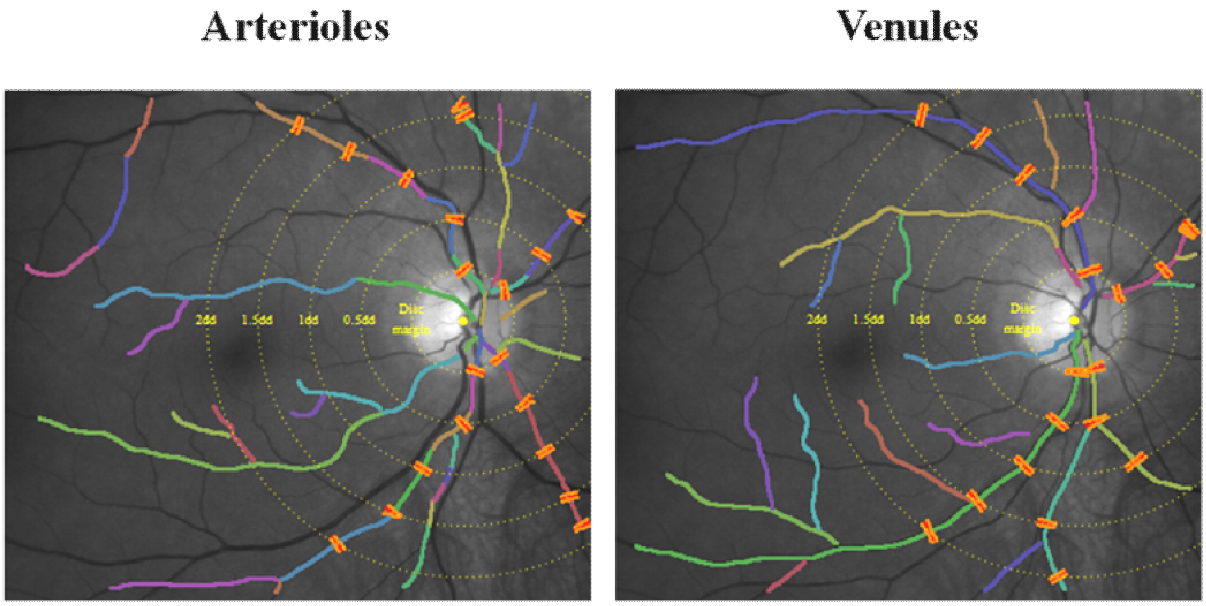

Each optical density profile was used to calculate the OS at their respective locations on the retinal blood vessels. OS calculations of the nasal arterioles and venules were excluded for two main reasons. Firstly, the majority of the segmentation lines often extended beyond the field of view of the retinal image. Secondly, the optical density profiles were often affected by noise, possibly from illumination variations towards the periphery of the nasal hemisphere in most retinal images. Therefore, only results from temporal arterioles and venules were included in the study. The mean optical density profiles at points along the blood vessel defined by the segmentation "lines of interest" of all 23 eyes were calculated and inspected visually. Subjects with "noisy" optical density measurements were excluded from further analysis (n = 9).

The mean OS of the superotemporal and inferotemporal retinal blood vessels (arterioles and venules) at the disc margin, ½ disc diameters (*dd*), 1 dd, 1½ dd and 2 dd from the disc margin were calculated in the remaining 14 eyes.

To confirm the validity of the choice of the optimal wavelength range (556 – 650 nm), each optical density profile at wavelength ranges of 500 – 650 nm (wavelengths used in the model eye) and 556 - 650 nm was used to calculate separate OS values. This was performed at points along the blood vessel defined by the segmentation "lines of interest". The mean OS for each subject was calculated and used to compare the OS calculations between the two wavelength ranges: 500 – 650 nm and 556 - 650 nm.

The OS calculations of the 14 normal eyes that were included in the study were checked for outlying OS results which were deleted, this was defined by: negative OS calculations, OS calculations greater than 200% for arterioles and OS calculations greater than 100% for venules. Forty-five (32%) arteriolar and forty-five (32%) venular OS calculations were excluded from further data analysis. The summary of the clinical findings in the 14 normal subjects included in the study are presented in Table 5.

Table 5: Summarized clinical data of the normal subjects included in the study.

Number of subjects		14
Mean age (range)		42.9 years (25 -74 years)
Mean best corrected visual acuity (LogMAR Equivalent)(± SD)		-0.07 (± 0.09)
Mean intraocular pressure (mmHg ± SD)		14.1 (± 2.0)
Mean systolic blood pressure (mmHg ± SD)		124.1 (± 10.1)
Mean diastolic blood pressure (mmHg ± SD)		78.5 (± 10.4)
Mean pulse oximeter oxygen saturation (% ± SD)		96.7 (± 0.8)
Mean lens opacity grade	Nuclear opalescence (± SD)	1.5 (± 0.8)
	nuclear colour (± SD)	1.3 (± 0.5)
	cortical (± SD)	1 (± 0)
	posterior subcapsular (± SD)	1 (± 0)

To study the OS of the macular circulation in more detail, the optical density profiles of selected macular branch arterioles and venules were evaluated. Fifty consecutive optical density profiles were generated proximal to and distal to (n = 101 optical density profiles) the selected point on each vessel. The mean optical density profile was calculated and used to calculate the OS of the macular vessel (and 95% confidence interval) from the nonlinear fitting oximetry algorithm. This was preferred to calculating the mean OS from each optical density profile separately to reduce the effect of outlying oxygen saturation calculations from spurious optical density profiles affecting the OS calculation of the macular vessels.

4.2.3.9. Statistical Analysis.

The normality of the data distribution were analyzed using the Shapiro-Wilk normality test, with the cutoff for non-normality set at $P < 0.05$. The calculated OS data for arterioles using 500 – 650 nm and 556 – 650 nm wavelength ranges and venules using the 500 – 650 nm sequence were not significantly different from a normal distribution (P = 0.173, 0.300 and 0.158 respectively). The calculated OS data for venules using the 556 – 650 nm was significantly different to a normal distribution (P = 0.011). Differences in the mean OS calculation using the two wavelength ranges (500 - 650 nm and 556 – 650 nm) in the retinal arterioles and venules were examined with a Student's t-test and Wilcoxon matched-pair signed-rank test respectively. Pearson's correlations between the mean OS calculation of the temporal retinal blood vessels (mean superotemporal and inferotemporal) and distance from the optic disc margin were calculated. Multiple linear regression ("enter" method) was used to determine the relationship between the mean OS of the temporal retinal vessels (calculated using the wavelength range 556 – 650 nm) and LOCS III grading scores (nuclear opalescence, nuclear colour, cortical and posterior subcapsular). To check for multicollinearity among the variables in the final model, the variance inflation factor and Durbin-Watson statistic were calculated. All statistical analysis was performed using commercial software (SPSS, ver. 16.0; SPSS Inc., Chicago, IL). In all statistical analyses, $P < 0.05$ was considered statistically significant. A summary of the methods and relevant statistical analyses are shown in a flow chart in Figure 4.21.

Figure 4.21: A flow chart of the image processing and analysis methods and the statistical analyses of the oxygen saturation (OS) data.

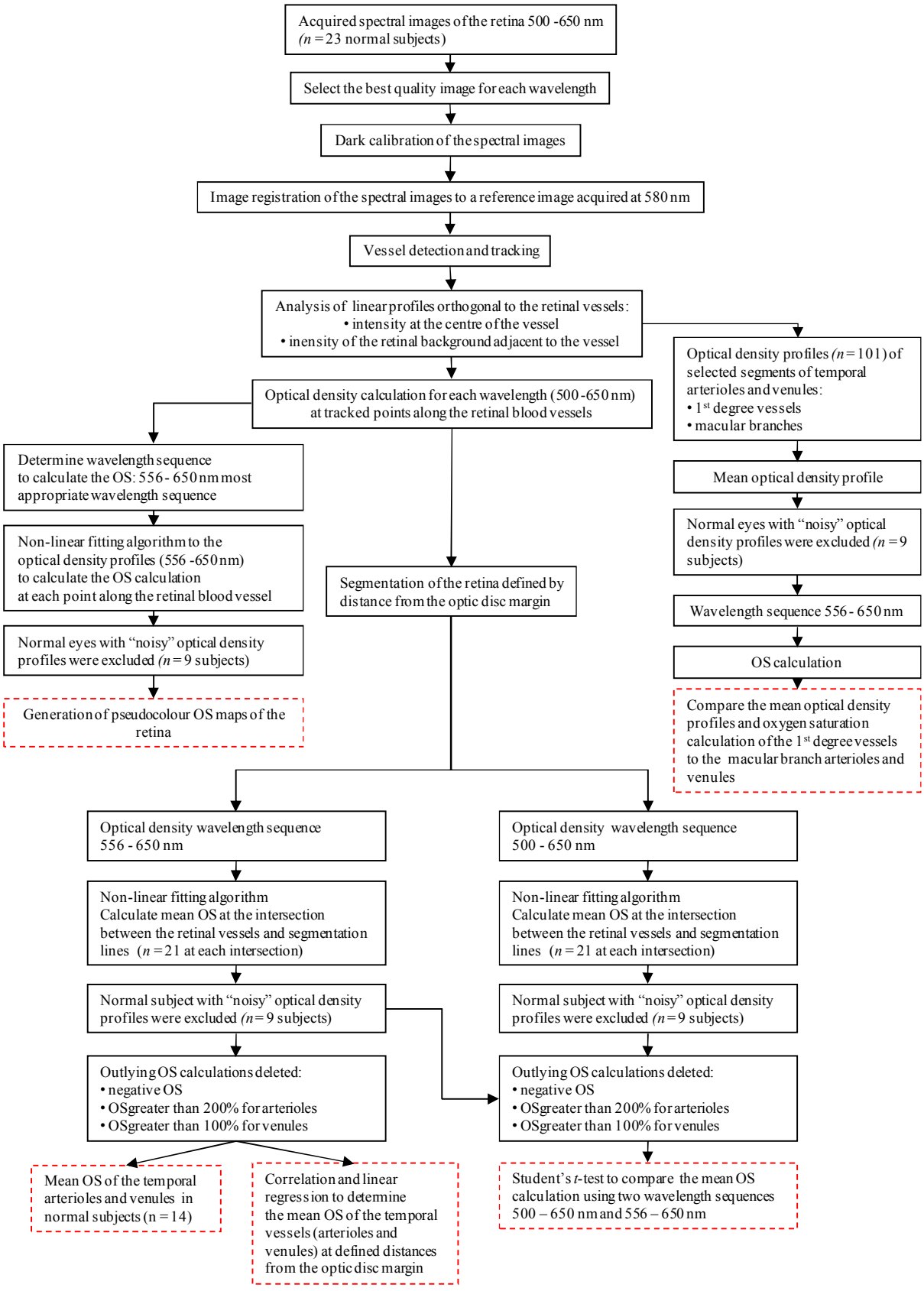

4.3. Results.

4.3.1. Comparison of the Oxygen Saturation Calculations between Two Wavelength Ranges (500 - 650 nm and 556 - 650 nm).

The mean OS calculation (± SD) of the temporal retinal arterioles and venules using a wavelength range of 500 - 650 nm were 61.7% (± 16.0%) and 30.4% (± 13.0.0%) respectively. The mean OS calculation (± SD) of the temporal retinal arterioles and venules using a wavelength range of 556 - 650 nm were 99.4% (± 16.6%) and 29.0% (± 10.2%) respectively. The mean OS calculation of the temporal retinal arterioles using a wavelength range of 500 - 650 nm were significantly lower than the mean OS calculation using a wavelength range of 556 - 650 nm ($p < 0.0001$, Student's *t*-test, two-tailed; Figure 4.22). No significant difference was found between the mean OS calculation of the temporal retinal venules using the two wavelength ranges ($p = 0.76$, Wilcoxon matched-pair signed-rank test, two-tailed; Figure 4.23).

Figure 4.22: A plot of the oxygen saturation (OS) calculations of the temporal (superotemporal and inferotemporal) retinal arterioles using a wavelength range of 500 - 650 nm (*filled circles*) and 556 – 650 nm (*filled squares*). Crossbars are at the mean and whiskers are the standard deviations.

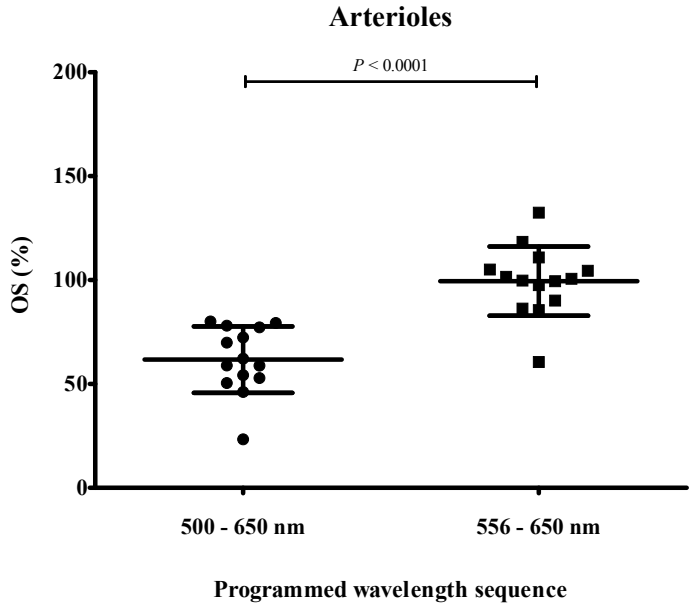

Figure 4.23: A plot of the oxygen saturations (OS) calculation of the temporal (superotemporal and inferotemporal) retinal venules using a wavelength range of 500 - 650 nm (*filled circles*) and 556 – 650 nm (*filled squares*). Crossbars are at the mean and whiskers are the standard deviations.

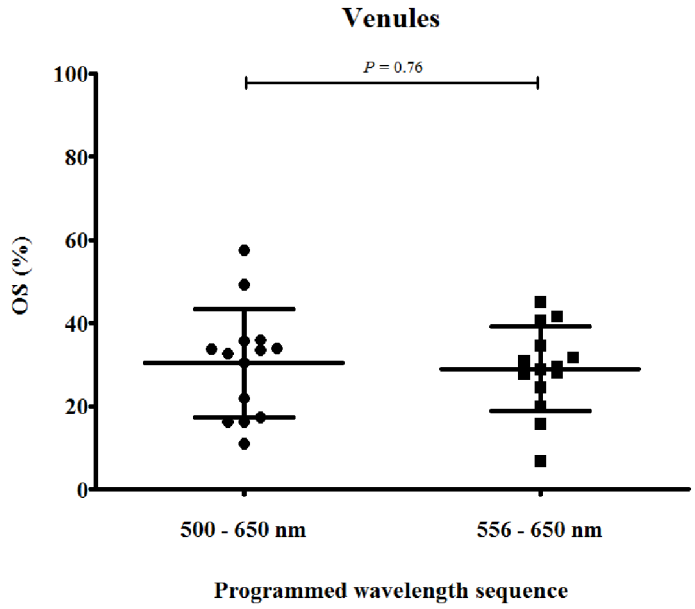

4.3.2. Observational Features of the Retinal Blood Vessels in the Spectral Images of the Retina.

Spectral images of the retina revealed characteristic optical features of the retinal blood vessels. Firstly, the retinal arterioles (Figure 4.24, *red arrow heads*) become less optically dense compared to the 1st degree retinal venules (Figure 4.24, *blue arrow heads*) at wavelengths greater than 590 nm. This feature indicates that the oxygenation of the 1st degree retinal arterioles can be differentiated by observation from the lower oxygenation of the 1st degree retinal venules. This feature is consistent with the modified extinction coefficients of oxy- and deoxyhaemoglobin, where the extinction (or optical density) of oxyhaemoglobin is lower than the extinction of deoxyhaemoglobin between 590 nm and 650 nm. Secondly, the macular branches of the retinal venules also appear to be less optically dense than the 1st degree retinal venules and suggest that the macular branches of the retinal venules appear to have oxygen saturations higher than that seen in the 1st degree retinal venules. Further, analysis to confirm this phenomenon is illustrated and discussed in later sections of this chapter.

Figure 4.24: The appearances of the arterioles and venules at 9 selected wavelengths (560, 570, 580, 590, 600, 610, 620 and 630 nm) in the dark calibrated spectral images of the retina in 3 normal subjects. The retinal arterioles (*red arrow heads*) become less optically dense compared to the venules (*blue arrow heads*) at wavelengths greater than 590 nm.

Subject 1. **Subject 2.**

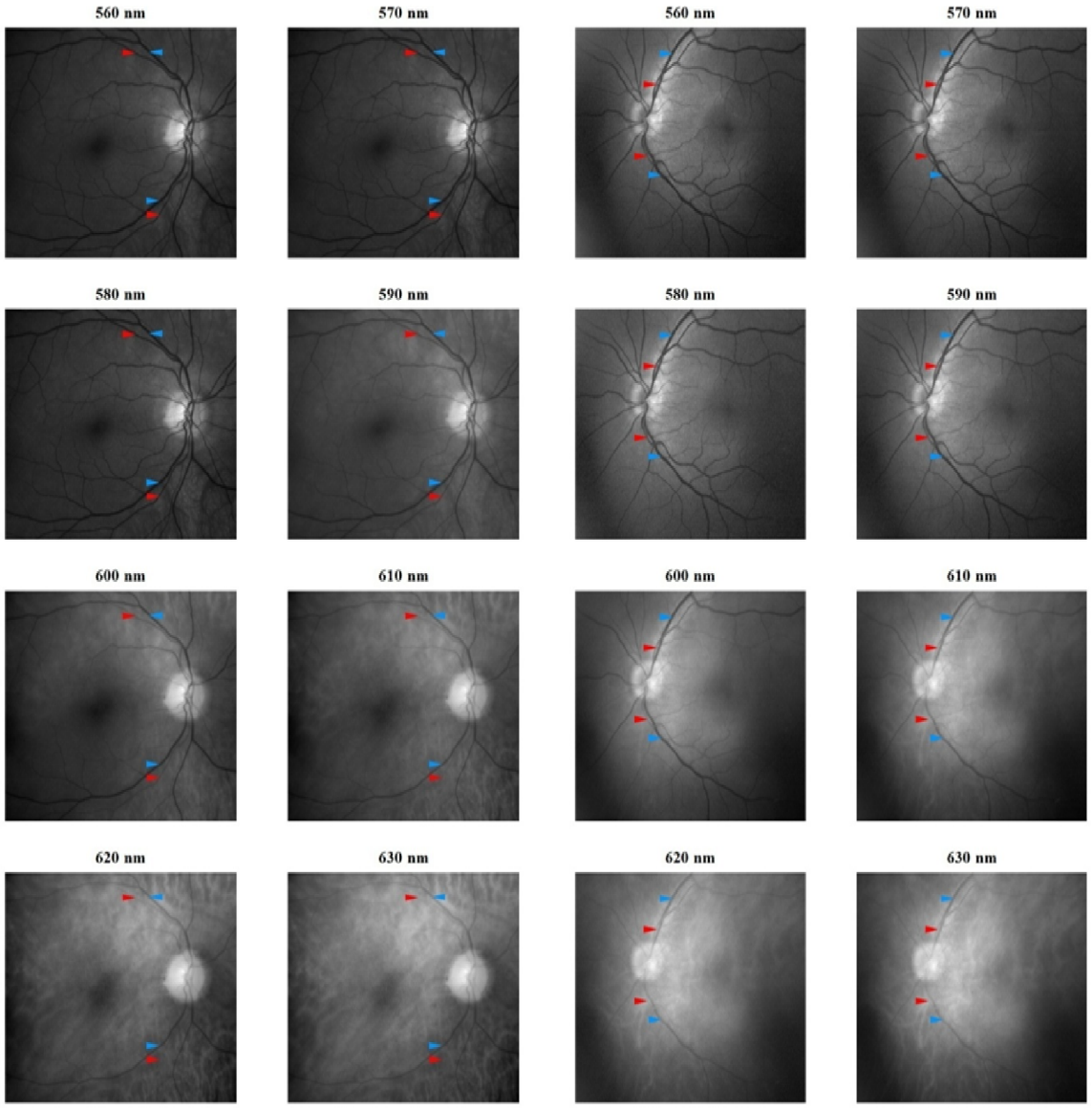

Subject 3.

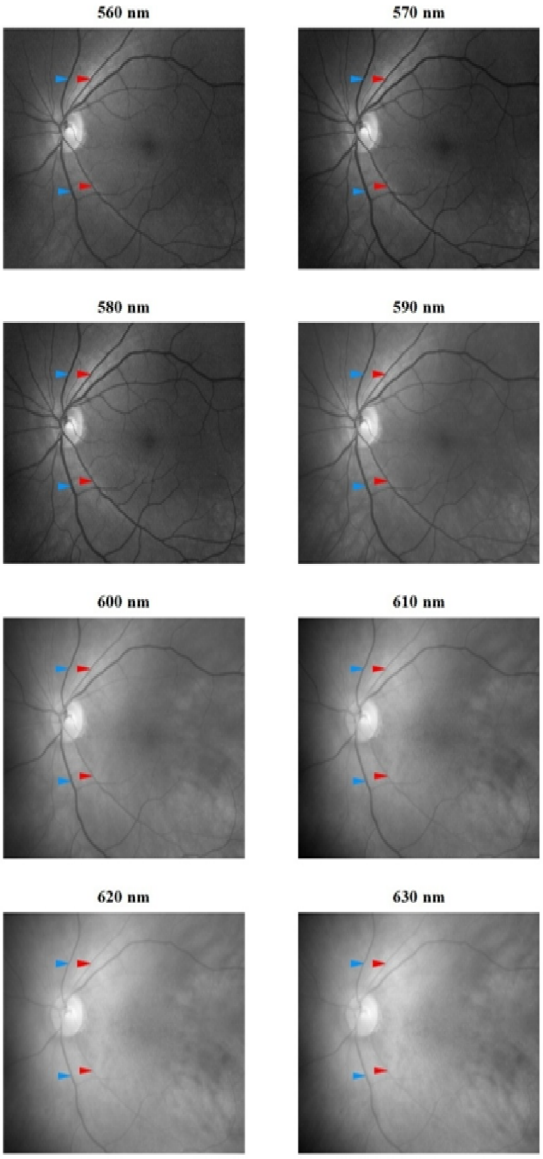

4.3.3. Oximetric Maps of the Retinal Vasculature in Normal Subjects.

Figure 4.25 show pseudocolour images of the calculated oxygen saturations along the retinal arterioles and venules in 14 normal subjects. It can be observed that the retinal arterioles generally have calculated oxygen saturations between greater than 70%. The calculated oxygen saturations of the retinal venules appear to be more varied, ranging between negative values to values above 100%.

The macular branches of the retinal venules generally appear to have higher calculated oxygen saturations compared to their respective main trunk 1st and 2nd degree retinal venules. This is consistent with the observations described previously, where the macular branches of the retinal venules appear to be optically less dense than the main retinal venules.

Figure 4.26 shows the optical profiles at defined points in the retinal vasculature with the resulting mean OS calculation in 5 representative normal subjects. The mean (± SD) OS of the superotemporal and inferotemporal retinal vessels (arterioles and venules) at points defined by the distance from the optic disc margin are summarized in Table 6. A summary box-and-whisker plot of the OS calculations in the temporal retinal arterioles and venules of the 14 normal subjects are shown in Figure 4.27. The mean OS (± SD) of the temporal retinal arterioles and venules were 110.8% (± 11.8%) and 27.7% (± 3.2%) respectively. Figure 4.28 shows the mean OS (and standard error of the mean) of the temporal retinal arterioles and venules at each defined distance from the optic disc margin (at the disc margin, ½ dd, 1 dd, 1½ dd and 2 dd from the disc margin). There was no statistically significant correlation between the distance from the optic disc margin and the mean OS of the temporal retinal arterioles ($r^2 = 0.071$, $p = 0.66$) and venules ($r^2 = 0.002$, $p = 0.95$)

Figure 4.25: Pseudocolour images of the oxygen saturation (OS) calculations overlayed onto the retinal arterioles (*left images*) and retinal venules (*right images*) in 14 normal subjects. A colour scale of the quantitative OS values is shown to the left of the images.

Subject 1.

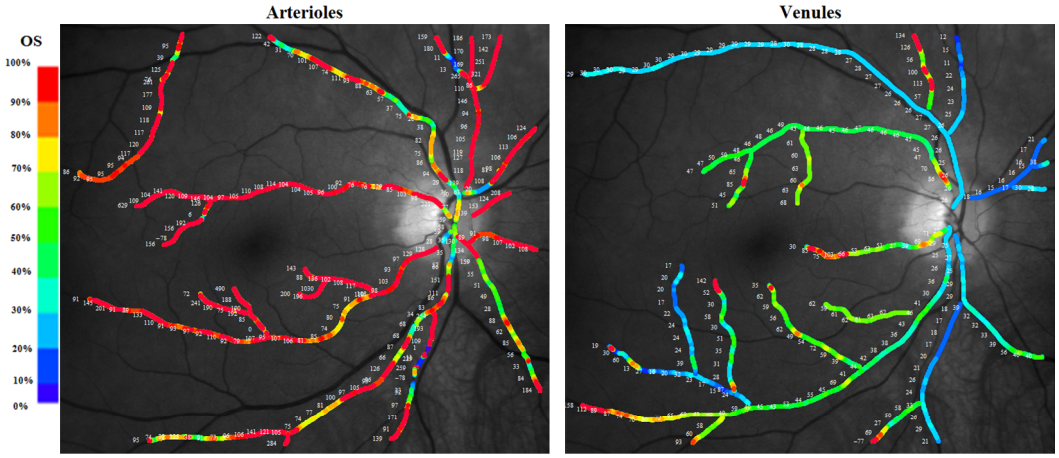

Subject 2.

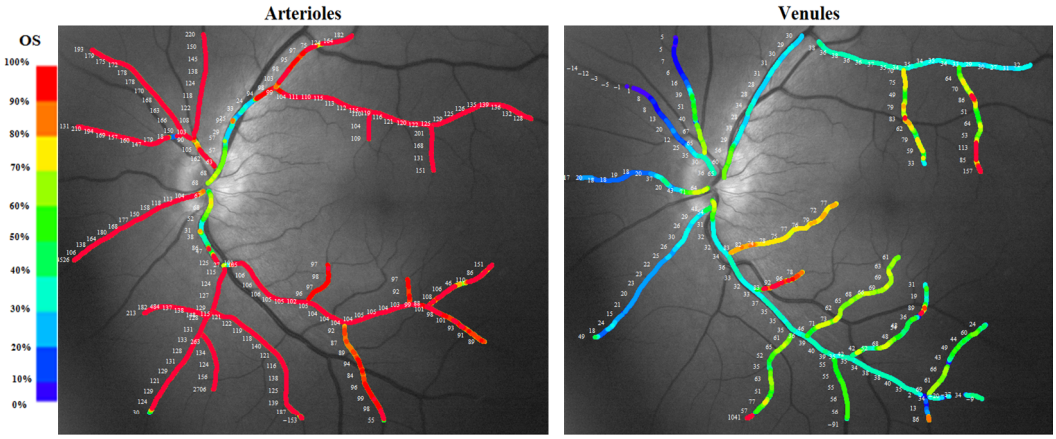

Subject 3.

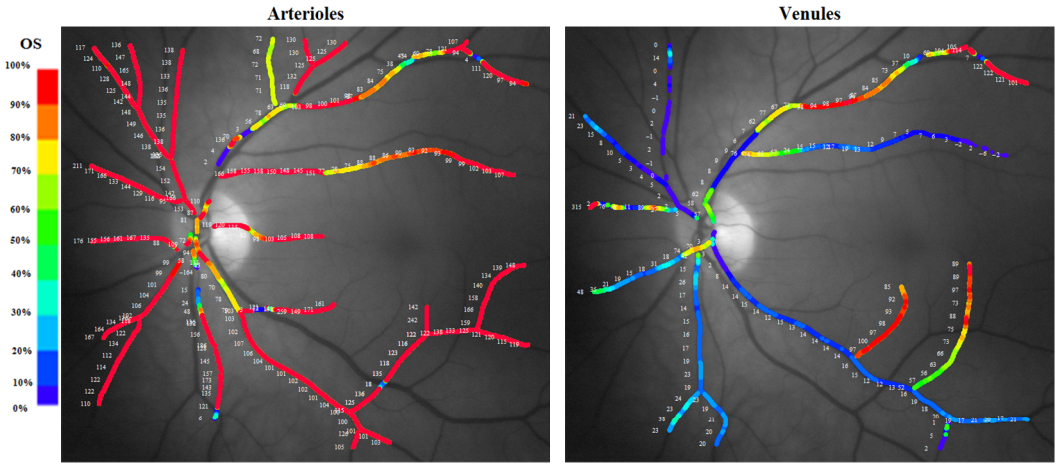

Subject 4.

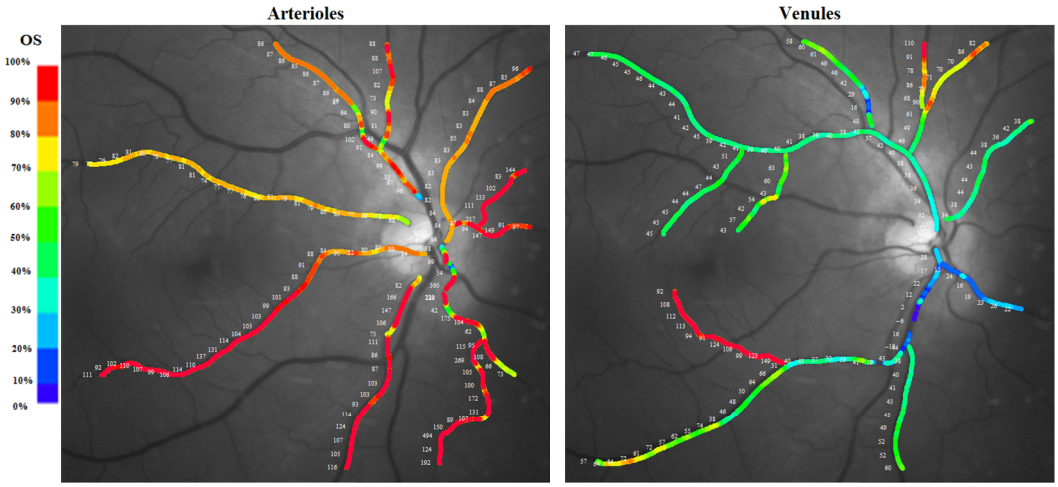

Subject 5.

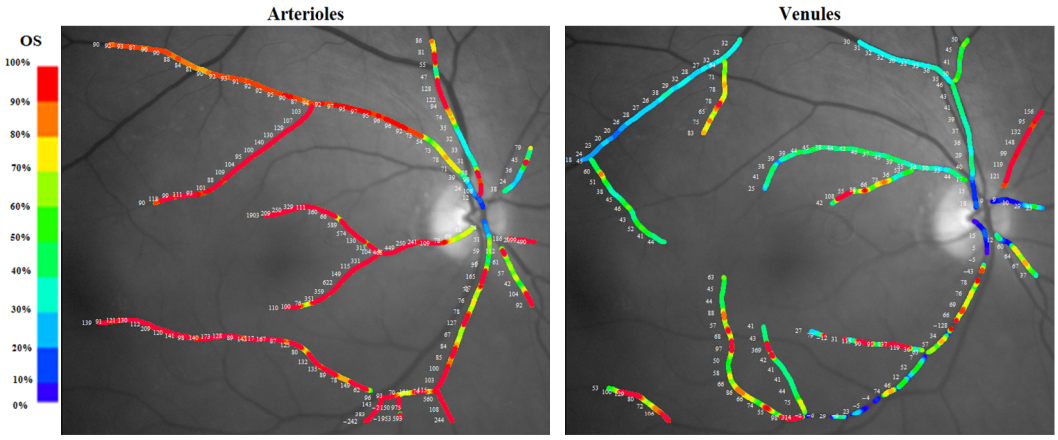

Subject 6.

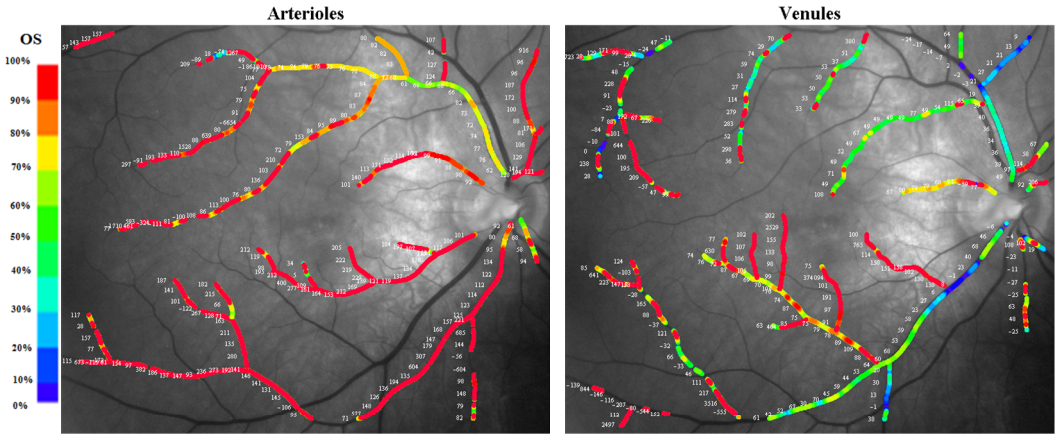

Subject 7.

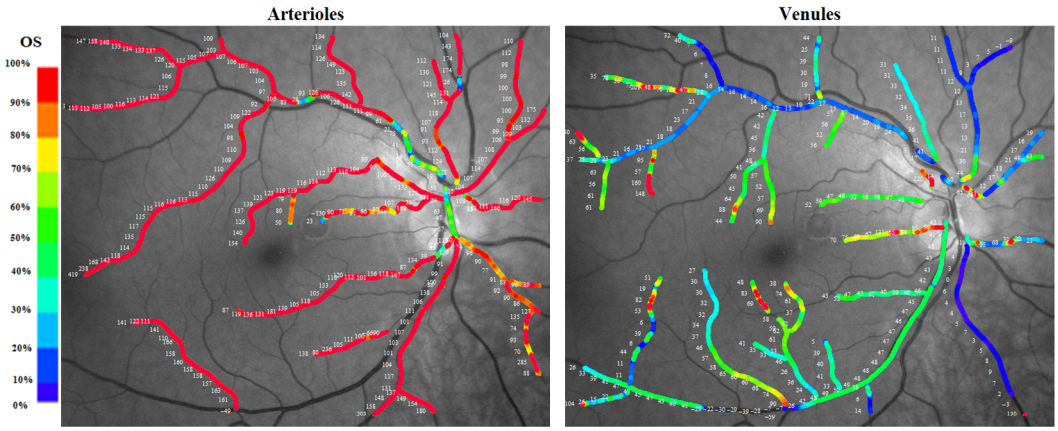

Subject 8.

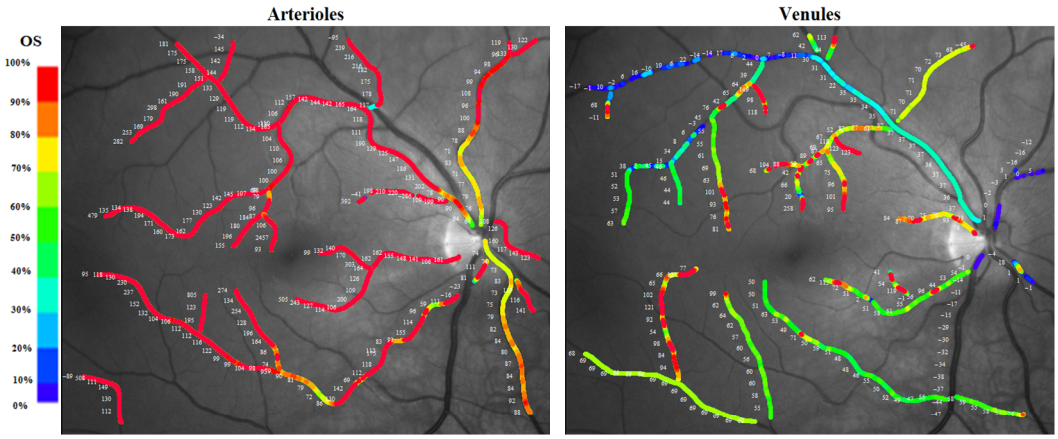

Subject 9.

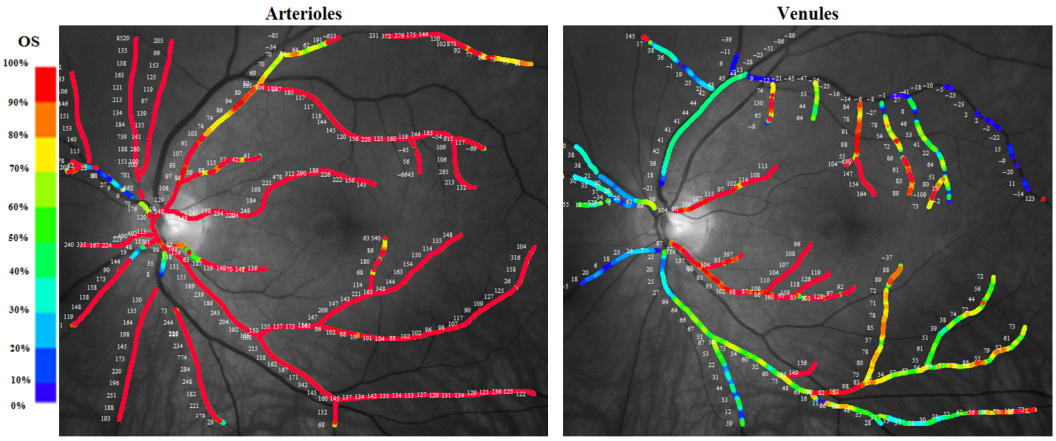

Subject 10.

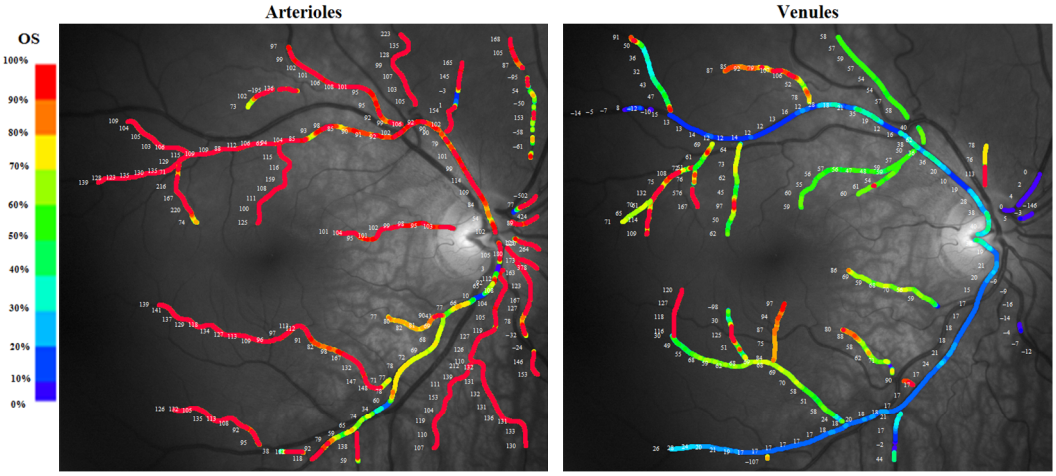

Subject 11.

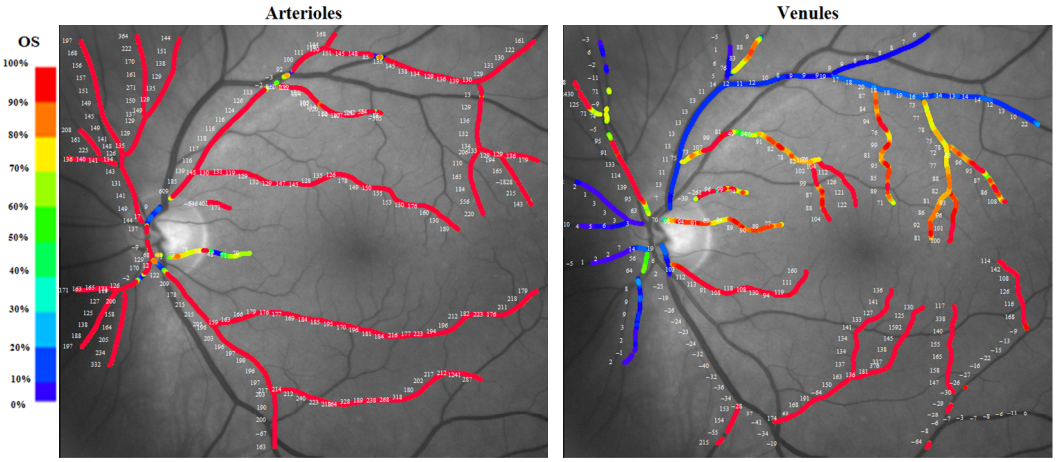

Subject 12.

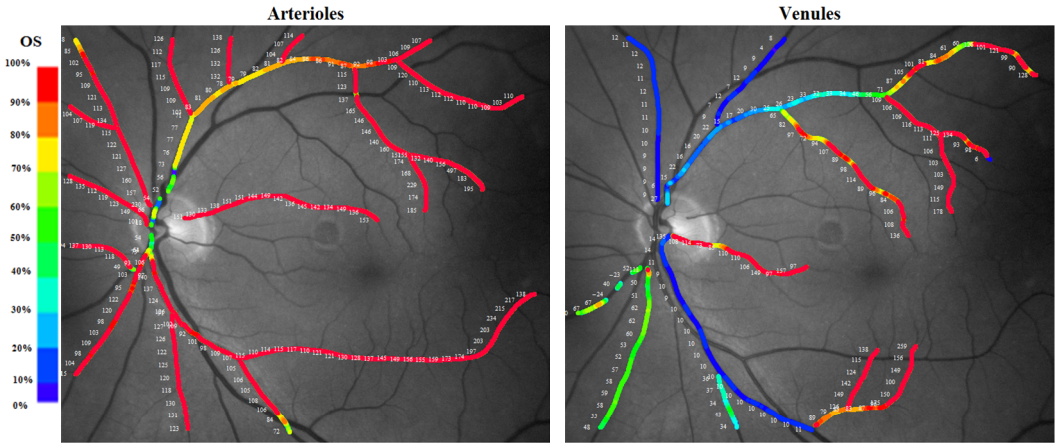

Subject 13.

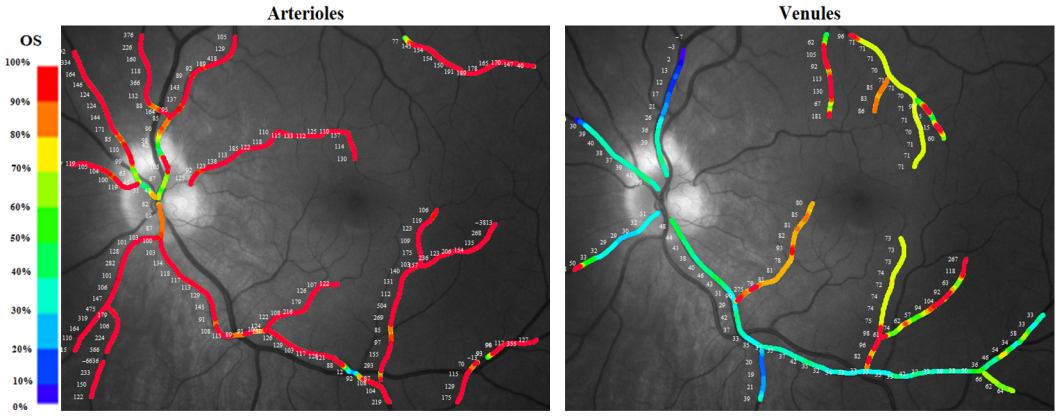

Subject 14.

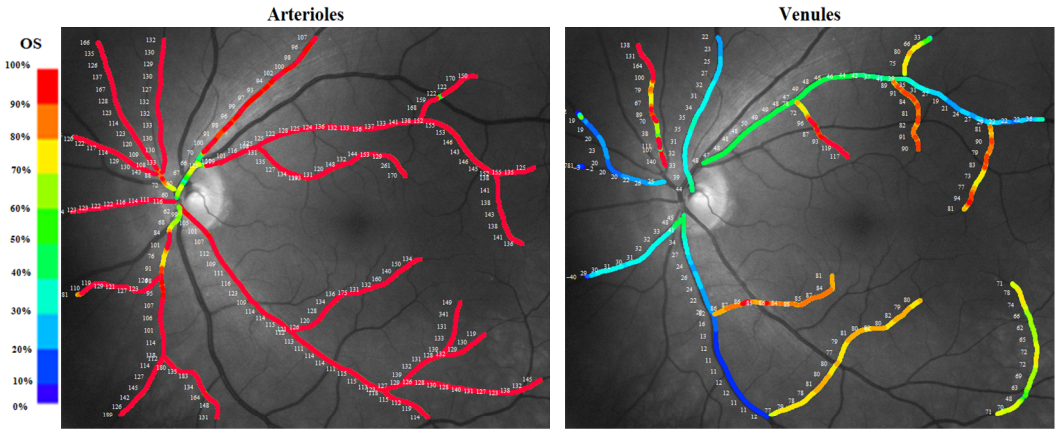

Figure 4.26: An illustration of the mean optical density profiles of selected points along the arterioles and venules in 5 representative normal subjects. The points along the retinal vessels are shown in the retinal grayscale images (*red and orange solid lines*) and were determined by disc diameter distance from the optic disc margin (*yellow dashed lines*). The plots of the mean optical density profiles (± SD; *red filled circle and whiskers*) of the respective points are shown below each grayscale retinal image. The respective mean oxygen saturation (OS) calculation of each point along the blood vessel is indicated above each retinal grayscale image.

Subject	Location	Arterioles	Venules
Subject 1	Superotemporal	Oxygen saturation: 87.9% 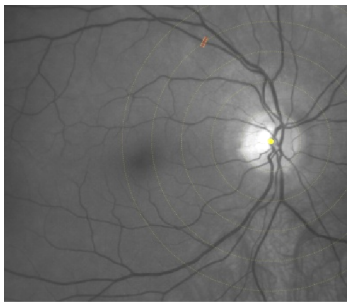 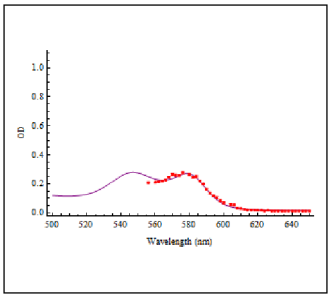	Oxygen saturation: 27.3% 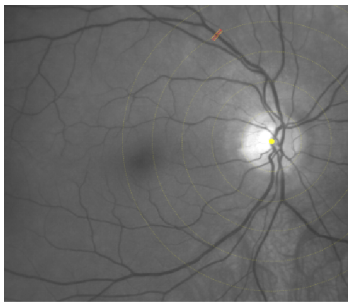 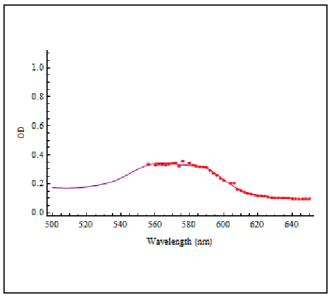
	Inferotemporal	Oxygen saturation: 106.7% 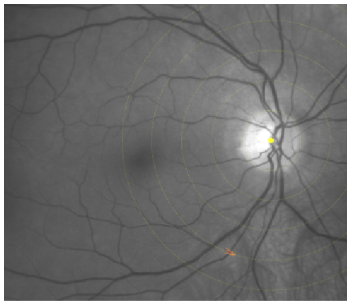 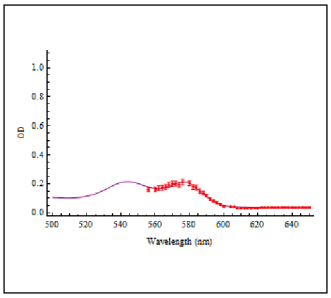	Oxygen saturation: 40.5% 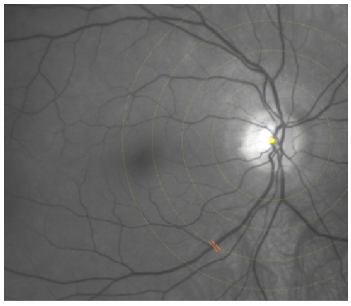 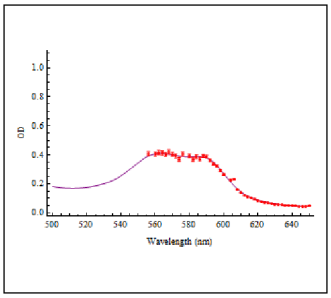

Subject	Location	Arterioles	Venules
Subject 2	Superotemporal	Oxygen saturation: 93.2% 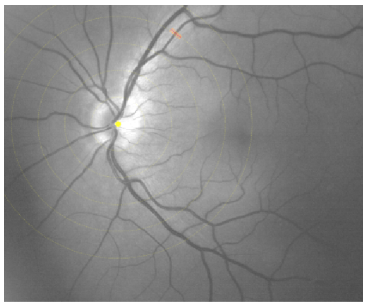 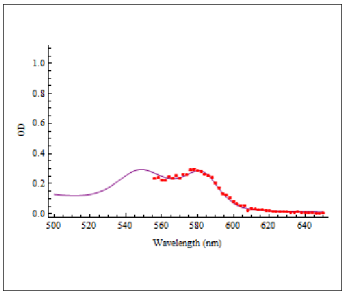	Oxygen saturation: 29.0% 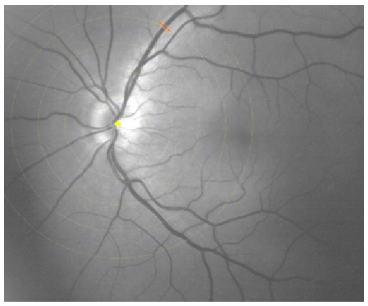 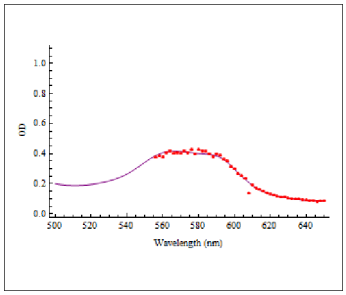
	Inferotemporal	Oxygen saturation: 102.0%  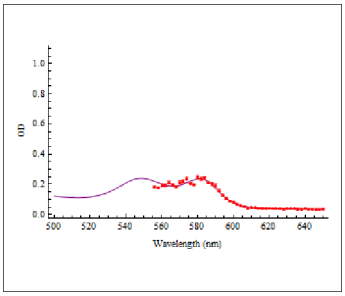	Oxygen saturation: 34.5% 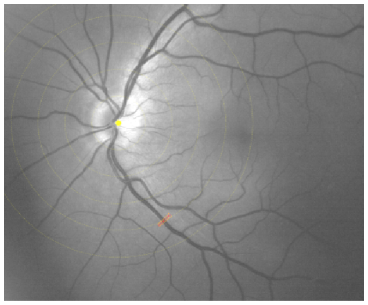 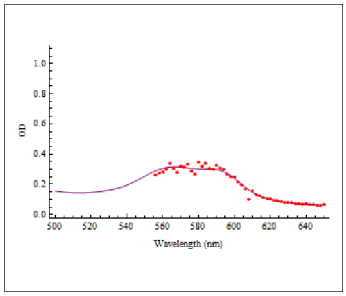

Subject	Location	Arterioles	Venules
Subject 10	Superotemporal	Oxygen saturation: 108.8% 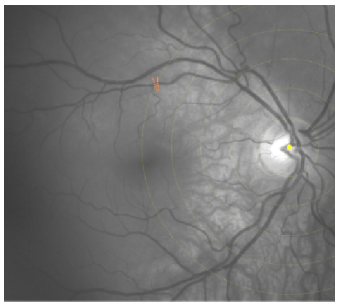 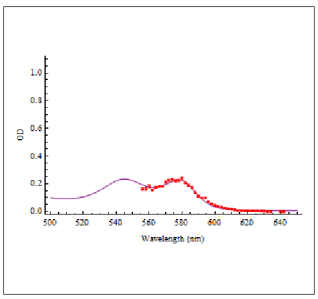	Oxygen saturation: 16.0% 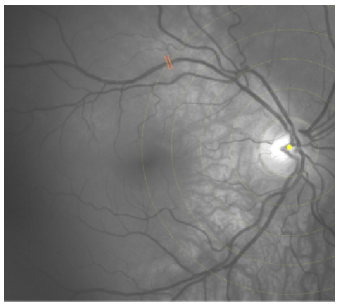 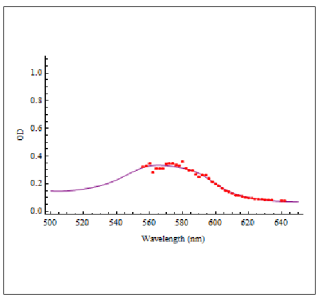
	Inferotemporal	Oxygen saturation: 76.8% 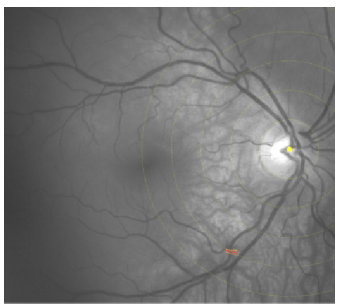 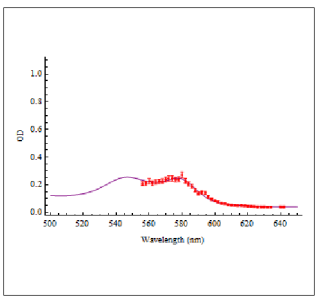	Oxygen saturation: 17.4% 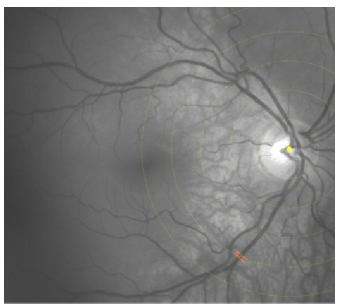 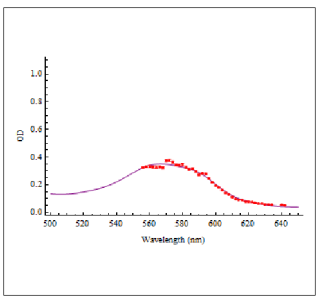

Subject	Location	Arterioles	Venules
Subject 11	Superotemporal	Oxygen saturation: 116.7% 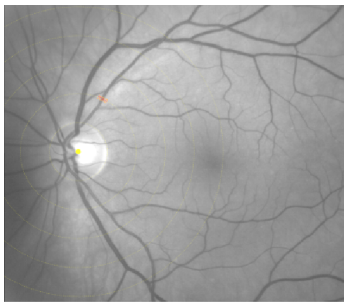 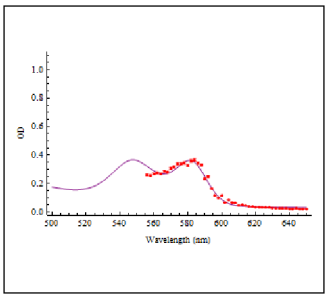	Oxygen saturation: 11.5% 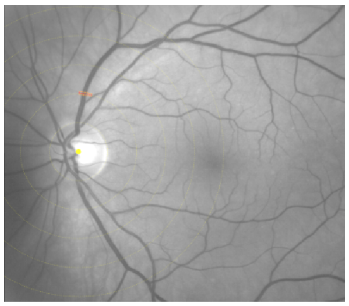 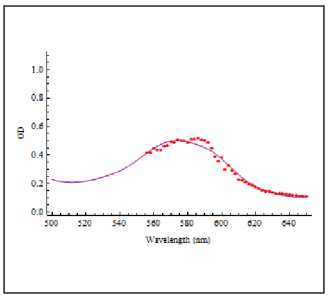
	Inferotemporal	Oxygen saturation: 221.6%* 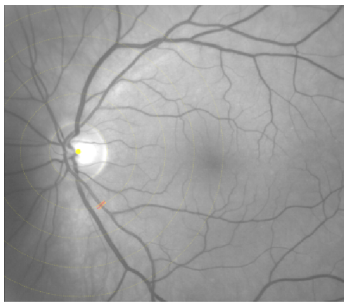 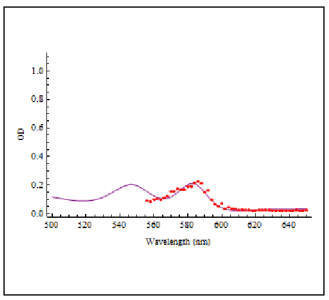	Oxygen saturation: -23.1%** 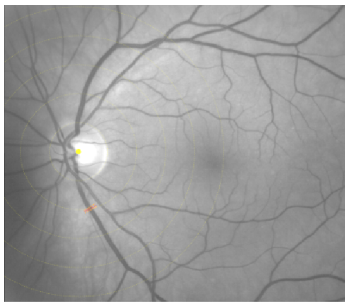 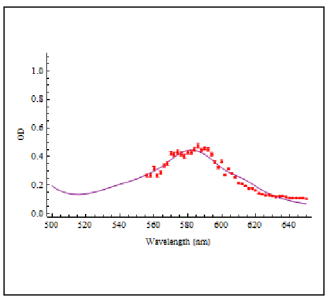

* Poor optical density profile and arteriolar OS calculation greater than 200%. These calculations were excluded from further analysis.

** Poor optical density profile and negative OS calculation. These calculations were excluded from further analysis.

Subject	Location	Arterioles	Venules
Subject 14	Superotemporal	Oxygen saturation: 89.3% 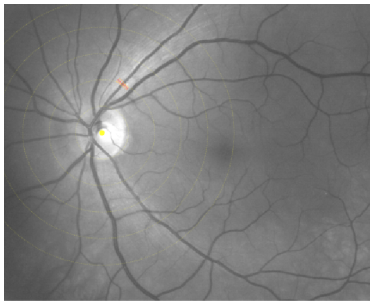 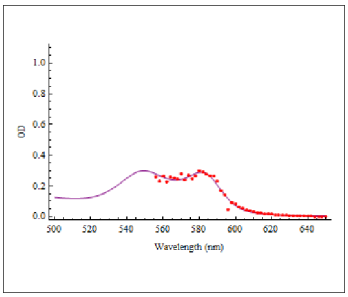	Oxygen saturation: 48.4% 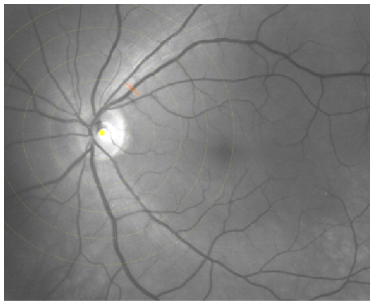 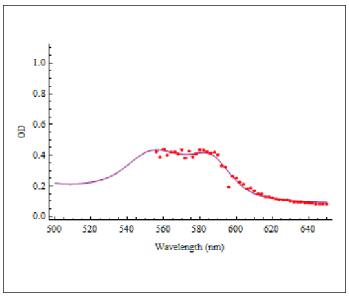
	Inferotemporal	Oxygen saturation: 109.5% 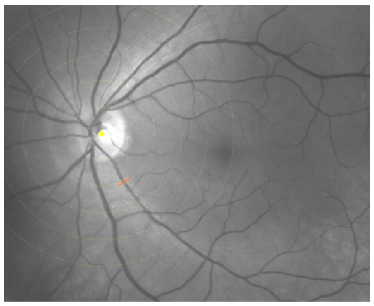 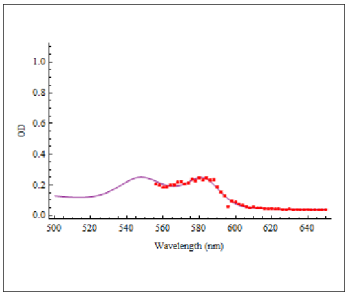	Oxygen saturation: 22.9% 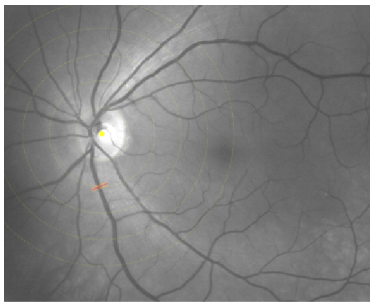 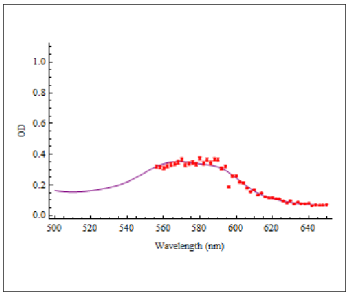

Table 6. Mean (± SD) oxygen saturation calculation of the temporal retinal arterioles and venules at points defined by the distance from the optic disc margin.

Location		Arterioles: mean oxygen saturation (± SD) (%)	Venules: mean oxygen saturation (± SD) (%)
Optic disc margin	Supero-Temporal	114.7 (± 28.3)	28.3 (± 10.1)
	Infero-Temporal	121.3 (± 19.1)	30.7 (± 14.6)
½ disc diameter from disc margin	Supero-Temporal	99.0 (± 36.5)	30.7 (± 10.8)
	Infero-Temporal	112.8 (± 20.9)	24.6 (± 12.9)
1 disc diameter from disc margin	Supero-Temporal	101.4 (± 19.9)	30.9 (± 11.1)
	Infero-Temporal	110.92 (± 21.9)	26.4 (± 7.3)
1½ disc diameter from disc margin	Supero-Temporal	96.7 (± 22.1)	28.9 (± 14.2)
	Infero-Temporal	129.1 (± 40.7)	20.7 (± 13.7)
2 disc diameter from disc margin	Supero-Temporal	97.9 (± 26.4)	29.1 (± 11.6)
	Infero-Temporal	124.5 (± 33.9)	27.0 (± 19.1)

Analysis of all temporal arterioles and venules	
Vessel	Mean oxygen saturation (± SD) (%)
All temporal arterioles	110.8 (± 11.8)
All temporal venules	27.7(± 3.2)

Figure 4.27: A box-and-whisker plot of the oxygen saturation (OS) of the temporal (superotemporal and inferotemporal) retinal arterioles and venules in normal subjects. The plot shows the median, the interquartile range, 95% central range and the minimum and maximum values.

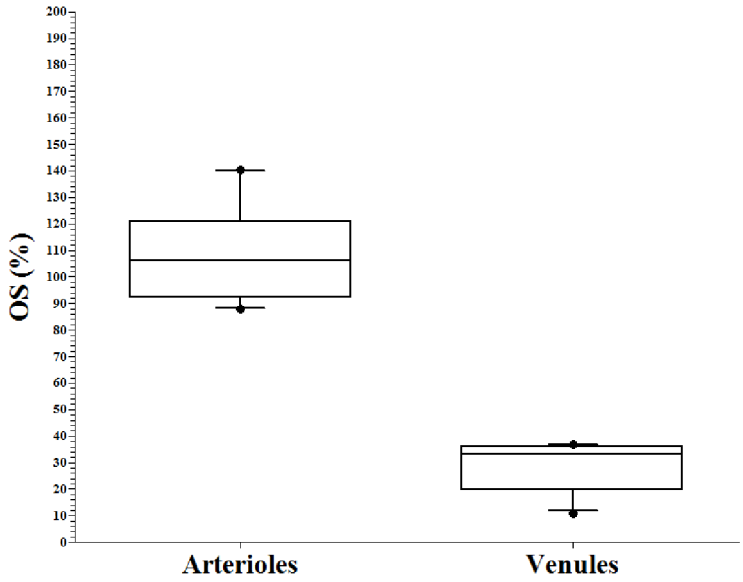

Figure 4.28: Plot of the mean oxygen saturation (OS) of the temporal (superotemporal and inferotemporal) arterioles (*left*) and venules (*right*) at points defined by the distance from the optic disc: at the disc margin (0.0), ½ disc diameter (0.5), 1 disc diameter (1.0), 1½ disc diameter (1.5) and 2 disc diameters (2.0) from the disc margin. The mean oxygen saturation (*central black filled circle*), the standard error of the mean (*vertical lines*), the best-fit line (*solid black line*) and the 95% confidence interval of the best-fit line (*dashed lines*) are shown in the plots.

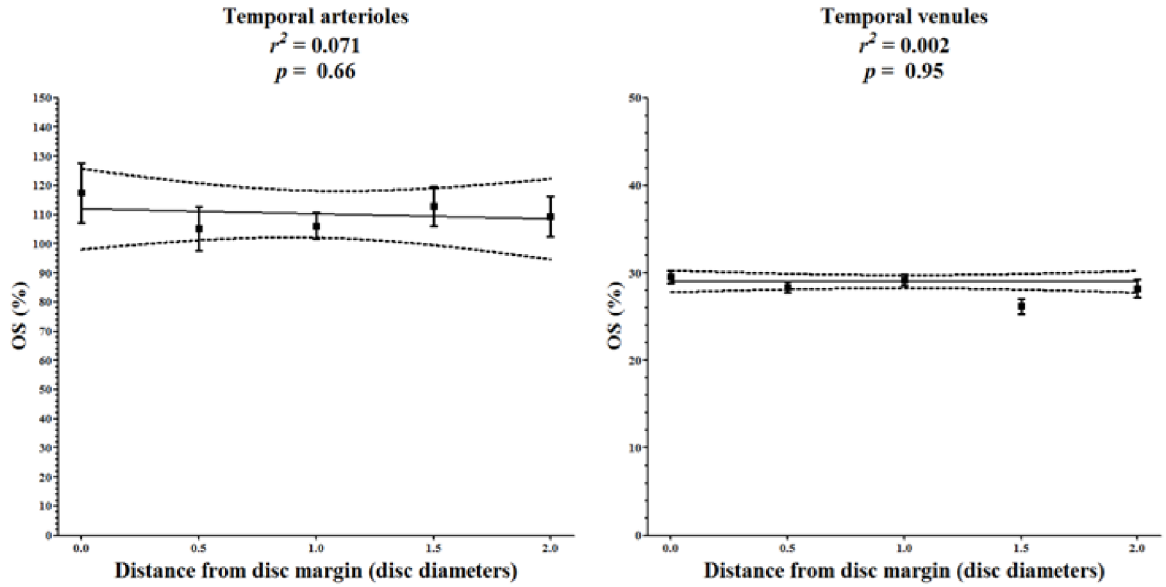

4.3.4. Relationship Between the Oxygen Saturation and LOCS III Grading Scores.

The multiple linear regression model predicting the OS of the temporal vessels in normal subjects using the LOCS III grading scores as independent variables did not produce a significant model ($F = 0.172$, $P = 0.843$, adjusted R squared = -0.065). The variance inflation factor and Durbin-Watson statistic of the model did not indicate the presence of multicollinearity. Cortical and posterior subcapsular LOCS III grades were constant in normal subjects and were not used in the analysis. The influence of the nuclear opalescence and nuclear colour lens grading scores were not statistically significant for OS in normal subjects ($\beta = 0.135$, $P = 0.609$ and $\beta = -0.142$, $P = 0.591$ respectively).

4.3.5. Analysis of the Macular Branches of the Retinal Arterioles and Venules.

Further analyses of the optical densities of the macular branches of the retinal arterioles and venules are illustrated in the Figure 4.29. The optical densities of the respective 1st degree arterioles and venules are displayed as a reference. In all three normal eyes the optical density profiles of the retinal arterioles appear consistent with the modified extinction coefficient of oxyhaemoglobin, that is the presence of two local maxima with a local minima. The calculated OS of these vessels exceed 80%. The optical density profiles of the 1st degree retinal venules appear consistent with the modified extinction coefficient of deoxyhaemoglobin, that is the presence of a single local maxima. In contrast, the macular branches of the retinal venules appear to have optical density profiles consistent with that of the modified extinction coefficient of oxyhaemoglobin, indicating that the OS of these macular branches of the retinal venules are higher than the respective 1st degree retinal venules. The calculated OS of the 1st degree retinal venules and its macular branches range from 16% - 52% and 47% - 98% respectively.

Figure 4.29: Mean optical density profiles and oxygen saturation calculation of selected 1st degree arterioles and venules and their macular branches in the superotemporal and inferotemporal quadrant of the retina of 3 normal eyes. For each eye, a series of retinal images are displayed with the locations of the analyzed optical density profiles (*orange* are the first and last profile *red solid lines* are the centre profiles). The mean optical density profile (between 556 – 650 nm, *red filled circle*) of the selected optical density profiles in each selected region are plotted with the standard deviation of the optical density for each wavelength between 556 - 650 nm (*red vertical lines*). The non-linear fitting algorithms to the optical density profiles are also shown (*red line*). The optical density profiles at wavelengths from 500 -554 nm are shown in gray in addition to the non-linear fitting at the respective wavelengths below 556 nm (*gray dashed line*). The oxygen saturation calculation from the non-linear fit is displayed above each retinal image and plotted together with the 95% confidence interval of the oxygen saturation calculation. The images and plots are separated into four rows (superotemporal arterioles, inferotemporal arterioles, superotemporal venules, inferotemporal venules) and two columns (1st degree retinal vessels and macular branches of the respective vessels). The red and blue arrows indicate the characteristic features of oxygenated blood (two local maxima and a local minima) and deoxygenated blood (single local maxima) respectively.

Subject 1.

Location	1st degree retinal arterioles	Macular branches of the retinal arterioles
Superotemporal	Oxygen saturation: 91.16% 95% confidence interval: 78.67% – 103.66% 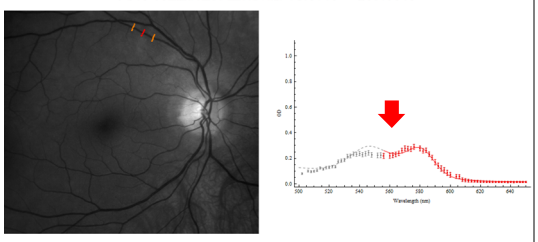	Oxygen saturation: 107.71% 95% confidence interval: 98.05% – 117.37% 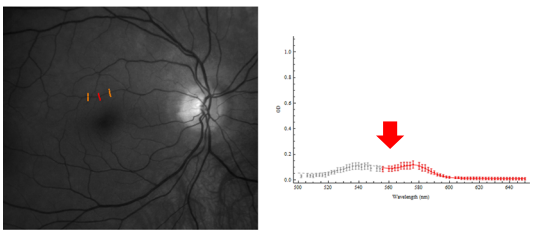
Inferotemporal	Oxygen saturation: 83.1% 95% confidence interval: 71.89% – 94.31% 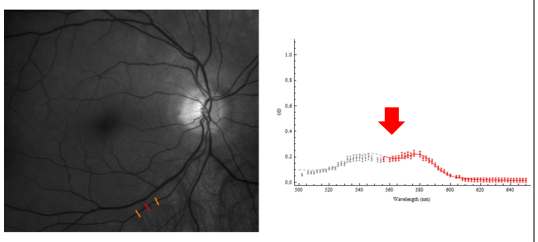	Oxygen saturation: 94.84% 95% confidence interval: 81.91% – 107.78% 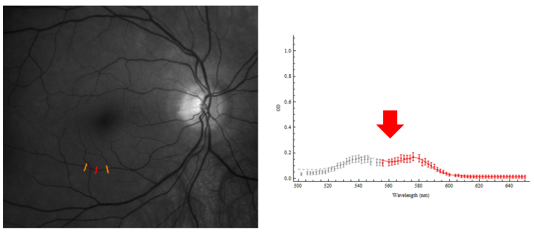
Location	**1st degree retinal venules**	**Macular branches of the retinal venules**
Superotemporal	Oxygen saturation: 27.25% 95% confidence interval: 20.54% – 33.96% 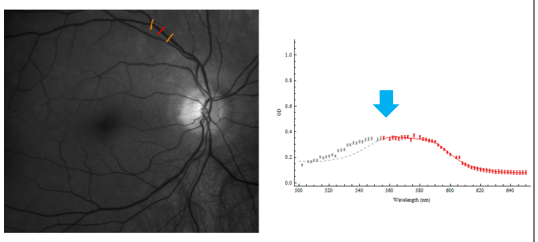	Oxygen saturation: 47.21% 95% confidence interval: 39.11% – 55.31% 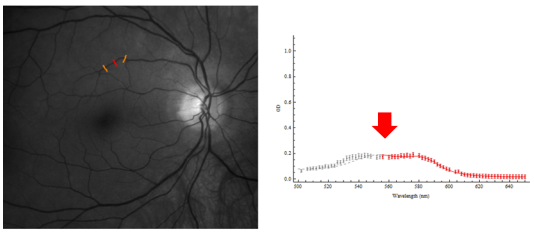
Inferotemporal	Oxygen saturation: 52.21% 95% confidence interval: 44.4% – 60.01% 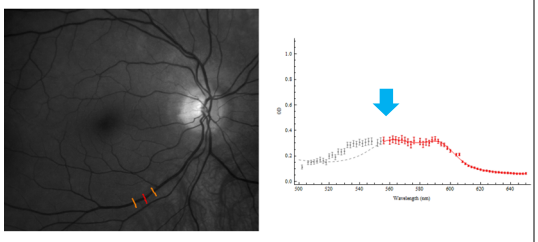	Oxygen saturation: 79.62% 95% confidence interval: 71.4% – 87.84% 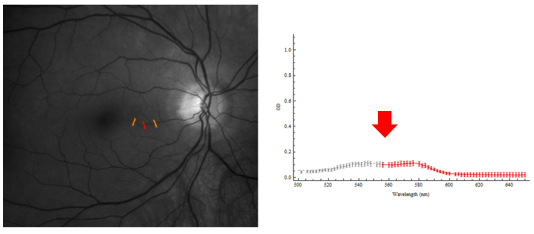

Subject 2.

Location	1st degree retinal arterioles	Macular branches of the retinal arterioles
Superotemporal	Oxygen saturation: 97.71% 95% confidence interval: 86.73% – 108.69% 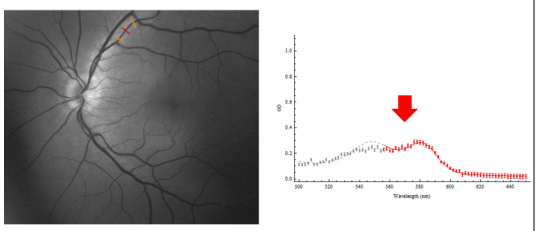	Oxygen saturation: 108.11% 95% confidence interval: 90.49% – 125.73% 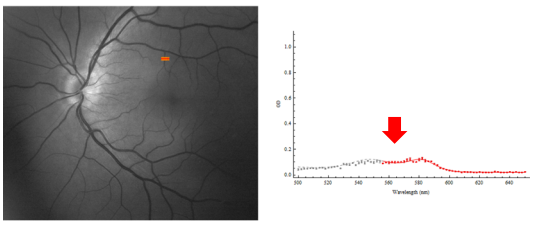
Inferotemporal	Oxygen saturation: 103.69% 95% confidence interval: 87.31% – 120.08% 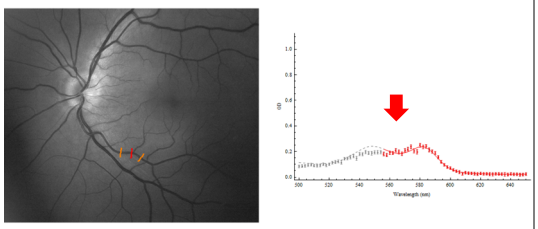	Oxygen saturation: 98.86% 95% confidence interval: 84.37% – 113.35% 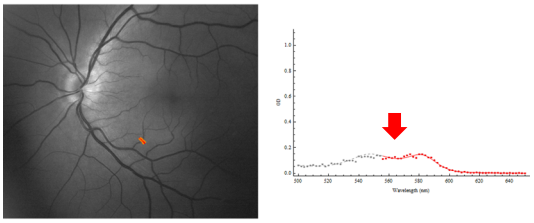
Location	**1st degree retinal venules**	**Macular branches of the retinal venules**
Superotemporal	Oxygen saturation: 29.78% 95% confidence interval: 20.63% – 38.92% 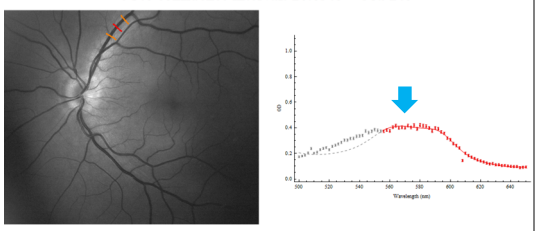	Oxygen saturation: 54.54% 95% confidence interval: 16.22% – 92.86% 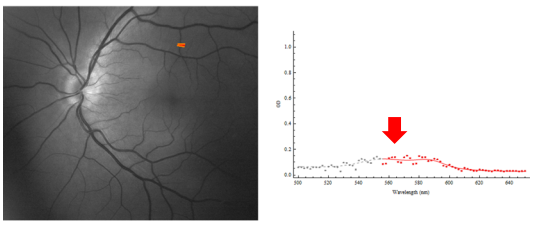
Inferotemporal	Oxygen saturation: 34.92% 95% confidence interval: 19.56% – 50.28% 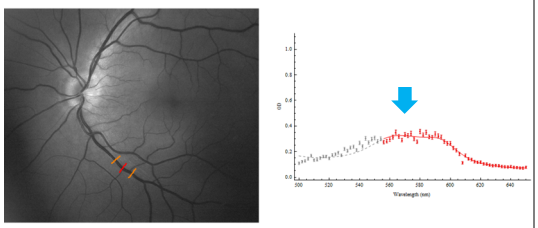	Oxygen saturation: 74.12% 95% confidence interval: 64.47% – 83.78% 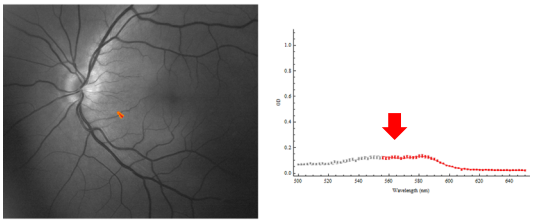

Subject 3.

Location	1st degree retinal arterioles	Macular branches of the retinal arterioles
Superotemporal	Oxygen saturation: 97.19% 95% confidence interval: 81.8% – 112.57% 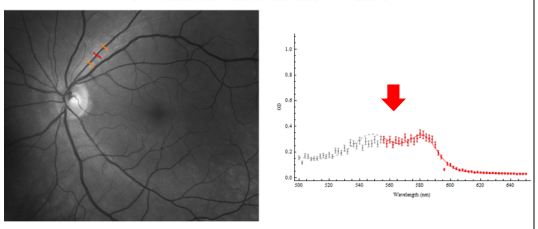	Oxygen saturation: 125.34% 95% confidence interval: 111.79% – 138.89% 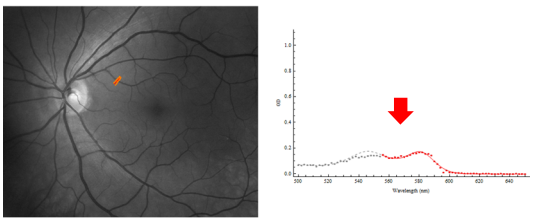
Inferotemporal	Oxygen saturation: 113.96% 95% confidence interval: 95.64% – 132.28% 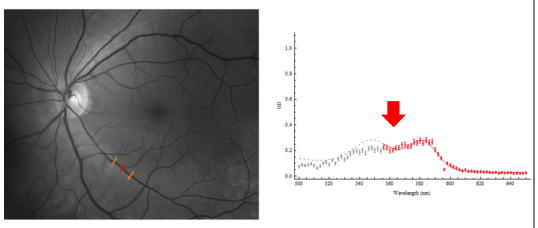	Oxygen saturation: 157.19% 95% confidence interval: 136.01% – 178.38% 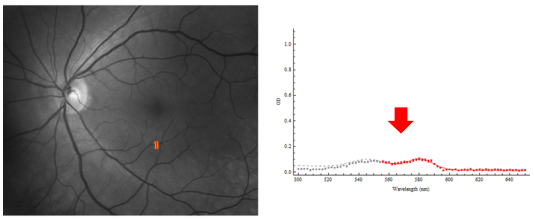
Location	**1st degree retinal venules**	**Macular branches of the retinal venules**
Superotemporal	Oxygen saturation: 41.87% 95% confidence interval: 24.62% – 59.12% 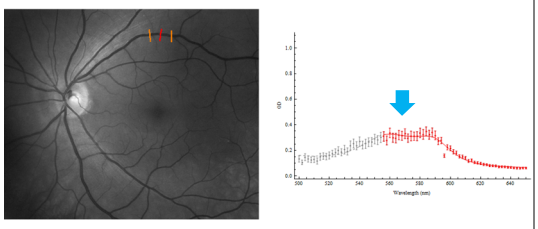	Oxygen saturation: 98.95% 95% confidence interval: 85.42% – 112.48% 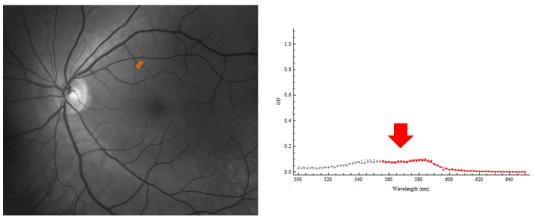
Inferotemporal	Oxygen saturation: 16.42% 95% confidence interval: 0.13% – 32.71% 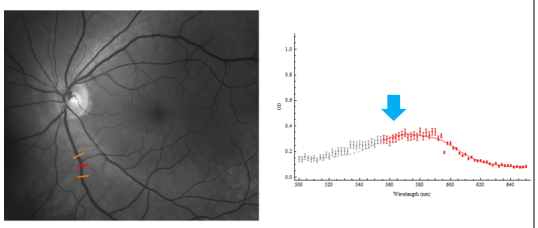	Oxygen saturation: 84.5% 95% confidence interval: 68.93% – 100.07% 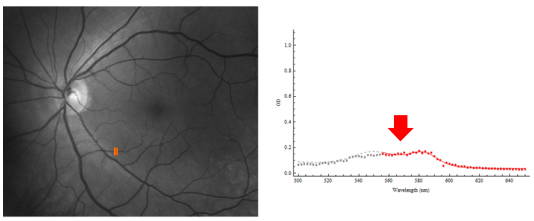

4.4. Discussion.

4.4.1. Oxygen Saturation of the Retina in Normal Subjects: Observational Features.

Dark calibrated registered spectral images of the retina from 3 normal subjects are illustrated in Figure 4.24. Direct observations of these images reveal similar optical features to that of the dark calibrated spectral images of the model eye (Figure 3.7, Chapter 3). The 1st degree arterioles and venules can be visibly distinguished from each other by their characteristic appearance as the wavelengths change. The arterioles appear less optically dense than the venules as the wavelengths used to acquire the retinal images are increased from 580 nm to 630 nm. This feature was seen in the model eye where quartz tubes containing arterial blood appeared less optically dense than tubes containing venous blood. This feature of the arterioles and venules is also consistent with that reported by Hardarson et al. (2006) and can be explained by the expected higher oxygen saturations of the retinal arterioles compared to the retinal venules which is consistent with the extinction coefficient of oxy- and deoxyhaemoglobin. The presence of this feature confirms that the hyperspectral camera is capable of detecting changes in the oxygen content of the retinal vasculature.

4.4.2. Wavelength Selection for Oxygen Saturation Calculations in the Retinal Vasculature.

The present study has described the acquisition of spectral images of the retina, the image processing and the analysis techniques used to calculate the OS of the retinal vasculature in normal subjects. The techniques used were similar to the techniques used in the model eye experiments described in Chapter 3. The important difference in the calculation of the OS in the model eye experiments and retinal images is that the wavelength range of the optical density profiles were shortened from 500 – 650 nm (model eye experiments) to 556 -650 nm (retinal images). The rationale for shortening the wavelength range of the optical density profiles has been illustrated in section 4.2.3.8. A wavelength range of 556 – 650 nm was decided to be the most appropriate wavelength range to accurately calculate the OS of the retinal vasculature. This wavelength range incorporates the important features of the extinction coefficient curves of oxyhaemoglobin (local minima and local maxima) and deoxyhaemoglobin (local maxima) to enable the non-linear fitting oximetry algorithm to accurately differentiate most optical density profiles of blood with varying oxygen

saturations. The evidence that using a wavelength range of 556 – 650 nm is more appropriate is supported by the finding that the oxygen saturations of the retinal arterioles were significantly lower when a wavelength range of 500 - 650 nm is used in comparison to a wavelength range of 556 - 650 nm (mean 61.7% vs. 99.4%; $p < 0.001$, Student's *t*-test). Furthermore, the mean OS calculation of the temporal retinal arterioles using a wavelength range of 556 - 650 nm is more consistent with the expected OS of the retinal arterioles.

The reason for the difference in the calculated OS using the two wavelength ranges is unclear. However, it is likely that the inaccurate modifications to the extinction coefficients of oxy- and deoxyhaemoglobin may be a significant attributing factor to this finding. Figure 4.16 illustrates the comparison between the modified extinction coefficients of oxy- and deoxyhaemoglobin and the published millimolar extinction coefficients of oxyhaemoglobin and deoxyhaemoglobin (van Assendelft, 1970). It can be seen that the extinction curves of deoxyhaemoglobin is similar. This may explain why the calculated oxygen saturations of the two wavelength ranges were comparable. The extinction curves of oxyhaemoglobin, however, appear to have two important differences. Firstly, the two local maxima at 542 nm and 577 nm of the published extinction coefficients of oxyhaemoglobin are greater than the two corresponding local maxima of the modified extinction coefficients. Secondly, the local maxima at 577 nm of the published extinction coefficients of oxyhaemoglobin is greater than the local maxima at 542 nm. This feature can also be observed in the optical density profiles of the temporal retinal arterioles in Figure 4.26. However, in the modified extinction coefficients of oxyhaemoglobin the reverse feature of the extinction curve is apparent: the local maxima at 577 nm is less than the local maxima at 542 nm. Therefore, the inaccuracy of the modified extinction coefficient may have contributed towards the underestimation of the OS of the temporal retinal arterioles when a wavelength range of 500 - 650 nm was used.

A further advantage of using a wavelength range of 556 - 650 nm is that it utilizes features of the oxyhaemoglobin (local minima at 560 nm and local maxima at 577 nm) and deoxyhaemoglobin (local maxima at 555 nm) extinction coefficient curves to enable the non-linear fitting algorithm to accurately distinguish a given optical density profile with a high OS from an optical density profile with a low oxygen saturation. Using a wavelength range of 556 - 650 nm was therefore a valid choice.

Interestingly, underestimation of the quartz tubes containing arterial blood in the model eye experiments (Chapter 3) did not occur when a wavelength range of 500 - 650 nm was used to calculate the OS. This could be explained by the shape of the calculated optical density profiles of the arterial blood samples whose two local maxima are approximately

equal (Chapter 3, Figure 3.10). In contrast, the first local minima of the optical density profiles of the temporal retinal arterioles appear to be more variable and less than the second local maxima (Figure 4.29). The variability in the optical densities at wavelengths less than approximately 550 nm could be explained by the variable pigment concentration of the retinal tissues resulting in variable contrast of the retinal vessels to the background retina. Excluding wavelengths less than 556 nm in the optical densities of the retinal vasculature therefore further reduces the inaccuracy of the OS calculations.

Figure 4.30: A comparison of the modified extinction coefficients of oxyhaemoglobin and deoxyhaemoglobin (*red and blue solid lines respectively*) to the published millimolar extinction coefficients of oxyhaemoglobin and deoxyhaemoglobin (*red and blue dashed lines respectively*)(van Assendelft, 1970). The wavelength at 556 nm is indicated as a gray dashed vertical line.

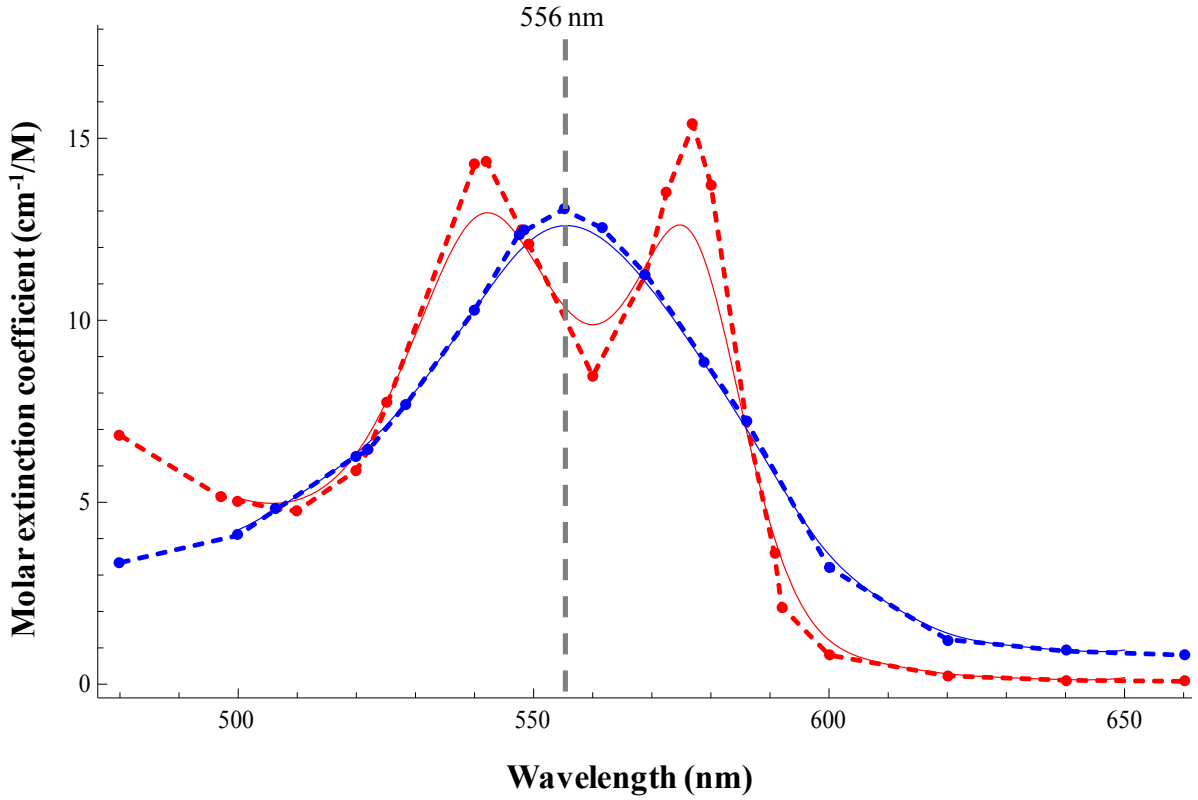

4.4.3. Oxygen Saturation of the 1st and 2nd Degree Vessels of the Retina in Normal Subjects: Quantitative features.

Pseudocolour images of the OS calculations overlayed onto the retinal arterioles and venules in 14 normal eyes are illustrated in Figure 4.25. The oxygen saturations of the retinal arterioles are generally greater than 80%. Lower than expected oxygen saturations of the retinal arterioles can be observed frequently at locations where the arterioles are in close proximity to the larger venules. This error is due to errors of the vessel profile analysis. The orthogonal vessel profiles of tracked arterioles adjacent to the larger venules will cross-over onto the spatial coordinates of the venules resulting in the inadvertent calculation of the optical density of the venule. Careful selection of appropriate points along the arterioles at given distances from the optic disc margin was performed to prevent in the inclusion of inaccurate OS calculations. Furthermore, OS calculations of small segments of the vessels were obtained from the segmentation analysis as opposed to large segments of the vessels to reduce the influence of spurious outlying results.

The pseudocolour images reveal highly variable oxygen saturations of the main (1st and 2nd degree) retinal venules which is consistent with studies reported by Hickam et al. (1963). The variability of the OS in the retinal venules is unclear and could be attributed to a number of factors such as noise in the optical density calculations as a result of variability in the illumination of the retina images (vignetting), retinal background (variable pigmentation) and retinal vasculature. Additionally, it could be explained by physiological variability in the function of the retina in the photopic conditions used to acquire the spectral retinal images (variable consumption of oxygen and blood flow). The non-significant relationship between the LOCS III grading score and the OS calculation, analyzed by multiple linear regression, suggest that the influence of the lens status on the oximetry values was not an important factor.

Analysis of the 1st and 2nd degree temporal retinal arterioles at defined points along its length determined by distances from the optic disc margin revealed a mean OS (± SD) of 110.8 % (± 11.8%). This is comparable to OS measurements of the retinal arterioles in healthy subjects reported by previous authors which range from 90% - 102% (see Table 7). Correlation analysis indicated that the OS of the 1st and 2nd degree temporal retinal arterioles did not significantly change at varying distances from the optic disc margin of up to 2 disc diameters. This is consistent with the findings of constant retinal arteriolar oxygen saturation measurements in the retinal arterioles of normal subjects reported by Schweitzer et al. (1992).

However, the mean OS of the 1st and 2nd degree temporal retinal venules was 27.7% (± 19.1%), which is a result much lower than the OS measurements of the retinal venules reported in previous studies (see Table 7). A possible explanation could be errors in the OS calculation caused by the inaccurate optical density profiles. However, this is unlikely as all the optical density profiles included in the analysis were carefully selected and examined. Poor optical density profiles were excluded from the analysis. Further analysis was warranted to investigate the OS calculations of the retinal venules. The constant OS measurements of the retinal venules at varying distances from the optic disc margin of up to 2 disc diameters indicate a consistency in the OS measurements. Furthermore, Figure 4.26 illustrates the mean optical density profiles and respective mean OS calculation of the retinal 1st degree vessels at selected points defined by the retinal segmentation in 5 representative normal subjects. It can be seen that the optical density profiles of the retinal venules with OS calculated at approximately 15 - 30% are consistent with the features of the modified extinction coefficients curves at the respective OS levels. Figure 4.31 illustrates the simulated modified extinction coefficient curves of haemoglobin at various oxygen saturations. The shapes of the optical density profiles are consistent with the shape of the modified extinction coefficients curves at the respective OS levels, i.e. the presence of a single local maxima at approximately 555 nm. It can also be seen in Figure 4.31 that the morphology of the modified extinction coefficients curves changes as the OS increases from 0% to 100% such that at approximately 40% OS the simulated modified extinction coefficient consists of 2 local maxima (at 542 nm and 577 nm) which becomes more apparent as the OS increases. The absence of the 2 maxima and the presence of a single maxima in the optical density profiles of the retinal venules, at least, indicates that the OS is less than 40%. Therefore, we can assume some confidence in the accuracy of the OS calculations of the retinal venules.

Previous retinal oximetry systems have reported retinal venous oxygen saturations ranging from 45% - 65% (Table 7). Most of these systems rely on two wavelength oximetry which has been reported to overestimate the true OS. It is possible that previous retinal oximetry systems may have been susceptible to the same flaws as those reported in two wavelength pulse oximeters (Sarnquist et al., 1980), i.e. scattering of red or infrared light in the blood vessels. However, Schweitzer et al. (1999) reported a mean OS of 57.9% (± 9.9). Their hyperspectral retinal oximetry system is the most comparable oximetry system to the one used in this present study. It is unclear why such a large difference in the OS calculation of the retinal venous system exists. A possible explanation could be the wavelengths used by Schweitzer et al. (1999) which ranged between 510 – 586 nm in 2 nm increments. At these

wavelengths, the hyperspectral retinal imaging system described in this present study yielded highly variable the optical densities of the retinal vessels which could contribute to errors in the OS calculations. Nonetheless, to date, no previous retinal oximetry studies have provided such an in depth demonstration and *in vivo* non-invasive validation of the OS calculation of the retinal venules.

Table 7. Oxygen saturation (OS) measurements of the retinal vessels in normal subjects reported in previous studies.

Authors	Oxygen saturation (± SD)		Wavelengths	Comments
	Arterioles	Venules		
This thesis	110.8% (± 11.8%)	27.7% (± 3.2%)	500 to 650 nm	*N* = 14
Hickam et al. (1963)		58% (± 10%) 60% (± 16%)	640 and 800 nm 640 and 505 nm	*N* = 55 *N* = 10
Delori et al. (1988)	98% (± 8%)	45% (± 7%)	558nm, 569 and 586 nm	*N* = 22
Schweitzer et al. (1998)	92.2% (± 4.1%)	57.9% (± 9.9%)	510 - 586 nm	*N* = 28 (30 eyes)
Michelson et al. (2006).	92.3% (± 3.4%)	55.7% (± 6.8%)	522, 560, 569 and 586 nm	*N* = 58
Denninghoff et al. (Drewes et al., 1999)	101-102% 98%	65% 63%	629, 678, 821 and 899 nm	*N* = 1 On the optic disc Away from the optic disc
Beach et al. (1999).		55% (± 3.38%)	569 and 600 nm	*N* = 5
Stefánsson et al. (Hardarson et al., 2006).	96% (± 9%)	55% (± 14%)	586 and 605nm	*N* = 18 Relative OS
Hammer et al. (2008)	98 (± 10.1 %)	65% (± 11.7 %)	548 ± 10 nm and 610 ± 10 nm (FWHM)	*N* = 20
Yoneya et al. (Ito et al., 2008)	90-98%	60-70%	480 - 600nm	*N* = 4 (normal fellow eyes of subjects with CRVO)
Johnson et al. (2007)	95%	60-65%	454 - 646 nm	*N* = 2 4nm bandwidth

Figure 4.31: Simulated modified extinction coefficients of haemoglobin at various oxygen saturations (*green solid line*). The extinction coefficient of oxyhaemoglobin (*red dashed line*) and deoxyhaemoglobin (*blue dashed line*) are shown for comparison.

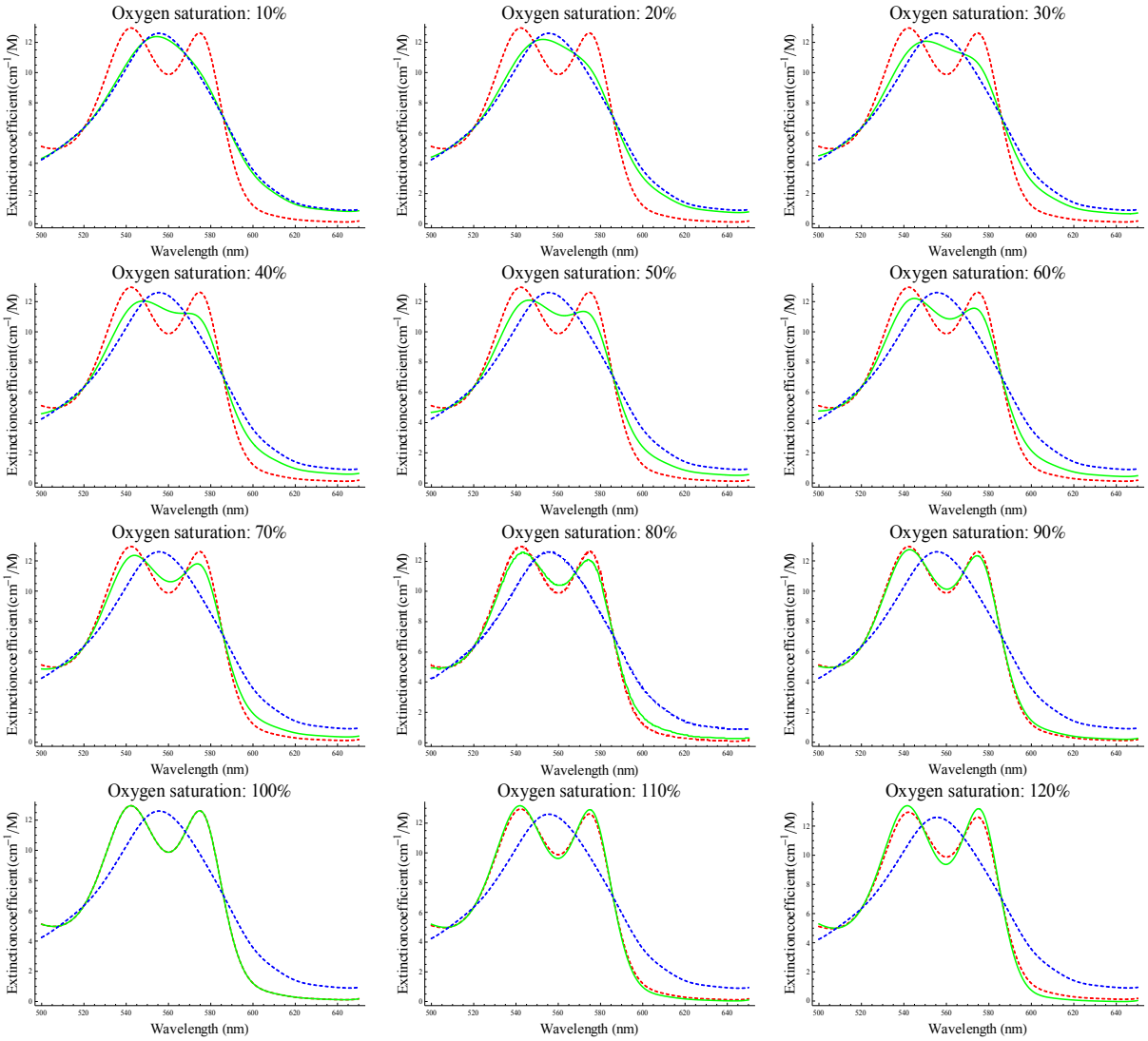

4.4.4. Oxygen Saturation of the Macular Branches of the Retinal Vasculature in Normal Subjects: Observational and Quantitative Features.

The macular branches of the retinal venules in the dark calibrated registered spectral images shown in Figure 4.24 appear to be less optically dense than their respective 1st and 2nd degree venules. This observation suggests that the macular branches of the retinal venous system have higher oxygen saturations than their parent venules. This observation is

confirmed by the quantitative OS calculations of the macular branches of the retinal venules. Figure 4.25 shows a series of pseudocolour images of the OS calculations overlayed onto the retinal vessels of normal subjects. These images generally indicate that the macular branches of the retinal venules contain blood with higher OS compared to their respective 1st and 2nd degree venules. Further analysis of the optical density profiles of selected segments of the macular venules and OS calculations was performed to confirm this finding (Figure 4.29). The optical density profiles of the macular branches of the retinal venules appear to have features similar to that of the retinal arterioles (two local maxima) providing evidence that these small venules contain blood with higher OS compared to the larger 1st and 2nd degree retinal venules into which they drain. To date, this phenomenon has not been reported in previous retinal oximetry studies. It is conceivable that the high OS of the blood in the macular branch venules are a result of the collection of high concentrations of unused excess oxygen in the foveal and perifoveal region which originate from the retinal and choroidal circulations.

4.4.5. Limitations of the Study.

This present study has a number of limitations. One of the main limitations is the small number of normal subjects recruited into the study. Unfortunately this was unavoidable as the majority of the work was placed into creating the software algorithms necessary to perform the oximetry calculations and analysis. The acquisition and processing of the images to generate oximetry maps of the retinal vasculature of one eye took on average approximately 50 hours of cumulative processing on a computer with a 2.5GHz dual-core processor with 4 GB of RAM. The processing and analysis steps were semi-automated and, in addition to this, further analysis of the large volumes of data had to be performed for the statistical analyses. Hence, this hyperspectral retinal oximetry system would be too cumbersome to be used as a general tool in the ophthalmology clinic. In addition to this, data from 9 normal subjects (40%) had to be excluded from the study due to “noisy” optical density calculations. Statistical bias in this process was minimized by blinding my evaluation of the optical density profiles from the OS calculation.

A further limitation of this study was that no investigation into the repeatability of the oximetry analysis has been performed. This would be desirable in future studies to evaluate the reliability of the hyperspectral retinal imaging system and image analysis algorithms to yield repeatable oxygen saturation calculations. Additionally, a number of previous retinal

oximetry studies have reported on the results of re-breathing exercises (Frayser and Hickam, 1964; Beach et al., 1999; Hardarson et al., 2006; Hammer et al., 2008) with varying mixtures of oxygen to "validate" the ability of the oximetry systems to detect changes in the oxygen saturation of the retinal vasculature. We did not perform these studies as our imaging system was not suited to acquiring a full image dataset in a short space of time necessary to adequately perform the experiments. In addition, these exercises only provide information on relative changes and not absolute quantitative changes in the oxygen saturation of the retinal vasculature which cannot be easily validated.

A significant amount of effort was applied to create the image processing and analysis algorithms to calculate the oxygen saturations of the retinal vasculature. However several aspects of the algorithms need to be addressed for future studies. Firstly, the dark calibration techniques applied to the images prior to oximetry analysis appear to significantly attenuate the gray scale intensity of the raw images. This can be seen in Figure 4.2 which compares the grayscale intensity profile of the linear region of interest before and after dark calibration. It is apparent that the dark calibration reduces the intensity profile to approximately 30% of its original value. This reduces the bit depth of the images from 12-bit to approximately 4-bits. It is possible that such a significant reduction in the bit depth of the images could affect the accuracy of the oximetry calculations. This is could explain frequent inaccuracies of the oxygen saturation calculations (negative values and values greater than 200%) of the smaller retinal vessels whose optical densities appear to be significantly attenuated. Careful evaluation of the optical density profiles and OS calculations were imposed when examining the oxygen saturation of the macular branches of the retinal vessels. Inaccurate optical densities and oxygen saturations were excluded.

The registration of the retinal images was perhaps the most challenging part of the image processing. A full series of retinal images with a wavelength range of 500 - 650 nm (76 spectral images) took on average approximately 8 to 10 hours to obtain the calculations of the offsets. This algorithm was designed to be automated; however, frequent errors in the calculations of the rotation, translational and scaling offsets due to features of the spectral images required the algorithm to be restarted. Furthermore, the results of the image registration had to be checked by visually inspecting the registered retinal images to remove significantly misregistered retinal images. As a result approximately 43% (10/23) of eyes had at least 1 retinal image of the wavelength range removed due to poor image registration. However, it is unlikely that small numbers of missing wavelengths would significantly affect the oxygen saturation calculation.

The detection and tracking of the retinal vessels is an integral part of the analysis of the retinal images. However, the Fast Marching Method preferentially tracks the darkest pixels in the filtered retinal image which frequently resulted in the tracking of the larger retinal venules instead of either retinal arterioles or smaller retinal vessels. A technique of tracking segments of the arterioles and smaller venules by trial-and-error was used as shown in Figure 4.7. As a consequence not all retinal vessels in the field of view of the retinal images were tracked. However, in this study sufficient numbers of retinal vessels were tracked for the analyses. Nonetheless, a further particular problem was that the analysis of the vessel profiles of the retinal arterioles in close proximity to the retinal venules often resulted in erroneous optical density and subsequently OS calculations often resulting in lower than expected OS calculations. This effect can be seen in the pseudocolour oximetry maps of the retinal vasculature (Figure 4.25). Careful evaluation of the optical density profiles and OS calculations was implemented to ensure that these erroneous measurements were not incorporated into the statistical analyses. Furthermore, inaccuracies of the optical density and OS calculations were frequently encountered in regions of the retinal images where there was poor illumination of the retina, particularly towards the periphery and nasal retina. As a result, analysis of segments of the retinal vasculature was limited to two disc diameters and analysis of the nasal retinal vasculature was not performed.

The non-linear fitting oximetry algorithm was used to calculate the free parameters such as the OS, vessel diameter, haemoglobin concentration, optical path length and scaling constants. In this study, the free parameters other than the OS were not evaluated. These free parameters would be difficult to validate and their influence on the accuracy of the OS calculation need further investigation. Furthermore, this study has shown that the oximetry algorithm frequently calculates OS beyond its physiological range (0 – 100%): negative values and OS greater than 100%. Further modifications to the oximetry algorithm to incorporate constraints on the OS (and other free parameters) would need to be implemented and evaluated. Additionally, the use of more accurate extinction coefficients needs to be addressed.

In this study, shortening of the wavelength range of the optical densities prior to oxygen calculations of the retinal vasculature was required to prevent gross underestimation of the arteriolar OS. The variability of the optical densities at wavelengths less than 556 nm is unclear. At these wavelengths, the retina appears dark in the spectral images. The lack of contrast between the retinal background and retinal vessels could be a plausible explanation for the variability in the optical density calculations at these wavelengths. This could indicate

that, the method of using the intensity of the retinal background as an estimate of the intensity of the incident light could possibly introduce a significant amount of noise in the calculations which is may be dependent on the amount of pigmentation in the retina. Although, shortening the wavelength range has reduced the effects of this variability, the wavelengths between 556 nm and 650 nm are possibly still susceptible to variations in the retinal pigmentation. This was noticeable in the analysis of 2 normal subjects (one Asian, one black Afro-Caribbean) with highly pigmented retina. These subjects had to be excluded because of erroneous calculations of the optical density and oxygen saturations. Further research is required to evaluate alternative methods of estimating the optical densities of the retinal vasculature which is not susceptible to the influence of retinal pigmentation.

4.4.6. Summary.

This present study has described the techniques used to perform OS calculations of the retinal vasculature in normal subjects. Retinal arteriolar OS calculations are consistent with previous studies. However, retinal venular OS calculations are considerably lower than the majority of those reported in the literature. Additionally, the OS of the macular branches of the retinal venules are higher than their respective 1st and 2nd degree retinal venules. This is an interesting, and novel finding, which needs further confirmation, but could be an important feature in understanding the normal physiology of the retina.

Chapter 5: Retinal Oximetry in Retinal Artery and Retinal Vein Occlusion.

5.1. Introduction.

In Chapter 4, the methods of calculating the oxygen saturation (OS) in the retinal vasculature in normal eyes were described. In particular, the method of validating the OS calculations by inspecting the retinal vasculature from the dark calibrated spectral images and the optical density profiles (used to calculate the OS) was described.

The applicability of the spectral imaging and the oximetry analysis techniques to diseased eyes required evaluation. An overview of retinal artery and venous occlusion has been provided in Chapter 1. These conditions are associated with altered blood flow (ischaemia) or stasis within the retinal vasculature which is thought to result in reduced oxygen supply to the retina from the systemic circulation. Additionally, histopathological studies have shown that retinal artery and vein occlusions are associated with inner retinal atrophy (Frangieh et al., 1982; Green et al., 1981; Wolter, 1961; Hayreh et al., 2004; Zimmerman, 1965). Therefore, these conditions, provide an opportunity to test the ability of a retinal oximeter to detect changes in the oxygenation of the retinal vasculature in terms of its supply (arteriolar oxygenation) and demand (venular oxygenation).

The aim of this study was:

- to demonstrate the ability of the hyperspectral fundus camera and our oximetry techniques to detect OS abnormalities in the retinal vasculature in patients with retinal arterial and venous occlusion.

5.2. Methods.

5.2.1. Recruitment of Subjects.

Nine patients previously diagnosed embolic retinal artery occlusion and 17 patients previously diagnosed with retinal vein occlusion were included in the study. The study protocol received institutional review board approval and adhered to the tenets of the Declaration of Helsinki.

All subjects underwent full clinical ophthalmic evaluation; visual acuity testing using a Snellen chart and intraocular pressure measurement (IOP) using Goldmann applanation tonometry. The pupils were dilated with 1% tropicamide (Minims; Chauvin Pharmaceuticals, Romford, UK) and slit lamp stereo biomicroscopy was performed to grade the degree of lens opacity (using the Lens Opacities Classification System III) (Chylack et al., 1993) and examine the fundus (at high magnification with a fundus +78D lens). Brachial blood pressure of all normal subjects was measured using an aneroid sphygmomanometer (Accoson 0342: A.C. Cossor & Son (Surgical) Ltd., Essex, UK).

5.2.2. Hyperspectral Retinal Image Processing and Oximetry Analysis.

The images acquisition techniques, processing and oximetry algorithms used to measure the OS of the retinal vasculature were the same as that described in Chapter 4. Briefly, retinal images were acquires at wavelengths using the time sequential hyperspectral fundus camera. The best quality images for each wavelength was selected, dark calibrated and aligned to a reference image obtained at 580 nm. The retinal vasculature of each eye was detected, and tracked to enable a vessel profile analysis algorithm to calculate optical density profiles of the tracked centreline points along the vessels.

The optical density profiles at wavelengths from 556 – 650 nm were used to calculate the OS of the respective centreline points along the tracked retinal vessels using a non-linear oximetry model. Pseudocolour maps of the OS calculations (oximetry maps) overlayed onto the retinal vasculature were generated. Six patients with retinal arterial occlusion and 8 patients with retinal vein occlusion were excluded from further analysis due to poor image quality, failed image registration and/or inaccurate optical density profile calculations. The remaining patients with retinal venous occlusion (n =9) were divided into two group: ischaemic and non-ischaemic.

In patients with retinal artery occlusion (n = 3) and retinal vein occlusion (n = 9) the mean optical density profile (n = 101 profiles) of selected segments of the temporal vessels were calculated and used to calculate the OS of the vessel segment. The mean optical density profiles of the selected segments of the arterioles and venules were studied and compared to those seen in corresponding regions in normal eyes.

In patients with ischaemic retinal vein occlusion (n = 6), the mean OS at points along the 1st and 2nd degree superotemporal, inferotemporal vessels (disc margin, ½ disc diameter (*dd*), 1 dd, 1½ dd and 2 dd from the disc margin) were calculated. The OS calculations were

checked for outlying OS results which were deleted and were defined by the same criteria as that described in Chapter 4 for normal subjects: negative OS calculations, OS calculations greater than 200% for arterioles and OS calculations greater than 100% for venules. Thirteen (14%) arteriolar and twenty-two (24%) venular OS calculations were excluded from further data analysis.

5.2.3. Statistical Analysis.

The normality of the data distributions were tested using the Shapiro-Wilk normality test, with the cutoff for non-normality set at $P < 0.05$. The OS data of the retinal arterioles in normal subjects and retinal arterioles and venules in patients with ischaemic retinal vein occlusion were not significantly different from a normal distribution ($P = 0.158$, 0.188, and 0.876 respectively). Multiple linear regression ("enter" method) was used to determine the relationship between the mean OS of the temporal retinal vessels and LOCS III grading scores (nuclear opalescence, nuclear colour, cortical and posterior subcapsular). To check for multicollinearity among the variables in the final model, the variance inflation factor and Durbin-Watson statistic were calculated. The OS data of the retinal venules in normal subjects was significantly different from a nomal distribution ($P = 0.011$). An unpaired *t*-test with Welch's correction (two-tailed) was used to compare the OS of the temporal arterioles between the normal subjects and patients with ischaemic retinal vein occlusion. A Mann-Whitney test (two-tailed) was used to compare the OS of the temporal venules between the normal subjects and patients with ischaemic retinal vein occlusion. A $P < 0.05$ was considered statistically significant. Statistical analyses were calculated using commercial software (SPSS, ver. 16.0; SPSS Inc., Chicago, IL).

5.3. Results.

This study included 3 patients with embolic retinal arterial occlusion (branch retinal artery occlusion $n = 2$, and central retinal artery occlusion $n = 1$) and 9 patients with retinal vein occlusion (6 ischaemic and 3 non-ischaemic). The baseline characteristics of the retinal vein occlusion patients included in this current study are presented in Table 8.

Table 8. Baseline characteristics of the patients with ischaemic and non-ischaemic retinal vein occlusion.

		Ischaemic	Non-ischaemic
Number		6	3
Mean age (years; range)		68.3 (53 - 81)	69 (68 - 70)
Male:Female ratio		2:4	3:0
Mean duration of retinal vein occlusion (months ± SD)		14.5 (± 13.4)	52 (± 79.2)
Mean best corrected visual acuity (LogMAR Equivalent)(± SD)		0.51 (± 0.21)	0.17 (± 0.13)
Mean intraocular pressure (mmHg ± SD)		14.5 (± 1.0)	14.7 (± 3.5)
Mean lens opacity grade	Nuclear opalescence (± SD)	2 (± 0.7)	2 (± 1.7)
	nuclear colour (± SD)	2 (± 0.7)	2 (± 1.7)
	cortical (± SD)	1 (± 0)	1.7 (± 0.6)
	posterior subcapsular (± SD)	1 (± 0)	1 (± 0)
Mean systolic blood pressure (mmHg ± SD)		155.8 (± 28.7)	166.7 (± 22.5)
Mean diastolic blood pressure (mmHg ± SD)		83.3 (± 12.9)	71.7 (± 5.8)
Mean pulse oximeter oxygen saturation (% ± SD)		96.5 (± 1.0)	96.7 (± 1.52)

5.3.1. Oxygen Saturation of the Retinal vasculature in Patients with Retinal Arterial Occlusion: Observational Features, Optical Density Profile Analysis and Quantitative Oximetry of the Retinal Vasculature.

The observational features, mean optical density profiles and OS calculation of the retinal blood vessels in 2 representative patients with retinal artery occlusion are presented in Figures 5.1 to 5.8. The third patient is illustrated in Appendix 5.

Subject A1 is a 79 year old male with a 25 day history of a left inferior branch retinal artery occlusion (Figure 5.1). The BCVA of the left eye was 6/18 at the time of imaging. The dark calibrated spectral images of the left retina at 9 selected wavelengths (560, 570, 580, 590, 600, 610, 620 and 630 nm) show two important features. Firstly, the inferotemporal arterioles appear more optically dense than in normal eyes at wavelengths greater than 590 nm indicating a lower OS (Figure 5.2; *yellow arrow heads*), and secondly the inferotemporal

venule appear to be less optically dense than in normal eyes at wavelengths greater than 600 nm indicating a higher OS (Figure 5.2; *green arrow heads*). Confirmation of these observational features can be seen when the optical density profiles and OS of selected segments of the arterioles and venules are assessed (Figure 5.3). The optical density of the inferotemporal arterioles (Figure 5.3, *red bordered images*) contrasts to the optical density profiles of the superotemporal arterioles and appear similar to that venous blood. This is confirmed by the lower OS calculations in the inferotemporal arterioles compared to the superotemporal arterioles. The optical density profiles of the 1st degree superotemporal and inferotemporal venules are relatively more "noisy" with calculated OS of 51% and 56% respectively. The pseudocolour oximetry maps of the retinal vessels show lower than normal OS in the inferotemporal retinal arterioles and slightly higher than normal OS in the inferotemporal venules (Figure 5.4).

Subject A2 is a 69 year old female with a 2 day history of a left central retinal artery occlusion (Figure 5.5). The BCVA of the left eye was detection of hand movements at 1 metre at the time of imaging. The dark calibrated spectral images of the left retina at the 9 selected wavelengths show abnormal appearances of the retinal arterioles and venules related to the OS. The arterioles appear to be more optically dense than in normal eyes at wavelengths greater than 590 nm indicating a lower OS (Figure 5.6; *yellow arrow heads*). The venules appear to be less optically dense than in normal eyes at wavelengths greater than 600 nm indicating a higher OS (Figure 5.6; *green arrow heads*). Confirmation of these observational features can be seen when the optical density profiles and OS of selected segments of the macular arterioles and venules are calculated (Figure 5.7, *red bordered images*). The optical density profiles of the macular branches arising from the superotemporal and inferotemporal arterioles have similar optical density profiles to the selected venules and extinction of deoxyhaemoglobin (single local maxima) indicating low OS which is confirmed by the OS calculations of 54% and 31% respectively. In contrast, the optical density of the cilio-retinal arteriole (traversing from the optic disc towards the fovea through the "spared" retina) is similar to that seen in a normal arteriole and extinction of oxyhaemoglobin (single local maxima) indicating that the OS is unaltered, this is confirmed by the OS calculation of 101%. The optical density profiles and OS of the 1st and 2nd degree venules are comparable to the venules in normal eyes. The optical density profiles and OS of the macular branches of the superotemporal and inferotemporal 1st degree venules adjacent to the cilio-retinal artery are similar to that seen in the macular venules in normal eyes. The pseudocolour oximetry

maps of the retinal vasculature suggest slightly lower OS in the inferotemporal retinal arteriole compared to the superotemporal retinal arteriole (Figure 5.8). The 1st and 2nd degree venules appear unremarkable when compared to the same vessels in normal eyes; however, the macular branches (except branches in close proximity to the cilio-retinal artery) appear to be generally lower than that seen in normal eyes.

In subject A1 (branch retinal artery occlusion), the pseudocolour oximetry maps of the retinal vasculature indicate that abnormally low oxygen saturations in the macular branches of the retinal venules are localised to the retinal hemisphere of the branch artery occlusion (Figure 5.4). In subject A2 (central retinal artery occlusion), the majority of the macular venules in both superior and inferior hemispheres appear to have lower oxygen saturation (Figure 5.8). This contrasts to the group of central retinal venules that traverse the central macular from the optic disc to the fovea which have comparatively higher OS than the other macular venules.

Figure 5.1. A colour image of the left fundus of subject A1. A 79 year old male with a 25 day history of a left inferior branch retinal artery occlusion (BCVA: 6/18).

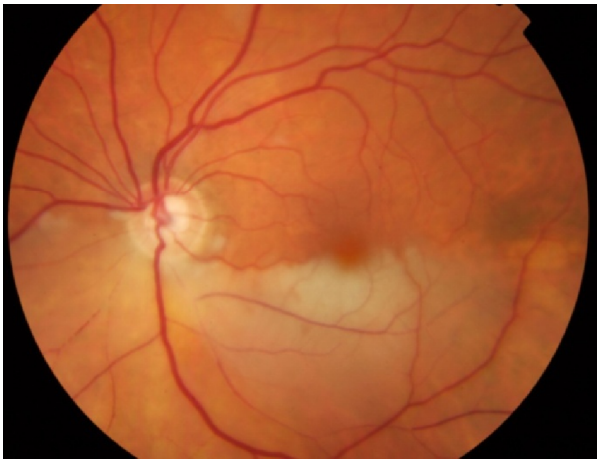

Figure 5.2. Subject A1: dark calibrated spectral images of the left retina at 9 selected wavelengths (560, 570, 580, 590, 600, 610, 620 and 630 nm). First degree retinal arterioles and venules are indicated by *red* and *blue arrow heads* respectively. Abnormal appearances of the retinal arterioles and venules related to the OS are indicated by the *yellow* and *green arrow heads* respectively.

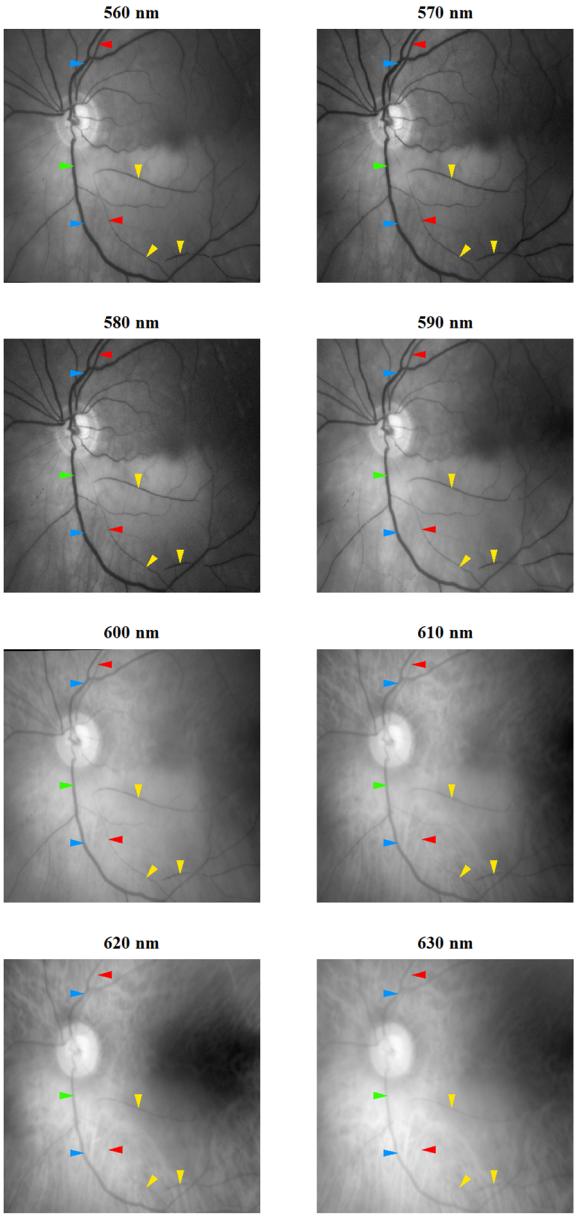

Figure 5.3. Subject A1: mean optical density profile (± SD; *red filled circle and whiskers*) of selected segments of the temporal arterioles and venules and the respective OS calculations (and 95% confidence interval). Locations of the analysis (red and orange lines) are shown in the grayscale image. Abnormal optical density profiles are indicated by *red borders*.

Location		1st degree vessels	Other vessel segments and macular branches
Arterioles	Superotemporal	Macular branch selected: 1st degree arteriole too close to venule for accurate oxygen saturation **Oxygen saturation: 126.88%** **95% confidence interval: 104.64% – 149.12%** 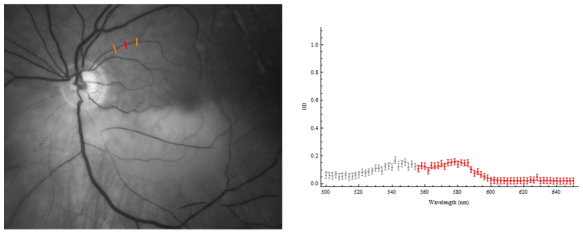	**Oxygen saturation: 84.95%** **95% confidence interval: 71.82% – 98.07%** 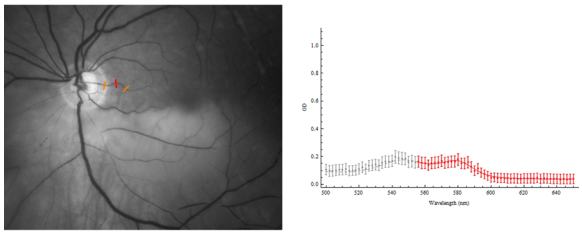
	Inferotemporal	**Oxygen saturation: 47.99%** **95% confidence interval: 24.% – 71.98%** 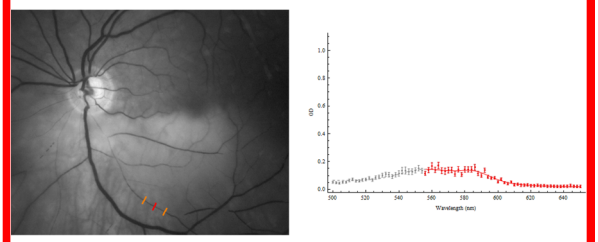	**Oxygen saturation: 34.07%** **95% confidence interval: 17.58% – 50.56%** 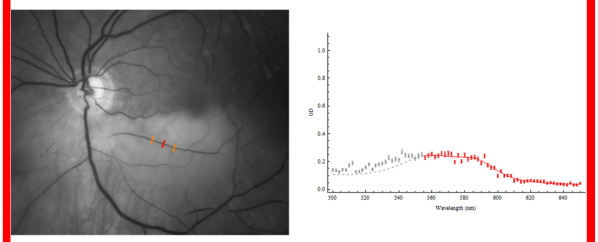
Venules	Superotemporal	**Oxygen saturation: 50.95%** **95% confidence interval: 31.29% – 70.6%** 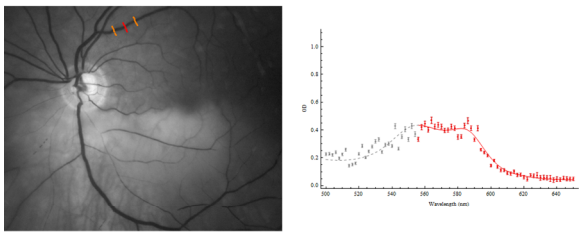	**Oxygen saturation: 68.86%** **95% confidence interval: 55.7% – 82.01%** 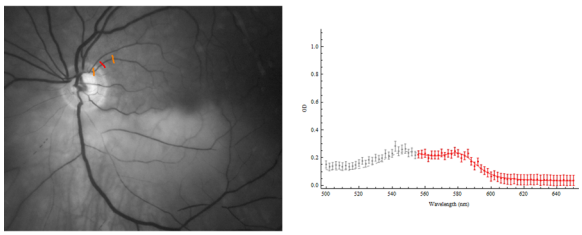
	Inferotemporal	**Oxygen saturation: 56.67%** **95% confidence interval: 33.63% – 79.72%** 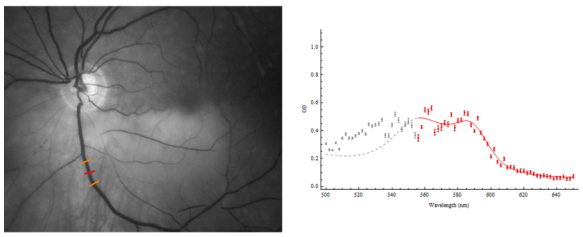	**Oxygen saturation: 66.75%** **95% confidence interval: 53.83% – 79.66%** 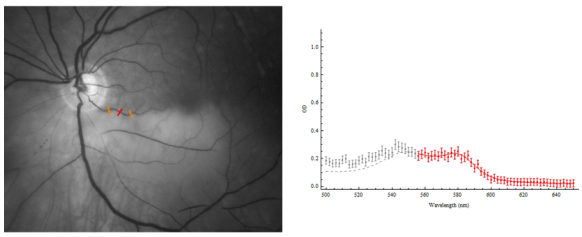

Figure 5.4. Subject A1: pseudocolour oximetry maps of the retinal arterioles (*left images*) and retinal venules (*right images*). A colour scale of the quantitative OS values is shown to the left of the images.

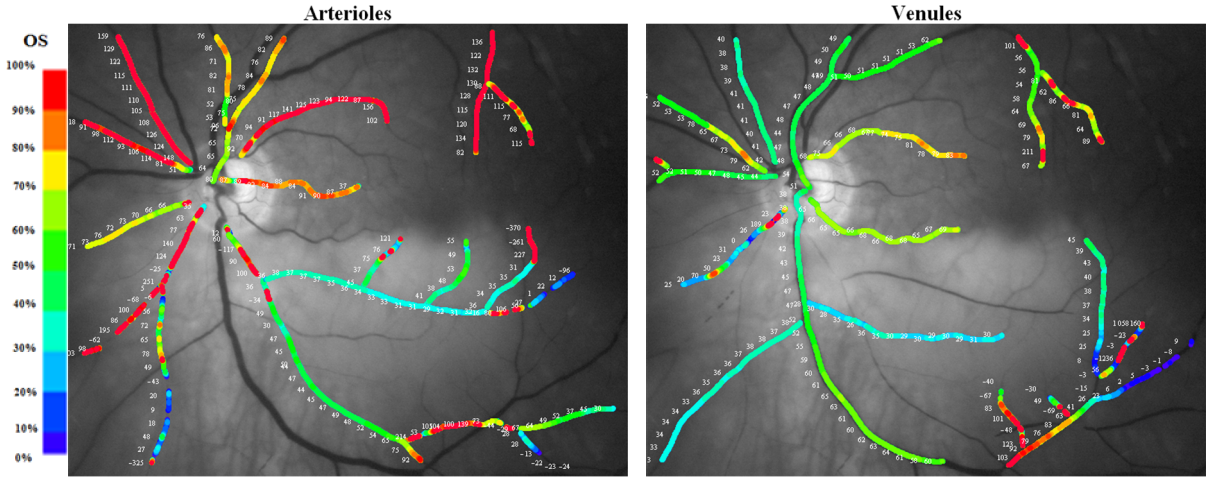

Figure 5.5. A colour image of the left fundus of subject A2. A 69 year old female with a 2 day history of a left central retinal artery occlusion (BCVA: hand movements at 1 metre).

Figure 5.6. Subject A2: dark calibrated spectral images of the left retina at 9 selected wavelengths (560, 570, 580, 590, 600, 610, 620 and 630 nm). First degree retinal arterioles and venules are indicated by *red* and *blue arrow heads* respectively. Abnormal appearances of the retinal arterioles and venules related to the OS are indicated by the *yellow* and *green arrow heads* respectively.

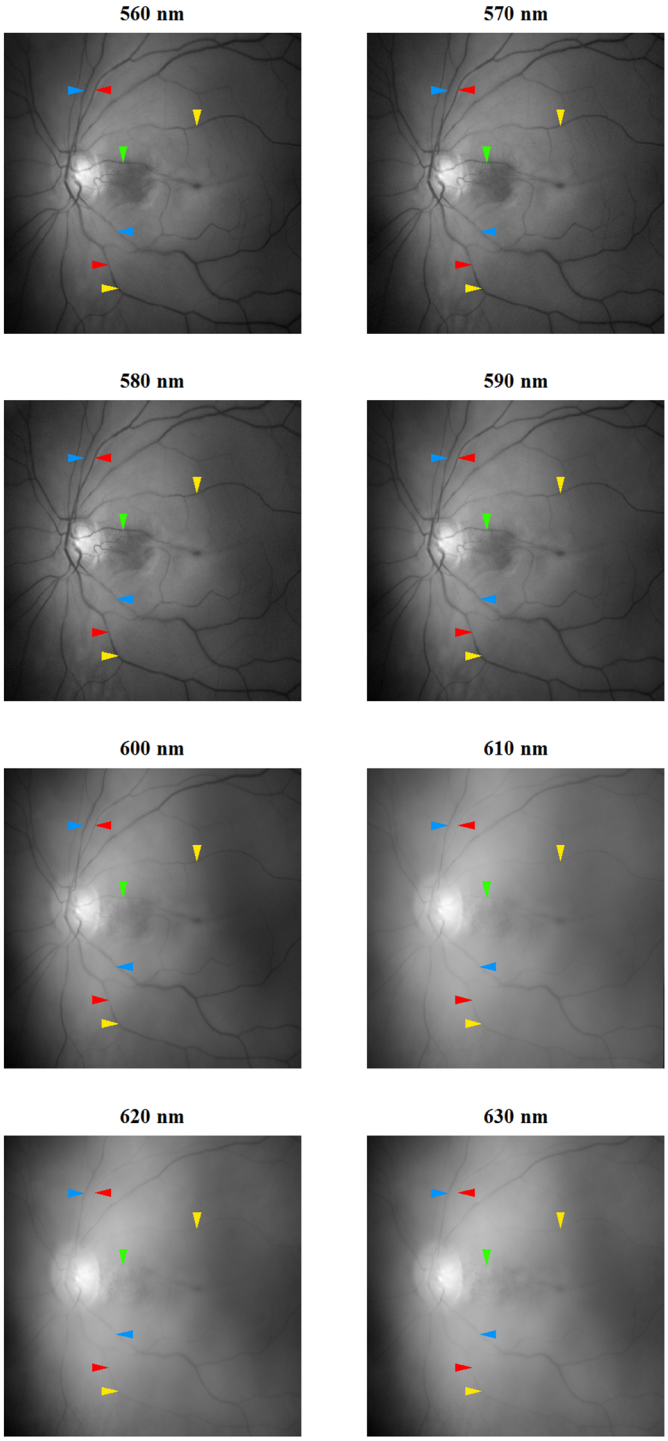

Figure 5.7. Subject A2: mean optical density profile (± SD; *red filled circle and whiskers*) of selected segments of the temporal arterioles and venules and the respective OS calculations (and 95% confidence interval). Locations of the analysis (red and orange lines) are shown in the grayscale image. Abnormal optical density profiles are indicated by *red borders*.

Location		1st degree vessels	Other vessel segments and macular branches
Arterioles	Superotemporal	Oxygen saturation: 103.27% 95% confidence interval: 80.84% – 125.71%	Oxygen saturation: 53.53% 95% confidence interval: 33.54% – 73.52%
	Inferotemporal	Oxygen saturation: 88.64% 95% confidence interval: 72.53% – 104.74%	Oxygen saturation: 30.72% 95% confidence interval: 16.31% – 45.13%
Venules	Superotemporal	Oxygen saturation: 21.22% 95% confidence interval: 8.86% – 33.57%	Oxygen saturation: 87.17% 95% confidence interval: 70.36% – 103.98%
	Inferotemporal	Oxygen saturation: 32.99% 95% confidence interval: 24.54% – 41.45%	Oxygen saturation: 69.55% 95% confidence interval: 54.08% – 85.01%

Figure 5.8. Subject A2: pseudocolour oximetry maps of the retinal arterioles (*left images*) and retinal venules (*right images*). A colour scale of the quantitative OS values is shown to the left of the images.

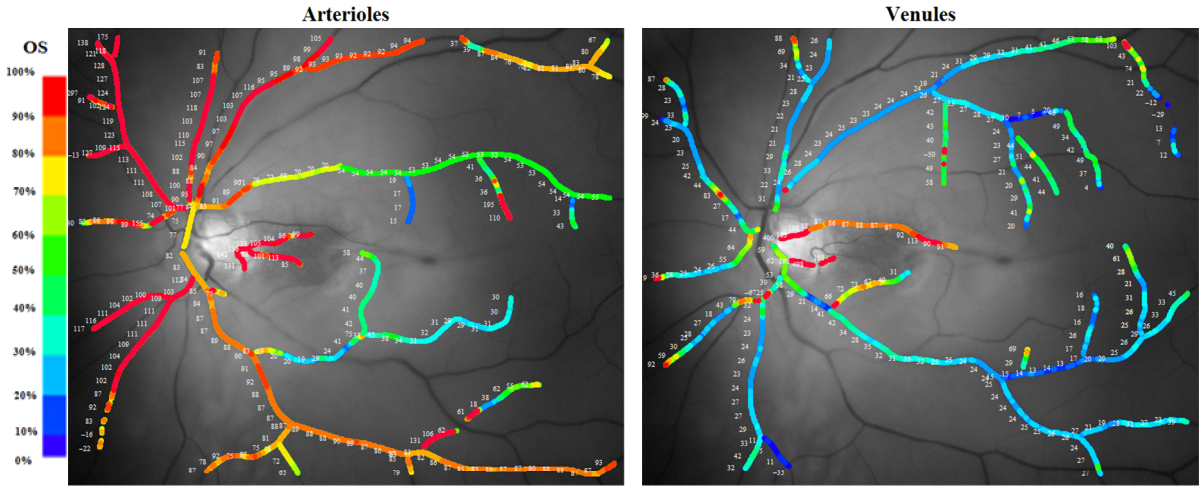

5.3.2. Oxygen Saturation of the Retinal vasculature in Patients with Retinal Vein Occlusion: Observational Features, Optical Density Profile Analysis and Quantitative Oximetry of the Retinal Vasculature.

Figures 5.9 to 5.28 present the observational features of the retinal vasculature, mean optical density profiles of selected segments of the retinal vessels and the respective OS calculations in 4 representative patients with retinal vein occlusion. (See Appendix 6 for the oximetry results of the remaining 5 patients). Pseudocolour oximetry maps of the retinal vasculature are also illustrated. No obvious abnormality of the oxygen distribution in the retinal arterioles is evident in patients with ether ischaemic or non-ischaemic retinal vein occlusion.

In patients with ischaemic retinal vein occlusion (subjects V1-V3), localized segments of the venules can be observed to have abnormal spectral characteristics indicating higher than normal venous oxygenation. These abnormal venules are commonly located in the ischaemic region of the retina (Figures 5.11, 5.16 and 5.21; *green arrow heads*). Optical density profiles and OS calculations of selected segments of the retinal venules confirm the presence of higher than normal venous oxygen saturations in 5 of the 6 patients with ischaemic retinal vein occlusion. Further, illustrations of abnormally high OS of the retinal

venules in regions of the afflicted retina are shown in the pseudocolour oximetry maps of the retinal vasculature (Figures 5.12, 5.17 and 5.22).

Figure 5.26 illustrates a selection of dark calibrated spectral images of the retina, the mean optical density profiles of selected segments of the retinal vessels and the respective OS calculations in a representative patient with a non-ischaemic retinal vein occlusion (subject V4). No abnormalities of the venular oxygen saturation could be identified from observing the retinal vasculature, inspecting the optical density profiles and pseudocolour oximetry maps of the retinal vasculature. This finding was seen in 2 of the 3 patients with non-ischaemic retinal vein occlusion.

Figure 5.9. A colour image of the left fundus of subject V1. A 46 year old female with a 9 month history of a left ischaemic superotemporal branch retinal vein occlusion (BCVA: 6/12).

Figure 5.10. Subject V1: fluorescein angiograms of the left fundus. There is a region of reduced background fluorescence (*yellow arrow head*; capillary "non-perfusion") associated with hyperfluorescent segments of the superotemporal vessels (*red arrow head*; vessel wall staining).

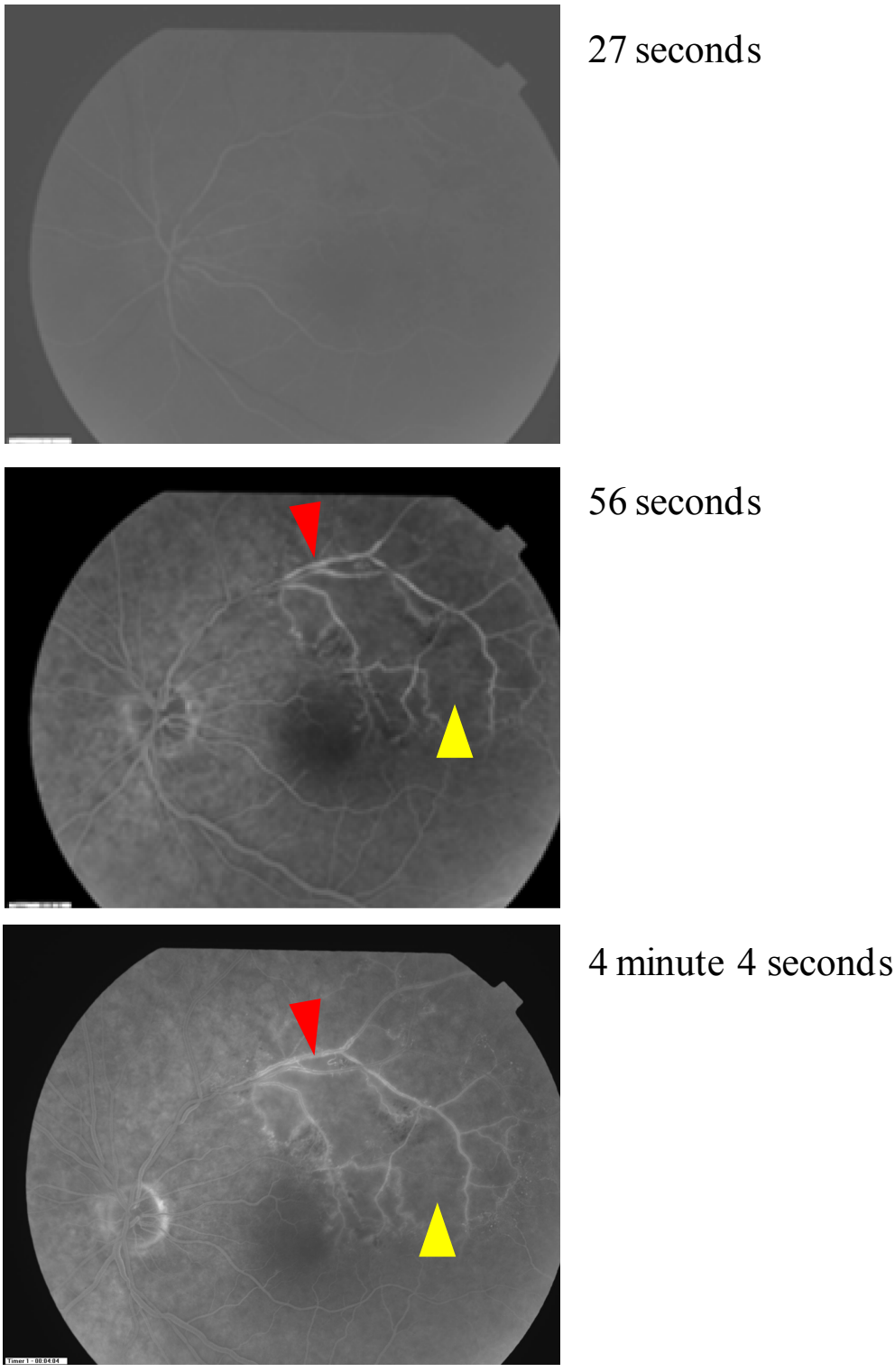

Figure 5.11. Subject V1: dark calibrated spectral images of the left retina at 9 selected wavelengths (560, 570, 580, 590, 600, 610, 620 and 630 nm). First degree retinal arterioles and venules are indicated by *red* and *blue arrow heads* respectively. Abnormal appearances of the retinal venules relating to the OS are indicated by the *green arrow heads*. These venules appear less optically dense than in normal eyes at wavelengths greater than 600 nm indicating a higher OS.

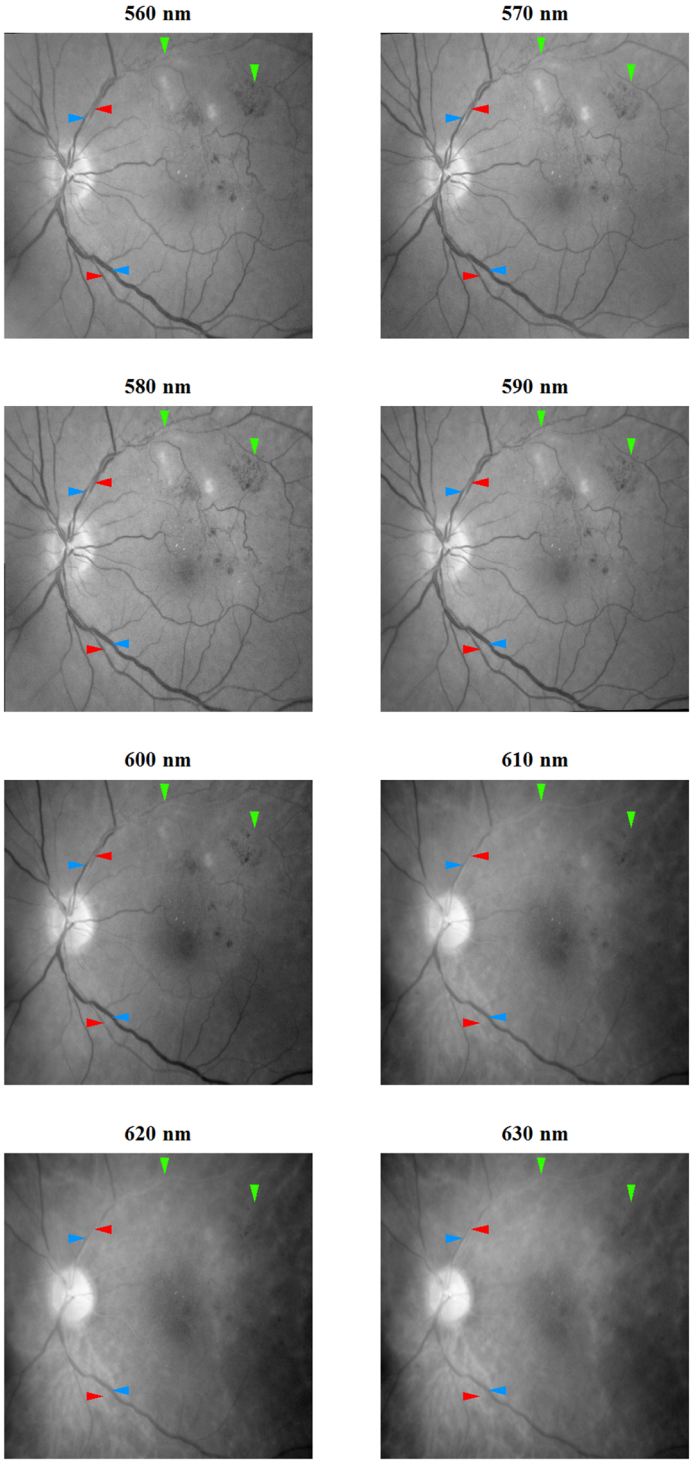

Figure 5.12. Subject V1: mean optical density profile (± SD; *red filled circle* and *whiskers*) of selected segments of the temporal arterioles and venules and the respective OS calculations (and 95% confidence interval). The locations of the optical density analysis (red and orange lines) are shown in the grayscale image. Abnormal optical density profiles are indicated by *red borders*.

Location		1st degree vessels	Macular branches
Arterioles	Superotemporal	Oxygen saturation: 204.99% 95% confidence interval: 176.56% – 233.42%	Oxygen saturation: 192.31% 95% confidence interval: 163.3% – 221.31%
	Inferotemporal	Oxygen saturation: 178.71% 95% confidence interval: 157.58% – 199.84%	Oxygen saturation: 156.19% 95% confidence interval: 140.11% – 172.26%
Venules	Superotemporal	Oxygen saturation: 163.57% 95% confidence interval: 121.45% – 205.68%	Oxygen saturation: 200.97% 95% confidence interval: 178.1% – 223.85%
	Inferotemporal	Oxygen saturation: 34.91% 95% confidence interval: 19.91% – 49.91%	Oxygen saturation: 84.64% 95% confidence interval: 71.46% – 97.82%

Figrure 5.13. Subject V1: pseudocolour oximetry maps of the retinal arterioles (*left images*) and retinal venules (*right images*). There is high venous oxygenation in the superotemporal venules. A colour scale of the quantitative OS values is shown to the left of the images.

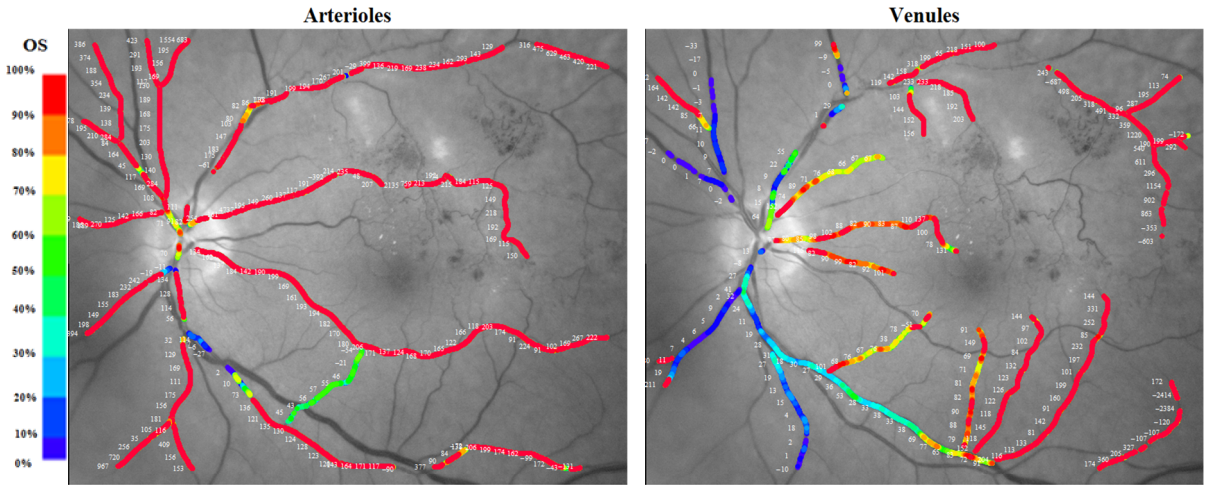

Figure 5.14. A colour image of the left fundus of subject V2. A 53 year old female with a 3 month history of a left ischaemic superotemporal branch retinal vein occlusion (BCVA: 6/12).

Figure 5.15. Subject V2: fluorescein angiograms of the left fundus. There is a region of reduced background fluorescence (*yellow arrow head*; capillary "non-perfusion") associated with hyperfluorescent segments of the superotemporal vessels (*red arrow head*; vessel wall staining).

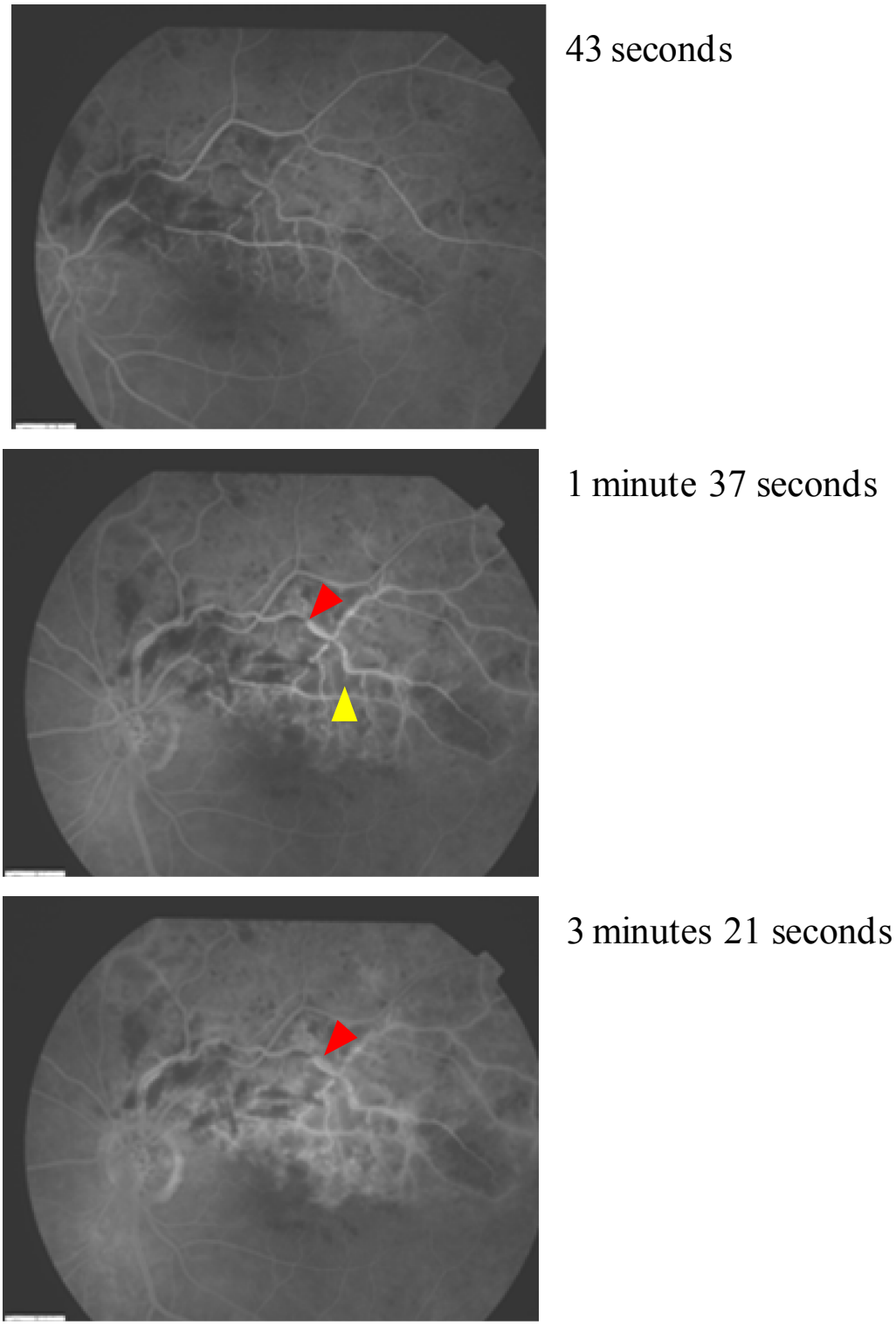

Figure 5.16. Subject V2: dark calibrated spectral images of the left retina at 9 selected wavelengths (560, 570, 580, 590, 600, 610, 620 and 630 nm). First degree retinal arterioles and venules are indicated by *red* and *blue arrow heads* respectively. Abnormal appearances of the retinal venules relating to the OS are indicated by the *green arrow head*. These venules appear less optically dense than in normal eyes at wavelengths greater than 600 nm indicating a higher OS.

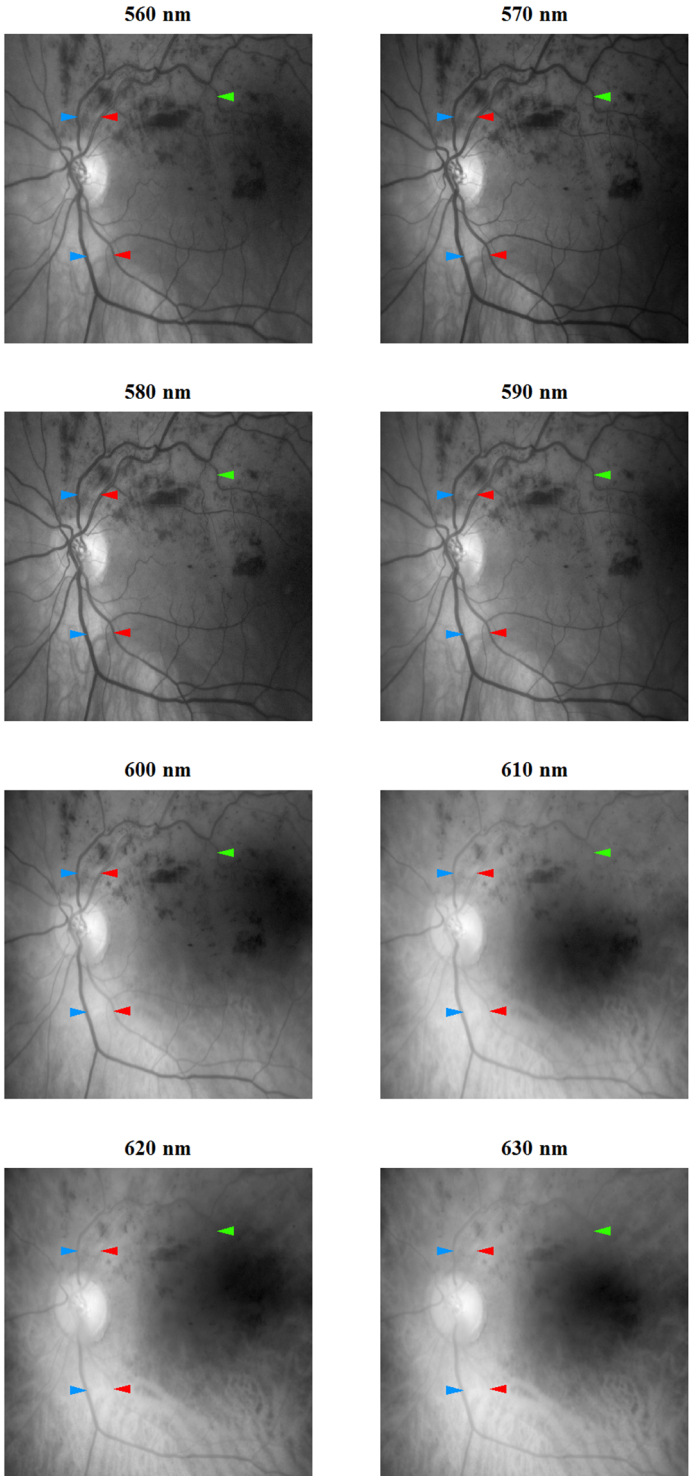

Figure 5.17. Subject V2: mean optical density profile (± SD; *red filled circle* and *whiskers*) of selected segments of the temporal arterioles and venules and the respective OS calculations (and 95% confidence interval). Locations of the analysis (red and orange lines) are shown in the grayscale image. Abnormal optical density profiles are indicated by *red borders*.

Location		1st degree vessels	Macular branches
Arterioles	Superotemporal	Oxygen saturation: 103.82% 95% confidence interval: 75.71% – 131.93% 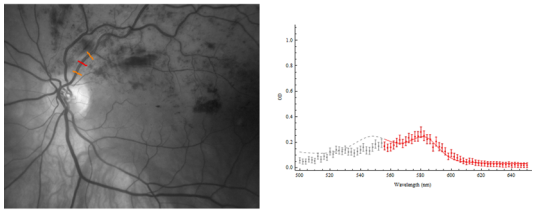	Oxygen saturation: 149.6% 95% confidence interval: 128.77% – 170.43% 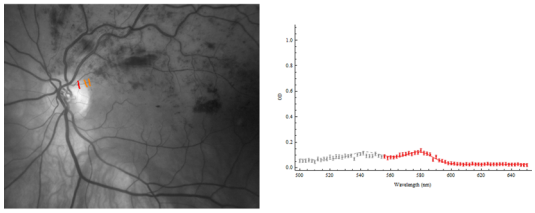
	Inferotemporal	Oxygen saturation: 86.85% 95% confidence interval: 69.09% – 104.62% 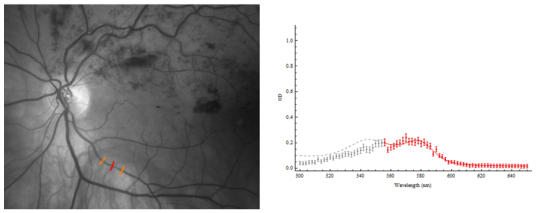	Oxygen saturation: 112.35% 95% confidence interval: 92.03% – 132.67% 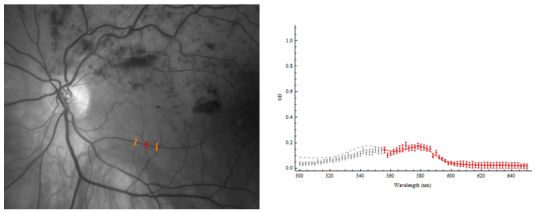
Venules	Superotemporal	Oxygen saturation: −13.24% 95% confidence interval: −28.16% – 1.68% 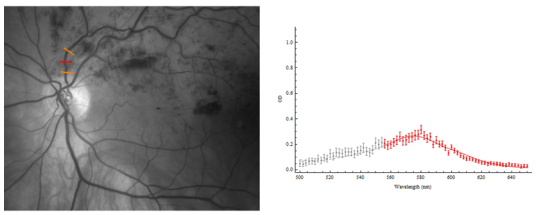	Oxygen saturation: 97.54% 95% confidence interval: 73.33% – 121.74% 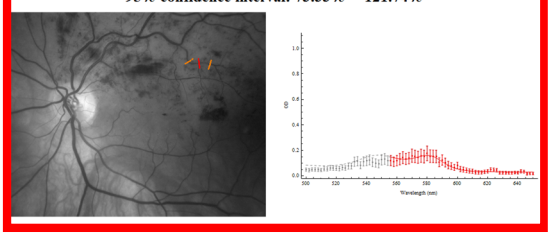
	Inferotemporal	Oxygen saturation: 5.48% 95% confidence interval: −6.52% – 17.47% 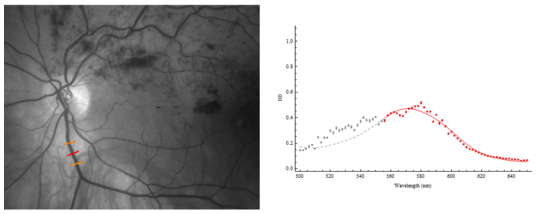	Oxygen saturation: 91.79% 95% confidence interval: 73.4% – 110.18% 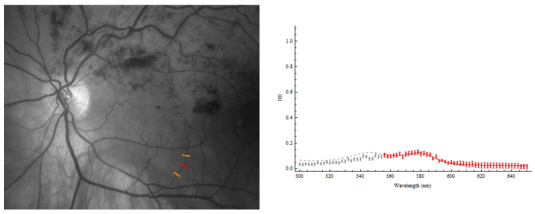

Figure 5.18. Subject V2: pseudocolour oximetry maps of the retinal arterioles (*left images*) and retinal venules (*right images*). There is high venous oxygenation in segments of the superotemporal venules. A colour scale of the quantitative OS values is shown to the left of the images.

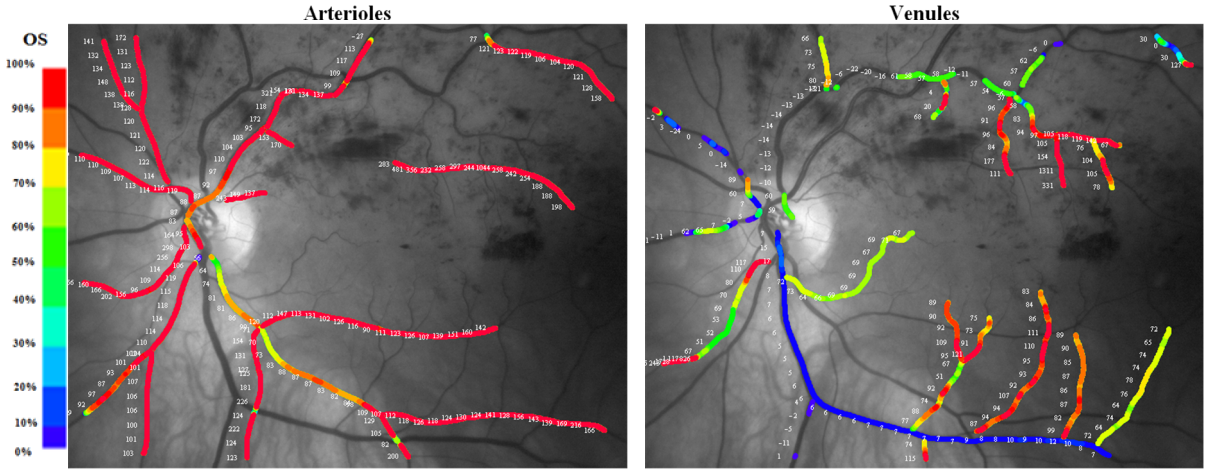

Figure 5.19. A colour image of the left fundus of subject V3. A a 61 year old male with a 36 month history of a left ischaemic superotemporal branch retinal vein occlusion with neovascularization of the temporal retina (BCVA: 6/24).

Figure 5.20. Subject V3: fluorescein angiograms of the left fundus. There are retinal new vessels (*red arrow heads*; vessel wall staining) and laser scars (*light blue arrow head*; capillary "non-perfusion").

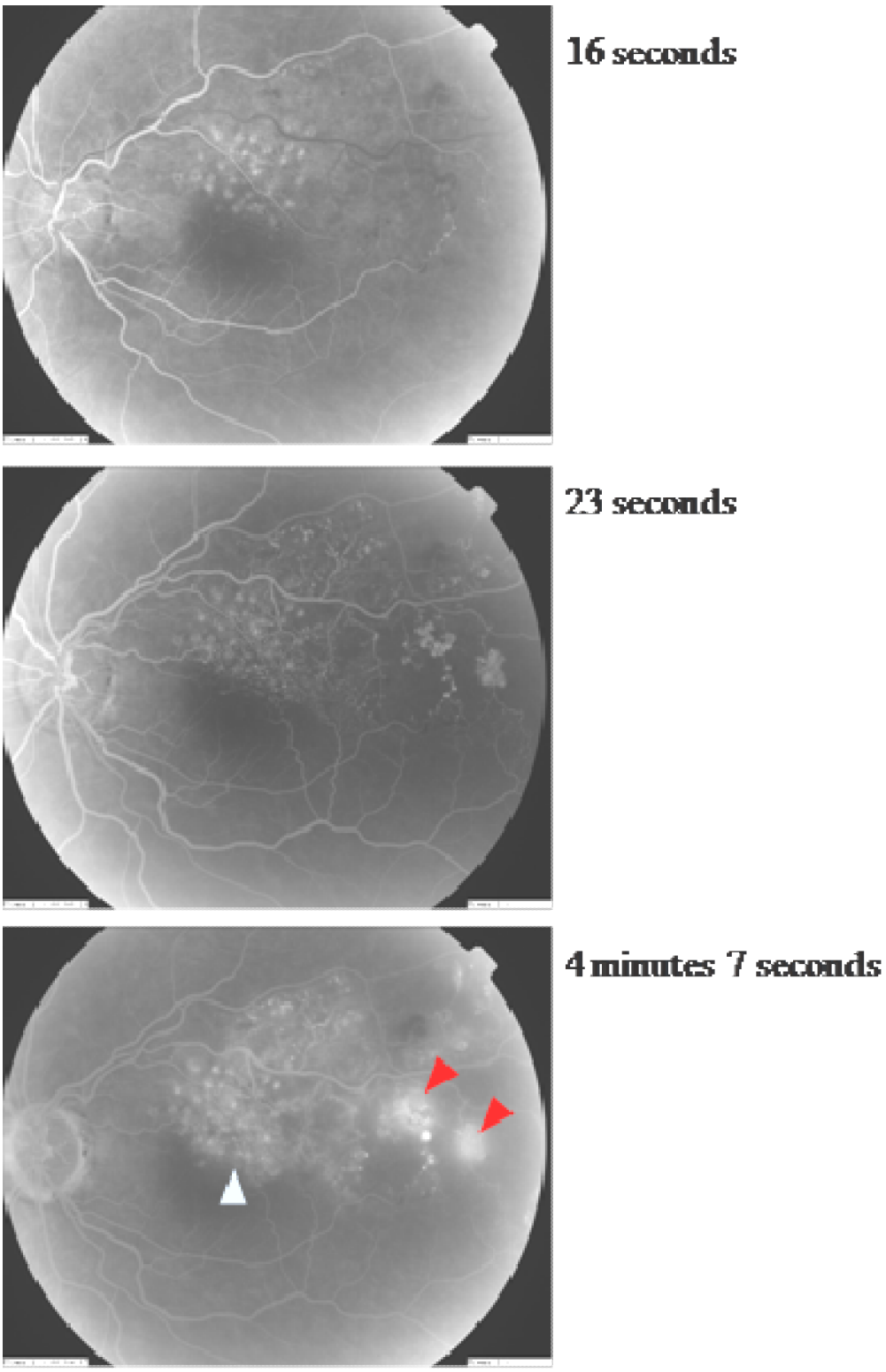

Figure 5.21. Subject V3: dark calibrated spectral images of the left retina at 9 selected wavelengths (560, 570, 580, 590, 600, 610, 620 and 630 nm). First degree retinal arterioles and venules are indicated by *red* and *blue arrow heads* respectively. Abnormal appearances of the retinal venules relating to the OS are indicated by the *green arrow head*. Theses venules appear less optically dense than in normal eyes at wavelengths greater than 600 nm indicating a higher OS.

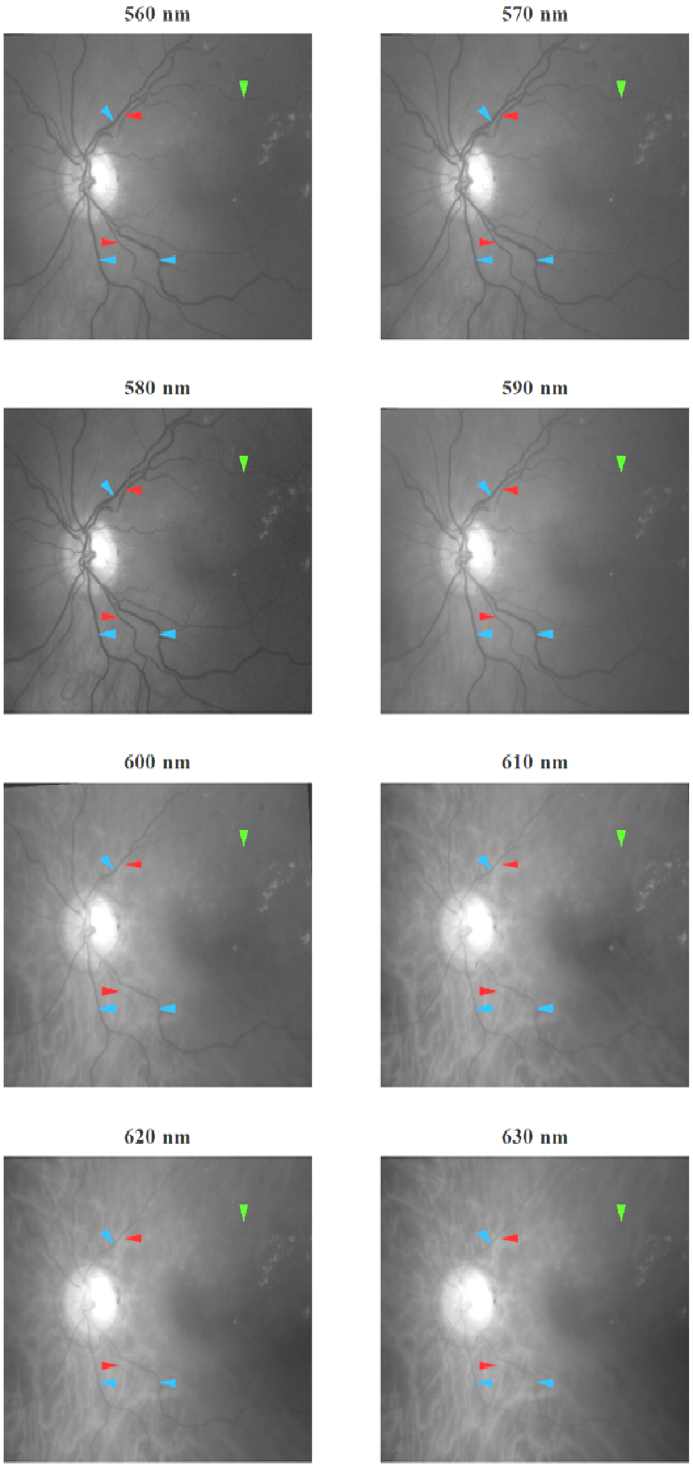

Figure 5.22. Subject V3: mean optical density profile (± SD; *red filled circle* and *whiskers*) of selected segments of the temporal arterioles and venules and the respective OS calculations (and 95% confidence interval). Locations of the analysis (red and orange lines) are shown in the grayscale image. Abnormal optical density profiles are indicated by *red borders*.

Location		1st degree vessels	Other vessel segments and macular branches
Arterioles	Superotemporal	Oxygen saturation: 192.71% 95% confidence interval: 165.82% – 219.59%	Oxygen saturation: 161.15% 95% confidence interval: 141.45% – 180.85%
	Inferotemporal	Oxygen saturation: 152.78% 95% confidence interval: 137.24% – 168.33%	Oxygen saturation: 153.03% 95% confidence interval: 130.99% – 175.06%
Venules	Superotemporal	Oxygen saturation: 73.37% 95% confidence interval: 59.41% – 87.33%	Oxygen saturation: 155.6% 95% confidence interval: 131.33% – 179.87%
	Inferotemporal	Oxygen saturation: 48.13% 95% confidence interval: 33.48% – 62.78%	Oxygen saturation: 69.16% 95% confidence interval: 50.82% – 87.49%

Figure 5.23. Subject V3: pseudocolour oximetry maps of the retinal arterioles (*left images*) and retinal venules (*right images*). There is high venous oxygenation in the superotemporal venules. A colour scale of the quantitative OS values is shown to the left of the images.

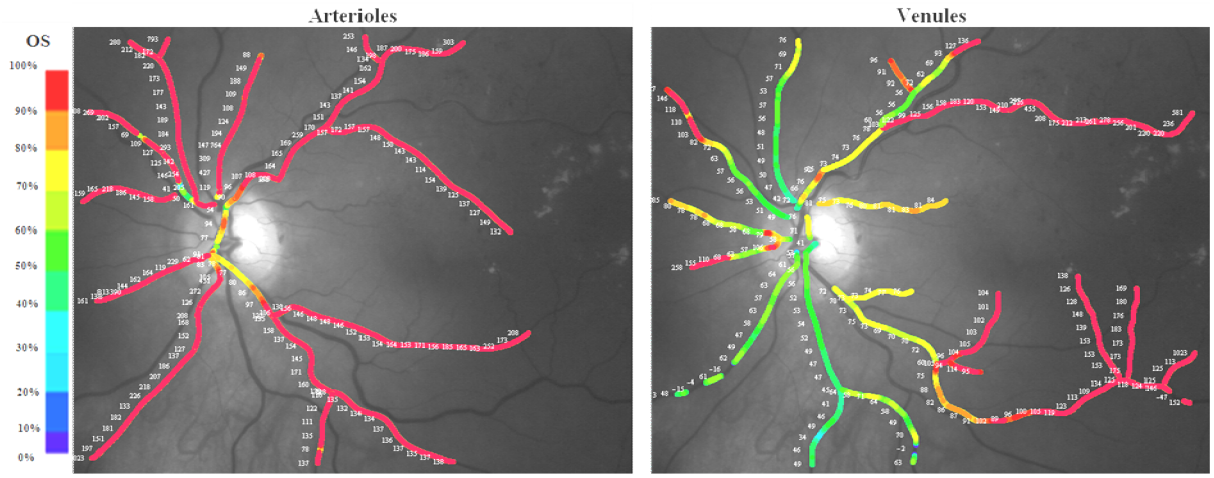

Figure 5.24. A colour image of the right fundus of subject V4. A 68 year old male with a 10 month history of a right non-ischaemic retinal vein occlusion (BCVA: 6/9).

Figure 5.25. Subject V4: Fluorescein angiograms of the right fundus.

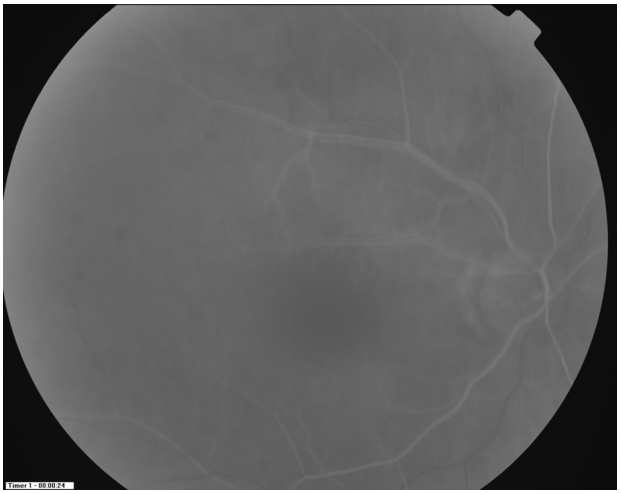

24 seconds

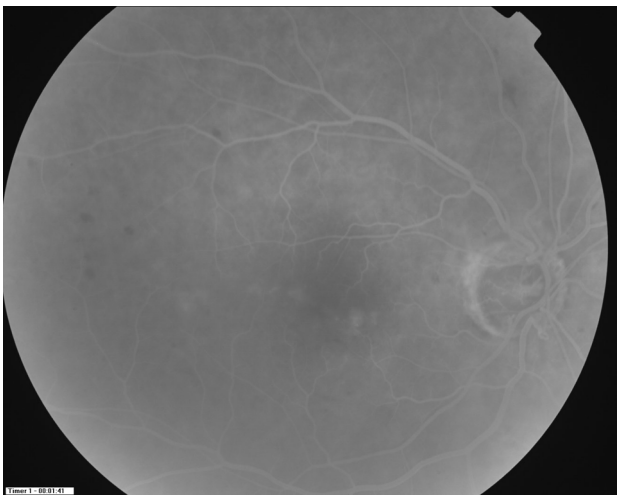

1 minute 41 seconds

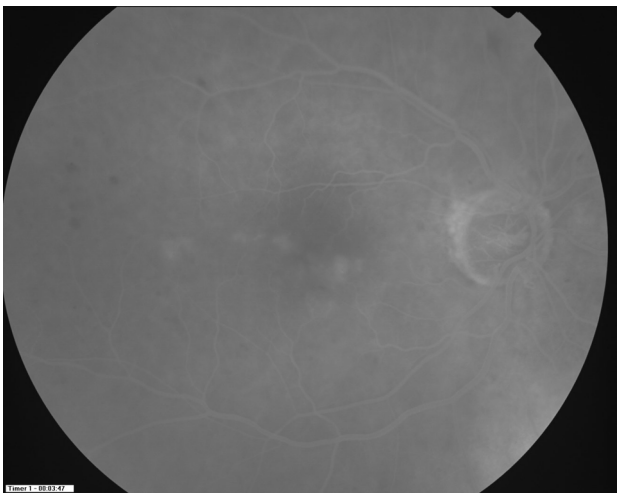

3 minutes 47 seconds

Figure 5.26. Subject V4: dark calibrated spectral images of the left retina at 9 selected wavelengths (560, 570, 580, 590, 600, 610, 620 and 630 nm). First degree retinal arterioles and venules are indicated by *red* and *blue arrow heads* respectively. Abnormal appearances of the retinal venules relating to the OS are not seen.

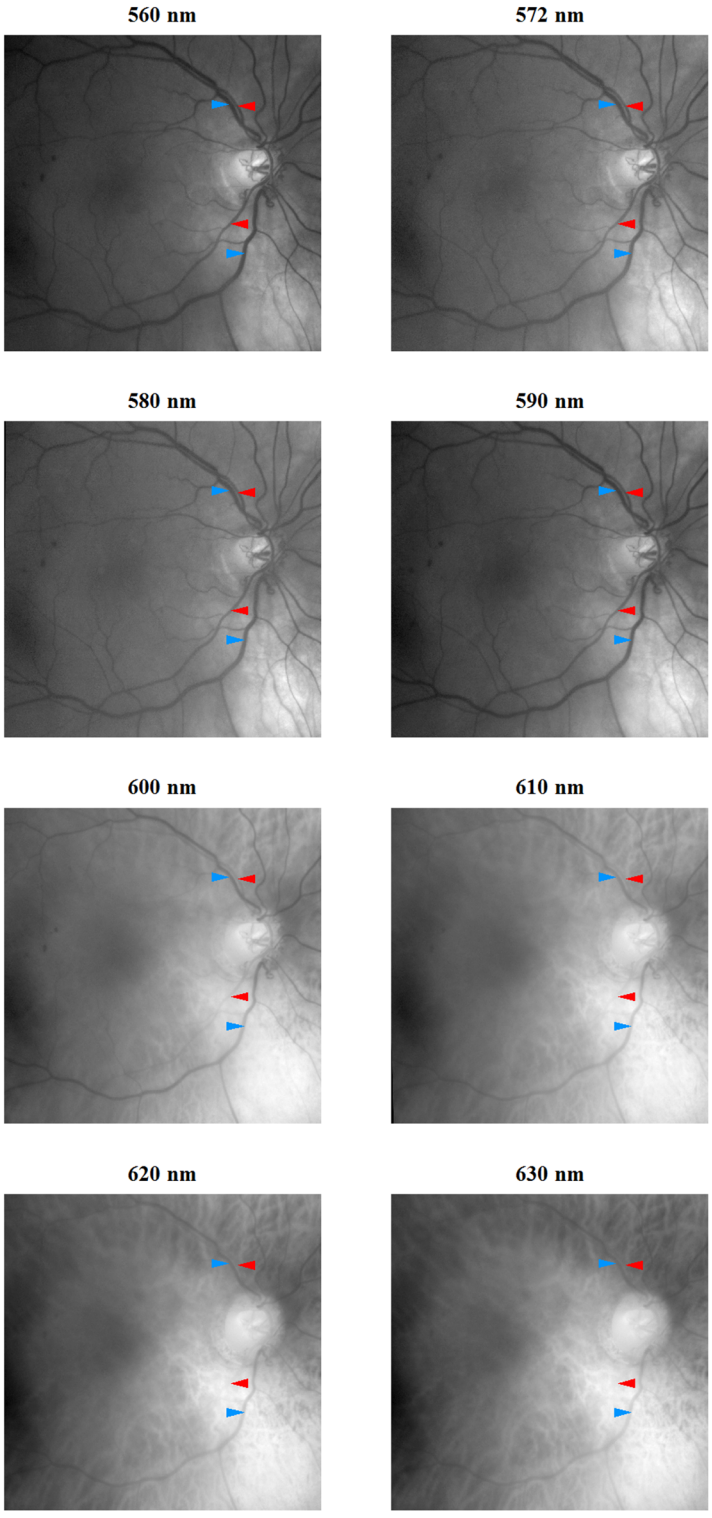

Figure 5.27. Subject V4: mean optical density profile (± SD; *red filled circle* and *whiskers*) of selected segments of the temporal arterioles and venules and the respective OS calculations (and 95% confidence interval). Locations of the analysis (red and orange lines) are shown in the grayscale image.

Location		1st degree vessels	
Arterioles	Superotemporal	Oxygen saturation: 107.79% 95% confidence interval: 90.07% – 125.51%	
	Inferotemporal	Oxygen saturation: 84.82% 95% confidence interval: 68.71% – 100.93%	
Venules	Superotemporal	Oxygen saturation: 15.3% 95% confidence interval: 3.73% – 26.88%	Oxygen saturation: 52.18% 95% confidence interval: 26.11% – 78.26%
	Inferotemporal	Oxygen saturation: 21.04% 95% confidence interval: 3.23% – 38.85%	Oxygen saturation: 83.96% 95% confidence interval: 43.07% – 124.86%

Figure 5.28. Subject V4: pseudocolour oximetry maps of the retinal arterioles (*left images*) and retinal venules (*right images*). A colour scale of the quantitative OS values is shown to the left of the images.

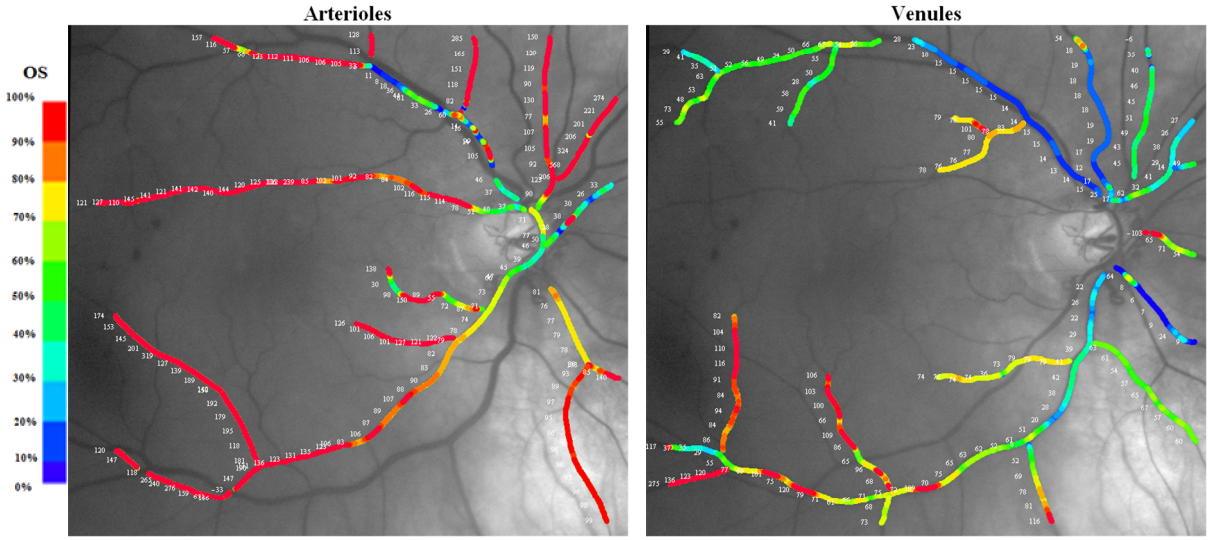

5.3.3. Relationship Between the Oxygen Saturation in Eyes with Ischaemic Retinal Vein Occlusion and LOCS III Grading Scores.

The multiple linear regression model predicting the OS of the temporal retinal vessels in eyes with ischaemic RVO using the LOCS III scores as independent variables did not produce a significant model ($F = 0.156$, $P = 0.857$, adjusted R squared = -0.110). Posterior subcapsular cataract grade were constant in eyes with ischaemic RVO and were not used in the analysis. Nuclear opalescence scores were excluded due to multicollinearity. The variance inflation factor and Durbin-Watson statistic of the final model did not indicate the presence of multicollinearity. The influence of the nuclear colour cataract and cortical grading scores were not statistically significant for temporal arteriolar OS in eyes with ischaemic RVO ($\beta = 0.109$, $P = 0.693$; $\beta = -0.135$, $P = 0.625$ respectively).

5.3.4. Comparison of the Oxygen Saturation between Normal Subjects and Patients with Ischaemic Retinal Vein Occlusion.

The mean (± SD) OS of the temporal retinal arterioles and venules in patients with ischaemic retinal vein occlusion were 103.0% (± 20%) and 37.9% (± 21.0%) respectively. Comparisons of the OS between normal subjects and patients with ischaemic retinal vein occlusion are shown in Figures 5.29 and 5.30 respectively. No significant differences were found in the OS of the temporal arterioles and venules between the patients with ischaemic retinal vein occlusion and normal subjects ($P = 0.54$ and 0.30 respectively; two-tailed, unpaired *t*-test with Welch's correction and Mann-Whitney test respectively).

Figure 5.29: A box-and-whisker plot of the oxygen saturation (OS) of the temporal (superotemporal and inferotemporal) retinal arterioles in normal subjects and patients with ischaemic retinal vein occlusion. The plot shows the median, the interquartile range, 95% central range and the minimum and maximum values.

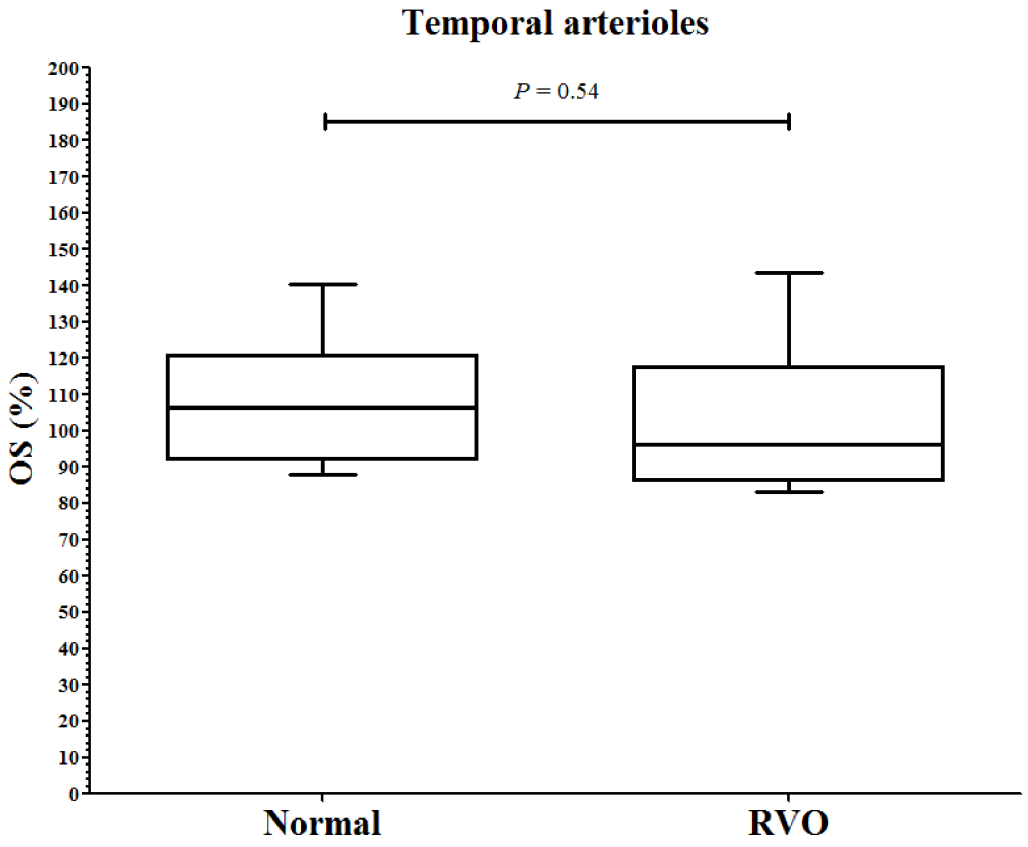

Figure 5.30: A box-and-whisker plot of the oxygen saturation (OS) of the temporal (superotemporal and inferotemporal) retinal venules in normal subjects and patients with ischaemic retinal vein occlusion. The plot shows the median, the interquartile range, 95% central range and the minimum and maximum values.

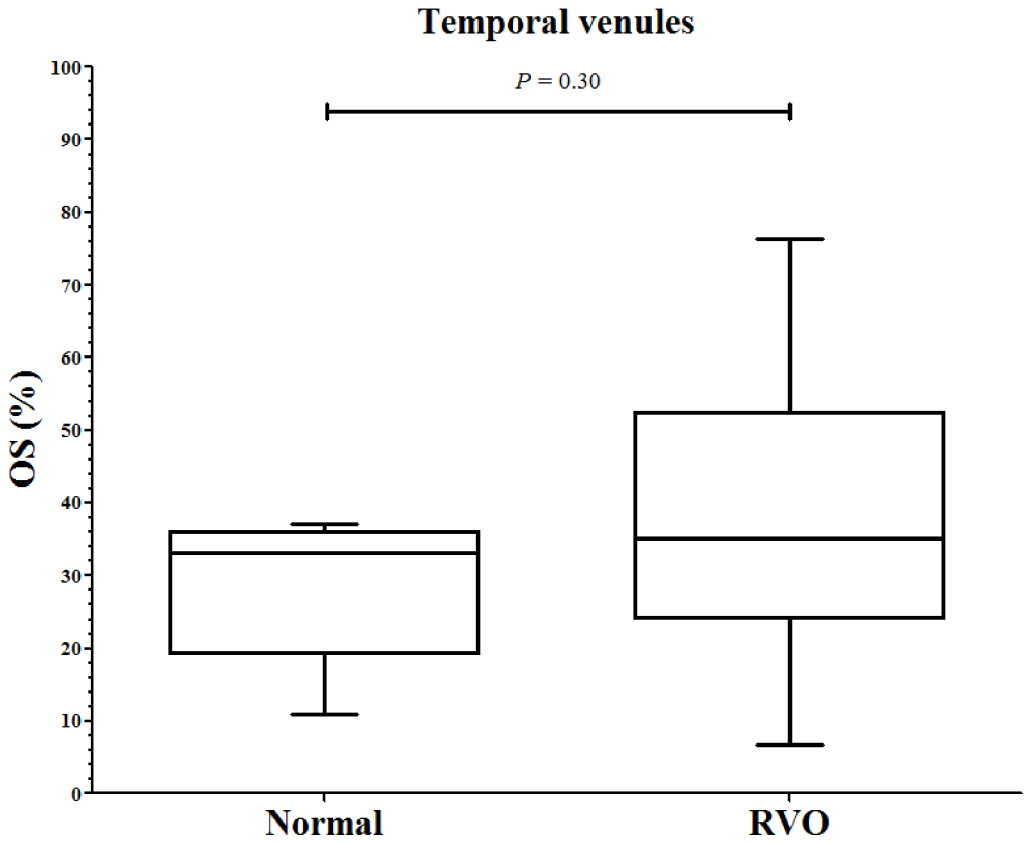

5.4. Discussion.

In this study, we have recruited patients with retinovascular pathologies to determine whether changes in the OS of the retinal vasculature can be detected using the hyperspectral fundus camera and our retinal oximetry techniques. These conditions are thought to result in damage to the inner retinal layers as a result of the vascular insufficiency (Frangieh et al., 1982; Green et al., 1981; Hayreh et al., 2004). This study has shown that OS abnormalities of the retinal vasculature can be detected in these patients from the spectral retinal images acquired by hyperspectral fundus camera. Three techniques have been described in analyzing the images to detect these changes. The first relies on observations of the spectral appearances of the retinal arterioles and venules in the dark calibrated images at different

wavelengths. In particular, arterioles with low OS appear optically more dense at wavelengths greater than 590 nm and venules with high OS appear optically less dense at wavelengths greater than 600 nm. The second technique involves inspecting the shape of the optical density profile from segments of the retinal vasculature. The third technique relies on the oximetry model to calculate the OS along the retinal vasculature. The observational features of the retinal vessels correspond (in most cases) with the calculated optical density profiles and OS. However, caution is required when interpreting the oximetry results because of the small numbers of patients included in this study.

5.4.1. Oxygen saturation in Retinal Artery Occlusion.

The patients with retinal artery occlusion presented in this study were shown to have abnormal segments of arteriolar and venular OS. Low calculated OS of selected arterioles and high calculated OS of selected venules in the region of the affected retina were validated by inspecting the shape of the optical density profiles.

The low OS of the retinal arteriole (arteriolar hypoxaemia) seen in subjects A1 and A2 (Figures 5.2 to 5.4 and 5.6 to 5.8 respectively) was confirmed by the similar appearance of the optical density profiles to that seen in normal retinal venules (single maxima). This finding of arterial hypoxaemia is supported by a recent study by Gehlert et al. (2010) who, using a two wavelength retinal oximeter, reported a mean arteriolar OS of 73% in affected arterioles of 10 patients with branch retinal artery occlusion. The lower OS of the arterioles in patients with retinal artery occlusion could be explained by the reduced blood flow resulting in the increased diffusion of oxygen from the slow flowing blood into the vitreous and surrounding retina. Alternatively, it could also reflect the consumption of oxygen in the slow flowing blood by the cells that comprise the arteriolar wall (such as the smooth muscles).

High OS of the small number of retinal venules (venular hyperoxaemia) were seen in subjects A1 and A2 (Figures 5.2 to 5.4 and 5.6 to 5.8 respectively). In subject A3 (see Appendix 5), this was confirmed by the similar appearance of its optical density profile to that seen in normal retinal arterioles (two maxima). However, this was less convincing in subject A1 as the optical density profiles were considerably “noisy” and errors in the OS calculation could not be excluded. Reduced metabolic consumption of oxygen due to dysfunction of the inner retina could explain the increase in the OS of the venules which may be collecting “unused” oxygenated blood. To date, no studies have reported high venular OS in retinal artery occlusion.

An interesting feature of the pseudocolour oximetry maps of the retinal vasculature in these patients with retinal arteriolar occlusion was the suggestion of a lower OS in the macular venules corresponding to the regions of the retina affected by the artery occlusion. In contrast, the OS of the macular venules in normal subjects were shown to be typically higher than that of the 1st and 2nd degree venules (ranging from 47% - 98%; see Chapter 4). Tissue hypoxia in laser induced occlusion of the retinal arteries in rats have been demonstrated using oxygen sensitive microelectrodes by Yu et al. (2007) The low OS in the macular branches of the venules could reflect the collection of hypoxaemic blood from the affected arterioles and regions of anoxic/hypoxic retinal tissues. Further research is required to confirm this observation to clarify the relationship between retinal blood flow, hypoxaemia and tissue hypoxia which is currently not well understood.

5.4.2. Oxygen saturation in Retinal Vein Occlusion.

The patients with ischaemic retinal vein occlusion presented in this study commonly had higher than normal venular OS in the venules supplying the regions of the "ischaemic" retina. In patients with non-ischaemic retinal vein occlusion this feature was not observed. No obvious oximetric abnormalities of the retinal arterioles were seen in patients with ischaemic or non-ischaemic retinal vein occlusion. The higher than normal venular OS in patients with retinal vein occlusion could reflect the reduced metabolic consumption of the oxygen supplied to the dysfunctional inner retina via the patent inner retinal arterial circulation or the choroid. However, this finding is not supported by previous studies. Hardarson and Stefánsson (2010), using a two wavelength retinal oximeter, reported lower OS in the retinal venules of eyes (n = 8) affected by central retinal vein occlusion (mean ± SD; 49% ± 12%) compared to the contralateral unaffected eye (65% ± 6%). Arteriolar OS was unaffected. Yoneya et al. (2002) using a Fourier transform-based spectral retinal imaging system demonstrated a correlation between the fluorescein angiogram and a decrease in retinal tissue oxygenation in patients (n =10) with ischaemic central retinal vein occlusion. In the latter study, it remains unclear as to the relationship between tissue hypoxia and intravascular oxygen saturation.

Multiple linear regression analysis demonstrated a non-significant relationship between the OS of the temporal vessels in eyes with ischaemic RVO and LOCS III grading scores suggesting that the influence of the lens status on the oximetry values was not an important factor.

A comparison of the OS of the temporal arterioles and venules between normal subjects and subjects with ischaemic retinal vein occlusion showed no significant differences between the two groups. This could be due to the lack of power of the statistical analysis as a result of the small numbers of subjects included in the study. Additionally, the nature of the analysis used calculated mean oxygen saturations of points along the temporal arterioles and venules (superotemporal and inferotemporal) at pre-defined distances from the optic disc margin of up to 2 disc diameters from the disc margin. Abnormalities of the retinal venular oxygen saturations were seen in localized venules typically more than 2 disc diameters from the optic disc margin which could explain the non-significant results. Furthermore, the oxygen saturations of the non-affected venules were included in the analysis. This limitation of the analysis technique indicates that further refinement is required in future studies to accurately characterize the oximetric abnormalities seen in patients with retinal vein (and artery) occlusion.

5.4.3. Summary.

The aim of this present study to demonstrate the ability of hyperspectral retinal imaging to detect abnormalities in the oxygen saturation of the retinal arterioles and venules has been achieved. Further studies are required to confirm the proposed theories which explain the detection of abnormally low arteriolar, and abnormally high venular oxygen saturations respectively in patients with retinal arterial and vein occlusion.

Chapter 6: Retinal Oximetry in Primary Open Angle Glaucoma.

6.1. Introduction.

.

The results in Chapter 5 demonstrated that abnormalities in the oxygen saturation (OS) of the retinal arterioles and venules can be detected and measured in patients with retinal arterial and venous occlusion. These oximetric abnormalities of the retinal vasculature were associated with localized areas of the retina where a disruption of the retinal blood supply was likely. In particular, hyperoxia of localised retinal venules suggested inner retinal dysfunction of the retina subserved by the affected venules.

Our subsequent interest was to evaluate whether the retinal oximetry techniques would be able to detect oximetric abnormalities of the retinal vasculature in other ophthalmic pathologies involving the inner retina.

Glaucoma is the second leading cause of blindness globally (Roodhooft, 2002) and in the UK (Bunce and Wormald, 2006) and is characterized by a combination of structural changes to the optic disc and nerve fibre layer and visual field deficits. Primary open-angle glaucoma (POAG) is the most common form of the disease accounting for 90% of glaucoma patients, and its onset is often insidious and progresses slowly with visual symptoms occurring in the late stage of the disease. The most important identifiable risk factor for POAG is an elevated IOP (above 21 mm Hg)(AGIS Investigators, 2000; Heijl et al., 2002; Gordon et al., 2002) which is the basis of current therapeutic strategies in the management of glaucoma to prevent progressive visual field loss and optic disc cupping. The clinical tools commonly used to aid in the management of glaucoma include IOP measurements, optic disc and nerve fibre layer evaluation and visual field analysis. However, specific limitations of these instruments in the management of glaucoma have been well documented and discussed in detail in Chapter 1. In essence, these limitations revolve around their respective sensitivity and specificity that relates to the ability to detect and monitor the progression of glaucomatous damage.

It is currently acknowledged that in glaucoma, the inner retinal layer is the site of primary damage manifested by retinal ganglion cell (RGC) death. Mounting evidence indicate that the mode of RGC death is characterized by apoptosis (Cordeiro et al., 2004;

Kerrigan et al., 1997; Quigley et al., 1995; Garcia-Valenzuela et al., 1994; Garcia-Valenzuela et al., 1995). Numerous mechanisms have been implicated but their role in relation to RGC apoptosis in glaucoma are yet to be fully understood.

Hypoxic stress, possibly as a result of blood flow abnormalities, in the tissues of the optic nerve head and retina is considered to be an important factor in the pathogenesis of glaucoma (Tezel and Wax, 2004; Semenza, 1999; Yamazaki and Drance, 1997; Fontana et al., 1998; Sugiyama et al., 2000). Currently, instruments designed to measure ocular/retinal blood flow are limited because of the uncertainty of the measurements and its relationship and relevance to glaucomatous damage and progression which remain poorly understood. As a consequence the usefulness of blood flow measurements in the management of glaucoma has yet to be established.

Measurements of tissue oxygenation could be a more informative method of determining the metabolic function of optic nerve and retina in health and in glaucoma. Measurements of oxygen tension overlying the optic nerve and retina have been reported in numerous animal studies (Ernest, 1973; Ernest, 1974, Stefánsson et al., 1999; la Cour et al., 2000; Pedersen et al., 2005). However, the technique involves the intraocular insertion of microelectrodes which is technically demanding and invasive. Phosphorescence imaging technique has been performed in experimental glaucoma in animals (Blumenröder et al., 1997; Shonat et al., 1992). However, this technique requires the injection of a bolus of an oxygen chemical probe whose safety in humans have yet to be determined.

Spectrophotometric techniques are currently the commonest non-invasive means of measuring the oxygen content of the retinal vasculature, retina and optic nerve head. Studies using various retinal oximetry devices to measure the OS of the retinal vasculature in glaucoma have been reported. Koobehi et al. (2004) demonstrated the use of a hyperspectral retinal imaging system to detect changes in the reflectance spectra of the optic nerve head tissue and vessels of cynomologus monkeys upon experimentally increasing the intraocular pressures. However, the hyperspectral retinal imaging system was only capable of measuring relative OS changes of a limited area overlying the optic nerve head.

The dual wavelength automatic retinal oximeter, used by Stefansson and co-workers, has shown that arteriolar and venular OS changes can be detected when using and changing topical glaucoma medications (Hardarson et al., 2006; Siesky et al., 2008). However following glaucoma filtration surgery the system did not detect oximetric changes in the retinal vasculature (Hardarson et al., 2009). Additionally, from these studies it appears that only small segments of the retinal vessels near the optic disc were measured and an

evaluation of the whole retinal vascular network is required since the disease process can affect various regions of the retina as well as the optic disc.

Retinal oxygen saturation measurements, using a Fourier transform-based spectral retinal imaging system, have found lower OS in the retinal tissue adjacent to the optic disc in patients with open angle glaucoma (particularly low tension glaucoma) compared to normal subjects (Ito et al., 2008). Additionally, reduced retinal tissue OS was shown to be associated with the severity of the visual field defects. However, this system is only capable of studying small areas of the retina (approximately 40 μm^2) and validation of the technique is both difficult and has yet to be performed.

Michelson and Scibor (2006), using the imaging ophthalmospectrometer, reported that the OS of the retinal arterioles was significantly lower in patients with normal tension glaucoma compared to normal subjects. Additionally, decreased retinal arteriolar OS was found to be associated with decreased optic rim area. The measurements in the study were restricted to retinal vessels located approximately 1-3 mm from the optic disc. Furthermore, the imaging system appears to be only capable of measuring a small section of a given retinal arteriole and venule in close proximity. Data regarding the OS of the retinal arterioles and venules in other parts of the retina was not reported.

Retinal oximetry studied of the retinal vascular network using a hyperspectral imaging system in glaucoma has not yet been reported.

The aims of this chapter are:

- to present the use of our hyperspectral fundus camera and oximetry algorithms in patients with asymmetrical primary open angle glaucoma (POAG)
- to determine whether there are detectable differences in the OS of the retinal vasculature between normal eyes and glaucomatous eyes
- to investigate whether oximetric differences could be detected between eyes with less advanced and eyes with more advanced glaucoma.

6.2. Methods.

This study was conducted in accordance with the ethical standards of the Declaration of Helsinki and was approved by the local Research and Ethics Committees at Gloucestershire Hospitals NHS Foundation Trust (REC reference number: 06/Q2005/132)

6.2.1. Recruitment, Assessment and Imaging of Subjects with Asymmetrical Primary Open Angle Glaucoma.

Seventeen subjects with a diagnosis of asymmetrical POAG were recruited prospectively from the eye departments in Cheltenham and Gloucester General Hospitals between 2007 and 2010. The subjects were diagnosed with POAG based on a history of IOP higher than 21 mm Hg, presence of visual field defects and/or optic disc cupping, normal irido-corneal angles on gonioscopy and no history of other ocular disease.

All subjects underwent full clinical ophthalmic evaluation; visual acuity testing using a Snellen chart; intraocular pressure measurement (IOP) using Goldmann applanation tonometry. The pupils were dilated with 1% tropicamide (Minims; Chauvin Pharmaceuticals, Romford, UK) and slit lamp stereo biomicroscopy was performed to grade the degree of lens opacity (using the Lens Opacities Classification System III) (Chylack et al., 1993) and examine optic nerve head (at high magnification with a fundus +78-D lens) using cup-to-disc ratio estimation and the disc damage likelihood scale (Bayer et al., 2002). All patients had been tested with SITA Standard 24-2 perimetry (Humphrey Field Analyzer II 740; Carl Zeiss Meditec, Inc.). The mean deviation (MD, a measure of the average deviation at each test location between the patient's sensitivity and that of the age-corrected normal value), the pattern standard deviation (PSD, measure of the variability in the shape of the tested field relative to the age-corrected normal reference field), Glaucoma Hemifield Test (measure of asymmetry between the superior and inferior hemifield) and reliability indices results were obtained automatically from a printout from the Humphrey Field Analyzer II. The stage of glaucoma was defined using the MD index. The eyes of each POAG subject were divided into two categories according to the MD index: eyes with more visual field loss (lower MD value) and eyes with less visual field loss (higher MD value).

Oximetry measurements of the index finger were performed in all volunteers using a pulse oximeter (Biox 3740, Ohmeda, Louisville, CO). Brachial blood pressure of all normal subjects was measured using an aneroid sphygmomanometer (Accoson 0342: A.C. Cossor & Son (Surgical) Ltd., Essex, UK).

Inclusion criteria included previously diagnosed open angles on gonioscopy, ocular hypertension (untreated IOP 22 mm Hg), glaucomatous optic neuropathy (GON) and glaucomatous visual field loss (at least two consecutive abnormal visual field test results, demonstrating a threshold sensitivity loss on the pattern deviation outside the 95% normal confidence limits, three or more such contiguous test locations with $P < 0.05$ with at least one

of the points depressed to $P < 0.01$, or a 10-dB difference across the nasal horizontal midline at two or more test locations). A reliable visual field perimetry result was defined as less than 20% fixation loss and less than 33% false-positive and false-negative responses. Exclusion criteria included other previous or current ocular pathology and previous ocular surgery (except successful cataract surgery and trabeculectomy). One patient was a current smoker and 7 patients were treated with anti-hypertensive therapy.

6.2.2. Hyperspectral Retinal Image Acquisition, Processing and Oximetry Analysis.

The acquisition, processing and algorithms used to measure the OS of the retinal vasculature were the same as that described in Chapter 4. Briefly, retinal images were acquired at wavelengths using the time sequential hyperspectral fundus camera. The best quality images for each wavelength selected, dark calibrated and aligned to a reference image obtained at 580 nm. The retinal vasculature of each eye was detected and tracked to enable a vessel profile analysis algorithm to calculate optical density profiles of the tracked centreline points along the vessels.

The optical density profiles at wavelengths from 556 – 650nm were used to calculate the OS of the respective centreline points along the tracked retinal vessels using a non-linear oximetry model. Pseudocolour maps of the oxygen saturation calculations (oximetry maps) overlayed onto retinal vasculature were generated. Six patients were excluded from further analysis due to poor image quality, failed image registration and/or inaccurate optical density profile calculations.

The mean OS at points along the 1st and 2nd degree superotemporal, inferotemporal vessels (disc margin, ½ disc diameters (*dd*), 1 dd, 1½ dd and 2 dd from the disc margin) were calculated in the remaining 11 patients. The OS calculations were checked for outlying oxygen saturation results which were deleted and were defined by the same criteria as that described in Chapter 4 for normal subjects: negative OS calculations, OS calculations greater than 200% for arterioles and OS calculations greater than 100% for venules. Twenty-five (32%) arteriolar and twenty-eight (25%) venular OS calculations were excluded from further data analysis.

The eyes of the POAG patients were divided into two categories according to the mean deviation index: eyes with worse mean deviation (more advanced POAG) and contralateral eyes with better mean deviation (less advanced POAG).

6.2.3. Statistical Analysis.

The normality of the data distributions were tested using the Shapiro-Wilk normality test, with the cutoff for non-normality set at $P < 0.05$. The OS data of the temporal retinal arterioles in normal subjects, temporal retinal arterioles and venules in less advanced glaucomatous eyes and temporal retinal arterioles and venules in more advanced glaucomatous eyes were confirmed to be normally distributed ($P = 0.158$, 0.329, 0.882, 0.868, 0.058 respectively). Multiple linear regression ("enter" method) was used to determine the relationship between the mean OS of the temporal retinal vessels and LOCS III grading scores (nuclear opalescence, nuclear colour, cortical and posterior subcapsular). To check for multicollinearity among the variables in the final model, the variance inflation factor and Durbin-Watson statistic were calculated. The OS data of the temporal retinal venules in normal subjects was significantly different from a nomal distribution ($P = 0.011$). Unpaired *t*-tests with Welch's correction (two-tailed) tests were used to compare the OS of the temporal arterioles between the normal subjects and less advanced and more advanced glaucomatous eyes of patients with POAG. Mann-Whitney (two-tailed) tests were used to compare the OS of the temporal venules between the normal subjects and less advanced and more advanced glaucomatous eyes of patients with POAG. Paired *t*-tests (two-tailed) were used to compare the OS of the temporal arterioles and venules between the eyes with more advanced POAG and the contralateral eyes with less advanced POAG. The association between mean OS of the temporal arterioles and venules of both eyes of POAG patients and visual field global indices were characterized by computing Pearson correlation coefficients. Linear regression analysis was performed to investigate the correlation between the OS calculations of the temporal arterioles and venules and perimetry indices (mean deviation and pattern standard deviation) and optic nerve head measurements (cup-to-disc ratio and disc damage likelihood scale). In all statistical analyses, $P < 0.05$ was considered statistically significant.

6.3. Results.

The baseline characteristics of the POAG patients ($n = 11$) included in this current study are presented in Table 9.

6.3.1. Oxygen Saturation of the Retinal Vasculature in Subjects with Asymmetrical POAG: Observational Features and Quantitative Oximetry Maps of the Retinal Vasculature.

Abnormalities in the spectral appearances of the retinal arterioles and venules could not be observed from the dark calibrated spectral images in patients with POAG. Figure 6.1 presents a 76 year old male POAG patient with asymmetrical glaucomatous visual field defect affecting the right eye more than the left eye. The spectral appearances of the arterioles and venules appear to be similar to that of normal subjects. Abnormal appearances of the retinal arterioles and venules that were seen in eyes with retinovascular conditions (Chapter 5: arterial hypoxaemia – arterioles appear more optically dense, venular hyperoxaemia – venules appear less optically dense) were not evident upon direct observation of the dark calibrated spectral images. In this case, the optical density profiles and OS of selected segments of the retinal arterioles and venules are illustrated which supports the observational findings. The optical density profiles of the supero- and inferotemporal retinal vessels and their respective macular branches were similar to that seen in normal eyes at the same locations.

Pseudocolour images oximetry maps of the retinal vasculature together with the respective colour fundus image and perimetry results of 4 representative POAG patients are illustrated in Figure 6.2 (see Appendix 7 for the results of the remaining 7 patients). Interpretation of the pseudocolour oximetry images in relation to the clinical findings is difficult due to the variability of the calculated OS in the retinal vasculature. The calculated OS of the retinal arterioles appear to be frequently greater than 100%. The calculated OS of the retinal venules appear to be more varied with frequent OS calculations below 0%. On direct inspection of the pseudocolour oximetry images were no characteristics pattern of oximetric abnormalities that corresponded with the severity of the disease, optic nerve head damage and visual field deficits.

Table 9. Summarized clinical data of the glaucoma subjects included in the study.

Number		11	
Mean age (years; range)		61.6 (37 - 82)	
Male:Female ratio		8:3	
Mean systolic blood pressure (mmHg ± SD)		146.5 (± 17.5)	
Mean diastolic blood pressure (mmHg ± SD)		75.1 (± 13.3)	
Mean pulse oximeter oxygen saturation (% ± SD)		96.4 (± 0.8)	
Ophthalmic assessment		Eye with less visual field loss	Eye with more visual field loss
Mean best corrected visual acuity (LogMAR Equivalent)(± SD)		0.10 (0.10)	0.17 (0.12)
Mean intraocular pressure (mmHg ± SD)		15.2 (± 3.6)	16.0 (± 3.3)
Mean lens opacity grade	Nuclear opalescence (± SD)	1.4 (± 0.5)	1.8 (± 1.0)
	nuclear colour (± SD)	1.4 (± 0.7)	1.7 (± 1.1)
	cortical (± SD)	1.4 (± 0.7)	1.3 (± 0.7)
	posterior subcapsular (± SD)	1 (± 0)	1.2 (± 0.4)
Mean optic disc measurement	Vertical cup–to-disc ratio	0.74 (± 0.22)	0.88 (± 0.06)
	Horizontal cup–to-disc ratio	0.70 (± 0.21)	0.79 (± 0.11)
	Disc damage likelihood scale	2.55 (± 2.66)	5.45 (± 1.37)
Mean visual field global indices	MD (dB ± SD)	-6.0 (± 6.8)	-15.9 (± 8.9)
	Pattern Standard Deviation (dB ± SD)	5.2 (± 4.3)	10.0 (± 3.2)
Glaucoma treatment (either single or combination therapy)		Xalatan (*n* = 5) Lumigan (*n* = 2) Timolol (*n* = 3) Betagan (*n* = 1) Travatan (*n* = 1) Trabeculectomy (*n* = 2)	Xalatan (*n* = 9) Lumigan (*n* = 2) Timolol (*n* = 3) Betagan (*n* = 1) Travatan (*n* = 1) Xalacom (*n* = 1) Trabeculectomy (*n* = 3)

Figure 6.1: Subject G1: a 76 year old male POAG patient with visual field defects affecting the right eye more than the left eye. Colour images and visual fields of both eyes are shown with corresponding dark calibrated spectral images at 9 selected wavelengths (560, 570, 580, 590, 600, 610, 620 and 630 nm). There is optic disc cupping in both eyes. There is a superior arcuate visual field defect in both eyes affecting the right eye more than the left. No obvious abnormalities of the retinal vasculature can be seen in the spectral images. The mean optical density profile (± SD; *red filled circle and whiskers*) of selected segments of the temporal arterioles and venules and the respective oxygen saturation calculations (and 95% confidence interval) are also illustrated. No abnormalities in the optical density profiles and oxygen saturation calculation are evident.

Subject G1	76 year old male	Right eye	Left eye
	BCVA (LogMAR)	0.22	0.12
	IOP (mm Hg)	12	13
	Colour Image	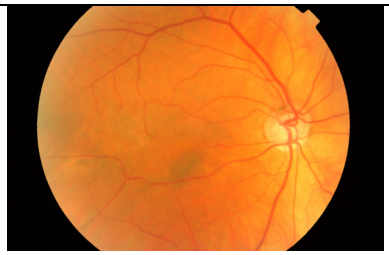	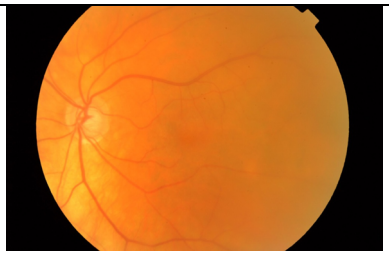
	Visual field	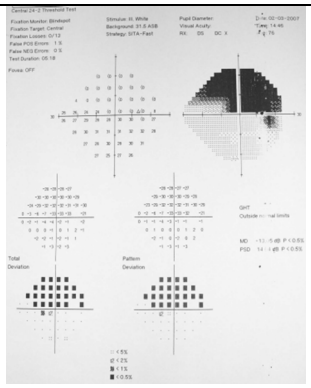	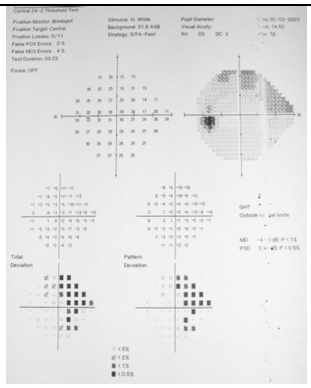
	Observational features of the spectral images		
	Selected dark calibrated registered spectral images	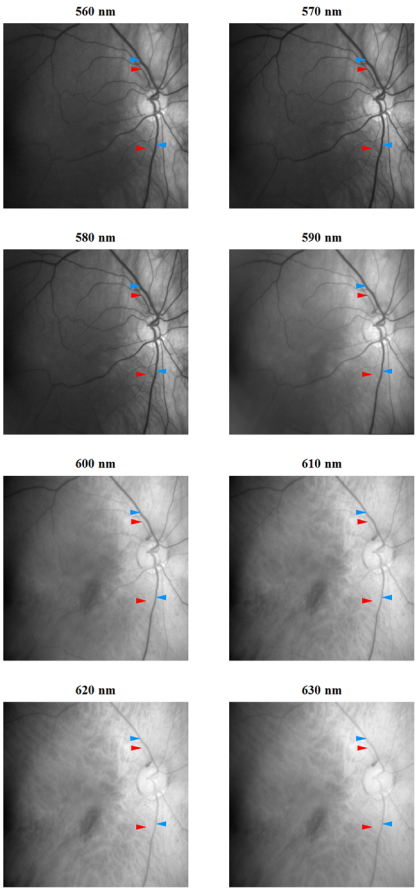	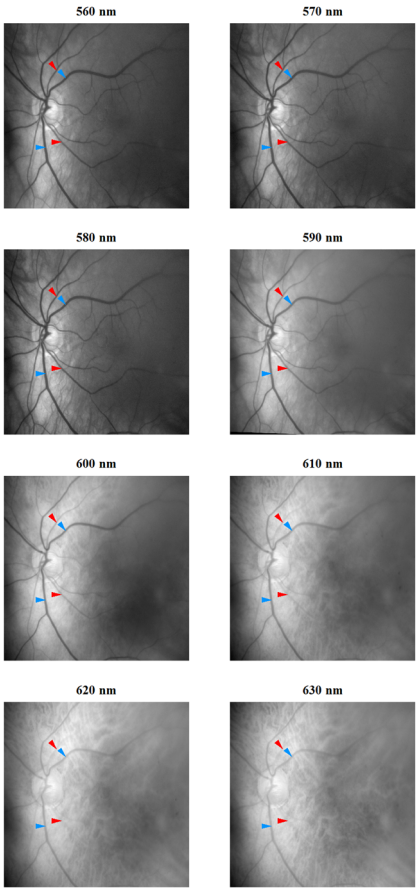

Mean optical density profile and oxygen saturation calculation of selected segments of the retinal blood vessels

Arterioles	Superotemporal		Oxygen saturation: 123.66% 95% confidence interval: 110.05% – 137.27% 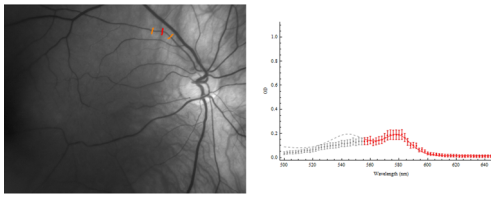	Oxygen saturation: 98.17% 95% confidence interval: 81.42% – 114.92% 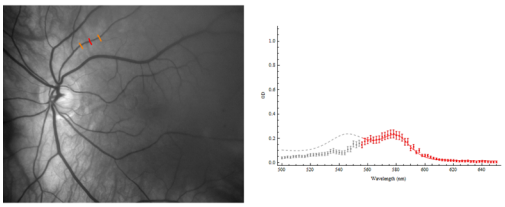
	Inferotemporal		Oxygen saturation: 149.16% 95% confidence interval: 117.56% – 180.76% 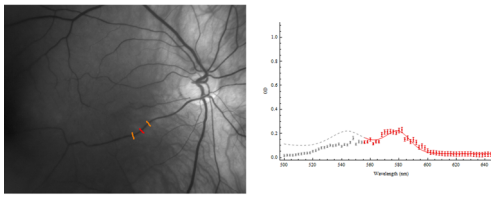	Oxygen saturation: 82.2% 95% confidence interval: 71.03% – 93.37% 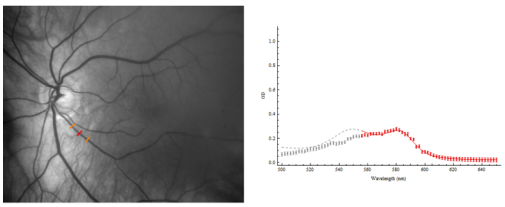
Venules	Superotemporal	1st degree	Oxygen saturation: 32.77% 95% confidence interval: 21.26% – 44.28% 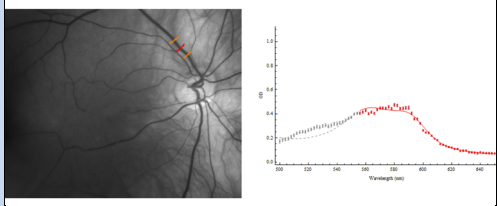	Oxygen saturation: 14.04% 95% confidence interval: 1.45% – 26.64% 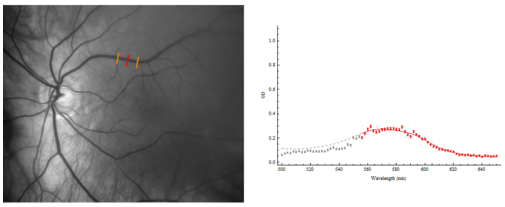
	Superotemporal	Macular branches	Oxygen saturation: 84.03% 95% confidence interval: 71.37% – 96.7% 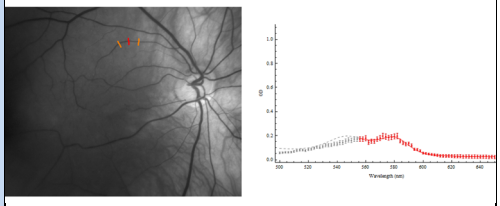	N/A
	Inferotemporal	1st degree	Oxygen saturation: 2.6% 95% confidence interval: −11.51% – 16.71% 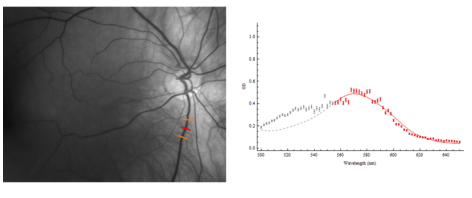	Oxygen saturation: 30.31% 95% confidence interval: 22.23% – 38.39% 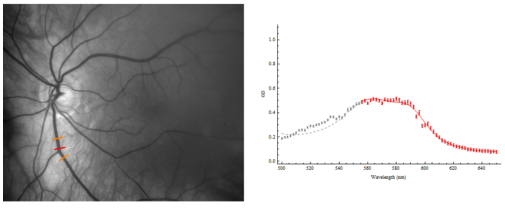
	Inferotemporal	Macular branches	Oxygen saturation: 106.87% 95% confidence interval: 89.3% – 124.45% 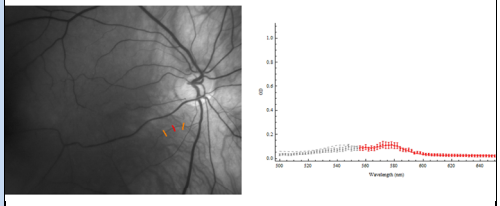	Oxygen saturation: 62.01% 95% confidence interval: 48.92% – 75.09% 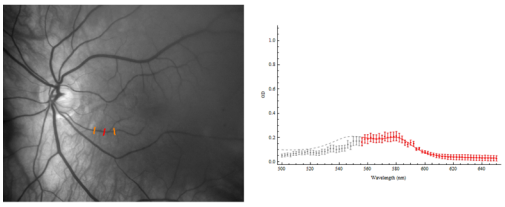

Figure 6.2: Colour images, Humphrey visual field analyses and pseudocolour quantitative oximetry maps of the retinal vasculature in 4 representative patients with asymmetrical POAG.

Subject G1 is a 76 year old male with asymmetrical POAG affecting the right eye more than the left. In both eyes there is optic disc cupping and superior arcuate visual field loss.

Subject G2 is a 77 year old female with asymmetrical POAG affecting the right eye more than the left. In both eyes there is optic disc cupping. Superior arcuate visual field loss is evident only in the right eye.

Subject G3 is a 47 year old male with asymmetrical POAG affecting the right eye more than the left. There is evidence of optic disc cupping in the right eye only. The Left optic disc appears normal. There is diffuse visual field loss in the right eye and an inferior nasal step in the left eye.

Subject G4 is a 63 year old female with asymmetrical POAG affecting the right eye more than the left. In both eyes there is optic disc cupping. There is diffuse visual field loss in both eyes affecting the right eye more than the left.

Pseudocolour quantitative oximetry maps of the retinal vasculature in all subjects are variable. There are no obvious characteristic features in the distribution of intravascular oxygen in these subjects that correlate with the morphology of the optic nerve head and visual field defects.

Subject G1

76 year old male			Right eye	Left eye
BCVA (LogMAR)			0.22	0.12
IOP (mm Hg)			12	13
Colour image				
Visual field			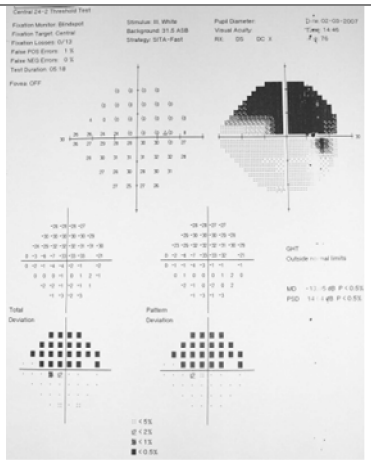	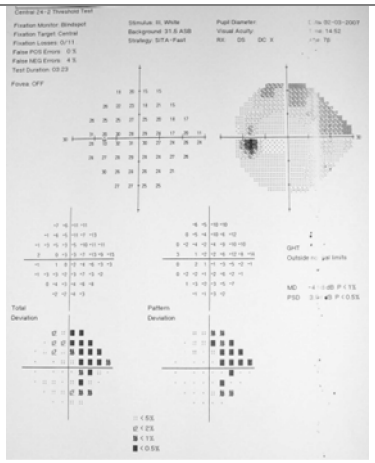
Visual field indices	Reliability	FL	0/13	0/11
		FP	1%	0%
		FN	0%	4%
	Global	MD	-13.05 dB	-4.98 dB
		PSD	14.64 dB	3.98 dB
	GHT		Outside normal limits	Outside normal limits
Quantitative oximetry maps: arterioles			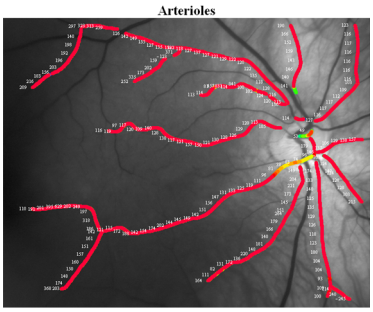	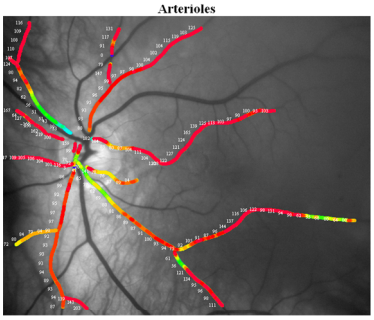
Quantitative oximetry maps: venules			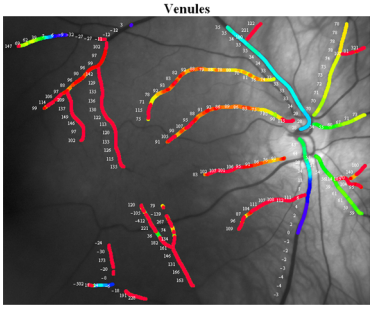	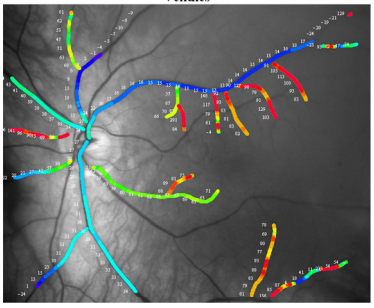

Subject G2

77 year old female			Right eye	Left eye
BCVA (LogMAR)			0.04	-0.04
IOP (mm Hg)			15	16
Colour image				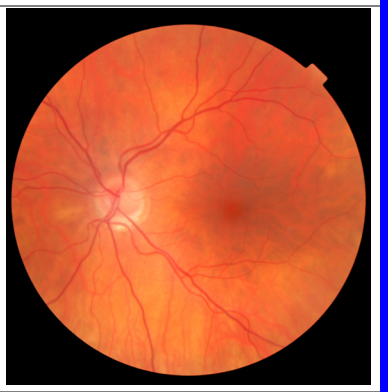
Visual field			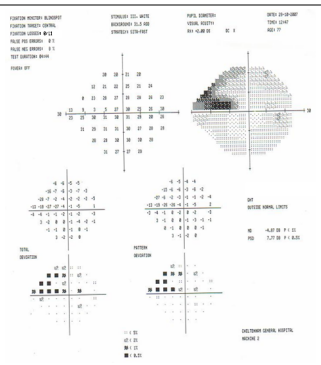	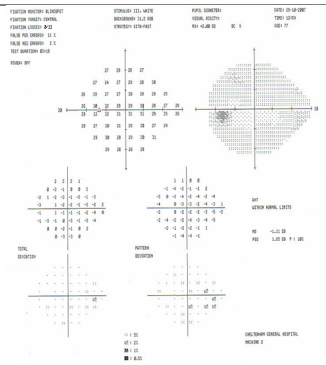
Visual field indices	Reliability	FL	0/11	0/11
		FP	0%	11%
		FN	0%	2%
	Global	MD	-4.87 dB	-1.11 dB
		PSD	7.77 dB	1.65 dB
	GHT		Outside normal limits	Outside normal limits
Quantitative oximetry maps: arterioles			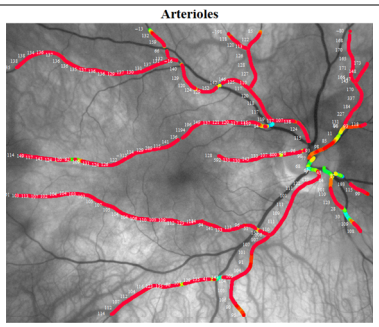	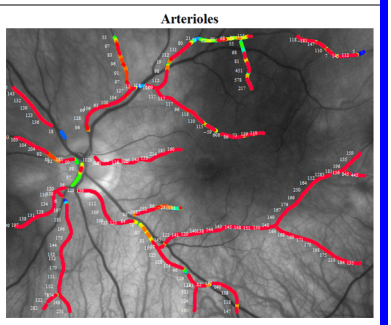
Quantitative oximetry maps: venules			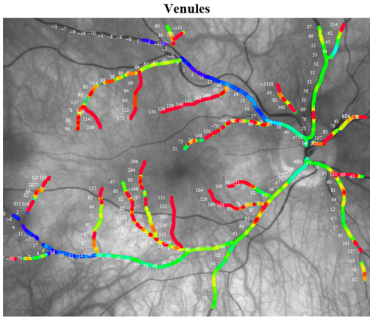	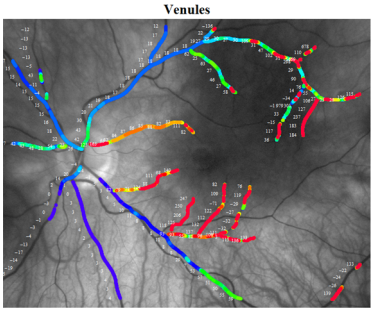

Subject G3

47 year old male			Right eye	Left eye
BCVA (LogMAR)			0.34	0.02
IOP (mm Hg)			16	16
Colour image			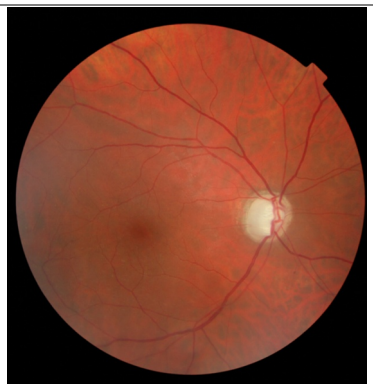	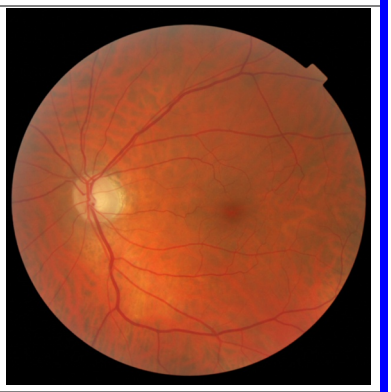
Visual field			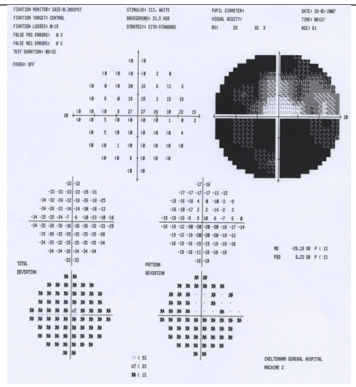	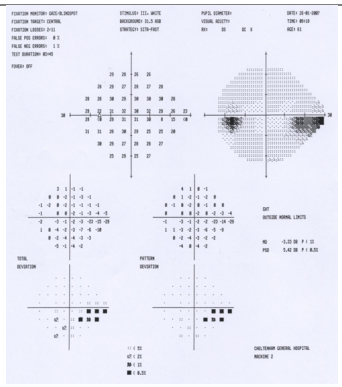
Visual field indices	Reliability	FL	0/19	2/11
		FP	1%	0%
		FN	0%	1%
	Global	MD	-29.19 dB	-3.33 dB
		PSD	8.23 dB	5.42 dB
	GHT		Outside normal limits	Outside normal limits
Quantitative oximetry maps: arterioles	OS		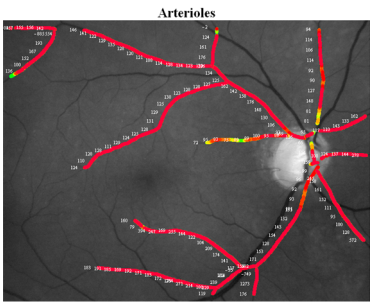	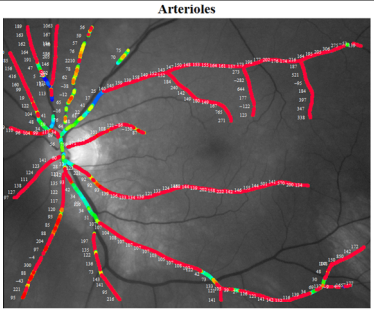
Quantitative oximetry maps: venules			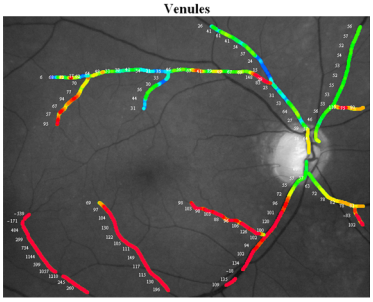	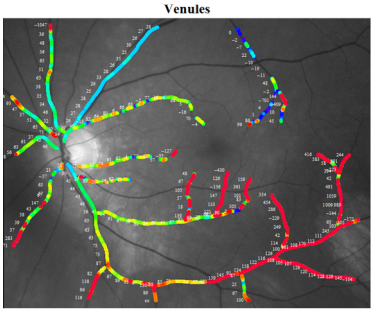

Subject G4

63 year old female			Right eye	Left eye
BCVA (LogMAR)			0.22	0.04
IOP (mm Hg)			20	19
Colour image			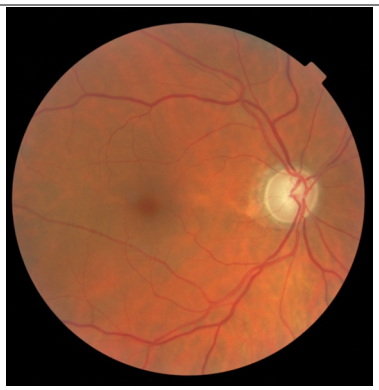	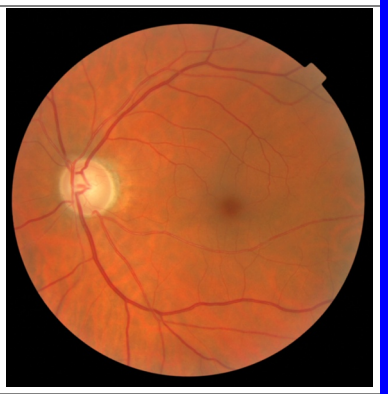
Visual field			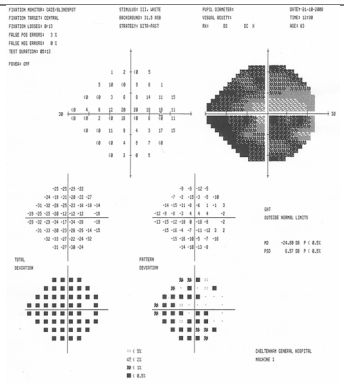	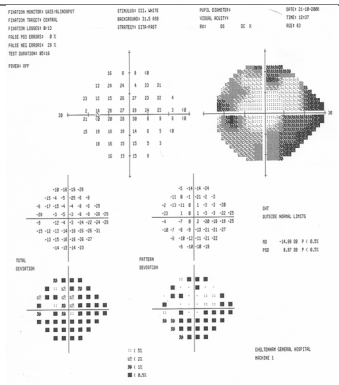
Visual field indices	Reliability	FL	0/13	0/13
		FP	3%	0%
		FN	0%	29%
	Global	MD	-24.80 dB	-14.98 dB
		PSD	6.57 dB	8.97 dB
	GHT		Outside normal limits	Outside normal limits
Quantitative oximetry maps: arterioles	OS		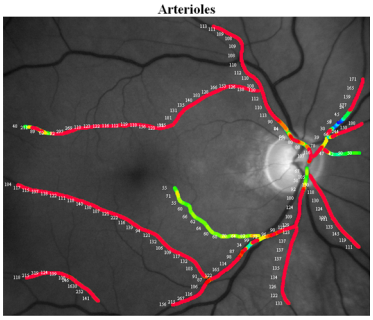	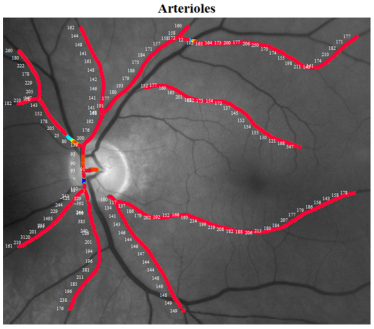
Quantitative oximetry maps: venules	OS		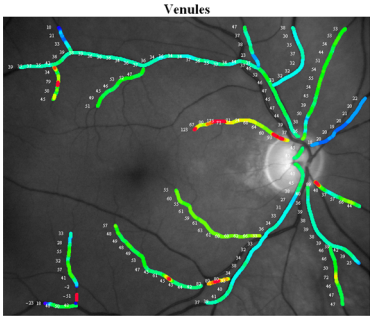	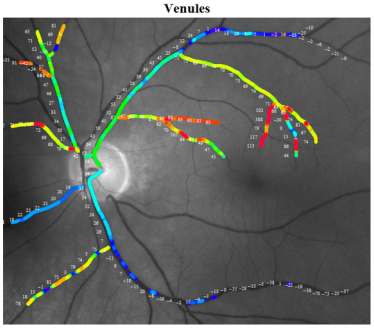

6.3.2. Relationship Between the Oxygen Saturation in Glaucomatous Eyes and LOCS III Grading Scores.

The multiple linear regression model predicting the OS of the temporal retinal vessels in glaucomatous eyes using the LOCS III scores as independent variables did not produce a significant model ($F = 0.602$, $P = 0.664$, adjusted R squared = -0.040). The variance inflation factor and Durbin-Watson statistic of the final model did not indicate the presence of multicollinearity. The influence of the nuclear opalescence, nuclear colour, cortical and posterior subcapsular lens grading scores were not statistically significant for OS in glaucomatous eyes ($\beta = -0.233$, $P = 0.532$; $\beta = 0.328$, $P = 0.418$, $\beta = -0.079$, $P = 0.733$ and $\beta = 0.181$, $P = 0.367$ respectively).

6.3.3. Comparison of the Oxygen Saturation Between Normal Subjects and Patients with Asymmetrical POAG.

Figures 6.3 and 6.4 summarizes the OS calculations of the temporal retinal arterioles and venules in normal subjects and patients with asymmetrical POAGs. In normal subject, the mean OS (± SD) of the temporal retinal arterioles and venules were 110.8% (± 11.8%) and 27.7% (± 3.2%) respectively. The mean (± SD) OS of the temporal retinal arterioles were 119.2% (± 21.9%) and 130.3% (± 21.33%) in the less advanced and more advanced glaucomatous eyes respectively. The mean (± SD) OS of the retinal venules were 35.8% (± 13.9%) and 44.8% (± 24.2%) in the less advanced and more advanced glaucomatous eyes respectively. The mean OS of the temporal retinal arterioles and venules were significantly higher in POAG eyes with more advanced visual field loss compared to the eyes of normal subjects ($P = 0.012$ and 0.046 respectively; unpaired t-test with Welch's correction (two-tailed) and Mann-Whitney test (two-tailed) respectively). No significant differences were found between the mean OS of the temporal retinal arterioles and venules in POAG eyes with less advanced visual field loss and the eyes of normal subjects ($P = 0.186$ and 0.218 respectively; unpaired t-test with Welch's correction (two-tailed) and Mann-Whitney test (two-tailed) respectively). Analysis of the two POAG sub-groups (less vs. more advanced visual field loss) showed no significant difference in the mean arteriolar and venular OS between the groups ($P = 0.202$ and 0.203 respectively (two-tailed); paired t-test).

Figure 6.3: A box-and-whisker plot of the oxygen saturation (OS) of the temporal (superotemporal and inferotemporal) retinal arterioles in normal subjects and POAG subjects with less advanced and more advanced visual field loss.

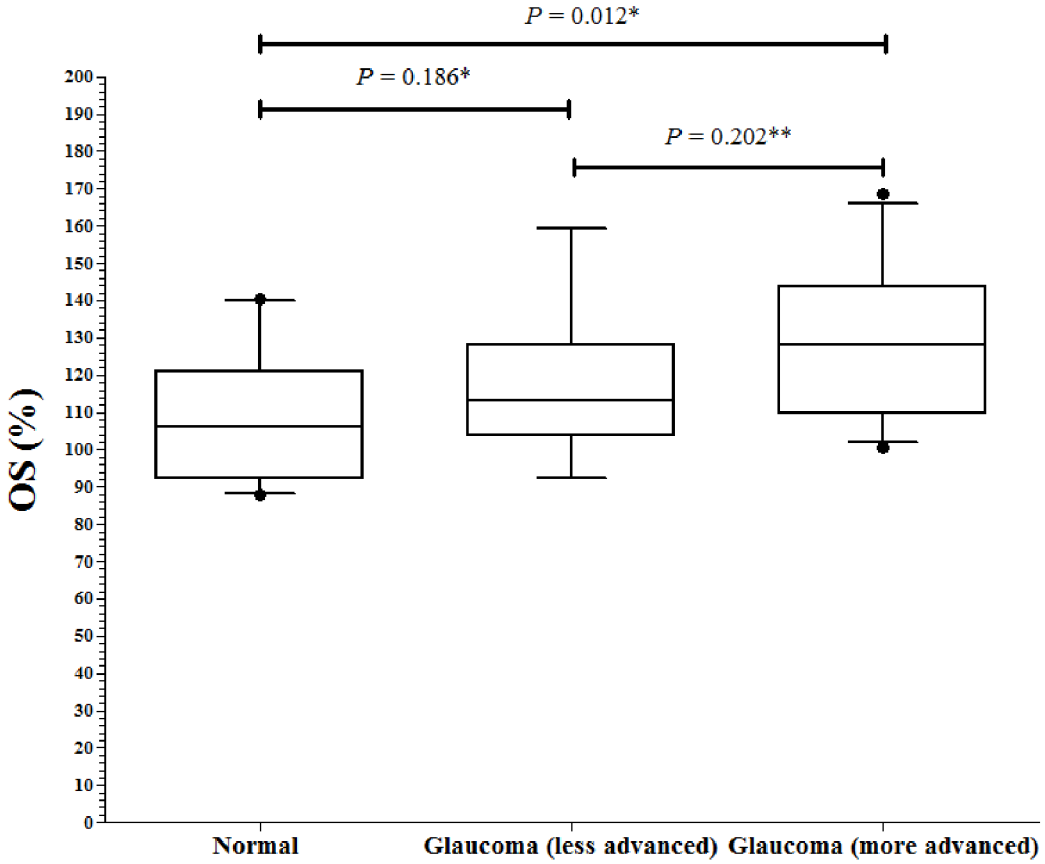

* Unpaired *t*-test with Welch's correction(two-tailed)
** Paired *t*-test (two-tailed)

Figure 6.4: A box-and-whisker plot of the oxygen saturation (OS) of the temporal (superotemporal and inferotemporal) retinal venules in normal subjects and POAG subjects with less advanced and more advanced visual field loss.

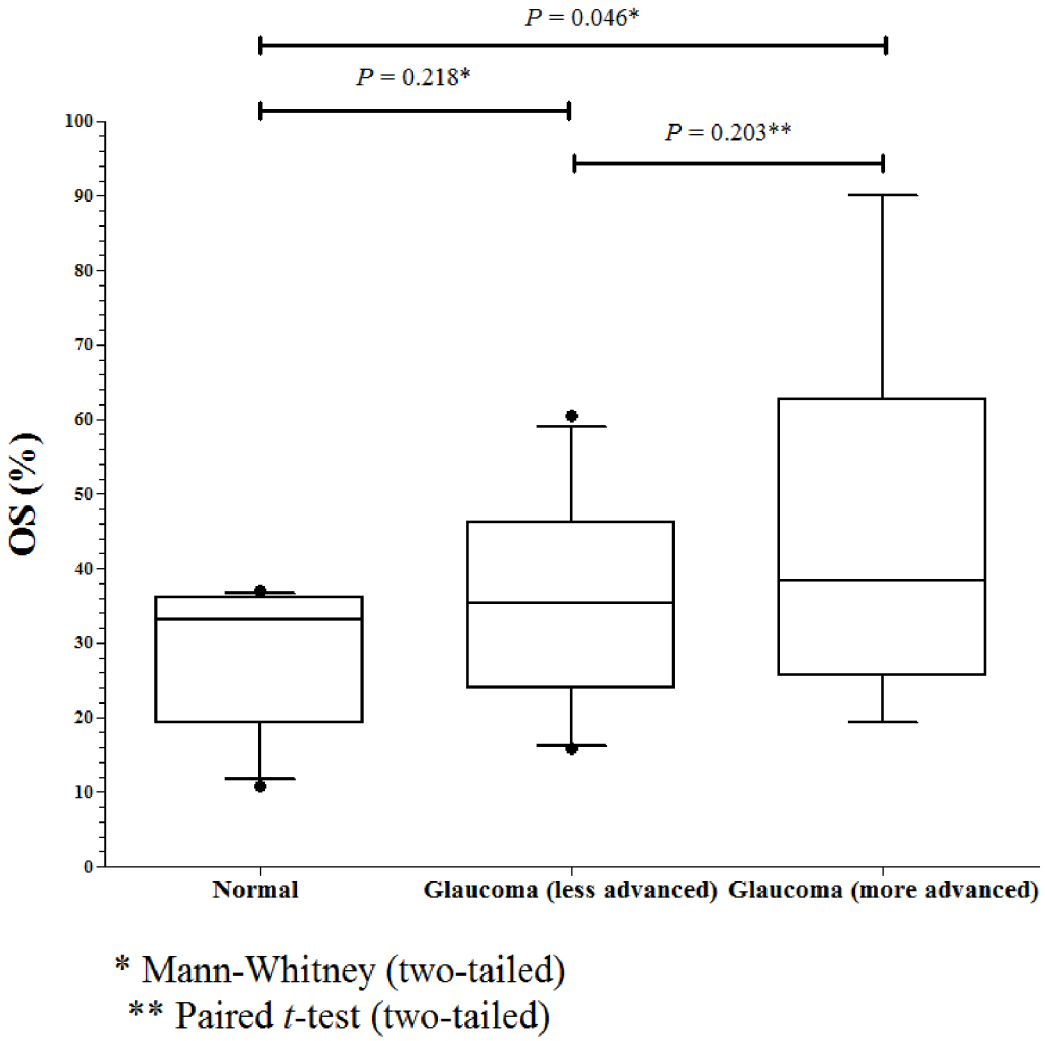

6.3.4. Correlation and Linear Regression Between the Oxygen Saturation of the Temporal Retinal Arterioles and Visual Field Global Indices.

The Pearson correlation analyses between the global indices (mean deviation and pattern standard deviation) and the mean OS of the temporal retinal arterioles and venules are presented in Table 10. The linear regression between the mean deviation and mean OS of the temporal retinal arterioles and venules was not statistically significant ($P = 0.06$ and 0.07 respectively; $R^2 = 0.17$ and 0.15 respectively; Figure 6.5 *left*). Similarly, the linear regression between the pattern standard deviation and mean OS of the temporal retinal arterioles and

venules was not statistically significant ($P = 0.06$ and 0.16 respectively; $R^2 = 0.17$ and 0.10 respectively; Figure 6.5 *right*).

Table 10. Correlation between the global indices and the mean oxygen saturation of the temporal arterioles and venules in POAG eyes ($n = 22$).

Global indices		Temporal arterioles	Temporal venules
MD	*r* (95% CI)	-0.41 (-0.71 – 0.02)	-0.39 (-0.70 – 0.04)
	R^2	0.17	0.15
	p-value	0.06	0.07
PSD	*r* (95% CI)	0.41 (-0.01 – 0.71)	0.31 (-0.13 – 0.65)
	R^2	0.17	0.10
	p-value	0.06	0.16

Figure 6.5: Scatter plots illustrating the relationship between the mean oxygen saturation calculation and visual field global indices. (*Left*) The relationship between the mean deviation (MD) and the mean oxygen saturation of the temporal arterioles (*red*) and venules (*blue*). (*Right*) The relationship between pattern standard deviation (PSD) and the mean oxygen saturation of the temporal arterioles (*red*) and venules (*blue*). The best-fit line (*solid black line*) and 95% confidence interval of the best-fit line (*dashed lines*) are shown in the plots.

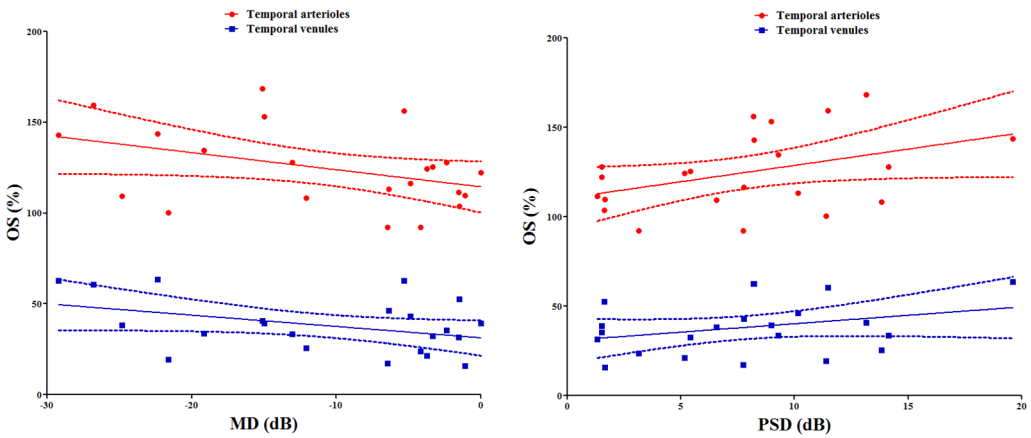

6.3.5. Correlation and Linear Regression Between the Oxygen Saturation of the Temporal Retinal Arterioles and Optic Nerve Head Evaluation.

The Pearson correlation analyses between the optic disc measurements (vertical and horizontal cup-to-disc ration and the disc damage likelihood scale) and the mean OS of the temporal retinal arterioles and venules are presented in Table 11. The linear regression between the disc damage likelihood scale and mean OS of the temporal retinal arterioles and venules was not statistically significant (P = 0.09 and 0.23 respectively; R^2 = 0.14 and 0.07 respectively; Figure 6.6).

Table 11. Correlation between the optic disc measurements (vertical and horizontal cup-to-disc ratio and the disc damage likelihood scale) and the mean retinal vessel oxygen saturation of the temporal arterioles and venules in POAG eyes (n = 22).

Global indices		Temporal arterioles	Temporal venules
Vertical cup-to-disc ratio	r (95% CI)	0.25 (-0.19 – 0.61)	-0.17 (-0.27 – 0.55)
	R^2	0.06	0.03
	p-value	0.26	0.46
Horizontal cup-to-disc ratio	r (95% CI)	0.11 (-0.33 – 0.51)	0.03 (-0.40 – 0.45)
	R^2	0.01	0.0009
	p-value	0.62	0.89
Disc damage likelihood scale	r (95% CI)	0.37 (-0.06 – 0.69)	0.26 (-0.18 – 0.62)
	R2	0.14	0.07
	p-value	0.09	0.23

Figure 6.6: Scatter plots illustrating the relationship between the retinal vessel oxygen saturation calculations and disc damage likelihood scale. The relationships are shown between the disc damage likelihood scale and the mean oxygen saturation of the temporal arterioles (*red*) and venules (*blue*). The best-fit line (*solid line*) and 95% confidence interval of the best-fit line (*dashed lines*) are shown in the plots.

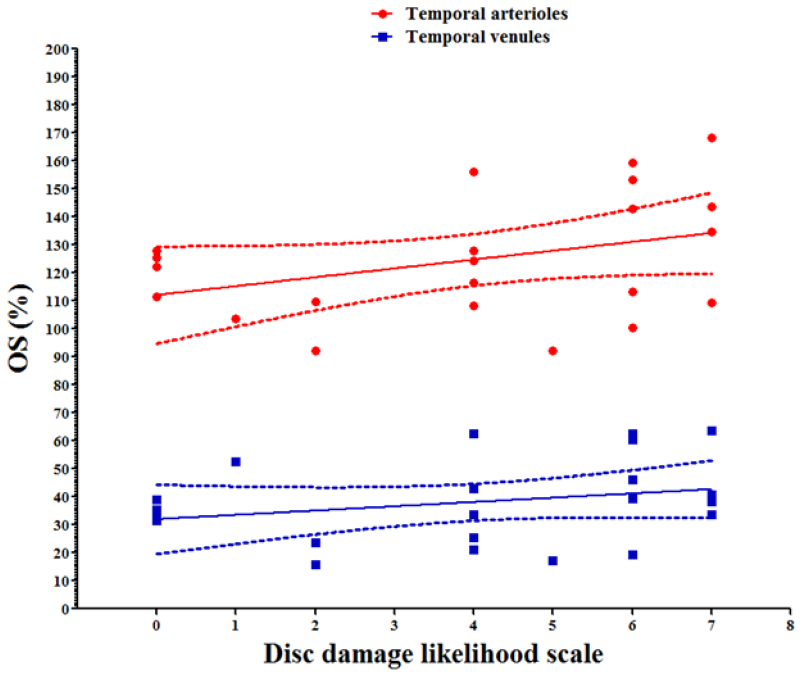

6.4. Discussion.

6.4.1. Oxygen Saturation of the Retina in POAG Patients: Observational Features, Quantitative Analysis and Oximetry Maps of the Retinal Vasculature.

The application of hyperspectral imaging to detect OS changes in the retinal vasculature of POAG patients has been presented in this study. Observational spectral features of the retinal vasculature, optical density profile and OS calculations of selected segments of the retinal vasculature in POAG patients have been illustrated in addition to the presentation of the pseudocolour oximetry maps of the retinal vasculature.

In contrast to the findings of patients with retinovascular occlusion presented in Chapter 5, the dark calibrated registered spectral images of the retina in patients with POAG did not reveal apparent spectral characteristic features of abnormal oxygenation in the retinal

vasculature upon inspection. This may indicate that either no abnormality was present or that only subtle abnormalities were present which could not be detected on visual inspection of the retinal vasculature. Further analysis of the retinal vasculature in POAG patients was necessary to determine whether abnormal OS within the blood vessels could be detected. Mean optical density profile analyses and OS calculations of selected segments of the retinal arterioles and venules in POAG patients were performed. These latter analyses did not reveal detectable OS abnormalities in the selected retinal vasculature. An illustration of the unremarkable spectral features of the retinal vasculature, optical density profiles and OS in a patient with asymmetrical POAG is presented in Figure 6.1 (subject G1).

Pseudocolour oximetry maps of the retinal vasculature in patients with POAG are presented together with the respective colour fundus images and Humphrey visual field analyses (Figure 6.2). These images were difficult to interpret in relation to the clinical investigations. There were no obvious patterns (on visual inspection of the pseudocolour images) to the distribution of the calculated OS in the retinal vasculature that correlated with the severity of glaucoma or localized glaucomatous damage. Structured analysis of the oximetry data was required to discern whether oximetric differences could be detected in glaucomatous eyes. This was subsequently performed.

6.4.2. Quantitative Oxygen Saturation: Comparison Between Normal Subjects and POAG Patients.

Statistical methods were subsequently used to determine the presence of abnormal oxygen saturations in the retinal vasculature of POAG patients. Structured collection of OS data from selected points along the retinal vessels in POAG patients was performed and compared to OS data performed using the same technique in normal subjects (described in Chapter 4). The results show that the mean OS of the temporal arterioles and venules were significantly higher in eyes with more advanced glaucomatous visual field loss compared to normal eyes (Figures 6.3 and 6.4). The mean OS of the temporal arterioles and venules of the contralateral POAG eyes were higher than in normal subjects, however this was not statistically significant. Similarly, sub-group analysis revealed no significant differences in the OS of the temporal arterioles and venules between POAG eyes with less advanced and more advanced visual field loss.

6.4.3. Retinal Arterioles.

The significantly higher OS of the temporal retinal arterioles in glaucomatous eyes is surprising and unclear. A possible explanation could be due to inaccuracies in the optical density profile and OS calculations in the population of normal subjects and patients with glaucoma included in the study which may have skewed the results. We anticipated no significant differences in the OS of the 1st and 2nd degree arterioles between our cohort of glaucoma patients and normal subjects. This is supported by comparing recent studies on normal subjects and glaucoma patients with the dual wavelength retinal oximeter. Hardarson et al. (2006) reported a mean (± SD) arterial OS of 96% (± 9%) in normal subjects. Traustason et al. (2009) reported a mean (± SD) OS of the 1st and 2nd degree retinal arterioles of 96% (± 2%) and 97% (± 2%) in glaucoma patients on topical timolol monotherapy and timolol-dorzolamide combination therapy respectively. Hardarson et al. (2009) reported a significant increase in the mean (± SD) OS of the 1st and 2nd degree retinal arterioles of 97% (± 4%) to 99% (± 6%) in glaucoma patients before and after glaucoma filtration surgery. In consideration of these studies, using the same retinal oximeter, it appears that the arteriolar OS are similar in normal subjects and patients with glaucoma.

In contrast, a study by Michelson and Scibor (2006), using a multi-wavelength imaging spectrometer, reported lower arteriolar OS in patients with normal tension and primary open angle glaucoma (89.7% ± 5.4% and 91.4% ± 4.0% respectively) compared to normal subjects (92.3% ± 3.4%). However, their measurements were limited to localized superotemporal arterioles approximately 1-3 mm from the optic disc. It is difficult to understand these findings as the commonly recognized causes of arterial hypoxaemia are pulmonary pathologies (alveolar hypoventilation, ventilation-perfusion mismatch, low inspired oxygen partial pressure) and right-to-left shunts. In Chapter 5, two cases of retinal arteriolar hypoxaemia were demonstrated in association with embolic retinal artery occlusion. Hypoxaemia of the retinal arterioles was explained by the presumed reduced blood flow and subsequent extraction and/or diffusion of oxygen from the intravascular haemoglobin into the adjacent vitreous and retinal tissues. Consumption of the intravascular oxygen by the vessel wall is another possibility. The quantitative relationship between blood flow in the 1st and 2nd degree retinal arterioles and extraction of oxygen leading to arteriolar hypoxaemia is not known. However, it would be reasonable to expect that arteriolar hypoxaemia would occur at extremely low blood flow rates in the 1st and 2nd degree retinal arterioles. Such conditions are unlikely to be present in the glaucoma patients included in this study.

6.4.4. Retinal Venules.

A higher mean oxygen saturation of the temporal retinal venules in glaucomatous eyes compared to normal eyes was observed in this study. A possible explanation could be a systematic error in the OS calculation, indicated by a concurrent higher mean arterial OS calculation in glaucomatous eyes, which could have offset the OS calculation of the retinal venules to a higher value. A plausible argument for a systematic error would be a difference in the fundal reflectance between normal and glaucomatous eyes where there is a loss of neuronal tissue in the inner retina. However, our model eye experiments described in Chapter 3 demonstrated that background reflectance had no significant influence on the OS measurements and did not appear to affect its accuracy. Other physiological factors that could contribute towards a systematic error, such as blood flow and vessel diameters differences between normal subjects and glaucoma patients, are unlikely as these factors do not significantly change the characteristic shapes of the optical density profile that enable the calculation of the OS. These physiological factors were previously studied by Schweitzer et al. (1999) who demonstrated that *in vitro* changes to the blood flow and blood column thickness resulted in a vertical displacement of the spectral transmission profile of fully oxygenated blood without a significant change to the shape of the transmission profile. Therefore, the curve fitting technique used in this study to generate the OS value is unlikely to be affected by such physiological features as each OS value is calculated from the specific shape of the optical density profiles. However, further research would be necessary to evaluate and confirm these statements.

Nonetheless, higher mean OS of the temporal retinal venules in glaucomatous eyes compared to normal eyes are contrary to the oximetry study in glaucoma reported by Michelson and Scibor (2006), where a mean (± SD) venular OS of 56.0% (± 8.3%) and 58.3% (± 10.5%) in patients with normal tension and primary open angle glaucoma were observed. These measurements were not significantly different to measurements made in normal subjects where a mean (± SD) venular OS of 55.7% (± 6.8%) was reported. However, combining the studies reported by Hardarson et al. (2006 and 2009) and Traustason et al. (2009), which used the same retinal oximeter, the mean (± SD) OS of the retinal venules in glaucoma patients on topical medical therapy were 66% (± 5%) and 65% (± 6%) respectively. In glaucoma patients undergoing filtration surgery the mean retinal venular OS were 63% (± 5%) before surgery and 64% (± 6%) after surgery (Hardarson et al., 2009). Importantly, an earlier study by Hardarson et al. (2006, 2009) found comparatively lower

retinal mean (± SD) venous OS in normal subjects of 55% (± 14%). As mentioned in previous chapters, a commonly accepted limitation of the two wavelength oximetry technique is the overestimation of the true blood oxygen saturation particularly at lower oxygen saturations (Sarnquist et al., 1980). This could explain the higher venular OS in glaucoma patients reported in these latter three studies compared to this study. The relative difference in the venular OS between normal subjects and glaucoma subjects (higher venular oxygen saturation in glaucoma patients), however, appear to support the findings in this study.

The increase in the OS of the temporal retinal venules could indicate reduced metabolic consumption of oxygen in the retinal tissues in glaucomatous eyes. However, microcirculatory shunting of arterial blood into the venous system and physiological changes within the tissue causing a left-shift of the haemoglobin oxygen dissociation curve in the capillaries (increased affinity of haemoglobin for oxygen) cannot be excluded from our findings. Increased venous OS is thought to be an indicator for reduced oxygen utilization as well as arteriovenous shunting (Marx and Reinhart, 2006). In normal human physiological conditions, the OS of the veins draining their respective organs within the body are highly variable which is thought to reflect variations in the oxygen extraction levels or metabolic activity of the tissues (Reinhart, 1989). This is most evident in the renal venules whose OS is approximately 92% as a result of relatively low oxygen extraction in the renal tissues which derives its energy requirements from non-oxidative phosphorylation (Byrick and Rose, 1990). In contrast, the OS of venous drainage from the heart is approximately 37% which reflects high oxygen extraction as a result of oxidative phosphorylation in the cardiac muscles (Reinhart, 1989). Rivers et al. (1992) reported venous hyperoxia in patients with following cardiac arrest which was hypothesized to be a result of deranged systemic oxygen consumption.

In glaucoma, the reduced metabolic consumption of the retina could reflect neuronal loss and/or dysfunction. Numerous studies have reported the loss of ganglion cells in glaucoma (Quigley and Addicks, 1981; Quigley et al., 1981; Morgan et al., 2000; Glovinsky et al., 1991; Glovinsky et al., 1993; Weber et al., 1998; Hitchings, 2000; Quigley et al., 1987) and the underlying process is thought to involve apoptosis (Kerrigan et al., 1997; Quigley et al., 1995; Garcia-Valenzuela et al., 1995; Guo et al., 2005). Further, ganglion cell drop out is thought to be preceded by structural morphological changes of the dendrites (Morgan et al., 2006; Shou et al., 2003; Weber et al., 1998) and reduced sensitivity to light stimuli (Porciatti, 2006; North et al., 2010) which suggests the presence of neuronal dysfunction which could be manifested by reduced oxygen consumption. At an intracellular level, it has been postulated

that mitochondrial function in the retinal ganglion cells are compromised by a multitude of insults which results in reduced energy production (reduced oxygen consumption) which subsequently induces cellular apoptosis (Osborne, 2008). Ganglion cell loss and/or dysfunction on its own may not necessarily result in increased venous OS as other neuronal cells and supportive cells within the retinal layers require oxygen to fuel their metabolic demands. There is emerging evidence from histological, electrophysiological and OCT studies that the processes involved in glaucomatous damage could also involve other neuronal cells such as amacrine cells (Raz et al., 2003), bipolar cells (North et al., 2010; Lei et al., 2008), horizontal cells (Janssen et al., 1996) and photoreceptors (Lei et al., 2008; Nork et al., 2000; Panda and Jonas, 1992; Velten et al., 2001; Guo et al., 2010). Therefore reduced mass tissue extraction of oxygen within the retinal layers would support our explanation of retinal venous hyperoxia.

However, regional intravenous hyperoxia associated with focal loss of perimetric sensitivity and/or neuroretinal rim in glaucoma patients was not observed in this study. It would be anticipated that, for example, a superior arcuate scotoma and/or inferior neuroretinal rim loss would be associated with higher OS of the inferotemporal retinal venules compared to the superotemporal retinal venules. In addition, with the increased density of retinal ganglion cells closer to the fovea compared to the peripheral retina (Perry and Cowey, 1985; Dacey and Peterson, 1992), it would be anticipated that localized visual field defects in regions close to fixation in glaucomatous eyes would result in higher OS of the respective venules draining the affected region of the retina. The absence of finding such features in this study could be explained by the lack of sensitivity of our oximetry technique to detect these differences or errors in the OS calculations. However, regional variations in the OS of the 1st degree venules in relation to visual field deficits may not necessarily be present as a given venule could be collecting blood from both hemispheres. Furthermore, Grewal et al. (2009) demonstrated diffuse patterns of reduced retinal nerve fibre layer thickness and retinal sensitivity in the normal regions of the perimetric tests in glaucoma patients with localized standard automated perimetry deficits. Therefore, despite focal visual field and neuroretinal rim loss, the presence of dysfunctional ganglion cells (and possibly other neuronal cells) in other regions of the retina could be manifested by higher venous OS in both the supero- and inferotemporal arcades.

6.4.5. Relationship Between Retinal Vascular Oxygen Saturation, LOCS III scores, Visual Field Analysis and Optic Nerve Head Measurements.

Multiple linear regression analysis demonstrated a non-significant relationship between the OS of the temporal vessels in glaucomatous eyes and LOCS III grading scores suggesting that the influence of the lens status on the oximetry values was not an important factor.

An intriguing finding in this study is the impression of an increasing trend of the mean venular OS calculation amongst normal subjects, glaucomatous eyes with less advanced visual field loss and glaucomatous eyes with more advanced visual field (Figure 6.4). Although no significant difference in the mean venular oxygen saturation was found between normal subjects and glaucomatous eyes with less advanced visual field loss and between glaucomatous eyes with less advanced visual field loss and glaucomatous eyes with more advanced visual field loss, the increasing trend implies some consistency with the results. The non-significant finding could reflect the presence of a mixture of eyes with little or no glaucomatous dysfunction in the less advanced visual field loss group. This is evident by the presence of 4 out of 11 eyes (36%) with normal Glaucoma Hemifield Tests in this group.

Further analysis was performed in this study to investigate the relationship between the OS calculations and both global indices of the automated perimetry (mean deviation and pattern standard deviation) and optic nerve head morphology (vertical and horizontal cup-to-disc ratio and disc damage likelihood scale) glaucoma patients. Both mean arteriolar and venular OS were negatively correlated with the mean deviation and positively correlated with the pattern standard deviation and optic nerve head measurements (Tables 8 and 9 and Figures 6.5 and 6.6 respectively). Although these findings were not statistically significant, the trends are consistent with the results of the aforementioned group comparisons. These observations, could lend support to the hypothesis that increasing retinal venular OS indicate decreasing tissue consumption of oxygen due to ganglion (and other neuronal) cell loss and/or dysfunction.

6.4.6. Limitations of the Study and Future Research.

A major limitation of this study, in addition to the limitations of the oximetry technique detailed in Chapter 4, is the small sample size of patients included in this study and low statistical power. Therefore, caution should be used when interpreting the results of the study. Further studies would be useful to fully investigate the relationship between the OS of the retinal vessels and glaucomatous damage with a larger population of matched subjects. This would reduce the potential for type 1 and type 2 errors which are likely to be present in this study. If the relationship between increasing venous oxygen saturation and increasing glaucomatous damage is confirmed it would indicate that measuring the venular OS could be a useful functional parameter in detecting and monitoring disease progression in glaucoma.

A further limitation of this study is that the oximetry technique was not capable of measuring the oxygen saturation of the retinal capillaries which is likely to be a more important indicator of oxygen supply and demand to the retinal tissues. Tissue hypoxia as a consequence of vascular dysregulation and reduced ocular blood flow are thought to be important in the pathogenesis of glaucoma (Tezel and Wax, 2004). Spectrophotometric techniques have previously been described to detect and characterize tissue and capillary oxygenation in animal and human studies. Selbach et al. showed that the OS of the capillaries of the anterior optic nerve head rim and centre was stable at experimentally induced intraocular pressures of up to 60 mm Hg and 40 mm Hg respectively in rabbits eyes (Selbach et al., 1999). Beyond these respective intraocular pressures the OS was shown to decrease presumably due to reduced (autoregulation) of blood flow and the resultant extraction of oxygen from haemoglobin located in the capillaries. Khoobehi et al. (2004) reported relative oxygen desaturation in the optic nerve head tissues and overlying arteriolar vessels in monkeys with experimentally increased intraocular pressures of up to 60 mm Hg. Ito et al. (2008) demonstrated lower OS in the retinal tissue adjacent to the optic disc in human patients with normal tension glaucoma and POAG compared to normal subjects. These studies are supported by a phosphorescence imaging technique performed by Shonat and colleagues (1992) who demonstrated that the oxygen tension of the optic nerve head and capillary bed in cats was stable at moderate increases in IOP. Hypoxia of the optic nerve head and capillary bed was only found when the IOP was increased and the blood flow, measured by laser Doppler flowmetry, stopped. It is apparent from these studies that measurements of oxygen content at the microvascular and tissue level could be important in contributing to our understanding of the vascular mechanisms which are thought to play a role in the

pathogenesis of glaucoma such as reperfusion injury and oxidative stress. From a clinical aspect, these measurements may be important in explaining the pressure dependent and pressure independent mechanisms of diffuse and focal visual field loss which have been postulated by Caprioli et al (1987). Furthermore, it is conceivable that full field oximetry of the retinal microvasculature and tissues could be a valuable tool in detecting and monitoring the progression of glaucoma. The oximetry technique presented in this study involved measuring the OS of the macular branches of the arterioles and venules. These measurements could potentially be used as a surrogate of indirectly estimating the oxygen saturation of the retinal capillaries. Further studies would be required to explore its usefulness.

Arterio-venous (AV) difference in OS of vessel pairs is thought to reflect tissue extraction of oxygen. This was not performed in study because of the errors in the OS calculation of retinal arterioles located in close proximity to the venules – this was described in detail in Chapter 4. Additionally, it is uncertain whether AV differences truly reflect oxygen extraction of a particular tissue region, as the contribution of oxygen from other regions of the retina collected by measured venule could compound the results.

An alternative method of measuring the oxygen content of the capillaries would involve hyperspectral image analysis techniques to quantify the relative amounts of oxy- and deoxyhaemoglobin within each hyperspectral voxel (volumetric pixel with the third dimension representing sequential wavelengths) of the retinal image plane. This was attempted in our early hyperspectral image analysis research using linear spectral unmixing of the hyperspectral retinal images obtained from glaucoma patients (Boardman, 1989), however, our results were highly variable, difficult to interpret and could not be accurately validated. (Mordant DJ et al. IOVS 2007;148: ARVO E-Abstract 148). Further research, and in particular, refinements to the registration of the retinal images and analysis of the hyperspectral images are required to establish the value of this alternative oximetry technique.

6.4.7. Summary.

This present study has described the application of the oximetry techniques to patients with primary open angle glaucoma. Retinal arteriolar and venular OS were significantly higher in eyes with more advanced visual field loss compared to normal eyes. We postulate that the increased OS of the retinal venules in glaucomatous eyes suggests reduced consumption within the retinal tissues. A trend of increasing OS within the retinal venules was associated with decreasing visual field sensitivities and increasing optic nerve head cupping and damage was observed in this study. However, the correlation was not statistically significant. To our knowledge, this is the first report of such findings and further research is required to support our results. Nonetheless, this study has provided a useful insight into the potential applications of retinal oximetry using spectral imaging in detecting glaucomatous damage and monitoring its progression.

Chapter 7: Summary and Future Work.

7.1. Summary

This thesis investigated the use of a hyperspectral fundus camera to measure the oxygen saturation (OS) of the retinal vasculature in humans. Initially, experiments were carried out to characterize the wavelengths of light emitted from the hyperspectral fundus camera. The results showed that the actual measured wavelength differed by several nanometres from the programmed wavelengths. Additionally, it was found that the difference between the measured and programmed wavelengths varied between imaging sessions. This was an important finding because the calculation of blood OS by photometric methods utilizes the extinction coefficient data of oxy- and deoxyhaemoglobin which is wavelength dependent. This finding contributed towards the modification of the OS algorithm which accounted for the difference between the measured and programmed wavelengths. The variability of the wavelengths emitted from the hyperspectral fundus camera provided a useful insight into the potential limitations of the fundus camera.

A subsequent experiment was performed which principally aimed at establishing the accuracy of our oximetry technique using a model eye. Whole arterial and venous human blood at varied measured OS were inserted into quartz tubes, placed within the model eye and imaged by the hyperspectral fundus camera using sequential wavelengths between 500 nm and 650 nm in 2 nm increments. Visible characteristic differences between arterial blood and venous blood (with low oxygen saturation) could be seen in the spectral images. This demonstrated that the hyperspectral fundus camera was capable of qualitatively detecting OS related differences in blood samples of varying oxygenation. The main steps in our oximetry technique were illustrated. The OS of the blood samples were calculated by our oximetry technique and compared to the gold standard measurement. We found that the accuracy of the OS calculation of the blood samples was reasonable and was not significantly influenced by the size of the quartz tube and the background reflectivity. We also found that at lower OS of blood, the oximetry technique had a tendency to overestimate the actual OS. We believed that this could have been attributed to by imperfections of our oximetry algorithm, in particular, the non-linear fitting to the optical density profiles. This overestimation of the true OS was comparable to previous studies. We believe that this overestimation of lower measured OS could have influenced the overall accuracy of the OS calculation.

Spectral images of the retina were acquired from normal subjects to determine whether our oximetry techniques could be applied to humans. The image processing and analysis techniques that were created in this research specifically for human retinal oximetry were illustrated. Visible characteristic features of the retinal arterioles and venules could be seen from the acquired spectral retinal images. These features were similar to that seen in the model eye and indicated that the differences in the OS of the retinal vasculature could be observed from the spectral retinal images. An important discovery was the effect of the choice of the optical density wavelength range on the accuracy of the OS calculation. We established that the wavelength range of 500 nm - 650 nm underestimated the OS in the retinal arterioles. Consequently, the wavelength range of the optical densities was changed to 556 nm – 650 nm for retinal oximetry calculations . This was determined to be an acceptable wavelength range. Our oximetry technique was used to generate pseudocolour oximetry maps of the retinal vasculature which was useful in providing an overview into the characteristic distribution of oxygen in the normal retinal vasculature. A more detailed examination of the oximetry technique was performed by evaluating the non-linear fitting of the oximetry model to the mean optical density profiles along segments of the retinal vessels. We found that the OS of the retinal venules in normal subjects were much lower than measurements reported in previous studies. We were able to support our findings by comparing the optical density profiles of the retinal venules of a normal subject to an interpolation of the published extinction coefficients of oxy- and deoxyhaemoglobin. We proposed that the OS calculation of the retinal venules in normal subjects using our oximetry technique was relatively more accurate and that it could reduce the possibility of overestimating the true OS of the retinal venules which may be inherent in other retinal oximetry systems. A new finding in our research which, to our knowledge, has never been previously reported relates to the observed and measured higher than anticipated oxygen saturation of the macular branches of the retinal venules. We were able to support our findings by demonstrating similarities between the optical density profiles of selected segments of the macular venules and the optical density profiles of the macular arterioles. We postulated that the higher than expected OS of the macular branches of the retinal venules could be explained by the collection of “un-used” oxygen in the venous system from an oxygen rich environment generated by both the choroidal and retinal supply of oxygen. However, there were a number of limitations of our study design and oximetry technique which requires further attention to confirm our findings.

Our subsequent studies involved evaluating whether the oximetry techniques were capable of detecting abnormal OS in the retinal vasculature in diseased eyes. Patients with retinal arterial and vein occlusions were imaged using the hyperspectral fundus camera. In patients with retinal arterial occlusion, we detected observable and measurable decreases in OS within selected retinal arterioles in regions of damaged retina. We proposed that the oxygen is lost either through diffusion into the surrounding vitreous, retina and/or consumption by the vessel walls. Additionally, in patients with retinal artery and vein occlusion we detected observable and measurable increased venular OS in selected vessels. This finding could be explained by the reduced consumption of oxygen in the damaged retina, shunting of arteriolar blood into the retinal venules or changes to the haemoglobin oxygen dissociation curve at the microvascular level. The study design involved a small cohort of patient and therefore further studies need to be performed to confirm our findings. Nonetheless, this study demonstrated that changes in the OS of the retinal arterioles and venules can be detected using our oximetry techniques.

The oximetry technique was subsequently applied to spectral images acquired from patients with primary open angle glaucoma, a common sight threatening condition which is thought to primarily cause damage to the ganglion cells located in the inner retina. We aimed to determine whether the oximetry technique was able to detect changes in the OS of the retinal vasculature. We found that the OS in the retinal venules were significantly higher in glaucomatous eye with more advanced visual field loss compared to normal subjects. Our finding was indirectly supported by reviewing the results of separate previously published peer-reviewed papers using the same dual wavelength retinal oximeter. We proposed that this finding, as with our cohort of patients with retinovascular occlusion, suggests reduced consumption of oxygen by damaged tissues in the retina. However, the main limitation of this study was the small sample size and further research is required to fully establish whether our oximetry techniques would be useful in the detection and monitoring of disease progression in glaucoma.

7.2. Future Work.

This thesis demonstrates that oxygen saturation measurements of the retinal vasculature can be performed using the described spectral imaging and image analysis techniques. Furthermore, our results suggest OS measurements of the retinal vasculature reflect the functional status of the retina and could be a potentially useful clinical tool to aid in the detection of ocular pathologies, such as glaucoma, and monitor its progression and response to treatment. It is hoped that this thesis would provide a framework for the direction of future research in this interesting and potentially useful topic.

The technical limitations have been addressed in detail in previous chapters. In relevance to its clinical applicability, the hyperspectral fundus camera and the oximetry techniques described are not suited for high volume imaging required for large scale population studies and use in a clinical setting. To achieve this, refinements to the imaging and analysis techniques needs to be addressed. A potential solution would be to implement multi-spectral imaging techniques without sacrificing the accuracy of the OS measurements. Currently, we are testing a snap-shot multispectral fundus camera which is capable of generating 8 registered spectral images of the fundus simultaneously which is achieved by using an Image Replicating Imaging Spectrometer system attached to a conventional fundus camera (Figure 7.1). The advantage is the rapid acquisition of retinal images (Figure 7.2) and generation of oximetry data with the omission of time-consuming processing steps such as image registration (Figure 7.3). Model eye experiments are being performed to validate the accuracy of a shortened number of wavelengths.

Figure 7.1: The multispectral fundus camera with the Image Replicating Imaging Spectrometer (IRIS) component attached to the viewing port of a fundus camera (*left*). The IRIS component functions by replicating a scene (retinal plane) into 8 images each image representing a defined wavelength.

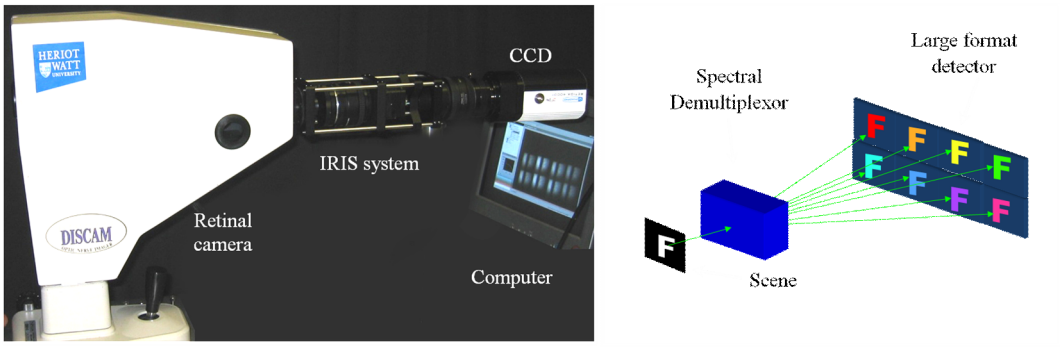

Figur

camer

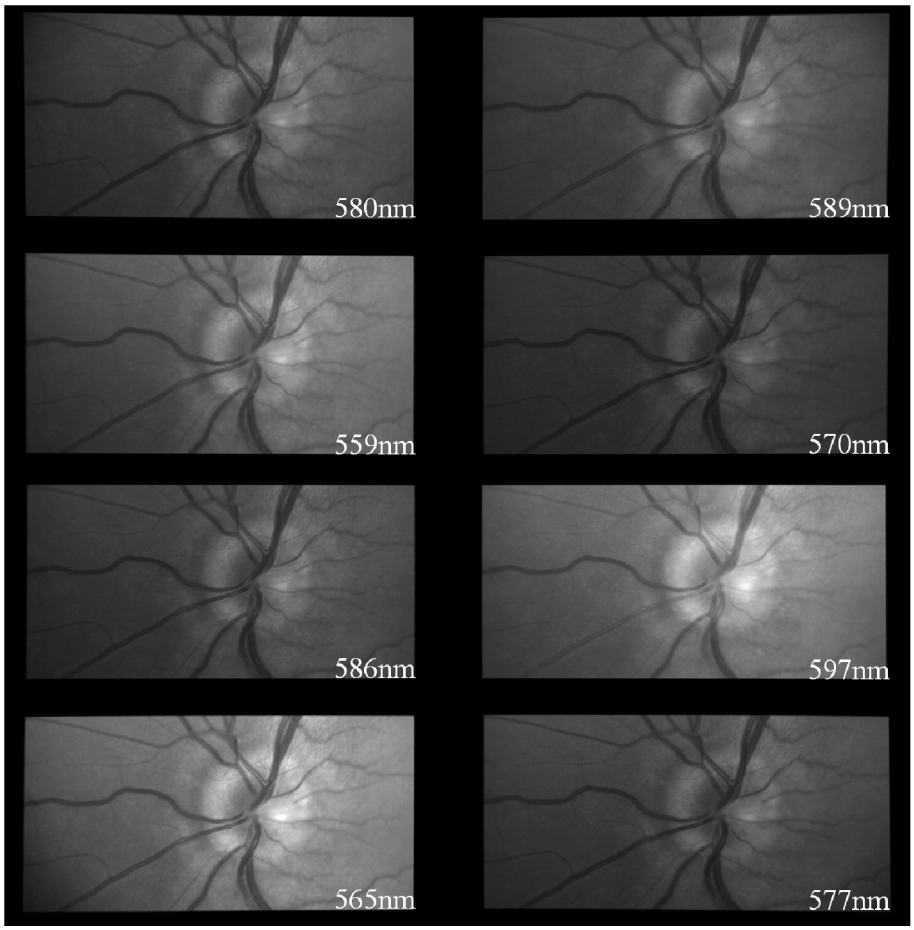

Figure 7.3: Oxygen saturation map of the retinal vasculature of a normal left retina. The oxygen saturation values are colour coded as shown in the scale bar to the right of the image.

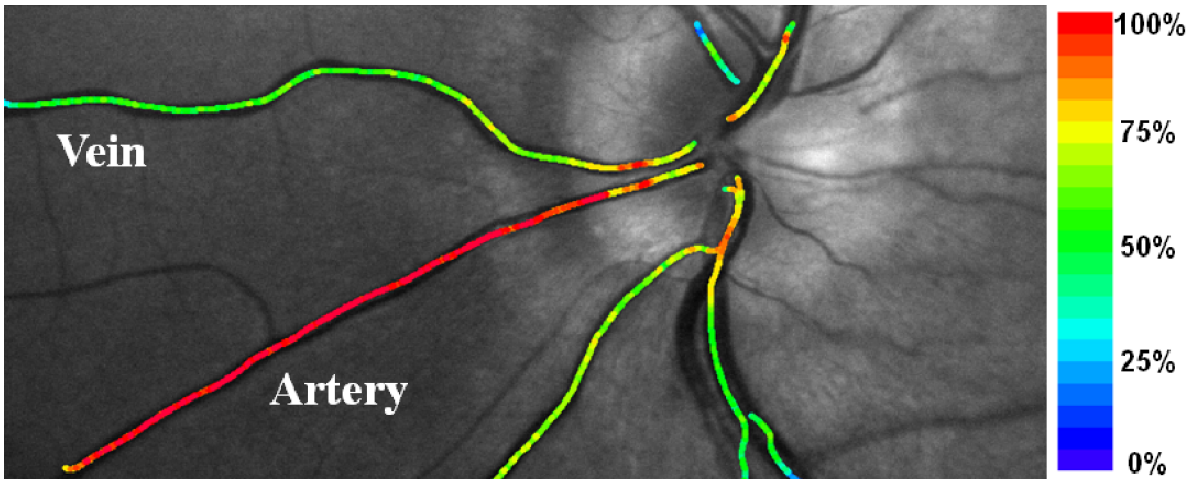

A further important aspect to retinal oximetry, which was alluded to in Chapter 6, is the requirement to explore a means to non-invasively measure the oxygen content within the tissues and capillaries. This can best be achieved using a snap-shot technique as the errors of misregistration are minimized. This would enable the characterization of oxygen distribution of in the whole retina in health and disease and provide a useful insight into the mechanisms of retinal pathologies. A different approach to the image analysis would need to be undertaken and is likely to involve the analysis of each voxel in the retinal image plane. This has been explored by our research group using a linear spectral unmixing approach and further research needs to be performed to determine the most accurate method of achieving tissue and capillary oximetry. Spectral analysis of each voxel in the image plane is particularly attractive because it has the potential of identifying other intracellular or extracellular chromophores, such as neuroglobin and cytochrome which could be a useful indicator of intracellular retinal function in severe sight-threatening ocular pathologies such as glaucoma, diabetic retinopathy and age-related macular degeneration.

Bibliography and References.

Abu-Amero K.K, Morales J, Bosley T.M. 2006. Mitochondrial abnormalities in patients with primary open-angle glaucoma. Invest Ophthalmol Vis Sci, 47: 2533-2541.

AGIS Investigators. 2000. The relationship between control of intraocular pressure and visual field deterioration. Am J Ophthalmol, 130: 429-440.

Alm A., 1992. Ocular circulation. In: Hart WM. ed. *Adler's physiology of the eye.* St Louis: Mosby-Year Book.

Alm A, Bill A. 1973. Ocular and optic nerve blood flow at normal and increased intraocular pressures in monkeys (Macaca irus): a study with radioactively labelled microspheres including flow determinations in brain and some other tissues. Exp Eye Res, 15(1): 15-29.

Alm A, Nilsson SF. 2009. Uveoscleral outflow--a review. Exp Eye Res, 88(4): 760-8.

Alvarado J, Murphy C, Juster R. 1984. Trabecular meshwork cellularity in primary open-angle glaucoma and nonglaucomatous normals. Ophthalmology, 91: 564-79.

Ames A III, Li YY, Heher EC, Kimble CR. 1992. Energy metabolism of rabbit retina as related to function: High cost of Na+ transport. J Neurosci, 12(3): 840–853.

Anderson DR, Hendrickson A. 1974. Effect of intraocular pressure on rapid axoplasmic transport in monkey optic nerve. Invest Ophthalmol Vis Sci, 13: 771-783.

Anderson NM, Sekelj P. 1967. Light-absorbing and scattering properties of nonhaemolysed blood. Phys. Med. Biol, 12: 173-184.

Andrews RM, Griffiths PG, Johnson MA, Turnbull DM. 1999. Histochemical localisation of mitochondrial enzyme activity in human optic nerve and retina. Br J Ophthalmol, 83(2): 231-5.

Aoyagi, T., Kishi, M., Yamaguchi, K., Watanabe, S., 1974. Improvement of the earpiece oximeter. Abstracts of the 13th annual meeting of the Japanese Society of Medical Electronics and Biological Engineering. Osaka.

Arimoto H, Furukawa H. 2007. Retinal blood oxygen saturation mapping by multispectral imaging and morphological angiography. Conf Proc IEEE Eng Med Biol Soc, 1627-30.

Artes PH, Iwase A, Ohno Y, Kitazawa Y, Chauhan BC. 2002. Properties of perimetric threshold estimates from Full Threshold, SITA Standard, and SITA Fast strategies. Invest Ophthalmol Vis Sci, 43(8): 2654-9.

Ashman RA, Reinholz F, Eikelboom RH. 2001. Oximetry with a multiple wavelength SLO. Int Ophthalmol, 23(4-6): 343-6.

Azuara-Blanco A, Katz LJ, Spaeth GL, Vernon SA, Spencer F, Lanzl IM. 2003. Clinical agreement among glaucoma experts in the detection of glaucomatous changes of the optic disk using simultaneous stereoscopic photographs. Am J Ophthalmol, 136: 949–50.

Ballerini L. 1997. Temporal matched filters for integration of ocular fundus images. Proc. IEEE Conf. Digital Signal Processing, 2: 1161–1164.

Bayer A, Harasymowycz P, Henderer JD, Steinmann WG, Spaeth GL. 2002. Validity of a new disk grading scale for estimating glaucomatous damage: correlation with visual field damage. Am J Ophthalmol, 133: 758–763.

Beach JM, Ning J, Khoobehi B. 2006. Hyperspectral Algorithm for Mapping Tissue Oxygen Saturation. Signal Processing Symposium. NORSIG 2006. Proceedings of the 7th Nordic, 142-145.

Beach JM, Schwenzer KJ, Srinivas S, Kim D, Tiedeman JS. 1999. Oximetry of retinal vessels by dual-wavelength imaging: calibration and influence of pigmentation. J Appl Physiol, 86(2): 748-58.

Bengtsson B, Heijl A. Evaluation of a new perimetric threshold strategy, SITA, in patients with manifest and suspect glaucoma. 1998. Acta Ophthalmol Scand, 76(3): 268-72.

Bill A, Sperber G, Ujiie K. 1983. Physiology of the choroidal vascular bed. Int Ophthalmol, 6(2): 101-7.

Birol G, Wang S, Budzynski E, Wangsa-Wirawan ND, Linsenmeier RA. 2007. Oxygen distribution and consumption in the macaque retina. Am J Physiol Heart Circ Physiol, 293(3): H1696 - H1704.

Bjärnhall G, Tomic L, Mishima HK, Tsukamoto H, Alm A. 2007. Retinal mean transit time in patients with primary open-angle glaucoma and normal-tension glaucoma. Acta Ophthalmol Scand, 85(1): 67-72.

Bland JM, Altman DG. 1986. Statistical methods for assessing agreement between 2 methods of clinical measurement. Lancet, 1: 307–310.

Blumenröder S, Augustin AJ, Koch FH. 1997. The influence of intraocular pressure and systemic oxygen tension on the intravascular pO2 of the pig retina as measured with phosphorescence imaging. Surv Ophthalmol, 42 Suppl 1: S118-26.

Blumenthal EZ, Sample PA, Berry CC, Lee AC, Girkin CA, Zangwill L, Caprioli J, Weinreb RN. 2003. Evaluating several sources of variability for standard and SWAP visual fields in glaucoma patients, suspects, and normals. Ophthalmology, 110(10): 1895-902.

Boardman JW. 1989. Inversion of imaging spectrometry data using singular value decomposition. Proceedings, IGARSS'89, 12th Canadian Symposium on Remote Sensing, 4: 2069-2072.

Boettner E, Wolter J. 1962. Transmission of the ocular media. Invest Ophthalmol Vis Sci, 1(6): 776-783.

Borja D, Manns F, Ho A, Ziebarth N, Rosen AM, Jain R, Amelinckx A, Arrieta E, Augusteyn RC, Parel JM. 2008. Optical power of the isolated human crystalline lens. Invest Ophthalmol Vis Sci, 49(6): 2541-8.

Briers JD, Fercher AF. 1982. Retinal blood-flow visualization by means of laser speckle photography. Invest Ophthalmol Vis Sci, 22: 255–259.

Bristow EA, Griffiths PG, Andrews RM, Johnson MA, Turnbull DM. 2002. The distribution of mitochondrial activity in relation to optic nerve structure. Arch Ophthalmol, 120(6): 791-6.

Brown JS, Flitcroft DI, Ying GS, Francis EL, Schmid GF, Quinn GE, Stone RA. 2009. In vivo human choroidal thickness measurements: evidence for diurnal fluctuations. Invest Ophthalmol Vis Sci, 50(1): 5-12.

Brown GC, Magaragal LE. 1982. Central retinal artery obstruction and visual acuity. Ophthalmology, 89: 14–19.

Brown GC, Magargal LE, Shields JA, Goldberg RE, Walsh PN. 1981. Retinal arterial obstruction in children and young adults. Ophthalmology, 88: 18–25.

Buhrmann RR, Quigley HA, Barron Y, West SK, Oliva MS, Mmbaga BB. 2000. Prevalence of glaucoma in a rural East African population. Invest Ophthalmol Vis Sci, 41: 40-48.

Bunce C, Wormald R. 2006. Leading causes of certification for blindness and partial sight in England & Wales. BMC Public Health, 6: 58.

Byrick RJ, Rose DK. 1990. Pathophysiology and prevention of acute renal failure: the role of the anaesthetist. Can J Anaesth, 37(4 Pt 1): 457-67.

Can A, Stewart CV, Roysam B, Tanenbaum HL. 2002. A feature based, robust, hierarchical algorithm for registering pairs of images of the curved human retina. IEEE Trans. Pattern Anal. Machine Intell, 24(3): 347–364.

Cancio LC, Batchinsky AI, Mansfield JR, Panasyuk S, Hetz K, Martini D, Jordan BS, Tracey B, Freeman JE. 2006. Hyperspectral imaging: a new approach to the diagnosis of hemorrhagic shock. J Trauma, 60(5): 1087-95.

Caprioli J, Coleman AL. 2010 Blood Flow in Glaucoma Discussion. Blood pressure, perfusion pressure, and glaucoma. Am J Ophthalmol. 2010 May;149(5):704-12

Caprioli J, Sears M, Miller JM. 1987. Patterns of early visual field loss in open-angle glaucoma. Am J Ophthalmol, 104(1): 98.

Carelli V, Ross-Cisneros FN, Sadun AA. 2004. Mitochondrial dysfunction as a cause of optic neuropathies. Progr Retin Eye Res, 23: 53-89.

Casson RJ, James B. 2006. Effect of cataract on frequency doubling perimetry in the screening mode. J Glaucoma, 15(1): 23-5.

Christoffersen NL, Larsen M. 1999. Pathophysiology and hemodynamics of branch retinal vein occlusion. Ophthalmology, 106: 2054–2062.

Chung HS, Harris A, Evans DW, Kagemann L, Garzozi HJ, Martin B. 1999. Vascular aspects in the pathophysiology of glaucomatous optic neuropathy. Surv Ophthalmol, 43(Suppl 1): S43-S50.

Chylack LT Jr, Wolfe JK, Singer DM, Leske MC, Bullimore MA, Bailey IL, Friend J, McCarthy D, Wu SY. 1993. The Lens Opacities Classification System III. The Longitudinal Study of Cataract Study Group. Arch Ophthalmol, 111(6): 831-6.

Cideciyan AV. 1995. Registration of ocular fundus images: An algorithm using cross-correlation of triple invariant image descriptors. IEEE Eng. Med. Biol. Mag, 14(1): 52–58.

Cioffi GA, Wang L, Fortune B, Cull G, Dong J, Bui B, Van Buskirk EM. 2004. Chronic ischemia induces regional axonal damage in experimental primate optic neuropathy. Arch Ophthalmol, 122: 1517-1525.

Clark AF, Miggans ST, Wilson K, Browder S, McCartney MD. 1995. Cytoskeletal changes in cultured human glaucoma trabecular meshwork cells. J Glaucoma, 4: 183-8.

Cohen AJ, Laing RA. 1976. Multiple scattering analysis of retinal blood oximetry. IEEE Trans Biomed Eng, 23(5): 391-400.

Collaborative Initial Normal-Tension Glaucoma Study Group. 1998a. Comparison of glaucomatous progression between untreated patients with normal-tension glaucoma and patients with therapeutically reduced intraocular pressures. Am J Ophthalmol, 126: 487–497.

Collaborative Initial Normal-Tension Glaucoma Study Group. 1998b. The effectiveness of intraocular pressure reduction in the treatment of normal-tension glaucoma. Am J Ophthalmol, 126: 498–505.

Comroe Jr JH, Botelho S. 1947. The unreliability of cyanosis in the recognition of arterial hypoxemia. Am J Med Sci, 214: 1.

Cordeiro MF, Guo L, Luong V, Harding G, Wang W, Jones HE, Moss SE, Sillito AM, Fitzke FW. 2004. Real-time imaging of single nerve cell apoptosis in retinal neurodegeneration. Proc Natl Acad Sci U S A, 101(36): 13352-6.

Costa VP, Arcieri ES, Harris A. 2009. Blood pressure and glaucoma. Br J Ophthalmol, 93(10): 1276-82.

Crittin M, Schmidt H, Riva CE. 2002. Hemoglobin oxygen saturation (So2) in the human ocular fundus measured by reflectance oximetry: preliminary data in retinal veins. Klin Monatsbl Augenheilkd, 219: 289–91.

Curcio CA, Allen KA. 1990. Topography of ganglion cells in human retina. J Comp Neurol, 300(1): 5-25.

Curcio CA, Sloan KR, Kalina RE, Hendrickson AE. 1990. Human photoreceptor topography. J. Comp Neurol, 22: 292(4): 497-523.

Curseifen C, Wisse M, Curseifen S, Junemann A, Martus P, Korth M. 2000. Migraine and tension headache in high-pressure and normal-pressure glaucoma. Am J Ophthalmol, 129: 102–4.

Dacey D, Peterson M. 1992. Dendritic field size and the morphology or midget and parasol retinal ganglion cell sof the human retina. Proc Natl Acad Sci, 89: 9666–70.

Dahrling BE. 1965. The histopathology of early central retinal artery occlusion. Arch Ophthalmol, 73: 506-10.

de Kock JP, Tarassenko L, Glynn CJ, Hill AR. 1993. Reflectance pulse oximetry measurements from the retinal fundus. IEEE Trans Biomed Eng, 40: 817–823.

Delgado MF, Nguyen NT, Cox TA, Singh K, Lee DA, Dueker DK, Fechtner RD, Juzych MS, Lin SC, Netland PA, Pastor SA, Schuman JS, Samples JR; American Academy of Ophthalmology. 2002. Ophthalmic Technology Assessment Committee 2001-2002 Glaucoma Panel. Automated perimetry: a report by the American Academy of Ophthalmology. Ophthalmology, 109(12): 2362-74.

Delori FC. 1988. Noninvasive technique for oximetry of blood in retinal vessels. Applied Optics, 27(6): 1113-1125.

Denninghoff KR, Smith MH. 2000. Optical model of the blood in large retinal vessels. J Biomed Opt, 5(4): 371-4.

Drabkin DL, Austin JH. 1935. Spectrophotometric studies. V. Technique for analysis of undiluted blood and concentrated hemoglobin solutions. J Biol Chem, 112: 105-115.

Drabkin DL, Schmidt CF. 1945. Observations of circulating blood in vivo, and the direct determination of the saturation of hemoglobin in arterial blood. J Biol Chem, 157: 69-83.

Drewes, J, Smith MH, Denninghoff KR, and Hillman LW. 1999. An instrument for the measurement of retinal vessel oxygen saturation. Optical Diagnostics of Biological Fluids IV. Proc SPIE, 3591: 114-120.

Dreyer EB, Zurakowski D, Schumer RA, Podos SM, Lipton SA. 1996. Elevated glutamate levels in the vitreous body of humans and monkeys with glaucoma. Arch Ophthalmol, 114: 299-305.

Duker, J., Weiter, J.J., 1991. Ocular circulation. In: W. Tasman, E.A. Jaeger, eds., *Duane's foundations of clinical ophthalmology*. New York: JB Lippincott.

Duker JS, Brown GC. 1989. Anterior location of the crossing artery in branch retinal vein obstruction. Arch Ophthalmol, 107: 998–1000.

Duong TQ, Ngan SC, Ugurbil K, Kim SG. 2002. Functional magnetic resonance imaging of the retina. Invest Ophthalmol Vis Sci, 43(4): 1176-81.

Ehinger B. 1966. Adrenergic nerves to the eye and to related structures in man and in the cynomolgus monkey (Macaca iris). Invest Ophthalmol Vis Sci, 5: 42-52.

Ernest JT. 1973. In vivo measurement of optic-disk oxygen tension. Invest Ophthalmol Vis Sci, 12(12): 927-31.

Ernest JT. 1974. Autoregulation of optic-disk oxygen tension. Invest Ophthalmol Vis Sci, 13(2): 101-6.

Falsini B, Riva CE, Logean E. 2002. Flicker-evoked changes in human optic nerve blood flow: relationship with retinal neural activity. Invest Ophthalmol Vis Sci, 43: 2309–2316.

Fatti I. 1977. Hydraulic flow conductivity of the vitreous gel. Invest Ophthalmol Vis Sci, 16(6): 565-8.

Faul F, Erdfelder E, Buchner A, Lang A.G. 2009. Statistical power analyses using G*Power 3.1: Tests for correlation and regression analyses. Behavior Research Methods, 41: 1149-1160.

Feke GT. 2006. Laser Doppler instrumentation for the measurement of retinal blood flow: theory and practice. Bull Soc Belge Ophtalmol, 302: 171–184.

Feke GT, Tagawa H, Deupree DM, Goger DG, Sebag J, Weiter JJ. 1989. Blood flow in the normal human retina. Invest Ophthalmol Vis Sci, 30(1): 58-65.

Ferguson, S.J., Nicholls, D., Ferguson, S., 2002. Bioenergetics. San Diego: Academic.

Ferreira SM, Lerner SF, Brunzini R, Evelson PA, Llesuy SF. 2004. Oxidative stress markers in aqueous humor of glaucoma patients. Am J Ophthalmol, 137: 62-69.

Findl O, Strenn K, Wolzt M, Menapace R, Vass C, Eichler HG, Schmetterer L. 1997. Effects of changes in intraocular pressure on human ocular haemodynamics. Curr Eye Res, 16(10): 1024-9.

Fitzgerald ME, Wildsoet CF, Reiner A. 2002. Temporal relationship of choroidal blood flow and thickness changes during recovery from form deprivation myopia in chicks. Exp Eye Res, 74(5): 561-70.

Flammer J. The vascular concept of glaucoma. 1994. Surv Ophthalmol, 38(Suppl): S3-S6.

Fontana L, Poinoosawmy D, Bunce CV, O'Brien C, Hitchings RA. 1998. Pulsatile ocular blood flow investigation in asymmetric normal tension glaucoma and normal subjects. Br J Ophthalmol, 82(7): 731-6.

Forrester, J.V., Dick, A.D., McMenamin, P.G., Lee, W.R.., 2002. Anatomy of the eye and orbit. In: J.V. Forrester, A.D. Dick, P.G. McMenamin, W.R. Lee, eds., *The eye: Basic sciences in practice*. London: WB Saunders.

Frangieh GT, Green WR, Barraquer-Somers E, Finkelstein D. 1982. Histopathologic study of nine branch retinal vein occlusions. Arch Ophthalmol, 100: 1132–1140.

Fraser S, Siriwardena D. 2002. Interventions for acute non-arteritic central retinal artery occlusion. Cochrane Database Syst Rev, CD001989.

Frayser R, Hickam JB. 1964. Retinal vascular response to breathing increased carbon dioxide and oxygen concentrations. Invest Ophthalmol Vis Sci, 3: 427-31.

Fuchsjäger-Mayrl G, Malec M, Polska E, Jilma B, Wolzt M, Schmetterer L. 2002. Effects of granulocyte colony stimulating factor on retinal leukocyte and erythrocyte flux in the human retina. Invest Ophthalmol Vis Sci, 43: 1520–1524.

Galassi F, Nuzzaci G, Sodi A, Casi P, Vielmo A. 1992 . Color Doppler imaging in evaluation of optic nerve blood supply in normal and glaucomatous subjects. Int Ophthalmol, 16(4-5): 273-6.

Gao H, Hollyfield JG. 1992. Aging of the human retina. Invest Ophthalmol Vis Sci, 33: 1–17.

Garcia-Valenzuela E, Gorczyca W, Darzynkiewicz Z, Sharma SC. 1994. Apoptosis in adult retinal ganglion cells after axotomy. J Neurobiol, 25(4): 431-8.

Garcia-Valenzuela E, Shareef S, Walsh J, Sharma SC. 1995. Programmed cell death of retinal ganglion cells during experimental glaucoma. Exp Eye Res, 61(1): 33-44.

Garway-Heath DF, Poinoosawmy D, Wollstein G, Viswanathan A, Kamal D, Fontana L, Hitchings RA. 1999. Inter- and intraobserver variation in the analysis of optic disc images: comparison of the Heidelberg retina tomograph and computer assisted planimetry. Br J Ophthalmol, 83(6): 664-9.

Gass A, Flammer J, Linder L, Romerio SC, Gasser P, Haefeli WE. 1997. Inverse correlation between endothelin-1-induced peripheral microvascular vasoconstriction and blood pressure in glaucoma patients. Graefes Arch Clin Exp Ophthalmol, 235: 634–8.

Gehlert S, Dawczynski J, Hammer M, Strobel J. 2010. Haemoglobin Oxygenation of Retinal Vessels in Branch Retinal Artery Occlusions over Time and Correlation with Clinical Outcome. Klin Monbl Augenheilkd, 227(12): 976-80.

Gherghel D, Griffiths HR, Hilton EJ. 2005. Systemic reduction in glutathione levels occurs in patients with primary open-angle glaucoma. Invest Ophthalmol Vis Sci, 46: 877-883.

Girkin CA, McGwin G, Jr, McNeal SF, Owsley C. 2006. Is there an association between pre-existing sleep apnoea and the development of glaucoma? Br J Ophthalmol, 90: 679–681.

Glovinsky Y, Quigley HA, Dunkelberger GR. 1991. Retinal ganglion cell loss is size dependent in experimental glaucoma. Invest Ophthalmol Vis Sci, 32: 484–491.

Glovinsky Y, Quigley HA, Pease ME. 1993. Foveal ganglion cell loss is size dependent in experimental glaucoma. Invest Ophthalmol Vis Sci, 34: 395–400.

Goebel W, Lieb WE, Ho A, Sergott RC, Farhoumand R, Grehn F. 1995. Color Doppler imaging: a new technique to assess orbital blood flow in patients with diabetic retinopathy. Invest Ophthalmol Vis Sc, 36(5): 864-70.

Goodacre R, Timmins EM, Burton R, Kaderbhai N, Woodward AM, Kell DB, Rooney PJ. 1998. Rapid identification of urinary tract infection bacteria using hyperspectral whole-organism fingerprinting and artificial neural networks. Microbiology, 144 (5): 1157-70.

Gordon MO, Beiser JA, Brandt JD, Heuer DK, Higginbotham EJ, Johnson CA, Keltner JL, Miller JP, Parrish RK 2nd, Wilson MR, Kass MA. 2002. The Ocular Hypertension Treatment Study: baseline factors that predict the onset of primary open-angle glaucoma. Arch Ophthalmol, 120: 714-720.

Greaney MJ, Hoffman DC, Garway-Heath DF, Nakla M, Coleman AL, Caprioli J. 2002. Comparison of optic nerve imaging methods to distinguish normal eyes from those with glaucoma. Invest Ophthalmol Vis Sci, 43: 140–5.

Green WR, Chan CC, Hutchins GM, Terry JM. 1981. Central retinal vein occlusion: A prospective histopathologic study of 29 eyes in 28 cases. Trans Am Ophthalmol Soc, 79: 371–422.

Greenman RL, Panasyuk S, Wang X, Lyons TE, Dinh T, Longoria L, Giurini JM, Freeman J, Khaodhiar L, Veves A. 2005. Early changes in the skin microcirculation and muscle metabolism of the diabetic foot. Lancet, 366(9498): 1711-7.

Grewal DS, Sehi M, Greenfield DS. 2009. Diffuse glaucomatous structural and functional damage in the hemifield without significant pattern loss. Arch Ophthalmol, 127(11): 1442-8.

Guglielmone R, Cantino D. 1982. Autonomic innervation of the ocular choroid membrane in the chicken: a fluorescence-histochemical and electron-microscopic study. Cell Tissue Res, 222(2): 417-31.

Guo L, Moss SE, Alexander RA, Ali RR, Fitzke FW, Cordeiro MF. 2005. Retinal ganglion cell apoptosis in glaucoma is related to intraocular pressure and IOP-induced effects on extracellular matrix. Invest Ophthalmol Vis Sci, 46(1): 175-82.

Guo L, Normando EM, Nizari S, Lara D, Cordeiro MF. 2010. Tracking Longitudinal Retinal Changes in Experimental Ocular Hypertension Using the cSLO and Spectral Domain-OCT. Invest Ophthalmol Vis Sci, 51(12): 6504-13.

Gutman FA, Zegarra H, Zakov ZN. 1974. The natural course of temporal retinal vein occlusion. Trans Am Acad Opthalmol Otolaryngol, 78: 178–192.

Guyton, A.C., Hall, J.E., 2006. Textbook of Medical Physiology. Philadelphia: Elsevier-Saunders.

Hammer M, Leistritz S, Leistritz L, Schweitzer D. 2001. Light paths in retinal vessel oxymetry. IEEE Trans Biomed Eng, 48(5): 592-8.

Hammer M, Thamm E, Schweitzer D. 2002. A simple algorithm for in vivo ocular fundus oximetry compensating for non-haemoglobin absorption and scattering. Phys. Med. Biol, 47: N233-N238.

Hammer M, Vilser W, Riemer T, Mandecka A, Schweitzer D, Kühn U, Dawczynski J, Liemt F, Strobel J. 2009. Diabetic patients with retinopathy show increased retinal venous oxygen saturation. Graefes Arch Clin Exp Ophthalmol, 247(8): 1025-30.

Hammer M, Vilser W, Riemer T, Schweitzer D. 2008. Retinal vessel oximetry-calibration, compensation for vessel diameter and fundus pigmentation, and reproducibility. J Biomed Opt, 13(5): 054015.

Hardarson SH, Basit S, Jonsdottir TE, Eysteinsson T, Halldorsson GH, Karlsson RA, Beach JM, Benediktsson JA, Stefansson E. 2009. Oxygen saturation in human retinal vessels is higher in dark than in light. Invest Ophthalmol Vis Sci, 50(5): 2308-11.

Hardarson SH, Gottfredsdottir MS, Halldorsson GH, Karlsson RA, Benediktsson JA, Eysteinsson T, Beach JM, Harris A, Stefansson E. 2009. Glaucoma filtration surgery and retinal oxygen saturation. Invest Ophthalmol Vis Sci, 50(11): 5247-50.

Hardarson SH, Harris A, Karlsson RA, Halldorsson GH, Kagemann L, Rechtman E, Zoega GM, Eysteinsson T, Benediktsson JA, Thorsteinsson A, Jensen PK, Beach J, Stefánsson E. 2006. Automatic retinal oximetry. Invest Ophthalmol Vis Sci, 47(11): 5011-6.

Hardarson SH, Stefánsson E. 2010. Oxygen Saturation in Central Retinal Vein Occlusion. Am J Ophthalmol, 150(6): 871.

Harman A, Abrahams B, Moore S, Hoskins R. 2000. Neuronal density in the human retinal ganglion cell layer from 16-77 years. Anat Rec, 260(2): 124-31.

Harris A, Joos K, Kay M, Evans D, Shetty R, Sponsel WE, Martin B. 1996. Acute IOP elevation with scleral suction: effects on retrobulbar haemodynamics. Br J Ophthalmol, 80: 1055–1059.

Harwerth RS, Crawford ML, Frishman LJ, Viswanathan S, Smith EL 3rd, Carter-Dawson L. 2002. Visual field defects and neural losses from experimental glaucoma. Prog Retin Eye Res, 21(1): 91-125.

Harwerth RS, Wheat JL, Rangaswamy NV. 2008. Age-related losses of retinal ganglion cells and axons. Invest Ophthalmol Vis Sci, 49(10): 4437-43.

Hayreh SS. 1962. The ophthalmic artery, Part III. Branches. Br J Ophthalmol, 46: 212-247.

Hayreh SS. 1985. Inter-individual variation in blood supply of the optic nerve head. Its importance in various ischemic disorders of the optic nerve head, and glaucoma, low-tension glaucoma and allied disorders. Documenta Ophthalmol, 59: 217-246.

Hayreh SS. 1994. Retinal vein occlusion. Indian J Ophthalmol, 42: 109–132.

Hayreh SS, Kolder HE, Weingeist TA. 1980. Central retinal artery occlusion and retinal tolerance time. Ophthalmology, 87: 75–78.

Hayreh SS, Rojas P, Podhajsky P, Montague P, Woolson RF. 1983. Ocular neovascularization with retinal vascular occlusion-III. Incidence of ocular neovascularization with retinal vein occlusion. Ophthalmology, 90: 488–506.

Hayreh SS, Zimmerman MB, Kimura A, Sanon A. 2004. Central retinal artery occlusion. Retinal survival time. Exp Eye Res, 78(3): 723-36.

Hayreh SS, Zimmerman MB, Podhajsky P, Alward WL. 1994. Nocturnal arterial hypotension and its role in optic nerve head and ocular ischemic disorders. Am J Ophthalmol, 117: 603–624.

Heijl A, Leske MC, Bengtsson B, Hyman L, Bengtsson B, Hussein M; Early Manifest Glaucoma Trial Group. 2002. Reduction of intraocular pressure and glaucoma progression: results from the Early Manifest Glaucoma Trial. Arch Ophthalmol, 120: 1268-1279.

Henne J, Pöttering S, Jeserich G. 2000. Voltage-gated potassium channels in retinal ganglion cells of trout: a combined biophysical, pharmacological, and single-cell RT-PCR approach. J Neurosci Res, 62(5): 629-37.

Hickam JB, Frayser R. 1949. Spectrophotometric determination of blood oxygen. J Biol Chem, 180(1): 457-65.

Hickam JB, Frayser R, Ross JC. 1963. A study of retinal venous blood oxygen saturation in human subjects by photographic means. Circulation, 27: 375-85.

Hirohara Y, OKawa Y , Mihashi T , Yamaguchi T , Nakazawa N , Tsuruga Y , Aoki H , Maeda N , Uchida I, Fujikado T. 2007. Validity of retinal oxygen saturation analysis: Hyperspectral imaging in visible wavelength with fundus camera and liquid crystal wavelength tunable filter. Opt Rev, 14(3): 151-158.

Hitchings RA. 2000. Selective ganglion cell death in glaucoma. Br J Ophthalmol, 84: 678–679.

Hogan MJ, Alvarado JA, Weddell JE. 1971. Histology of the Human Eye, an Atlas and Textbook. Philadelphia: WB Saunders.

Huebschman ML, Schultz RA, Garner HR. 2002. Characteristics and capabilities of the hyperspectral imaging microscope. IEEE Eng Med Biol Mag, 21(4): 104-17.

Hung L, Wallman J, Smith ER. 2000. Vision-dependent changes in the choroidal thickness of macaque monkeys. Invest Ophthalmol Vis Sci, 41: 1259–1269.

Iester M, Mikelberg FS, Courtright P, Burk RO, Caprioli J, Jonas JB, Weinreb RN, Zangwill L. 2001. Interobserver variability of optic disk variables measured by confocal scanning laser tomography. Am J Ophthalmol, 132(1): 57-62.

Ito M, Murayama K, Deguchi T, Takasu M, Gil T, Araie M, Peyman G, Yoneya S. 2008. Oxygen saturation levels in the juxta-papillary retina in eyes with glaucoma. Exp Eye Res, 86(3): 512-8.

Iwabe S, Lamas M, Vásquez Pélaez CG, Carrasco FG. 2010. Aqueous humor endothelin-1 (Et-1), vascular endothelial growth factor (VEGF) and cyclooxygenase-2 (COX-2) levels in Mexican glaucomatous patients. Curr Eye Res, 35(4): 287-94.

Jampel HD, Friedman D, Quigley H, Vitale S, Miller R, Knezevich F, Ding Y. 2009. Agreement among glaucoma specialists in assessing progressive disc changes from photographs in open-angle glaucoma patients. Am J Ophthalmol, 147: 39–44.

Janssen FJ. 1972. A study of the absorption and scattering factors of light in whole blood. Med. & Biol. Eng, 10: 231-240.

Janssen MC, den Heijer M, Cruysberg JR, Wollersheim H, Bredie SJ. 2005. Retinal vein occlusion: a form of venous thrombosis or a complication of atherosclerosis? A meta-analysis of thrombophilic factors. Thromb Haemost, 93(6): 1021-6.

Janssen P, Naskar R, Moore S, Thanos S, Thiel H. 1996. Evidence for glaucoma-induced horizontal cell alterations in the human retina. Ger J Ophthalmol, 5: 378 –385.

Joachim SC, Pfeiffer N, Grus FH. 2005. Autoantibodies in patients with glaucoma: a comparison of IgG serum antibodies against retinal, optic nerve, and optic nerve head antigens. Graefes Arch Clin Exp Ophthalmol, 243: 817-823.

Johnson CC. 1970. Near infrared propagation in blood. J Ass Adv Med Instr, 4: 22-27.

Johnson EC, Deppmeier LM, Wentzien SK. 2000. Chronology of optic nerve head and retinal responses to elevated intraocular pressure. Invest Ophthalmol Vis Sci, 41: 431-442.

Johnson WR, Wilson DW, Fink W, Humayun M, Bearman G. 2007. Snapshot hyperspectral imaging in ophthalmology. J Biomed Opt, 12(1): 014036.

Jones CE, Atchison DA, Meder R, Pope JM. 2005. Refractive index distribution and optical properties of the isolated human lens measured using magnetic resonance imaging (MRI). Vision Res, 45(18): 2352–2366.

Justice J, Lehmann RP. 1976. Cilioretinal arteries. A study based on review of stereo fundus photographs and fluorescein angiographic findings. Arch Ophthalmol, 94(8): 1355-8.

Kagemann L, Wollstein G, Wojtkowski M, Ishikawa H, Townsend KA, Gabriele ML, Srinivasan VJ, Fujimoto JG, Schuman JS. 2007. Spectral oximetry assessed with high-speed ultra-high-resolution optical coherence tomography. J Biomed Opt, 12(4): 041212.

Kanamori A, Nagai-Kusuhara A, Escano MF, Maeda H, Nakamura M, Negi A. 2006. Comparison of confocal scanning laser ophthalmoscopy, scanning laser polarimetry and optical coherence tomography to discriminate ocular hypertension and glaucoma at an early stage. Graefes Arch Clin Exp Ophthalmol, 244: 58–68.

Kass MA, Heuer DK, Higginbotham EJ, Johnson CA, Keltner JL, Miller JP, Parrish RK 2nd, Wilson MR, Gordon MO. 2002. The Ocular Hypertension Treatment Study: a randomized trial determines that topical ocular hypotensive medication delays or prevents the onset of primary open-angle glaucoma. Arch Ophthalmol, 120(6): 701–713.

Keltner JL, Johnson CA, Levine RA, Fan J, Cello KE, Kass MA, Gordon MO. 2005. Normal visual field test results following glaucomatous visual field end points in the Ocular Hypertension Treatment Study. Arch Ophthalmol, 123(9): 1201-6.

Kerrigan LA, Zack DJ, Quigley HA, Smith SD, Pease ME. 1997. TUNEL-positive ganglion cells in human primary open-angle glaucoma. Arch Ophthalmol, 115(8): 1031-5.

Khoobehi B, Beach JM, Kawano H. 2004. Hyperspectral imaging for measurement of oxygen saturation in the optic nerve head. Invest Ophthalmol Vis Sci, 45(5): 1464-72.

Klein R, Klein BE, Moss SE, Meuer SM. 2000. The epidemiology of retinal vein occlusion: The Beaver Dam Eye Study. Trans Am Ophthalmol Soc, 98: 133–141.

Kramer K, ElamJO, Saxton GA, Elam WN Jr. 1951. Influence of oxygen saturation, erythrocyte concentration and optical depth upon the red and near-infrared light transmittance of whole blood. Am J Physiol, 165: 229-246.

Kremmer S, Kreuzfelder E, Klein R, Bontke N, Henneberg-Quester KB, Steuhl KP, Grosse-Wilde H. 2001. Antiphosphatidylserine antibodies are elevated in normal tension glaucoma. Clin Exp Immunol, 125: 211-215.

Kubelka P, Munk F. 1931. Ein Betrag zur Optik der Farbanstriche. Z. Techn. Phys, 12: 593-601.

Kuhli-Hattenbach C, Scharrer I, Lüchtenberg M, Hattenbach LO. 2010. Coagulation disorders and the risk of retinal vein occlusion. Thromb Haemost, 103(2): 299-305.

la Cour M, Kiilgaard JF, Eysteinsson T, Wiencke AK, Bang K, Dollerup J, Jensen PK, Stefánsson E. 2000. Optic nerve oxygen tension: effects of intraocular pressure and dorzolamide. Br J Ophthalmol, 84(9): 1045-9.

Laing RA, Cohen AJ, Friedman E. 1975. Photographic measurements of retinal blood oxygen saturation: falling saturation rabbit experiments. Invest Ophthalmol Vis Sci, 14(8): 606–610.

Lampert PW, Vogel MH, Zimmerman LE. 1968. Pathology of the optic nerve in experimental acute glaucoma: electron microscopic studies. Invest Ophthalmol Vis Sci, 7: 199-213.

Lei Y, Garrahan N, Hermann B, Becker DL, Hernandez MR, Boulton ME, Morgan JE. 2008. Quantification of retinal transneuronal degeneration in human glaucoma: a novel multiphoton-DAPI approach. Invest Ophthalmol Vis Sci, 49: 1940–1945.

Leskea MC, Heijl A, Hyman L, Bengtsson B, Komaroff E. 2003. Factors for glaucoma progression and the effect of treatment: the Early Manifest Glaucoma Trial. Arch Ophthalmol, 121(1): 48–56.

Levkovitch-Verbin H, Martin KR, Quigley HA, Baumrind LA, Pease ME, Valenta D. 2002. Measurement of amino acid levels in the vitreous humor of rats after chronic intraocular pressure elevation or optic nerve transection. J Glaucoma, 11: 396-405.

Li H, Chutatape O. 2004. Automated feature extraction in color retinal images by a model based approach. IEEE Trans. Biomed. Eng, 51(2): 246–254.

Lichter PR, Musch DC, Gillespie BW, Guire KE, Janz NK, Wren PA, Mills RP; CIGTS Study Group. 2001. Interim clinical outcomes in the Collaborative Initial Glaucoma Treatment Study comparing initial treatment randomized to medications or surgery. Ophthalmology, 108(11): 1943–1953.

Linsenmeier RA, Braun RD. 1992. Oxygen distribution and consumption in the cat retina during normoxia and hypoxemia. J Gen Physiol, 99(2): 177-97.

Linsenmeier RA, Goldstick TK, Blum RS, Enroth-Cugell C. 1981. Estimation of retinal oxygen transients from measurements made in the vitreous humor. Exp Eye Res, 32(4): 369-79.

Lipton S.A. 2003. Possible role for memantine in protecting retinal ganglion cells from glaucomatous damage. Surv Ophthalmol, 48(1): S38-S46.

Lo LW, Koch CJ, Wilson DF. 1996. Calibration of oxygen-dependent quenching of the phosphorescence of Pd-meso-tetra [4-carboxylphenyl] porphine: A phosphor with general application for measuring oxygen concentration in biological systems. Anal. Biochem, 236: 153-160.

Loewinger E, Gordon A, Weinreb A, Gross J. 1964. Analysis of a micromethod for transmission oximetry of whole blood. J Appl Physiol, 19: 1179-1184.

Longini RL, Zdrojkowski R. 1968. A note on the theory of backscattering of light by living tissue. IEEE Trans. Biomed. Eng, BME-15: 4-10.

Lloret D, Serrat J, Lopez AM, Soler A, Villaneuva JJ. 2000. Retinal image registration using creases as anatomical landmarks. IEEE Proc. Int. Conf. Pattern Recognition, 3: 203–206.

Lyot, B., 1933. Optical apparatus with wide field using interference of polarized light. C. R. Acad. Sci: Paris.

Maes F, Collignon A, Vandermeulen D, Marchal G, Suetens P. 1997. Multimodality image registration by maximization of mutual information. IEEE Trans. Med. Imag, 16(2): 187–198.

Marr D, Hildreth E. 1980. Theory of edge detection. Proc R Soc Lond B Biol Sci, 207(1167): 187-217.

Martin ME, Wabuyele MB, Chen K, Kasili P, Panjehpour M, Phan M, Overholt B, Cunningham G, Wilson D, Denovo RC, Vo-Dinh T. 2006. Development of an Advanced Hyperspectral Imaging (HSI) System with Applications for Cancer Detection. Ann Biomed Eng, 34(6): 1061-8.

Marx G, Reinhart K. 2006. Venous oximetry. Curr Opin Crit Care, 12(3): 263-8.

Masland RH. 1996. Processing and encoding of visual information in the retina. Curr Opin Neurobiol, 6: 467-74.

Matsopoulos G, Mouravliansky N, Delibasis K, Nikita K. 1999. Automatic retinal image registration scheme using global optimization techniques. IEEE Trans. Inform. Technol. Biomed, 3(1): 47–60.

Matthes K, Gross F. 1939a. Untersuchungen fiber die Absorption yon rotem und ultraotem Licht durch kohlenoxydgesittigtes und reduziertes Blut. Arch Exp Pathol Pharmacol, 191: 369-380.

Matthes K, Gross F. 1939b. Fortlaufende Registrierung der Lichtabsorption des Blutes in zwei verschiedenen pektralbezirken. Arch Exp Pathol Pharmacol, 191: 381-390.

McNaught AI, Allen JG, Healey DL, McCartney PJ, Coote MA, Wong TL, Craig JE, Green CM, Rait JL, Mackey DA. 2000. Accuracy and implications of a reported family history of glaucoma: experience from the Glaucoma Inheritance Study in Tasmania. Arch Ophthalmol, 118: 900-904.

Medeiros FA, Zangwill LM, Bowd C, Weinreb RN. 2004. Comparison of the GDx VCC scanning laser polarimeter, HRT II confocal scanning laser ophthalmoscope, and stratus OCT optical coherence tomograph for the detection of glaucoma. Arch Ophthalmol, 122: 827–37.

Meinke M, Müller G, Helfmann J, Friebel M. 2007. Empirical model functions to calculate hematocrit-dependent optical properties of human blood. Applied Optics, 46(10): 1742-53.

Michels RG, Gass JDM. 1974. Natural course of temporal retinal branch occlusion. Trans Am Acad Ophthalmol Otolaryngol, 78: 166–177.

Michelson G, Scibor M. 2006. Intravascular oxygen saturation in retinal vessels in normal subjects and open-angle glaucoma subjects. Acta Ophthalmol. Scand, 84: 89–295.

Miglior S, Albé E, Guareschi M, Rossetti L, Orzalesi N. 2002. Intraobserver and interobserver reproducibility in the evaluation of optic disc stereometric parameters by Heidelberg Retina Tomograph. Ophthalmology, 109(6): 1072-7.

Minckler DS, Tso MO, Zimmerman LE. 1976. A light microscopic, autoradiographic study of axoplasmic transport in the optic nerve head during ocular hypotony, increased intraocular pressure, and papilledema. Am J Ophthalmol, 82: 741-757.

Mitchell P, Hourihan F, Sandbach J, Wang JJ. 1999. The relationship between glaucoma and myopia: the Blue Mountains Eye Study. Ophthalmology, 106: 2010-2015.

Mitchell P, Smith W, Chang A. 1996. Prevalence and associations of retinal vein occlusion in Australia. The Blue Mountains Eye Study. Arch Ophthalmol, 114: 1243–1247.

Morgan JE, Datta AV, Erichsen JT, Albon J, Boulton ME. 2006. Retinal ganglion cell remodelling in experimental glaucoma. Adv Exp Med Biol, 572: 397–402.

Morgan JE, Jeffery G, Foss AJ. 1998. Axon deviation in the human lamina cribrosa. Br J Ophthalmol, 82(6): 680-3.

Morgan JE, Sheen NJ, North RV, Goyal R, Morgan S, Ansari E, Wild JM. 2005. Discrimination of glaucomatous optic neuropathy by digital stereoscopic analysis. Ophthalmology, 112(5): 855-62.

Morgan JE, Uchida H, Caprioli J. 2000. Retinal ganglion cell death in experimental glaucoma. Br J Ophthalmol, 84: 303–310.

Muqit MM, Denniss J, Nourrit V, Marcellino GR, Henson DB, Schiessl I, Stanga PE. 2010. Spatial and Spectral Imaging of Retinal Laser Photocoagulation Burns. Invest Ophthalmol Vis Sci. 2010 Sep 22. [Epub ahead of print]

Nelson DA, Krupsky S, Pollack A, Aloni E, Belkin M, Vanzetta I, Rosner M, Grinvald A. 2005. Special report: Noninvasive multi-parameter functional optical imaging of the eye. Ophthalmic Surg Lasers Imaging, 36(1): 57-66.

Nickla D, Wildsoet C, Wallman J. 1998. The circadian rhythm in intraocular pressure and its relation to diurnal ocular growth changes in chicks. Exp Eye Res, 66: 183–193.

Nickla D, Wildsoet C, Troilo D. 2002. Diurnal rhythms in intraocular pressure, axial length, and choroidal thickness in a primate model of eye growth, the common marmoset. Invest Ophthalmol Vis Sci, 43: 2519–2528.

Nork TM, Ver Hoeve JN, Poulsen GL, Nickells RW, Davis MD, Weber AJ, Vaegan, Sarks SH, Lemley HL, Millecchia LL. 2000. Swelling and loss of photoreceptors in chronic human and experimental glaucomas. Arch Ophthalmol, 118: 235–245

North RV, Jones AL, Drasdo N, Wild JM, Morgan JE. 2010. Electrophysiological evidence of early functional damage in glaucoma and ocular hypertension. Invest Ophthalmol Vis Sci, 51(2): 1216-22.

Nuffer LL, Medvick PA, Foote HP, Solinsky JC. 2006. Multispectral/hyperspectral image enhancement for biological cell analysis. Cytometry A, 69(8): 897-903.

O'Brien C, Butt Z. 1999. Blood flow velocity in the peripheral circulation of glaucoma patients. Ophthalmologica, 213: 150–3.

Okawa H, Sampath AP, Laughlin SB, Fain GL. 2008. ATP consumption by mammalian rod photoreceptors in darkness and in light. Curr Biol, 18(24): 1917–1921.

Okisaka S, Murakami A, Mizukawa A, Ito J. 1997. Apoptosis in retinal ganglion cell decrease in human glaucomatous eyes. Jap J Ophthalmol, 41: 84-88.

Olver JM, Spalton DJ, McCartney AC. 1990. Microvascular study of the retrolaminar optic nerve in man: the possible significance in anterior ischaemic optic neuropathy. Eye, 4 (Pt 1): 7-24.

Onda E, Cioffi GA, Bacon DR, Van Buskirk EM. 1995. Microvasculature of the human optic nerve. Am J Ophthalmol,120(1): 92-102.

Osborne NN. 2008. Pathogenesis of ganglion "cell death" in glaucoma and neuroprotection: focus on ganglion cell axonal mitochondria. Prog Brain Res, 173: 339-52.

Osborne NN, Melena J, Chidlow G, Wood JP. 2001. A hypothesis to explain ganglion cell death caused by vascular insults at the optic nerve head: possible implication for the treatment of glaucoma. Br J Ophthalmol, 85: 1252-1259.

Panda S, Jonas JB. 1992. Decreased photoreceptor count in human eyes with secondary angle-closure glaucoma. Invest Ophthalmol Vis Sci. 33: 2532-2536.

Pang IH, Johnson EC, Jia L, Cepurna WO, Shepard AR, Hellberg MR, Clark AF, Morrison JC. 2005. Evaluation of inducible nitric oxide synthase in glaucomatous optic neuropathy and pressure-induced optic nerve damage. Invest Ophthalmol Vis Sci, 46: 1313-1321.

Pease ME, McKinnon SJ, Quigley HA, Kerrigan-Baumrind LA, Zack DJ. 2000. Obstructed axonal transport of BDNF and its receptor TrkB in experimental glaucoma. Invest Ophthalmol Vis Sci, 41: 764-774.

Pedersen DB, Koch Jensen P, la Cour M, Kiilgaard JF, Eysteinsson T, Bang K, Wiencke AK, Stefánsson E. 2005. Carbonic anhydrase inhibition increases retinal oxygen tension and dilates retinal vessels. Graefes Arch Clin Exp Ophthalmol, 243(2): 163-8.

Perry V, Cowey A. 1985. The ganglion cell and cone distributions in the monkey's retina: implications for central magnification factors. Vis Res, 25: 1795–810.

Pillunat LE, Anderson DR, Knighton RW, Joos KM, Feuer WJ. 1997. Autoregulation of human optic nerve head circulation in response to increased intraocular pressure. Exp Eye Res, 64(5): 737-44.

Pittman RN, Duling BR. 1975a. A new method for the measurement of percent oxyhemoglobin. J Appl Physiol, 38(2): 315-20.

Pittman RN, Duling BR. 1975b. Measurement of percent oxyhemoglobin in the microvasculature. J Appl Phys, 38(2): 321-327.

Porciatti V. 2006. Pattern electroretinogram in glaucoma. Curr Opin Ophthalmol, 17(2): 196-202.

Quigley HA, Addicks EM. 1981. Chronic experimental glaucoma in primates, II: effect of extended intraocular pressure elevation on optic nerve head and axonal transport. Invest Ophthalmol Vis Sci, 19: 137–152.

Quigley HA, Addicks EM, Green WR, Maumenee AE. 1981. Optic nerve damage in human glaucoma. II. The site of injury and susceptibility to damage. Arch Ophthalmol, 99: 635–649.

Quigley HA, Broman AT. 2006. The number of people with glaucoma worldwide in 2010 and 2020. Br J Ophthalmol, 90(3): 262-7.

Quigley HA, McKinnon SJ, Zack DJ, Pease ME, Kerrigan-Baumrind LA, Kerrigan DF, Mitchell RS. 2000. Retrograde axonal transport of BDNF in retinal ganglion cells is blocked by acute IOP elevation in rats. Invest Ophthalmol Vis Sci, 41: 3460-3466.

Quigley HA, Nickells RW, Kerrigan LA, Pease ME, Thibault DJ, Zack DJ. 1995. Retinal ganglion cell death in experimental glaucoma and after axotomy occurs by apoptosis. Invest Ophthalmol Vis Sci, 36: 774–86

Quigley HA, Sanchez RM, Dunkelberger GR, L'Hernault NL, Baginski TA. 1987. Chronic glaucoma selectively damages large optic nerve fibers. Invest Ophthalmol Vis Sci, 28: 913–920.

Quinlan PM, Elman MJ, Bhatt AK, Mardesich P, Enger C. 1990. The natural course of central retinal vein occlusion. Am J Ophthalmo, 110: 118–123.

Radius RL, Anderson DR. 1981. Morphology of axonal transport abnormalities in primate eyes. Br J Ophthalmol, 65(11): 767-77.

Radius RL, Pederson JE. 1984. Laser-induced primate glaucoma. II. Histopathology. Arch Ophthalmol, 102(11): 1693-8.

Ramella-Roman J, Mathews SA. 2007. Spectroscopic Measurements of Oxygen Saturation in the Retina. IEEE Journal of Selected Topics in Quantum Electronics, 13(6): 1697-1703.

Ramella-Roman JC, Mathews SA, Kandimalla H, Nabili A, Duncan DD, D'Anna SA, Shah SM, Nguyen QD. 2008. Measurement of oxygen saturation in the retina with a spectroscopic sensitive multi aperture camera. Opt Express, 28; 16(9): 6170-82.

Raz D, Perlman I, Percicot CL, Lambrou GN, Ofri R. 2003. Functional damage to inner and outer retinal cells in experimental glaucoma. Invest Ophthalmol Vis Sci, 44(8): 3675-84.

Reinhart, K., 1989. Monitoring O2 transport and tissue oxygenation in critically ill patients. In: K. Reinhart and K. Eyrich, eds., *Clinical aspects of O2 transport and tissue oxygenation*. Berlin, Heidelberg: Springer.

Remington, L., 1998. Ocular embryology. In: L. Remington, eds., *Clinical Anatomy of the Visual System*. Oxford: Butterworth-Heinemann.

Remky A, Arend O, Jung F, Kiesewetter H, Reim M, Wolf S. 1996. Haemorheology in patients with branch retinal vein occlusion with and without risk factors. Graefes Arch Clin Exp Ophthalmol, 234 Suppl 1: S8-12.

Ritter N, Owens R, Cooper J, Eikelboom R, Van Saarloos P. 1999. Registration of stereo and temporal images of the retina. IEEE Trans. Med. Imag, 18(5): 404–418.

Riva CE, Falsini B. 2008. Functional laser Doppler flowmetry of the optic nerve: physiological aspects and clinical applications. Prog Brain Res, 173: 149–163.

Rivers EP, Rady MY, Martin GB, Fenn NM, Smithline HA, Alexander ME, Nowak RM. 1992. Venous hyperoxia after cardiac arrest. Characterization of a defect in systemic oxygen utilization. Chest, 102: 1787-1793.

Roh, S., Weiter, J.J., 2008. Retina and vitreous: Basic science: Retinal and choroidal circulation. In: M. Yanoff, J.S. Duker, eds., *Ophthalmology*. London: Mosby.

Roodhooft JM. Leading causes of blindness worldwide. 2002. Bull Soc Belge Ophtalmol, 283: 19-25.

Rumelt S, Dorenboim Y, Rehany U. 1999. Aggressive systemic treatment for central retinal artery occlusion. Am J Ophthalmol, 128: 733–8.

Sadun, A.A., 2008. Neuro-ophthalmology: The afferent visual system: Anatomy and physiology. In: M. Yanoff, J.S. Duker, eds., *Ophthalmology*. London: Mosby.

Salyer DA, Beaudry N, Basavanthappa S, Twietmeyer K, Eskandari M, Denninghoff KR, Chipman RA, Park RI. 2006. Retinal oximetry using intravitreal illumination. Curr Eye Res, 31(7-8): 617-27.

Sample PA, Johnson CA. Functional assessment of glaucoma. 2001. J Glaucoma, 10(5 Suppl 1): S49-52.

Sarnquist F, Todd C, Whitcher C. 1980. Accuracy of a new non-invasive oxygen saturation monitor. Anesthesiology, 53: S163.

Schubert, H.D., 2008. Retina and vitreous: Basic science: Structure and function of the neural retina. In: M. Yanoff, J.S. Duker, eds., *Ophthalmology*. London: Mosby.

Schultz RA, Nielsen T, Zavaleta JR, Ruch R, Wyatt R, Garner HR. 2001. Hyperspectral imaging: a novel approach for microscopic analysis. Cytometry, 43(4): 239-47.

Schwartz B. 1994. Circulatory defects of the optic disk and retina in ocular hypertension and high pressure open-angle glaucoma. Surv Ophthalmol, 38(Suppl): S23–S34.

Schweitzer D, Hammer M, Kraft J, Thamm E, Königsdörffer E, Strobel J. 1999. In vivo measurement of the oxygen saturation of retinal vessels in healthy volunteers. IEEE Trans Biomed Eng, 46(12): 1454-65.

Schweitzer D, Guenther S, Scibor M, Hammer M. 1992. Spectrometric investigations in ocular hypertension and early stages of primary open angle glaucoma and of low tension glaucoma--multisubstance analysis. Int Ophthalmol, 16(4-5): 251-7.

Schweitzer D, Lang GE, Remsch H, Beuermann B, Hammer M, Thamm E, Spraul CW, Lang GK. 2000. [Age-related maculopathy: comparative studies of patients, their children and healthy controls]. Ophthalmologe, 97: 84–90.

Schweitzer D, Thamm E, Hammer M, Kraft J. 2001. A new method for the measurement of oxygen saturation at the human ocular fundus. Int Ophthalmol, 23(4-6): 347-53.

Sebag J, Delori FC, Feke GT, Weiter JJ. 1989. Effects of optic atrophy on retinal blood flow and oxygen saturation in humans. Arch Ophthalmol, 107(2): 222-6.

Selbach MJ, Wonka F, Höper J, Funk RH. 1999. Effects of elevated intraocular pressure on haemoglobin oxygenation in the rabbit optic nerve head: a microendoscopical study. Exp Eye Res, 69(3): 301-9.

Semenza GL. 1999. Regulation of mammalian O2 homeostasis by hypoxia-inducible factor 1. Annu Rev Cell Dev Biol, 15: 551–578.

Sethian, JA., 1999. Level Set Methods and Fast Marching Methods. Cambridge, MA: Cambridge University Press.

Sharma S, Grown GC, Cruess AF, for the RECO Study Group. 1998. The accuracy of visible retinal emboli for the detection of cardio-embolic lesions requiring anticoagulation or cardiac surgery. Br J Ophthalmol, 82: 655–658.

Sheen NJ, Morgan JE, Poulsen JL, North RV. 2004. Digital stereoscopic analysis of the optic disc: evaluation of a teaching program. Ophthalmology, 111(10): 1873-9.

Shimada Y, Yoshiya I, Oka N, Hamaguri K. 1984. Effects of multiple scattering and peripheral circulation on arterial oxygen saturation measured with a pulse-type oximeter. Med Biol Eng Comput, 22: 475-478.

Shimizu, K., Kazuyoshi, U., 1978. Structure of ocular vessels. New York, Igaku-Shoin.

Shonat RD, Wilson DF, Riva CE, Cranstoun SD. 1992. Effect of acute increases in intraocular pressure on intravascular optic nerve head oxygen tension in cats. Invest Ophthalmol Vis Sci, 33(11): 3174-80.

Shonat RD,Wilson DF, Riva CE, Pawlowski M. 1992. Oxygen distribution in the retinal and choroidal vessels of the cat as measured by a new phosphorescence imaging method. Applied Optics, 31: 3711-8.

Shou T, Liu J, Wang W, Zhou Y, Zhao K. 2003. Differential dendritic shrinkage of alpha and beta retinal ganglion cells in cats with chronic glaucoma. Invest Ophthalmol Vis Sci, 44: 3005–3010.

Siesky B, Harris A, Cantor LB, Kagemann L, Weitzman Y, McCranor L, Marques C, Werne A, Stefansson E. 2008. A comparative study of the effects of brinzolamide and dorzolamide on retinal oxygen saturation and ocular microcirculation in patients with primary open-angle glaucoma. Br J Ophthalmol, 92(4): 500-4.

Siesky B, Harris A, Kagemann L, Stefansson E, McCranor L, Miller B, Bwatwa J, Regev G, Ehrlich R. 2010. Ocular blood flow and oxygen delivery to the retina in primary open-angle glaucoma patients: the addition of dorzolamide to timolol monotherapy. Acta Ophthalmol, 88(1):142-9.

Sivak, J.G., 1988. Corneal optics in aquatic animals: how they see above and below. In: H.D. Cavanagh, ed., *The Cornea: Transactions of the World Congress on the Cornea III*. New York: Raven Press.

Skokan M, Skoupy A, Jan J. 2002. Registration of multimodal images of retina. Proc. IEEE Conf. Eng. Med. Biol, 2: 1094–1096.

Smith G. 2003. The optical properties of the crystalline lens and their significance. Clin Exp Optom, 86(1): 3-18.

Smith MH. 1999. Optimum wavelength combinations for retinal vessel oximetry. Appl Opt, 38(1): 258-67.

Smith MH, Denninghoff KR, Lompado A, Hillman LW. 2000. Effect of multiple light paths on retinal vessel oximetry. Applied Optics, 29: 1183-1193.

Snell, R.S., Lemp M.A. 1998. The eyeball. In: R.S. Snell, M.A. Lemp, eds., *Clinical Anatomy of the Eye*. Cambridge, MA: Blackwell Scientific Publication.

Sofka M, Stewart CV. 2006. Retinal vessel centerline extraction using multiscale matched filters, confidence and edge measures. IEEE Trans Med Imaging, 12: 1531-46.

Sorg BS, Moeller BJ, Donovan O, Cao Y, Dewhirst MW. 2005. Hyperspectral imaging of hemoglobin saturation in tumor microvasculature and tumor hypoxia development. J Biomed Opt, 10(4): 44004.

Spaeth GL. 1975. Fluorescein angiography: its contributions towards understanding the mechanisms of visual loss in glaucoma. Trans Am Ophthalmol Soc, 73: 491–553.

Spitznas, M., 1977. Anatomical features of the human macula. In: F.A. l'Esperance, ed., *Current diagnosis and management of retinal disorders.* St Louis: CV Mosby.

Stefánsson E, Jensen PK, Eysteinsson T, Bang K, Kiilgaard JF, Dollerup J, Scherfig E, la Cour M. 1999. Optic nerve oxygen tension in pigs and the effect of carbonic anhydrase inhibitors. Invest Ophthalmol Vis Sci, 40(11): 2756-61.

Stefánsson E, Machemer R, de Juan E, McCuen BW II. 1992. Retinal oxygenation and laser treatment in patients with diabetic retinopathy. Am J Ophthalmol, 113: 36-38.

Stewart CV, Tsai CL, Roysam B. 2003. The dual-bootstrap iterative closest point algorithm with application to retinal image registration. IEEE Trans Med Imaging, 22(11): 1379-94.

Sugiyama T, Schwartz B, Takamoto T, Azuma I. 2000. Evaluation of the circulation in the retina, peripapillary choroid and optic disk in normal-tension glaucoma. Ophthalmic Res, 32(2-3): 79-86.

Sugiyama T, Utsunomiya K, Ota H, Ogura Y, Narabayashi I, Ikeda T. 2006. Comparative study of cerebral blood flow in patients with normal-tension glaucoma and control subjects. Am J Ophthalmol, 141: 394–396.

Tamaki Y, Araie M, Kawamoto E, Eguchi S, Fujii H. 1995. Non-contact, two-dimensional measurement of tissue circulation in choroid and optic nerve head using laser speckle phenomenon. Exp Eye Res, 60: 373–383.

Tamaki Y, Araie M, Tomita K, Nagahara M, Tomidokoro A, Fujii H. 1997. Real-time measurement of human optic nerve head and choroid circulation, using the laser speckle phenomenon. Jpn J Ophthalmol, 41: 49–54.

Tatton WG, Chalmers-Redman RM, Tatton NA. 2001. Apoptosis and anti-apoptosis signalling in glaucomatous retinopathy. Eur J Ophthalmol, 11(2): S12-S22.

Tatton W, Chen D, Chalmers-Redman R, Wheeler L, Nixon R, Tatton N. 2003. Hypothesis for a common basis for neuroprotection in glaucoma and Alzheimer's disease: anti-apoptosis by alpha-2-adrenergic receptor activation. Surv Ophthalmol, 48(Suppl 1): S25-S37.

Tezel G, Edward DP, Wax MB. 1999. Serum autoantibodies to optic nerve head glycosaminoglycans in patients with glaucoma. Arch Ophthalmol, 117: 917-924.

Tezel G, Wax MB. 2004. Hypoxia-inducible factor 1alpha in the glaucomatous retina and optic nerve head. Arch Ophthalmol, 122: 1348-1356.

Tezel G, Yang X. 2004. Caspase-independent component of retinal ganglion cell death, in vitro. Invest Ophthalmol Vis Sci, 45: 4049-4059.

Tezel G, Yang X, Cai J. 2005. Proteomic identification of oxidatively modified retinal proteins in a chronic pressure-induced rat model of glaucoma. Invest Ophthalmol Vis Sci, 46: 3177-3187.

Thamm E, Schweitzer D, Hammer M. 1998. A data reduction scheme for improving the accuracy of oxygen saturation calculations from spectrometric in vivo measurements. Phys. Med. Biol, 43: 1401-1411.

The Branch Retinal Vein Occlusion Study Group. 1984. Argon laser photocoagulation for macular edema in branch vein occlusions. Am J Ophthalmol, 98: 271–282.

The Eye Disease Case-Control Study Group. 1993. Risk factors for branch retinal vein occlusion. Am J Ophthalmol, 116: 286–296.

The Central Vein Occlusion Study. 1993. Baseline and early natural history report. Arch Ophthalmol, 111: 1087–1095.

Tiedeman JS, Kirk SE, Srinivas S, Beach JM. 1998. Retinal oxygen consumption during hyperglycemia in patients with diabetes without retinopathy. Ophthalmology, 105(1): 31-6.

Tielsch JM, Katz J, Sommer A, Quigley HA, Javitt JC. 1994. Family history and risk of primary open angle glaucoma. The Baltimore Eye Survey. Arch Ophthalmol, 112: 69-73.

Tielsch JM, Sommer A, Katz J, Royall RM, Quigley HA, Javitt J. 1991. Racial variations in the prevalence of primary open-angle glaucoma. The Baltimore Eye Survey. Jama, 266: 369-374.

Timlin JA, Haaland DM, Sinclair MB, Aragon AD, Martinez MJ, Werner-Washburne M. 2005. Hyperspectral microarray scanning: impact on the accuracy and reliability of gene expression data. BMC Genomics, 11: 6(1): 72.

Tomic L, Mäepea O, Sperber GO, Alm A. 2001. Comparison of retinal transit times and retinal blood flow (A study in monkeys). Invest Ophthalmol Vis Sci, 42: 752–755.

Törnquist P, Alm A. 1979. Retinal and choroidal contribution to retinal metabolism in vivo. A study in pigs. Acta Physiol Scand, 106(3): 351-7.

Traustason S, Hardarson SH, Gottfredsdottir MS, Eysteinsson T, Karlsson RA, Stefánsson E, Harris A. 2009. Dorzolamide-timolol combination and retinal vessel oxygen saturation in patients with glaucoma or ocular hypertension. Br J Ophthalmol, 93(8): 1064-7.

Troilo D, Nickla D, Wildsoet C. 2000. Choroidal thickness changes during altered eye growth and refractive state in a primate. Invest Ophthalmol Vis Sci, 41: 1249–1258.

Tsuchihashi T, Mori K, Peyman G, Shimada Y, Yoneya S. 2009. Photodynamic effects on retinal oxygen saturation, blood flow, and electrophysiological function in patients with neovascular age-related macular degeneration. Retina, 29(10): 1450-6.

Twersky V. 1962. Multiple scattering of waves and optical phenomena. J Opt Soc Amer, 52: 145-171.

Twersky V. 1970. Interface effects in multiple scattering by large, low refracting absorbing particles. J Opt Soc Amer, 60: 908-914.

Twersky V. 1970. Absorption and multiple scattering by biological suspensions. J Opt Soc Amer, 60: 1084-1093.

van Assendelft, O., 1970. Spectrophotometry of Haemoglobin Derivatives. The Netherlands: Royal van Gorcum Assen.

Velten IM, Korth M, Horn FK. 2001. The a-wave of the dark adapted electroretinogram in glaucomas: are photoreceptors affected? Br J Ophthalmol, 85: 397-402.

Vorwerk CK, Gorla MS, Dreyer EB. 1999. An experimental basis for implicating excitotoxicity in glaucomatous optic neuropathy. Surv Ophthalmol, 43(1): S142-S150.

Wajer SD, Taomoto M, McLeod DS, McCally RL, Nishiwaki H, Fabry ME, Nagel RL, Lutty GA. 2000. Velocity measurements of normal and sickle cell red blood cells in the rat retinal and choroidal vasculatures. Microvasc Res, 60(3): 281-93.

Wamsley S, Gabelt BT, Dahl DB, Case GL, Sherwood RW, May CA, Hernandez MR, Kaufman PL. 2005. Vitreous glutamate concentration and axon loss in monkeys with experimental glaucoma. Arch Ophthalmol, 123: 64-70.

Wang JJ, Mitchell P, Smith W. 1997. Is there an association between migraine headache and open-angle glaucoma? Findings of the Blue Mountains Study. Ophthalmol, 104:1714–9.

Wang L, Dong J, Cull G, Fortune B, Cioffi GA. 2003. Varicosities of intraretinal ganglion cell axons in human and nonhuman primates. Invest Ophthalmol Vis Sci, 44(1): 2-9.

Wangsa-Wirawan ND, Linsenmeier RA. 2003. Retinal oxygen: Fundamental and clinical aspects. Arch Ophthalmol, 121(4): 547–557.

Wax MB, Barrett DA, Pestronk A. 1994. Increased incidence of paraproteinemia and autoantibodies in patients with normal-pressure glaucoma. Am J Ophthalmol, 117: 561-568.

Wetzig PC. 1979. The treatment of acute branch vein occlusion by photocoagulation. Am J Ophthalmol, 87: 65–73.

Weber AJ, Kaufman PL, Hubbard WC. 1998. Morphology of single ganglion cells in the glaucomatous primate retina. Invest Ophthalmol Vis Sci, 39: 2304–2320.

Wild JM, Cubbidge RP, Pacey IE, Robinson R. 1998. Statistical aspects of the normal visual field in short-wavelength automated perimetry. Invest Ophthalmol Vis Sci, 39(1): 54-63.

Williamson TH. 1977. Central retinal vein occlusion: what's the story? Br J of Ophthalmol, 81: 698–704.

Wolfs RC, Klaver CC, Ramrattan RS, van Duijn CM, Hofman A, de Jong PT. 1998. Genetic risk of primary open-angle glaucoma. Population-based familial aggregation study. Arch Ophthalmol, 116: 1640-1645.

Wolf S, Jung F, Kiesewetter H, Körber N, Reim M. 1989. Video fluorescein angiography: method and clinical application. Graefes Arch Clin Exp Ophthalmol, 227: 145–151.

Wolter JR. 1961. Retinal pathology after central retinal vein occlusion. Br J Ophthalmol, 45: 683-694.

Xu J,Chutatape O, Sung E, Zheng C, ChewTecKuan P. 2007. Optic disk feature extraction via modified deformable model technique for glaucoma analysis. Pattern Recog, 40(7): 2063–2076.

Yamazaki Y, Drance SM. 1997. The relationship between progression of visual field defects and retrobulbar circulation in patients with glaucoma. Am J Ophthalmol, 124(3): 287-95.

Yan X, Tezel G, Wax MB, Edward DP. 2000. Matrix metalloproteinases and tumor necrosis factor alpha in glaucomatous optic nerve head. Arch Ophthalmol, 118: 666-673.

Yoneya S, Saito T, Nishiyama Y, Deguchi T, Takasu M, Gil T, Horn E. 2002. Retinal oxygen saturation levels in patients with central retinal vein occlusion. Ophthalmology, 109(8):1521-6.

Yu DY, Cringle SJ. 2002. Outer retinal anoxia during dark adaptation is not a general property of mammalian retinas. Comp Biochem Phys A, 132(1): 47–52.

Yu DY, Cringle SJ, Yu PK, Su EN. 2007. Intraretinal oxygen distribution and consumption during retinal artery occlusion and graded hyperoxic ventilation in the rat. Invest Ophthalmol Vis Sci, 48(5): 2290-6.

Zana F, Klein J. 1999. A multimodal registration algorithm of eye fundus images using vessels detection and hough transform. IEEE Trans. Biomed. Eng, 18(5): 419–428.

Zangwill LM, Bowd C, Berry CC, Williams J, Blumenthal EZ, Sánchez-Galeana CA, Vasile C, Weinreb RN. 2001. Discriminating between normal and glaucomatous eyes using the Heidelberg retina tomograph, GDx nerve fiber analyzer, and optical coherence tomograph. Arch Ophthalmol, 119: 985–93.

Zangwill LM, Weinreb RN, Beiser JA, Berry CC, Cioffi GA, Coleman AL, Trick G, Liebmann JM, Brandt JD, Piltz-Seymour JR, Dirkes KA, Vega S, Kass MA, Gordon MO. 2005. Baseline topographic optic disc measurements are associated with the development of primary open-angle glaucoma: the Confocal Scanning Laser Ophthalmoscopy Ancillary Study to the Ocular Hypertension Treatment Study. Arch Ophthalmol, 123: 1188-1197.

Zdrojkowski RJ, Pisharoty NR. 1970. Optical transmission and reflection by blood. IEEE Trans. Biomed. Eng, BME-17: 122-128.

Zelefsky JR, Harizman N, Mora R, Ilitchev E, Tello C, Ritch R, Liebmann JM. 2006. Assessment of a race-specific normative HRT-III database to differentiate glaucomatous from normal eyes. J Glaucoma, 15(6): 548-51.

Zhao J, Sastry SM, Sperduto RD, Chew EY, Remaley NA. 1993. Arteriovenous crossing patterns in branch retinal vein occlusion. Ophthalmology, 100: 423–428.

Zimmerman L.E. 1965. Embolism of the central retinal artery secondary to myocardial infarction with mural thrombosis. Arch Ophthalmol, 73:822-6.

Zinn IG. 1755. Descriptio anatomica oculi humani. Göttingen, B. Abrami Vandenhoeck.

Zuckerman R. 1993. Optical mapping of inner retinal tissue PO_2. Curr Eye Res, 12: 809-25.

Zuzak KJ, Gladwin MT, Cannon RO 3rd, Levin IW. 2003. Imaging hemoglobin oxygen saturation in sickle cell disease patients using noninvasive visible reflectance hyperspectral techniques: effects of nitric oxide. Am J Physiol Heart Circ Physiol, 285(3): H1183-9.

Zuzak KJ, Schaeberle MD, Gladwin MT, Cannon RO 3rd, Levin IW. 2001. Noninvasive determination of spatially resolved and time-resolved tissue perfusion in humans during nitric oxide inhibition and inhalation by use of a visible-reflectance hyperspectral imaging technique. Circulation, 104(24): 2905-10.

Zuzak KJ, Schaeberle MD, Lewis EN, Levin IW. 2002. Visible reflectance hyperspectral imaging: characterization of a noninvasive, in vivo system for determining tissue perfusion. Anal Chem, 74(9): 2021-8.

Appendices

Appendix 1: Mathematical Concept of the Two Wavelength Method of Calculating the Oxygen Saturation.

The Lambert-Beer law in transmission blood oximetry assumes that for any given wavelength of light its absorption is dependent on the extinction coefficient of the blood solution (ε), its concentration or haematocrit (c) and the distance (d) the light has to travel through the solution (path length):

$$I_T = I_O \times 10^{-\epsilon \times c \times d} \qquad \text{(Eq. A1.1)}$$

Where I_T is the amount of light transmitted through a solution and I_O is the amount of incident light.

The optical density (OD) of a solution is a measure of its transmittance, and is defined by:

$$OD = -\log_{10}\left(\frac{I_T}{I_O}\right) = \epsilon \times c \times d \qquad \text{(Eq. A1.2)}$$

Therefore the optical density of a solution of blood is a function of its extinction coefficient, concentration and the path length the light has to travel.

The two main haemoglobin derivatives in blood are deoxyhaemoglobin (Hb) and oxyhaemoglobin (HbO_2), also known as the functional haemoglobin derivatives.

$$Blood = Hb + HbO_2 \qquad \text{(Eq. A1.3)}$$

Therefore the optical density of blood (OD_{Blood}) at a given wavelength can be expressed as a function of the extinction coefficients (ε_{Hb} and ε_{HbO2}) and concentrations (c_{Hb} and c_{HbO2}) of the functional haemoglobin derivatives:

$$OD_{Blood} = (\epsilon_{Hb} \times c_{Hb} \times d) + (\epsilon_{HbO_2} \times c_{HbO_2} \times d) \qquad \text{(Eq. A1.4)}$$

Functional oxygen saturation (OS) is defined as:

$$OS = \frac{c_{HbO_2}}{c_{Hb} + c_{HbO_2}} = \frac{c_{HbO_2}}{c_{HbTotal}} \qquad \text{(Eq. A1.5)}$$

Equation A1.5 can be rearranged to obtain the following:

$$c_{HbO_2} = OS \times c_{HbTotal} \quad \text{(Eq. A1.6)}$$

$$c_{Hb} = c_{HbTotal} \times (1 - OS) \quad \text{(Eq. A1.7)}$$

Equation A1.4 can be rewritten using Equations 1.6 and 1.7 to include the oxygen saturation:

$$OD_{Blood} = (\epsilon_{Hb} \times c_{HbTotal} \times (1 - OS) \times d) + (\epsilon_{HbO_2} \times OS \times c_{HbTotal} \times d) \quad \text{(Eq. A1.8)}$$

This can be simplified to:

$$OD_{Blood} = c_{HbTotal} \times d[OS \times (\epsilon_{HbO_2} - \epsilon_{Hb}) + \epsilon_{Hb}] \quad \text{(Eq. A1.9)}$$

In Equation A1.9 there are 2 known variables (the extinction coefficients), 1 measurable variable (the optical density of blood) and 3 unknown variables (concentration of blood, path length and oxygen saturation). A minimum of two wavelengths of light ($\lambda 1$ and $\lambda 2$) are required to perform oximetry which enables the calculation of the oxygen saturation which is not assumed to be independent on the concentration of blood and the path length:

$$OD_{\lambda 1} = c_{HbTotal} \times d[OS \times (\epsilon_{HbO_2}{}^{\lambda 1} - \epsilon_{Hb}{}^{\lambda 1}) + \epsilon_{Hb}{}^{\lambda 1}]$$

$$OD_{\lambda 2} = c_{HbTotal} \times d[OS \times (\epsilon_{HbO_2}{}^{\lambda 2} - \epsilon_{Hb}{}^{\lambda 2}) + \epsilon_{Hb}{}^{\lambda 2}] \quad \text{(Eq. A1.10)}$$

These two equations (1.10) can be solved for *s*, resulting in the oximetry equation:

$$OS = \frac{(OD_{\lambda 1} - \epsilon_{Hb}{}^{\lambda 2}) - (OD_{\lambda 2} - \epsilon_{Hb}{}^{\lambda 1})}{OD_{\lambda 2} (\epsilon_{HbO_2}{}^{\lambda 1} - \epsilon_{Hb}{}^{\lambda 1}) - OD_{\lambda 1} (\epsilon_{HbO_2}{}^{\lambda 2} - \epsilon_{Hb}{}^{\lambda 2})} \quad \text{(Eq. A1.11)}$$

The oximetry Equation A1.11 no longer require values for the haemoglobin concentration or path length and oxygen saturation can be calculated from optical density measurements and the extinction coefficients of the haemoglobin derivatives at the two wavelengths.

This equation can be further simplified when one isobestic wavelength (where the absorption of light by Hb and HbO_2 is equal; oxygen insensitive) is chosen. Therefore if $\lambda 1$ is the isobestic wavelength:

$$\epsilon_{HbO_2}{}^{\lambda 1} = \epsilon_{Hb}{}^{\lambda 1}$$
$$\epsilon_{HbO_2}{}^{\lambda 1} - \epsilon_{Hb}{}^{\lambda 1} = 0 \quad \text{(Eq. A1.12)}$$

Substituting Equation A1.12 into Equation A1.11 can further simplify the oxygen saturation equation to:

$$OS = \left(\frac{OD_{\lambda 2}}{OD_{\lambda 1}} \times \frac{\epsilon_{HbO_2}{}^{\lambda 1}}{\epsilon_{HbO_2}{}^{\lambda 2} - \epsilon_{Hb}{}^{\lambda 2}} \right) - \left(\frac{\epsilon_{Hb}{}^{\lambda 2}}{\epsilon_{HbO_2}{}^{\lambda 2} - \epsilon_{Hb}{}^{\lambda 2}} \right) \quad \text{(Eq. A1.13)}$$

Equation A1.13 is a linear equation:

$$OS = \left(\frac{OD_{\lambda 2}}{OD_{\lambda 1}} \right) A - B \quad \text{(Eq. A1.14)}$$

Where:

$$A = \left(\frac{\epsilon_{HbO_2}{}^{\lambda 1}}{\epsilon_{HbO_2}{}^{\lambda 2} - \epsilon_{Hb}{}^{\lambda 2}} \right)$$

$$B = \left(\frac{\epsilon_{Hb}{}^{\lambda 2}}{\epsilon_{HbO_2}{}^{\lambda 2} - \epsilon_{Hb}{}^{\lambda 2}} \right) \quad \text{(Eq. A1.15)}$$

Appendix 2. Image Selection.

All raw retinal images for each eye were saved onto a computer hard disk as 8-bit bitmap and 12-bit PNG (signed integer) images for further processing. Selection of the best retinal images for each wavelength was performed manually. This was done by inspecting the raw 12bit retinal images on a computer using image viewing software (Windows picture and fax viewer, Microsoft, Redmond, WA). Images of the same wavelength were compared.

Features within each image such as the presence of artefacts (Figure A2.1), focus (Figures A2.3 and A2.4) and illumination pattern (Figures A2.5 and A2.6) were evaluated to determine the best quality image for each wavelength. The other images were removed from further image processing.

The images shown in Figures A2.1 – A2.6 are the saved raw 12-bit PNG images displayed in the Windows picture and fax viewer software (Microsoft, Redmond, WA). The light grey background of the retina in the 12-bit PNG images is a consequence of the incompatibility of the Windows viewing software and the raw images. Although the saved 8-bit bitmap images can be viewed using the Windows viewing software without compatibility issues, the low contrast of the 8-bit images made it too difficult to effectively determine differences in the features of the images to enable the selection of the best quality retinal image for each wavelength. Displaying the 12-bit PNG images was determined to be the quickest and most effective way of selecting the best quality images.

Figure A2.1: Retinal images of a normal left eye obtained at 536 nm. Images with artefacts are deleted. Image ***A*** has no artefact. Image ***B*** contains an artefact and was removed from further processing.

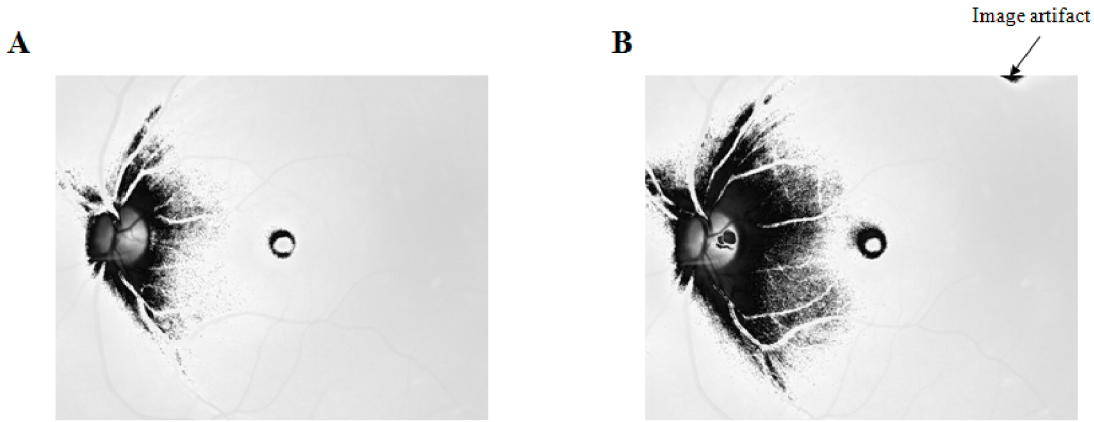

Figure A2.3: Retinal images of a normal left eye obtained at 542 nm. Images that are out of focus or comparatively more out of focus were removed from further processing. The edges of the retinal blood vessels appear sharper in image ***A*** than in image ***B***. Image ***A*** is more in focus compared to image ***B***. Image ***B*** was removed from further processing.

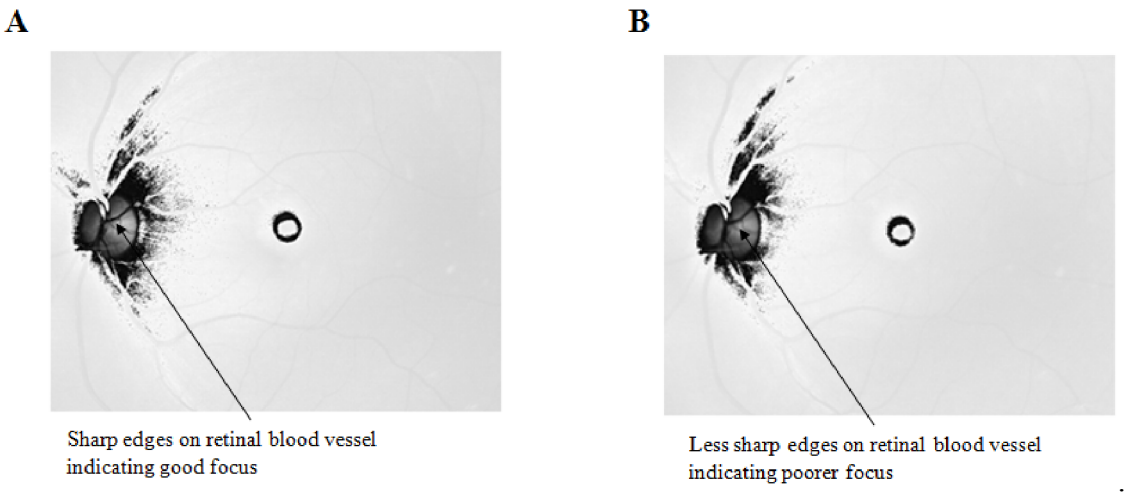

Figure A2.4: Retinal images of a normal left eye obtained at 580 nm. The focus of the images can also be determined by the edges of the retinal blood vessels and sharpness of the retinal reflex. **Image *A*** has a sharp retinal reflex and the blood vessels appear in focus. **Image *B*** has a faint retinal reflex and was removed from further processing. Image ***C*** has no retinal reflex and was removed from further processing. Image ***D*** has sharp edges to the retinal blood vessel and the retinal reflex appears sharp but the illumination pattern was skewed with darker areas inferiorly. This image was removed from further processing. Image ***E*** has a clear retinal reflex but its sharpness and the edges of the blood vessels appear to be less sharp compared to image ***A*** and therefore more out of focus. This image was removed from further processing.

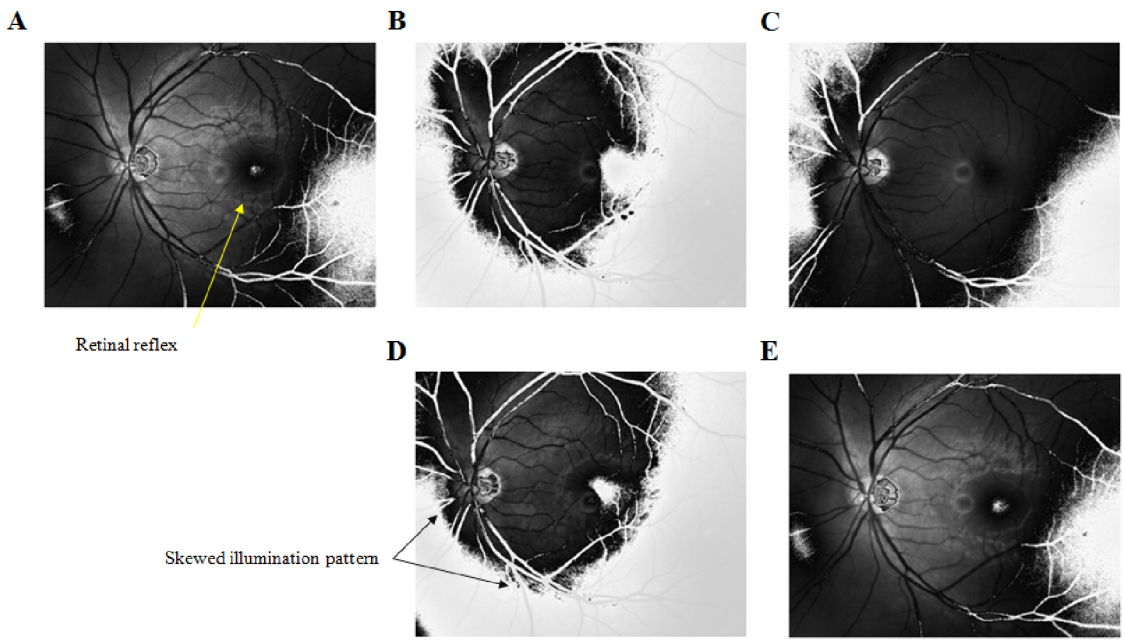

FigureA 2.5: Retinal images of a normal left eye obtained at 532 nm. Illumination of the optic disc and its surroundings is comparatively better in image ***A*** compared to image ***B***. Image ***B*** is removed from further processing.

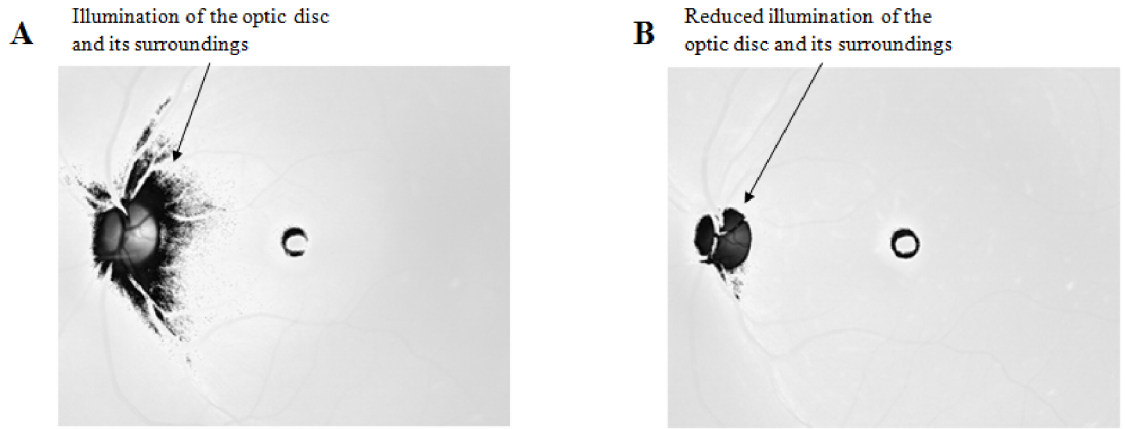

Figure A2.6: Retinal images of a normal left eye obtained at 574 nm. The illumination pattern in image ***A*** is more uniform around the optic disk compared to image ***B*** where the illumination is brighter in the superotemporal region adjacent to the optic disc. Image ***A*** was used for processing and image ***B*** was removed from further processing.

A

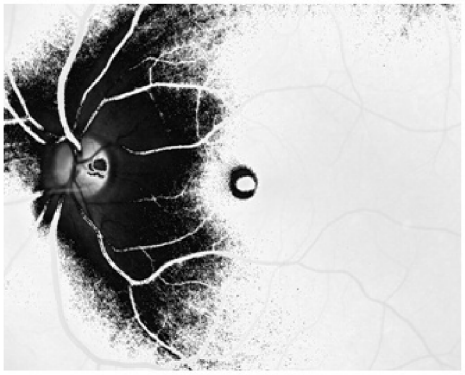

More uniform illumination pattern

B

Skewed illumination pattern

Appendix 3: Histogram of a sample raw retinal image acquired at 580 nm (portable network graphics format)

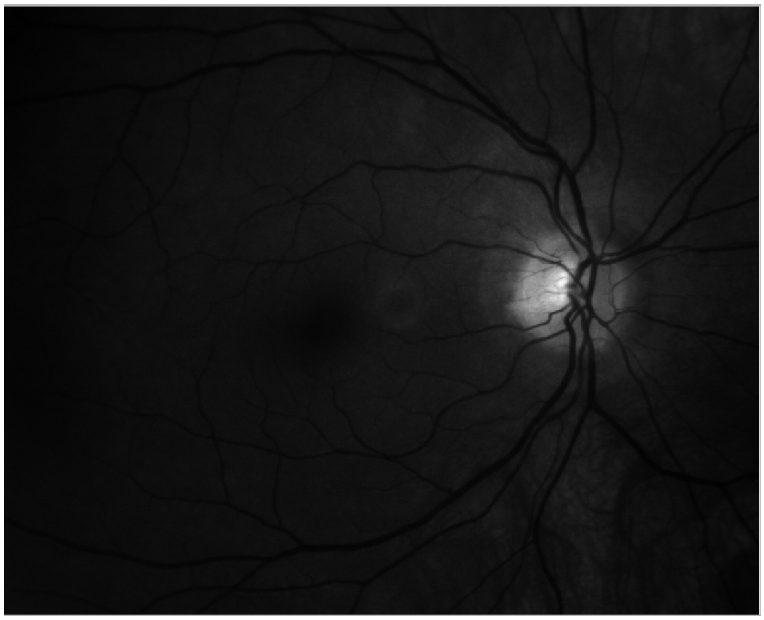

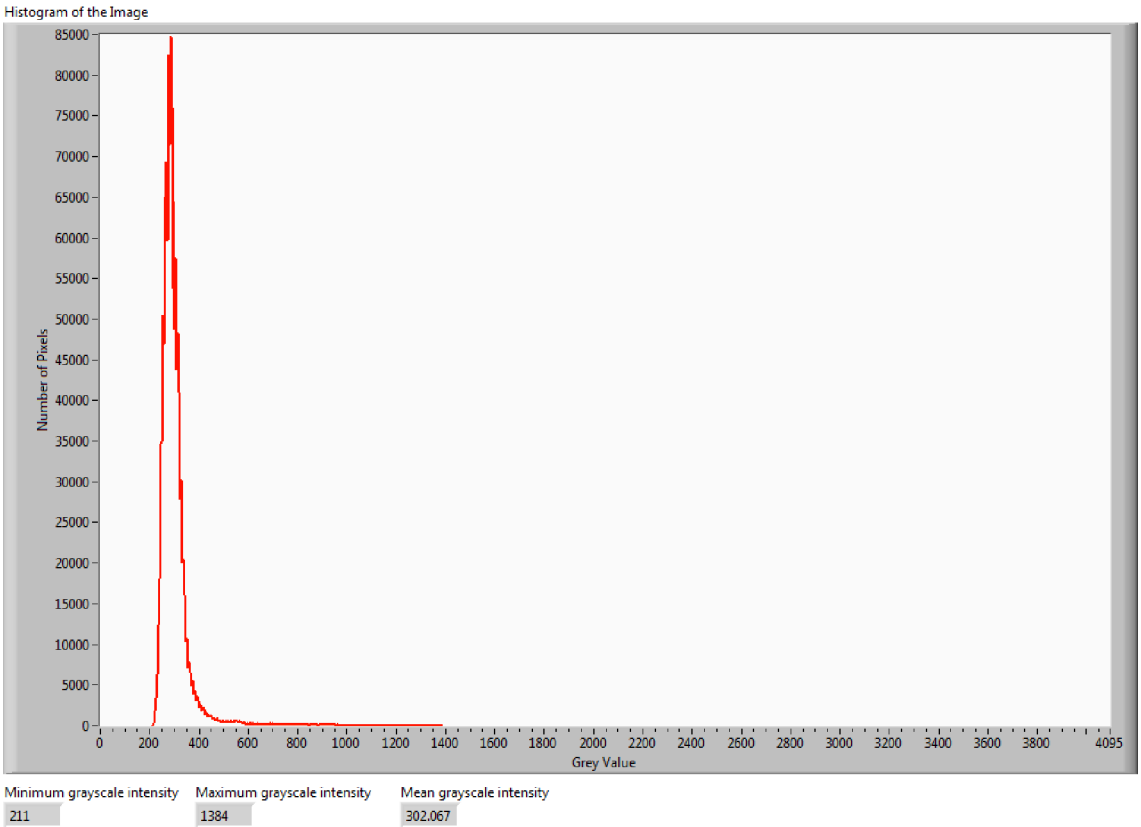

Appendix 4: Retinal Image Segmentation and Vessel Intersection Detection - Mathematica Programming Codes

SETTING THE DIRECTORY AND DEFINING FILES

```
<< ImageProcessing`
Needs["LinearRegression`"]
Needs["NonlinearRegression`"]
Needs["ErrorBarPlots`"];
pn = P24 (* THE PATIENT RESEARCH NUMBER *) ;
(* CHANGE *)
es = L; (* THE SIDE OF THE EYE *)
(* CHANGE *)
SetDirectory[
  name = "G:\\2010_02_15 MD Normals\\P24 [L] images coreg\\"];
(* CHANGE *)
```

THE RESULTS OF THE VESSEL DETECTION

```
pic = Import[
   ToString[name] <> "DC_" <> ToString[pn] <> ToString[" ["] <>
    ToString[es] <> ToString["]"] <> " REF VESSEL DETECTION 2.bmp"];
aa = FileNames["xy_P*.txt"];
bb = FileNames["xy_n*.txt"];
xys = Table[Round[Get[aa[[i]]]], {i, 1, Length[aa]}];
xyn = Table[Round[Get[bb[[i]]]], {i, 1, Length[bb]}];
Show[pic, ListPlot[xys, PlotStyle -> {RGBColor[1, 1, 0]}],
 ImageSize -> 500, PlotLabel -> "Location of Detected Vessels"]
```

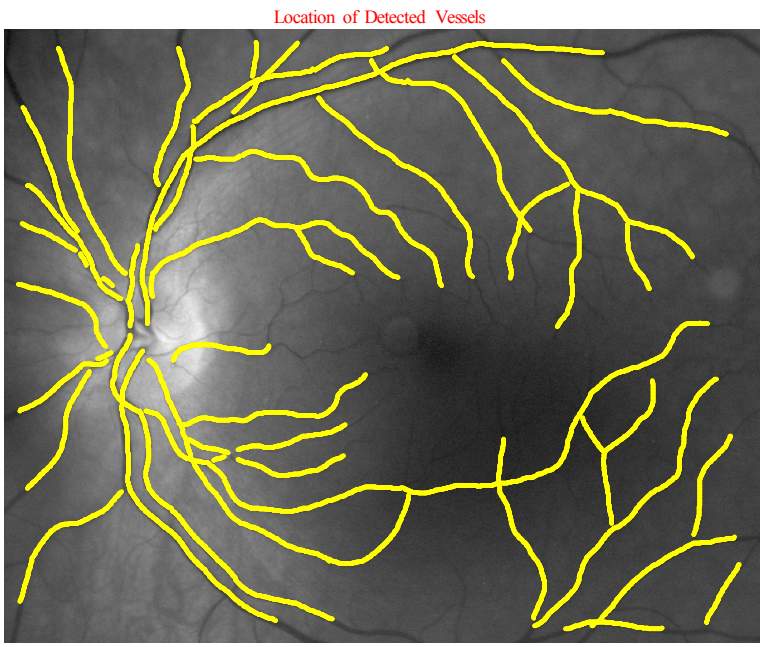

SEGMENT THE IMAGE FOR OXIMETRY ANALYSIS

```
r=92 ;(* RADIUS OF THE OPTIC DISC *)
(* DIAMETER IS 2r, 1DD = 3r FROM CENTRE OF THE CIRCLE *)
{x1,y1}={235,482}; (* X, Y COORDINATES OF THE CENTRE OF THE OPTIC DISC - USED
MATHEMATICA 7 TO DETERMINE CO-ORDINATES *)
p1={x1,y1};
dm=Circle[Round[{x1,y1}],r]; (* DISC MARGIN *)
dd05=Circle[Round[{x1,y1}],2r];
dd1=Circle[Round[{x1,y1}],3r];
dd15=Circle[Round[{x1,y1}],4r];
dd2=Circle[Round[{x1,y1}],5r];
(*ImageDimensions[ImageRead["G:\\2010_02_15 MD Normals\\P11 [R] images coreg\\DC_P11 [R] REF
VESSEL DETECTION.bmp"]][[2]]
l1=Line[Round[{{0,y1},{1061,y1}}]];*)
segtext1={Text["Disc\nmargin",{x1+r,y1}],Text["0.5dd",{x1+2r,y1}],Text["1dd",{x1+3r,y1}],Text["1.5dd",{x
1+4r,y1}],Text["2dd",{x1+5r,y1}]};

segimage=Show[pic,ImageSize□500,PlotLabel□"Location of retinal image
segmentation",Epilog□{Dotted,Yellow,PointSize[0.015],{dm,dd05,dd1,dd15,dd2,Point[p1],segtext1
    }}]
```

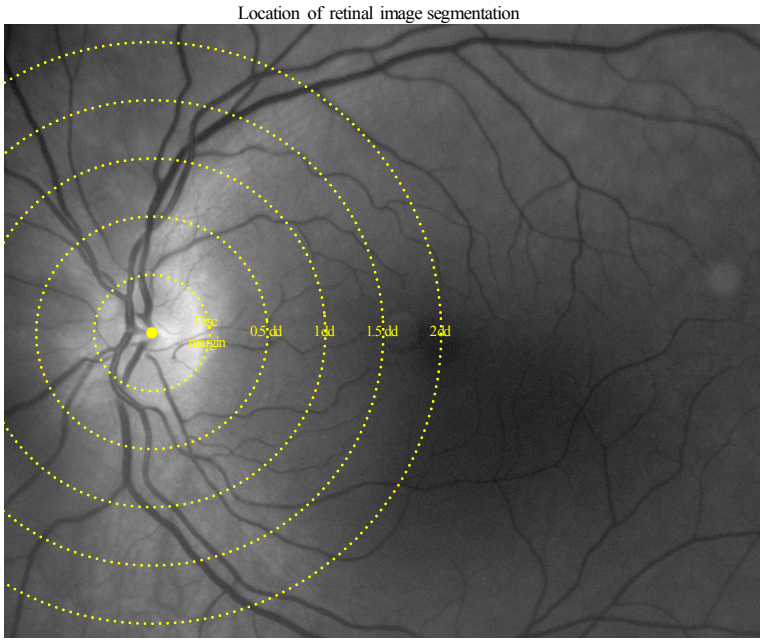

LOCATE COORDINATES OF THE INTERSECTIONS BETWEEN THE RETINAL BLOOD VESSELS AND SEGMENTATION RINGS

```
(* LOAD THE PROFILES *)
prosa = Get[
  smoothedprosa =
   ToString[name] <> "smoothed_pros_" <> ToString[pn] <>
    ToString["["] <> ToString[es] <> ToString["]"] <> "_art.txt"];
prosv = Get[
  smoothedprosv =
   ToString[name] <> "smoothed_pros_" <> ToString[pn] <>
    ToString["["] <> ToString[es] <> ToString["]"] <> "_vein.txt"];
pros = Join[prosa, prosv];

(* DEFINE THE VESSEL PROFILE LOCATION AND REGION FOR MEAN PROFILE \
```

```
ANALYSIS-ARTERIOLES AND VENULES *)
aaart = FileNames["xy_P*a00*.txt"];
bbart = FileNames["xy_n*a00*.txt"];
xysart = Table[Round[Get[aaart[[i]]]], {i, 1, Length[aaart]}];
xynart = Table[Round[Get[bbart[[i]]]], {i, 1, Length[bbart]}];

aavein = FileNames["xy_P*v00*.txt"];
bbvein = FileNames["xy_n*v00*.txt"];
xysvein = Table[Round[Get[aavein[[i]]]], {i, 1, Length[aavein]}];
xynvein = Table[Round[Get[bbvein[[i]]]], {i, 1, Length[aavein]}];

(* SHOW VESSEL DETECTION ARTERIOLES AND VENULES WITH SEGMENTATION *)
DisplayTogetherArray[
 Show[pic, ListPlot[xysart],
  PlotLabel -> "Locations of arteriolar vessel tracking",
  Epilog -> {Dotted, Yellow,
    PointSize[0.015], {dm, dd05, dd1, dd15, dd2, Point[p1],
     segtext1}}],
 Show[pic, ListPlot[xysvein],
  PlotLabel -> "Locations of venular vessel tracking",
  Epilog -> {Dotted, Yellow,
    PointSize[0.015], {dm, dd05, dd1, dd15, dd2, Point[p1],
     segtext1}}],
 ImageSize -> 1000]

(* SHOW THE INTERSECTION BETEWEEN THE VESSEL POSITION AND \
SEGMENTATION *)
xyvessels = FileNames["xy_P*vessel*.txt"];
(*Table of xy coordinates for all vessels*)
xyvessels1 =
  Table[Round[Get[xyvessels[[i]]]], {i, 1, Length[xyvessels]}];

(*How close in pixels should intersection be to count*)
CloseEnough = r/50;

(*Table for intersections*)
VesselIntersections = Table[0, {Length[xyvessels]}];

(*Loop through vessels *)
For[VesNo = 1, VesNo <= Length[xyvessels], VesNo++,

  DimVes = Dimensions[xyvessels1[[VesNo]]];
  Dist = Flatten[
    Total[(xyvessels1[[
         VesNo]] - (Table[{x1,
          y1}, {DimVes[[
           1]]}]))^2, {2}]^0.5];  (*Distance of each vessel point \
from centre of optic disk*)
  Intersect = Table[0, {5}];  (*Table to hold intersections*)
  q = 1;
  (*Loop to find intersections for vessel from 1r to 5r*)
  For[j = 1, j <= 5, j++,
   IntDist = Abs[Dist - j r];  (*Distance from jth circle*)
   If[Min[IntDist] <
     CloseEnough,  (*Check if vessel is close enough to circle to \
count as intersection*)
    Intersect[[q]] =
     Ordering[IntDist, 1];  (*Find index of closest intersection*)
    q = q + 1;
    ];
```

```
  ];
  VesselIntersections[[VesNo]] =
   Intersect; (*Index number of coordinate pair *)
  ];

TableForm[
 Transpose[{
   bb,
   Table[i + 1, {i, 0, Length[bb] - 1, 1}],
   Table[Length[Transpose[Get[bb[[i]]]][[All, 1]]], {i, 1,
     Length[bb]}],
   Table[Length[xyn[[i, 1]]], {i, 1, Length[bb]}],
   VesselIntersections
   }],
 TableHeadings -> {Automatic, {"Filename", "FileNumber",
    "Number of \nxyn profiles", "Check number \nin each pros",
    "XY Intersection Position\n (Higher number closest to optic \
disc)"}},
 TableSpacing -> {1, 2}]
```

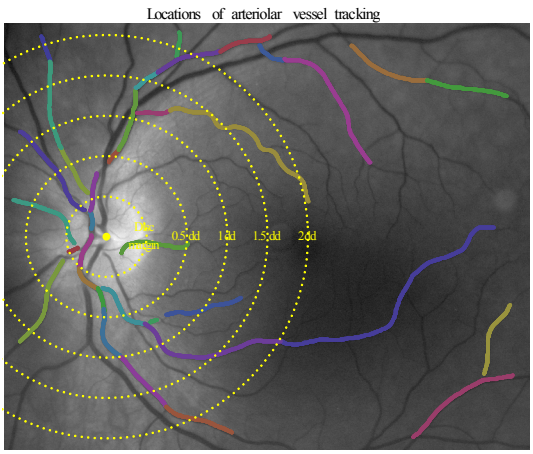

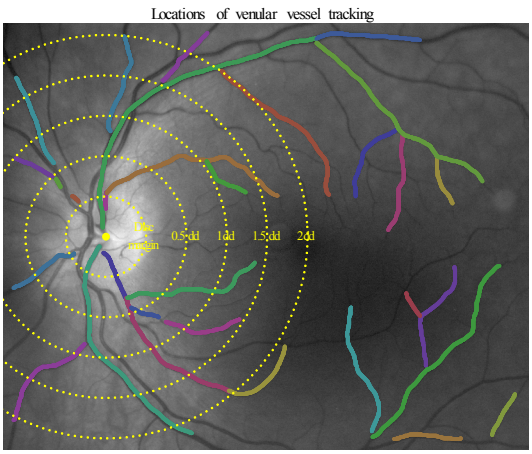

METHODS:

1. CUT, PASTE AND RUN THE MANIPULATION TO FIND THE 1ST DEGREE VESSEL FILE NUMBER - ENTER NUMBER IN "iv*" VARIABLES

2. CUT, PASTE THE TABLE WITH THE INTERSECTION VALUES ONTO SEPARATE NOTEBOOK AND USETO DEFINE THE POSITION OF THE XY COORDINATES THAT INTERSECT WITH THE SEGMENTATION

SHOW LOCATION OF A SELECTED PROFILE AND THE CORRESPONDING TRACKED VESSEL

```
Manipulate[
 profilelocation = 20;

 Show[pic,

  ListPlot[Join[xysart, xysvein][[profilevessel]],
   PlotStyle -> {Yellow}],
  ListPlot[
   xyn[[profilevessel,
    1, {Round[Length[xyn[[profilevessel, 1]]]/2]}]],
   PlotStyle -> {Red}],
  PlotLabel ->
   ToString[bb[[profilevessel]]] <> "\nPosition of intersections: " <>
    ToString[VesselIntersections[[profilevessel]]] <>
    "\nLength of profiles: " <>
```

```
   ToString[Length[xyn[[profilevessel, 1]]]], ImageSize -> 500,
  Epilog -> {Dotted, Yellow,
    PointSize[0.015], {dm, dd05, dd1, dd15, dd2, Point[p1], segtext1}}]
 , {profilevessel, 1, Length[xyvessels], 1}
 ]
```

INSERT THE VESSEL FILE NUMBER "iv*" AND USE THE TABLE TO DEFINE THE POSITION OF THE XY COORDINATES THAT INTERSECT WITH THE SEGMENTATION

```
(* vp DEFINES THE RANGE OF THE VESSEL POSITIONS FOR THE MEAN OD \
ANALYSIS *)
vpr = 10;

(* iv DEFINES THE VESSEL; 1 IS THE FIRST VESSEL  *)
(* vp DEFINES THE VESSEL POSITION OF THE ANALYSIS
REMEMBER THAT THE POSITION CLOSEST TO THE OPTIC DISC HAS A HIGHER \
VALUE (I.E REVERSE POSITION NUMBERING)*)
        (* ST ARTERIOLES *)
ivstadm = 10;
ivstadd05 = 11;
ivstadd1 = 12;
ivstadd15 = 13;
ivstadd2 = 14;

vpstadm = 119;
vpstadd05 = 47;
vpstadd1 = 129;
vpstadd15 = 76;
vpstadd2 = 115;

        (* IT ARTERIOLES *)
ivitadm = 23;
ivitadd05 = 26;
ivitadd1 = 27;
ivitadd15 = 27;
ivitadd2 = 28;

vpitadm = 12;
vpitadd05 = 208;
vpitadd1 = 292;
vpitadd15 = 91;
vpitadd2 = 190;

        (* IN ARTERIOLES *)
ivinadm = 32;
ivinadd05 = 33;
ivinadd1 = 33;
ivinadd15 = 33;
ivinadd2 = 33;

vpinadm = 12;
vpinadd05 = 273;
vpinadd1 = 70;
vpinadd15 = 22;
vpinadd2 = 12;

        (* SN ARTERIOLES *)
ivsnadm = 35;
ivsnadd05 = 35;
ivsnadd1 = 35;
```

```
ivsnadd15 = 35;
ivsnadd2 = 35;

vpsnadm = 449;
vpsnadd05 = 259;
vpsnadd1 = 73;
vpsnadd15 = 22;
vpsnadd2 = 12;

        (* ST VENULES *)
ivstvdm = 39;
ivstvdd05 = 39;
ivstvdd1 = 39;
ivstvdd15 = 39;
ivstvdd2 = 39;

vpstvdm = 1348;
vpstvdd05 = 1159;
vpstvdd1 = 963;
vpstvdd15 = 731;
vpstvdd2 = 479;

        (* IT VENULES *)
ivitvdm = 52;
ivitvdd05 = 52;
ivitvdd1 = 52;
ivitvdd15 = 52;
ivitvdd2 = 52;

vpitvdm = 957;
vpitvdd05 = 755;
vpitvdd1 = 544;
vpitvdd15 = 305;
vpitvdd2 = 85;

        (* IN VENULES *)
ivinvdm = 61;
ivinvdd05 = 61;
ivinvdd1 = 61;
ivinvdd15 = 61;
ivinvdd2 = 61;

vpinvdm = 309;
vpinvdd05 = 115;
vpinvdd1 = 32;
vpinvdd15 = 22;
vpinvdd2 = 12;

        (* SN VENULES *)
ivsnvdm = 63;
ivsnvdd05 = 64;
ivsnvdd1 = 65;
ivsnvdd15 = 65;
ivsnvdd2 = 65;

vpsnvdm = 27;
vpsnvdd05 = 30;
vpsnvdd1 = 286;
vpsnvdd15 = 98;
vpsnvdd2 = 12;
```

```
(* vp DEFINES THE LOCATION OF THE PROFILES NOTE: SOMETIMES THE START
OF THE VESSEL DETECTION IS AT THE POSITION OF THE PROFILE SO CLOSEST PROFILES
INCORPORATING 20 PROFILES ARE TAKEN*)
        (* ST ARTERIOLES *)
staddm = xyn[[ivstadm, 1, {vpstadm, vpstadm - vpr, vpstadm + vpr}]];
stadd05 =
  xyn[[ivstadd05, 1, {vpstadd05, vpstadd05 - vpr, vpstadd05 + vpr}]];
stadd1 = xyn[[ivstadd1,
   1, {vpstadd1, vpstadd1 - vpr, vpstadd1 + vpr}]];
stadd15 =
  xyn[[ivstadd15, 1, {vpstadd15, vpstadd15 - vpr, vpstadd15 + vpr}]];
stadd2 = xyn[[ivstadd2,
   1, {vpstadd2, vpstadd2 - vpr, vpstadd2 + vpr}]];
        (* IT ARTERIOLES *)
itaddm = xyn[[ivitadm, 1, {vpitadm, vpitadm - vpr, vpitadm + vpr}]];
itadd05 =
  xyn[[ivitadd05, 1, {vpitadd05, vpitadd05 - vpr, vpitadd05 + vpr}]];
itadd1 = xyn[[ivitadd1,
   1, {vpitadd1, vpitadd1 - vpr, vpitadd1 + vpr}]];
itadd15 =
  xyn[[ivitadd15, 1, {vpitadd15, vpitadd15 - vpr, vpitadd15 + vpr}]];
itadd2 = xyn[[ivitadd2,
   1, {vpitadd2, vpitadd2 - vpr, vpitadd2 + vpr}]];
        (* IN ARTERIOLES *)
inaddm = xyn[[ivinadm, 1, {vpinadm, vpinadm - vpr, vpinadm + vpr}]];
inadd05 =
  xyn[[ivinadd05, 1, {vpinadd05, vpinadd05 - vpr, vpinadd05 + vpr}]];
inadd1 = xyn[[ivinadd1,
   1, {vpinadd1, vpinadd1 - vpr, vpinadd1 + vpr}]];
inadd15 =
  xyn[[ivinadd15, 1, {vpinadd15, vpinadd15 - vpr, vpinadd15 + vpr}]];
inadd2 = xyn[[ivinadd2,
   1, {vpinadd2, vpinadd2 - vpr, vpinadd2 + vpr}]];
        (* SN ARTERIOLES *)
snaddm = xyn[[ivsnadm, 1, {vpsnadm, vpsnadm - vpr, vpsnadm + vpr}]];
snadd05 =
  xyn[[ivsnadd05, 1, {vpsnadd05, vpsnadd05 - vpr, vpsnadd05 + vpr}]];
snadd1 = xyn[[ivsnadd1,
   1, {vpsnadd1, vpsnadd1 - vpr, vpsnadd1 + vpr}]];
snadd15 =
  xyn[[ivsnadd15, 1, {vpsnadd15, vpsnadd15 - vpr, vpsnadd15 + vpr}]];
snadd2 = xyn[[ivsnadd2,
   1, {vpsnadd2, vpsnadd2 - vpr, vpsnadd2 + vpr}]];

        (* ST VENULES *)
stvddm = xyn[[ivstvdm, 1, {vpstvdm, vpstvdm - vpr, vpstvdm + vpr}]];
stvdd05 =
  xyn[[ivstvdd05, 1, {vpstvdd05, vpstvdd05 - vpr, vpstvdd05 + vpr}]];
stvdd1 = xyn[[ivstvdd1,
   1, {vpstvdd1, vpstvdd1 - vpr, vpstvdd1 + vpr}]];
stvdd15 =
  xyn[[ivstvdd15, 1, {vpstvdd15, vpstvdd15 - vpr, vpstvdd15 + vpr}]];
stvdd2 = xyn[[ivstvdd2,
   1, {vpstvdd2, vpstvdd2 - vpr, vpstvdd2 + vpr}]];
        (* IT VENULES *)
itvddm = xyn[[ivitvdm, 1, {vpitvdm, vpitvdm - vpr, vpitvdm + vpr}]];
itvdd05 =
  xyn[[ivitvdd05, 1, {vpitvdd05, vpitvdd05 - vpr, vpitvdd05 + vpr}]];
itvdd1 = xyn[[ivitvdd1,
```

```
   1, {vpitvdd1, vpitvdd1 - vpr, vpitvdd1 + vpr}]];
itvdd15 =
  xyn[[ivitvdd15, 1, {vpitvdd15, vpitvdd15 - vpr, vpitvdd15 + vpr}]];
itvdd2 = xyn[[ivitvdd2,
   1, {vpitvdd2, vpitvdd2 - vpr, vpitvdd2 + vpr}]];
          (* IN VENULES *)
invddm = xyn[[ivinvdm, 1, {vpinvdm, vpinvdm - vpr, vpinvdm + vpr}]];
invdd05 =
  xyn[[ivinvdd05, 1, {vpinvdd05, vpinvdd05 - vpr, vpinvdd05 + vpr}]];
invdd1 = xyn[[ivinvdd1,
   1, {vpinvdd1, vpinvdd1 - vpr, vpinvdd1 + vpr}]];
invdd15 =
  xyn[[ivinvdd15, 1, {vpinvdd15, vpinvdd15 - vpr, vpinvdd15 + vpr}]];
invdd2 = xyn[[ivinvdd2,
   1, {vpinvdd2, vpinvdd2 - vpr, vpinvdd2 + vpr}]];
          (* SN VENULES *)
snvddm = xyn[[ivsnvdm, 1, {vpsnvdm, vpsnvdm - vpr, vpsnvdm + vpr}]];
snvdd05 =
  xyn[[ivsnvdd05, 1, {vpsnvdd05, vpsnvdd05 - vpr, vpsnvdd05 + vpr}]];
snvdd1 = xyn[[ivsnvdd1,
   1, {vpsnvdd1, vpsnvdd1 - vpr, vpsnvdd1 + vpr}]];
snvdd15 =
  xyn[[ivsnvdd15, 1, {vpsnvdd15, vpsnvdd15 - vpr, vpsnvdd15 + vpr}]];
snvdd2 = xyn[[ivsnvdd2,
   1, {vpsnvdd2, vpsnvdd2 - vpr, vpsnvdd2 + vpr}]];


(* -SHOWS THE SEGMENTATION OF THE RETINA AND LOCATION OF THE PROFILES AND THE
VESSEL TRACKING *)
DisplayTogetherArray[
 Show[pic,
  ListPlot[#, PlotStyle -> {Red, Orange, Orange}] & /@ {staddm,
    stadd05, stadd1, stadd15, stadd2, itaddm, itadd05, itadd1,
    itadd15, itadd2, inaddm, inadd05, inadd1, inadd15, inadd2, snaddm,
     snadd05, snadd1, snadd15, snadd2},
  PlotLabel ->
   "Locations of arteriolar profile analysis\n and retinal image \
segmentation", ImageSize -> 500,
  Epilog -> {Dotted, Yellow,
    PointSize[0.015], {dm, dd05, dd1, dd15, dd2, Point[p1],
     segtext1}}],
 Show[pic,
  ListPlot[xysart],
  ListPlot[#, PlotStyle -> {Red, Orange, Orange}] & /@ {staddm,
    stadd05, stadd1, stadd15, stadd2, itaddm, itadd05, itadd1,
    itadd15, itadd2, inaddm, inadd05, inadd1, inadd15, inadd2, snaddm,
     snadd05, snadd1, snadd15, snadd2},
  PlotLabel ->
   "Locations of arteriolar profile analysis\n and arteriolar vessel \
tracking", ImageSize -> 500,
  Epilog -> {Dotted, Yellow,
    PointSize[0.015], {dm, dd05, dd1, dd15, dd2, Point[p1],
     segtext1}}],
 ImageSize -> 1000
 ]

DisplayTogetherArray[
 Show[pic,
  ListPlot[#, PlotStyle -> {Red, Orange, Orange}] & /@ {stvddm,
    stvdd05, stvdd1, stvdd15, stvdd2, itvddm, itvdd05, itvdd1,
```

```
    itvdd15, itvdd2, invddm, invdd05, invdd1, invdd15, invdd2, snvddm,
     snvdd05, snvdd1, snvdd15, snvdd2},
  PlotLabel ->
   "Locations of venular profile analysis\n and retinal image \
segmentation", ImageSize -> 500,
  Epilog -> {Dotted, Yellow,
    PointSize[0.015], {dm, dd05, dd1, dd15, dd2, Point[p1],
     segtext1}}],
 Show[pic,
  ListPlot[xysvein],
  ListPlot[#, PlotStyle -> {Red, Orange, Orange}] & /@ {stvddm,
    stvdd05, stvdd1, stvdd15, stvdd2, itvddm, itvdd05, itvdd1,
    itvdd15, itvdd2, invddm, invdd05, invdd1, invdd15, invdd2, snvddm,
     snvdd05, snvdd1, snvdd15, snvdd2},
  PlotLabel ->
   "Locations of venular profile analysis\n and arteriolar vessel \
tracking", ImageSize -> 500,
  Epilog -> {Dotted, Yellow,
    PointSize[0.015], {dm, dd05, dd1, dd15, dd2, Point[p1],
     segtext1}}],
 ImageSize -> 1000
 ]
```

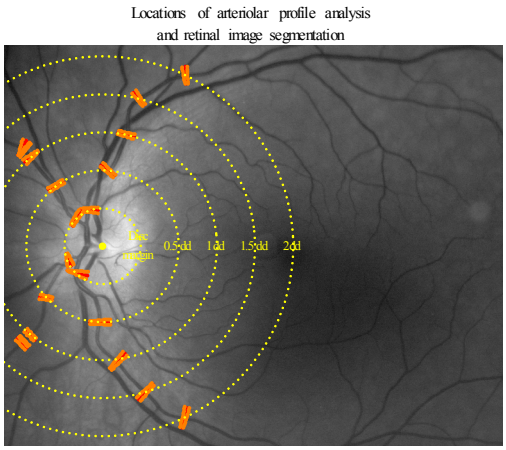

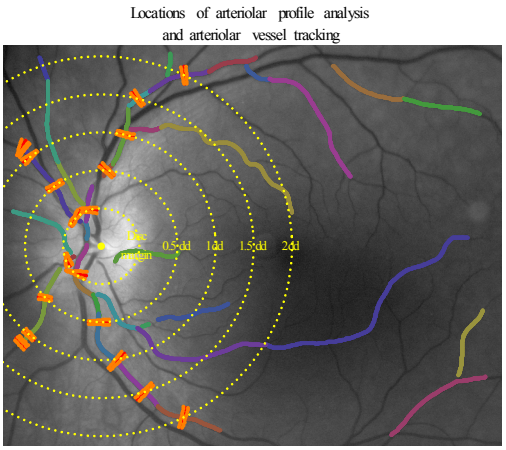

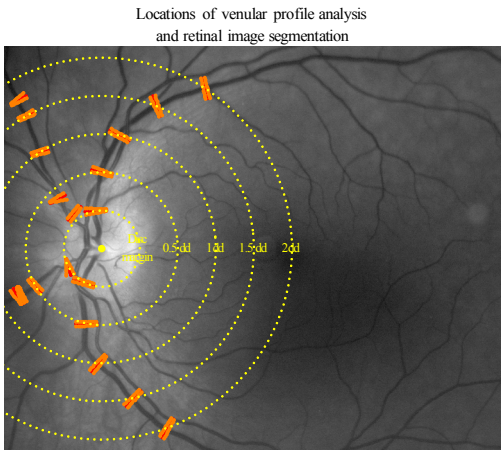

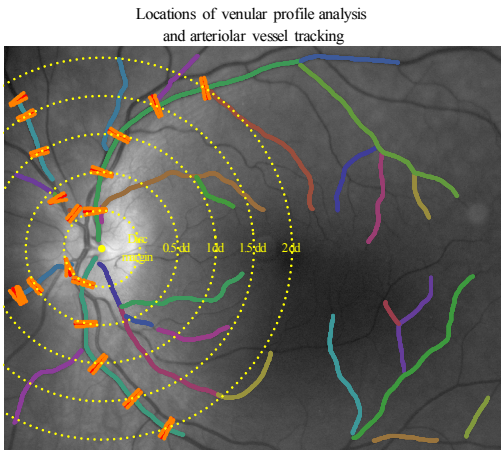

Appendix 5: Oximetry Results in Retinal Artery Occlusion

Subject A3 is a 67 year old male with a 10 day history of a left superior branch retinal artery occlusion (Figure A3.1A). The BCVA of the left eye was 6/9 at the time of imaging. In contrast to subject A1, the dark calibrated spectral images of the left retina at the same 9 selected wavelengths show a macular branch of the superotemporal arteriole appearing slightly more optically dense than in normal eyes at wavelengths greater than 590 nm indicating a lower OS (Figure A3.1B; *yellow arrow head*). The optical density profile and OS calculation of the selected macular branch of the superotemporal arteriole indicate a slightly lower OS of 86% compared to other selected arterioles. (Figure A3.1C, *red bordered image*). Observational abnormalities of the superotemporal and inferotemporal 1st degree venules are not apparent – the optical densities are similar to normal eyes at wavelengths above 600 nm. However, the OS calculation of the superotemporal venule is considerably higher than that of the inferotemporal venule, 32% vs. 5%. The pseudocolour oximetry maps of the retinal vessels show a slightly lower than normal OS in the superotemporal retinal arteriole traversing the macula (Figure A3.1D).

Subject A3

Figure A3.1: Subject A3: a 67 year old male with a 10 day history of a left superior branch retinal artery occlusion (BCVA: 6/9). **A.** A spectral image of the left fundus acquired at 580 nm (colour image was not obtained). **B.** Dark calibrated spectral images of the left retina at 9 selected wavelengths (560, 570, 580, 590, 600, 610, 620 and 630 nm). First degree retinal arterioles and venules are indicated by *red* and *blue arrow heads* respectively. An abnormal appearance of the retinal arteriole related to the OS is indicated by the *yellow arrow head*. **C**. The mean optical density profile (± SD; *red filled circle and whiskers*) of selected segments of the temporal arterioles and venules and the respective OS calculations (and 95% confidence interval). Locations of the analysis (red and orange lines) are shown in the grayscale image. Abnormal optical density profiles are indicated by *red borders*. **D**. Pseudocolour oximetry maps of the retinal arterioles (*left images*) and retinal venules (*right images*). A colour scale of the quantitative OS values is to the left of the images.

A. Spectral image at 580 nm

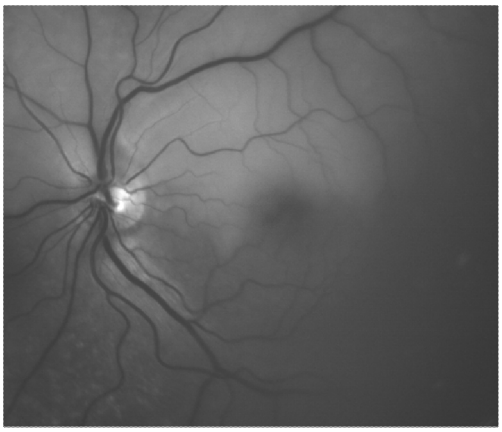

B. Observational features of the spectral images

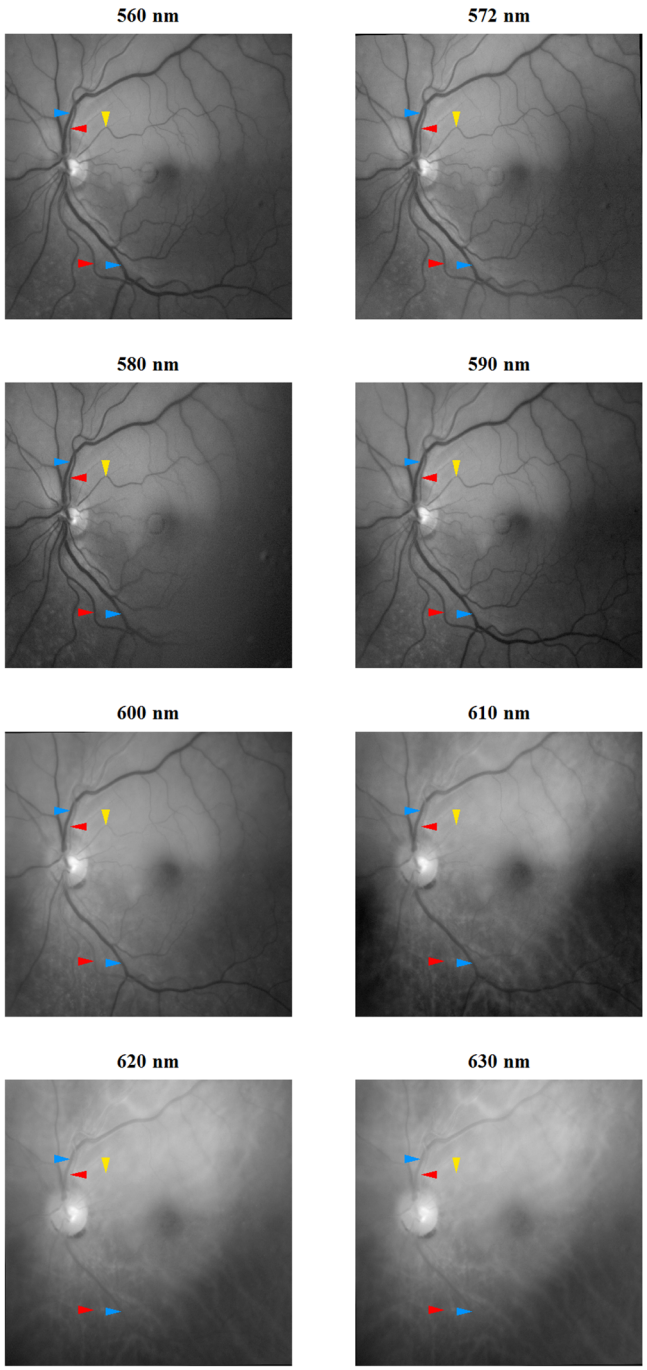

C. Mean optical density profile and oxygen saturation of selected segments of the retinal blood vessels

Location		1st degree vessels	Other vessel segments and macular branches
Arterioles	Superotemporal	Oxygen saturation: 96.44% 95% confidence interval: 81.64% – 111.25% 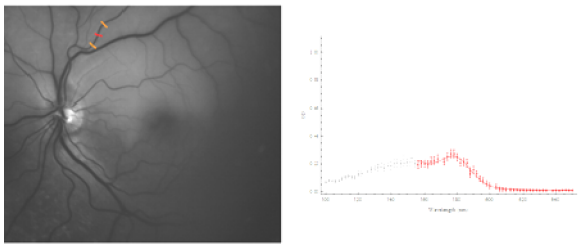	Oxygen saturation: 86.34% 95% confidence interval: 70.44% – 102.24% 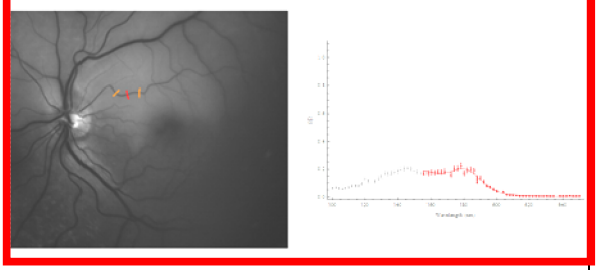
	Inferotemporal	Oxygen saturation: 99.53% 95% confidence interval: 76.24% – 122.83% 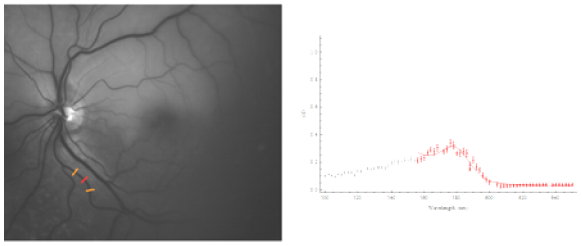	Oxygen saturation: 99.15% 95% confidence interval: 67.35% – 130.94% 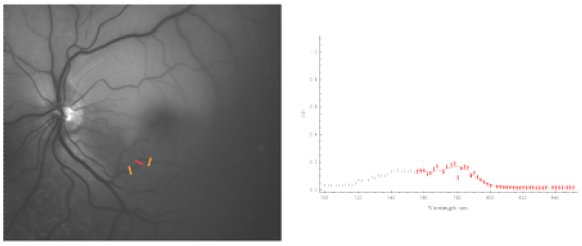
Venules	Superotemporal	Oxygen saturation: 32.6% 95% confidence interval: 21.34% – 43.85% 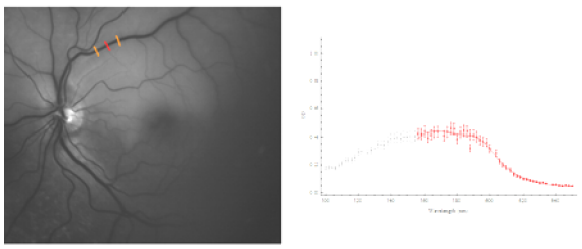	Oxygen saturation: 33.68% 95% confidence interval: 17.6% – 49.77% 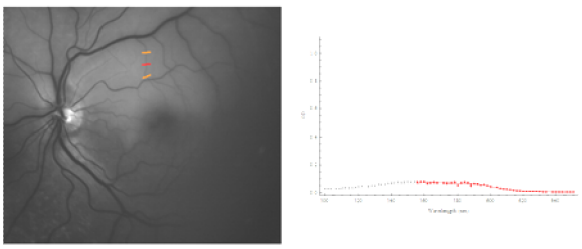
	Inferotemporal	Oxygen saturation: 5.18% 95% confidence interval: −7.9% – 18.26% 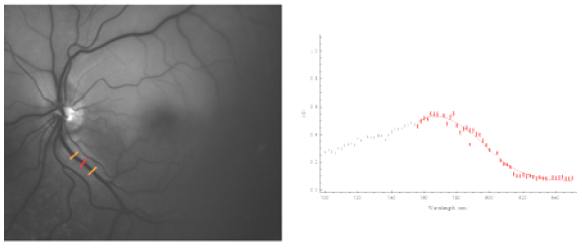	Oxygen saturation: 52.01% 95% confidence interval: 22.96% – 81.06% 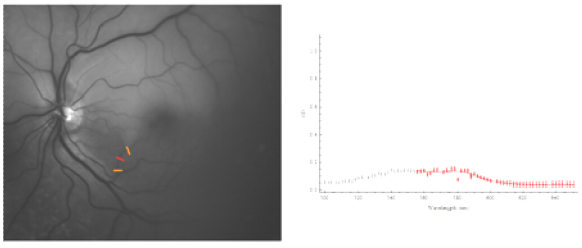

D. Oxygen saturation of the retinal vasculature

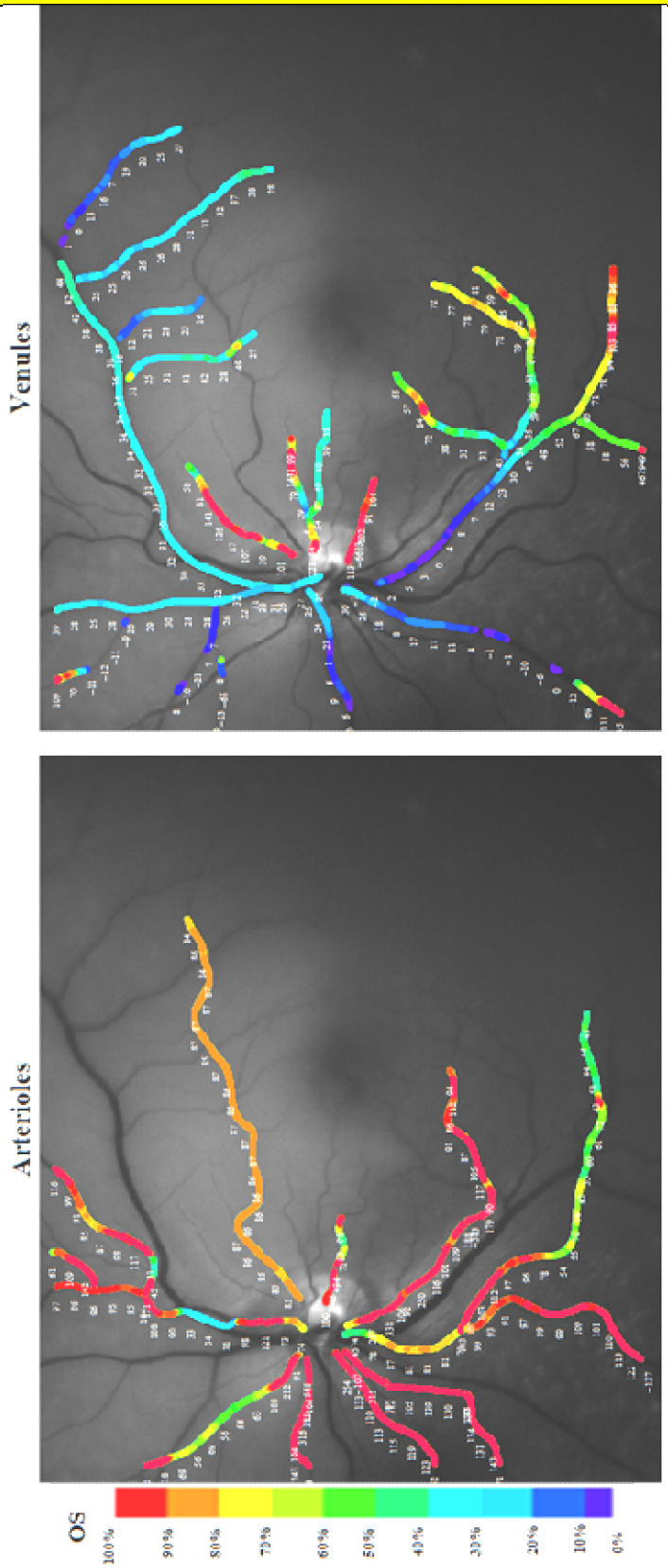

Appendix 6: Oximetry Results in Retinal Vein Occlusion

Figure A4.1: Analyses of subject V1 with spectral images acquired of the superotemporal retina (superotemporal branch retinal vein occlusion). **A.** Dark calibrated spectral images of the left retina at 9 selected wavelengths (560, 570, 580, 590, 600, 610, 620 and 630 nm). First degree retinal arterioles and venules are indicated by *red* and *blue arrow heads* respectively. Abnormal appearances of the retinal venules relating to the OS are indicated by the *green arrow heads*. These venules appear to be less optically dense than in normal eyes at wavelengths greater than 600 nm indicating a higher OS. **B**. The mean optical density profile (± SD; *red filled circle and whiskers*) of selected segments of the temporal arterioles and venules and the respective OS calculations (and 95% confidence interval). Locations of the analysis (red and orange lines) are shown in the grayscale image. Abnormal optical density profiles are indicated by *red borders*. **C**. Pseudocolour oximetry maps of the retinal arterioles (*left images*) and retinal venules (*right images*). There is high venous oxygenation in the superotemporal venules. A colour scale of the quantitative OS values is to the left of the images.

Subject V1 – superotemporal field of view

A. Observational features of the spectral images

560 nm

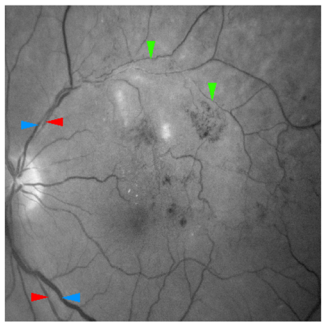

570 nm

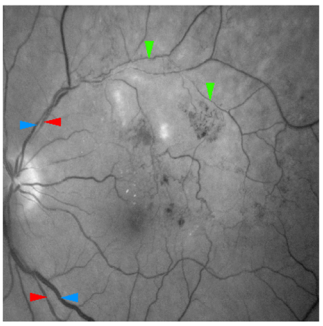

580 nm

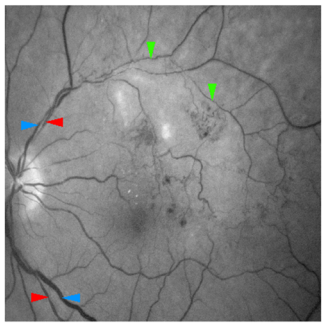

590 nm

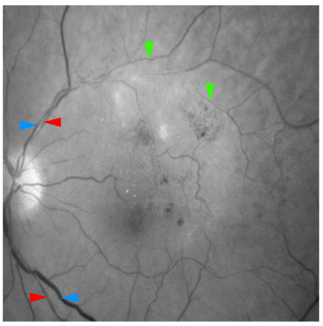

600 nm

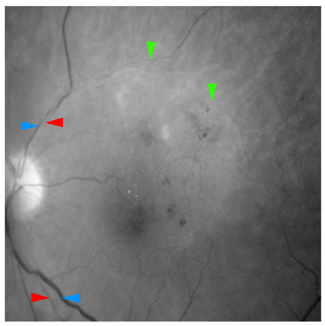

610 nm

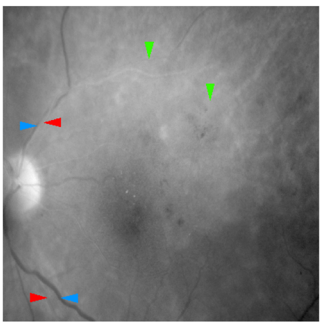

620 nm

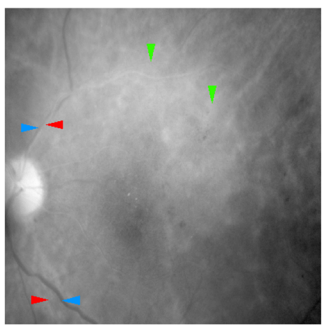

630 nm

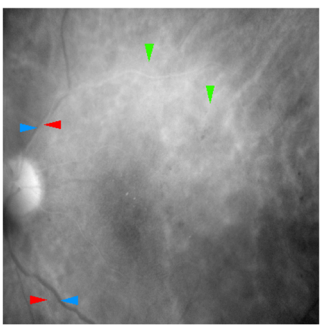

B. Mean optical density profile and oxygen saturation of selected segments of the retinal blood vessels

Location		1st degree vessels	Macular branches
Arterioles	Superotemporal	Oxygen saturation: 126.06% 95% confidence interval: 111.86% – 140.27% 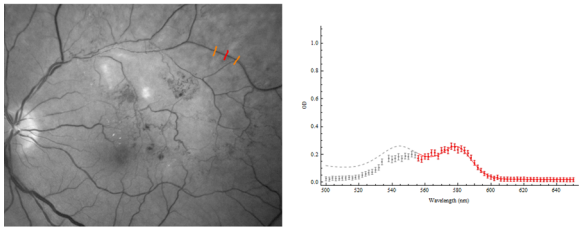	Oxygen saturation: 126.06% 95% confidence interval: 111.86% – 140.27% 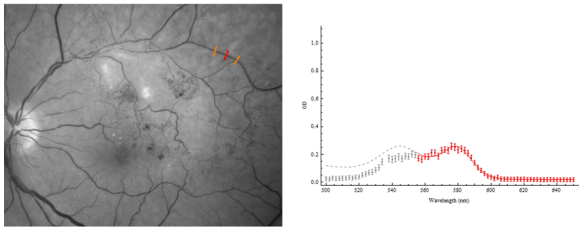
	Inferotemporal	Oxygen saturation: 112.53% 95% confidence interval: 93.61% – 131.46% 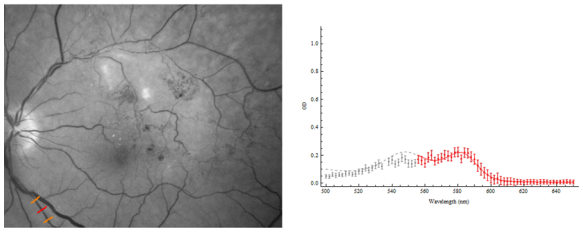	Oxygen saturation: 144.42% 95% confidence interval: 128.45% – 160.39% 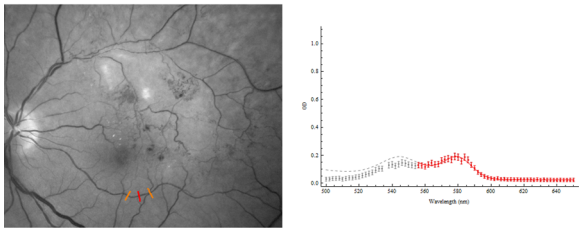
Venules	Superotemporal	Oxygen saturation: 87.29% 95% confidence interval: 75.25% – 99.33% 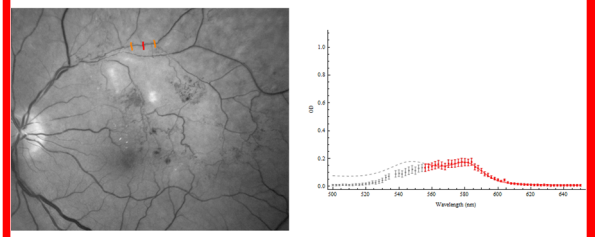	Oxygen saturation: 129.49% 95% confidence interval: 115.98% – 142.99% 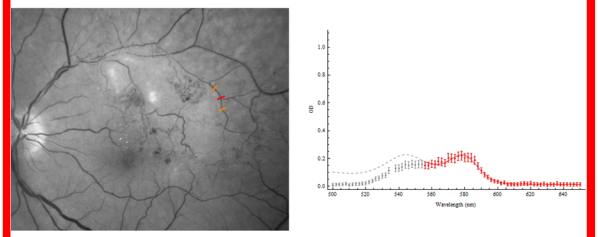
	Inferotemporal	Macular branch Oxygen saturation: 68.04% 95% confidence interval: 57.87% – 78.22% 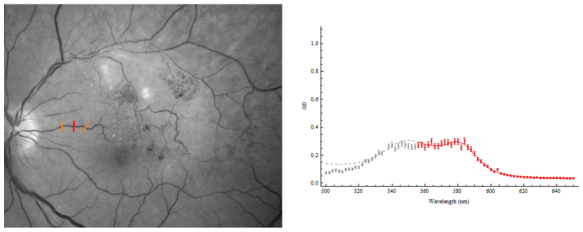	Oxygen saturation: 52.27% 95% confidence interval: 34.05% – 70.48% 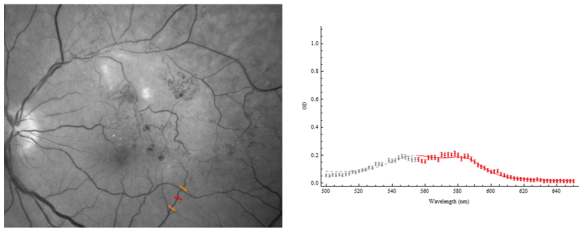

C. Oxygen saturation of the retinal vasculature

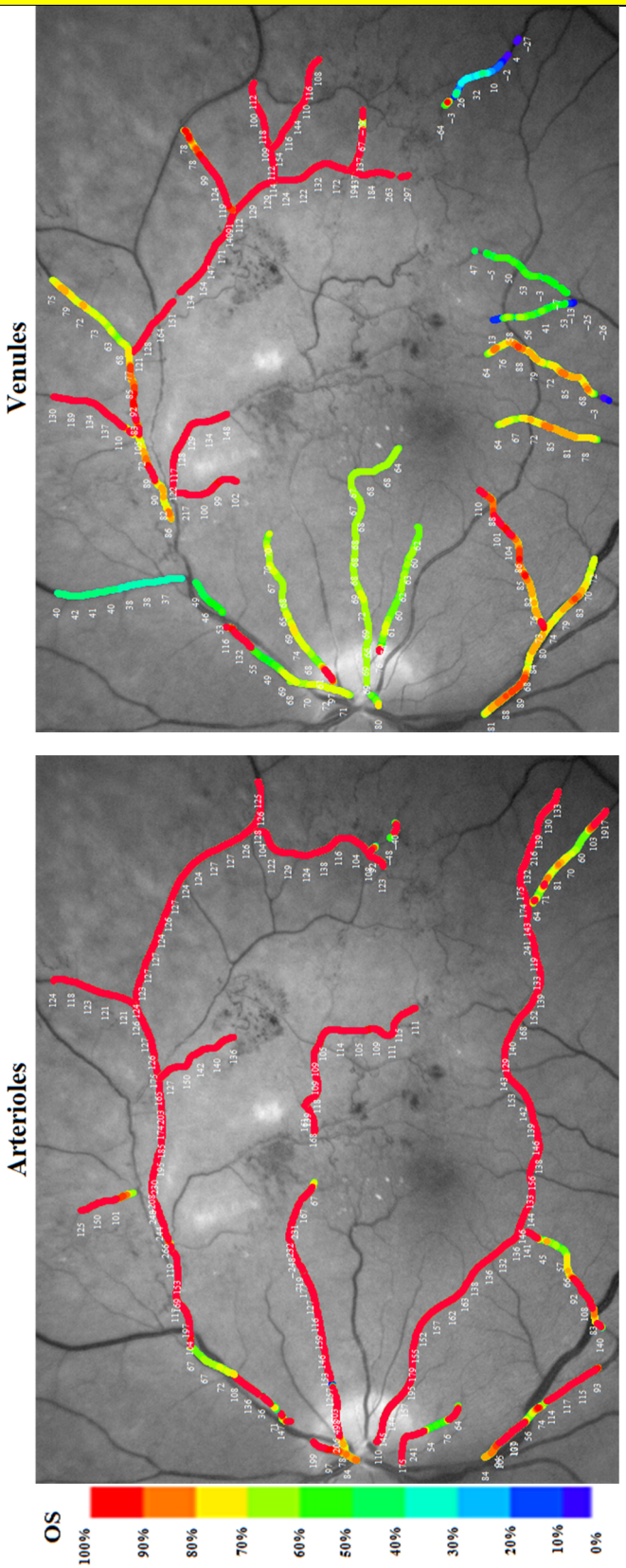

Figure A4.2: Analyses of subject V3 with spectral images acquired of the temporal retina (left ischaemic superotemporal branch retinal vein occlusion with neovascularization of the temporal retina). **A.** A colour image of the left fundus. **B.** Dark calibrated spectral images of the left retina at 9 selected wavelengths (560, 570, 580, 590, 600, 610, 620 and 630 nm). First degree retinal arterioles and venules are indicated by *red* and *blue arrow heads* respectively. Abnormal appearances of the retinal venules relating to the OS are indicated by the *green arrow head*. Theses venules appear less optically dense than in normal eyes at wavelengths greater than 600 nm indicating a higher OS. **C**. The mean optical density profile (± SD; *red filled circle* and *whiskers*) of selected segments of the temporal arterioles and venules and the respective OS calculations (and 95% confidence interval). Locations of the analysis (red and orange lines) are shown in the grayscale image. Abnormal optical density profiles are indicated by *red borders*. **D**. Pseudocolour oximetry maps of the retinal arterioles (*left images*) and retinal venules (*right images*). There is high venous oxygenation in the superotemporal venules. A colour scale of the quantitative OS values is to the left of the images.

Subject V3 - temporal field of view	
A. Colour image	**B. Observational features of the spectral images**
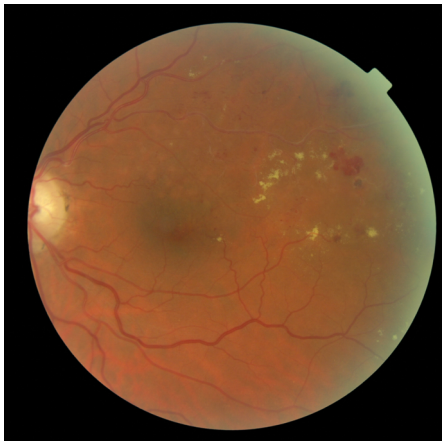	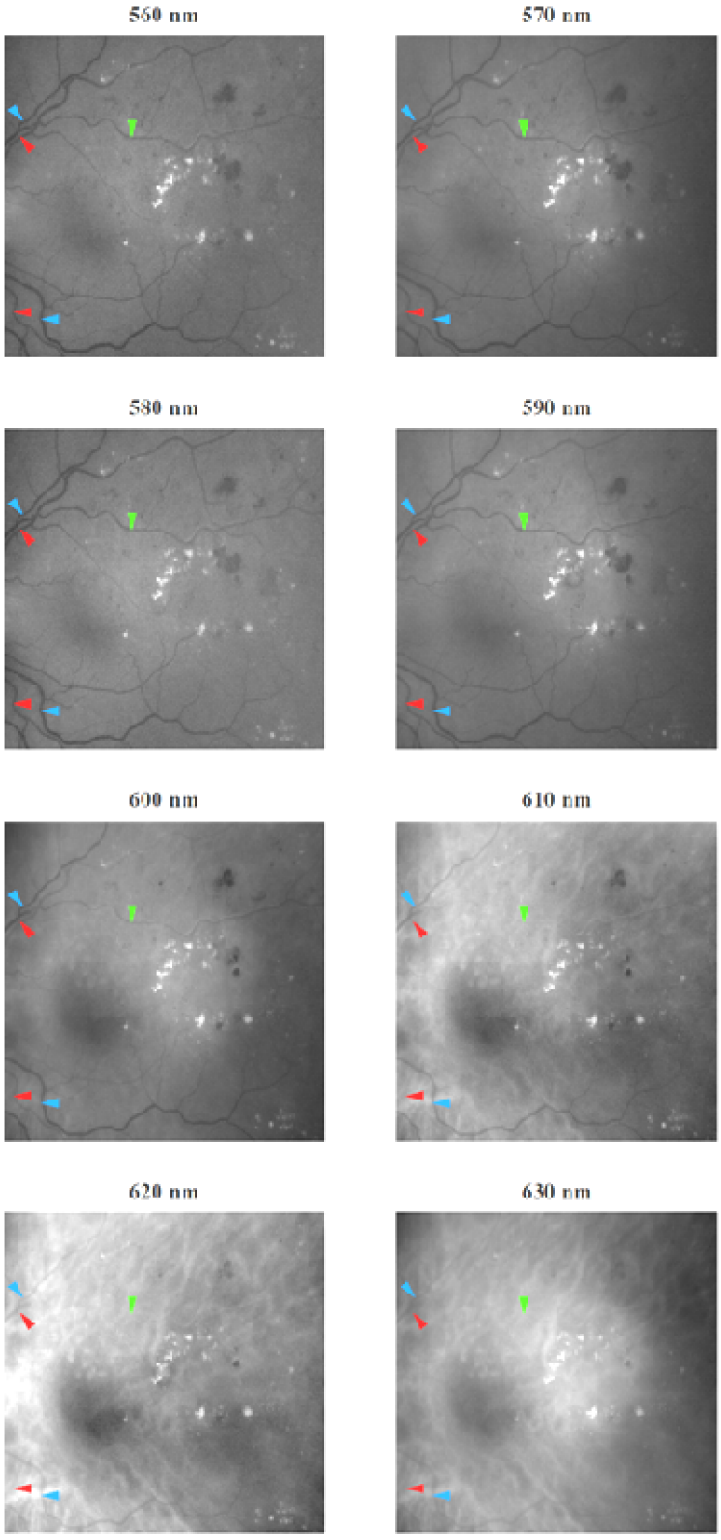

C. Mean optical density profile and oxygen saturation of selected segments of the retinal blood vessels

Location		1st degree vessels	Other vessel segments and macular branches
Arterioles	Superotemporal	Oxygen saturation: 151.01% 95% confidence interval: 125.93% – 176.1% 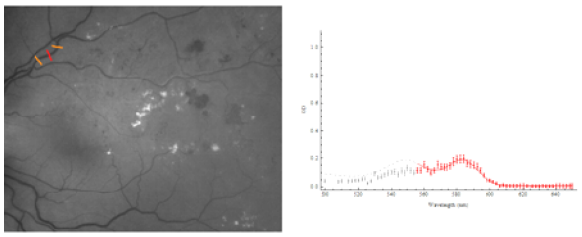	Oxygen saturation: 206.26% 95% confidence interval: 177.29% – 235.23% 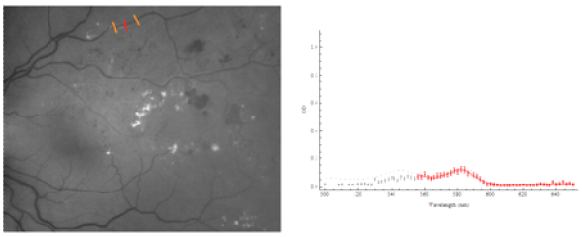
	Inferotemporal	Oxygen saturation: 186.37% 95% confidence interval: 151.08% – 221.67% 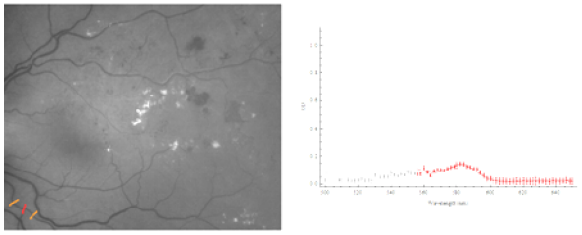	Oxygen saturation: 184.99% 95% confidence interval: 152.37% – 217.62% 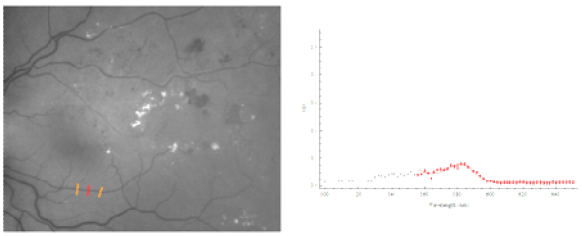
Venules	Superotemporal	Oxygen saturation: 79.92% 95% confidence interval: 57.32% – 102.51% 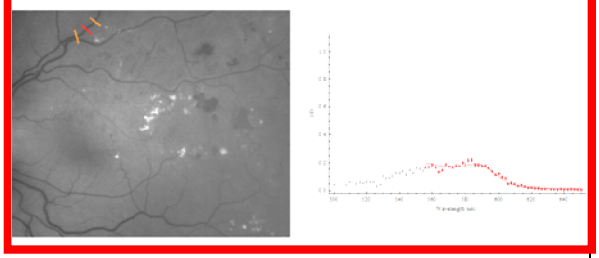	Oxygen saturation: 153.57% 95% confidence interval: 119.32% – 187.81% 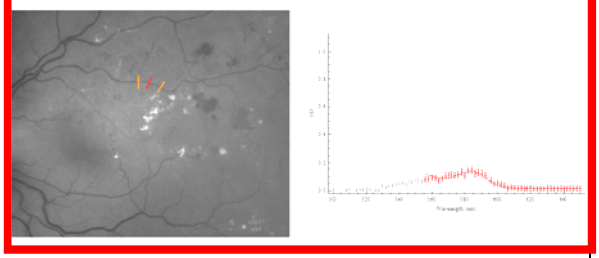
	Inferotemporal	Oxygen saturation: –12.28% 95% confidence interval: –34.09% – 9.52% 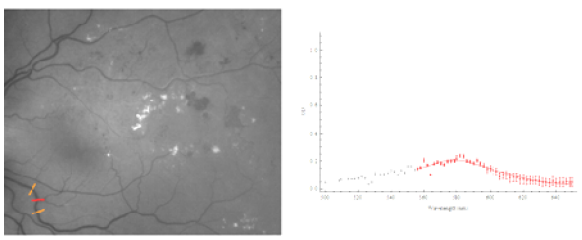	Oxygen saturation: –23.61% 95% confidence interval: –49.37% – 2.15% 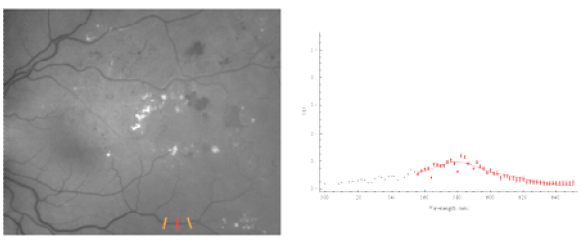

D. Oxygen saturation of the retinal vasculature

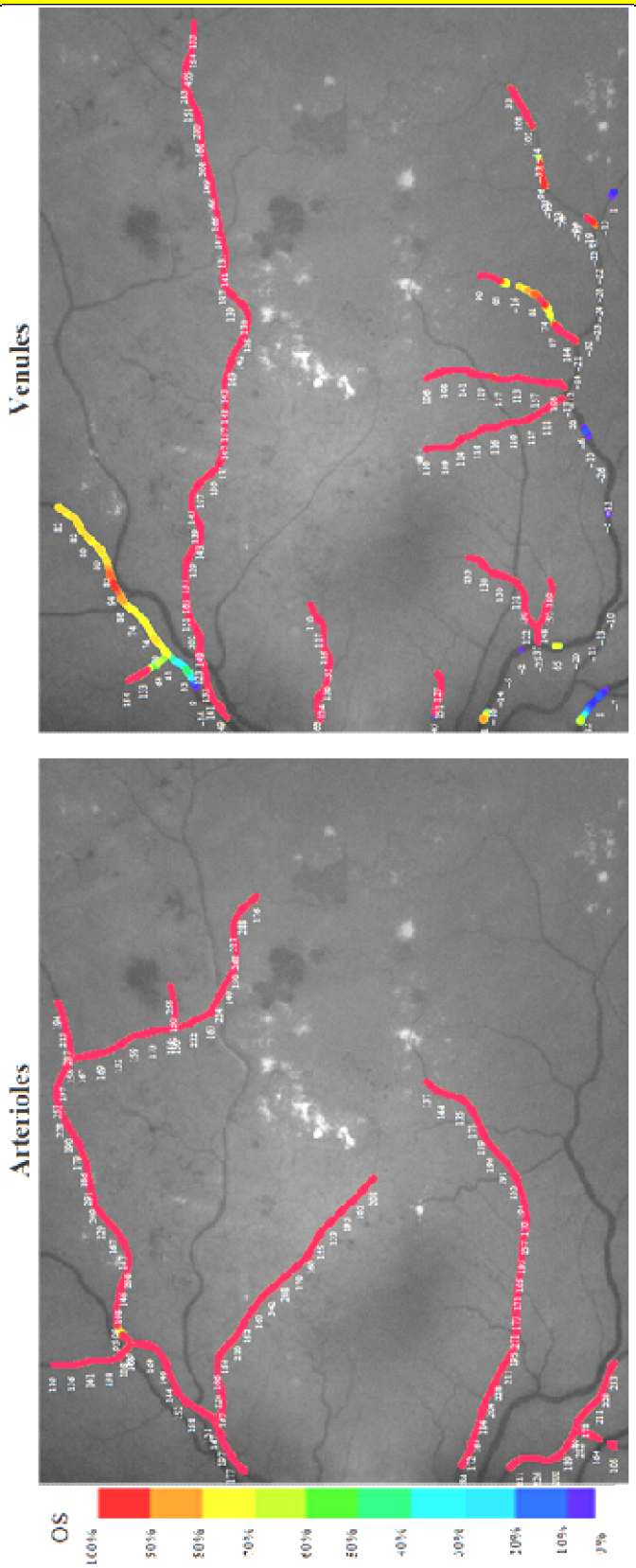

Figure A4.3: Subject V5: a 73 year old female with a 26 month history of a left ischaemic superotemporal branch retinal vein occlusion (BCVA: 6/36). **A.** A colour image of the left fundus. **B.** Fluorescein angiograms of the left fundus 2 years (*left*) and 1 week (*right*) prior to spectral imaging. There is a region of reduced background fluorescence (*yellow arrow head*; capillary "non-perfusion") associated with hyperfluorescent segments of the superotemporal vessels (*red arrow head*; vessel wall staining) **C.** Dark calibrated spectral images of the left retina at 9 selected wavelengths (560, 570, 580, 590, 600, 610, 620 and 630 nm). First degree retinal arterioles and venules are indicated by *red* and *blue arrow heads* respectively. Abnormal appearances of the retinal venules relating to the OS are indicated by the *green arrow heads*. These venules appear less optically dense than in normal eyes at wavelengths greater than 600 nm indicating a higher OS. **D**. The mean optical density profile (± SD; *red filled circle* and *whiskers*) of selected segments of the temporal arterioles and venules and the respective OS calculations (and 95% confidence interval). Locations of the analysis (red and orange lines) are shown in the grayscale image. Abnormal optical density profiles are indicated by *red borders*. **E**. Pseudocolour oximetry maps (t*op image*: standard view of the posterior pole; *bottom image*: superotemporal field of view) of the retinal arterioles (*left images*) and retinal venules (*right images*). There is high venous oxygenation in the superotemporal venules. A colour scale of the quantitative OS values is to the left of the images

.

Subject V5

A. Colour image

2 years prior to spectral imaging

1 week prior to spectral imaging

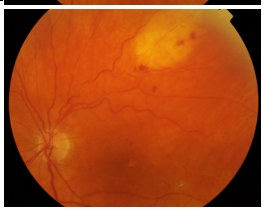

B. Fluorescein Angiogram

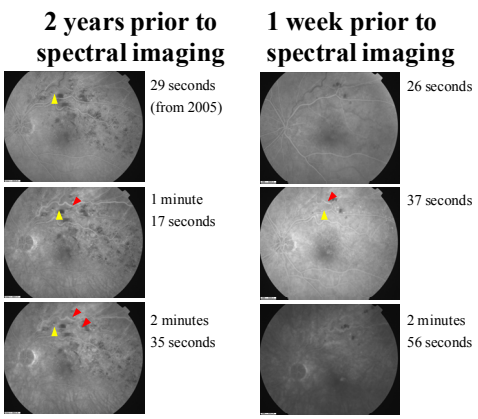

C. Observational features of the spectral images

560 nm

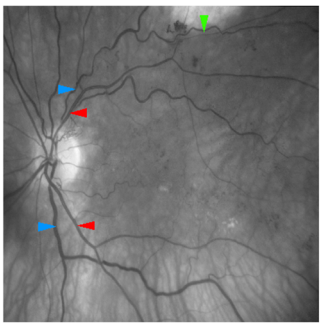

570 nm

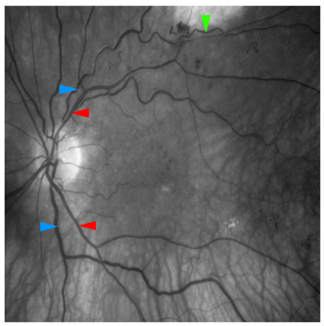

580 nm

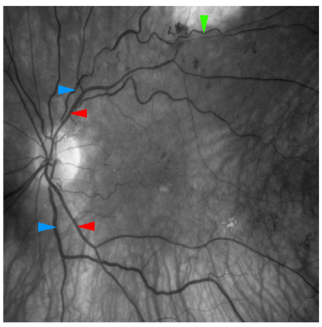

590 nm

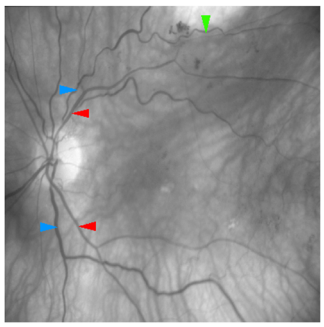

600 nm

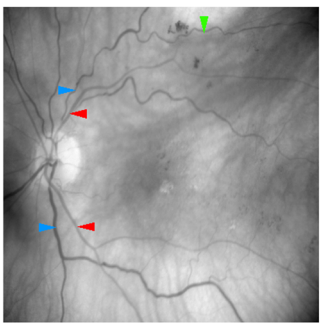

610 nm

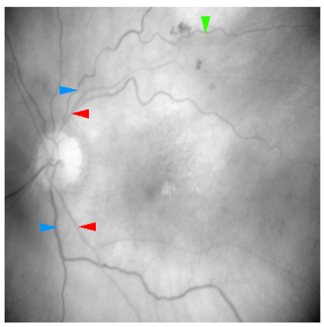

620 nm

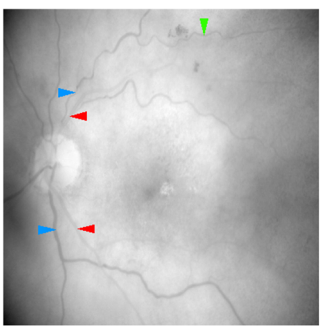

630 nm

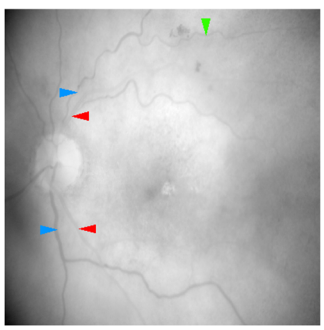

D. Mean optical density profile and oxygen saturation of selected segments of the retinal blood vessels

Location		1st degree vessels	Macular branches
Arterioles	Superotemporal	Oxygen saturation: 114.78% 95% confidence interval: 93.06% – 136.49% 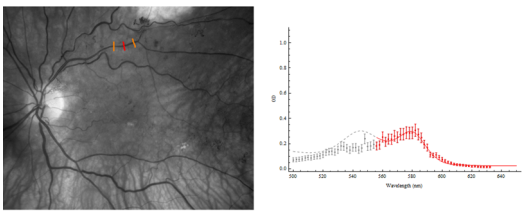	Oxygen saturation: 114.86% 95% confidence interval: 101.03% – 128.69% 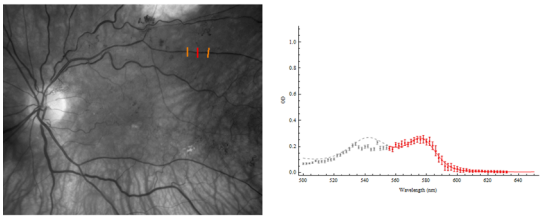
	Inferotemporal	Oxygen saturation: 72.77% 95% confidence interval: 59.48% – 86.06% 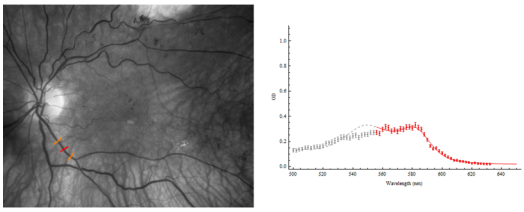	Oxygen saturation: 101.% 95% confidence interval: 82.6% – 119.4% 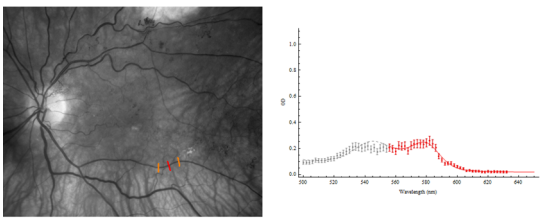
Venules	Superotemporal	Oxygen saturation: 79.77% 95% confidence interval: 53.66% – 105.88% 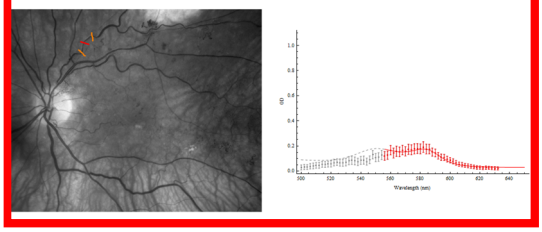	Oxygen saturation: 82.42% 95% confidence interval: 57.9% – 106.94% 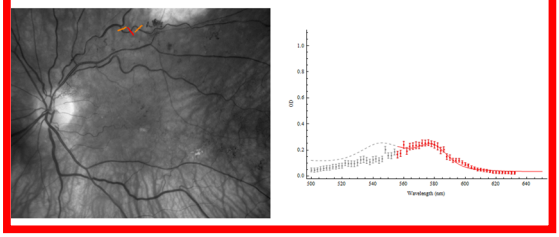
	Inferotemporal	Oxygen saturation: 45.22% 95% confidence interval: 32.96% – 57.48% 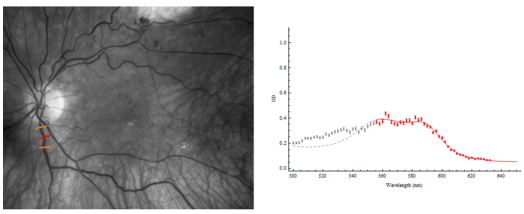	Oxygen saturation: 38.12% 95% confidence interval: –5.59% – 81.82% 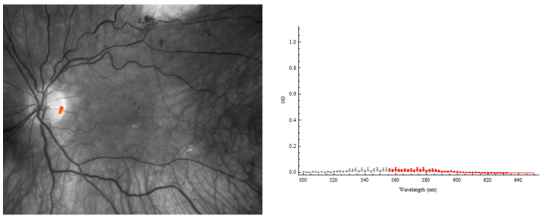

E. Oxygen saturation of the retinal vasculature

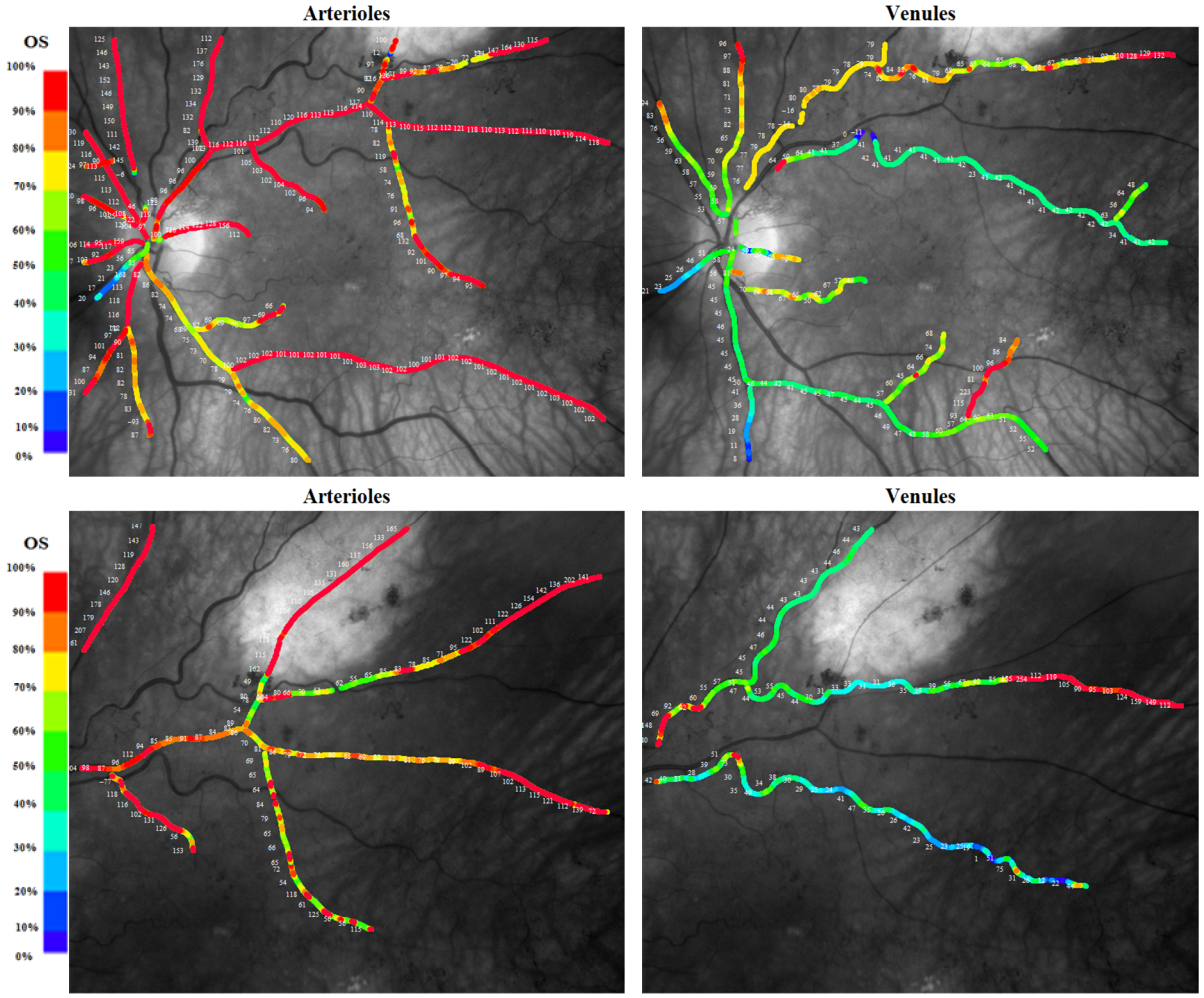

Figure A4.4: Subject V6: a 53 year old female with a 4 month history of a right ischaemic superotemporal branch retinal vein occlusion (BCVA: 6/24). **A.** A colour image of the right fundus. **B.** Fluorescein angiograms of the right fundus. There is a region of reduced background fluorescence (*yellow arrow head*; capillary "non-perfusion"). **C.** Dark calibrated spectral images of the left retina at 9 selected wavelengths (560, 570, 580, 590, 600, 610, 620 and 630 nm). First degree retinal arterioles and venules are indicated by *red* and *blue arrow heads* respectively. Abnormal appearances of the retinal venules relating to the OS are indicated by the *green arrow head*. The venules appear less optically dense than in normal eyes at wavelengths greater than 600 nm indicating a higher OS. **D**. The mean optical density profile (± SD; *red filled circle* and *whiskers*) of selected segments of the temporal arterioles and venules and the respective OS calculations (and 95% confidence interval). Locations of the analysis (red and orange lines) are shown in the grayscale image. **E**. Pseudocolour oximetry maps of the retinal arterioles (*left images*) and retinal venules (*right images*). A colour scale of the quantitative OS values is to the left of the images.

Subject V6

A. Colour image

B. Observational features of the spectral images

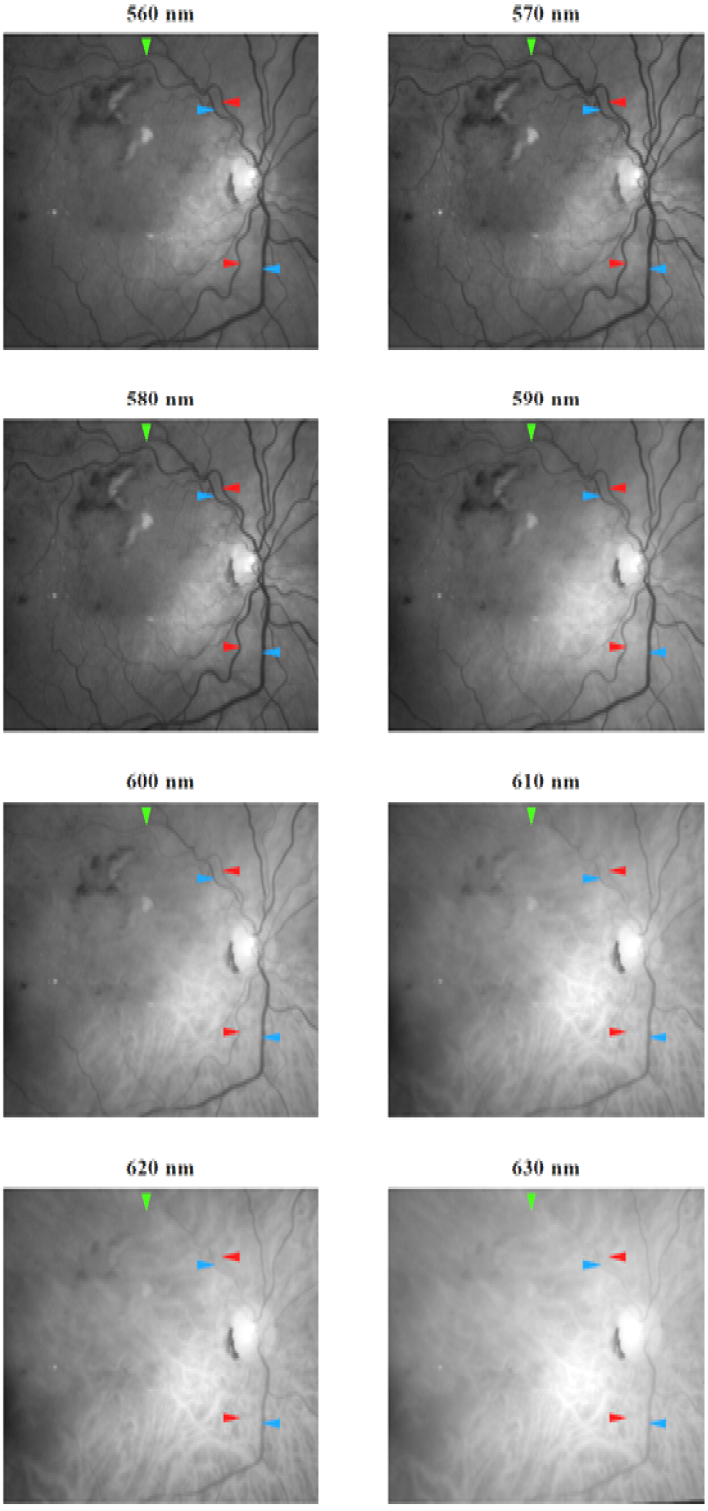

C. Fluorescein Angiogram

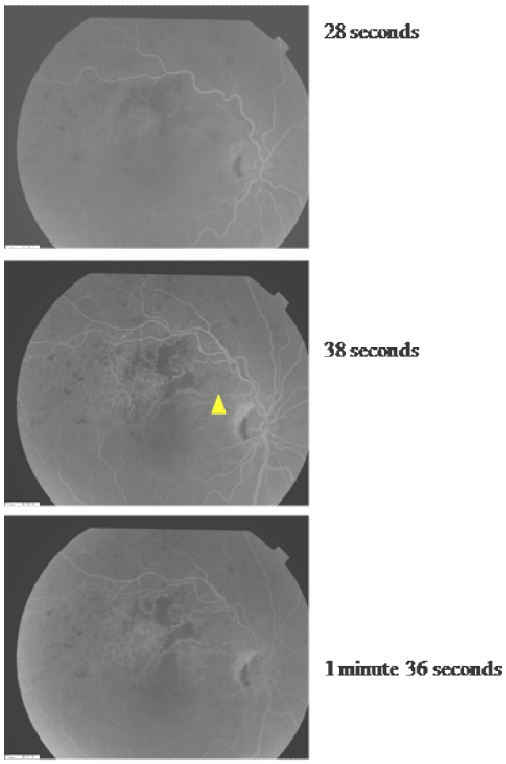

D. Mean optical density profile and oxygen saturation of selected segments of the retinal blood vessels

Location		1st degree vessels	Other vessel segments and macular branches
Arterioles	Superotemporal	Oxygen saturation: 112.19% 95% confidence interval: 97.45% – 126.93% 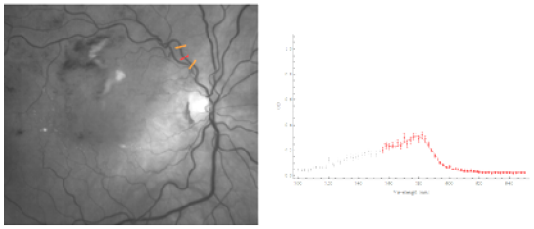	Oxygen saturation: 174.94% 95% confidence interval: 151.05% – 198.83% 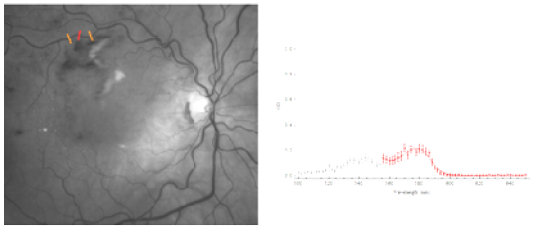
	Inferotemporal	Oxygen saturation: 108.3% 95% confidence interval: 96.72% – 119.87% 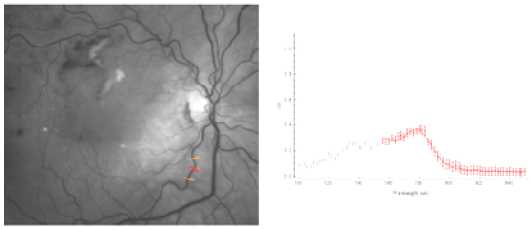	Oxygen saturation: 123.67% 95% confidence interval: 105.22% – 142.12% 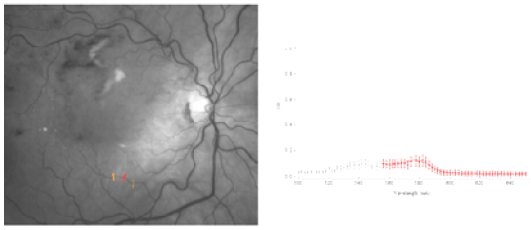
Venules	Superotemporal	Oxygen saturation: 44.85% 95% confidence interval: 34.76% – 54.95% 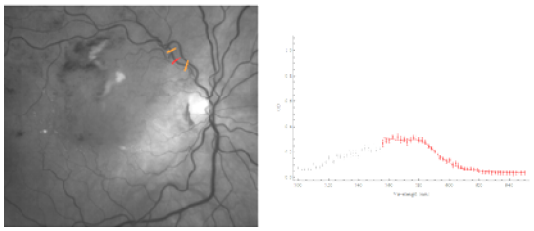	Oxygen saturation: 23.1% 95% confidence interval: 6.23% – 39.97% 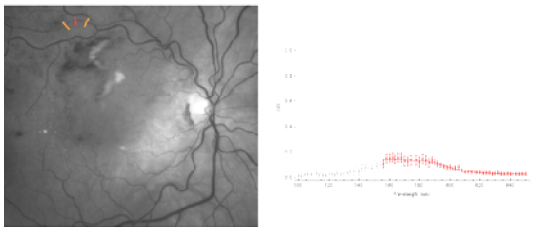
	Inferotemporal	Oxygen saturation: 19.93% 95% confidence interval: 4.9% – 34.97% 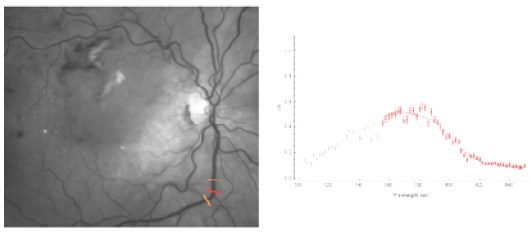	Oxygen saturation: 73.41% 95% confidence interval: 56.76% – 90.06% 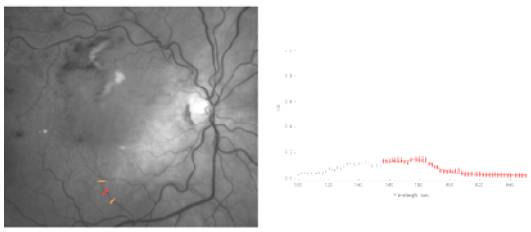

E. Oxygen saturation of the retinal vasculature

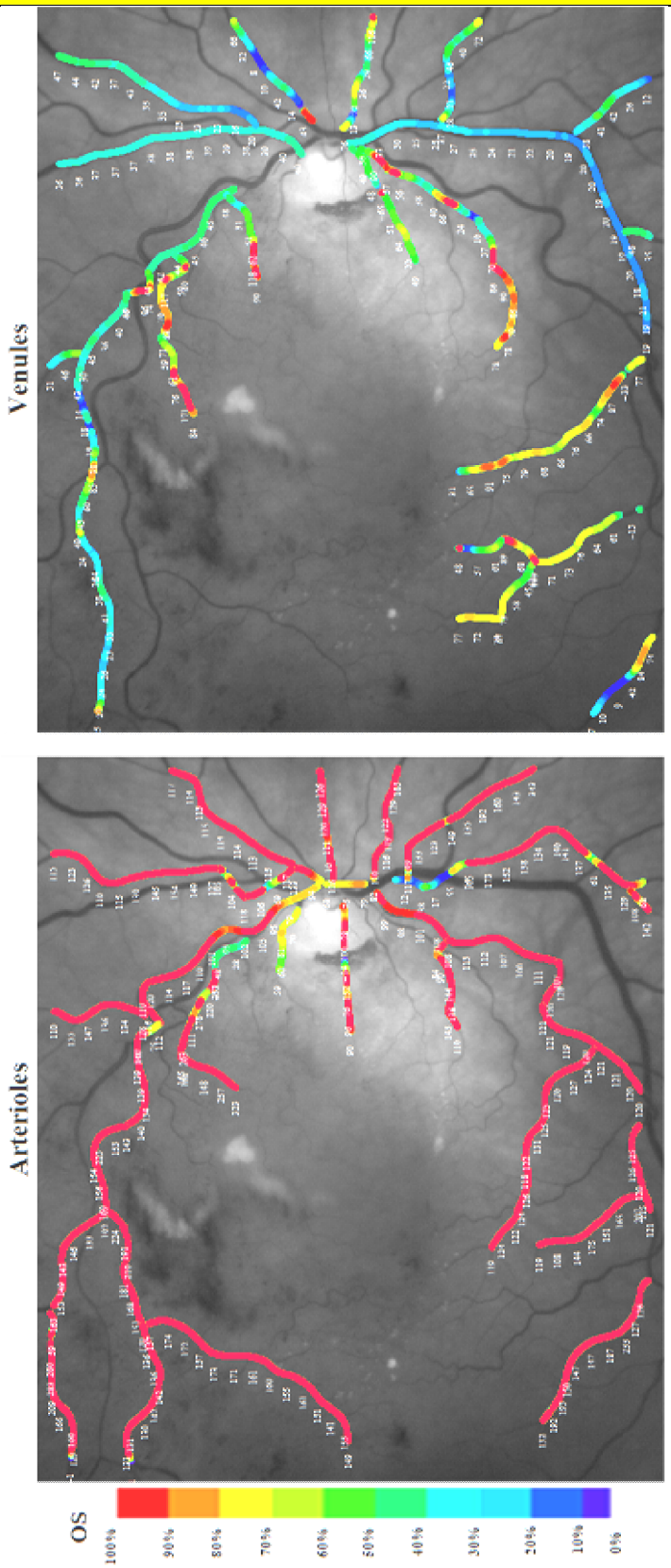

Figure A4.5: Subject V7: a 53 year old male with a 9 month history of a right ischaemic superior hemi-retinal vein occlusion (BCVA: 6/18). **A.** A colour image of the right fundus. **B.** Fluorescein angiograms of the right fundus. Hyperfluorescent segments of the superotemporal vessels are present (*red arrow head*; vessel wall staining). **C.** Dark calibrated spectral images of the left retina at 9 selected wavelengths (560, 570, 580, 590, 600, 610, 620 and 630 nm). First degree retinal arterioles and venules are indicated by *red* and *blue arrow heads* respectively. Abnormal appearances of the retinal venules relating to the OS are indicated by the *green arrow head*. The venule appears less optically dense than in normal eyes at wavelengths greater than 600 nm indicating a higher OS. **D**. The mean optical density profile (± SD; *red filled circle* and *whiskers*) of selected segments of the temporal arterioles and venules and the respective OS calculations (and 95% confidence interval). Locations of the analysis (red and orange lines) are shown in the grayscale image. **E**. Pseudocolour oximetry maps of the retinal arterioles (*left images*) and retinal venules (*right images*). A colour scale of the quantitative OS values is to the left of the images.

Subject V7

A. Colour image

B. Fluorescein Angiogram

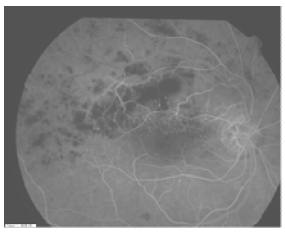

39 seconds

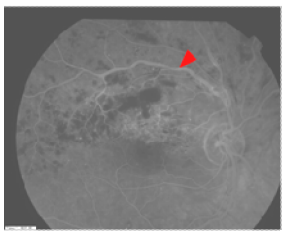

1 minute 48 seconds

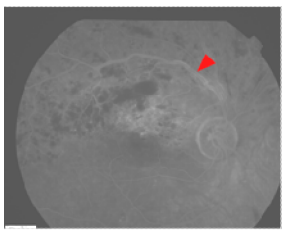

3 minutes 17 seconds

C. Observational features of the spectral images

560 nm

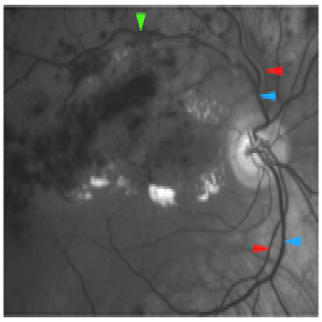

570 nm

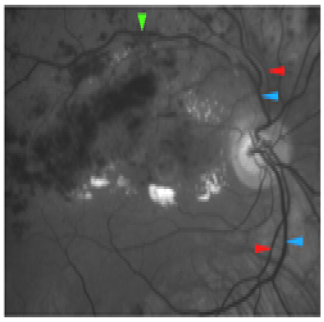

580 nm

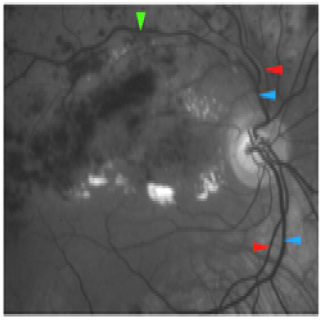

590 nm

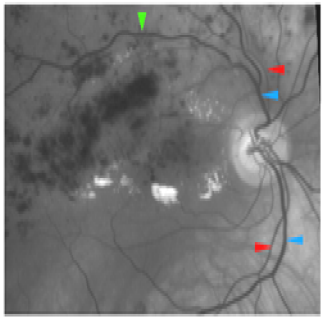

600 nm

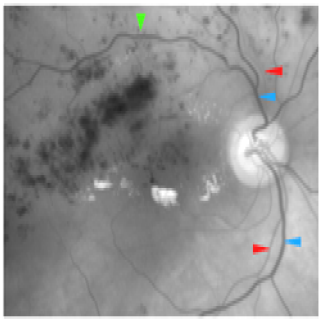

610 nm

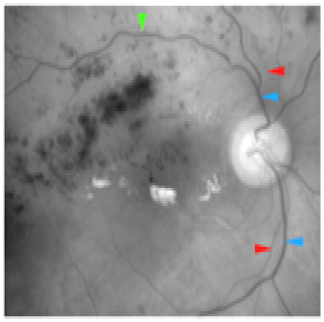

620 nm

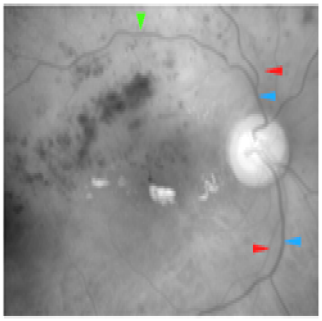

630 nm

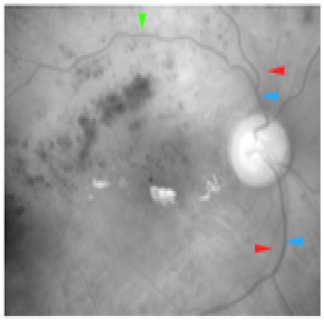

D. Mean optical density profile and oxygen saturation of selected segments of the retinal blood vessels			
Location		**1st degree vessels**	**Macular branches**
Arterioles	**Superotemporal**	Oxygen saturation: 71.27% 95% confidence interval: 46.81% – 95.74% 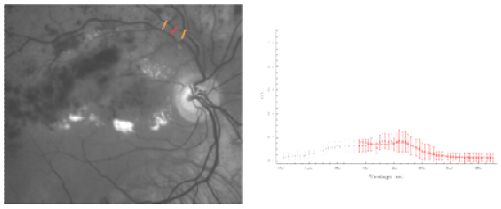	Oxygen saturation: 94.95% 95% confidence interval: 75.51% – 114.4% 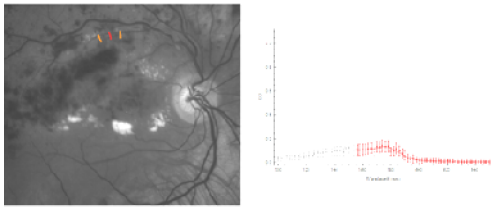
	Inferotemporal	Oxygen saturation: 93.29% 95% confidence interval: 79.88% – 106.7% 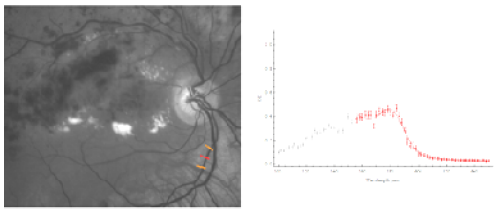	Oxygen saturation: 93.25% 95% confidence interval: 78.9% – 107.61% 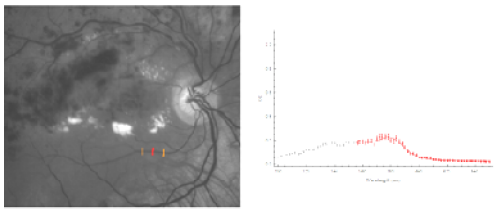
Venules	**Superotemporal**	Oxygen saturation: 25.84% 95% confidence interval: 8.04% – 43.64% 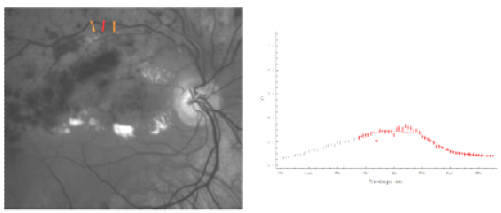	Oxygen saturation: 39.96% 95% confidence interval: 28.55% – 51.37% 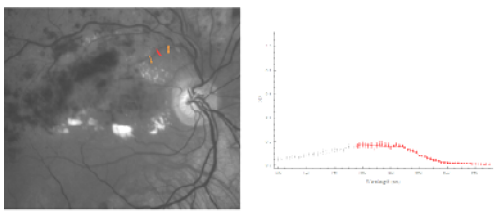
	Inferotemporal	Oxygen saturation: 64.86% 95% confidence interval: 48.16% – 81.56% 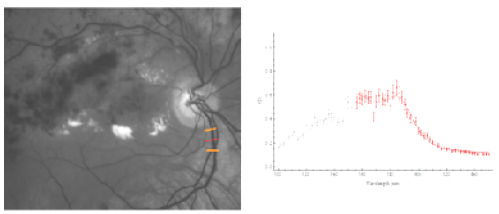	Oxygen saturation: 64.9% 95% confidence interval: 52.39% – 75.61% 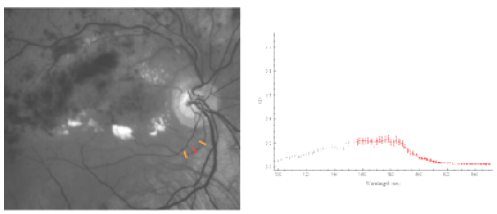

E. Oxygen saturation of the retinal vasculature

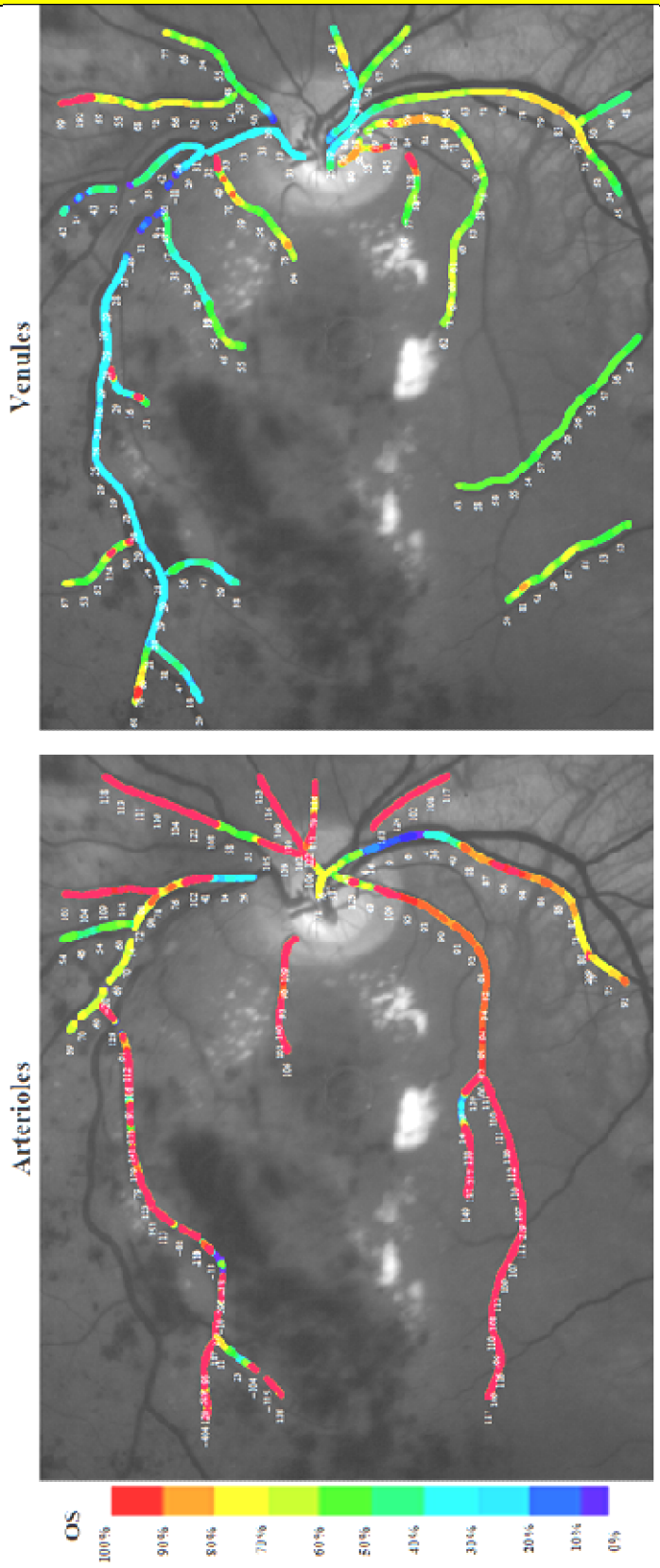

Figure A4.6: Subject V8: a 70 year old male with a 4 month history of a right non-ischaemic superior hemi-retinal vein occlusion (BCVA: 6/12). **A.** A colour image of the right fundus (fluorescein angiogram was not performed). **B.** Dark calibrated spectral images of the left retina at 9 selected wavelengths (560, 570, 580, 590, 600, 610, 620 and 630 nm). First degree retinal arterioles and venules are indicated by *red* and *blue arrow heads* respectively. Abnormal appearances of the retinal venules relating to the OS are not present. **C**. The mean optical density profile (± SD; *red filled circle* and *whiskers*) of selected segments of the temporal arterioles and venules and the respective OS calculations (and 95% confidence interval). Locations of the analysis (red and orange lines) are shown in the grayscale image. **D**. Pseudocolour oximetry maps of the retinal arterioles (*left images*) and retinal venules (*right images*). A colour scale of the quantitative OS values is to the left of the images.

Subject V8	
A. Colour image	**B. Observational features of the spectral images**
	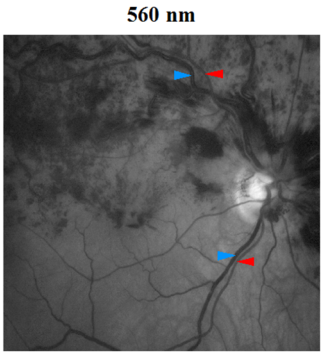 560 nm 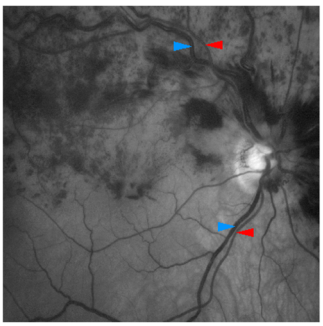 570 nm 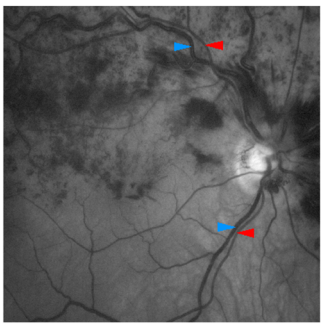 580 nm 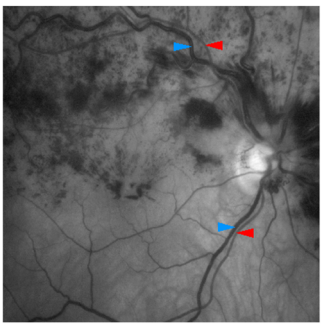 590 nm 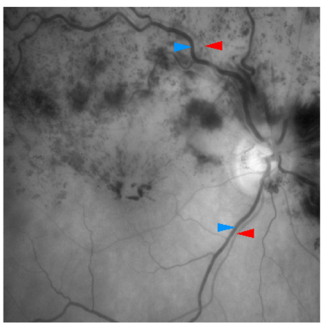 600 nm 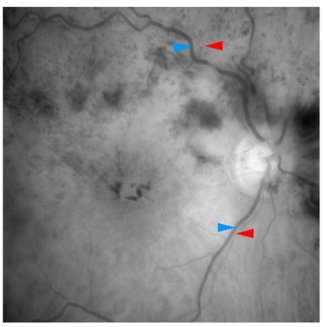 610 nm 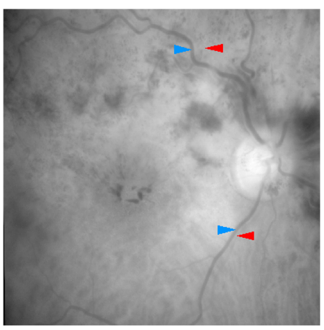 620 nm 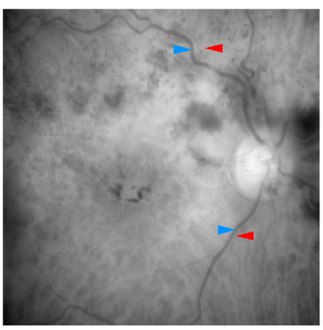 630 nm
Fluorescein angiogram not performed	

C. Mean optical density profile and oxygen saturation of selected segments of the retinal blood vessels

Location		1st degree vessels	Other vessel segments and macular branches
Arterioles	Superotemporal	Oxygen saturation: 170.27% 95% confidence interval: 142.73% – 197.81% 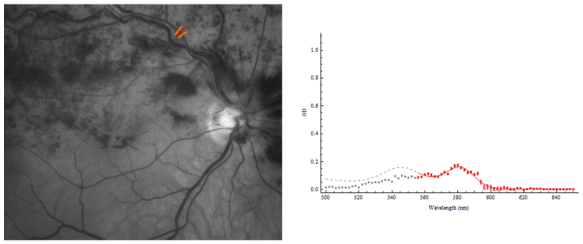	Oxygen saturation: 130.86% 95% confidence interval: 113.11% – 148.61% 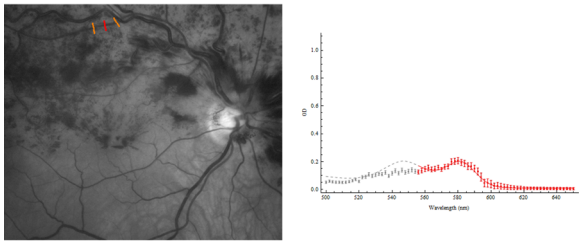
	Inferotemporal	Oxygen saturation: 72.65% 95% confidence interval: 54.97% – 90.33% 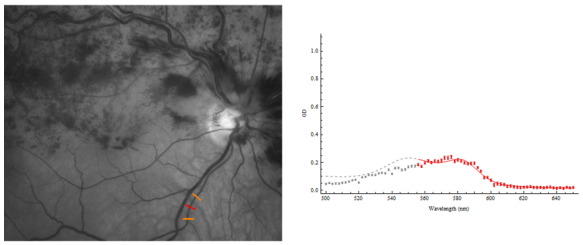	Oxygen saturation: 105.73% 95% confidence interval: 89.47% – 121.99% 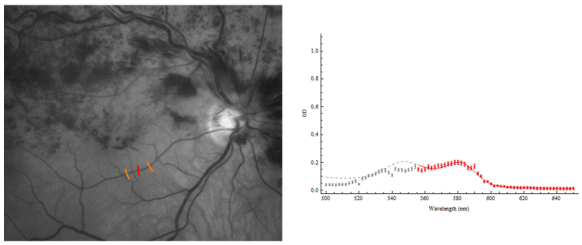
Venules	Superotemporal	Oxygen saturation: –15.72% 95% confidence interval: –33.2% – 1.76% 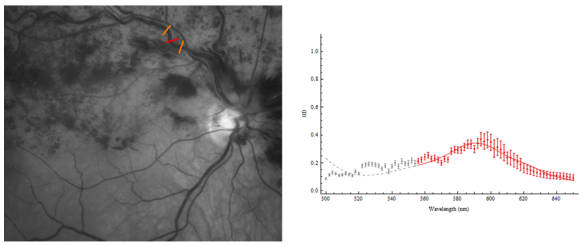	Oxygen saturation: 9.32% 95% confidence interval: –9.1% – 27.74% 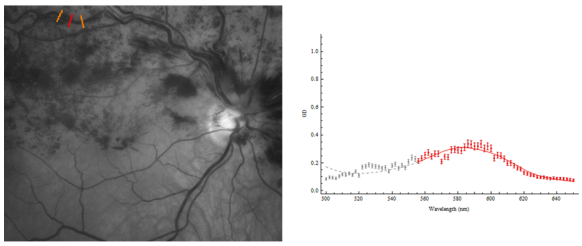
	Inferotemporal	Oxygen saturation: 37.79% 95% confidence interval: 27.91% – 47.67% 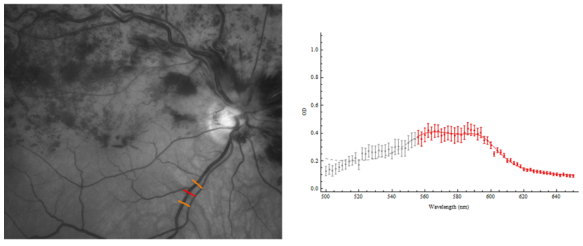	Oxygen saturation: 57.63% 95% confidence interval: 46.43% – 68.82% 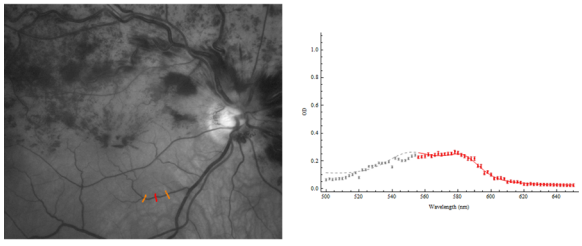

D. Oxygen saturation of the retinal vasculature

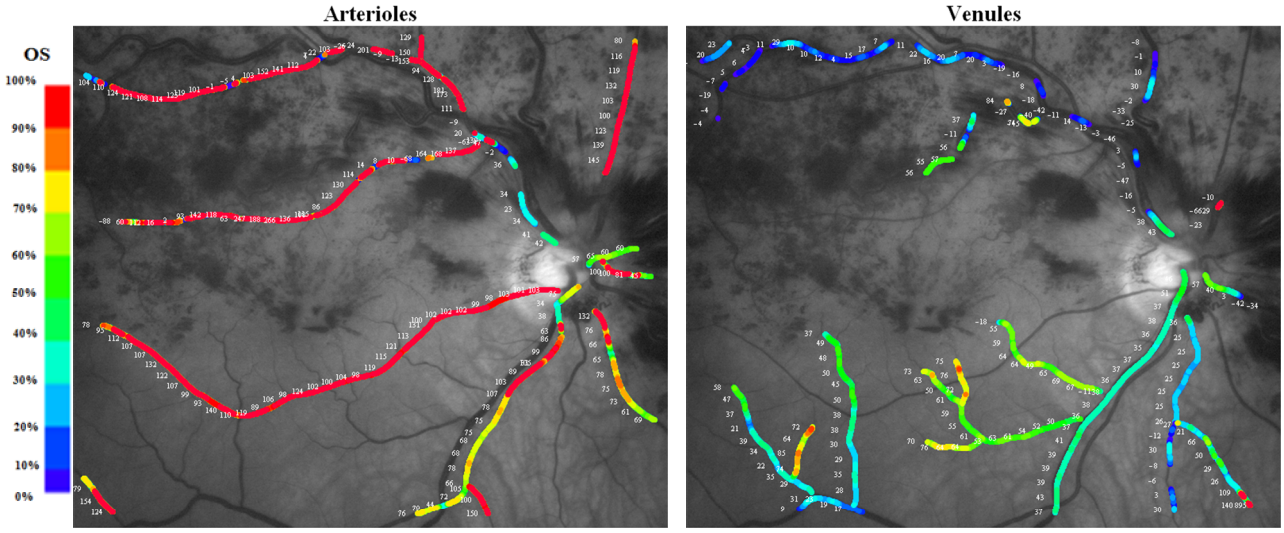

Figure A4.7: Subject V9: a 70 year old male with a 12 year history of a left non-ischaemic inferotemporal branch retinal vein occlusion (BCVA: 6/12). **A.** A colour image of the left fundus. **B.** Fluorescein angiograms of the left fundus. **C.** Dark calibrated spectral images of the left retina at 9 selected wavelengths (560, 570, 580, 590, 600, 610, 620 and 630 nm). First degree retinal arterioles and venules are indicated by *red* and *blue arrow heads* respectively. Abnormal appearances of the retinal venules relating to the OS are indicated by the *green arrow head*. The venules appear less optically dense than in normal eyes at wavelengths greater than 600 nm indicating a higher OS. **D**. The mean optical density profile (± SD; *red filled circle* and *whiskers*) of selected segments of the temporal arterioles and venules and the respective OS calculations (and 95% confidence interval). Locations of the analysis (red and orange lines) are shown in the grayscale image. Negative OS values were calculated in the inferotemporal venules. **E**. Pseudocolour oximetry maps of the retinal arterioles (*left images*) and retinal venules (*right images*). There is low venous oxygenation (< 0%) in the superotemporal venules. A colour scale of the quantitative OS values is to the left of the images.

Subject V9

A. Colour image

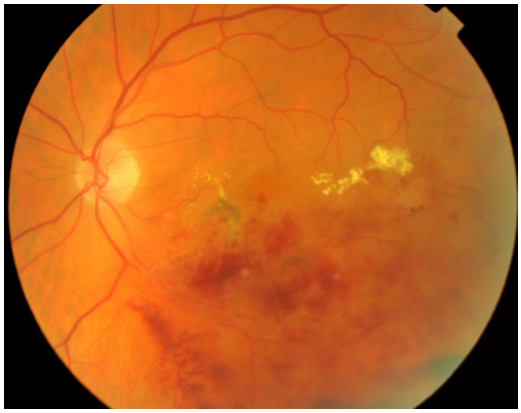

B. Fluorescein Angiogram

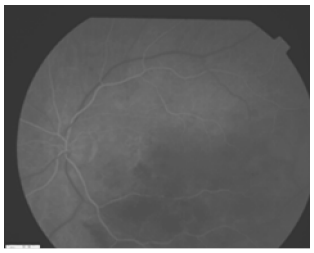

33 seconds

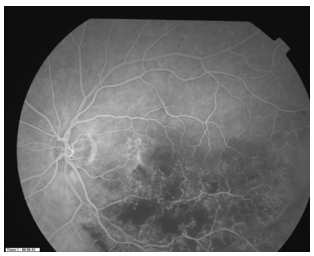

43 seconds

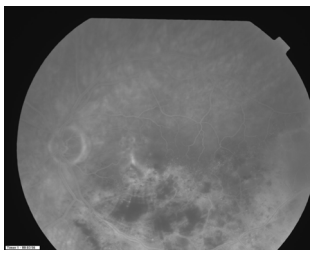

3 minutes 56 seconds

F. Observational features of the spectral images

560 nm

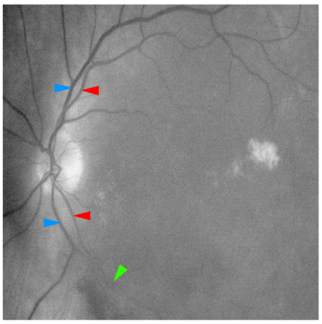

570 nm

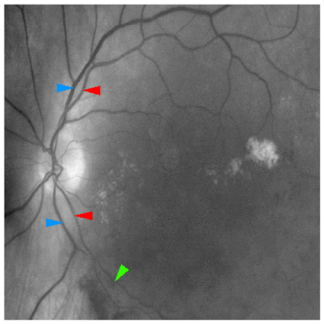

580 nm

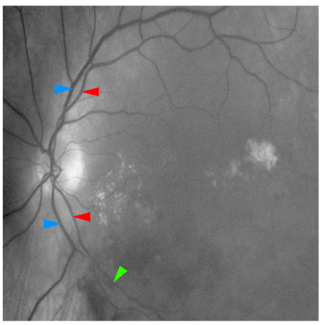

590 nm

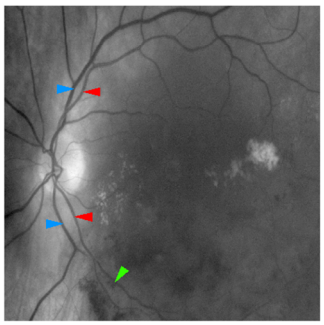

600 nm

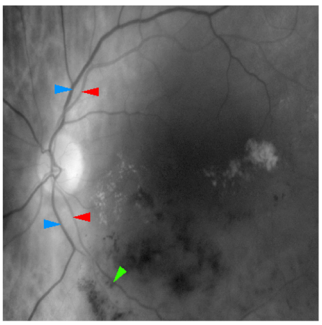

610 nm

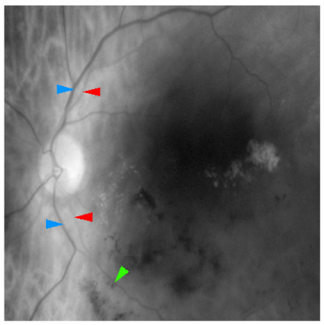

620 nm

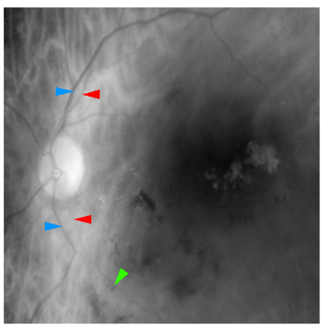

630 nm

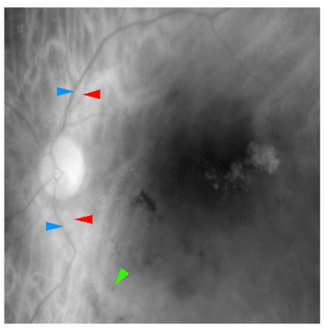

D. Mean optical density profile and oxygen saturation of selected segments of the retinal blood vessels

Location		1st degree vessels	Other vessel segments and macular branches
Arterioles	Superotemporal	Oxygen saturation: 128.04% 95% confidence interval: 99.09% – 157.% 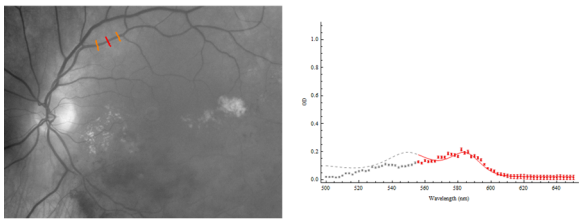	Oxygen saturation: 176.69% 95% confidence interval: 130.07% – 223.3% 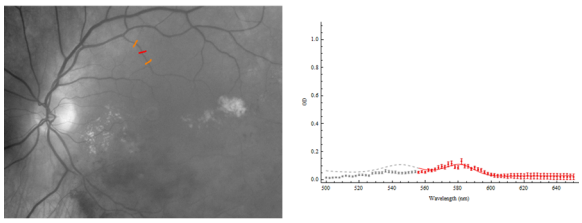
	Inferotemporal	Oxygen saturation: 108.64% 95% confidence interval: 81.66% – 135.62% 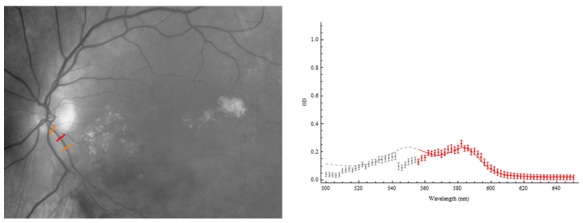	
Venules	Superotemporal	Oxygen saturation: 39.12% 95% confidence interval: 23.04% – 55.19% 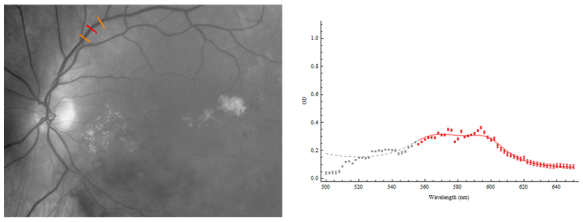	Oxygen saturation: 0.1% 95% confidence interval: –18.53% – 18.74% 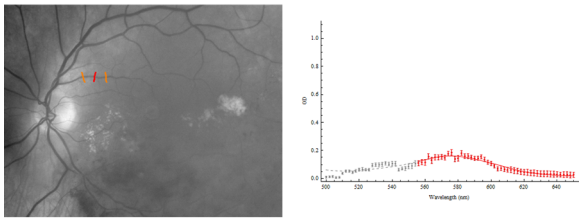
	Inferotemporal	Oxygen saturation: –5.29% 95% confidence interval: –20.6% – 10.02% 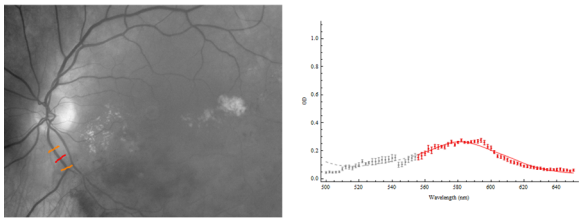	Oxygen saturation: –42.23% 95% confidence interval: –66.92% – –17.54% 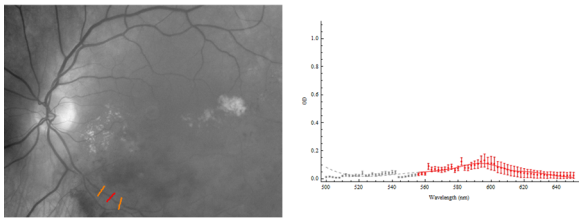

E. Oxygen saturation of the retinal vasculature

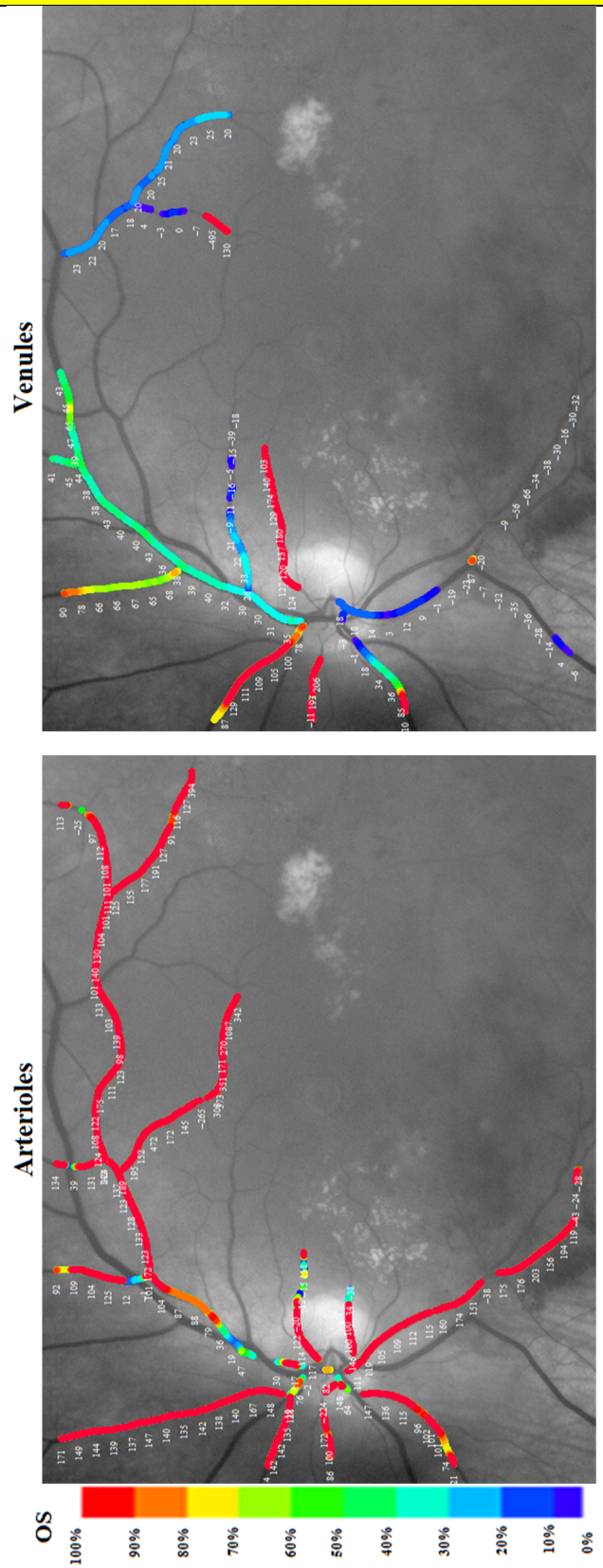

Figure A4.7: Analyses of subject V9 with spectral images acquired of the inferotemporal retina (non-ischaemic inferotemporal branch retinal vein occlusion). **A.** Dark calibrated spectral images of the left retina at 9 selected wavelengths (560, 570, 580, 590, 600, 610, 620 and 630 nm). First degree retinal arterioles and venules are indicated by *red* and *blue arrow heads* respectively. Abnormal appearances of the retinal venules related to the OS are indicated by the *green arrow head*. The venules appear less optically dense than in normal eyes at wavelengths greater than 600 nm indicating a higher OS. **B.** The mean optical density profile (± SD; *red filled circle* and *whiskers*) of selected segments of the temporal arterioles and venules and the respective OS calculations (and 95% confidence interval). Locations of the analysis (red and orange lines) are shown in the grayscale image. Negative OS values were calculated in the inferotemporal venules. **C.** Pseudocolour images of the oxygen saturation calculations overlayed onto the retinal arterioles (*left images*) and retinal venules (*right images*).

Subject V9 – inferotemporal field of view

A. Observational features of the spectral images

560 nm

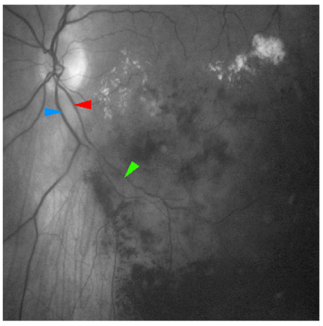

570 nm

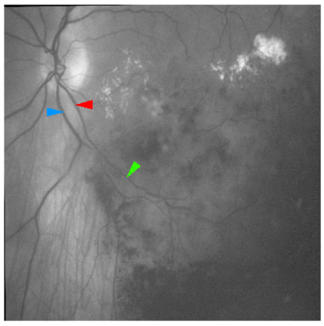

580 nm

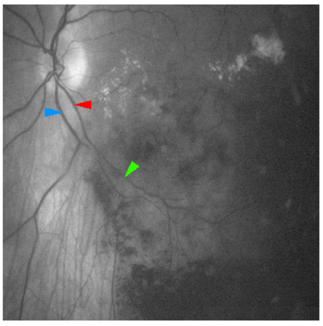

590 nm

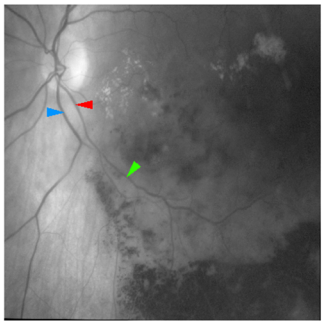

600 nm

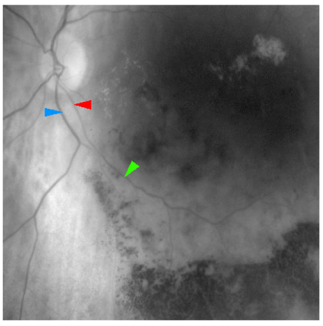

610 nm

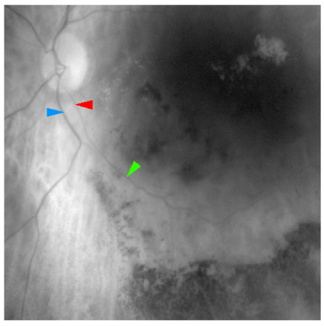

620 nm

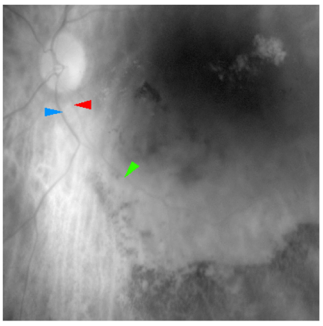

630 nm

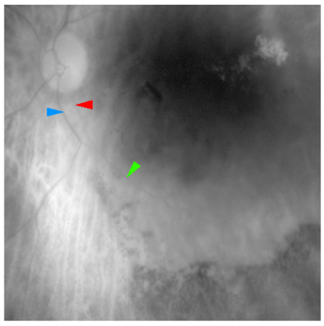

B. Mean optical density profile and oxygen saturation of selected segments of the retinal blood vessels

Location		1st degree vessels	Other vessel segments and macular branches
Arterioles	Inferotemporal	Oxygen saturation: 96.86% 95% confidence interval: 69.67% – 124.04% 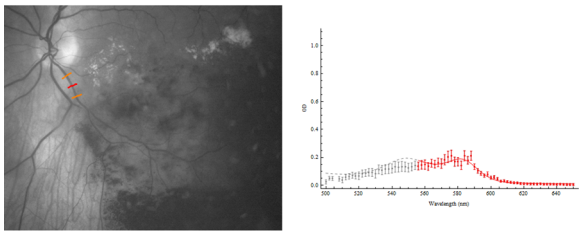	
Venules	Inferotemporal	Oxygen saturation: 16.98% 95% confidence interval: 2.99% – 30.97% 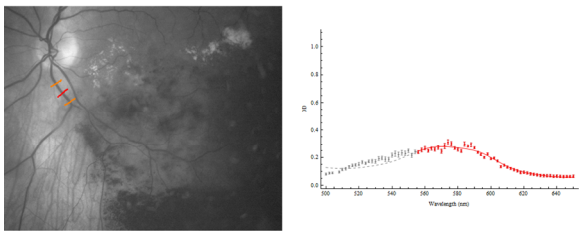	Oxygen saturation: −7.2% 95% confidence interval: −29.32% – 14.93% 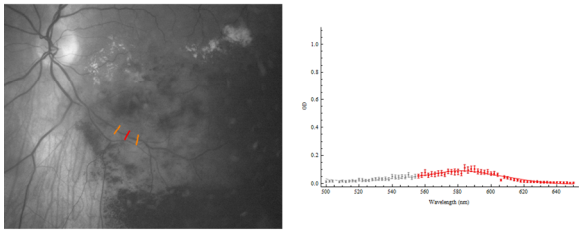 Oxygen saturation: 16.47% 95% confidence interval: 2.09% – 30.84% 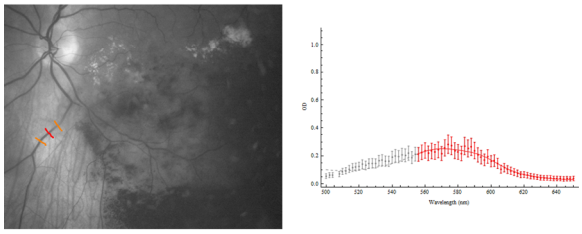

C. Oxygen saturation of the retinal vasculature

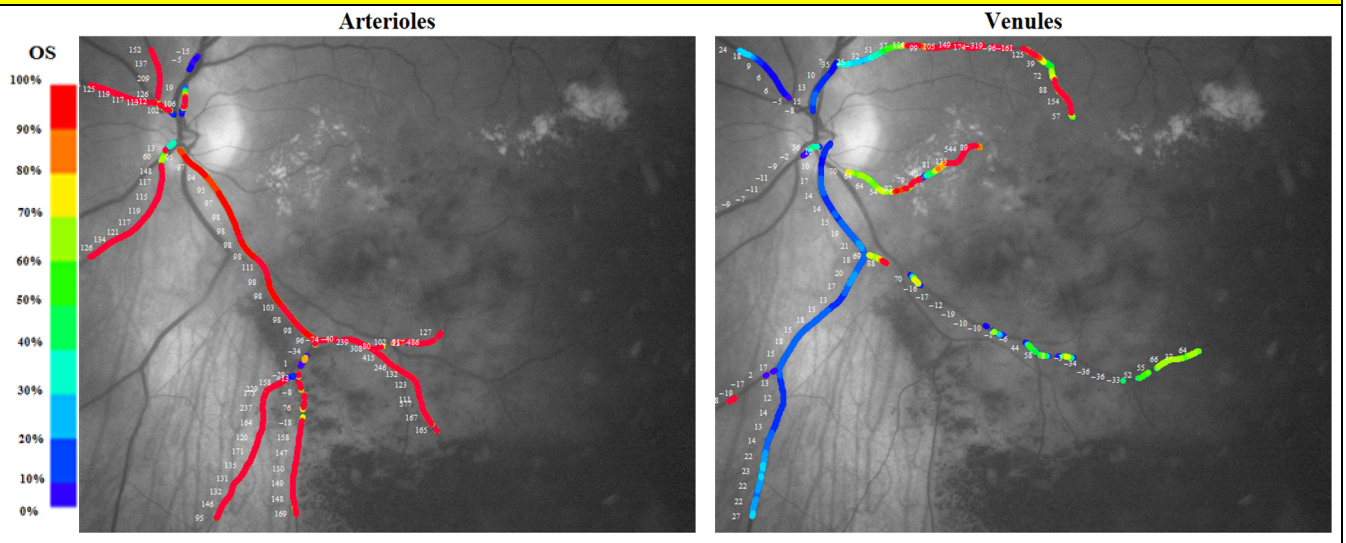

Appendix 7: Oximetry Results in Primary Open Angle Glaucoma.

Figure A5.1: Colour images, Humphrey visual field analyses and pseudocolour quantitative oxygen saturation calculations of the retinal vasculature in patients with asymmetrical POAG.

Subject G5

82 year old male			Right eye	Left eye
BCVA (LogMAR)			0.24	0.24
IOP (mm Hg)			15	15
Colour image			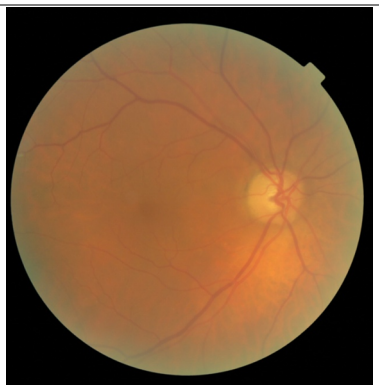	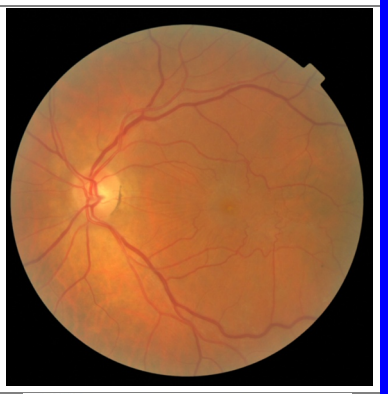
Visual field			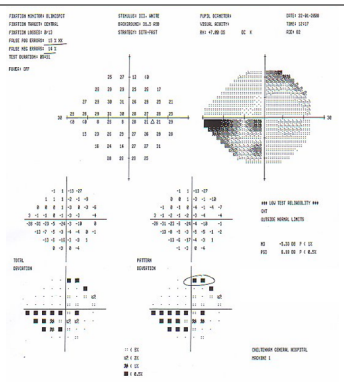	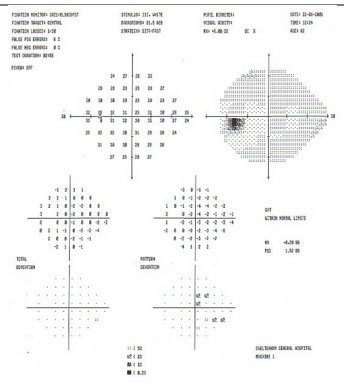
Visual field indices	Reliability	FL	0/13	1/10
		FP	15%	6%
		FN	14%	0%
	Global	MD	-5.33 dB	-0.20 dB
		PSD	8.18 dB	1.52 dB
	GHT		Outside normal limits	Within normal limits
Quantitative oximetry maps: arterioles			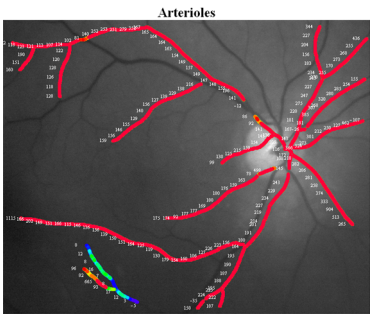	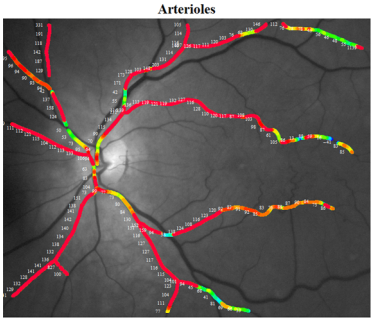
Quantitative oximetry maps: venules			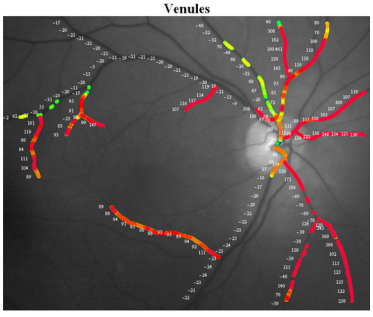	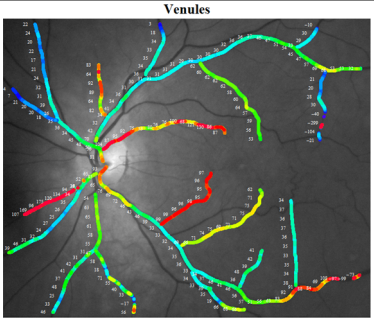

Subject G6

54 year old male			Right eye	Left eye
BCVA (LogMAR)			0.20	0.20
IOP (mm Hg)			17	15
Colour image				
Visual field			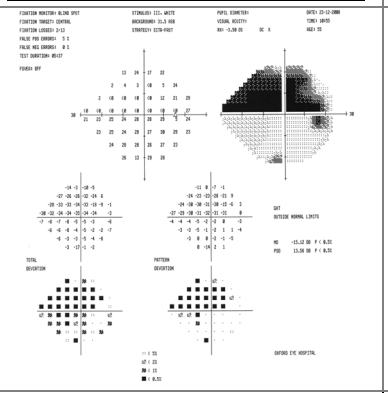	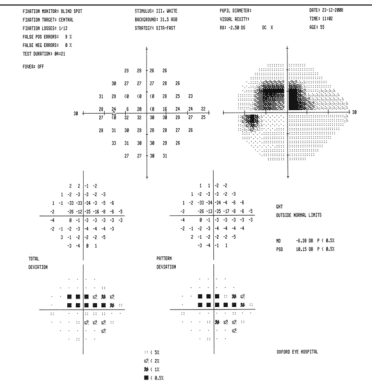
Visual field indices	Reliability	FL	2/13	1/13
		FP	5%	9%
		FN	0%	0%
	Global	MD	-15.12 dB	-6.38 dB
		PSD	13.56 dB	10.15 dB
	GHT		Outside normal limits	Outside normal limits
Quantitative oximetry maps: arterioles	OS		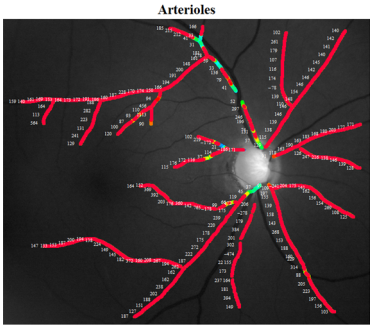	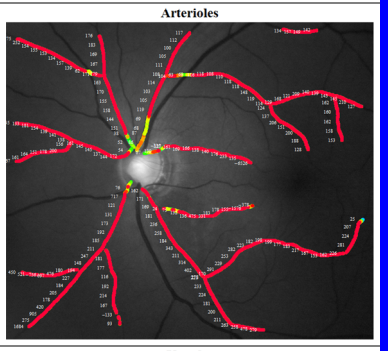
Quantitative oximetry maps: venules			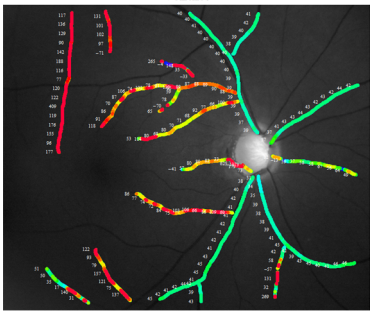	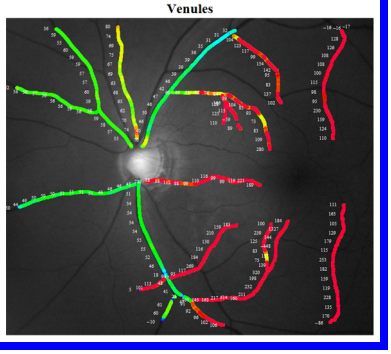

Subject G7

65 year old male			Right eye	Left eye
BCVA (LogMAR)			0.00	0.00
IOP (mm Hg)			22	22
Colour image			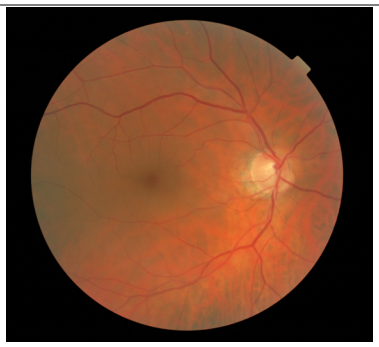	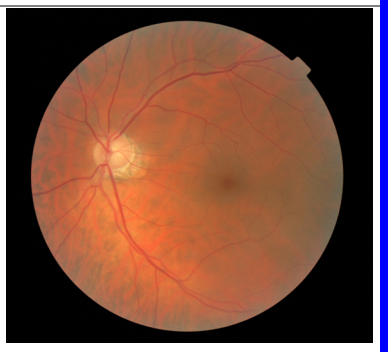
Visual field			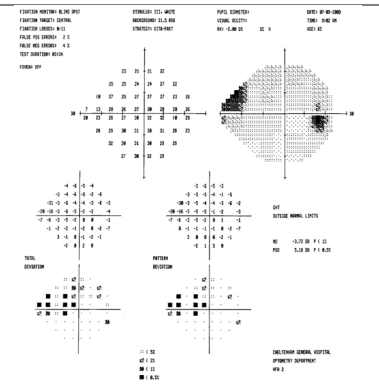	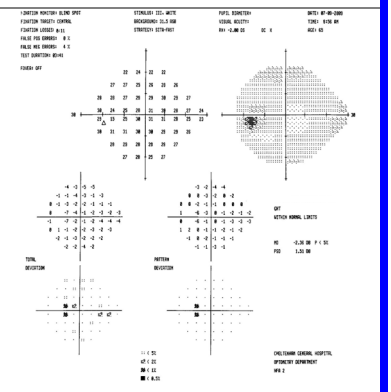
Visual field indices	Reliability	FL	0/11	0/11
		FP	2%	0%
		FN	4%	4%
	Global	MD	-3.72 dB	-2.36 dB
		PSD	5.18 dB	1.51 dB
	GHT		Outside normal limits	Within normal limits
Quantitative oximetry maps: arterioles	OS		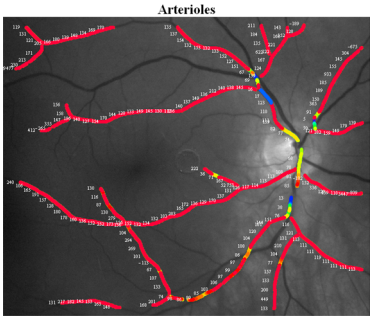	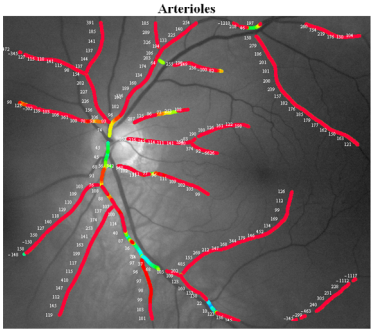
Quantitative oximetry maps: venules			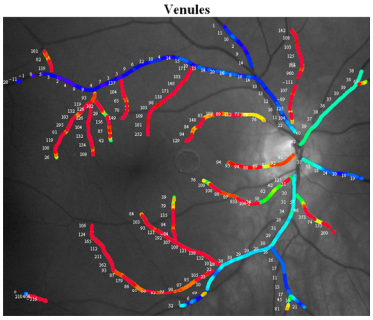	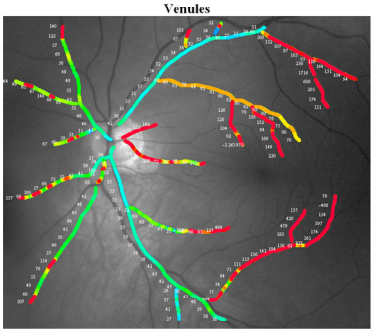

Subject G8

37 year old male			Right eye	Left eye
BCVA (LogMAR)			0.26	0.18
IOP (mm Hg)			14	14
Spectral image (580 nm) (Colour image not available)				
Visual field			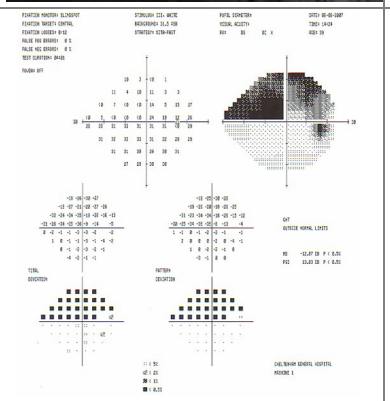	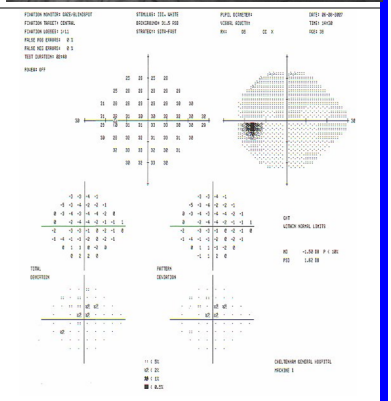
Visual field indices	Reliability	FL	0/12	0/11
		FP	0%	0%
		FN	0%	0%
	Global	MD	-12.87 dB	-1.50 dB
		PSD	13.83 dB	1.62 dB
	GHT		Outside normal limits	Within normal limits
Quantitative oximetry maps: arterioles	OS 100% 90% 80% 70% 60% 50% 40% 30% 20% 10% 0%		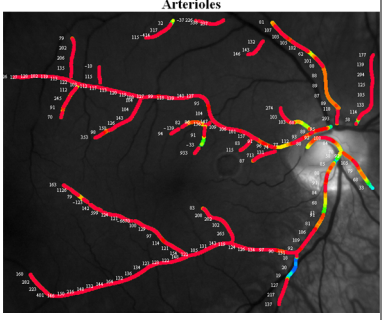	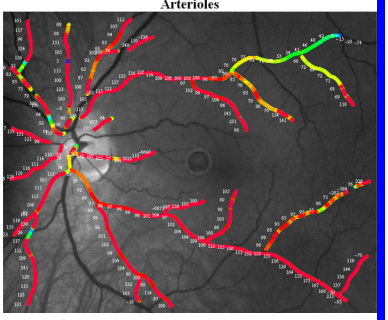
Quantitative oximetry maps: venules			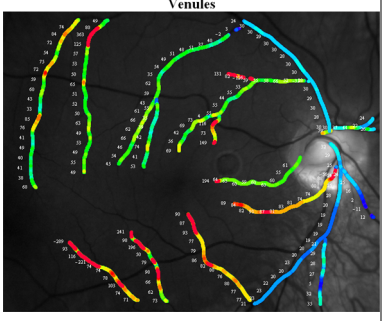	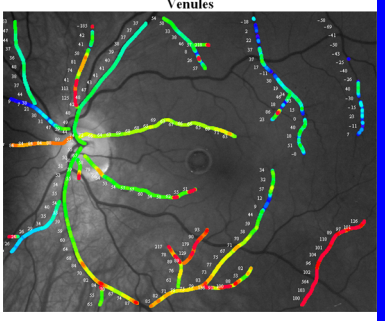

Subject G9

64 year old female			Right eye	Left eye
BCVA (LogMAR)			-0.06	-0.06
IOP (mm Hg)			18	18
Colour image			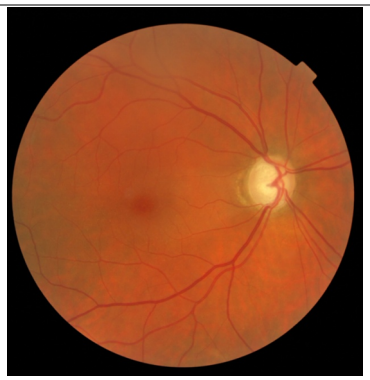	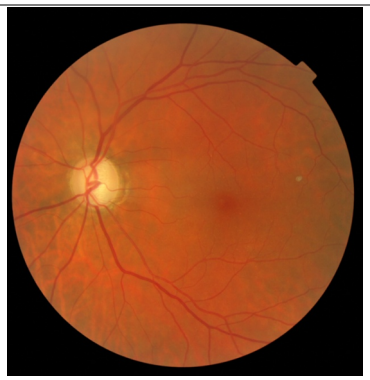
Visual field			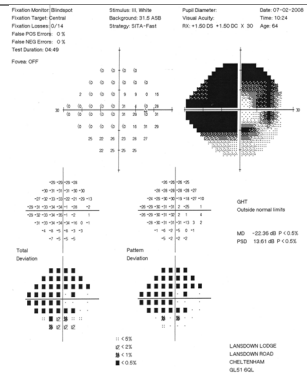	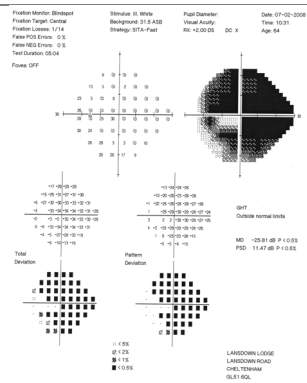
Visual field indices	Reliability	FL	0/14	1/14
		FP	0%	0%
		FN	0%	0%
	Global	MD	-22.36 dB	-25.81 dB
		PSD	13.61 dB	11.47 dB
	GHT		Outside normal limits	Outside normal limits
Quantitative oximetry maps: arterioles			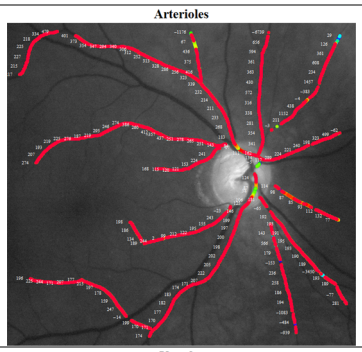	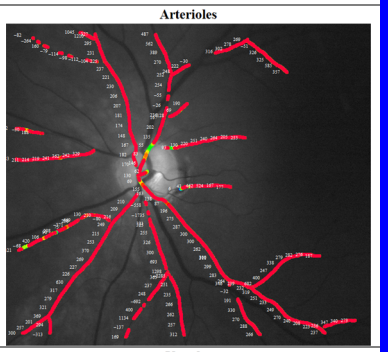
Quantitative oximetry maps: venules			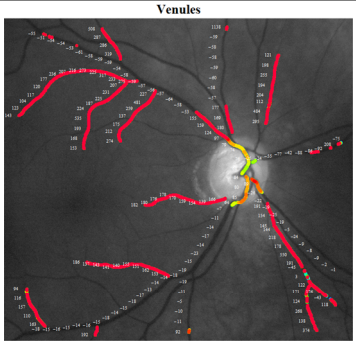	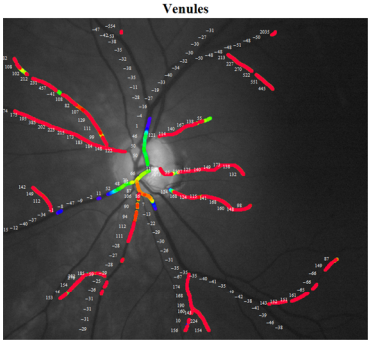

Subject G10

48 year old male			Right eye	Left eye
BCVA (LogMAR)			0.20	0.16
IOP (mm Hg)			14	49
Colour image				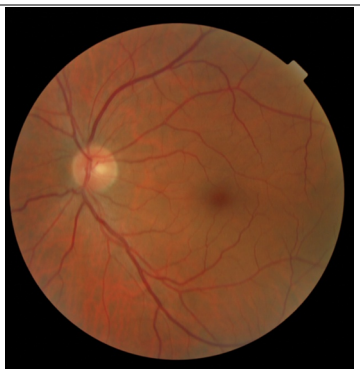
Visual field			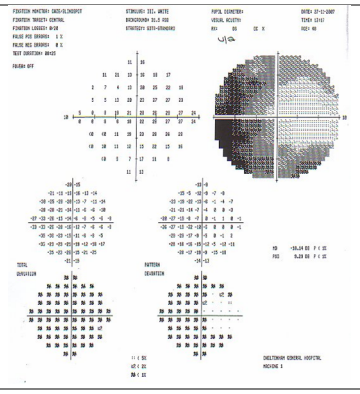	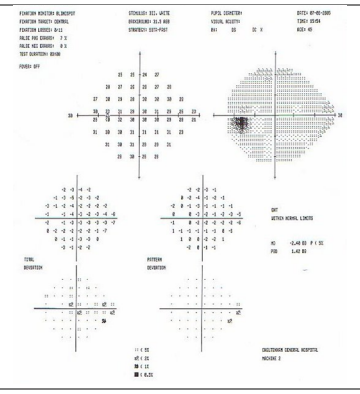
Visual field indices	Reliability	FL	0/20	0/11
		FP	1%	7%
		FN	0%	0%
	Global	MD	-18.14 dB	-2.40 dB
		PSD	9.29 dB	1.42 dB
	GHT		Outside normal limits	Within normal limits
Quantitative oximetry maps: arterioles	OS 100% 90% 80% 70% 60% 50% 40% 30% 20% 10% 0%		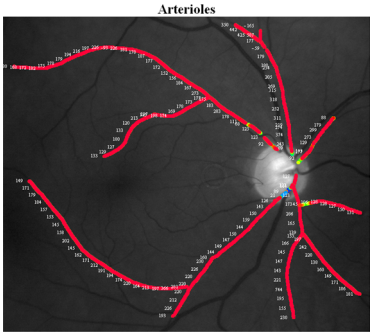	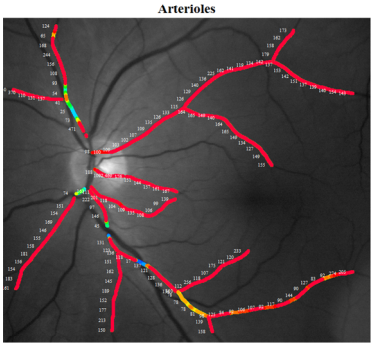
Quantitative oximetry maps: venules			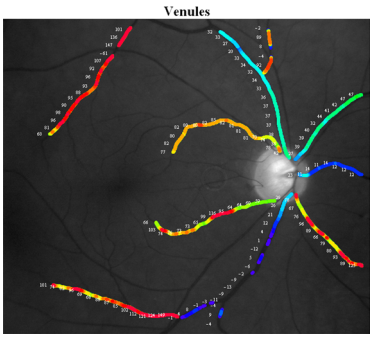	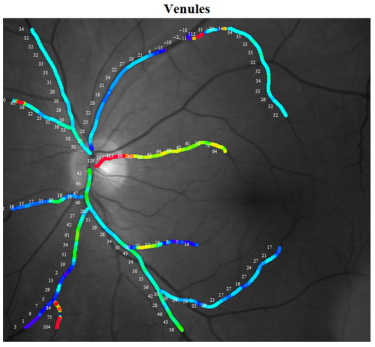

Subject G11

65 year old male			Right eye	Left eye
BCVA (LogMAR)			0.20	0.22
IOP (mm Hg)			11	10
Colour image				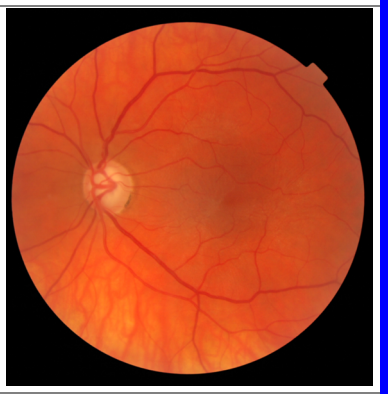
Visual field			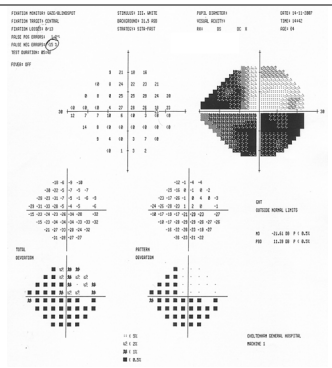	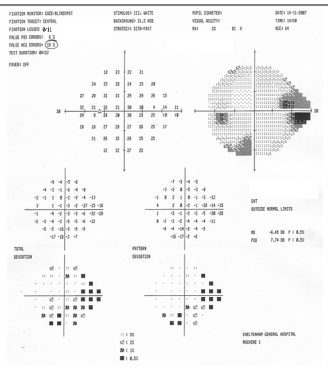
Visual field indices	Reliability	FL	0/13	0/11
		FP	15%	6%
		FN	1%	19%
	Global	MD	-21.61 dB	-6.45 dB
		PSD	11.39 dB	7.74 dB
	GHT		Outside normal limits	Outside normal limits
Quantitative oximetry maps: arterioles			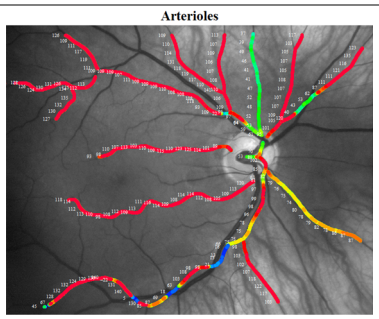	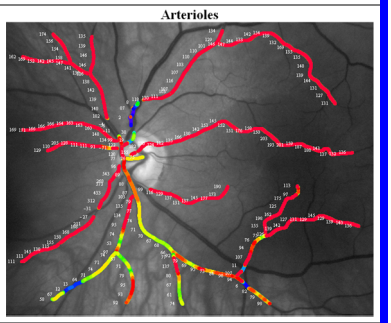
Quantitative oximetry maps: venules			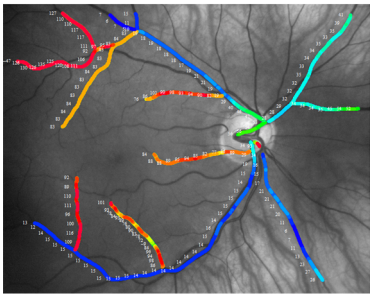	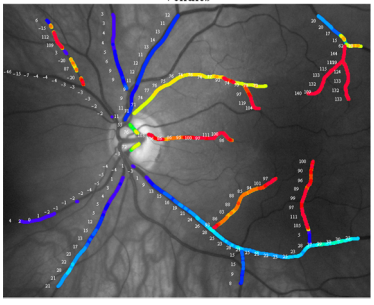

Appendix 8: Peer Reviewed Publications Originating from this Thesis